Pediatric Oncology
Series Editors: Gregory H. Reaman · Franklin O. Smith

Stephan D. Voss
Kieran McHugh *Editors*

Imaging in Pediatric Oncology

Springer

Pediatric Oncology

More information about this series at http://www.springer.com/series/5421

Stephan D. Voss • Kieran McHugh
Editors

Imaging in Pediatric Oncology

Springer

Editors
Stephan D. Voss
Boston Children's Hospital
Harvard Medical School
Boston, MA
USA

Kieran McHugh
Department of Radiology
Great Ormond Street Hospital for Children
London, UK

ISSN 1613-5318 ISSN 2191-0812 (electronic)
Pediatric Oncology
ISBN 978-3-030-03776-5 ISBN 978-3-030-03777-2 (eBook)
https://doi.org/10.1007/978-3-030-03777-2

Library of Congress Control Number: 2019930552

Preface

When the Series Editors for the Springer Verlag Pediatric Oncology Series first approached us to consider developing a comprehensive text focused on Imaging in Pediatric Oncology, we were enthusiastic. Not since 1992, when Cohen published his text *Imaging of Children with Cancer*, has there been a textbook dedicated to pediatric oncologic imaging. To be sure, there have been numerous clinical pediatric oncology texts with chapters devoted to imaging, as well as a variety of pediatric imaging textbooks with chapters or sections describing the imaging features of particular tumor types, in addition to textbooks focusing on radiology/pathology correlation in pediatric oncology. But a comprehensive reference text that could serve both pediatric oncologists and pediatric radiologists, and that focused primarily on the imaging techniques used in caring for children with cancer, was lacking.

In approaching this project we had two major considerations: firstly, this text was not simply to be focused on providing detailed discussions of the role of imaging and the imaging characteristics for each individual cancer observed in the pediatric age group—while of interest, there are ample other reference materials devoted to these topics. Rather we chose to focus on the imaging techniques available and currently in use, including guidelines for response assessment, use of functional imaging techniques and molecular imaging, as well as newer developments within the field of radiology. Secondly, in an effort to appeal to a broad readership and to provide a balanced perspective, we were encouraged to invite colleagues from both North America and Europe to serve as chapter coauthors, taking advantage of the insights and expertise of pediatric imaging experts active in multiple international consortia, such as the Children's Oncology Group (COG) and the International Society of Pediatric Oncology (SIOP).

The result has been better than we could have anticipated. We were thrilled by the willingness of so many of our colleagues from institutions around the world to contribute their knowledge and expertise in putting together the various chapters contained in this text. In many cases chapters were written together by colleagues from both the USA and Europe, and that is a testament to the close working relationships that have developed among pediatric radiologists with a major interest in oncology. The result is a series of contributions that span the breadth of pediatric radiology as it relates to the imaging of children with cancer. All of the authors are well-known leaders in their respective fields, and most also contribute their imaging expertise and knowledge by being active in ongoing clinical trials. By inviting input from both

North American and European institutions, we feel we have been able to provide a varied perspective on the different approaches to imaging, particularly as it is used in the context of both North American and European clinical trials. In another edition we will endeavor to make this effort an even more global phenomenon with contributions from Australasia and hopefully elsewhere also.

The text initially focuses on technical aspects of pediatric oncologic imaging, and then moves into how the multiple imaging techniques are applied to specific challenges inherent to the imaging of children being treated for cancer, such as assessing response to therapy and treatment-associated complications. Chapters focused on radiation safety considerations and on radiotherapy are necessary in any text such as this, as are the sections related to interventional techniques. We conclude with chapters focusing on emerging techniques (molecular imaging) as well as on the use of imaging to guide new clinical management paradigms, such as for screening patients with a cancer predisposition syndrome, and considerations related to survivorship and imaging surveillance.

Understandably, some topics could not be specifically addressed in this text. For example, the topics of quality of life, ethical considerations, global disparities, and communication with patients are all worthy topics, but beyond the scope of this text. There is no doubt that differences in healthcare economics between countries can and do influence how imaging is utilized and which techniques are deployed in the management of children with cancer. For example, whole body MRI is not currently reimbursed in the USA as there is presently no CPT billing code. As such many institutions must either forgo these exams or develop creative strategies for reimbursement. In most Canadian and European centers, in contrast, whole body MRI is reimbursed as with other examinations and there are no barriers to performing the studies in the majority of patients.

We hope you will agree that a book such as this is long overdue and that you find it to be a valuable reference and resource for imaging and imaging-based therapy used in the care of children with cancer.

Boston, MA, USA — Stephan D. Voss
London, UK — Kieran McHugh

Contents

Imaging in Pediatric Oncology: New Advances and Techniques

1

Daniel A. Morgenstern, Carlos Rodriguez-Galindo, and Mark N. Gaze

1.1 Introduction

The discovery of X-rays by Wilhelm Röntgen in 1895 was translated with remarkable speed into routine clinical practice. Less than 1 year later, the world's first radiology department was established at the Glasgow Royal Infirmary. One of the earliest images was of a foreign body lodged in the esophagus of a 6-month-old boy, and thus pediatric radiology was born [1, 2]. Since that time there has been astonishing progress in imaging technology, including the development of medical ultrasound in the 1950s and computerized tomography (CT), magnetic resonance imaging (MRI), and positron emission tomography (PET) from the 1970s to the 1990s. Over time, technological advances coupled with clinical research have led to an expanding array of more sophisticated and sometimes more costly imaging investigations. These include the use of various types of contrast, additional functional MRI sequences such as diffusion weighting and arterial spin labeling, a wider choice of molecular imaging tracers, and image fusion with hybrid imaging platforms bringing together single photon emission computed tomography (SPECT) and PET with CT and MRI. This bewildering range of imaging options brings with it a requirement to choose wisely, to get the most clinically important information from the smallest number of scans.

Radiologists have emerged from an initial role, focused on the technical aspects of obtaining images and their interpretation, to become a vital part of the multidisciplinary team caring for pediatric oncology patients. Imaging is now central to the management of patients with a variety of CNS and non-CNS solid tumors, including for initial diagnosis, staging and risk stratification, treatment response assessment, surgical and radiotherapy planning, and surveillance both after completion of therapy and in patients with cancer predisposition syndromes. In addition, children with all types of cancer are at risk of infective and other treatment-related complications for which radiological investigations are required. The new subspecialty of pediatric interventional radiology is essential to modern pediatric oncology, its practitioners undertaking a range of image-guided minimally invasive techniques

D. A. Morgenstern (✉)
Division of Haematology/Oncology, Hospital for Sick Children, Toronto, ON, Canada
e-mail: daniel.morgenstern@sickkids.ca

C. Rodriguez-Galindo
Department of Global Pediatric Medicine, St Jude Children's Research Hospital, Memphis, TN, USA
e-mail: carlos.rodriguez-galindo@stjude.org

M. N. Gaze
University College London Hospitals NHS Foundation Trust, London, UK

Great Ormond Street Hospitals for Children NHS Foundation Trust, London, UK
e-mail: mgaze@nhs.net; mark.gaze@uclh.nhs.uk

S. D. Voss, K. McHugh (eds.), *Imaging in Pediatric Oncology*, Pediatric Oncology,
https://doi.org/10.1007/978-3-030-03777-2_1

including core biopsies, central venous catheter placement, fluid drainage, stent placement, arteriography and tumor embolization, and lesion ablation.

Cancer in children is comparatively rare, representing only 1% of all cancer diagnoses, yet the burden of disease is significant, and in North America and Western Europe, cancer remains the leading cause of childhood death by disease occurring after infancy. While breast, prostate, lung, and gastrointestinal carcinomas represent the most common diagnoses in adults, the pattern of disease in children is radically different. Acute lymphoblastic leukemia (26%), brain tumors (21%), neuroblastoma (7%), and non-Hodgkin lymphoma (6%) represent the most common diagnoses in patients aged 0–14 years, with Hodgkin lymphoma (15%), thyroid carcinoma (11%), brain tumors (10%), testicular germ cell tumors (8%), and bone cancers (including osteosarcoma and Ewing sarcoma) most common in the 15–19-year-old adolescent population [3]. Most well-recognized pediatric embryonal tumors such as neuroblastoma, Wilms tumor (nephroblastoma), hepatoblastoma, and retinoblastoma rarely occur in adults. Thus, the varying spectrum of disease across the pediatric age group and in adolescents and young adults is very different from that in older adults, and an understanding of these changing disease patterns within childhood and adolescence is crucial to interpretation of imaging (see Fig. 1.1).

There has been remarkable progress in improving the outcomes for patients with childhood cancer, resulting from various factors, not least of which has been the development of better imaging for diagnosis, risk stratification, treatment planning, response assessment, and surveillance. In addition, the implementation of multi-agent chemotherapy regimens, and more

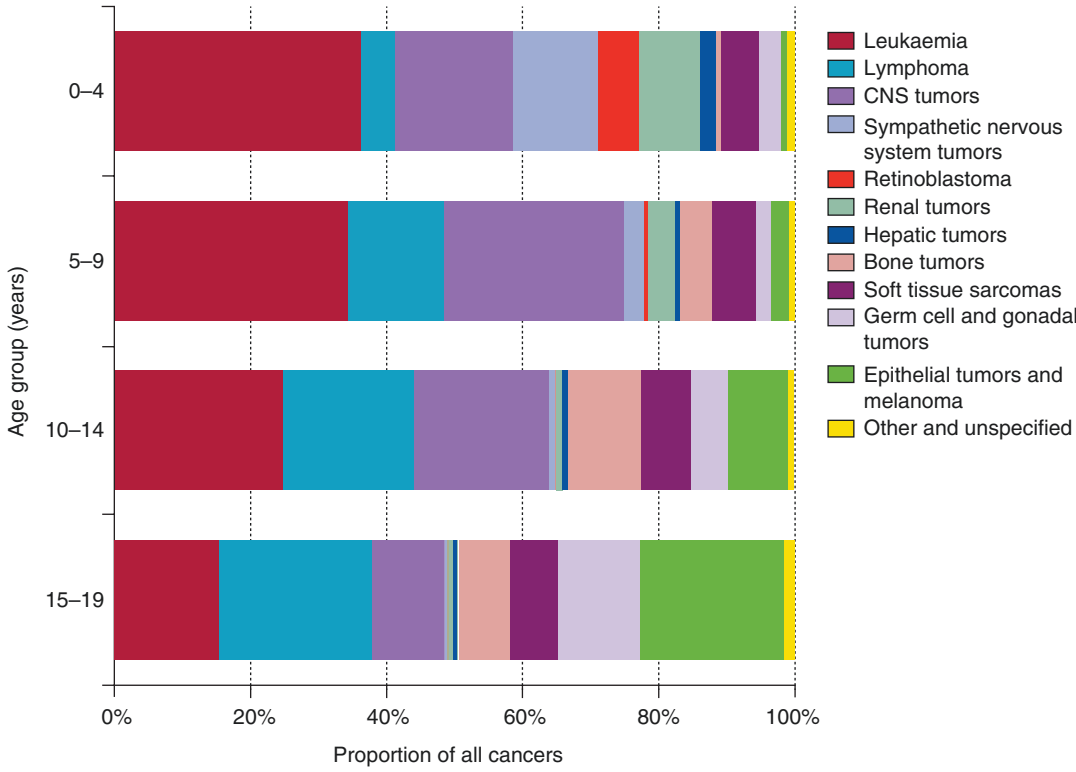

Fig. 1.1 Distribution of cancer types by age group. Summary from multiple international pediatric and general cancer datasets showing the dramatic changes in proportions of different cancer diagnoses depending on age. From [5] with permission

refined use of the local treatment modalities of surgery and radiotherapy, coupled with a strong ethos of clinical research built on national and international collaborations has been transformative. Overall childhood cancer mortality rates have more than halved in the period 1975–2006 from 5.14 to 2.48 per 100,000 [4]. Currently the combined 5-year overall survival (OS) rate is around 80%, although this single figure masks a wide range of outcomes, depending on the underlying diagnosis (see Fig. 1.2). For acute lymphoblastic leukemia (ALL), 5-year OS is nearly 90%, while for non-infant neuroblastoma (>12 months of age), 5-year OS is 65% [4]; for diagnoses such as diffuse intrinsic pontine glioma (DIPG), outcomes remain dire with 5-year OS less than 1%. Overall childhood cancer incidences have been slowly increasing since 1975 (for reasons that are not entirely clear), with a current incidence rate around 170 per 100,000 in North America and Western Europe. However, there is incomplete knowledge on the incidence and epidemiology of childhood cancer globally since large proportions of the world's population are not covered by cancer registries; this is particularly true in the areas of the world where predictions indicate that the cancer burden is growing with the fastest rates, such as in Asia and Africa. Existing data suggest noticeable differences in incidence and patterns of disease by ethnicity, race, and geography [5]. In the United States, it is estimated that 1 in 408 children will be diagnosed with cancer before the age of 15 and 1 in 285 before the age of 20 years [3].

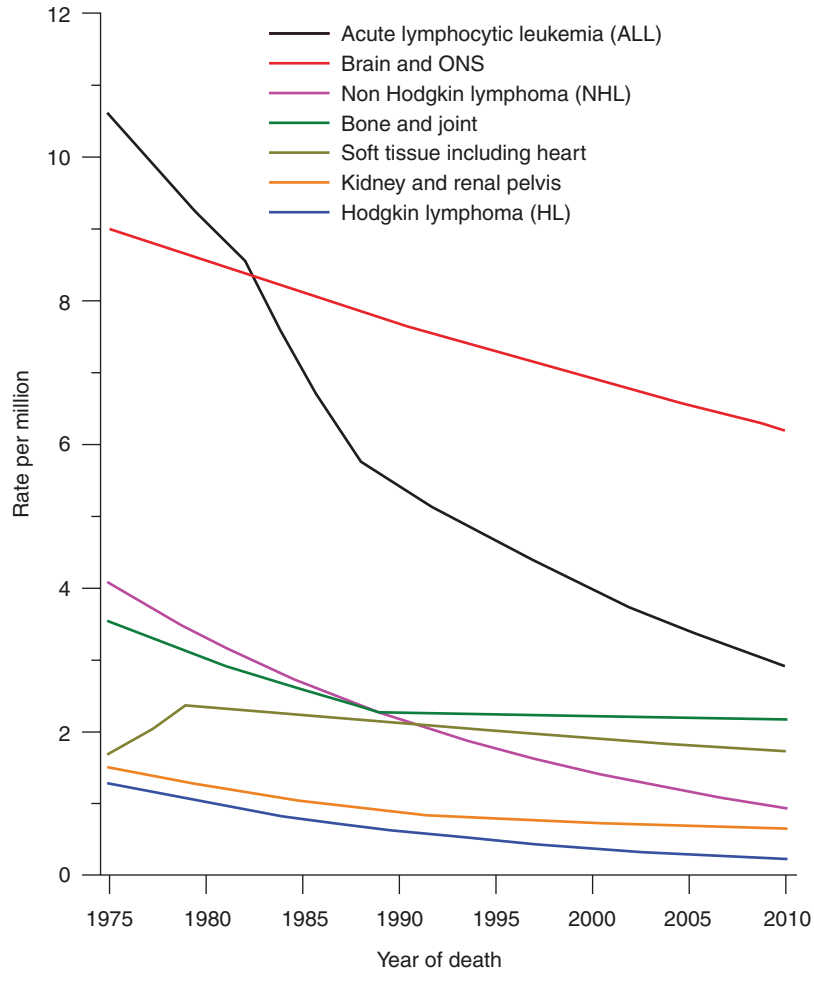

Fig. 1.2 Trends in pediatric cancer mortality rates by site. Data showing changes in pediatric cancer mortality in the United States obtained from National Center for Health Statistics, Centers for Disease Control and Prevention. ONS indicates other nervous system. Overall mortality rates have declined dramatically since 1975, particularly for ALL but also across the range of most solid tumors. From [3] with permission

Improved survival rates have also led to a growing number of adult survivors of childhood cancer, many of whom will be at risk of significant late effects as a result of their original oncology treatment, prompting new considerations related to off-treatment surveillance, both for detecting late relapses and the late effects resulting from the original therapies.

Most children with cancer will initially present to a primary care doctor or general practitioner or to a local hospital emergency department and be referred to a general pediatrician for further investigation. Patients in secondary care settings with suspected or confirmed malignancies will then be referred on to an appropriate regional specialist tertiary center. Those with brain tumors will normally be managed initially by a pediatric neurosurgical service, while those with extracranial solid tumors or leukemia/lymphoma will be referred directly to a pediatric oncology center. Different pathways may exist for adolescents and younger adults suspected to have cancer compared with those for younger children, depending on the local structure of health services. Once at a pediatric oncology center, the care of patients with proven or suspected cancer is usually coordinated by a site-specialized pediatric or adolescent oncologist or hematologist working together with members of a diagnostic and therapeutic multidisciplinary team (MDT). As subsequent care, including imaging, may be shared between the tertiary principal treatment center and local secondary services at the pediatric oncology shared care unit, it is good practice for there to be close communication between radiologists and clinicians regarding any radiological investigations requested closer to home, established protocols for the secure transfer of imaging studies between institutions, and taking steps to ensure that the optimal imaging examinations are performed in order to avoid the need for suboptimal investigations to be repeated.

Initial management is focused on stabilizing the patient, obtaining a diagnosis, and defining risk factors which will guide treatment options. The choice of imaging technique is dependent on the history and clinical examination indicating the body part affected. For suspected brain tumors, contrast-enhanced MRI of the whole central nervous system (CNS) with functional sequences including diffusion weighting will give the best information. For neck, abdominal, pelvic, chest wall, and extremity lesions, ultrasound may be a very useful first step, followed by either CT or MRI. Intrathoracic lesions may be better demonstrated by chest X-ray and CT. These cross-sectional imaging techniques will contribute to determining disease burden and delineate the primary tumor prior to interventional radiology percutaneous (or surgical) biopsy to provide a histological diagnosis and tissue for relevant biological studies. These studies are also essential for demonstrating the presence of lymph node or distant metastatic disease and establishing disease stage. In some cases, such as diffuse intrinsic pontine glioma, retinoblastoma, or Wilms tumor, a presumptive diagnosis may be made on imaging appearances alone. In other cases, typical imaging appearances coupled with elevated blood, cerebrospinal fluid, or urinary tumor marker levels may be sufficient to diagnose, for example, hepatoblastoma, cortical or medullary adrenal tumors, and gonadal, extra-gonadal, and intracranial germ cell tumors. Biopsy may still be required to obtain tissues to complete diagnosis and facilitate risk stratification.

Part of the role of the MDT discussion is to decide on the most appropriate imaging investigations and the order in which they should be performed in individual patients. Because of the carcinogenic risk of ionizing radiation exposure [6], investigations such as ultrasound and MRI are preferred, especially in undiagnosed children who may not, in fact, have cancer. Even in those with a confirmed diagnosis, a balance has to be struck between obtaining the most useful clinical information for disease management and minimizing radiation exposure. The aim of keeping the radiation exposure as low as reasonably achievable (ALARA) can be helped by the selection of optimal technical parameters in imaging protocols, avoiding unnecessary over-investigation, and minimizing the frequency of reassessment and surveillance imaging by following evidence-based guidelines.

Staging investigations depend on an understanding of the likely (or confirmed) diagnosis and anticipated potential sites of metastatic spread. Patients with CNS malignancies typically require imaging of the entire neuraxis. Many extracranial solid tumors (such as sarcomas and Wilms tumor) metastasize preferentially to the lungs requiring CT evaluation, with many sarcomas additionally requiring ^{99m}Tc bone scintigraphy or ^{18}F-fluorodeoxyglucose (FDG) PET/CT evaluation for distant metastases. For neuroblastoma, ^{123}I-mIBG (meta-iodobenzylguanidine) scintigraphy has now largely replaced ^{99m}Tc bone scans for the evaluation of skeletal metastases [7]. This is an important element in the diagnostic process as it can define future therapeutic options with the use of ^{131}I-mIBG for relapsed or refractory disease [8]. FDG-PET/CT has now been routinely adopted for staging and response evaluation in Hodgkin lymphoma and is increasingly used for metastatic evaluation in patients with rhabdomyosarcoma, Ewing sarcoma, and other pediatric sarcomas [9].

There are considerable complexities around the details of primary tumor evaluation and staging that require a detailed knowledge of the underlying diagnosis and relevant clinical trial protocols. Improvements to the resolution of thoracic CT have led to the identification of more sub-centimeter nodules, raising difficult questions about defining lung metastases on the basis of imaging appearances alone [10]. Improving imaging resolution leading to the identification of ever smaller lesions also risks leading to stage migration (i.e., upstaging of patients in whom metastases might not previously have been identified)—the so-called Will Rogers phenomenon [11]. For many pediatric cancers, staging strategies have moved from those based on a surgical evaluation to those based on imaging alone. For neuroblastoma, for example, the International Neuroblastoma Staging System (INSS) definitions are based on tumor surgical resectability and disease involvement of nearby lymph nodes [12]. In contrast, the more recent International Neuroblastoma Risk Group (INRG) staging system focuses on imaging-defined risk factors [13]. Thus, radiological interpretation coupled with a detailed understanding of the relevant staging systems and newly developed imaging-based risk-stratification criteria is crucial to appropriate staging. Other diagnoses have disease-specific staging systems that are based on relevant anatomy and future decisions relating to surgical resectability, for example, the pretreatment extent of disease (PRETEXT) staging system for hepatoblastoma [14].

The role of imaging in pediatric oncology of course extends well beyond the initial diagnostic work-up and staging. For both CNS and extracranial solid tumor imaging, evaluation of tumor response to therapy is crucial for treatment decisions, and again a detailed understanding of relevant diagnoses and treatment protocols is important for appropriate interpretation. In the research context, response of solid tumors is often defined on the basis of the response evaluation criteria in solid tumors (RECIST) guidance [15]. However, for many pediatric cancer diagnoses, disease-specific criteria have been established, often using three-dimensional volume assessments. For example, the European Paediatric Soft Tissue Sarcoma Study Group (EpSSG) guidelines are not interchangeable with RECIST [16], whereas for neuroblastoma, a multinational analysis concluded that none of the methods of primary tumor response assessment was predictive of outcome, and therefore future tumor response assessment will be based on the RECIST guidance [17], together with semiquantitative assessment (such as Curie scoring) of MIBG-positive disease response. Similar issues arise in neuro-oncology, particularly in the evaluation of malignant embryonal tumors such as medulloblastoma that have the propensity to disseminate throughout the neuraxis, leading to the development of disease-specific response criteria [18]. The example of medulloblastoma also further highlights the critical importance of comprehensive disease evaluation and the potential role for central radiology review. The Children's Oncology Group (COG) ACNS9961 study reported significantly inferior EFS for patients with inadequate studies, compared with those with centrally reviewed adequate examinations [19]. Outcome was particularly poor for patients

in whom disseminated disease was only detected retrospectively upon central review. Nuclear medicine modalities also play an important role in response evaluation. In Hodgkin lymphoma, early response assessment based on FDG-PET predicts outcome [20], and resolution of FDG-avid lesions is now used to guide decisions about radiotherapy, while for patients with high-risk metastatic neuroblastoma, post-induction mIBG response predicts outcome [21] and is used to determine adequacy of response for the patient to progress to consolidation therapy.

Imaging also plays an important role in surveillance after the end of therapy for early detection of disease recurrence and the late effects of therapy. Clinical trials that incorporate event-free survival as a primary endpoint have detailed schedules of disease evaluation post-therapy, typically requiring cross-sectional imaging with CT/MRI every 3 months initially. These schedules have frequently been adopted for routine monitoring of patients outside the context of therapeutic trials, although the benefit of intensive surveillance in improving overall outcomes (through the early detection of relapse) has rarely been established. Growing concerns about the risks of exposure to CT-associated radiation [22], gadolinium contrast for MRI [23], and the impact on the developing brain of recurrent general anesthesia often required to facilitate imaging in young children [24] mean that the appropriateness of such imaging needs to be carefully considered.

In summary, the excellent outcomes seen today for the majority of children and young people with cancer, and hope for future improvements for those tumor types where the prognosis is less good, are based in no small part on the wide range of imaging techniques now available and the knowledge and skills of diagnostic and interventional radiologists working as part of the wider pediatric oncology MDT. The selection of the most appropriate investigations for an individual patient should be evidence-based and made in discussion with experienced pediatric radiologists. The radiologist will identify the site, extent, and nature of the primary tumor and demonstrate the presence or absence of metastases. The radiologist may biopsy the tumor for histological diagnosis and molecular pathology subtyping and may well support care by insertion of a central venous catheter and other interventions. The radiologist is an essential supporter of surgeons and clinical oncologists as they plan complex radical tumor surgery and sophisticated modern radiation treatments and provide continuing evaluation with the assessment of response to chemotherapy, surgery, and radiation therapy. Finally, the involvement of the radiologist in the follow-up of the patient after completing therapy is critical in the evaluation of local or metastatic recurrence or treatment-related complications and second tumors.

For future improvements in the care of children and young people with cancer, it is essential that pediatric radiologists are not simply fully integrated as core members of the pediatric oncology MDTs in principal treatment centers but are also involved in national and international clinical trial groups. Further research into imaging biomarkers and the best use of radiological investigations is as fundamental to the progress of pediatric oncology as randomized trials of treatment.

References

1. Sweet E. Paediatric radiology in Great Britain and Ireland. In: Kaufmann HJ, Ringertz H, Sweet E, editors. The first 30 years of the ESPR. Berlin: Springer; 1993. p. 1–2.
2. Thomas AM, Banerjee AK. The history of radiology. Oxford: Oxford University Press; 2013.
3. Ward E, DeSantis C, Robbins A, Kohler B, Jemal A. Childhood and adolescent cancer statistics, 2014. CA Cancer J Clin. 2014;64(2):83–103.
4. Smith MA, Seibel NL, Altekruse SF, Ries LAG, Melbert DL, O'Leary M, et al. Outcomes for children and adolescents with cancer: challenges for the twenty-first century. J Clin Oncol. 2010;28(15):2625–34.
5. Steliarova-Foucher E, Colombet M, Ries LAG, Moreno F, Dolya A, Bray F, et al. International incidence of childhood cancer, 2001-10: a population-based registry study. Lancet Oncol. 2017;18(6):719–31.
6. Linet MS, Kim KP, Rajaraman P. Children's exposure to diagnostic medical radiation and cancer risk: epidemiologic and dosimetric considerations. Pediatr Radiol. 2009;39(Suppl 1):S4–26.
7. Matthay KK, Shulkin B, Ladenstein R, Michon J, Giammarile F, Lewington V, et al. Criteria for evaluation of disease extent by (123)

I-metaiodobenzylguanidine scans in neuroblastoma: a report for the International Neuroblastoma Risk Group (INRG) Task Force. Br J Cancer. 2010;102(9):1319–26.
8. Wilson JS, Gains JE, Moroz V, Wheatley K, Gaze MN. A systematic review of 131I-meta iodobenzylguanidine molecular radiotherapy for neuroblastoma. Eur J Cancer. 2014;50(4):801–15.
9. Norman G, Fayter D, Lewis-Light K, Chisholm J, McHugh K, Levine D, et al. An emerging evidence base for PET-CT in the management of childhood rhabdomyosarcoma: systematic review. BMJ Open. 2015;5(1):e006030.
10. Grundy PE, Green DM, Dirks AC, Berendt AE, Breslow NE, Anderson JR, et al. Clinical significance of pulmonary nodules detected by CT and Not CXR in patients treated for favorable histology Wilms tumor on national Wilms tumor studies-4 and -5: a report from the Children's Oncology Group. Pediatr Blood Cancer. 2012;59(4):631–5.
11. Feinstein AR, Sosin DM, Wells CK. The Will Rogers phenomenon. Stage migration and new diagnostic techniques as a source of misleading statistics for survival in cancer. N Engl J Med. 1985;312(25):1604–8.
12. Brodeur GM, Pritchard J, Berthold F, Carlsen NL, Castel V, Castelberry RP, et al. Revisions of the international criteria for neuroblastoma diagnosis, staging, and response to treatment. J Clin Oncol. 1993;11(8):1466–77.
13. Monclair T, Brodeur GM, Ambros PF, Brisse HJ, Cecchetto G, Holmes K, et al. The International Neuroblastoma Risk Group (INRG) staging system: an INRG Task Force report. J Clin Oncol. 2009;27(2):298–303.
14. Roebuck DJ, Aronson D, Clapuyt P, Czauderna P, de Ville de Goyet J, Gauthier F, et al. 2005 PRETEXT: a revised staging system for primary malignant liver tumours of childhood developed by the SIOPEL group. Pediatr Radiol. 2007;37(2):123–32. quiz249–50.
15. Eisenhauer EA, Therasse P, Bogaerts J, Schwartz LH, Sargent D, Ford R, et al. New response evaluation criteria in solid tumours: revised RECIST guideline (version 1.1). Eur J Cancer. 2009;45(2):228–47.
16. Schoot RA, McHugh K, van Rijn RR, Kremer LCM, Chisholm JC, Caron HN, et al. Response assessment in pediatric rhabdomyosarcoma: can response evaluation criteria in solid tumors replace three-dimensional volume assessments? Radiology. 2013;269(3):870–8.
17. Bagatell R, McHugh K, Naranjo A, Van Ryn C, Kirby C, Brock P, et al. Assessment of primary site response in children with high-risk neuroblastoma: an international multicenter study. J Clin Oncol. 2016;34(7):740–6.
18. Warren KE, Vezina G, Poussaint TY, Warmuth-Metz M, Chamberlain MC, Packer RJ, et al. Response assessment in medulloblastoma and leptomeningeal seeding tumors: recommendations from the response assessment in pediatric neuro-oncology committee. Neuro Oncol. 2018;20:13.
19. Packer RJ, Gajjar A, Vezina G, Rorke-Adams L, Burger PC, Robertson PL, et al. Phase III study of craniospinal radiation therapy followed by adjuvant chemotherapy for newly diagnosed average-risk medulloblastoma. J Clin Oncol. 2006;24(25):4202–8.
20. Furth C, Steffen IG, Amthauer H, Ruf J, Misch D, Schönberger S, et al. Early and late therapy response assessment with [18F]fluorodeoxyglucose positron emission tomography in pediatric Hodgkin's lymphoma: analysis of a prospective multicenter trial. J Clin Oncol. 2009;27(26):4385–91.
21. Matthay KK, Edeline V, Lumbroso J, Tanguy ML, Asselain B, Zucker JM, et al. Correlation of early metastatic response by 123I-metaiodobenzylguanidine scintigraphy with overall response and event-free survival in stage IV neuroblastoma. J Clin Oncol. 2003;21(13):2486–91.
22. Owens C, Li BK, Thomas KE, Irwin MS. Surveillance imaging and radiation exposure in the detection of relapsed neuroblastoma. Pediatr Blood Cancer. 2016;63(10):1786–93.
23. Fraum TJ, Ludwig DR, Bashir MR, Fowler KJ. Gadolinium-based contrast agents: a comprehensive risk assessment. J Magn Reson Imaging. 2017;46:338.
24. Sinner B, Becke K, Engelhard K. General anaesthetics and the developing brain: an overview. Anaesthesia. 2014;69(9):1009–22.

2 Imaging in Paediatric Oncology: Pitfalls, Acceptable and Unacceptable Imaging

Joy Barber and Kieran McHugh

2.1 Introduction

Cancer in the paediatric age group is rare and in most countries is usually managed in a small number of specialist centres in order to maximise expertise. The first presentation of a child with cancer is most frequently however at a smaller local hospital where the initial diagnostic tests are often undertaken. Some follow-up imaging may also be performed locally for patient convenience. This arrangement results in imaging from a wide variety of district hospitals being sent to regional cancer centres for review. Our chapter sets out to illustrate potential errors made in the imaging of children with cancer, from selecting an incorrect modality or using suboptimal protocols to incorrect identification and interpretation of abnormalities. Whilst this chapter illustrates some of the pitfalls in the imaging of childhood cancer we have encountered, it comes with a plea for a collaborative approach to imaging between specialist and general hospitals with an encouragement of an open dialogue and constructive feedback to referring centres.

J. Barber (✉)
St. George's Hospital, London, UK
e-mail: joy.barber1@nhs.net

K. McHugh
Great Ormond Street Hospital for Children, London, UK
e-mail: Kieran.McHugh@gosh.nhs.uk

2.2 How to Scan

2.2.1 Choosing Imaging Modalities

Survival rates for childhood cancer are very good, with a 5-year survival of 82% for children diagnosed between 2006 and 2010 [1]. For this reason, it is particularly important to minimise potential morbidity due to the side-effects of radiation exposure incurred during diagnosis, treatment and later surveillance. The risks of treatment-dose radiation in children are well established [2]. More controversial currently are the risks attributable to diagnostic level radiation, with arguments both for [3, 4] and against [5] it posing significant hazard. At worst, a lifetime risk of cancer in the order of 1 in 550 has been quoted for a 1 year old child following a CT of the abdomen [6]. Given the uncertainty regarding the risk of diagnostic radiation doses, the ALARA principle is recommended for safety. On the other hand, MRI is not an entirely risk-free alternative, with sedation or anaesthesia required for long scans in young children carrying an associated morbidity [7]. There is growing concern in the literature regarding the effects of gadolinium deposition in tissues albeit without any evidence of harm to children as yet [8]. Certainly, if CT or other techniques involving ionising radiation are to be used, the protocol must be optimised to ensure the maximum useful information will be gained.

S. D. Voss, K. McHugh (eds.), *Imaging in Pediatric Oncology*, Pediatric Oncology,
https://doi.org/10.1007/978-3-030-03777-2_2

2.2.2 Plain Radiographs

2.2.2.1 Chest Radiographs

Chest radiographs will, quite reasonably, be performed in most patients with a suspected new tumour for staging purposes. With the exception of children with obvious pulmonary metastases, most abnormalities identified on chest radiographs will be inflammatory/infective abnormalities such as round pneumonia or occasionally congenital lesions such as bronchopulmonary foregut malformations. This is largely due to the low incidence of primary thoracic malignancy in children although bronchogenic tumours, carcinoids, pleuropulmonary blastomas and mesenchymal tumours are occasionally seen.

Misidentification of normal structures on plain film is easily done on a rotated radiograph. The thymus can look particularly large in infants and toddlers, however should always maintain its normal gently lobulated contour and not exert any mass effect (Fig. 2.1). Malignant mediastinal masses however do also occur in children. Locating the mass within the anterior or posterior mediastinum can help to narrow the differential, lymphoma being the most common malignant anterior mediastinal mass and neuroblastoma (Fig. 2.2) being a posteriorly located mass often erodes or splays the posterior ribs. Chest radiographs are used as part of follow-up of patients following treatment for cancers with a risk of lung metastatic disease, for instance, Wilms tumour, rhabdomyosarcoma, osteosarcoma and Ewing sarcoma. In addition to the usual sites where pathology is commonly missed on chest radiographs—for instance, behind the clavicles (Fig. 2.3), behind the heart and in the costophrenic recesses projected below the diaphragm—another potential pitfall which is peculiar to paediatrics is misidentification of sternal ossification centres. Although more commonly mistaken for rib fracture on oblique chest

Fig. 2.2 A posterior mediastinal mass (neuroblastoma) on chest radiograph—note the distortion of the posterior ribs, helping to confirm the posterior location

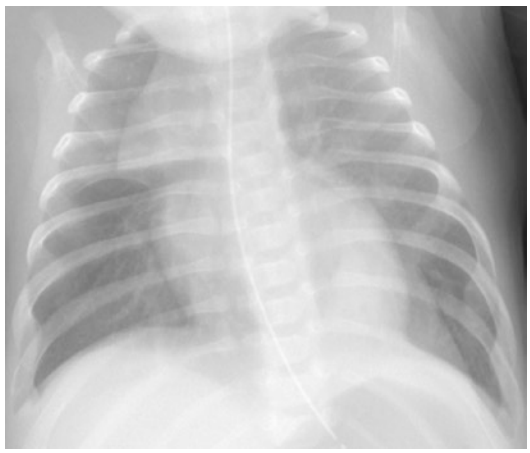

Fig. 2.1 Normal gently lobulated thymic contour on chest radiograph, conforming to the overlying ribs. Note also the added left lower lobe density in this example—a sequestration

Fig. 2.3 This Ewing tumour is located behind the right clavicle but is also detectable by the deviation it causes to the adjacent trachea—demonstrating the importance of systematic review areas

radiographs, sternal ossification centres may on occasion be mistaken for calcified metastases. Thankfully with patient age and progressive ossification, this becomes a less common pitfall.

The bones imaged on chest radiographs are a minefield for potential missed diagnoses. In addition to the posterior rib distortion and erosion that may help to identify a mediastinal mass as a posterior thoracic neuroblastoma (Fig. 2.2), metastatic bone disease and non-malignant but nonetheless aggressive processes may also be demonstrated. Lucency within the proximal humeral metaphyses may be the first manifestation of metastatic bone disease, for instance, in neuroblastoma, or diffuse marrow space involvement in the setting of haematological malignancy (Fig. 2.4). Whilst metabolic bone disease should also be considered in cases where the abnormality is symmetrical and the margins ill-defined, the imaging features of cupping and fraying of the metaphyses in rickets are well described and quite characteristic and distinct from the bony changes seen in malignancy. It is well recognised that ifosfamide treatment for tumours can also be complicated by rickets. The presence of abnormality elsewhere in the skeleton and the overall clinical picture usually allow differentiation.

The ribs, whilst also a site of potential metastatic disease, may also be affected by primary bone lesions including PNET/Ewings (Fig. 2.5). Non-malignant lesions such as enchondromas, fibrous dysplasia and mesenchymal hamartoma may also be seen (Fig. 2.6). Of note, osteochondromas are the commonest rib tumour induced by

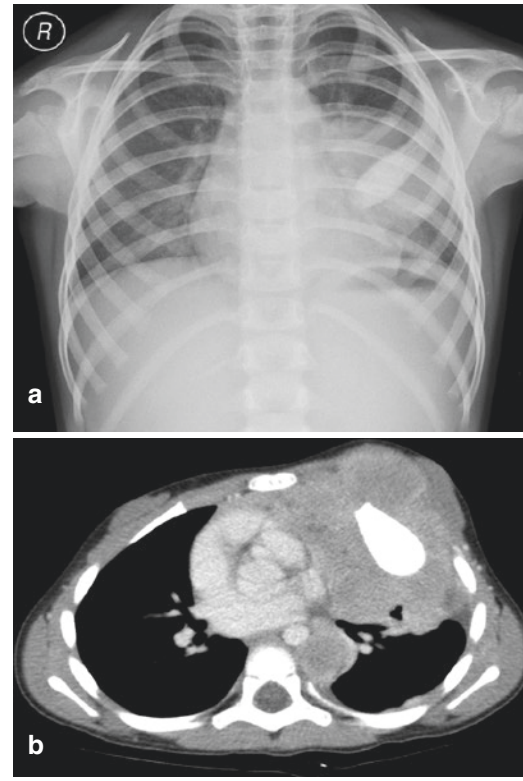

Fig. 2.5 (**a**, **b**) Note the sclerotic, expanded left third rib, with associated soft tissue mass—an Ewing sarcoma

Fig. 2.4 Infiltrative lucency in both proximal humeri was the presenting abnormality in this child with metastatic neuroblastoma

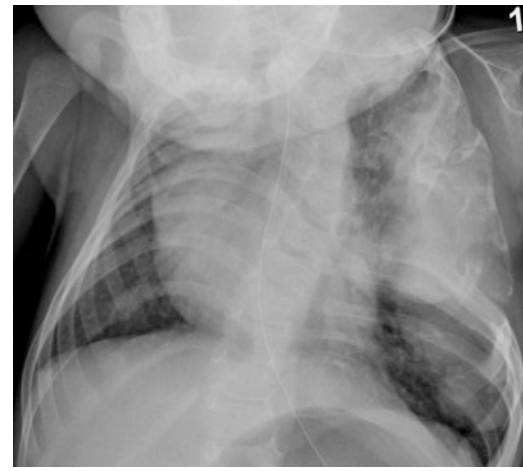

Fig. 2.6 Unusual but characteristic chest radiograph appearance of a mesenchymal hamartoma

radiation, and these were frequently seen in the era when children had total body irradiation prior to bone marrow transplant and are still encountered following mediastinal radiation for Hodgkin lymphoma. The likelihood of each differential is influenced by patient age at presentation and the often distinctive imaging appearances.

Vertebral lesions may also be detectable on chest radiograph although easily missed if not looked for—in particular vertebral collapse which may be secondary to infiltration in haematological malignancy and metastatic disease or secondary to Langerhans cell histiocytosis (LCH) (Fig. 2.7).

2.2.2.2 Abdominal Radiographs

A calcified neuroblastoma mass can often be seen on a plain abdominal radiograph in the upper abdomen or pelvis. Calcification in a germ cell tumour or teratoma of the ovary may also be evident occasionally. These findings may help in the diagnosis of those tumours but seldom provide any other useful information. In addition, these findings are generally evident at initial ultrasound examination also. In rare cases of high-risk metastatic neuroblastoma, lytic skeletal metastases may be visible, but that is an exception rather than the rule. Abdominal radiographs for abdominal masses in children usually show a nonspecific mass in the abdomen, with pelvic masses appearing often identical to a distended bladder. Their role is virtually always superseded by cross-sectional imaging, notably ultrasound. In general an abdominal radiograph at initial presentation of an abdominal mass may be avoided unless there is a concern over bowel obstruction or perforation.

2.2.2.3 Appendicular Radiographs

Whilst they are performed for LCH, extended skeletal surveys are not recommended for routine identification of metastatic disease in children with malignancy, and where clinically required, radiographs should be targeted to a specific indication. Whilst not as sensitive as scintigraphy or

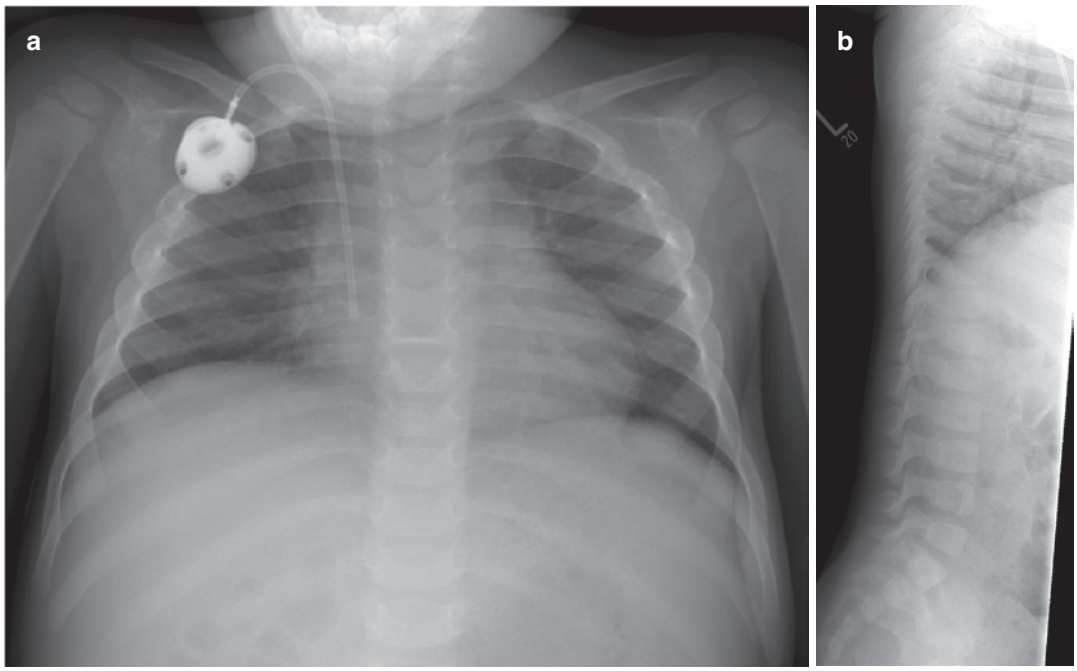

Fig. 2.7 (**a**, **b**) There is collapse of the T7 vertebral body, secondary to infiltration by Langerhans cell histiocytosis

Fig. 2.8 The plain radiograph appearance is sometimes sufficiently distinctive to allow identification of specific patterns of calcification or ground glass changes—such as in fibrous dysplasia shown here

MRI for detecting bone lesions, plain radiographs are particularly valuable in identifying patterns of calcification or typical osseous changes which may assist in identifying 'don't touch' lesions—such as the ground-glass appearance in fibrous dysplasia (Fig. 2.8).

2.2.3 Ultrasound

There are many merits of ultrasound in paediatric oncology. Ultrasound requires neither ionising radiation nor sedation and is low risk and potentially high yield. The dynamic nature of the study and direct patient interaction allow for assessment of mobility of structures relative to each other and on respiration. For instance, ultrasound can allow relatively easy assessment of whether a right upper quadrant tumour is tethered to adjacent liver—allowing the oncologic surgeon to more accurately assess operative risk and take mitigating steps as appropriate. In the authors' experience, this useful information is often overlooked on preoperative ultrasound scanning.

With a distressed or uncooperative child, it can take time and patience to acquire an optimal ultrasound study, sometimes requiring 'time-out' for both child and operator. A systematic approach can help avoid critical components of the study being missed. Colour Doppler should always be applied to lesions—to assist in differentiation between solid and cystic lesions and to help establish the relationship to adjacent vessels (Fig. 2.9). Regional lymph nodes should always be systematically assessed when soft tissue lesions are examined and followed up (Fig. 2.10).

High-frequency linear probes (at least 10–12 MHz) should be used to interrogate the solid organs when metastases are suspected or when fungal infection is suspected in a neutropenic child following treatment. Use of lower-frequency curvilinear probes may mask pathology or at the very least may make it much more difficult to identify lesions which are present (Fig. 2.11).

Ultrasound microbubble contrast (Sonovue/Lumason, Bracco, Milan, Italy) has recently been approved by the FDA in the United States for intravascular use in adults and children for assessment of focal liver lesions. It continues to be used 'off label' in Europe for a multitude of indications in children. There is a paucity of literature currently regarding the accuracy of intravascular ultrasound contrast in assessing paediatric solid organ lesions, although the limited data available is encouraging with one study reporting a specificity of 98% for identifying benign lesions and a negative predictive value of 100% [9]. It is anticipated with the recent FDA approval that the body of evidence surrounding paediatric ultrasound contrast will be significantly expanded in the coming years.

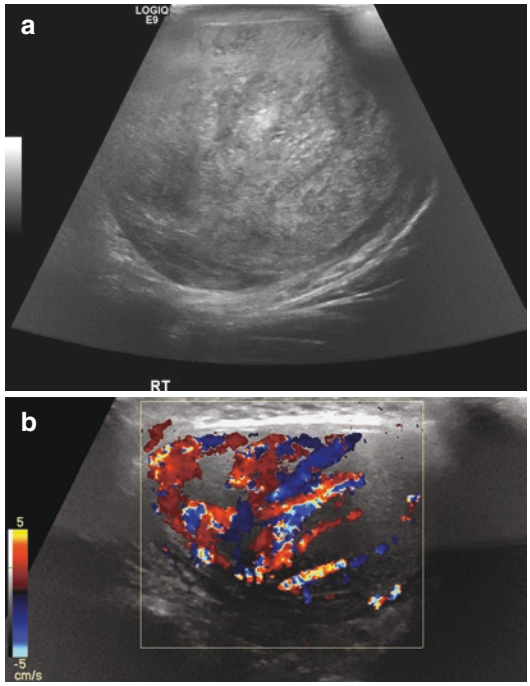

Fig. 2.9 (**a**, **b**) Colour Doppler interrogation allows characterisation of this para-testicular mass as a solid lesion (rhabdomyosarcoma) rather than, for instance, a heterogenous haematoma

Fig. 2.10 Regional lymph node recurrence of rhabdomyosarcoma, identified at follow-up ultrasound

An easy error on ultrasound is to mistake a calcified left upper quadrant mass for gas in the stomach and vice versa (Fig. 2.12). Similarly a cystic mass in the low midline can be dismissed as bladder. In both of these cases, careful delineation of the surrounding anatomy can avoid these pitfalls. For instance, correct identification

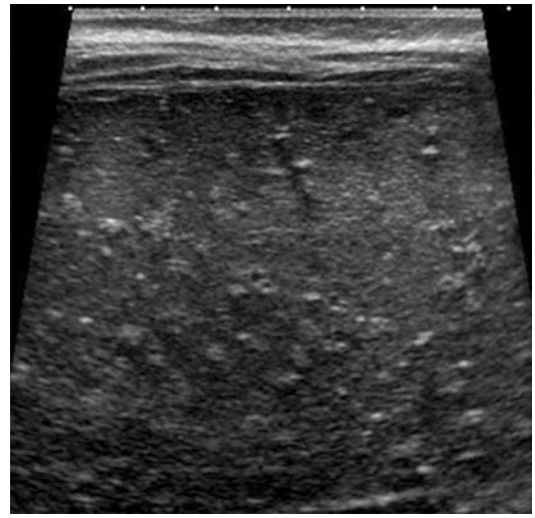

Fig. 2.11 Focal parenchymal lesions in the liver, spleen and kidneys are more apparent on high-frequency ultrasound scanning with a linear probe—such as these hepatic fungal deposits

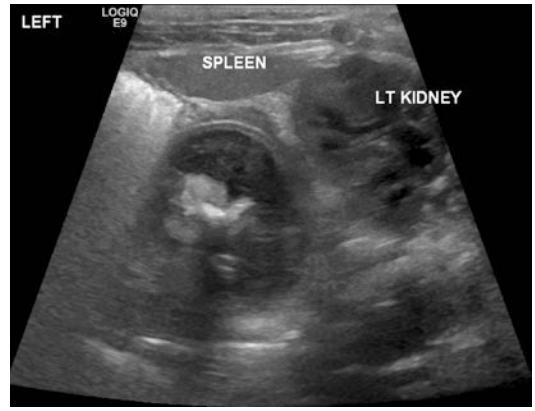

Fig. 2.12 The echogenic foci casting posterior acoustic shadows are not gas within the stomach but calcification within a left upper quadrant solid mass

of the stomach can be confirmed with recognition of the pylorus, and correct identification of the bladder can be confirmed with recognition of the urethral opening.

2.2.4 CT

Whilst the risks of diagnostic level ionisation are debated [3–6], the ALARA principle has driven the development of technology centred around

reducing dose. Choice of scanner plays a role in the dose reduction techniques available, and it would be remiss for a paediatric radiologist to not be involved in specifying the requirements for new acquisitions of CT scanners and establishing paediatric-specific CT protocols. From optimising pitch and collimation to tube current modulation and iterative reconstruction, there are a wealth of techniques that can be implemented to ensure radiation can be minimised without impairing image quality [10]. At our institutions, paediatric chest CT is currently delivered with an effective dose in the range 0.5–1 mSv. Dose reference levels have been developed by Image Gently and the European Society of Radiology through the Eurosafe project [11] and should be used as a guide to optimise departmental protocols. However even a perfectly optimised, paediatric-friendly CT scanner can be used in error if the wrong scan or protocol is performed.

2.2.4.1 Only Perform Necessary Studies

For children with radiation sensitivity syndromes such as Li-Fraumeni, ataxia telangiectasia, Nijmegen breakage syndrome, or Fanconi anaemia, extra effort should be made to avoid CT and substitute with US or MRI whenever possible.

CT imaging of the chest is not required in all tumour types; in particular it has been shown to be unnecessary in neuroblastoma [12], where pulmonary metastatic disease is uncommon, although including the thorax may be helpful in characterising potential supraclavicular lymph node involvement (Virchow's node) identified by MIBG. Chest CT is nonetheless more sensitive for detecting metastatic lung disease than plain radiographs and is invaluable in pathologies with a tendency to spread to the lungs including osteosarcoma, Ewing sarcoma, rhabdomyosarcoma, hepatoblastoma and Wilms tumours.

The frequency of follow-up imaging in children can also be moderated. For instance, most tumour relapses can be detected clinically, and repeated surveillance CT does little to improve outcome in tumour types including lymphoma [13, 14].

CT of the abdomen/pelvis provides poorer soft tissue resolution than MRI, particularly important in young children who have high body water contents and little internal fat to separate organs. New MRI sequences allow excellent spatial resolution, and well-performed MRI is now generally preferable for investigation of a new abdominal mass. The main drawback is regarding the risk of sedation or anaesthesia, which may be required for longer MRI studies and can often be avoided for CT.

2.2.4.2 Do Not Use Thick or Noncontiguous Slices

This should rarely occur; however, where a scanner has acquired thin section data, this needs to be available for review and reformat by the reporting radiologist. Some lesions are much easier to identify and characterize on coronal or sagittal reformats than the standard provided axial images. Indeed, review of properly reformatted images in axial, sagittal and coronal planes using soft tissue, lung and bone windows is considered standard of care and should take place with every examination. Noncontiguous slices are unacceptable in cancer staging.

2.2.4.3 Eliminating Movement

Whilst the increased speed of scanners reduces the severity to which images are degraded due to patient movement, it is not acceptable to repeatedly image a child with CT due to poor immobilisation. Whilst sedation or anaesthesia was previously widely employed to ensure children were sufficiently still for CT, this is less necessary in the era of sub-second scan times. Immobilisation techniques such as trauma evacuation-style 'vacuum' bags are well tolerated by most children, easy to use and compatible with CT and MRI. A small number of children will nonetheless require anaesthetic support for CT, in particular those with neck or mediastinal masses at risk of compromising the airway. In these patients, if the risk of lying supine is felt to be too great, such as in a child with T-cell non-Hodgkin lymphoma and a large anterior mediastinal mass compressing the trachea, lateral decubitus or prone imaging may still be possible.

2.2.4.4 Intravascular Contrast

Iodinated contrast is not inherently safe, with potential risks of extravasation, anaphylactoid reactions and contrast-induced nephropathy. Thankfully these are uncommon in children. Extravasation can be reduced by careful IV line placement, line flushing and auto cut-offs on injector pumps in the case of a rapid rise in resistance. Mild or moderate anaphylactoid reactions occur in up to 0.5% of patients and severe anaphylactoid reactions only in approximately 0.02% [15, 16]. The risk of unexpected contrast-induced nephropathy can be mitigated by checking of renal function in at-risk patients.

With their higher body water content and lower body fat content compared with adults, giving contrast for paediatric CT is rarely an error. With the exception of spotting lung nodules, non-contrast scans in children often result in relatively homogenous shades of grey with poor differentiation between tissues (Fig. 2.13) and should be avoided in the assessment of a new mass [17]. The only useful information gleaned from a non-contrast CT in a child is whether a lesion is calcified or not, but this is also readily apparent after contrast administration (see Table 2.1). Even for CT studies primarily assessing for metastatic lung disease, contrast can be useful to delineate the mediastinal and vascular structures.

There has been some debate in the literature regarding the timing of contrast boluses in oncologic CT [18, 19] with some advocates of a dual-bolus approach—achieving both arterial and portal venous phase contrast in a single pass. This can be helpful in certain scenarios but is not normally required. Arterial phase imaging is generally preferred for the chest.

Ideally, the abdomen and pelvis should be imaged with MRI. Where CT imaging of the abdomen is necessary, the phase of imaging must be tailored to the question. Single-phase imaging at CT is all that is necessary for the majority of abdominal mass lesions in young patients. Triple-phase scanning (arterial, portal, delayed venous) seldom adds useful additional information and triples the effective dose. It should be borne in mind that prior ultrasound with Doppler vascular assessment of any abdominal mass should have been performed before CT. If both arterial and portal venous phase imaging are required simultaneously, the dual-bolus technique can be considered.

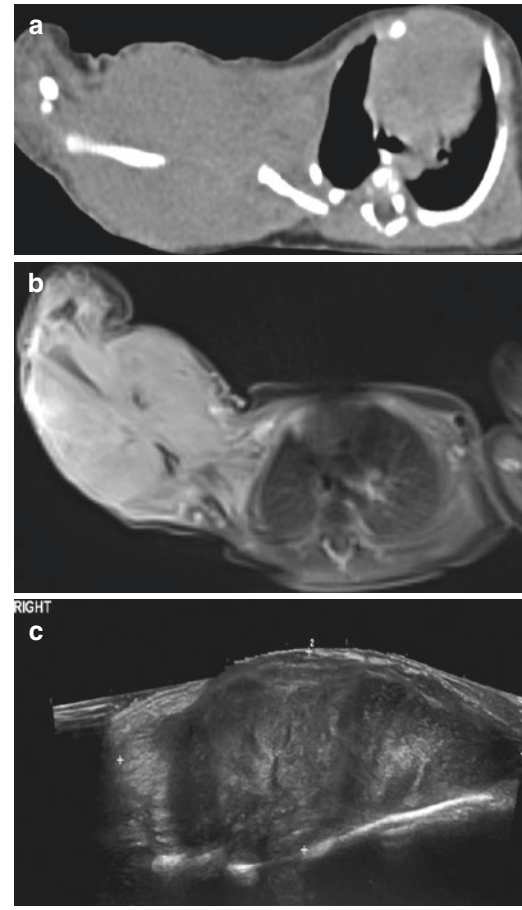

Fig. 2.13 This right upper limb soft tissue lesion is poorly delineated on non-contrast CT (**a**) but much better seen and assessed on both MRI (**b**) and ultrasound (**c**)

2.2.5 MRI

2.2.5.1 MRI Sequences

MRI sequences can generally be grouped into those which aid detection of disease (fat-suppressed T2 imaging/STIR, DWI), those which allow assessment of lesion contents

Table 2.1 Important 'Do's' and 'Don'ts' in paediatric oncology imaging

Don't do non-contrast CT. Post-contrast scanning should generally suffice
Don't do multiphase CT scanning; single-phase scans should be sufficient. Remember that ultrasound to assess vascularity should have been performed before CT
Do perform ultrasound evaluation initially of superficial lesions
Don't forget to assess the regional lymph nodes with ultrasound and MRI. For limb tumours this means assessing the popliteal and inguinal nodes of a leg or the epitrochlear and axillary nodes for an upper limb primary
For MRI do try to perform diffusion weighted imaging (DWI) and ADC maps for all new tumours. This helps assess lesion cellularity and may guide biopsy
At MRI a volumetric sequence is useful for reconstruction in the other orthogonal planes for surgical planning
Don't routinely perform an abdominal radiograph for an abdominal mass; it is seldom useful
Do consider performing MRI instead of CT for all limb, abdominal (particularly pelvic and liver), paravertebral and neck tumours

Fig. 2.14 High-resolution T2 SPACE/CUBE imaging provides excellent delineation of a left renal tumour and surrounding vascular anatomy but at the cost of a long study time often requiring general anaesthetic in younger children

(T1, in- and out-of-phase, T2, and contrast-enhanced imaging) and those which are particularly good at anatomic localisation and resection planning (isotropic, small voxel T2 imaging). An oncology protocol needs to satisfy all these demands but will be tailored to an individual institution's machine and coil capabilities and adapted based on the patient and pathology.

The plane of imaging is important. Midline lesions, for instance thymus or prostatic/vaginal lesions, are difficult to delineate on coronal imaging, and sagittal imaging is often a better choice for the second acquired plane.

MRI sequence selection involves trade-offs. High-resolution MR imaging has the ability to replace CT of the abdomen and pelvis in terms of spatial resolution (Fig. 2.14) but takes a long time to acquire in order to maintain an adequate signal-to-noise ratio (10–15 min for a T2-SPACE/CUBE of the abdomen and pelvis) and therefore often requires sedation/anaesthesia.

2.2.5.2 Gadolinium

Although the risk of NSF is low with modern macrocyclic gadolinium agents, it should not be given to children with known renal impairment without a careful risk-benefit assessment [20]. Gadolinium carries lower but non-zero risk of anaphylaxis compared with CT-iodinated contrast. More recently, concerns have increased regarding deposition of gadolinium within brain and bone tissue. Although the long-term effects of this are unknown, it has been found to occur both in patients with normal renal function and with macrocyclic agents previously thought to be more stable [21, 22]. The need to give gadolinium to assess enhancement needs to be weighed carefully against potential risks in each child.

2.2.6 Nuclear Medicine

SPECT and PET/CT are increasingly used in the investigation of childhood malignancies. [^{18}F]fluo-

rodeoxyglucose (FDG) remains the most commonly used tracer, and FDG-PET can be used in staging disease, in evaluating the response to chemotherapy and as a surveillance test. Pitfalls with FDG are its relatively low specificity—with inflammatory lesions also FDG avid—and exposure to ionising radiation. It is also possible to misinterpret normal physiologic uptake of FDG in the body as disease. Physiologic FDG uptake can be seen within the lymphoid tissue, salivary glands, muscles, heart, liver, spleen, breast tissue and bowel, and it is seen excreted in the renal tract and bladder. Metabolically active brown fat can also show increased FDG uptake, which can be reduced by keeping the child warm and still during preparation for the scan. Each tracer in nuclear medicine has a different distribution in normal tissues with which the interpreting radiologist needs to be familiar.

Treatment effects can also cause confusion in FDG-PET, with both radiotherapy and chemotherapy causing posttreatment flare effects. At least 2 months should elapse between radiotherapy and a follow-up FDG-PET scan, and ideally 1 month after chemotherapy, to reduce the chance of misinterpreting flare. The flare following chemotherapy can in part be due to bone marrow hyperplasia, and a similar effect is seen post-granulocyte colony-stimulating factor (GCSF) with homogenously increased uptake in the skeleton.

The most common gamma-emitting radiopharmaceuticals used in paediatric oncology are likely [123I]MIBG and [99mTc]methylendiphosphonates (MDP). [123I]MIBG scan is used in assessment of neurogenic tumours, most commonly neuroblastoma, at diagnosis and in monitoring response to treatment. Radiolabelling of MIBG with 123I is highly preferable to 131I, as it gives better quality images and a much lower radiation burden. A number of drugs can interfere with MIBG uptake, in particular antihypertensives, anti-depressants and sympathomimetics [23]. Not all neurogenic tumours are MIBG positive, with a sensitivity of approximately 90% for neuroblastomas. Non-avid primaries may result in non-avid metastases, and a negative MIBG scan in this case cannot rule out metastatic disease. Approximately 10% of neuroblastomas are MIBG negative, and FDG-PET is the recommended alternative tracer in this context. More differentiated neurogenic tumours show a lower avidity for MIBG.

Technetium bone scans, whilst sensitive for detecting metastatic bone disease when scrupulously performed, are not particularly good at assessing response to chemotherapy or radiotherapy, as reactive changes can persist even when viable tumour is no longer present. Bone scans are only indicated at diagnosis for staging in some tumours, but their utility has recently been questioned for the evaluation of several paediatric tumours, including rhabdomyosarcomas [24] and neuroblastoma [25].

2.2.6.1 Imaging at the Wrong Time

There are several time points when children with cancer will require imaging: at diagnosis, to assess response to treatment, on surveillance and when imaging for complications of treatment. Chong et al. have clearly demonstrated how easy it is for excess non-mandated CT scanning in particular to be done during the course of treatment, adding to the radiation burden [26]. In their lymphoma cohort, 66% of studies were non-mandated, described as discretionary (for disease surveillance, good patient care or radiologist request). Given the excellent outcome of this group and the long-term risks, rational use of discretionary surveillance procedures is necessary. Guidelines for the appropriate use of surveillance imaging based on probability of risk recurrence must be developed in order to minimise ionising radiation exposure, and this advice applies not just to lymphoma but to all tumour types.

One of the most common pitfalls in timing of imaging is to not perform a baseline study prior to changing treatment—for instance, making it difficult to assess whether changes in disease appearance truly represent progression on treatment or are due to a deterioration prior to commencing the latest treatment.

When planning for surgical resection, high-resolution imaging (CT or MRI) should be performed just prior to the planned operation, to ensure disease status is up to date. This is particularly relevant in cases of delayed resection of low malignant potential lesions in order to allow for child growth

(for instance, a neonatal teratoma) and in patients receiving induction chemotherapy in an effort to reduce tumour size prior to surgical resection (e.g. neuroblastoma and hepatoblastoma).

2.2.6.2 Imaging the Wrong Area

Whilst few would fail to image the primary mass lesion, it is surprisingly easy to not image correctly for local or metastatic disease. A common error is not imaging the entire limb for soft tissue and boney lesions and miss second skip lesions or nodal spread. Locoregional spread of a tumour such as rhabdomyosarcoma upstages the disease and thus has important therapeutic implications.

Conversely, it is surprisingly easy to become fixated on detailed imaging of a soft tissue or bony lesion and not recognise that it is a manifestation of metastatic or systemic disease and not the primary site (Fig. 2.15).

Another pitfall is not considering variations in lymphatic drainage pathways—for instance, for testicular tumours—and therefore not including sufficient coverage of the draining lymph nodes of the abdomen and pelvis in imaging.

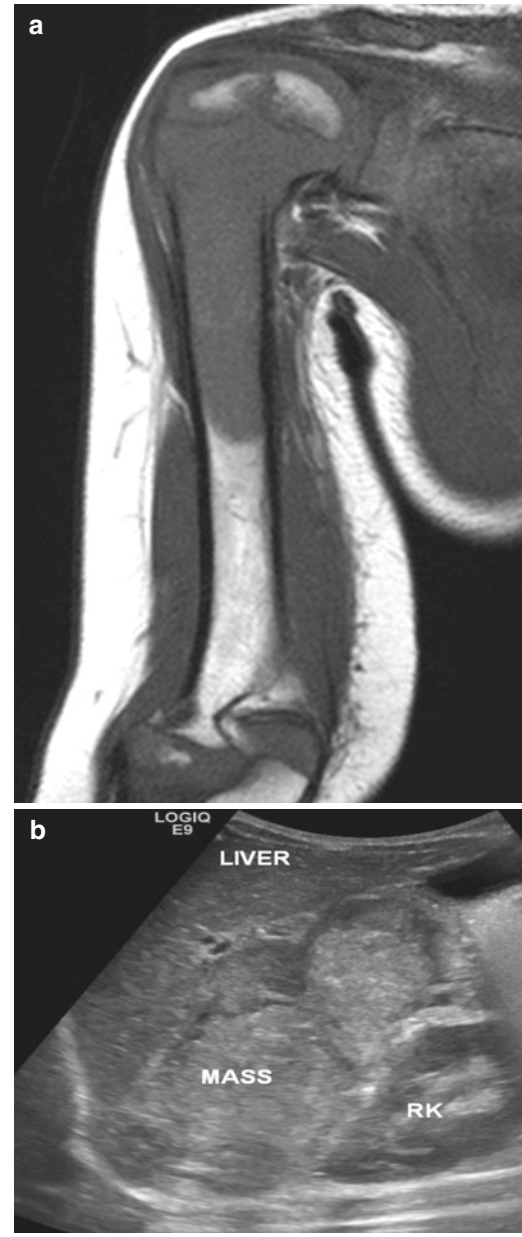

Fig. 2.15 Initial assessment of this right proximal humerus bony lesion included MRI of the site (**a**), before evaluation of the abdomen with ultrasound demonstrated that it represented a site of metastatic disease from neuroblastoma (**b**) rather than a bony primary

2.3 Pitfalls in Identifying and Characterising Abnormality

2.3.1 Missing and Overcalling Lung Disease

Using transverse maximum intensity projections (MIPs) when reviewing for lung metastases increases the sensitivity of detection of lung nodules, particularly for less experienced readers [27]. MIP images are easy to generate from available axial data, and it is hard to justify not using them. However, it is not just lung metastases that can be identified on chest CT. Pulmonary emboli are also critical to look for, and the detection of embolic disease is an argument for giving contrast even when the primary question is detection of lung nodules (Fig. 2.16).

Deciding whether a lung nodule is or is not metastatic disease is not straightforward. Despite suggestions in some early guidelines for rhabdomyosarcoma and Ewing sarcoma that size thresholds could be used for identifying metastatic disease, subsequent research has shown no clear relationship between nodule size or indeed any

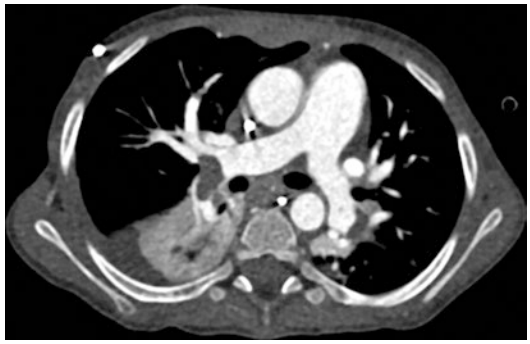

Fig. 2.16 Acute right pulmonary artery embolus is demonstrated on a contrast-enhanced CT thorax performed for staging of Wilms tumour

Table 2.2 Definition of pulmonary metastases in the European Paediatric Soft Tissue Sarcoma Study Group (EpSSG)

Nodule size	Classified as
≥1 nodules >10 mm	Metastatic disease
≥2 nodules 5–10 mm	Metastatic disease
≥5 nodules <5 mm	Metastatic disease
≤4 nodules <5 mm	Equivocal disease, treat as localised disease
0 nodules	Localised disease

other imaging factor and likelihood of representing metastatic versus benign/inflammatory disease [28, 29]. As a result different arbitrary thresholds as to what is considered to represent unequivocal pulmonary metastatic disease are now used in some collaborative cooperative paediatric oncology trials. For example, the next European Wilms tumour study (UMBRELLA) will categorise all lung nodules ≥3 mm as lung metastases, having used 1 cm nodules as the lesion threshold size for pulmonary metastatic disease in the prior study. Local radiologists should be aware of these definitions within the various trials, or they should be made aware by their paediatric oncology colleagues (Table 2.2, definition of lung metastases in the EpSSG study). That said, the dilemma of what constitutes a normal chest CT, equivocal and unequivocal pulmonary metastatic disease is probably best dealt with by central radiology review.

2.3.2 Finding Fat

Sometimes the identification of fat in a lesion can help to significantly narrow a differential diagnosis. Recognition of the characteristics of different MRI imaging sequences is crucial for this. Whilst both short-tau inversion-recovery (STIR) and chemical selective fat suppression sequences can demonstrate macroscopic fat, gradient-echo in and out-of-phase imaging is the technique of choice for demonstrating microscopic fat. Pre-contrast T1 imaging is typically performed with chemical fat suppression (gadolinium enhancement being more clearly assessed on fat-suppressed images) and can provide a 'free' opportunity to detect macroscopic fat if other fat-suppressed sequences have not been performed. Indeed, not fat suppressing for contrast-enhanced MR images can make it extremely difficult to differentiate true enhancement from surrounding fat and other intrinsically high T1 signal structures (Fig. 2.17).

Modified Dixon techniques are also increasingly used and generate four sets of images from a single acquisition—in/out of phase, water only and fat only images—allowing for efficient characterisation. Where CT imaging is performed, macroscopic fat is clearly seen, although microscopic fat is less accurately assessed.

2.3.3 Calcification and Bone Lesions on MRI vs. CT

Calcification and abnormal ossification can be much more subtle on MRI than on CT, with the surrounding soft tissue abnormality often the dominant feature on MRI. In some cases, this can lead to the causative lesion being overlooked in favour of secondary soft tissue changes, such as oedema (Fig. 2.18). An awareness of the subtlety of calcification on MRI can help to mitigate this risk. On CT, when identification of bone erosion is critical to diagnosing or staging disease—such as pterygoid plate involvement in parameningeal rhabdomyosarcoma—the bones need to be very carefully interrogated on dedicated bone windows as subtle erosion is easily overlooked.

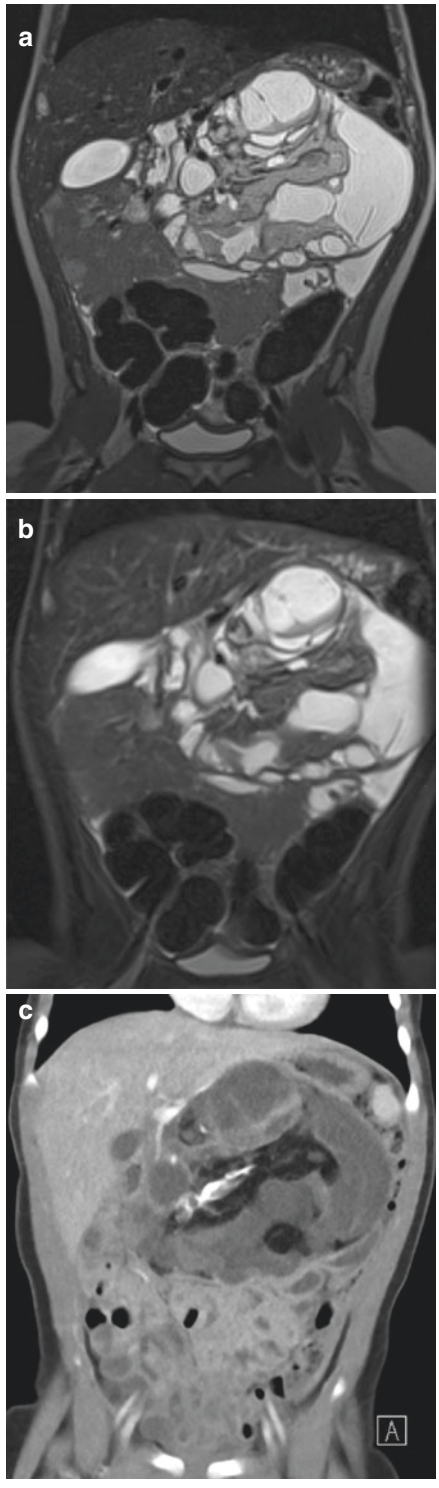

Fig. 2.17 An abdominal teratoma containing macroscopic fat, demonstrated as an area of signal drop-out on the fat-sat T2 (**b**) compared to the non-fat-suppressed T2 sequence (**a**). The macroscopic fat is easily seen on a CT study also performed (**c**) but at the expense of radiation

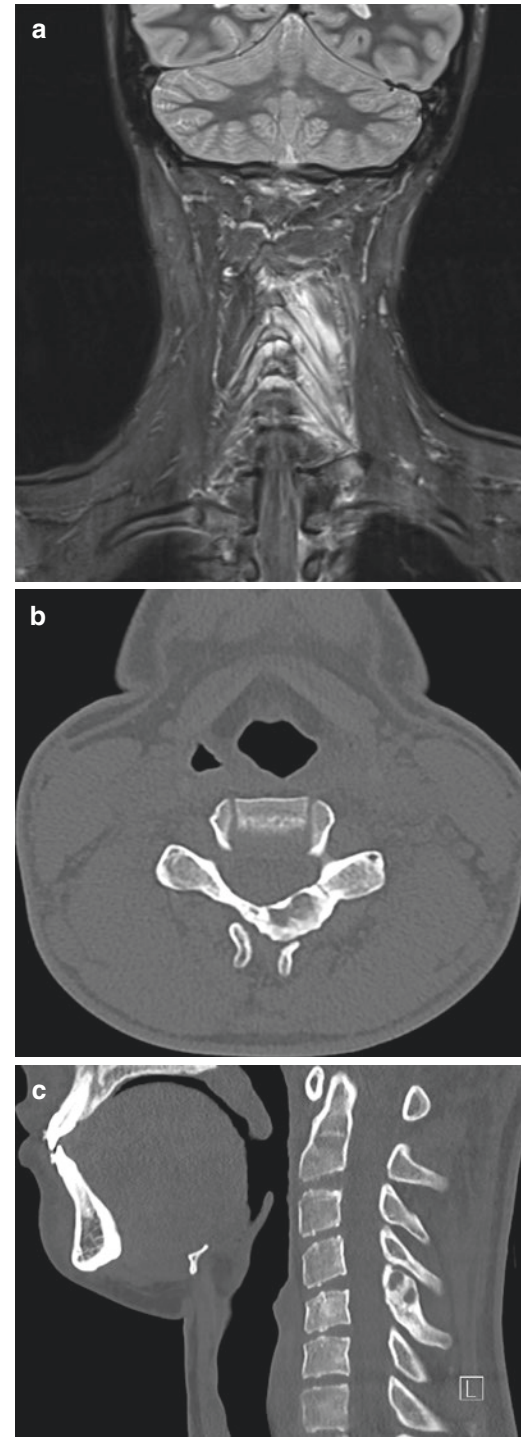

Fig. 2.18 An osteoid osteoma of the cervical spine. The dominant feature on MRI is the associated soft tissue inflammation (**a**) with the primary bony abnormality easily overlooked. The bony lesion is more clearly delineated on CT (**b**, **c**)

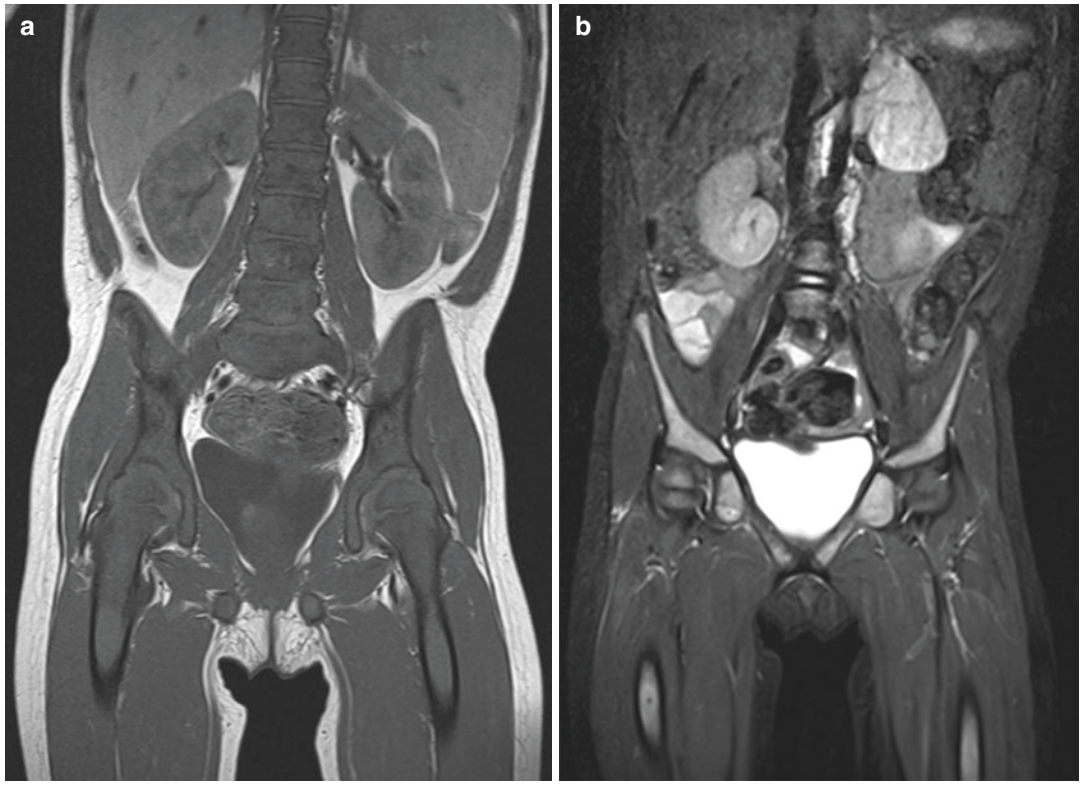

Fig. 2.19 There is diffusely abnormal marrow signal in the bones in keeping with metastatic infiltration—best appreciated in the femoral heads which should contain fatty marrow which should be high signal on T1 (**a**). The primary left suprarenal neuroblastoma is also seen (**b**)

CT is relatively poor at identifying bone marrow infiltration, for instance, in neuroblastoma, which is more clearly seen on MRI and bone marrow biopsy.

2.3.4 Missing the Symmetrical Abnormality

Diffuse or symmetrical processes can be very difficult to detect unless they are systematically assessed for and normal appearances are known. This can be particularly difficult with bone marrow changes, as this requires a knowledge of how the pattern of red/yellow marrow changes with age. A good guide is that epiphyses should be bright on T1 imaging, that is, they contain fat, within months of developing ossification. Low T1 signal epiphyses therefore are concerning for abnormal marrow infiltration (Fig. 2.19).

An additional possible pitfall here however is children who have received granulocyte colony-stimulating factor (GCSF) to combat bone marrow suppression, for instance, during treatment for leukaemia, which can drive reconversion of fatty bone marrow to haematopoietic bone marrow and simulate marrow infiltration or metastases. Clinical history here is key.

2.3.5 Over-Interpreting Artefact

Particular tumour types lend themselves well to particular types of error in identification of abnormality. The known diffuse cortical abnormality in nephroblastomatosis can be misdiagnosed with overcalling of thin rims of reduced T2 signal along the renal cortex as ‘rinds’ of abnormal tissue when they may in fact be attributable to chemical shift artefact (Fig. 2.20). Similarly, it can be tempting to overcall rims of abnormally restricted diffusion along the renal cortex in this context as persistent nephrogenic rests, particularly in the

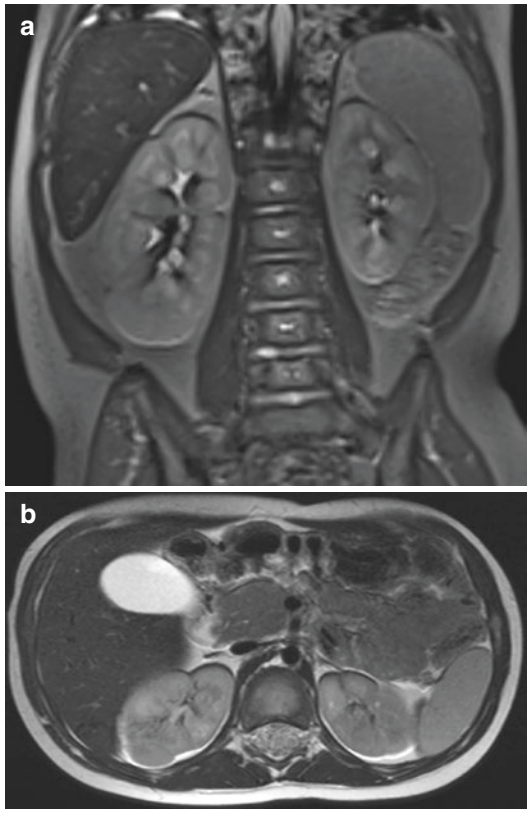

Fig. 2.20 Originally described as 'rinds' of abnormal T2 signal, the dark rings along the margins of the kidneys represent chemical shift artefact, not nephroblastomatosis (**a**, **b**)

presence of convincing more nodular sites of cortical disease elsewhere. When in doubt on the DWI imaging, the high *b*-value images should be turned to, as failure to recognise subtle misregistration on ADC maps or combined DWI/ADC images can lead to overcalling of disease.

Concern over intravascular extension associated with Wilms tumour can lead to overenthusiasm in diagnosing IVC thrombus in cases where the low attenuation in the IVC at the level of the renal veins is often due to mixing effects at CT. Vascular artefact and flow voids at MRI can also produce a pseudothrombus appearance. These artefacts should easily be identifiable by normal opacification and non-expansion of the draining renal vein (Fig. 2.21), and in cases where confusion persists, ultrasound can usually clarify. Altering the phase and frequency direction during MRI acquisitions can usually eliminate flow-related artefacts. Foot vein contrast injections in addition should be avoided at CT as the unopacified blood from one lower limb may also mimic thrombus in the IVC.

Fig. 2.21 There is mixing artefact within the IVC on this contrast-enhanced CT, generating a 'pseudo-thrombus' appearance

2.4 Pitfalls in Interpreting Findings and Reaching a Differential Diagnosis

2.4.1 Patient Age Is Critical to the Most Likely Diagnosis

The differential diagnosis of masses in children is age-dependent, with very different pathologies at birth, in infancy and in an older age group. For instance, embryonal tumours including neuroblastoma, PNET, Ewing sarcoma, Wilms tumour, retinoblastoma and rhabdomyosarcoma are most common in the first few years of life and rare in older children, whereas lymphoma is rare in children under 2 years of age, and the incidence increases thereafter with age.

Renal tumours are a good example of how the likelihood of pathology changes with age, with mesoblastic nephroma the most common renal mass in neonates, Wilms tumour more likely after 6 months of age and into early childhood and renal cell carcinoma increasingly common in older adolescents.

For instance, a suprarenal cystic lesion presenting immediately after birth is most likely to be an adrenal haemorrhage, whereas a suprarenal lesion presenting in an infant is statistically more likely to be a neuroblastoma even if it does contain cystic elements. Where diagnosis is uncertain, biopsy may be required for confirmation prior to commencing treatment. This point, of course, emphasises the importance of knowing which tumours are common in each age group. For example, a soft tissue scalp lesion initially detected by physical exam and further characterised by US and MRI (Fig. 2.22) was the presenting feature of lymphoblastic leukaemia in this child.

2.4.2 Anterior Mediastinal Masses

It is worth making a specific comment on anterior mediastinal masses. Unless routinely reporting paediatric imaging, the appearance of the thymus in children of different ages can be confusing and easily over- and under-called. The thymus can appear large in neonates, and 'benign' thymic hyperplasia can occur in some children after cessation of chemotherapy or other physiologic insult, persisting for up to 3–4 months after completing treatment. However, the normal thymus should always be homogenous, never exert mass effect and rebound thymic hyperplasia should resolve [30].

Anterior mediastinal soft tissue in children which exerts mass effect raises the possibility of tumour (Fig. 2.23). Most commonly in the

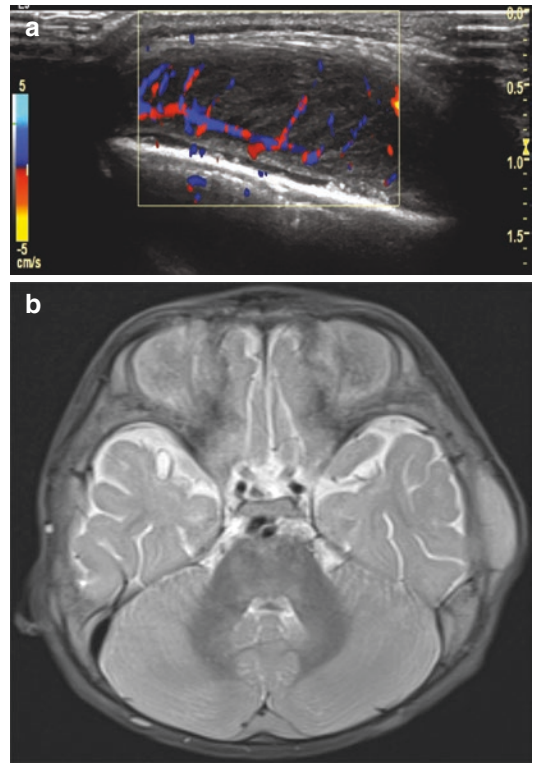

Fig. 2.22 This soft tissue scalp lesion was the presenting feature of acute lymphoblastic leukaemia in this child, seen on ultrasound (**a**) and MRI (**b**)

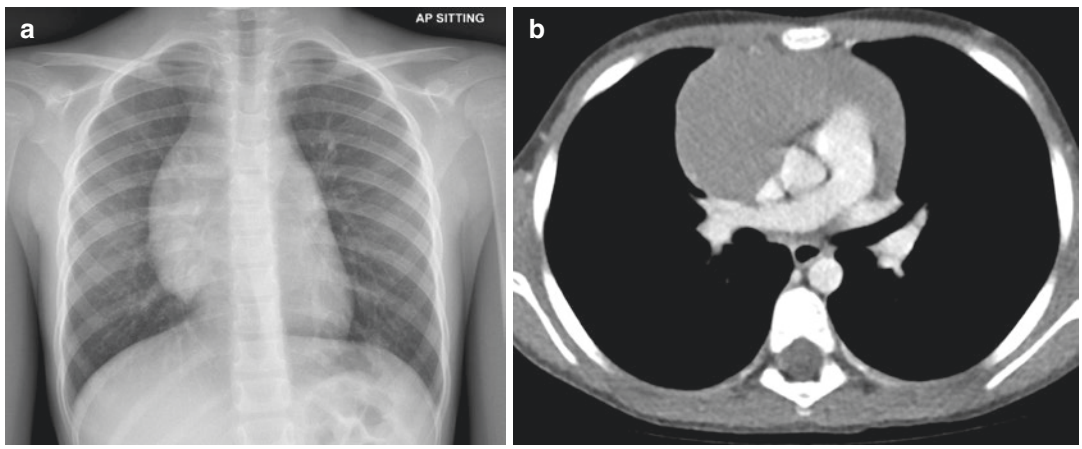

Fig. 2.23 Normal thymus should cause no mass effect on mediastinal structures. Although difficult to appreciate on plain film, (**a**) the anterior mediastinal mass causes posterior displacement of the heart and great vessels (**b**) in keeping with lymphoma

paediatric age group, this is lymphoma, although it is rare to see it before 2 years of age. Alternative anterior mediastinal masses are less common but do occur, including germ cell tumours which typically contain fat and calcium and are more commonly seen in children less than 2 years of age.

2.4.3 Reaching the Limits of Imaging Assessment

Whilst imaging is invaluable in assessing the extent of disease and assessing for response, it generally does not allow a definitive histological diagnosis of a lesion, which requires biopsy. Even with ultrasound it can be difficult to be sure whether lesions are adherent to or invading adjacent organs. Clinical examination is often invaluable in addition to determining the level of suspicion of tethering to surrounding structures, with lesions that are not mobile on palpation more likely to be difficult to excise intact at surgery.

Soft tissue lesions in particular can be very nonspecific on imaging or indeed show features which can be misleading and correlation with clinical findings, and a healthy level of scepticism regarding definitive diagnosis on imaging is required. For instance, despite having clearly defined borders and a homogenous cystic appearance on imaging suggesting a vascular malformation, a lesion which is firm to palpation on clinical examination needs to be treated with suspicion (Fig. 2.24). Vascular malformations where palpable should be soft and fluctuant. Soft tissue sarcomas in particular can look similar to venous malformations on imaging, and synovial sarcoma is often initially misinterpreted. A low threshold for biopsy is recommended.

Alternative investigations such as endoscopy or bronchoscopy can also be better than standard radiological imaging in determining the cause of pathology in certain situations. For instance, a lobar collapse may be due to bronchial obstruction due to foreign body or endobronchial tumour (Fig. 2.25), but differentiation between these is better achieved with bronchoscopy than CT, and bronchoscopy also may allow for therapeutic removal of a benign polypoid lesion.

2.4.4 Non-neoplastic Differentials

Non-neoplastic differentials also need to be considered when assessing new lesions, including Langerhans cell histiocytosis (LCH) and infec-

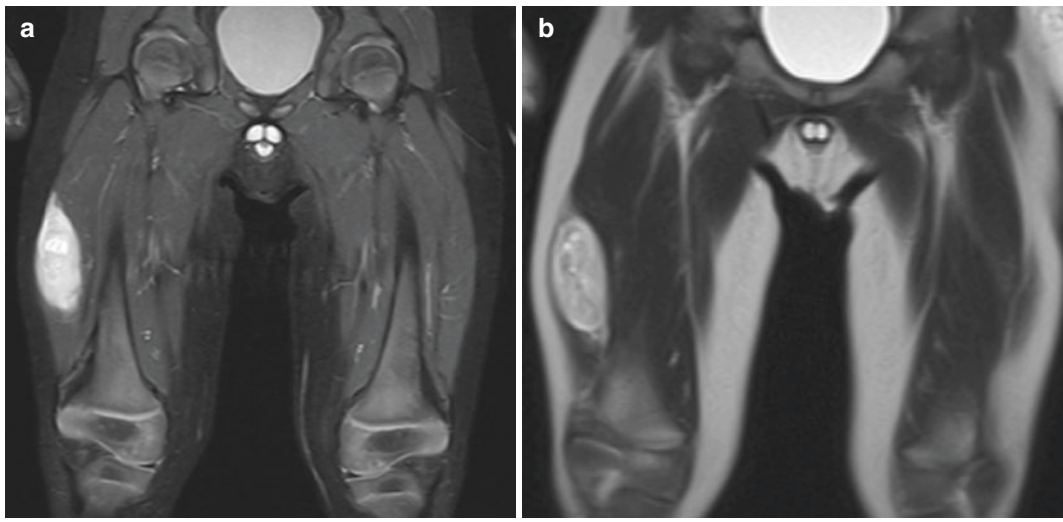

Fig. 2.24 A cystic-looking lesion on STIR (**a**) and T2 (**b**) MRI sequences that enhanced homogenously was hard on palpation raising the suspicion that it represented a mass lesion rather than a vascular malformation. It was found to represent a rhabdomyosarcoma on biopsy

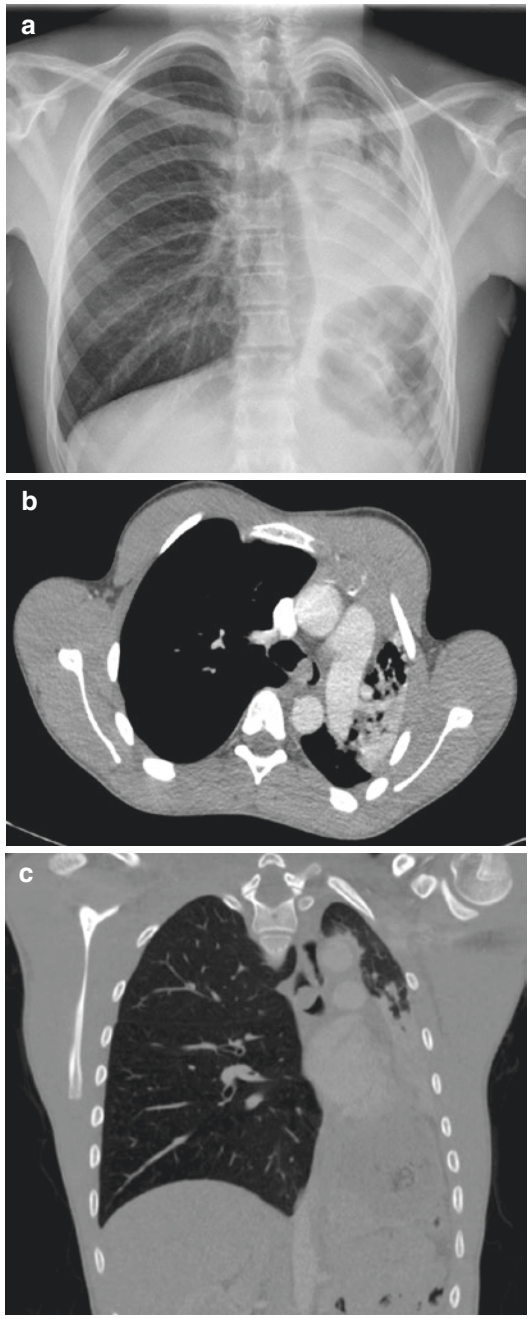

Fig. 2.25 An endobronchial tumour causes collapse of the left lower lobe seen on plain radiograph (**a**). Although the intraluminal lesion is detectable in the airway on CT (**b**, **c**), bronchoscopy was required for definitive characterisation and initial treatment

tion for lytic bone lesions. Some non-neoplastic differentials are diagnoses of exclusion and require treating with suspicion initially such as chronic recurrent multifocal osteomyelitis (CRMO) which may require biopsy to differentiate it from malignant bone lesions such as Ewing sarcoma (Fig. 2.5).

Fig. 2.26 A homogenous echogenic suprarenal lesion in keeping with an extralobar sequestration, which progressively reduced in size on follow-up

Congenital lesions may also present as masses, and it is an awareness of their typical features which can be most helpful in making the diagnosis. Close monitoring to ensure expected regression, for instance, is also prudent in cases of extralobar sequestrations (Fig. 2.26) or infantile hepatic haemangioma (Fig. 2.27). In other instances the distinction between a benign congenital lesion such as a CPAM and a similar appearing malignant pleuropulmonary blastoma cannot be reliably made based on imaging, and surgical resection is indicated.

2.5 Conclusion

Here we have reviewed common pitfalls in oncological imaging and how to avoid them, including selecting the correct modality and protocol, avoiding pitfalls in identification of abnormalities and correctly interpreting findings.

In particular, low-yield approaches such as unenhanced CT should be avoided, and imaging should be performed only when it is going to affect patient management. Protocols should be optimised to allow the reader to glean the maximum useful information from imaging studies at the least cost in terms of radiation and sedation. Readers need to be familiar with the common age-specific diagnoses and remember

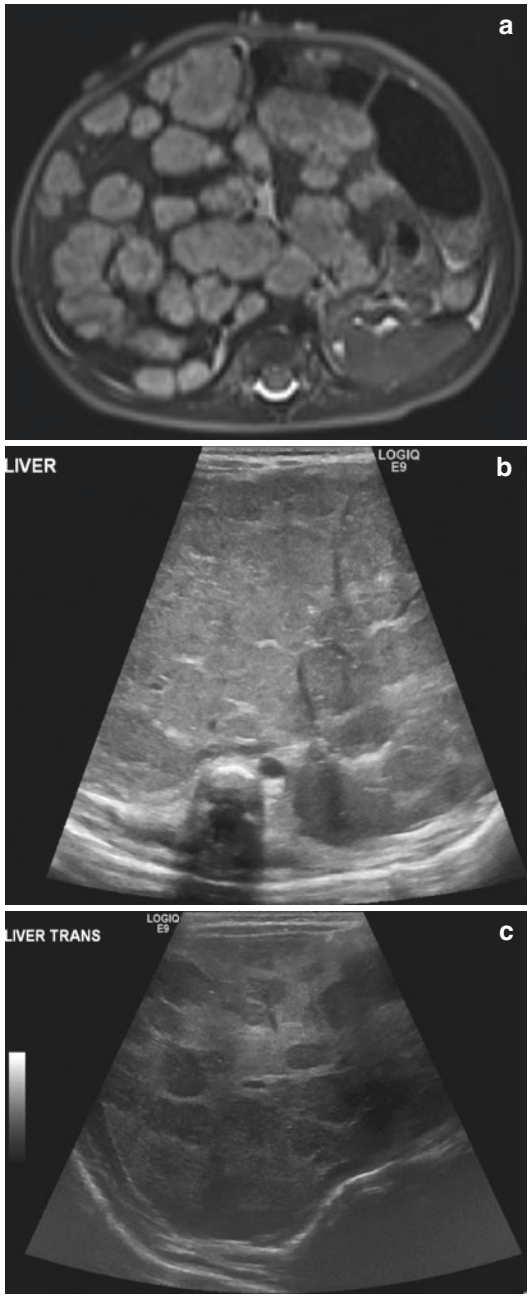

Fig. 2.27 Although MRI (**a**) was used for the early characterisation of these extensive infantile hepatic haemangiomas, they were well seen on ultrasound (**b**), allowing radiation and anaesthesia-free follow-up during which time they became progressively lower echogenicity before reducing in size and extent (**c**)

that unusual presentations of common tumours including metastatic disease are more likely than very rare tumours. The limitations of imaging also need to be borne in mind, with the need for correlation with clinical findings and biopsy.

References

1. National Cancer Intelligence Network. National registry of childhood tumours progress report, 2012. Oxford: NRCT; 2013.
2. Armstrong GT, Stovall M, Robison LL. Long-term effects of radiation exposure among adult survivors of childhood cancer: results from the childhood cancer survivor study. Radiat Res. 2010;174(6):840–50.
3. Pearce MS, Salotti JA, Little MP, et al. Radiation exposure from CT scans in childhood and subsequent risk of leukaemia and brain tumours: a retrospective cohort study. Lancet. 2012;380(9840):499–505.
4. Mathews JD, Forsythe AV, Brady Z, et al. Cancer risk in 680 000 people exposed to computed tomography scans in childhood or adolescence: data linkage study of 11 million Australians. Br Med J. 2013;346:f2360.
5. Andronikou S. Letting go of what we believe about radiation and the risk of cancer in children. Pediatr Radiol. 2017;47(1):113–5.
6. Brenner DJ, Elliston CD, Hall EJ, Berdon WE. Estimated risks of radiation-induced fatal cancer from pediatric CT. Am J Roentgenol. 2001;176(2):289–96.
7. Schmidt MH, Marshall J, Downie J, Hadskis MR. Pediatric magnetic resonance research and the minimal-risk standard. IRB. 2011;33(5):1.
8. Adin ME, Kleinberg L, Vaidya D, Zan E, Mirbagheri S, Yousem DM. Hyperintense dentate nuclei on T1-weighted MRI: relation to repeat gadolinium administration. Am J Neuroradiol. 2015;36(10):1859–65.
9. Jacob J, Deganello A, Sellars ME, Hadzic N, Sidhu PS. Contrast enhanced ultrasound (CEUS) characterization of grey-scale sonographic indeterminate focal liver lesions in pediatric practice. Ultraschall Med. 2013;34(6):529–40.
10. Nelson TR. Practical strategies to reduce pediatric CT radiation dose. J Am Coll Radiol. 2014;11(3):292–9.
11. http://www.eurosafeimaging.org/wp/wp-content/uploads/2014/02/European-Guidelines-on-DRLs-for-Paediatric-Imaging_Revised_18-July-2016_clean.pdf. Accessed 26 Mar 2017.
12. Federico SM, Brady SL, Pappo A, Wu J, Mao S, McPherson VJ, Young A, Furman WL, Kaufman R, Kaste S. The role of chest computed tomography (CT) as a surveillance tool in children with high-risk neuroblastoma. Pediatr Blood Cancer. 2015;62(6):976–81.
13. McHugh K, Roebuck DJ. Pediatric oncology surveillance imaging: two recommendations. Abandon CT scanning, and randomize to imaging or solely clinical follow-up. Pediatr Blood Cancer. 2014;61(1):3–6.
14. Voss S, Chen L, Constine LS, et al. Surveillance CT and detection of relapse in intermediate-and advanced-stage pediatric Hodgkins lymphoma: a report from the Children's Oncology Group. J Clin Oncol. 2012;30:2635–40.

15. Callahan MJ, Poznauskis L, Zurakowski D, Taylor GA. Nonionic iodinated intravenous contrast material–related reactions: incidence in large urban children's hospital—retrospective analysis of data in 12 494 patients. Radiology. 2009;250(3):674–81.
16. Dillman JR, Strouse PJ, Ellis JH, Cohan RH, Jan SC. Incidence and severity of acute allergic-like reactions to iv nonionic iodinated contrast material in children. Am J Roentgenol. 2007;188(6):1643–7.
17. McHugh K, Disini L. Commentary: for the children's sake, avoid non-contrast CT. Cancer Imaging. 2011;11:16–8.
18. Scialpi M, Schiavone R, D'ANDREA AL, Palumbo I, Magli M, Gravante S, Falcone G, De Filippi C, Palumbo B. Single-phase whole-body 64-MDCT split-bolus protocol for pediatric oncology: diagnostic efficacy and dose radiation. Anticancer Res. 2015;35(5):3041–8.
19. Tomà P. Monophasic computed tomography for pediatric oncology using a split-bolus protocol: an unnecessary complication? Pediatr Radiol. 2017;47(3):366.
20. Weller A, Barber JL, Olsen OE. Gadolinium and nephrogenic systemic fibrosis: an update. Pediatr Nephrol. 2014;29(10):1927–37.
21. Kanda T, Ishii K, Kawaguchi H, Kitajima K, Takenaka D. High signal intensity in the dentate nucleus and globus pallidus on unenhanced T1-weighted MR images: relationship with increasing cumulative dose of a gadolinium-based contrast material. Radiology. 2014;270:834–41.
22. Murata N, Gonzalez-Cuyar LF, Murata K, Fligner C, Dills R, Hippe D, Maravilla KR. Macrocyclic and other non–group 1 gadolinium contrast agents deposit low levels of gadolinium in brain and bone tissue: preliminary results from 9 patients with normal renal function. Invest Radiol. 2016;51(7):447–53.
23. Solanki KK, Bomanji JB, Moyes J, et al. A pharmacological guide to medicines which interfere with the biodistribution of radiolabelled meta-iodobenzylguanidine (MIBG). Nucl Med Commun. 1992;13:51321.
24. Weiss AR, Lyden ER, Anderson JR, Hawkins DS, Spunt SL, Walterhouse DO, Wolden SL, Parham DM, Rodeberg DA, Kao SC, Womer RB. Histologic and clinical characteristics can guide staging evaluations for children and adolescents with rhabdomyosarcoma: a report from the Children's Oncology Group Soft Tissue Sarcoma Committee. J Clin Oncol. 2013;31(26):3226–32.
25. Gauguet JM, Pace-Emerson T, Grant FD, Shusterman S, DuBois SG, Frazier AL, Voss SD. Evaluation of the utility of 99mTc-MDP bone scintigraphy versus MIBG scintigraphy and cross-sectional imaging for staging patients with neuroblastoma. Pediatr Blood Cancer 2017;64(11).
26. Lee Chong A, Grant RM, Ahmed BA, Thomas KE, Connolly BL, Greenberg M. Imaging in pediatric patients: time to think again about surveillance. Pediatr Blood Cancer. 2010;55(3):407–13.
27. Gruden JF, Ouanounou S, Tigges S, Norris SD, Klausner TS. Incremental benefit of maximum-intensity-projection images on observer detection of small pulmonary nodules revealed by multidetector CT. AJR Am J Roentgenol. 2002;179(1):149–57.
28. Silva CT, Amaral JG, Moineddin R, Doda W, Babyn PS. CT characteristics of lung nodules present at diagnosis of extrapulmonary malignancy in children. Am J Roentgenol. 2010;194(3):772–8.
29. McCarville MB, Lederman HM, Santana VM, Daw NC, Shochat SJ, Li CS, Kaufman RA. Distinguishing benign from malignant pulmonary nodules with helical chest CT in children with malignant solid tumors. Radiology. 2006;239(2):514–20.
30. Sams CM, Voss SD. Imaging of the pediatric thymus and thymic disorders. In: Pediatric chest imaging. Berlin, Heidelberg: Springer; 2014. p. 327–48.

PET/CT in Pediatric Oncology

3

Lisa J. States and Stephan D. Voss

3.1 Introduction

Positron emission tomography (PET) combined with computed tomography (CT) has transformed the diagnosis, evaluation, and treatment of cancer in adults. In pediatric practice, PET/CT has evolved as an imaging technique and is increasingly becoming integral to the treatment of pediatric cancer patients [1]. Oncologic imaging with ^{18}F-fluorodeoxyglucose (FDG) is now considered standard of care for the diagnosis, staging, and posttreatment response assessments in both common and rare pediatric malignancies [2–4]. Factors that have contributed to the relatively slow early adoption and standardization of PET/CT practices in the pediatric population include the relative rarity of pediatric tumors, availability of PET/CT scanners, access to PET/CT scanners shared with adult practices, development of pediatric-specific protocols, and rapidly changing technology that has focused largely on the imaging needs of adult patients. Pediatric-specific challenges have included radiation dose concerns, intravenous contrast use, and impaired neurodevelopment related to the need for sedation/anesthesia. This chapter will focus on the use of FDG PET/CT and review the current technology, protocol options, normal variations in the pediatric patient, and present evidence-based literature for specific cancer types and tumor-like non-cancerous lesions. Multiparametric imaging and personalized medicine are drivers in the development of treatment protocols and technologic advances in hybrid PET technology and in the field of molecular imaging, which includes use of novel radiotracers and molecular imaging-based therapies, and will continue to drive development of enhanced PET/CT acquisition, processing, and quantitative data analysis techniques.

3.2 Technology

PET/CT is a hybrid imaging technology that continues to evolve [5]. Positrons emitted from PET tracers such as FDG annihilate on contact with electrons after traveling a short distance (~1 mm) within the body. Each annihilation event results in liberation of two 511 keV photons that travel in opposite directions, and the simultaneous or coincident detection of these photons is central to all PET imaging technologies. In conventional PET the coincidence detection electronics are

L. J. States
Department of Radiology, The Children's Hospital of Philadelphia (CHOP), Perelman School of Medicine, University of Pennsylvania, Philadelphia, PA, USA
e-mail: STATES@email.chop.edu

S. D. Voss (✉)
Department of Radiology, Boston Children's Hospital, Harvard Medical School, Boston, MA, USA
e-mail: Stephan.Voss@childrens.harvard.edu

S. D. Voss, K. McHugh (eds.), *Imaging in Pediatric Oncology*, Pediatric Oncology,
https://doi.org/10.1007/978-3-030-03777-2_3

used to determine the line of response (LOR) along which an annihilation event has occurred. With advances in detector technology and processing hardware, the development of time-of-flight (TOF) PET takes coincidence detection one step further, using measured differences in arrival times between the two emitted 511 keV photons to more precisely determine the approximate position of the annihilation event along the line of response (Fig. 3.1). Advances such as the development of time-of-flight techniques (which are available from all major vendors) contribute to improved image resolution and potentially decreased acquisition time. The increasing use of solid-state digital detector technology in place of conventional systems based on scintillator crystals such LSO and photomultiplier tubes [6] allows for further improvements in PET imaging

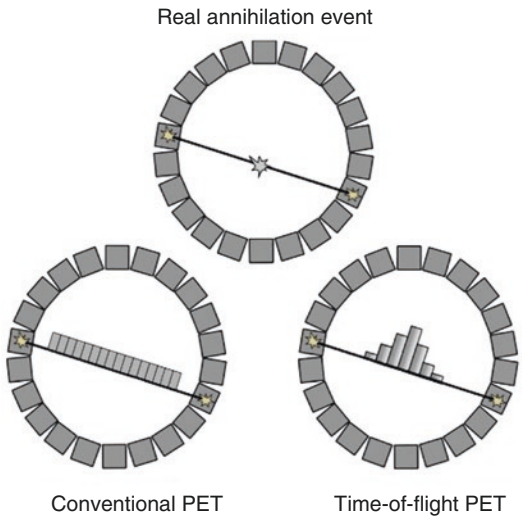

Fig. 3.1 Time-of-flight PET. Positron emission tomography (PET) is based on the principle of an annihilation event occurring when an emitted positron encounters a nearby electron, triggering the release of two opposed 511 keV photons originating from the point of annihilation. In conventional PET, the two photons travel along the line of response (LOR) from which an annihilation event has occurred. Coincidence electronics are used to determine the path along which a given event arose and with tomographic image reconstruction techniques, the approximate origin of the annihilation event can be determined from multiple LORs. Time-of-flight (TOF)-PET extends this principle, and by using measured differences in arrival times for the respective coincident photons, a more precise approximation of the point of annihilation can be determined along the line of response. Reproduced with permission from Vandenberghe et al. [6]

techniques. Options for the computed tomography (CT) component of hybrid PET/CT systems include multi-slice, multi-detector imaging up to 128 slices, allowing diagnostic quality CT images to be produced, single-source dual-energy imaging, and the use of continuous table motion in place of existing step-and-shoot mode PET acquisition techniques [7]. Future advances include a long axial field of view total-body PET capability (Fig. 3.2), with predictions of up to 40-fold gains in sensitivity, leading to enhanced lesion detection, reduction in artifacts, and significant decreases in overall scan duration [8, 9]. As with all hybrid imaging techniques, optimizing each component of the examination, i.e., both the PET scan and the CT scan, is essential for the success of this technique. It is well recognized that the acquisition and interpretation of integrated PET/CT examinations is superior to interpreting either the CT or PET study alone [10], capitalizing on both the increased sensitivity for lesion detection afforded by FDG PET and the specificity and correlative anatomic detail provided by CT, all of which are necessary for accurate lesion localization and characterization, and which are essential for disease staging, surgical management, and radiation treatment planning.

3.3 Radiopharmaceuticals

PET imaging in children, at present, primarily involves the use of ^{18}F-fluorodeoxyglucose (FDG), although a number of other radiopharmaceuticals are either in development or undergoing early-phase clinical testing in children. These include the DNA thymidine nucleoside analogue ^{18}F-FLT [11], neurotransmitter analogues ^{18}F-fluorodopa, ^{18}F-fluorodopamine [12], amino acid analogue ^{11}C methionine [13, 14], somatostatin receptor targeting peptides ^{68}Ga-DOTATATE [15] and ^{64}Cu-SARTATE [16], and ^{18}F-MFBG, targeting neuroendocrine/neuroblastoma tumors overexpressing the norepinephrine transporter (NET) [17].

FDG is a glucose analog, the uptake of which provides a measure of metabolic activity in the cell. In contrast to most normal tissues, the mechanism of glucose uptake in cancer cells

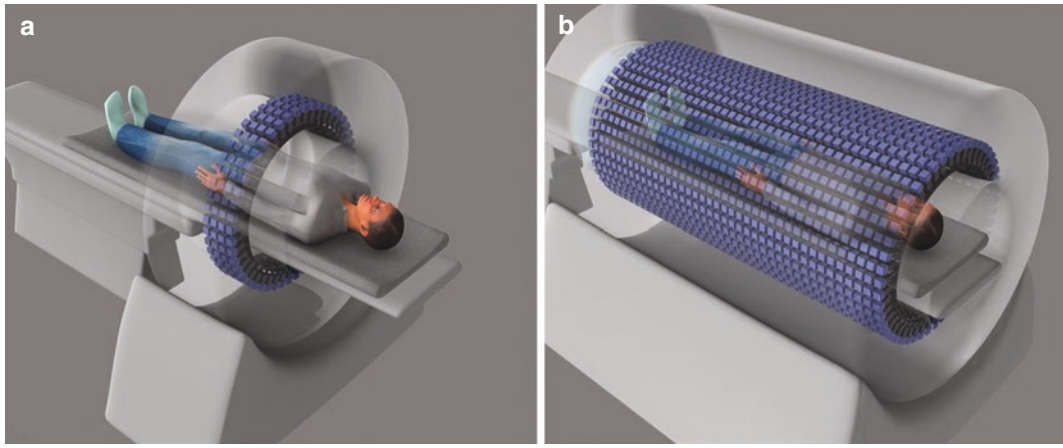

Fig. 3.2 Whole-body PET (**a**) vs. total-body PET (**b**). The principle of total-body PET is based on a scanner that encompasses and images the entire body within a single FOV, without requiring table movement and co-registration of multiple bed positions. A single acquisition FOV allows imaging of all the tissues and organs of the body simultaneously, and the increase in geometric coverage of total-body PET results in increased sensitivity, improved signal to noise, and potentially decreases in injected activity and scan length, all of which are important considerations in pediatric imaging. (Note: The first clinical total-body PET/CT scanner (uEXPLORER, United Imaging Healthcare) was recently cleared by the FDA for clinical use and will be available in the U.S. in 2019). Reproduced from Cherry et al. [9], with permission

does not require insulin. Just as with glucose, FDG is transported into cancer cells by a group of structurally related glucose transport (GLUT) receptors present on the cell membrane [18]. These receptors have been found to be upregulated in cancer cells and provide the malignant cells with continuous anaerobic glycolytic activity, known as the Warburg effect [19]. When the radiolabeled glucose analogue FDG is taken up by cancer cells, the FDG is phosphorylated by hexokinase as the first step in glycolysis. FDG cannot, however, enter the glycolytic pathway and is trapped, allowing high intracellular concentrations of FDG to accumulate within the cell. Together with the increased metabolic activity characteristic of tumors, the high levels of FDG retained in the cells results in the relatively intense patterns of FDG uptake characteristic of tumor PET imaging. FDG uptake is not specific for malignancy, and high levels of FDG uptake may also be seen with inflammatory cells, which—while nonspecific—can play a pivotal role in the body's ability to fight cancer. In addition, local factors, systemic treatment response, tumor physiology, presence of necrosis, and histopathology can all influence the amount of FDG taken up by the tumor.

3.4 Accuracy

The diagnostic and prognostic accuracy of FDG PET/CT is superior to conventional anatomic imaging [3, 4, 20]. In a recent comprehensive meta-analysis of FDG PET imaging in pediatric malignancy, the reported sensitivities and specificities of ^{18}F-FDG PET/CT for tumor staging ranged from 90–97% and 99–100%, respectively [4]. While these data referred primarily to the common pediatric malignancies such as lymphoma and small round blue cell neoplasms such as Ewing sarcoma, RMS, and LCH, they underscore the fact that PET/CT was found to be the accurate modality in the majority of cases, with the PET/CT results impacting clinical decision-making in a significant number of cases. In addition to providing a comprehensive whole-body survey of disease burden, FDG PET addresses problematic issues with conventional imaging, including defining local extension versus reactive edema, distinguishing residual nonviable soft tissue from tumor, and providing characterization of potential false-positive and false-negative lesions evaluated by conventional imaging techniques.

Treatment protocols using conventional anatomic imaging rely on size criteria as the primary

determinant of tumor stage, response to therapy, and presence of malignant lymphadenopathy. For the majority of non-lymphomatous solid tumors, the most commonly used criteria for assessing response to therapy are the RECIST criteria (Table 3.1) [21]. RECIST 1.1 provides a guideline for radiologists to choose, measure, and report target and nontarget lesions and lymph nodes, both at the time of initial staging and in response to therapy (see Chap. 9 for additional details). Target lesions are characterized by their single longest dimension, typically measured in the axial plane, although other planes (e.g. sagittal and coronal) are allowed, provided the images are acquired with isotropic resolution. Lymph nodes are characterized by their short axis; to be considered as measureable target lesions enlarged lymph nodes must have a short axis measurement of ≥ 15 mm. The tumor burden used for response determination is defined by the sum of these measurements from up to five representative target lesions. However, as has been highlighted by several recent reviews [22–24], there are many limitations to relying solely on changes in tumor size to assess response to therapy, particularly in the era of molecularly targeted and metabolically active agents, agents that have unequivocal antitumor activity, but that do not produce the immediate changes in tumor size that are typical of conventional cytotoxic agents.

In part to address these limitations, and in acknowledgement of the widespread use of FDG PET in oncologic imaging, a corresponding method for response assessment using PET has been proposed: the so-called PERCIST (PET Response Criteria in Solid Tumors) criteria (Table 3.1) [25, 26]. Based on the PERCIST criteria, which propose use of a consistent PET methodology to allow quantitative assessments of tumor response, target lesions characterized as having achieved a partial response (PR) to therapy show >30% decrease in FDG uptake based on standardized uptake value (SUV) measurements normalized to lean body mass, while progressive disease (PD) requires an increase in SUV of >30% relative to baseline or the presence of new lesions. Stable disease (SD) identifies those patients whose

Table 3.1 Brief summary of imaging response assessment criteria

	Complete response	Partial response	Stable disease	Progressive disease
RECIST	Complete disappearance of all target lesions Complete disappearance of all non-target lesions (if present)	Decrease of at least 30% in sum of the longest diameters of target lesions Non-target lesions (if present) either stable or complete response	Not meeting criteria for partial response or progressive disease Non-target lesions (if present) either stable or complete response	Increase of at least 20% in sum of longest diameters of target lesions, or presence of new lesions Unequivocal progression of non-target lesions
PERCIST	Decrease in FDG uptake similar to background blood pool	Reduction in peak SUV of at least 30%	Not meeting criteria for partial response or progressive disease	Increase in peak SUV of greater than 30% Presence of new lesions
iRECIST[a]	Complete disappearance of all target and non-target lesions	Decrease of at least 30% in sum of the longest diameters of target lesions	Not meeting criteria for partial response or progressive disease	Increase of at least 20% in sum of longest diameters of target lesions = iUPD (unconfirmed PD). If confirmed to be PD at next timepoint = iCPD; otherwise either iSD or iPR. PD if new lesions develop.

[a]iRECIST accounts for transient flares or apparent increases in target lesion size that accompany a robust immune response, followed by return to baseline (iSD) or showing further decrease in size (iPR)

Table 3.2 Response criteria for FDG-avid malignant lymphoma: Lugano classification

	Complete response	Partial response	Stable disease	Progressive disease
Soft tissue, nodal and extranodal sites	Deauville Score of 1, 2, or 3. Residual mass, nodal or extranodal sites may be present if FDG-negative	Deauville Score of 3 or 4. Residual mass(es) permitted provided the degree of FDG uptake is decreased compared to baseline	Deauville Score of 4 or 5, with no change in FDG uptake compared to baseline	Deauville Score of 4 or 5. Either increased intensity of FDG uptake (from baseline) at nodal or extranodal sites, new FDG avid foci compatible with lymphoma, or both.
Bone Marrow	No FDG avid marrow disease	Residual marrow uptake at baseline sites of disease; uptake is higher than normal marrow uptake but reduced compared to baseline. Persistent focal marrow findings to be evaluated by MRI, biopsy or close f/u	No change in bone marrow FDG uptake from baseline. No new marrow findings	New or recurrent FDG-avid marrow disease

disease does not meet either complete response (CR), PR, or PD criteria. This promising approach has not yet been validated and incorporated into routine practice in the pediatric population.

The use of functional imaging, initially with ^{68}Gallium citrate, and now with ^{18}F-FDG is the standard of care for staging and response assessment in pediatric Hodgkin [27, 28] and non-Hodgkin lymphoma [29, 30]. Multiple studies have confirmed the superiority of FDG PET for staging and assessing treatment response in pediatric lymphoma. Specific lymphoma response criteria have been proposed and widely adopted in both adult and pediatric practice. The so-called Lugano classification (Table 3.2) [31, 32] was established by the International Malignant Lymphoma Working Group, following many years of work, in an effort to standardize posttreatment response assessments in lymphoma patients and provide semiquantitative criteria for defining response both by PET and conventional imaging techniques.

The development of novel immunotherapeutic agents aimed at stimulating antitumor immune activity and providing improved survival via prolonged stable disease has also led to new response criteria that reflect the unique mechanisms by which these agents produce their antitumor responses. In particular, based on studies investigating cytokines, cancer vaccines, monoclonal antibodies, and immune checkpoint inhibitors, we have learned that measurable responses, both by conventional techniques and by PET, may take longer to achieve than for cytotoxic therapies and responses to immunotherapies (particularly with the checkpoint inhibitors) may occur after an initial apparent progression of disease. This so-called pseudo-progression is now well recognized in this treatment setting and is the basis for the iRECIST criteria for immune-based therapies (Table 3.1) [33, 34].

3.5 Image Analysis

In clinical practice, most analysis is based on a combination of qualitative visual assessment and assessment of semiquantitative FDG uptake (standardized uptake value, SUV) data. Visual analysis in most cases is adequate for the detection of metastatic lesions at the time of initial staging and as a baseline for assessing response to therapy. 3D-MIP images provide a rapid and comprehensive global assessment and provide PET imaging results that are the easiest to recognize and understand for non-imaging specialists. All other analyses of the PET imaging data, independent of the choice of radiopharmaceutical, should include a systemic and comprehensive review of all imaging data [1]. Images should be reviewed in axial, coronal, and sagittal planes, with and without fusion of the PET and CT data (Fig. 3.3). This should be done either on a dedicated nuclear medicine processing and viewing workstation or using a PACS-integrated nuclear medicine viewing functionality. Regardless of the viewing environment chosen, the PET fusion workstation should have adjustable and scalable

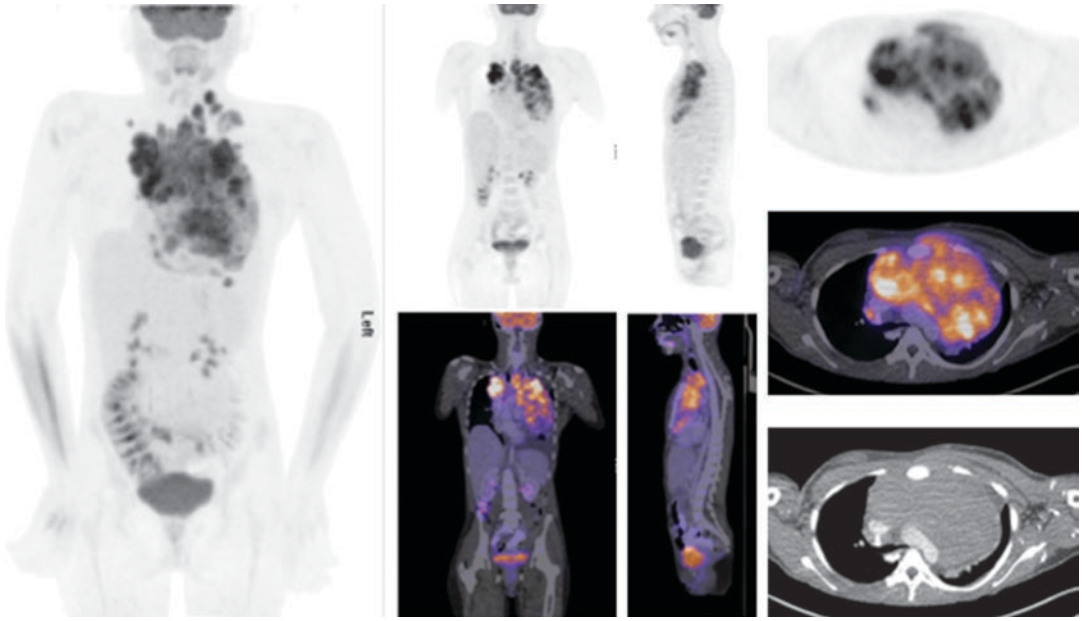

Fig. 3.3 PET/CT multimodality viewing workstation. The PET/CT viewing console should be configured to display the PET/CT as a 3-D MIP reconstruction, in addition to presenting the PET images in axial, sagittal, and coronal planes, both fused and unfused to the co-registered diagnostic or attenuation CT images. CT images should be reviewed separately at the PACS workstation

image thresholds and should be able to display fused images with different percentages of PET and CT blending. PET quantitation requires options for measuring SUV, both from single slices and from volumetric ROIs. The CT images should be viewed in soft tissue, bone, and lung windows. Review of non-attenuation corrected images may be helpful in the assessment of unusual foci of uptake or artifacts of reconstruction.

To the extent that tumor metabolic activity can be viewed as reflecting the relative aggressiveness of a lesion, in some settings higher levels of FDG uptake have been seen with more aggressive malignant lesions as compared with low grade or benign tumors [35–37], thus providing potential prognostic information regarding tumor type. There has been great interest in using semiquantitative analysis with SUV as a prognostic tool and imaging biomarker for tumor grade and aggressiveness by evaluating SUVmax at diagnosis [38]. Similarly, establishing SUV-based response criteria to guide response-based treatment decisions provides an attractive noninvasive means of determining which patients will benefit from continuation of treatment and which may benefit from alternative therapies. Semiquantitative methods to evaluate response to therapy include determining an absolute SUV_{max} cutoff value and tumor to background ratio at baseline as compared to post-therapy scans or simply using % change in SUV relative to baseline as indicative of response to therapy [39]. Dual-time-point imaging can potentially provide information regarding the aggressiveness of a lesion but is not realistic in routine practice due to workflow considerations [40]. Measurements of total lesion glycolysis and metabolic tumor volume may prove to be useful in characterizing the entire tumor rather than a representative region of interest; however, workflow considerations have hampered the incorporation of these rigorous quantitative methods into routine practice, and they remain investigational.

3.6 Patient Preparation

3.6.1 Precautions

In many institutions part of the standard procedure is the determination of lack of pregnancy prior to

injection in menstruating females. A urine or serum pregnancy test is recommended by the SNMMI as part of the Standard Procedure Guideline for General Imaging (although not specifically for PET/CT), while published EANM guidelines do not specifically recommend pre-procedure pregnancy testing in all patients, with the caveat that in Europe national guidelines may apply [41]. In two studies of women being staged for malignancy during pregnancy estimates of absorbed dose to the fetus from the ^{18}F-FDG were low, "below the threshold for non-cancer health effects throughout pregnancy" [42] and "significantly below the threshold dose for deterministic effects due to radiation exposure" [43]. Inasmuch as the guidelines do not provide specific recommendations, different centers should develop their own respective procedural requirements based on institutional policy. For example, at Boston Children's Hospital all post-menarchal female patients age 12 and older undergo urine pregnancy testing prior to the PET/CT exam only if they are also having a diagnostic CT of the abdomen or pelvis; pregnancy tests are not obtained for routine PET/CT studies. In contrast, at the Children's Hospital of Philadelphia (CHOP) pregnancy tests are routinely conducted on all PET/CT patients aged 10 and older.

3.6.2 Preparation

The main objective of patient preparation for FDG PET imaging is to insure that both circulating insulin and blood glucose levels are low. As noted earlier, uptake of glucose by metabolically active tumor cells is not insulin dependent; increased serum glucose and insulin levels result in non-specific uptake of FDG by non-tumor cells, thereby reducing the sensitivity of the PET examination (Fig. 3.4). Standard guidelines recommend NPO status for at least 4 h prior to injection, with no other exogenous sources of glucose, such as dextrose in IV fluids or tube feeds. Non-caloric artificial sweeteners such as Nutrasweet® can also stimulate insulin secretion and are contraindicated [44]. Strenuous activity should be avoided during the 24 h prior to arrival, as this has been shown to result in high levels of skeletal muscle uptake (Fig. 3.4). Blood glucose should be <200 mg/dL prior to injection. In most cases having the patient void prior to starting the exam is sufficient to eliminate excreted FDG in the bladder. For infants undergoing sedation, or if a pelvic mass is the focus of concern, catheterization of the bladder may be indicated.

Another focus of preparation is aimed at reducing the uptake of FDG into brown adipose tissue (BAT), which is more common in adolescents than adults or younger children [45]. Brown adipose tissue can be seen in up to one third of patients [44] undergoing FDG PET imaging and can compromise lesion detection and characterization (Fig. 3.4). Methods used to decrease BAT should be as noninvasive as possible, and in many instances simply insuring adequate warming of the patient 30 min prior to and during the 60-min FDG uptake period may be sufficient [46]. Arrival in warm clothes and being placed in a warm uptake room with warm blankets has been shown to be effective. A warm towel can be placed around the neck. Medications that have been found to be effective in inhibiting BAT include short-acting opioids such as fentanyl, benzodiazepines such as midazolam (Versed) or diazepam (Valium), or beta-blockers such as propranolol [44, 47], although in practice this may not be practical for institutions in which administration of such agents is under the supervision of sedation and anesthesia services.

The overall process of preparing the patient, including the uptake room environment, should be focused on decreasing the anxiety of the child. Child life specialists and technologists can also make a significant difference in reducing anxiety in older children, which may result in the exam being completed without sedation or anxiolytics, although children younger than 6 years of age typically require sedation.

Pediatric consensus guidelines for performing the PET portion of the PET/CT examination have been published and are widely accepted [48]. However, because of differences in scanner technology, technologist and physician training, child age and indications for the examination, and institutional practice, it has been challenging to implement a universally accepted CT scanning protocol that could be integrated into the PET/CT examination for pediatric patients. All PET/CT examinations utilize the CT for photon attenuation correction (AC CT); however, the degree to which this AC CT can

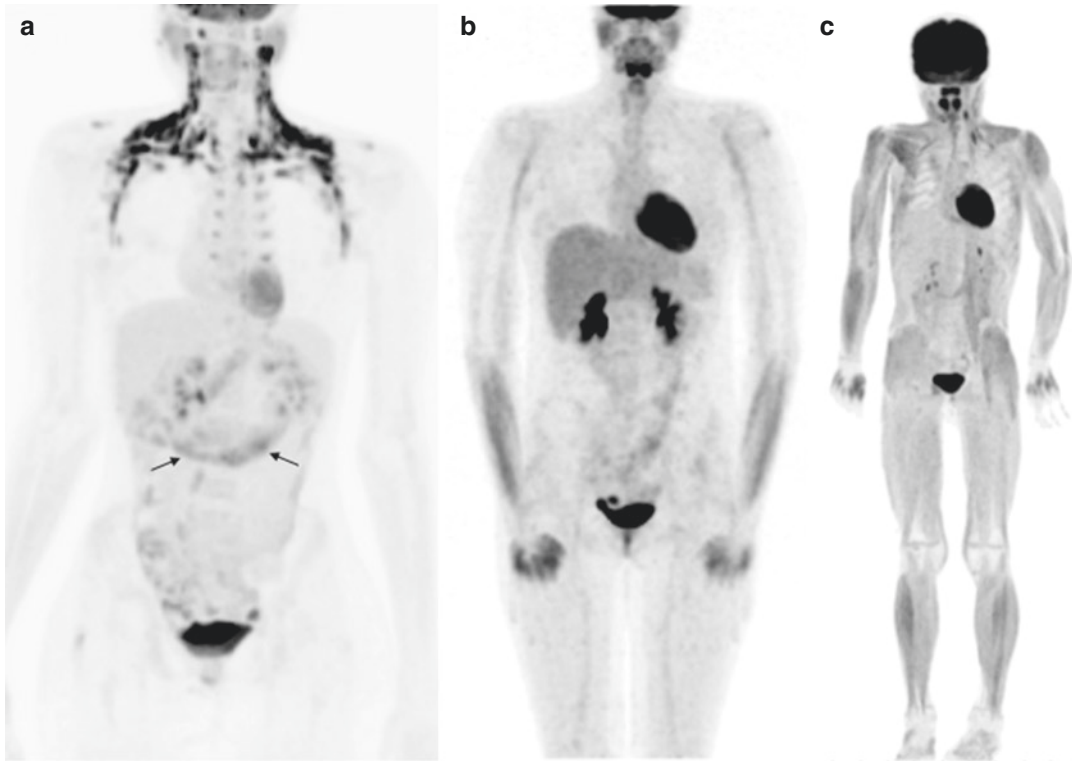

Fig. 3.4 Brown adipose tissue and skeletal muscle uptake. (**a**) 17-year-old with DSRCT of the abdomen/peritoneal cavity, with multiple sites of nodal involvement at diagnosis. A f/u scan after two cycles of chemotherapy shows an excellent metabolic response at prior sites of disease (arrows), but the examination in the neck and upper thorax is limited by extensive brown fat uptake. (**b**) 16-year-old with Ewing sarcoma of the mandible. Diffuse muscle uptake is related to recent vigorous exercise prior to the PET examination. (**c**) 7-year-old with metastatic Ewing sarcoma undergoing off-therapy evaluation. The scan is nondiagnostic secondary to diffuse muscle uptake, related to the patient having eaten less than 4 h prior to the exam. Serum glucose levels were normal, but postprandial insulin levels were likely still sufficiently high to drive FDG uptake into muscle

also be used for diagnostic purposes will depend on the CT dose, as well as other acquisition parameters, such as the use of IV contrast material. In general, the ALARA principle should be adhered to; various CT protocols have been described for PET/CT imaging [1, 5, 49] and include:

- Lowest-dose non-contrast CT (NCCT) for attenuation correction only
- Low-dose NCCT for attenuation correction and anatomic localization
- Low-dose NCCT for attenuation correction combined with diagnostic contrast-enhanced CT (CECT) on same scanner
- Diagnostic quality CECT for both attenuation correction and anatomic localization

The CT scanner tube current (mA) and peak voltage (kVp) vary with intended use and anatomic site imaged. For an attenuation correction-only CT, the effective mAs can be as low as 10–30 mAs [50], depending on patient size and vendor options. Alessio et al. have proposed comprehensive weight-based whole-body protocols using the NCCT for attenuation correction and anatomic localization, with the CT dose optimized to reduce the effective dose to the patient, while preserving image quality [51]. They propose a kVp of 120 with variable mAs settings, ranging from 10 to 40 based on patient weight. While this approach complies with the ALARA principal, it results in 11 distinct weight-based PET/CT protocols, which may not be practical in

many institutions. We have chosen a modification of the Alessio protocol, using a weight-based protocol with 55 kg as the cutoff between small and large child. For children >55 kg, the AC CT is performed at 120 kVp, with a reference mAs of 35 mA. For smaller children weighing less than 55 kg the AC CT is performed at 100-120 kVp, but with a reference mAs of 20 mA. In all cases, automatic tube current modulation is activated to further optimize the mA and adapt the AC CT exam to account for tissues with large differences in attenuation, such as the chest, abdomen, and pelvis, which are included in nearly all PET/CT exams. Further reductions in kVp are also possible for small children but may result in underestimation of the linear attenuation coefficient for the 511 keV PET photons and lead to attenuation correction artifacts [50].

At many institutions, the protocol chosen will depend on whether a diagnostic study has already been performed. For example, if a diagnostic contrast-enhanced CT has already been performed, an attenuation correction only CT may be sufficient. If a diagnostic study has not been performed, a diagnostic CT can be obtained as part of the PET/CT exam and serve both as the attenuation correction CT and the anatomic co-localization CT. This provides the necessary diagnostic quality cross-sectional imaging needed, but avoids repeat CT imaging over the same anatomic region of interest, thereby reducing the unnecessary radiation exposure from duplicate CT examinations. The use of intravenous contrast media for the low-dose attenuation correction CT can improve the quality of the AC CT examination (Fig. 3.5) and in many cases may provide sufficient anatomical information to obviate the need for a dedicated diagnostic quality CT [1], although the routine use of intravenous contrast for all PET/CT examinations is not standard practice in most centers. A novel approach implemented at several pediatric hospitals, referred to as a multiseries PET/CT exam, uses a combination of CT techniques, depending on the area of concern. For example, a PET/CT examination of the torso for follow-up of stage 2 Hodgkin lymphoma with cervical and mediastinal disease could be performed with a diagnostic quality CECT in the neck and chest, combined with a low-dose localization only AC CT in the abdomen and pelvis (Fig. 3.6) [1, 49]. These options can have a significant impact on radiation dose delivered, in addition to providing diagnostic quality CT data to aid in co-localization of abnormalities identified on the PET examination. Further discussion and collaboration are necessary to provide a standardized approach to pediatric PET/CT imaging.

3.7 Normal Physiologic Patterns of Uptake and Variations

Normal physiologic uptake patterns in children are well recognized (Table 3.3) [44, 52] and vary with age, activity, or diet or may be related to therapy. Normal uptake can be seen in the lymphatic tissue of Waldeyer's ring—the tonsils and adenoids, the cervical lymph nodes, and lymphoid follicles in the terminal ileum. Patterns of uptake unique to children include oral muscle and pharyngeal uptake due to pacifier use and diaphragm and intercostal muscle uptake due to crying, along with activity in the vocal cords (Fig. 3.7). Toddlers may have extremity muscle uptake due to physical activity the day before the scan or during the uptake period. The use of smart phones and other distracting devices commonly results in upper extremity muscle uptake. Asymmetric lower extremity uptake may be seen with altered weight bearing due to limp, presence of a lower extremity prosthesis, or pain. Uptake patterns in the shoulder girdle can be related to crutches or a heavy backpack. Alterations in uptake related to physical activity resulting in diffuse uptake in the muscles may obscure local pathology and limit the sensitivity of the scan (Fig. 3.4). Diffuse muscle uptake can also be seen with steroid therapy, carbohydrate load, or meal within 4 h of FDG administration (Fig. 3.4) [44].

Many benign bone lesions unique to the pediatric age group have been shown to be FDG avid. The list is long and includes benign bone lesions, such as non-ossifying fibroma, fibrous cortical defect, fracture, and fibrous dysplasia, which have pathognomonic radiographic features, as well as other more aggressive lesions such as osteomyelitis.

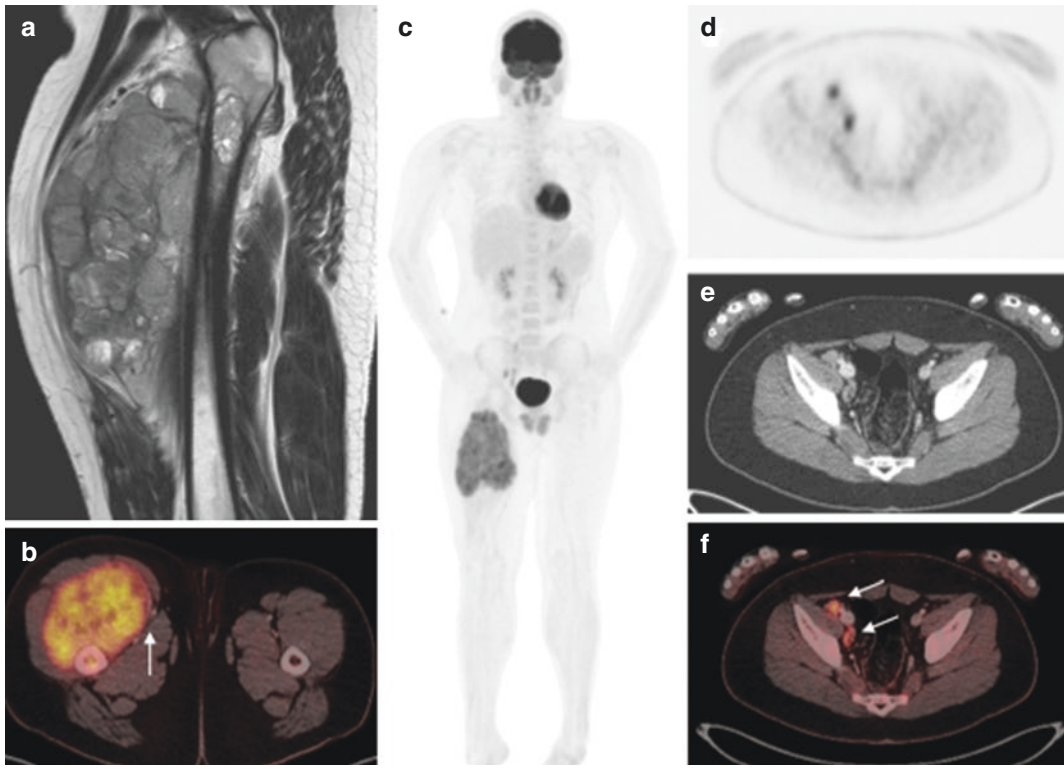

Fig. 3.5 Contrast-enhanced attenuation correction CT. Fifteen-year-old with newly diagnosed rhabdomyosarcoma of the right thigh. MRI (**a**) and PET/CT (**b**–**f**) with contrast-enhanced low-dose attenuation correction CT, which nicely delineates right external iliac nodal uptake from adjacent vessels (**f**, arrows) and complements the earlier MRI examination by showing the relationship of the tumor mass to the femoral vasculature (**b**, arrow)

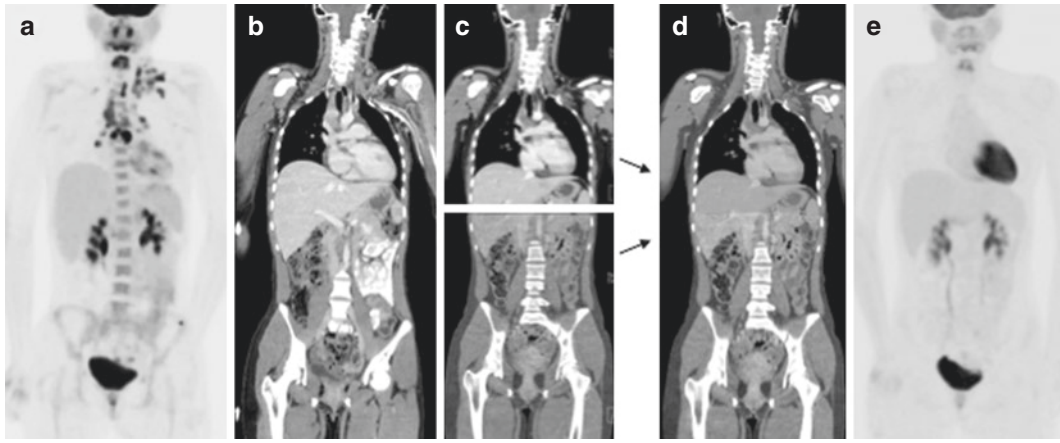

Fig. 3.6 Multi-series PET/CT. Stage 2A nodular sclerosing Hodgkin lymphoma, with neck MRI at outside facility for left lower neck adenopathy; biopsy showed HL. Staging FDG PET (**a**) and diagnostic CT (**b**) show left supraclavicular, anterior mediastinal, paratracheal, hilar, and subcarinal disease, consistent with stage 2 disease. Post-cycle two PET/CT using multi-series technique (**c**, **d**) merges a diagnostic quality neck and chest CT with low-dose AC CT of the abdomen and pelvis to yield a composite CT image composed from both the diagnostic and AC CT data. The merged CT (**d**) is used for diagnostic interpretation and attenuation correction of the accompanying FDG PET scan (**e**) and reveals a complete metabolic response to therapy

Table 3.3 Normal uptake and pitfalls

Location	Etiology
Diaphragm	Crying
Ovaries, endometrium	Menstrual cycle specific
Testes	Normal heterogeneous uptake
Facial uptake	Steroids with induction chemotherapy
Marrow, spleen uptake	Cytokines, therapy with G-CSF/GM-CSF, anemia
Photopenic bones	Radiation therapy, treated disease
Surgical scar uptake	Granulation tissue/healing
Thymus uptake	Thymic rebound
GI uptake	Graft vs. host disease, clostridium difficile, Neutropenic typhlitis, esophagitis, gastritis
Terminal ileum, appendix	Lymphoid follicles
Bowel	Peristalsis, swallowed radiotracer
Breast tissue	Puberty
Brain	Varies with age
Thyroid	Normal, thyroiditis, focal lesion, e.g. papillary thyroid cancer (PTC)
Bones	Benign bone lesions (see text)

Diffusely increased activity in the axial skeleton, proximal extremities, and spleen can be seen in the setting of anemia, due to physiologic stimulation of the marrow. Diffuse bone marrow uptake of FDG is also commonly seen in patients with Hodgkin lymphoma and is thought to be related to the generalized inflammatory state (elevated ESR, CRP levels) present at the time of diagnosis [53] and should not be interpreted as diffuse infiltration of the bone marrow by lymphoma (Fig. 3.8). Uptake in focal bone or bone marrow lesions is typically distinctive and easily distinguished from the surrounding low-level diffuse marrow uptake (Fig. 3.8). A diffuse FDG uptake pattern of marrow activation can also be seen following treatment with colony-stimulating factors such as granulocyte colony-stimulating factor (G-CSF; Neulasta®), and photopenic foci on post-therapy scans may be related to radiation therapy or sites of treated disease (Fig. 3.9). In order to reduce the confounding effect of treatment-related changes on the PET scan, consensus guidelines recommend

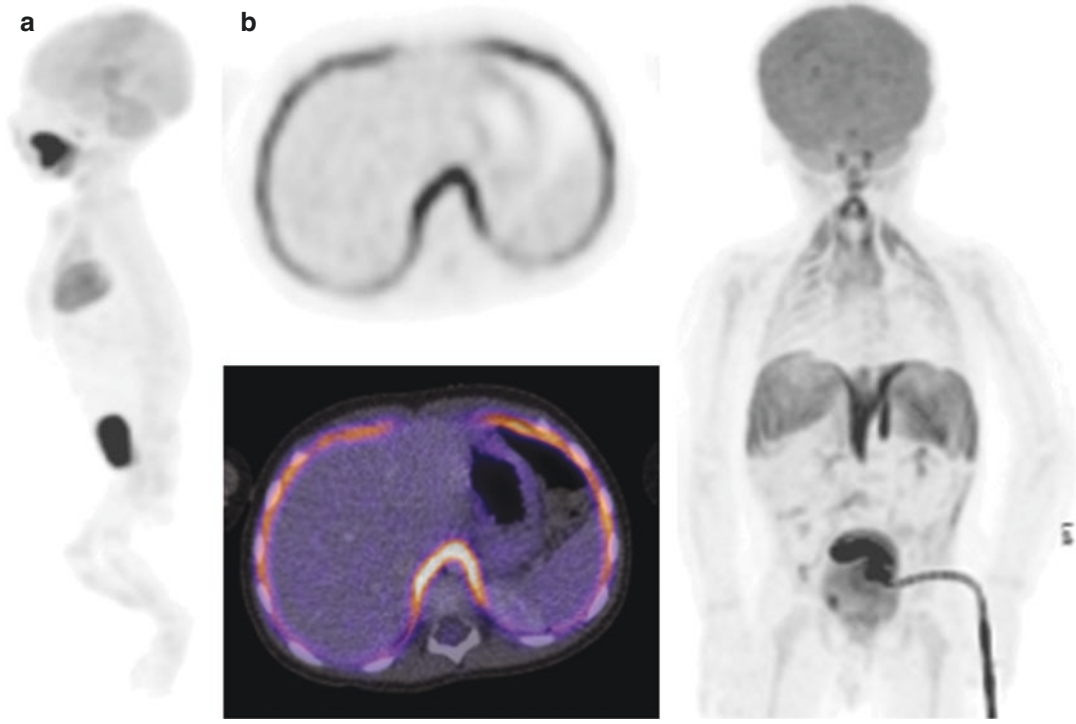

Fig. 3.7 Physiologic patterns of uptake. (**a**) Focal uptake in the tongue related to vigorous sucking on a pacifier during the uptake period. (**b**) Diffuse diaphragmatic and intercostal muscle uptake in an inconsolable 28-month-old child with bladder rhabdomyosarcoma, crying throughout the uptake period

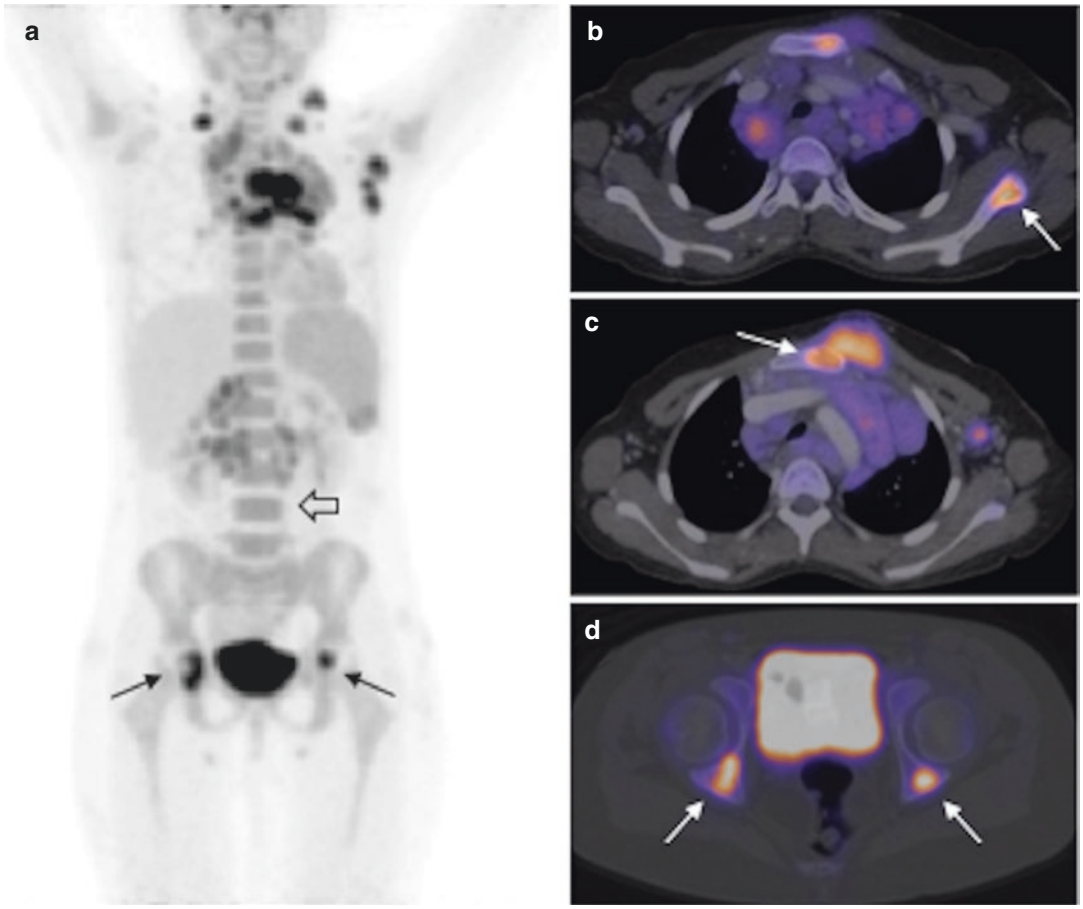

Fig. 3.8 Hodgkin lymphoma staging. FDG PET/CT and diffuse vs. focal bone uptake. Eleven-year-old with stage 4 Hodgkin lymphoma (HL) with mediastinal adenopathy, focal osseous lesions in both acetabula (**a**, **d**, arrows), sternum (**c**, arrow), and left scapulae (**b**, arrow) which have patterns of focal uptake that are distinct from the diffuse bone marrow uptake commonly seen at diagnosis throughout the axial skeleton in HL (open arrow), the latter of which is presumed to be related to a generalized heightened inflammatory state

an interval of at least 2–3 weeks following completion of the last cycle of chemotherapy and 3 months following completion of radiation therapy before follow-up PET imaging is performed [41, 54]. A questionnaire completed by the parents on the day of imaging should include the time and date of most recent chemotherapy, radiation therapy, and surgery to aid in the interpretation.

Normal physiologic uptake can be seen at the gastroesophageal junction, in the stomach, or scattered throughout small bowel and colon. A more diffuse pattern of uptake in the esophagus, stomach, and colon is often related to inflammation due to complications of therapy such as esophagitis or graft-versus-host disease (GVHD). Sharp et al. described a transient pattern of altered FDG uptake in the superficial soft tissues and reduced hepatic uptake in 6/11 children with lymphoblastic lymphoma 1 month after initiation of induction chemotherapy and high-dose steroids [55]. Other treatment-related effects can be seen, such as diffuse colonic uptake related to infectious or inflammatory colitis, or following immunotherapy with checkpoint inhibitors (Fig. 3.10), or focal nodal uptake related to recent immunizations, and knowledge of the patient's treatment history is crucial.

Another common finding in the pediatric patient is thymic rebound. Thymic rebound or

Fig. 3.9 G-CSF (Neulasta) stimulated reactive bone marrow. Five-year-old with Ewing sarcoma of the left humerus (arrows), showing intense uptake in primary tumor at baseline (**a**), and after three cycles of induction chemotherapy and G-CSF, showing diffuse marrow stimulation from G-CSF but no uptake in the bone marrow at the original site of primary tumor involvement (**b**)

benign thymic hyperplasia was first described in children after treatment of childhood tumors [56] and occurs following episodes of physiologic stress. Thymic rebound is defined by regrowth of thymic tissue up to 50% greater than baseline. With the advent of FDG PET, it was noted that normal thymic uptake on FDG PET scan is common in children younger than 10 years of age prior to therapy and can usually be distinguished from pathologic uptake associated with a mediastinal mass [52]. In the oncology patient, thymic rebound is most commonly seen after completion of chemotherapy but can also occur as a result of stress due to surgery or radiation therapy [57].

3.8 FDG PET in the Management of Specific Pediatric Cancers

FDG PET/CT imaging is increasingly being used for the management of many pediatric malignancies. Table 3.4 provides a brief summary of typical patterns of disease spread for the most commonly encountered pediatric cancers. An exhaustive discussion of the role that PET plays in staging, monitoring treatment response, and detecting recurrence in each of the many pediatric cancers is beyond the scope of this chapter, and the reader is referred both to the primary literature pertinent to the specific malignancies and to recent comprehensive reviews of the value of PET/CT in pediat-

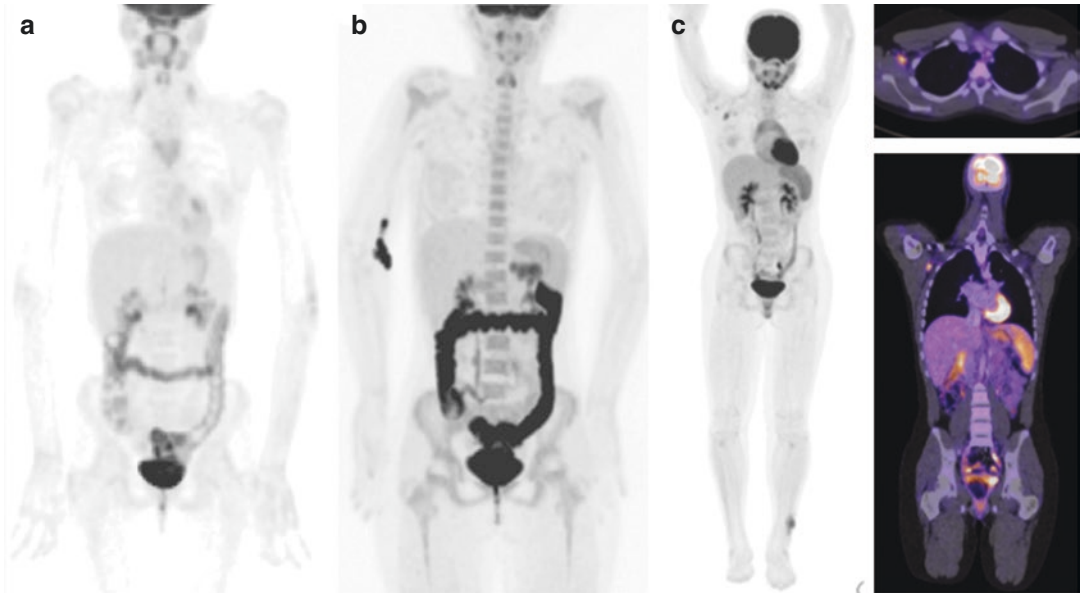

Fig. 3.10 Treatment-related causes of FDG-uptake. (**a**) 13-year-old with scalp melanoma, on the PD-1 inhibitor Nivolumab, known to result in diffuse colonic inflammation and FDG uptake. (**b**) Teenage patient with new-onset colitis and concern for lymphoma, showing diffuse colonic uptake related to colitis. (**c**). Fourteen-year-old with distal fibular Ewing sarcoma. Staging PET/CT shows primary lesion in the left fibula and FDG-avid lymph nodes in the right axilla. Upon further questioning, the patient had received a flu vaccine in the right arm just days prior to the PET scan

Table 3.4 Typical patterns of spread

	Lymph node	Marrow	Cortical/osseous	Lungs	Peritoneum	Vascular
Osteogenic sarcoma			x	x		
Rhabdomyosarcoma	x	x	x	x		
Ewing sarcoma/PNET		x	x	x		
Germ cell- chest/mediastinum	x			x		
Germ cell- abdomen/pelvis	x			x	x	
Gastrointestinal stromal tumor					x	
Hepatoblastoma				x	x	x
Wilms tumor	x			x	x	x
Hodgkin disease	x	x		x		
Non-Hodgkin lymphoma	x	x	x	x		
Neuroblastoma	x	x	x	x	x	x

ric oncology [4, 58, 59]. What follows is a brief summary of the role PET imaging plays in the most common pediatric cancers.

3.8.1 Lymphoma

The use of FDG PET imaging in the treatment of children with lymphoma is now considered standard of care and has provided clinicians and researchers alike with a reproducible, reliable method for initial staging, evaluation of treatment response, and response-based modifications of therapy. FDG PET is more sensitive and specific, as compared to conventional imaging with CT, in the detection of nodal and extranodal disease, splenic involvement, and bone marrow disease [28]. In the USA, staging bone marrow aspirates are still included in most protocols to assess for bone marrow involvement. European investigators, however, now rely on FDG PET imaging to determine the presence of bone

marrow involvement based on several studies showing both sensitivity and accuracy of PET in identifying sites of marrow involvement [60, 61].

FDG PET/CT is increasingly being used to predict response and to guide response-based treatment decisions following initial chemotherapy. Many studies have now shown that early metabolic responses after two cycles of chemotherapy correlate with outcome and the so-called post-cycle 2 PET/CT is now being used to predict response to therapy, guide radiotherapy decisions, and stratify treatment. In contrast to the metabolic response to therapy, changes in tumor size, measured either by CT or MRI, are not predictive of outcome [28]. Indeed it is common to encounter Hodgkin lymphoma patients with large bulky FDG-avid mediastinal tumors at diagnosis who achieve a complete metabolic response after just two cycles of chemotherapy, despite having a significant residual non-avid mediastinal mass (Fig. 3.11). Whether FDG PET responses alone can dictate treatment decisions,

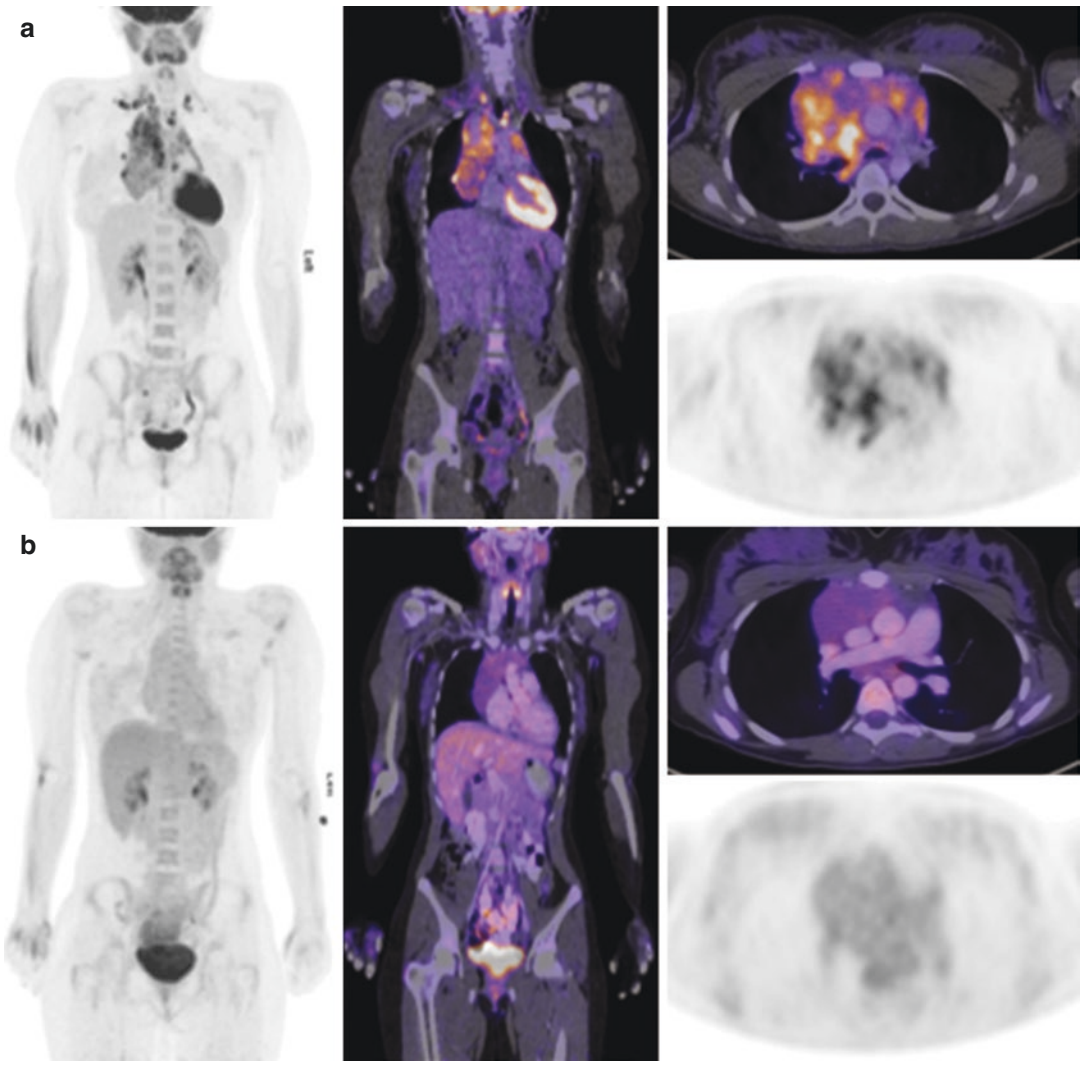

Fig. 3.11 PET/CT in Hodgkin lymphoma. Eighteen-year-old female with stage 4 nodular sclerosing Hodgkin lymphoma with bulky mediastinal, supraclavicular, and hilar adenopathy at diagnosis (panel **a**). After two cycles of chemotherapy (panel **b**), there is only faint uptake in the residual mediastinal mass, the degree of which is below the level of background liver uptake (Deauville 3), consistent with a complete metabolic response to therapy

in particular reductions in therapy for "good responders," or whether both changes in tumor size and metabolic activity better correlate with outcome is under investigation.

As more investigators began to incorporate PET imaging into response-based treatment algorithms, it became clear that establishing criteria for interpreting PET findings was needed. The Lugano classification [31, 32] is now widely used in the evaluation of malignant lymphoma and was established by consensus of an international working group, in an effort to standardize post-treatment response assessments in lymphoma patients. The Lugano classification provides for both CT and MRI-based response criteria (Table 3.2) and establishes a semiquantitative 5-point scale (the Deauville scale, Table 3.5) for determining responses based on FDG PET, using mediastinal blood pool and hepatic uptake to define normal levels of background FDG activity. By providing easily implemented visual criteria (SUV-based assessments are not used) for classifying FDG uptake as representative of disease versus normal background, the Lugano criteria have been widely accepted and incorporated into both pediatric and adult practice. At baseline, diagnostic quality CT or MRI images of the torso are obtained, with coverage including Waldeyer's ring of lymphoid tissue in the neck and extending through the inguinal nodal basin; the PET imaging field of view should provide the same coverage. Some investigators have advocated for whole-body PET imaging in lymphoma so as not to miss peripheral sites of disease [62], but in practice most centers rely on so-called "eyes-to-thighs" imaging for their lymphoma patients. At the time of interim response assessment, the diagnostic CT coverage may be limited to initial sites of disease. For example, in a patient with stage 2 Hodgkin lymphoma, follow-up imaging need not include diagnostic CT or MRI imaging of the abdomen and pelvis; rather the diagnostic CT coverage can be limited to the neck and chest. As noted above, use of a multi-series PET/CT acquisition can further reduce radiation exposure by eliminating duplicate scanning over the same anatomic regions (Fig. 3.6).

Table 3.5 Deauville criteria for interim FDG-PET assessment

Score	Description of FDG uptake findings
1	No FDG uptake above surrounding background
2	FDG uptake is less than or equal to mediastinal blood pool
3	FDG uptake is greater than mediastinal blood pool but less than or equal to liver
4	Moderate increase in FDG uptake, greater than liver
5	Marked increase in FDG uptake, greater than liver

The use of FDG PET/CT in the management of non-Hodgkin lymphoma (NHL) is also standard of care; however, the heterogeneous nature of NHL has made it more difficult to standardize the use of PET/CT in the various treatment algorithms. For example, T-lymphoblastic lymphoma and Burkitt lymphoma often present acutely with rapidly growing tumors that can result in critical airway compromise, vascular occlusion, and acute abdominal symptoms, which precludes the use of PET/CT for initial staging. For other tumors such as diffuse large B-cell lymphoma or ALCL, PET imaging can be effective in determining response to initial chemotherapy and is being incorporated into many treatment algorithms (Fig. 3.12). A complete discussion of posttransplant lymphoproliferative disease (PTLD) is beyond the scope of this review, but inasmuch as PTLD represents a premalignant lymphoma-like proliferation and can degenerate into a Burkitt-like lymphoma, the use of PET imaging for patients suspected of developing PTLD, and in the management of patients being treated for PTLD has been shown to be effective in staging, establishing disease burden, and in guiding therapy (Fig. 3.13). As with HL, response criteria for NHL have been proposed [29, 30]. These incorporate FDG PET imaging results, anatomic imaging, and other clinical criteria into the overall response assessment and acknowledge the challenge of establishing a single set of criteria for all non-Hodgkin lymphomas. These challenges aside, FDG PET imaging plays a crucial role in the management of NHL and when feasible should be incorporated into all NHL staging and response assessments.

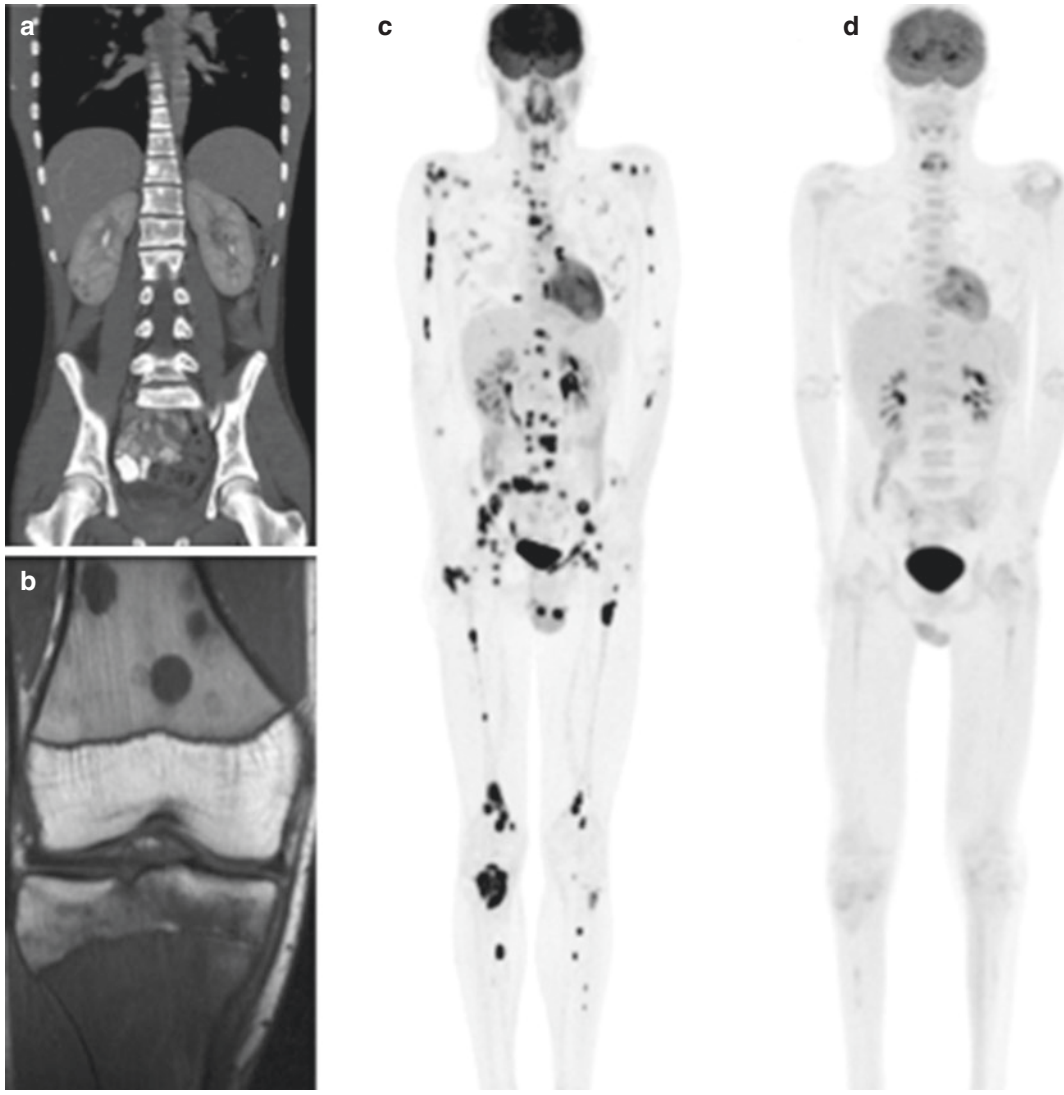

Fig. 3.12 FDG PET/CT in non-Hodgkin lymphoma. Fifteen-year-old with Crohn's disease, on immunosuppression with knee pain. CT (**a**), and MRI (**b**) showed multiple osseous lesions, renal lesions, and diffuse marrow replacement. Biopsy confirmed DLBCL. Staging PET (**c**) shows widespread osseous disease, extensive nodal disease, and multiple renal lesions. Restaging after four cycles of chemotherapy showed complete response to therapy (**d**)

3.8.2 Sarcoma

3.8.2.1 Soft Tissue Sarcomas

Rhabdomyosarcoma is the most common soft tissue tumor in children. Compared to adults, children have a more favorable prognosis [63]. Prognostic factors include patient age, histologic type, primary site of disease, local/regional spread, and distant metastases [64]. Staging includes CT or MRI of the primary tumor site, chest CT and bone marrow aspirate. If available, FDG PET is the imaging study of choice for detection of lymph node (LN) metastases and a whole-body screen, vertex to toes, for cortical bone and marrow metastases. Locoregional or "sentinel" lymph nodes are the most common site of tumor spread, particularly for extremity tumors, followed by metastatic spread to the lungs. Although FDG-avid hypermetabolic lymph nodes may be reactive, PET imaging plays

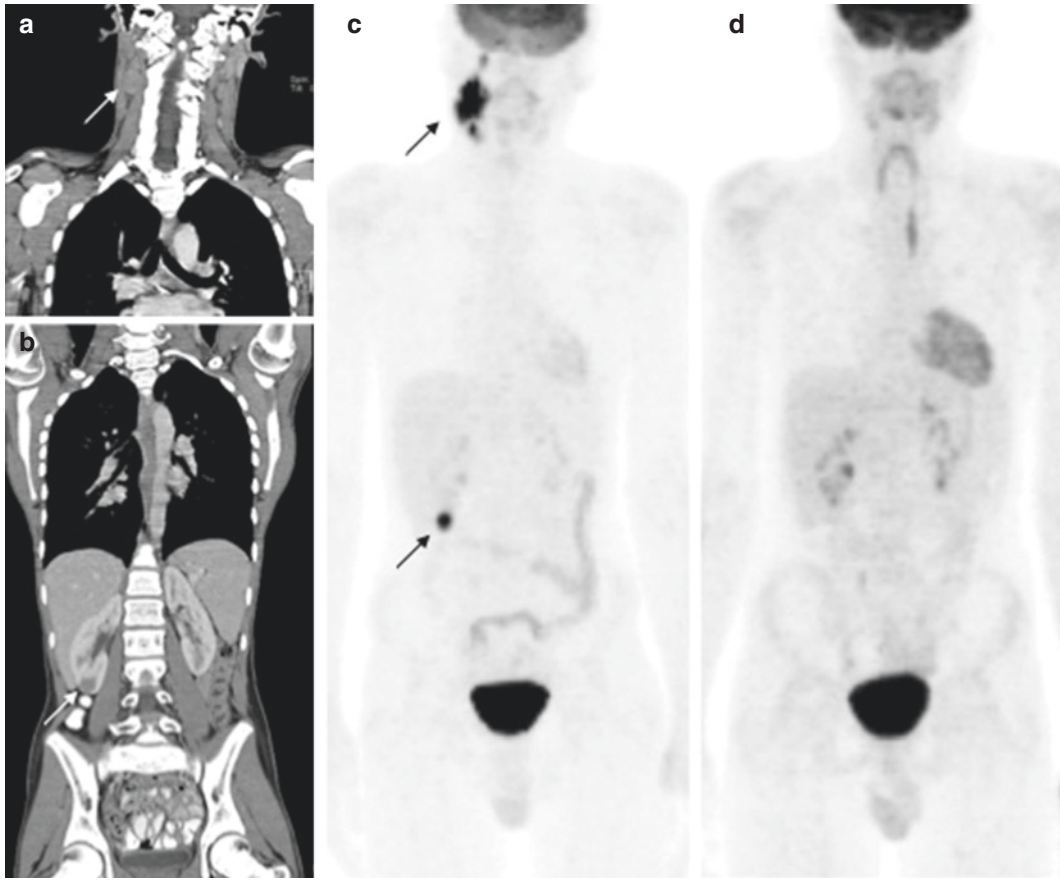

Fig. 3.13 FDG PET/CT and PTLD. Eleven-year-old s/p heart transplant with palpable neck nodes (**a**) and CT showing renal lesion (**b**, arrows). PET/CT (**c**) shows FDG-avid cervical lymph node enlargement and right lower pole FDG-avid renal lesion, all compatible with the diagnosis of PTLD. After two cycles of rituximab, no residual FDG-avid disease is demonstrated (**d**)

an important role in identifying potential sites of regional lymph node involvement and contributes to preoperative planning for intraoperative lymph node dissection and/or postoperative local control [65]. The presence of lymph node metastasis impacts outcome, and survival can be improved by intensification of therapy and irradiation of the affected region [64]. Lymphoscintigraphy is still used for intraoperative localization of sentinel lymph nodes and may complement PET imaging for guiding sentinel lymph node biopsy (Fig. 3.14) [66, 67]. The presence of pulmonary metastases also impacts survival in this patient group, and dedicated chest CT remains the imaging study of choice for detection of pulmonary metastases [65–67].

Non-rhabdomyomatous soft tissue sarcomas are rare and include desmoplastic sarcoma, malignant rhabdoid tumor, synovial sarcoma, undifferentiated sarcoma, and angiosarcoma. FDG PET imaging is not yet routinely performed as a standard part of staging and response evaluations but in selected cases has been found to be useful in determining extent of disease and metastases at diagnosis, response to therapy, and recurrence [68]. Non-rhabdomyomatous tumors of the head and neck in children include nasopharyngeal carcinoma (NPC), adenoid cystic carcinoma, and mucoepidermoid tumor. Cheuk et al. compared FDG PET with MRI in 18 children with NPC and found FDG PET to be useful in the evaluation of response to therapy, and in patients

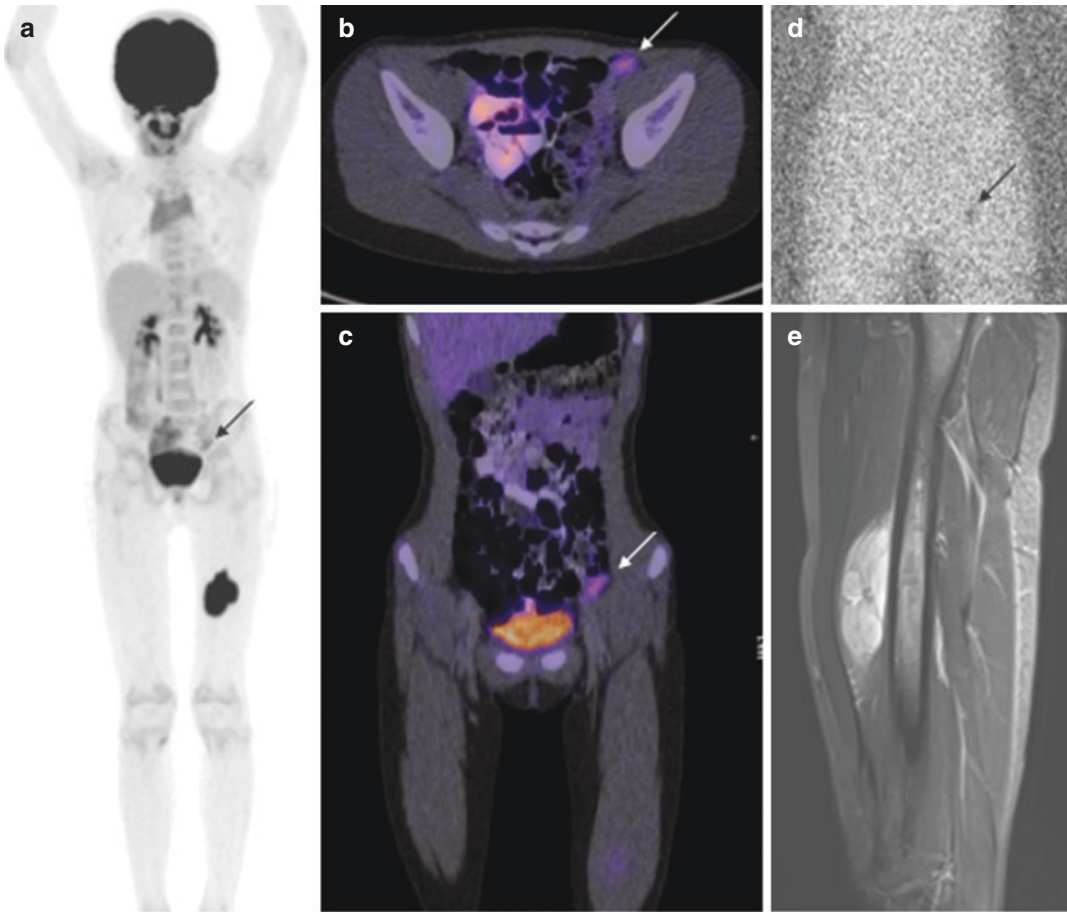

Fig. 3.14 Sentinel lymph node identification in rhabdomyosarcoma (RMS). Ten-year-old with palpable left thigh swelling, evaluated by MRI (**e**); biopsy showed RMS. PET/CT (**a**–**c**) shows subtle uptake in an external iliac lymph node, just above the inguinal ligament (**a**–**c**, arrow). Sentinel lymph node lymphoscintigraphy shows this to be the sentinel node (**d**, arrow). Two non-avid femoral lymph nodes were negative. This external iliac lymph node was positive

who achieved complete remission, FDG PET/CT showed disease clearance 3–6 months earlier than MRI [69].

3.8.2.2 Bone Sarcomas

Osteosarcoma

Osteogenic sarcoma (OS) is the most common primary bone tumor in the pediatric population, with the peak incidence occurring during puberty and the adolescent growth spurt [70]. Osteosarcomas occur most often in the long bones of the extremities, and the primary tumor is typically located in the metaphyses of the distal femur, proximal tibia, or proximal humerus. Less commonly, lesions can arise in the axial skeleton, in the ribs, and in the flat bones of the pelvis and sacrum. In the pediatric population, OS may be a secondary tumor at the site of previous radiation therapy, with a lag time of 7–15 years. Cancer predisposition syndromes, such as Li-Fraumeni and bilateral retinoblastoma also put children at risk for osteogenic sarcoma [70]. Predictors of poor outcome include pelvic site, the presence of metastatic disease at diagnosis, pathologic fracture at diagnosis, positive tumor margins, and a poor histologic response to chemotherapy [71].

At presentation, most patients with OS are considered to have subclinical micrometastatic disease that is below the limits of detection by conventional imaging [70]. The most common site of hematogenously spread metastatic disease is the lungs, followed by the bone and bone marrow. Metastatic disease to the same bone, called a skip lesion, is a feature of OS in the long bones and can be detected by MRI or FDG PET/CT. In rare cases, osseous metastases can be disseminated. Up to 20% of cases have detectable metastases at diagnosis [70]. When present, lung metastases are often calcified, and non-contrast CT of the thorax is the imaging methodology of choice. The staging work-up for OS includes imaging of the primary site with MRI or combination of MRI and CT and lung evaluation with non-contrast chest CT. Whole-body imaging with bone scintigraphy is still used for staging and long-term follow-up, but recent studies with FDG PET/CT have shown superiority of PET/CT for both staging and response assessment [72, 73]. FDG PET is not a reliable tool for the evaluation of metastases to the lungs; however, it is superior to bone scintigraphy and MRI in the detection of bone marrow and cortical bone metastases [74, 75], although small calcified lesions may not have increased uptake on FDG PET.

In addition to staging, FDG PET imaging plays an important role in determining a biopsy site that is safe and has the highest yield. Tumor histology is an important determinant of outcome, and FDG PET/CT can be used to guide and increase the diagnostic yield of core needle biopsies. Core biopsy has comparable yield to surgical excisional biopsy and by virtue of being less invasive than surgical biopsy is increasingly the initial method of choice for obtaining a tissue diagnosis. Bone sarcomas often appear heterogeneous by imaging. By identifying metabolically active sites of FDG uptake, the PET scan can be used to guide the localization of an optimal biopsy site. Histological response to treatment and the ability to achieve complete surgical resection remain the best predictors of outcome in OS [70]. Repeat imaging is performed after neoadjuvant chemotherapy for evaluation of response and includes MRI of the primary tumor site and chest CT. FDG PET has recently been shown to be useful in evaluating response to therapy [72] and is increasingly being incorporated into OS treatment and response assessment algorithms [73].

Inasmuch as the goal of surgical resection for osteosarcoma is achieving a wide margin, the decision to proceed with amputation or rotationplasty versus a limb salvage procedure depends on the tumor response to neoadjuvant chemotherapy, the presence of disease progression, and the location of the tumor [76]. Limb salvage surgery is associated with a higher rate of local recurrence, without decreasing overall survival, and is usually accompanied by multidrug chemotherapy. FDG PET is not routinely in use but can be helpful in the evaluation of local tumor recurrence, especially in the presence of a metallic prosthesis (Fig. 3.15) [77].

Ewing Sarcoma

Ewing sarcoma (EWS) is a small, round, blue cell tumor that derives from a primitive neuroectodermal cell with variable differentiation. Ewing sarcoma accounts for 2–3% of all childhood cancers and is the second most common pediatric bone tumor, after osteosarcoma [78]. EWS affects primarily adolescents, with a peak age range at diagnosis between 10 and 20 years. The majority of EWS occur in the long bones of the upper and lower extremities, followed by the pelvis, thorax, and spine [78]. Although EWS tumors more commonly arise from the bone, soft tissue primary tumors are frequently seen. Factors associated with a worse prognosis include older age, pelvic primary tumor, tumor size, and metastatic disease at time of diagnosis [79]. The staging evaluation for EWS includes evaluation of the primary tumor with either CT or MRI and non-contrast chest CT for pulmonary metastases. FDG PET/CT has been found to be superior to bone scintigraphy for the detection of skeletal metastases, particularly bone marrow metastases, and also had a higher sensitivity for detecting bone marrow involvement than bone marrow biopsy [80, 81]. Based on these and other retrospective studies, the data now point to replacing

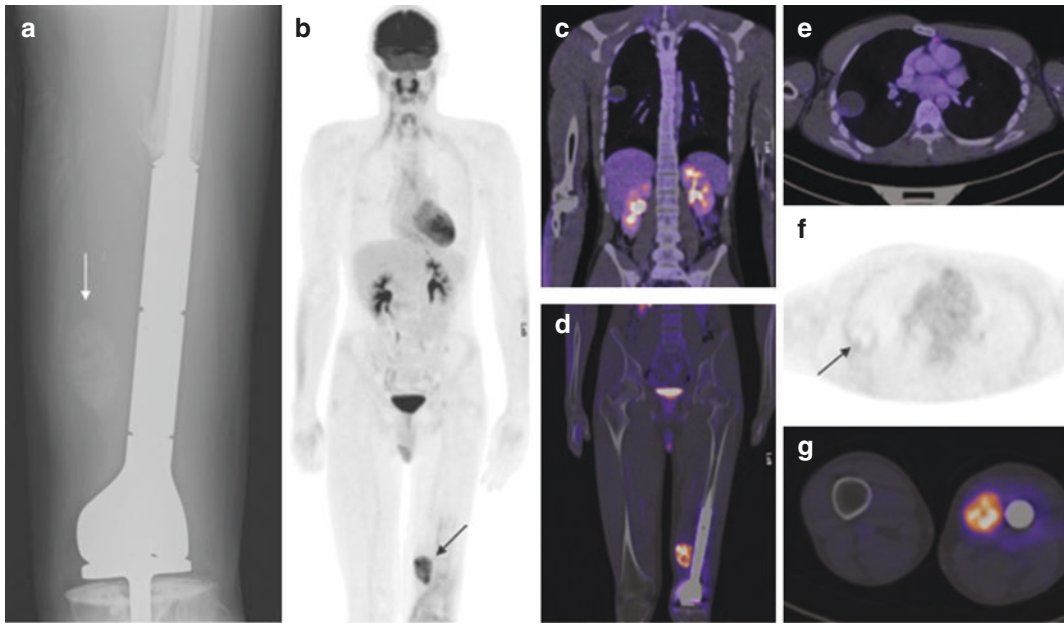

Fig. 3.15 FDG PET/CT in osteosarcoma. Nineteen-year-old with metastatic osteosarcoma who initially presented with pathologic fracture of the left femur, s/p resection, and distal femoral prosthesis. At followup he presented with a palpable mass along the medial thigh. X-Ray shows a radiodense mass medial to prosthesis, in the adductor compartment (**a**, arrow). FDG PET/CT shows intense uptake at the site of recurrence (**b**, arrow; **d**, **g**), which is easily distinguishable from adjacent hardware. Also seen is a new lung lesion (**c**, **e**, **f**), faintly FDG avid (**f**, arrow), and localizing to a right lung mass identified on the attenuation correction CT (**c**, **e**). Biopsy showed multifocal disease recurrence

bone scintigraphy and bone marrow biopsy with FDG PET/CT for staging EWS [73].

As with osteosarcoma, response to neoadjuvant chemotherapy is a prognostic factor in patients with Ewing sarcoma [82]. In studies aimed at investigating the accuracy of FDG PET/CT in predicting response to chemotherapy, Raciborska et al. investigated the diagnostic accuracy and the potential of FDG PET to predict response to chemotherapy, with FDG PET/CT imaging performed at diagnosis, after induction chemotherapy, and prior to local control [83]. SUV at diagnosis was significantly lower in patients with good histological response than in patients with poor histological response, a finding supported by results showing that SUVmax at diagnosis was the only independent pretreatment prognostic factor to retain statistical significance [83, 84]. Several studies have also shown significantly improved outcome in patients with favorable metabolic responses to therapy as measured by reductions in tumor SUV on posttreatment FDG PET/CT (Fig. 3.16) [82–84]. As encouraging as these small retrospective studies have been in establishing the potential utility of PET imaging in EWS, larger prospective studies are needed to confirm the utility of FDG PET in predicting response and outcome.

3.8.3 Malignant Peripheral Nerve Sheath Tumor

Neurofibromatosis type 1 is an autosomal dominant disorder characterized by the development of benign plexiform neurofibromas with the potential for sarcomatous transformation to malignant peripheral nerve sheath tumors. Malignant transformation is often suspected with the development of new lesions, change in lesion size, or increased localized pain. PET/CT has been valuable in detecting hypermetabolic lesions with possible malignant transformation and is most useful in identifying sites for biopsy or resection

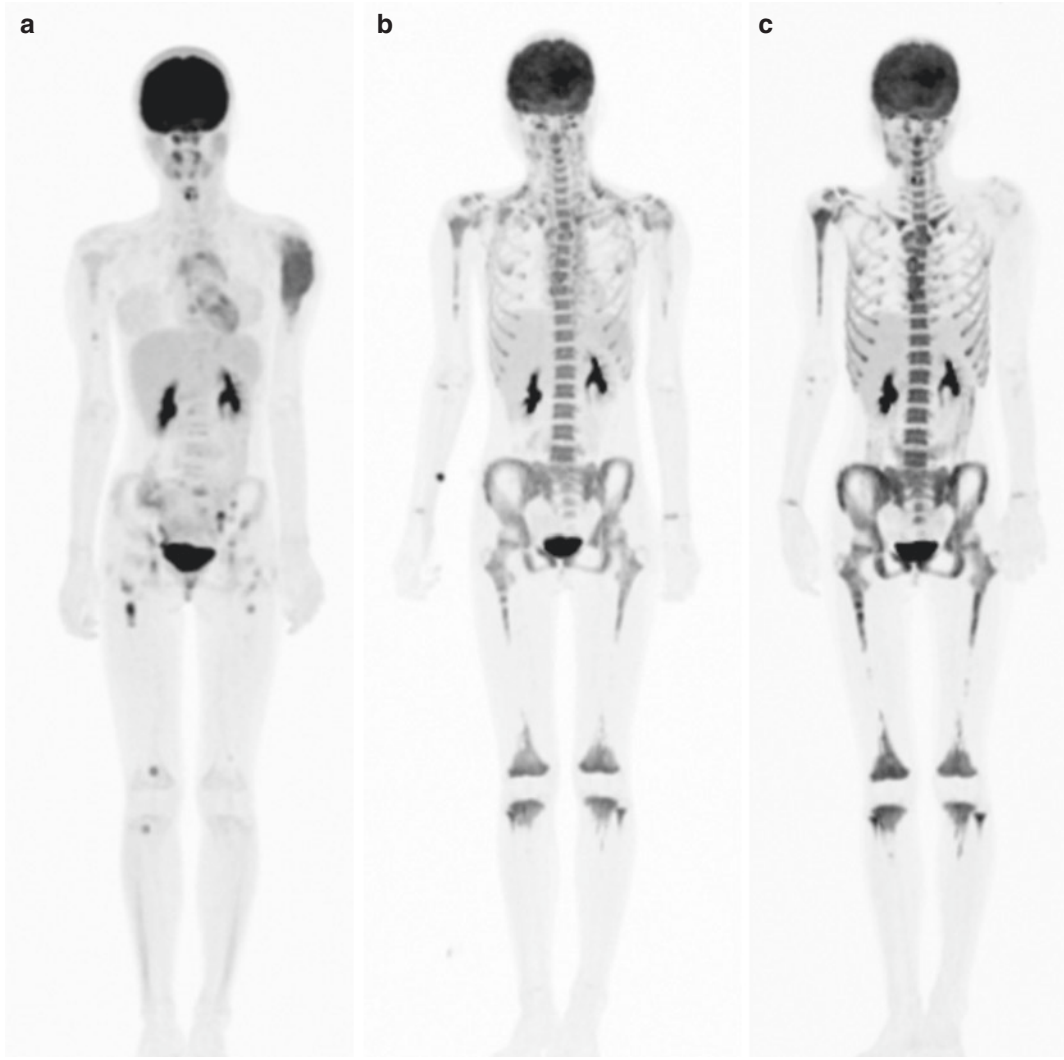

Fig. 3.16 FDG PET/CT response assessment in Ewing sarcoma. Eleven-year-old with left humeral Ewing sarcoma. FDG PET shows multifocal metastatic disease at diagnosis (**a**). After six cycles of chemotherapy (**b**), there has been near complete metabolic response at all sites of disease. No residual disease was evident at completion of induction and consolidation chemotherapy (**c**), with diffuse bone marrow uptake throughout the skeletal related to cellular marrow stimulation by G-CSF. Note the absence of post-treatment marrow uptake in the left humeral metaphysis at the primary disease site, indicating a metabolic response of the tumor, but with no normal cellular marrow recovery as yet at the treatment site

(Fig. 3.17). Several studies have evaluated the use of SUVmax cutoffs to distinguish benign versus malignant lesions [36, 85]; however, there is significant overlap, and benign aggressive lesions and premalignant atypical neurofibromas can also show increased FDG uptake. A meta-analysis by Tovmassian et al. provides a comprehensive review of the literature and concludes that the use of FDG PET/CT for predicting malignant degeneration of plexiform neurofibromas in NF-1 patients is a useful noninvasive diagnostic tool with excellent sensitivity and negative predictive value, although further prospective trials are needed to establish SUVmax values that optimally predict malignant degeneration and minimize false-positive lesion detection [86].

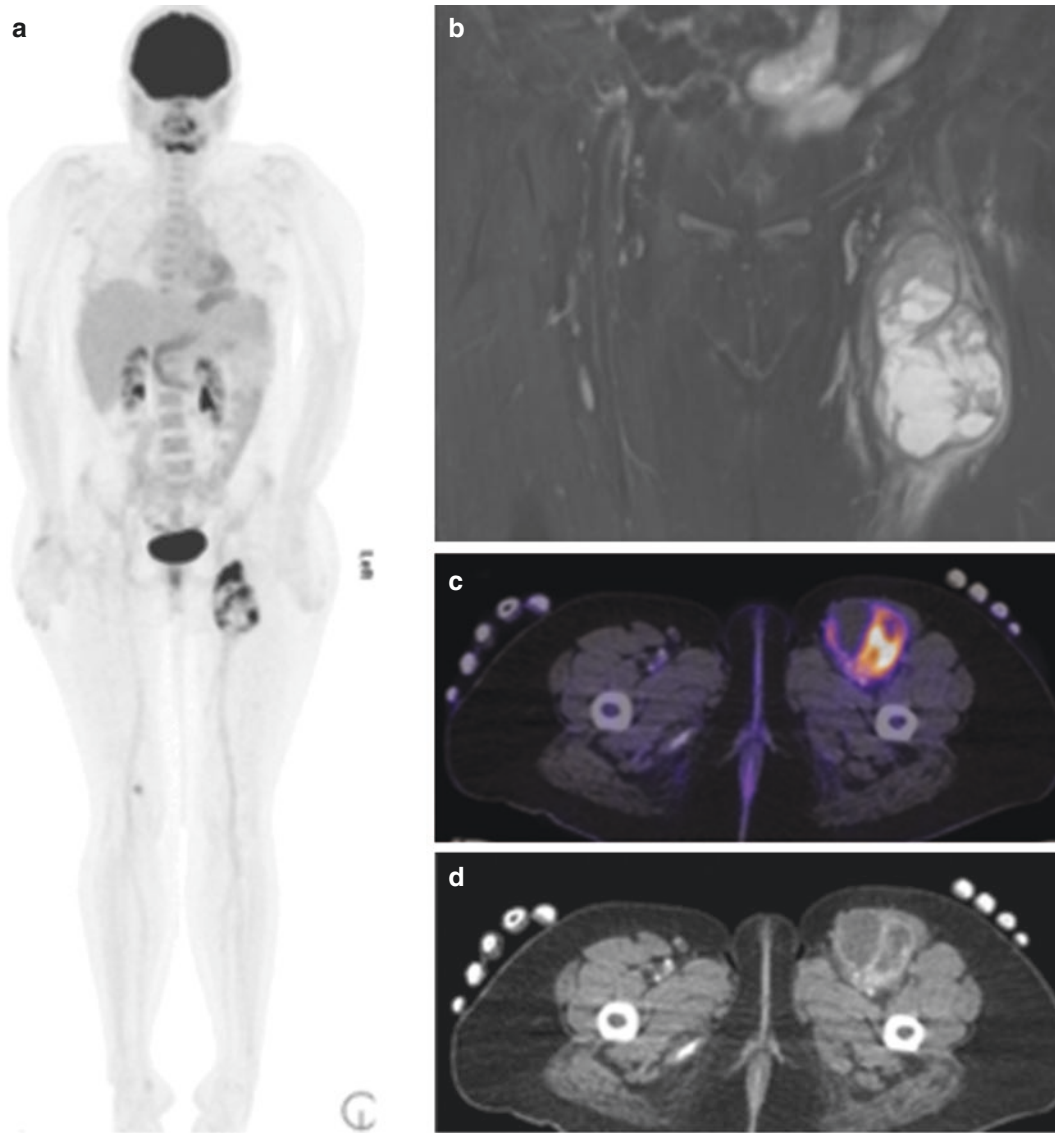

Fig. 3.17 FDG PET/CT and MPNST in NF-1. Twenty-five-year-old with NF-1 and optic pathway gliomas, now with enlarging left thigh mass. FDG PET/CT shows heterogeneously FDG-avid mass (**a**, **c**) with SUVmax along the upper margin of the lesion of 13.9. The earlier MRI (**b**) also showed heterogeneously increased T2 signal, but the areas of intense FDG uptake (**a**, **c**) helped guide biopsy and resection. The contrast-enhanced AC CT (**d**) provides adequate localization of the FDG-avid mass relative to the femoral vasculature

3.8.4 Hepatoblastoma

MRI and CT are the imaging modalities of choice for the initial evaluation of patients with hepatoblastoma, and functional imaging with FDG PET plays little role in hepatoblastoma staging. However, FDG PET imaging can play a role in the evaluation of tumor recurrence in select cases of hepatoblastoma, particularly when rising AFP levels raise concern for disease relapse and conventional imaging techniques are unrevealing [87]. In a study of nine patients, Cistaro et al. showed that in the evaluation of hepatoblastoma recurrence, FDG PET may better delineate and be more predictive of tumor recurrence than conventional imaging, noting regenerative nodules

and necrotizing granulomas may cause false-positive results [87]. Clearly larger studies are needed to better determine the role of PET imaging in hepatoblastoma.

3.8.5 Neuroblastoma

Neuroblastoma is the most common extracranial soft tissue tumor in children. Up to 50% of patients have metastatic disease at diagnosis. Whole-body imaging with ^{123}I-metaiodobenzylguanidine (MIBG) is generally felt to be superior to FDG PET in evaluation of metastatic osseous disease and remains the imaging test of choice to determine the extent of disease for staging, for evaluation of treatment response, and for determining prognosis [88–90]. Tumor biopsy is the gold standard for diagnosis and provides key information including histopathology, genetic abnormalities and cellular differentiation, which are essential elements used for treatment planning and prognosis. MIBG is taken up by the norepinephrine transporter (NET), and the majority of neuroblastomas express NET. However, approximately 10% of neuroblastomas cases do not take up MIBG, and FDG PET is a useful adjunctive tool for imaging these non-MIBG-avid neuroblastoma tumors. In the evaluation of high-risk patients, FDG PET can also be used to identify poorly differentiated tumor which may be weakly or non-MIBG avid, and in some cases, FDG PET/CT may show more lesions than MIBG scintigraphy (Fig. 3.18), although in practice most investigators rely on MIBG and reserve FDG PET/CT for those few patients who are MIBG-negative or when there are inclusive or discrepant findings between MIBG and conventional imaging techniques [89, 91].

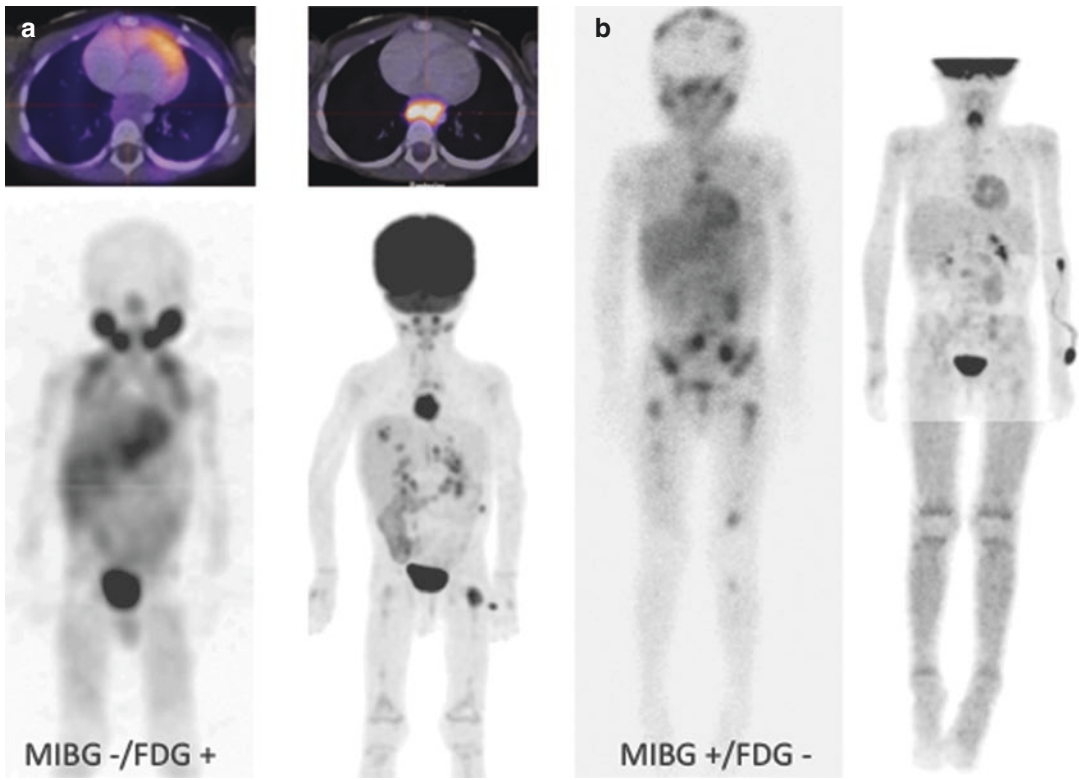

Fig. 3.18 Examples of discordant patterns of ^{123}I-MIBG and ^{18}F-FDG uptake in neuroblastoma. Patient (**a**) shows no MIBG-avid disease, despite multiple foci of FDG-avid disease, most notably an intensely FDG-avid posterior mediastinal mass, while another patient (**b**) shows extensive MIBG-avid disease throughout the axial and appendicular skeleton with no corresponding FDG uptake

3.8.6 Wilms Tumor

Wilms tumor is the most common malignant renal tumor in children with a mean age at presentation of 3.5 years. In the USA, initial treatment is based on histology and surgical staging, and there has been very little use of FDG PET/CT for initial disease characterization. Conventional imaging with CT and/or MRI can provide information regarding metastatic disease and local extent for surgical planning. In the setting of bilateral disease or when extrarenal spread of disease is suspected, FDG PET may play a role, although excretion of the FDG radiopharmaceutical via the kidneys limits its utility for characterizing subtle renal parenchymal abnormalities. Hossain et al. showed that Wilms tumor is a metabolically active tumor and that FDG PET/CT can help in defining extent of tumor involvement and presence of metastatic disease, although FDG PET cannot distinguish between tumors with favorable histology and those with anaplasia, a distinction that has prognostic and therapeutic significance in Wilms tumor [92]. Another potential role for PET imaging in Wilms tumor is for assessing treatment response in patients not undergoing upfront surgical resection and the evaluation of metastatic disease in patients with recurrence.

3.8.7 Langerhans Cell Histiocytosis

In the evaluation of LCH, FDG PET has been shown to be superior to conventional imaging, including bone scintigraphy and radiographic skeletal survey, in the detection of active disease and in the determination of response to therapy (Fig. 3.19). Several small series have shown its utility in the evaluation of responses to therapy that precede changes on bone scintigraphy [93, 94]. Comparison with other whole-body imaging techniques such as wbMRI has not been well studied, although the use of combined PET/MR techniques for assessing pediatric LCH has shown promise [95].

3.8.8 CNS Malignancies

Brain tumors are the most common solid tumors occurring in childhood and are a significant cause of morbidity and mortality in the pediatric population. The use of FDG PET/CT imaging to stage, assess response to therapy, and evaluate potential sites of recurrence in pediatric brain tumors has been hampered by the high levels of physiologic FDG uptake that occur in the normal brain, which makes identifying and characterizing subtle lesions challenging against the high levels of

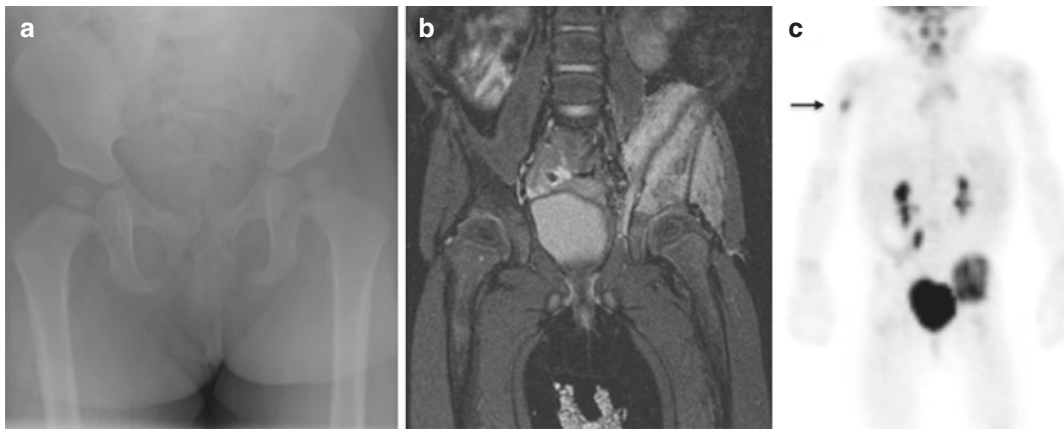

Fig. 3.19 FDG PET/CT in LCH. Thirty-month-old with multifocal LCH, on treatment, with new refusal to weight bear. Radiographs (**a**) showed subtle periosteal reaction in the left ilium; MRI confirmed iliac involvement with soft tissue extension (**b**). FDG PET showed left iliac uptake and additional site of uptake in the right humerus (**c**), consistent with progressive disease

surrounding background activity. Although the systematic use of FDG PET/CT in pediatric brain tumor management has been difficult to implement, a study from the Pediatric Brain Tumor Consortium suggested that ^{18}F-FDG PET and MR imaging provide complementary information in the evaluation of pediatric brain tumors [96]. More aggressive tumors such as GBM and medulloblastoma tended to be more FDG avid, whereas more indolent neoplasms such as brain stem gliomas and ependymomas were less FDG avid. While some have suggested that the intensity of FDG uptake correlates with histologic grade, low-grade lesions such as pilocytic astrocytoma can also be hypermetabolic, arguing against a strict association between FDG avidity and aggressiveness [97]. In an effort to improve the sensitivity and specificity of pediatric brain tumor characterization, ^{18}F-FLT has been investigated as an alternative to ^{18}F-FDG, with lower physiologic background uptake in the brain and greater specificity for actively dividing tumor (Fig. 3.20) [98]. Whether this technique, or use of other tracers such as ^{11}C-methionine, will be proven useful in the management of pediatric CNS malignancies is the object of ongoing investigation.

3.8.9 PET/CT and Pulmonary Nodules

Evaluation of pulmonary nodules by PET/CT deserves special attention. Nodule size cannot be used to distinguish between benign and malignant lesions. In a small series of solid tumors, predominantly sarcomas, McCarville et al. found that 43% of nodules smaller than 0.5 cm were malignant [99]. Comparison of PET/CT with the diagnostic CT did not improve sensitivity, specificity or accuracy for predicting histologic diagnosis. Assessment of nodules larger than 0.5 cm was also limited. Concurrent review of PET/CT and diagnostic CT did improve the specificity in the prediction of malignancy in the larger nodules; however, there was significant interreviewer variability. In addition, the sensitivity and accuracy of chest CT alone, performed at end-inspiration with diagnostic technique, remained superior to PET/CT. The added value of PET may be in using semiquantitative analysis with SUVmax. Although the number of nodules in this series was small, the median SUVmax of malignant nodules was significantly higher than benign nodules.

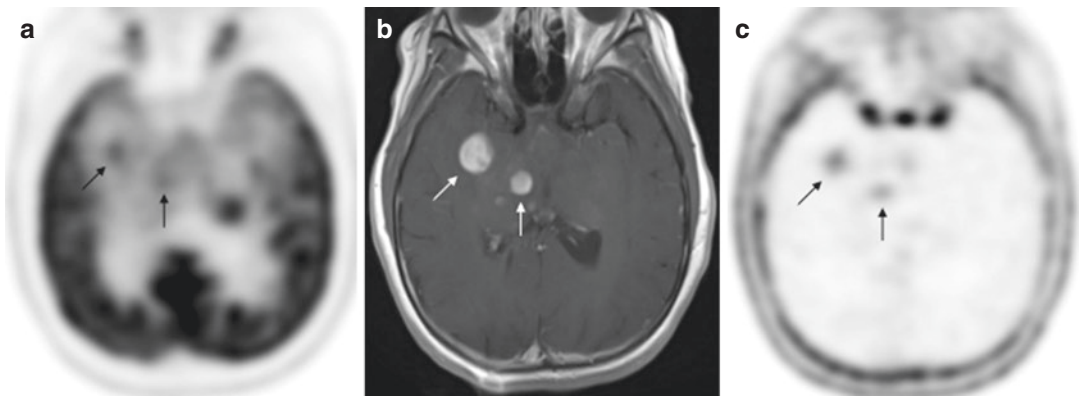

Fig. 3.20 ^{18}FLT PET in pediatric CNS malignancies. Twelve-year-old with bithalamic fibrillary astrocytoma and new lesions seen on MRI. ^{18}F-FDG PET (**a**), contrast-enhanced brain MRI (**b**), and ^{18}F-FLT PET (**c**) were obtained. The FLT PET shows increased uptake, indicating cellular proliferative activity and DNA turnover in the enhancing lesions demonstrated by MRI (arrows). Because of the low background with FLT, uptake in the lesions is easily seen. Only subtle FDG uptake is demonstrated on the accompanying ^{18}F-FDG PET, with the intense physiologic uptake in the brain limiting sensitivity for lesion detection and characterization

3.9 Non-FDG Tracers for Oncologic Imaging

This chapter has focused largely on the use of ^{18}F-FDG in pediatric PET/CT applications. However, there are several new PET tracers on the horizon that are currently either experimental or not yet FDA approved for use in the USA, but that will likely be of interest for pediatric oncologic imaging.

^{18}F-MFBG has recently been shown to be comparable to ^{123}I-MIBG for staging neuroblastoma and once it becomes more widely available could offer a more sensitive and quantitative means of evaluating neuroblastoma, in addition to providing a shorter time interval between injection and imaging (2–4 h for ^{18}F-MFBG compared to 24 h with ^{123}I-MIBG) [17]. Other tracers being developed for neuroblastoma include ^{68}Ga-DOTATATE, which has recently been approved for us in the USA, and the dopamine analogues ^{18}F-DOPA and ^{18}F-Fluorodopamine (Fig. 3.21). ^{18}F-DOPA has also been shown to be effective in localizing focal pancreatic lesions in congenital hyperinsulinism [100].

Amino acid analogues such as ^{11}C-methione have been evaluated in lymphoma and in pediatric CNS tumors [13, 14], although high levels of background uptake in the bone marrow and the short half-life of ^{11}C (~20 min), requiring an onsite cyclotron to facilitate production, have limited the use of this tracer. The thymidine nucleoside analogue ^{18}F-FLT offers promise for evaluating tumor DNA turnover, but high uptake in the bone marrow has limited its utility for the most common pediatric tumors.

Finally, the use of ^{18}F-sodium fluoride (^{18}F-Na) deserves mention as a potential replacement for conventional bone scintigraphy. ^{18}F-Na is rapidly incorporated into bone and can be used to assess for skeletal metastatic disease. In addition, owing to its favorable pharmacokinetics and the superior imaging features of PET/CT, ^{18}F-Na has increased sensitivity over conventional ^{99m}Tc MDP bone scintigraphy [101]. Osteosarcoma metastases frequently calcify, increasing the likelihood of calcified nodules being malignant. However smaller nodules, or non-calcified nodules, may still have osteoblastic activity but have indeterminate features by CT. We have taken advantage of the sensitivity and high resolution provided by ^{18}F-NaF PET/CT and used it in a small number of osteosarcoma patients suspected of having recurrent or progressive disease, in whom indeterminate pulmonary nodules or intrathoracic lymph nodes were identified, but for which more definitive imaging was desired prior to proceeding with thoracotomy. Figure 3.22 shows one example of a small non-calcified pulmonary nodule showing intense accumulation of ^{18}F-fluoride, consistent with osteosarcomatous metastasis.

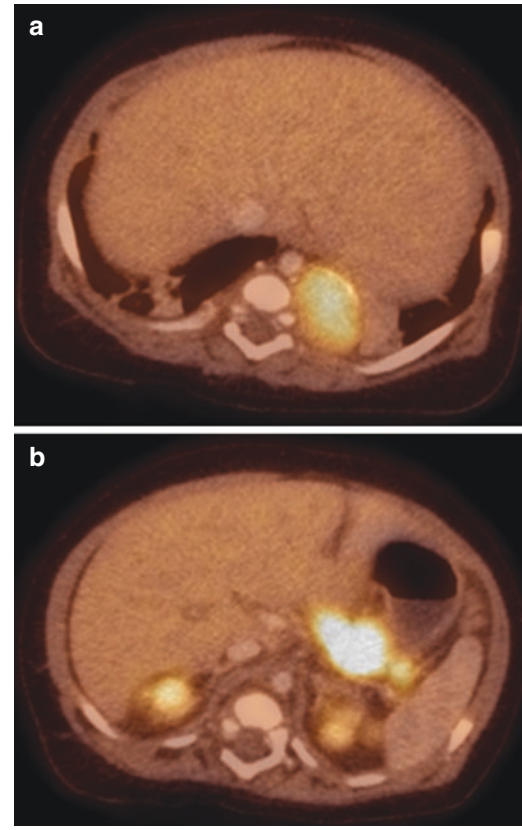

Fig. 3.21 ^{18}F-DOPA PET/CT. Two-month-old with Beckwith-Wiedemann syndrome and hyperinsulinism underwent PET/CT with ^{18}F-DOPA. Increased ^{18}F-DOPA uptake is demonstrated in a left thoracic paraspinal lesion (**a**) as well as in the markedly enlarged pancreatic body and tail (**b**) Pathology revealed a poorly differentiated favorable histology neuroblastoma and pancreatic findings of increased endocrine tissue and nucleomegaly consistent with diffuse disease of congenital hyperinsulinism

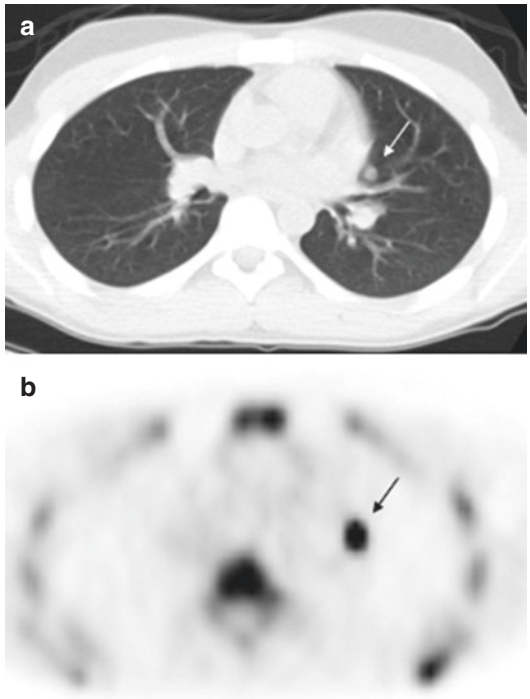

Fig. 3.22 (**a**, **b**) ^{18}F-NaF bone PET in osteosarcoma. Sixteen-year-old with distal left femur osteosarcoma and chest CT (**a**) showing a non-calcified indeterminate but suspicious pulmonary nodule (arrow). ^{18}F-NaF bone PET (**b**) shows radiotracer localizing to the nodule, consistent with metastatic osteosarcoma

3.10 Summary

PET/CT provides a noninvasive, quantitative, physiologic method of detecting metabolically active malignant processes. The use of imaging in response assessment continues to evolve. Current research is focused on the combination of anatomical and functional imaging techniques to determine how to best predict which patients will benefit from modified, less toxic treatment regimens, and which patients will require more aggressive therapy. As we evolve from risk-adapted treatment strategies to guide these decisions and enter an era of response-based therapy, the development of imaging surrogates of response to therapy should give us more specific information related to disease activity and response to therapy. Discovery and validation of noninvasive imaging biomarkers will contribute to development of new response assessment paradigms. The development of standardized protocols and reproducible image acquisition techniques will allow the collection of standardized, multi-institutional data. Further technological advances are likely to further refine the information provided by FDG PET imaging as well as contribute to development of novel imaging strategies with new more specific radiotracers.

References

1. Colleran GC, Kwatra N, Oberg L, Grant FD, Drubach L, Callahan MJ, MacDougall RD, Fahey FH, Voss SD. How we read pediatric PET/CT: indications and strategies for image acquisition, interpretation and reporting. Cancer Imaging. 2017;17(1):28. https://doi.org/10.1186/s40644-017-0130-8.
2. Kiratli PO, Tuncel M, Bar-Sever Z. Nuclear medicine in pediatric and adolescent tumors. Semin Nucl Med. 2016;46(4):308–23. https://doi.org/10.1053/j.semnuclmed.2016.01.004.
3. Franzius C. FDG-PET/CT in pediatric solid tumors. Q J Nucl Med Mol Imaging. 2010;54(4):401–10.
4. Uslu L, Donig J, Link M, Rosenberg J, Quon A, Daldrup-Link HE. Value of 18F-FDG PET and PET/CT for evaluation of pediatric malignancies. J Nucl Med. 2015;56(2):274–86. https://doi.org/10.2967/jnumed.114.146290.
5. Parisi MT, Bermo MS, Alessio AM, Sharp SE, Gelfand MJ, Shulkin BL. Optimization of pediatric PET/CT. Semin Nucl Med. 2017;47(3):258–74. https://doi.org/10.1053/j.semnuclmed.2017.01.002.
6. Vandenberghe S, Mikhaylova E, D'Hoe E, Mollet P, Karp JS. Recent developments in time-of-flight PET. EJNMMI Phys. 2016;3(1):3. https://doi.org/10.1186/s40658-016-0138-3.
7. Rausch I, Cal-Gonzalez J, Dapra D, Gallowitsch HJ, Lind P, Beyer T, Minear G. Performance evaluation of the biograph mCT Flow PET/CT system according to the NEMA NU2-2012 standard. EJNMMI Phys. 2015;2(1):26. https://doi.org/10.1186/s40658-015-0132-1.
8. Cherry SR, Jones T, Karp JS, Qi J, Moses WW, Badawi RD. Total-body PET: maximizing sensitivity to create new opportunities for clinical research and patient care. J Nucl Med. 2018;59:3–12.
9. Cherry SR, Badawi RD, Karp JS, Moses WW, Price P, Jones T. Total-body imaging: transforming the role of positron emission tomography. Sci Transl Med. 2017;9(381) https://doi.org/10.1126/scitranslmed.aaf6169.
10. Furth C, Denecke T, Steffen I, Ruf J, Voelker T, Misch D, Vondran F, Plotkin M, Stover B, Henze G,

Lemke AJ, Amthauer H. Correlative imaging strategies implementing CT, MRI, and PET for staging of childhood Hodgkin disease. J Pediatr Hematol Oncol. 2006;28(8):501–12. https://doi.org/10.1097/01.mph.0000212962.68007.12.
11. Yamamoto Y, Ono Y, Aga F, Kawai N, Kudomi N, Nishiyama Y. Correlation of 18F-FLT uptake with tumor grade and Ki-67 immunohistochemistry in patients with newly diagnosed and recurrent gliomas. J Nucl Med. 2012;53(12):1911–5. https://doi.org/10.2967/jnumed.112.104729.
12. Timmers HJ, Chen CC, Carrasquillo JA, Whatley M, Ling A, Havekes B, Eisenhofer G, Martiniova L, Adams KT, Pacak K. Comparison of 18F-fluoro-L-DOPA, 18F-fluoro-deoxyglucose, and 18F-fluorodopamine PET and 123I-MIBG scintigraphy in the localization of pheochromocytoma and paraganglioma. J Clin Endocrinol Metab. 2009;94(12):4757–67. https://doi.org/10.1210/jc.2009-1248.
13. Kaste SC, Snyder SE, Metzger ML, Sandlund JT, Howard SC, Krasin M, Shulkin BL. Comparison of (11)C-methionine and (18)F-FDG PET/CT for staging and follow-up of pediatric lymphoma. J Nucl Med. 2017;58(3):419–24. https://doi.org/10.2967/jnumed.116.178640.
14. Lucas JT Jr, Serrano N, Kim H, Li X, Snyder SE, Hwang S, Li Y, Hua CH, Broniscer A, Merchant TE, Shulkin BL. (11)C-methionine positron emission tomography delineates non-contrast enhancing tumor regions at high risk for recurrence in pediatric high-grade glioma. J Neurooncol. 2017;132(1):163–70. https://doi.org/10.1007/s11060-016-2354-z.
15. Kong G, Hofman MS, Murray WK, Wilson S, Wood P, Downie P, Super L, Hogg A, Eu P, Hicks RJ. Initial experience with gallium-68 DOTA-octreotate PET/CT and peptide receptor radionuclide therapy for pediatric patients with refractory metastatic neuroblastoma. J Pediatr Hematol Oncol. 2016;38(2):87–96. https://doi.org/10.1097/MPH.0000000000000411.
16. Paterson BM, Roselt P, Denoyer D, Cullinane C, Binns D, Noonan W, Jeffery CM, Price RI, White JM, Hicks RJ, Donnelly PS. PET imaging of tumours with a 64Cu labeled macrobicyclic cage amine ligand tethered to Tyr3-octreotate. Dalton Trans. 2014;43(3):1386–96. https://doi.org/10.1039/c3dt52647j.
17. Pandit-Taskar N, Zanzonico P, Staton KD, Carrasquillo JA, Reidy-Lagunes D, Lyashchenko S, Burnazi E, Zhang H, Lewis JS, Blasberg R, Larson SM, Weber WA, Modak S. Biodistribution and dosimetry of (18)F-meta-fluorobenzylguanidine: a first-in-human PET/CT imaging study of patients with neuroendocrine malignancies. J Nucl Med. 2018;59(1):147–53. https://doi.org/10.2967/jnumed.117.193169.
18. Sai KKS, Zachar Z, Bingham PM, Mintz A. Metabolic PET imaging in oncology. AJR Am J Roentgenol. 2017;209(2):270–6. https://doi.org/10.2214/AJR.17.18112.
19. Koppenol WH, Bounds PL, Dang CV. Otto Warburg's contributions to current concepts of cancer metabolism. Nat Rev Cancer. 2011;11(5):325–37. https://doi.org/10.1038/nrc3038.
20. Samuel AM. PET/CT in pediatric oncology. Indian J Cancer. 2010;47(4):360–70. https://doi.org/10.4103/0019-509X.73551.
21. Eisenhauer EA, Therasse P, Bogaerts J, Schwartz LH, Sargent D, Ford R, Dancey J, Arbuck S, Gwyther S, Mooney M, Rubinstein L, Shankar L, Dodd L, Kaplan R, Lacombe D, Verweij J. New response evaluation criteria in solid tumours: revised RECIST guideline (version 1.1). Eur J Cancer. 2009;45(2):228–47. https://doi.org/10.1016/j.ejca.2008.10.026.
22. Litiere S, Collette S, de Vries EG, Seymour L, Bogaerts J. RECIST - learning from the past to build the future. Nat Rev Clin Oncol. 2017;14(3):187–92. https://doi.org/10.1038/nrclinonc.2016.195.
23. Schwartz LH, Seymour L, Litiere S, Ford R, Gwyther S, Mandrekar S, Shankar L, Bogaerts J, Chen A, Dancey J, Hayes W, Hodi FS, Hoekstra OS, Huang EP, Lin N, Liu Y, Therasse P, Wolchok JD, de Vries E. RECIST 1.1 - standardisation and disease-specific adaptations: perspectives from the RECIST Working Group. Eur J Cancer. 2016;62:138–45. https://doi.org/10.1016/j.ejca.2016.03.082.
24. Tirkes T, Hollar MA, Tann M, Kohli MD, Akisik F, Sandrasegaran K. Response criteria in oncologic imaging: review of traditional and new criteria. Radiographics. 2013;33(5):1323–41. https://doi.org/10.1148/rg.335125214.
25. JH O, Lodge MA, Wahl RL. Practical PERCIST: a simplified guide to PET response criteria in solid tumors 1.0. Radiology. 2016;280(2):576–84. https://doi.org/10.1148/radiol.2016142043.
26. Wahl RL, Jacene H, Kasamon Y, Lodge MA. From RECIST to PERCIST: evolving considerations for PET response criteria in solid tumors. J Nucl Med. 2009;50(Suppl 1):122S–50S. https://doi.org/10.2967/jnumed.108.057307.
27. Flerlage JE, Kelly KM, Beishuizen A, Cho S, De Alarcon PA, Dieckmann U, Drachtman RA, Hoppe BS, Howard SC, Kaste SC, Kluge R, Kurch L, Landman-Parker J, Lewis J, Link MP, McCarten K, Punnett A, Stoevesandt D, Voss SD, Wallace WH, Mauz-Korholz C, Metzger ML. Staging evaluation and response criteria harmonization (SEARCH) for childhood, adolescent and young adult hodgkin lymphoma (CAYAHL): methodology statement. Pediatr Blood Cancer. 2017;64(7) https://doi.org/10.1002/pbc.26421.
28. Kluge R, Kurch L, Georgi T, Metzger M. Current role of FDG-PET in pediatric Hodgkin's lymphoma. Semin Nucl Med. 2017;47(3):242–57. https://doi.org/10.1053/j.semnuclmed.2017.01.001.
29. Rosolen A, Perkins SL, Pinkerton CR, Guillerman RP, Sandlund JT, Patte C, Reiter A, Cairo MS. Revised international pediatric non-hodgkin lymphoma staging system. J Clin Oncol. 2015;33(18):2112–8. https://doi.org/10.1200/JCO.2014.59.7203.

30. Sandlund JT, Guillerman RP, Perkins SL, Pinkerton CR, Rosolen A, Patte C, Reiter A, Cairo MS. International pediatric non-hodgkin lymphoma response criteria. J Clin Oncol. 2015;33(18):2106–11. https://doi.org/10.1200/JCO.2014.59.0745.
31. Barrington SF, Mikhaeel NG, Kostakoglu L, Meignan M, Hutchings M, Mueller SP, Schwartz LH, Zucca E, Fisher RI, Trotman J, Hoekstra OS, Hicks RJ, O'Doherty MJ, Hustinx R, Biggi A, Cheson BD. Role of imaging in the staging and response assessment of lymphoma: consensus of the International Conference on Malignant Lymphomas Imaging Working Group. J Clin Oncol. 2014;32(27):3048–58. https://doi.org/10.1200/JCO.2013.53.5229.
32. Cheson BD, Fisher RI, Barrington SF, Cavalli F, Schwartz LH, Zucca E, Lister TA, Alliance AL, Lymphoma G, Eastern Cooperative Oncology G, European Mantle Cell Lymphoma C, Italian Lymphoma F, European Organisation for R, Treatment of Cancer/Dutch Hemato-Oncology G, Grupo Espanol de Medula O, German High-Grade Lymphoma Study G, German Hodgkin's Study G, Japanese Lymphorra Study G, Lymphoma Study A, Group NCT, Nordic Lymphoma Study G, Southwest Oncology G, United Kingdom National Cancer Research I. Recommendations for initial evaluation, staging, and response assessment of Hodgkin and non-Hodgkin lymphoma: the Lugano classification. J Clin Oncol. 2014;32(27):3059–68. https://doi.org/10.1200/JCO.2013.54.8800.
33. Seymour L, Bogaerts J, Perrone A, Ford R, Schwartz LH, Mandrekar S, Lin NU, Litiere S, Dancey J, Chen A, Hodi FS, Therasse P, Hoekstra OS, Shankar LK, Wolchok JD, Ballinger M, Caramella C, de Vries EG, group Rw. iRECIST: guidelines for response criteria for use in trials testing immunotherapeutics. Lancet Oncol. 2017;18(3):e143–52. https://doi.org/10.1016/S1470-2045(17)30074-8.
34. Eleneen Y, Colen RR. Cancer imaging in immunotherapy. Adv Exp Med Biol. 2017;995:141–53. https://doi.org/10.1007/978-3-319-53156-4_7.
35. Subhawong TK, Winn A, Shemesh SS, Pretell-Mazzini J. F-18 FDG PET differentiation of benign from malignant chondroid neoplasms: a systematic review of the literature. Skeletal Radiol. 2017;46(9):1233–9. https://doi.org/10.1007/s00256-017-2685-7.
36. Tsai LL, Drubach L, Fahey F, Irons M, Voss S, Ullrich NJ. [18F]-fluorodeoxyglucose positron emission tomography in children with neurofibromatosis type 1 and plexiform neurofibromas: correlation with malignant transformation. J Neurooncol. 2012;108(3):469–75. https://doi.org/10.1007/s11060-012-0840-5.
37. Chirindel A, Chaudhry M, Blakeley JO, Wahl R. 18F-FDG PET/CT qualitative and quantitative evaluation in neurofibromatosis type 1 patients for detection of malignant transformation: comparison of early to delayed imaging with and without liver activity normalization. J Nucl Med. 2015;56(3):379–85. https://doi.org/10.2967/jnumed.114.142372.
38. Lisle JW, Eary JF, O'Sullivan J, Conrad EU. Risk assessment based on FDG-PET imaging in patients with synovial sarcoma. Clin Orthop Relat Res. 2009;467(6):1605–11. https://doi.org/10.1007/s11999-008-0647-z.
39. Lodge MA. Repeatability of SUV in oncologic 18F-FDG PET. J Nucl Med. 2017;58(4):523–32. https://doi.org/10.2967/jnumed.116.186353.
40. Costantini DL, Vali R, Chan J, McQuattie S, Charron M. Dual-time-point FDG PET/CT for the evaluation of pediatric tumors. AJR Am J Roentgenol. 2013;200(2):408–13. https://doi.org/10.2214/AJR.12.8930.
41. Boellaard R, Delgado-Bolton R, Oyen WJ, Giammarile F, Tatsch K, Eschner W, Verzijlbergen FJ, Barrington SF, Pike LC, Weber WA, Stroobants S, Delbeke D, Donohoe KJ, Holbrook S, Graham MM, Testanera G, Hoekstra OS, Zijlstra J, Visser E, Hoekstra CJ, Pruim J, Willemsen A, Arends B, Kotzerke J, Bockisch A, Beyer T, Chiti A, Krause BJ, European Association of Nuclear M. FDG PET/CT: EANM procedure guidelines for tumour imaging: version 2.0. Eur J Nucl Med Mol Imaging. 2015;42(2):328–54. https://doi.org/10.1007/s00259-014-2961-x.
42. Zanotti-Fregonara P, Laforest R, Wallis JW. Fetal radiation dose from 18F-FDG in pregnant patients imaged with PET, PET/CT, and PET/MR. J Nucl Med. 2015;56(8):1218–22. https://doi.org/10.2967/jnumed.115.157032.
43. Takalkar AM, Khandelwal A, Lokitz S, Lilien DL, Stabin MG. 18F-FDG PET in pregnancy and fetal radiation dose estimates. J Nucl Med. 2011;52(7):1035–40. https://doi.org/10.2967/jnumed.110.085381.
44. Grant FD. Normal variations and benign findings in pediatric 18F-FDG-PET/CT. PET Clin. 2014;9(2):195–208. https://doi.org/10.1016/j.cpet.2013.12.002.
45. Hong TS, Shammas A, Charron M, Zukotynski KA, Drubach LA, Lim R. Brown adipose tissue 18F-FDG uptake in pediatric PET/CT imaging. Pediatr Radiol. 2011;41(6):759–68. https://doi.org/10.1007/s00247-010-1925-y.
46. Zukotynski KA, Fahey FH, Laffin S, Davis R, Treves ST, Grant FD, Drubach LA. Seasonal variation in the effect of constant ambient temperature of 24 degrees C in reducing FDG uptake by brown adipose tissue in children. Eur J Nucl Med Mol Imaging. 2010;37(10):1854–60. https://doi.org/10.1007/s00259-010-1485-2.
47. Gelfand MJ, O'Hara SM, Curtwright LA, Maclean JR. Pre-medication to block [(18)F]FDG uptake in the brown adipose tissue of pediatric and adolescent patients. Pediatr Radiol. 2005;35(10):984–90. https://doi.org/10.1007/s00247-005-1505-8.
48. Lassmann M, Treves ST, Group ESPDHW. Paediatric radiopharmaceutical administration: harmonization of the 2007 EANM paediatric dosage card (version 1.5.2008) and the 2010 North American consensus guidelines. Eur J Nucl Med Mol Imaging.

2014;41(5):1036–41. https://doi.org/10.1007/s00259-014-2731-9.
49. Fahey FH, Goodkind A, MacDougall RD, Oberg L, Ziniel SI, Cappock R, Callahan MJ, Kwatra N, Treves ST, Voss SD. Operational and dosimetric aspects of pediatric PET/CT. J Nucl Med. 2017;58:1360. https://doi.org/10.2967/jnumed.116.182899.
50. Fahey FH. Dosimetry of pediatric PET/CT. J Nucl Med. 2009;50(9):1483–91. https://doi.org/10.2967/jnumed.108.054130.
51. Alessio AM, Kinahan PE, Manchanda V, Ghioni V, Aldape L, Parisi MT. Weight-based, low-dose pediatric whole-body PET/CT protocols. J Nucl Med. 2009;50(10):1570–7. https://doi.org/10.2967/jnumed.109.065912.
52. Shammas A, Lim R, Charron M. Pediatric FDG PET/CT: physiologic uptake, normal variants, and benign conditions. Radiographics. 2009;29(5):1467–86. https://doi.org/10.1148/rg.295085247.
53. Salaun PY, Gastinne T, Bodet-Milin C, Campion L, Cambefort P, Moreau A, Le Gouill S, Berthou C, Moreau P, Kraeber-Bodere F. Analysis of 18F-FDG PET diffuse bone marrow uptake and splenic uptake in staging of Hodgkin's lymphoma: a reflection of disease infiltration or just inflammation? Eur J Nucl Med Mol Imaging. 2009;36(11):1813–21. https://doi.org/10.1007/s00259-009-1183-0.
54. Surasi DS, Bhambhvani P, Baldwin JA, Almodovar SE, O'Malley JP. (1)(8)F-FDG PET and PET/CT patient preparation: a review of the literature. J Nucl Med Technol. 2014;42(1):5–13. https://doi.org/10.2967/jnmt.113.132621.
55. Sharp SE, Gelfand MJ, Absalon MJ. Altered FDG uptake patterns in pediatric lymphoblastic lymphoma patients receiving induction chemotherapy that includes very high dose corticosteroids. Pediatr Radiol. 2012;42(3):331–6. https://doi.org/10.1007/s00247-011-2228-7.
56. Cohen M, Hill CA, Cangir A, Sullivan MP. Thymic rebound after treatment of childhood tumors. AJR Am J Roentgenol. 1980;135(1):151–6. https://doi.org/10.2214/ajr.135.1.151.
57. Jerushalmi J, Frenkel A, Bar-Shalom R, Khoury J, Israel O. Physiologic thymic uptake of 18F-FDG in children and young adults: a PET/CT evaluation of incidence, patterns, and relationship to treatment. J Nucl Med. 2009;50(6):849–53. https://doi.org/10.2967/jnumed.108.058586.
58. Kleis M, Daldrup-Link H, Matthay K, Goldsby R, Lu Y, Schuster T, Schreck C, Chu PW, Hawkins RA, Franc BL. Diagnostic value of PET/CT for the staging and restaging of pediatric tumors. Eur J Nucl Med Mol Imaging. 2009;36(1):23–36. https://doi.org/10.1007/s00259-008-0911-1.
59. Portwine C, Marriott C, Barr RD. PET imaging for pediatric oncology: an assessment of the evidence. Pediatr Blood Cancer. 2010;55(6):1048–61. https://doi.org/10.1002/pbc.22747.
60. Adams HJ, Nievelstein RA, Kwee TC. Opportunities and limitations of bone marrow biopsy and bone marrow FDG-PET in lymphoma. Blood Rev. 2015;29(6):417–25. https://doi.org/10.1016/j.blre.2015.06.003. Epub 2015 Jun 17
61. Cheng G, Alavi A. Value of 18F-FDG PET versus iliac biopsy in the initial evaluation of bone marrow infiltration in the case of Hodgkin's disease: a meta-analysis. 2013. Nucl Med Commun. 34(1):25–31. https://doi.org/10.1097/MNM.0b013e32835afc19.
62. Sammer MB, Shulkin BL, Alessio A, Parisi MT. Role of limited whole-body PET/CT in pediatric lymphoma. AJR Am J Roentgenol. 2011;196(5):1047–55. https://doi.org/10.2214/AJR.10.6074.
63. Sultan I, Qaddoumi I, Yaser S, Rodriguez-Galindo C, Ferrari A. Comparing adult and pediatric rhabdomyosarcoma in the surveillance, epidemiology and end results program, 1973 to 2005: an analysis of 2,600 patients. J Clin Oncol. 2009;27(20):3391–7. https://doi.org/10.1200/JCO.2008.19.7483.
64. Borinstein SC, Steppan D, Hayashi M, Loeb DM, Isakoff MS, Binitie O, Brohl AS, Bridge JA, Stavas M, Shinohara ET, Meyer WH, Reed DR, Wagner LM. Consensus and controversies regarding the treatment of rhabdomyosarcoma. Pediatr Blood Cancer. 2018;65(2) https://doi.org/10.1002/pbc.26809.
65. Federico SM, Spunt SL, Krasin MJ, Billup CA, Wu J, Shulkin B, Mandell G, McCarville MB. Comparison of PET-CT and conventional imaging in staging pediatric rhabdomyosarcoma. Pediatr Blood Cancer. 2013;60(7):1128–34. https://doi.org/10.1002/pbc.24430.
66. Alcorn KM, Deans KJ, Congeni A, Sulkowski JP, Bagatell R, Mattei P, Minneci PC. Sentinel lymph node biopsy in pediatric soft tissue sarcoma patients: utility and concordance with imaging. J Pediatr Surg. 2013;48(9):1903–6. https://doi.org/10.1016/j.jpedsurg.2013.04.013.
67. De Corti F, Dall'Igna P, Bisogno G, Casara D, Rossi CR, Foletto M, Alaggio R, Carli M, Cecchetto G. Sentinel node biopsy in pediatric soft tissue sarcomas of extremities. Pediatr Blood Cancer. 2009;52(1):51–4. https://doi.org/10.1002/pbc.21777.
68. Walter F, Federman N, Apichairuk W, Nelson S, Phelps ME, Allen-Auerbach M, Walter MA, Czernin J. 18F-fluorodeoxyglucose uptake of bone and soft tissue sarcomas in pediatric patients. Pediatr Hematol Oncol. 2011;28(7):579–87. https://doi.org/10.3109/08880018.2011.602180.
69. Cheuk DK, Sabin ND, Hossain M, Wozniak A, Naik M, Rodriguez-Galindo C, Krasin MJ, Shulkin BL. PET/CT for staging and follow-up of pediatric nasopharyngeal carcinoma. Eur J Nucl Med Mol Imaging. 2012;39(7):1097–106. https://doi.org/10.1007/s00259-012-2091-2.
70. Taran SJ, Taran R, Malipatil NB. Pediatric osteosarcoma: an updated review. Indian J Med Paediatr Oncol. 2017;38(1):33–43. https://doi.org/10.4103/0971-5851.203513.
71. Janeway KA, Barkauskas DA, Krailo MD, Meyers PA, Schwartz CL, Ebb DH, Seibel NL, Grier HE,

Gorlick R, Marina N. Outcome for adolescent and young adult patients with osteosarcoma: a report from the Children's Oncology Group. Cancer. 2012;118(18):4597–605. https://doi.org/10.1002/cncr.27414.
72. Davis JC, Daw NC, Navid F, Billups CA, Wu J, Bahrami A, Jenkins JJ, Snyder SE, Reddick WE, Santana VM, McCarville MB, Guo J, Shulkin BL. (18)F-FDG uptake during early adjuvant chemotherapy predicts histologic response in pediatric and young adult patients with osteosarcoma. J Nucl Med. 2018;59(1):25–30. https://doi.org/10.2967/jnumed.117.190595.
73. Harrison DJ, Parisi MT, Shulkin BL. The role of (18) F-FDG-PET/CT in pediatric sarcoma. Semin Nucl Med. 2017;47(3):229–41. https://doi.org/10.1053/j.semnuclmed.2016.12.004.
74. Hurley C, McCarville MB, Shulkin BL, Mao S, Wu J, Navid F, Daw NC, Pappo AS, Bishop MW. Comparison of (18) F-FDG-PET-CT and bone scintigraphy for evaluation of osseous metastases in newly diagnosed and recurrent osteosarcoma. Pediatr Blood Cancer. 2016;63(8):1381–6. https://doi.org/10.1002/pbc.26014.
75. Quartuccio N, Fox J, Kuk D, Wexler LH, Baldari S, Cistaro A, Schoder H. Pediatric bone sarcoma: diagnostic performance of (1)(8)F-FDG PET/CT versus conventional imaging for initial staging and follow-up. AJR Am J Roentgenol. 2015;204(1):153–60. https://doi.org/10.2214/AJR.14.12932.
76. Anderson ME. Update on survival in osteosarcoma. Orthop Clin North Am. 2016;47(1):283–92. https://doi.org/10.1016/j.ocl.2015.08.022.
77. Sharp SE, Shulkin BL, Gelfand MJ, McCarville MB. FDG PET/CT appearance of local osteosarcoma recurrences in pediatric patients. Pediatr Radiol. 2017;47(13):1800–8. https://doi.org/10.1007/s00247-017-3963-1.
78. Jackson TM, Bittman M, Granowetter L. Pediatric malignant bone tumors: a review and update on current challenges, and emerging drug targets. Curr Probl Pediatr Adolesc Health Care. 2016;46(7):213–28. https://doi.org/10.1016/j.cppeds.2016.04.002.
79. Rodriguez-Galindo C, Liu T, Krasin MJ, Wu J, Billups CA, Daw NC, Spunt SL, Rao BN, Santana VM, Navid F. Analysis of prognostic factors in ewing sarcoma family of tumors: review of St. Jude Children's Research Hospital studies. Cancer. 2007;110(2):375–84. https://doi.org/10.1002/cncr.22821.
80. Franzius C, Sciuk J, Daldrup-Link HE, Jurgens H, Schober O. FDG-PET for detection of osseous metastases from malignant primary bone tumours: comparison with bone scintigraphy. Eur J Nucl Med. 2000;27(9):1305–11.
81. Newman EN, Jones RL, Hawkins DS. An evaluation of [F-18]-fluorodeoxy-D-glucose positron emission tomography, bone scan, and bone marrow aspiration/biopsy as staging investigations in Ewing sarcoma. Pediatr Blood Cancer. 2013;60(7):1113–7. https://doi.org/10.1002/pbc.24406.
82. Hawkins DS, Schuetze SM, Butrynski JE, Rajendran JG, Vernon CB, Conrad EU III, Eary JF. [18F] Fluorodeoxyglucose positron emission tomography predicts outcome for Ewing sarcoma family of tumors. J Clin Oncol. 2005;23(34):8828–34. https://doi.org/10.1200/JCO.2005.01.7079.
83. Raciborska A, Bilska K, Drabko K, Michalak E, Chaber R, Pogorzala M, Polczynska K, Sobol G, Wieczorek M, Muszynska-Roslan K, Rychlowska-Pruszynska M, Rodriguez-Galindo C, Dziuk M. Response to chemotherapy estimates by FDG PET is an important prognostic factor in patients with Ewing sarcoma. Clin Transl Oncol. 2016;18(2):189–95. https://doi.org/10.1007/s12094-015-1351-6.
84. Palmerini E, Colangeli M, Nanni C, Fanti S, Marchesi E, Paioli A, Picci P, Cambioli S, Donati D, Cevolani L, De Paolis M, Gambarotti M, Ferrari S. The role of FDG PET/CT in patients treated with neoadjuvant chemotherapy for localized bone sarcomas. Eur J Nucl Med Mol Imaging. 2017;44(2):215–23. https://doi.org/10.1007/s00259-016-3509-z.
85. Meany H, Dombi E, Reynolds J, Whatley M, Kurwa A, Tsokos M, Salzer W, Gillespie A, Baldwin A, Derdak J, Widemann B. 18-fluorodeoxyglucose-positron emission tomography (FDG-PET) evaluation of nodular lesions in patients with Neurofibromatosis type 1 and plexiform neurofibromas (PN) or malignant peripheral nerve sheath tumors (MPNST). Pediatr Blood Cancer. 2013;60(1):59–64. https://doi.org/10.1002/pbc.24212.
86. Tovmassian D, Abdul Razak M, London K. The role of [(18)F]FDG-PET/CT in predicting malignant transformation of plexiform neurofibromas in neurofibromatosis-1. Int J Surg Oncol. 2016;2016:6162182. https://doi.org/10.1155/2016/6162182.
87. Cistaro A, Treglia G, Pagano M, Fania P, Bova V, Basso ME, Fagioli F, Ficola U, Quartuccio N. A comparison between (1)(8)F-FDG PET/CT imaging and biological and radiological findings in restaging of hepatoblastoma patients. Biomed Res Int. 2013;2013:709037. https://doi.org/10.1155/2013/709037.
88. Sharp SE, Parisi MT, Gelfand MJ, Yanik GA, Shulkin BL. Functional-metabolic imaging of neuroblastoma. Q J Nucl Med Mol Imaging. 2013;57(1):6–20.
89. Sharp SE, Shulkin BL, Gelfand MJ, Salisbury S, Furman WL. 123I-MIBG scintigraphy and 18F-FDG PET in neuroblastoma. J Nucl Med. 2009;50(8):1237–43. https://doi.org/10.2967/jnumed.108.060467.
90. DuBois SG, Mody R, Naranjo A, Van Ryn C, Russ D, Oldridge D, Kreissman S, Baker DL, Parisi M, Shulkin BL, Bai H, Diskin SJ, Batra V, Maris JM, Park JR, Matthay KK, Yanik G. MIBG avidity correlates with clinical features, tumor biology, and outcomes in neuroblastoma: a report from the Children's Oncology Group. Pediatr Blood Cancer. 2017;64(11) https://doi.org/10.1002/pbc.26545.
91. Melzer HI, Coppenrath E, Schmid I, Albert MH, von Schweinitz D, Tudball C, Bartenstein P, Pfluger T.

(1)(2)(3)I-MIBG scintigraphy/SPECT versus (1)(8) F-FDG PET in paediatric neuroblastoma. Eur J Nucl Med Mol Imaging. 2011;38(9):1648–58. https://doi.org/10.1007/s00259-011-1843-8.
92. Moinul Hossain AK, Shulkin BL, Gelfand MJ, Bashir H, Daw NC, Sharp SE, Nadel HR, Dome JS. FDG positron emission tomography/computed tomography studies of Wilms' tumor. Eur J Nucl Med Mol Imaging. 2010;37(7):1300–8. https://doi.org/10.1007/s00259-010-1396-2.
93. Mueller WP, Melzer HI, Schmid I, Coppenrath E, Bartenstein P, Pfluger T. The diagnostic value of 18F-FDG PET and MRI in paediatric histiocytosis. Eur J Nucl Med Mol Imaging. 2013;40(3):356–63. https://doi.org/10.1007/s00259-012-2278-6.
94. Phillips M, Allen C, Gerson P, McClain K. Comparison of FDG-PET scans to conventional radiography and bone scans in management of Langerhans cell histiocytosis. Pediatr Blood Cancer. 2009;52(1):97–101. https://doi.org/10.1002/pbc.21782.
95. Sher AC, Orth R, McClain K, Allen C, Hayatghaibi S, Seghers V. PET/MR in the assessment of pediatric histiocytoses: a comparison to PET/CT. Clin Nucl Med. 2017;42(8):582–8. https://doi.org/10.1097/RLU.0000000000001717.
96. Zukotynski K, Fahey F, Kocak M, Kun L, Boyett J, Fouladi M, Vajapeyam S, Treves T, Poussaint TY. 18F-FDG PET and MR imaging associations across a spectrum of pediatric brain tumors: a report from the pediatric brain tumor consortium. J Nucl Med. 2014;55(9):1473–80. https://doi.org/10.2967/jnumed.114.139626.
97. Patil S, Biassoni L, Borgwardt L. Nuclear medicine in pediatric neurology and neurosurgery: epilepsy and brain tumors. Semin Nucl Med. 2007;37(5):357–81. https://doi.org/10.1053/j.semnuclmed.2007.04.002.
98. Bading JR, Shields AF. Imaging of cell proliferation: status and prospects. J Nucl Med. 2008;49(Suppl 2):64S–80S. https://doi.org/10.2967/jnumed.107.046391.
99. McCarville MB, Billups C, Wu J, Kaufman R, Kaste S, Coleman J, Sharp S, Nadel H, Charron M, Lederman H, Don S, Shochat S, Daw NC, Shulkin B. The role of PET/CT in assessing pulmonary nodules in children with solid malignancies. AJR Am J Roentgenol. 2013;201(6):W900–5. https://doi.org/10.2214/AJR.12.10205.
100. Laje P, States LJ, Zhuang H, Becker SA, Palladino AA, Stanley CA, Adzick NS. Accuracy of PET/CT scan in the diagnosis of the focal form of congenital hyperinsulinism. J Pediatr Surg. 2013;48(2):388–93. https://doi.org/10.1016/j.jpedsurg.2012.11.025.
101. Bastawrous S, Bhargava P, Behnia F, Djang DS, Haseley DR. Newer PET application with an old tracer: role of 18F-NaF skeletal PET/CT in oncologic practice. Radiographics. 2014;34(5):1295–316. https://doi.org/10.1148/rg.345130061.

PET/MRI

4

Sergios Gatidis and Jürgen F. Schäfer

4.1 Introduction

In contrast to other imaging techniques discussed in this book, combined PET/MR is a relatively new modality that was first introduced in 2010 for clinical applications [1]. Pediatric imaging was identified as a potential key application of PET/MRI from the beginning mainly due to the significantly reduced diagnostic radiation exposure compared to PET/CT [2]. From this starting point, the discussion about PET/MR applications in pediatric oncology moved forward with the first clinical studies demonstrating technical feasibility, diagnostic equivalence to PET/CT, and the potential for advanced multiparametric and functional tumor characterization [2, 3].

The backbone of pediatric PET/MR is a dedicated MR examination providing detailed anatomical and a significant amount of functional information about tumor localization and biology. The simultaneously acquired PET data offers highly specific information about functional tumor properties such as tumor vitality that cannot be obtained using MRI. Thus, the combination of these two modalities promises comprehensive assessment of oncologic disorders [4].

S. Gatidis (✉) · J. F. Schäfer
Pediatric Imaging, Department of Radiology, University Hospital Tübingen, Tübingen, Germany
e-mail: Sergios.Gatidis@med.uni-tuebingen.de; Juergen.Schaefer@med.uni-tuebingen.de

The discussion about differential indications of PET/MR compared to PET/CT has evolved from a technical and diagnostic comparison of these two hybrid imaging modalities to a careful consideration of strengths and weaknesses of CT, MRI, and PET. Thus, there is a consensus that—wherever available—PET/MR can be used in pediatric oncology whenever a PET is indicated and MRI provides equal or better diagnostic information compared to CT [5].

In this chapter we will give an overview of technical aspects of PET/MR imaging, review practical aspects related to performing pediatric PET/MR, and present a discussion of potential clinical as well as scientific applications.

4.2 Technical Aspects of PET/MRI

4.2.1 Acquisition

The primary challenge for the development of a PET/MR system is the compatibility of high magnetic field strengths of MRI and complex detector design and electronics of PET. Specifically, photomultiplier tubes conventionally used in PET detector systems are highly sensitive to strong magnetic fields. Thus, the introduction of semiconductor-based PET detectors has paved the way for integrated PET/

S. D. Voss, K. McHugh (eds.), *Imaging in Pediatric Oncology*, Pediatric Oncology,
https://doi.org/10.1007/978-3-030-03777-2_4

MRI. Recent PET/MR scanner generations have a fully integrated design with PET detectors being placed within the MR gantry [1, 6]. In contrast to PET/CT, this allows for truly simultaneous acquisition of both modalities.

In contrast to PET/CT, in which CT-based attenuation correction factors can be calculated directly from Hounsfield unit-based tissue density measurements, PET attenuation correction in PET/MR presents unique challenges, as tissue densities cannot be directly measured by MRI. Thus, MR-based PET attenuation correction has been a field of research for many years. The state of the art for MR-based attenuation correction is a combination of a segmentation approach and atlas-based bone estimation. Using a T1-weighted gradient-echo MR sequence, tissues are first segmented into distinct classes (usually fat, lean tissue, lung tissue, and air), and known attenuation coefficients for these tissue classes are inserted; subsequently, the location of bone structures is estimated using a preacquired skeletal atlas. Using this method of attenuation correction, PET SUV deviations compared to CT-based attenuation correction can be reduced to values below 5% [7]. For brain imaging, bone structures can alternatively be visualized using ultrashort echo time (UTE) MR imaging [8].

Because the PET and MR acquisitions can be obtained simultaneously, PET/MR offers the potential for improved image quality compared to sequential hybrid imaging techniques (Fig. 4.1). Where physiological motion or varying urinary bladder volume can cause substantial displacement of adjacent structures, it has been shown in early studies that spatial alignment of PET and MRI is more accurate than with PET and CT in PET/CT [9] (Fig. 4.2). Also, motion information obtained by fast MR imaging can be used to perform motion correction on PET data. So-called joint reconstruction techniques can potentially enhance diagnostic PET quality yielding better spatial and quantitative accuracy in moving organs [10].

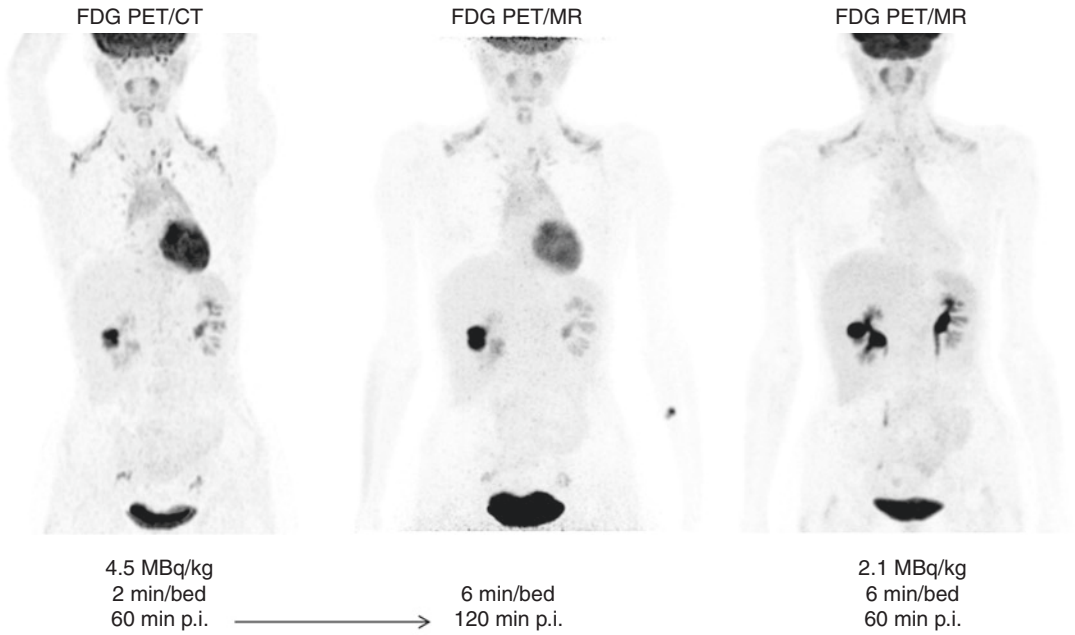

Fig. 4.1 PET in PET/CT and PET/MR. Direct comparison of PET from PET/CT (left figure, arms elevated) and from PET/MR (middle figure, arms down) showing equivalent diagnostic image quality. Increase in PET acquisition time (e.g., 6 min, right figure) allows for substantial reduction in administered tracer activity (here from 4.5 to 2.1 MBq/kg) in PET/MR while maintaining high diagnostic quality

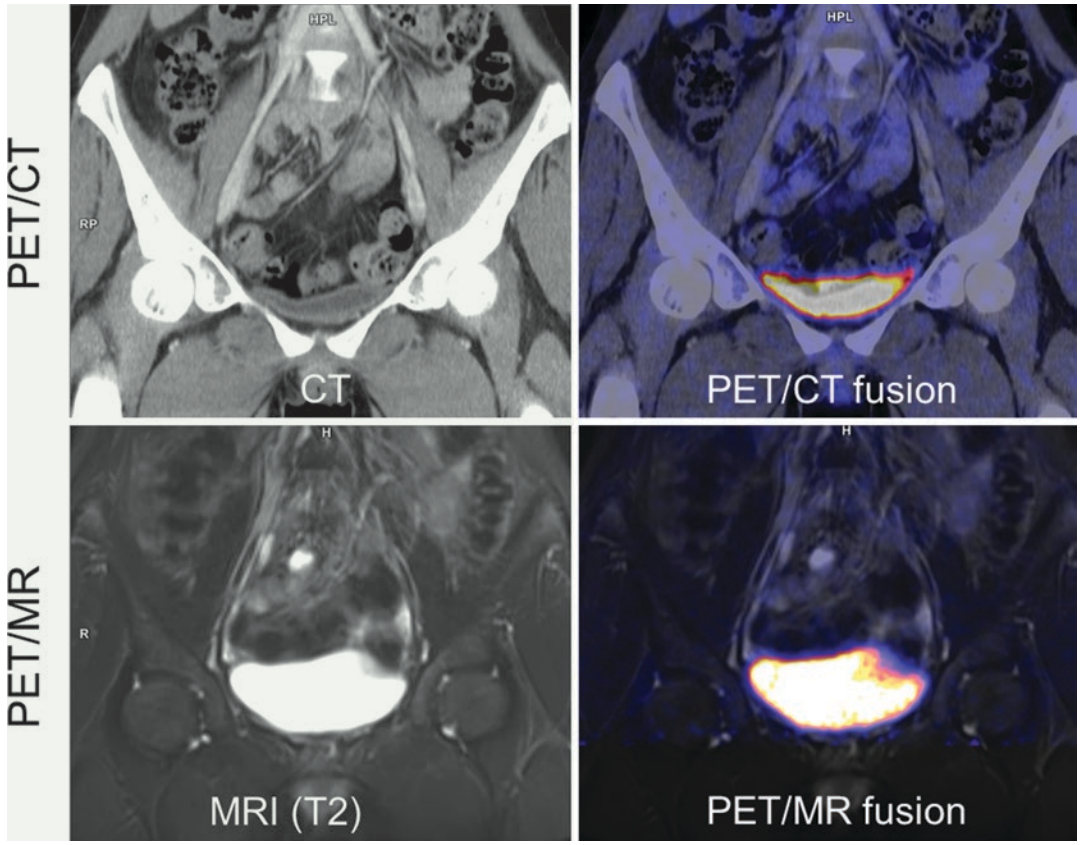

Fig. 4.2 Alignment quality in PET/CT and PET/MR. Simultaneous PET/MR acquisition enables more accurate alignment of anatomic structures between PET and MRI compared to PET and CT in sequential PET/CT. In this example, the bladder volume is different between PET and CT resulting in misalignment compared to perfect alignment in PET/MR

4.2.2 Dose Aspects

The fundamental motivation for implementing pediatric PET/MRI is the significantly reduced diagnostic radiation exposure compared to conventional PET/CT examinations. This can be of considerable importance, as children with cancer are often examined numerous times during the course of disease resulting in high cumulative radiation exposure with potential related risks in long-term survivors. Depending on CT imaging protocols, dose reduction of about 50–70% can be thus achieved [2, 3, 11].

Moreover, simultaneous acquisition of MRI and PET in combination with a large field of view and highly sensitive PET detectors allows for reduction in administered tracer activities. In theory, PET image quality is identical if the product of administered tracer dose and PET sampling time is the same [11]. Compared to PET/CT, PET sampling time is two to three times longer in PET/MR, with MRI usually the time-limiting modality. Thus, tracer doses in PET/MR can be reduced (Fig. 4.1) and are generally on the low side of international ^{18}F-FDG recommendations. It is expected that these recommendations will be revised in the future, with improving detector technology, introduction of solid-state detectors, and corresponding increases in detector sensitivity.

4.3 Practical Aspects

4.3.1 Preparation

Simultaneous PET/MR, mostly performed as a whole-body examination in children, can be considered one of the most complex of the hybrid imaging modalities and thus requires thorough preparation and planning. Indication and choice of PET tracer should be defined in a common effort between pediatric oncologists, pediatric radiologists, and nuclear medicine physicians. Before performing the study, patients and legal guardians should be informed about the rationale and the nature of the examination including information about total examination time and preparation procedures. In this context, potential contraindications should be addressed which are in principle equivalent to MR contraindications such as noncompatible implants and claustrophobia. In addition, necessary preparation steps for oncologic FDG-PET imaging, such as fasting and minimizing strenuous activity, have to be conveyed. Importantly, the necessity for patient sedation should also be evaluated early on in the process. In general, the preparation steps before the examination are in principle the same as for wbMRI and PET/CT examinations, which are described in detail in the respective chapters of this book.

4.3.2 Protocol

Due to the high versatility of MRI, PET/MR protocols can vary significantly depending on the clinical question, patient compliance, anatomical site, and particular local preferences [5, 12, 13]. For pediatric imaging, two aspects should be considered in particular: patient compliance can be limited, and the repetition of diagnostic radiation exposure (related to repeat FDG tracer administrations) should be avoided if possible. Thus, it is advisable to begin pediatric PET/MR examinations with the PET acquisition combined with the essential MR sequences. Typically, oncologic whole-body PET/MR protocols include simultaneous bed-per-bed measurement of PET and whole-body MR sequences, mostly a T1-weighted sequence (also used for attenuation correction), a T2-weighted fat-saturated sequence, and potentially diffusion-weighted imaging (DWI) (Fig. 4.3). Subsequently, MR-only acquisitions can be performed freely, including local tumor imaging, contrast-enhanced MRI, or CNS imaging.

Neuro-oncologic protocols are simpler as the acquisition is mostly performed over a single stationary position allowing for continuously simultaneous PET/MR measurements.

Despite developments in MR sequence design, with increased availability of motion-robust

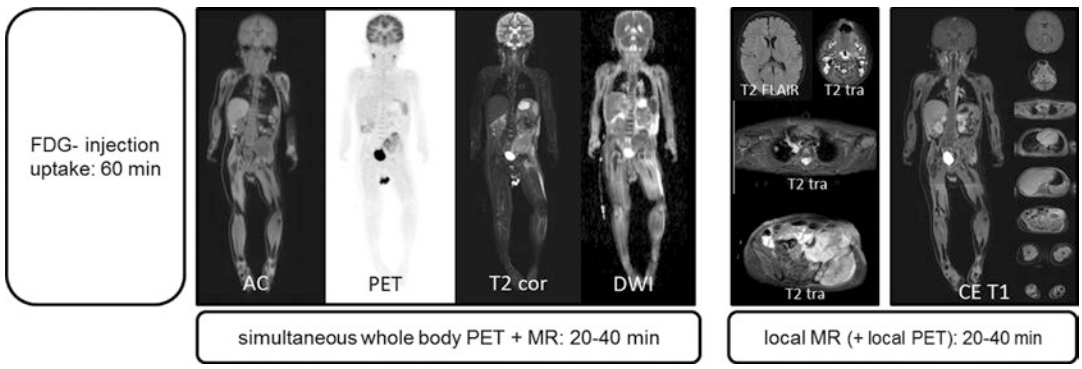

Fig. 4.3 Typical oncologic whole-body FDG-PET/MR protocol in children (2-year-old boy). After 60 min of uptake time, simultaneous whole-body PET and MR measurements are performed including a sequence for attenuation correction (AC), morphological imaging (in this case coronal T2w STIR sequence), and optionally diffusion-weighted imaging (DWI). Subsequently, local MRI and contrast-enhanced (CE) MRI can be performed as in any other MR scanner with the option of additional simultaneous local PET imaging

ultrafast sequences, examination times are still relatively long for combined PET/MR examinations, reaching between 45 and 90 min for whole-body imaging studies, depending largely on the extent of MR measurements.

As PET/MR is considered a comprehensive oncologic imaging tool, image quality should be as high as possible, even in children who cannot cooperate well. Thus, acceleration techniques and motion-robust MR techniques (e.g., radial sampling) should be implemented where available. Furthermore, dedicated morphological lung imaging is a central requirement in oncologic PET/MR in order to avoid additional chest CT if possible, although the routine use of MRI, as opposed to CT, for detecting pulmonary nodules has not been universally accepted. Advanced MR techniques such as UTE sequences are being developed and are of considerable value in obtaining high-quality MR images of the thorax.

4.3.3 Post-processing and Interpretation

PET/MR data are complex with respect to the usually large number of acquired images as well as their multidimensional and multiparametric nature. Thus, post-processing is an essential step prior to reading and interpretation. High-performance software solutions that provide image processing tools for image fusion, image reformation, and advanced analysis of both PET imaging results and functional MR imaging data such as DWI or DCE are an absolute prerequisite and are available from multiple commercial vendors. Furthermore, examination results should be visualized in a way that they can be presented to referring pediatricians as well as patients and parents.

Similarly, image interpretation is a challenge in PET/MRI. PET/MR examinations should be interpreted by pediatric imaging specialists (radiologists and nuclear medicine physicians) and finally presented and discussed in an interdisciplinary setting with referring clinicians.

Specific attention should be paid to possible artifacts in MR-based attenuation correction that can affect PET images. Thus the evaluation of the attenuation map and of non-corrected PET images are part of structured reading in PET/MR. Pitfalls when reading the PET images are in large part the same as in PET/CT. However, the danger of insufficient attention to single sequences must be emphasized and is mainly caused by overly lengthy MR protocols, resulting in large volumes of often redundant image information (Fig. 4.4). This is especially the case when focal lesions are PET-negative, and the tendency to add multiple additional MR sequences to the exam usually adds little additional diagnostic information while dramatically lengthening exam duration. Therefore, in order to avoid misinterpretation, sufficient time, technical expertise, optimal work environment including a dedicated image viewer, and a high level of experience by a team of dedicated pediatric imaging specialists are essential to the success of any PET/MR program.

4.4 PET/MR Applications and Potential Advantages

In general, PET/MR can be used for children whenever PET/CT is indicated, and no contraindications for MRI are present. In general, a major advantage of PET/MR is the possibility of both whole-body staging and local tumor assessment in a single session rendering additional examinations unnecessary and thus potentially reducing the number of necessary sedations. Moreover, particularly in cases of equivocal or nonspecific uptake (e.g., bowel uptake), the excellent soft-tissue contrast of MRI offers the opportunity for higher confidence differentiating between normal and abnormal findings [14].

4.4.1 Lymphoma

FDG-PET is indicated for staging, therapy response assessment, and detection of recurrence in Hodgkin lymphoma and high-grade lymphoma in children. As described in the previous chapter, PET/CT in most centers remains the modality of choice for this purpose. PET/MR offers equivalent diagnostic information as PET/CT with respect to

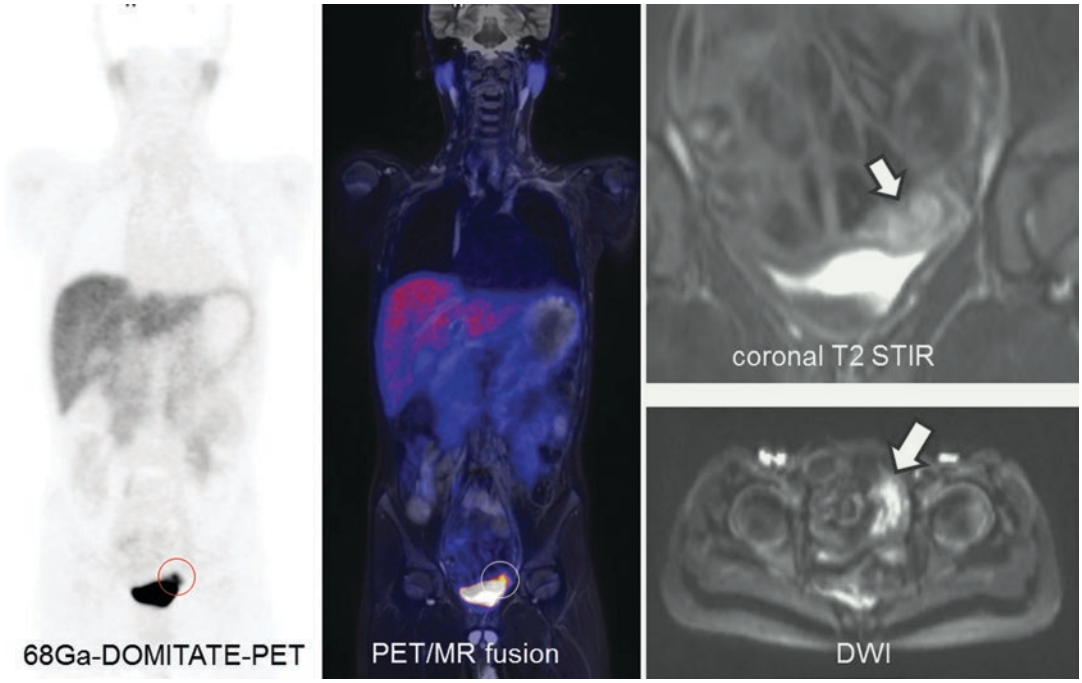

Fig. 4.4 Patient with recurrent paraganglioma. DOMITATE-PET/MR reveals a mass adjacent to the urinary bladder with marked diffusion restriction (DWI). Due to the adjacent bladder, however, this uptake could easily be missed in PET in this case showing how important careful evaluation of all available image data is

PET and potential advantages by MRI for assessing bone marrow infiltration and involvement of solid organs (Fig. 4.5). Concerning assessment of pulmonary involvement in lymphoma, PET/MRI using state-of-the-art lung MRI and MR-based PET motion correction can be regarded as diagnostically equivalent to PET/CT. A significant diagnostic advantage of PET/MR over PET/CT can be expected in lymphoma with low or heterogeneous FDG avidity. In these cases, high soft-tissue contrast and functional information (e.g., DWI) from MRI can provide decisive diagnostic information [15].

4.4.2 Sarcoma

Due to its high soft-tissue contrast, MRI is the modality of choice for imaging of children with sarcoma offering information about local tumor extent as well as whole-body staging [16] (Fig. 4.6). FDG-PET can add information about initial tumor metabolism that can be prognostically relevant as well as about tumor vitality after neoadjuvant therapy [4, 17]. Furthermore, PET/MR can help in distinguishing therapy effects from residual or recurrent tumor after therapy and thus increase specificity compared to MRI alone [4]. A possible limitation of PET/MR over PET/CT is the limited sensitivity for small pulmonary metastases that can be prognostically and therapeutically highly relevant in children with sarcoma [18]. Thus, an additional chest CT should initially be performed in these patients, as well as in other patients with malignancies carrying a high risk of pulmonary metastases. This limitation may potentially be overcome with further developments in MR lung imaging techniques in the future.

4.4.3 Neuroblastoma

Although the 123I-mIBG scan is established as the reference modality, MRI and FDG-PET play important roles for the diagnostic work-up in children with neuroblastoma [19, 20]. MRI provides information about local tumor spread

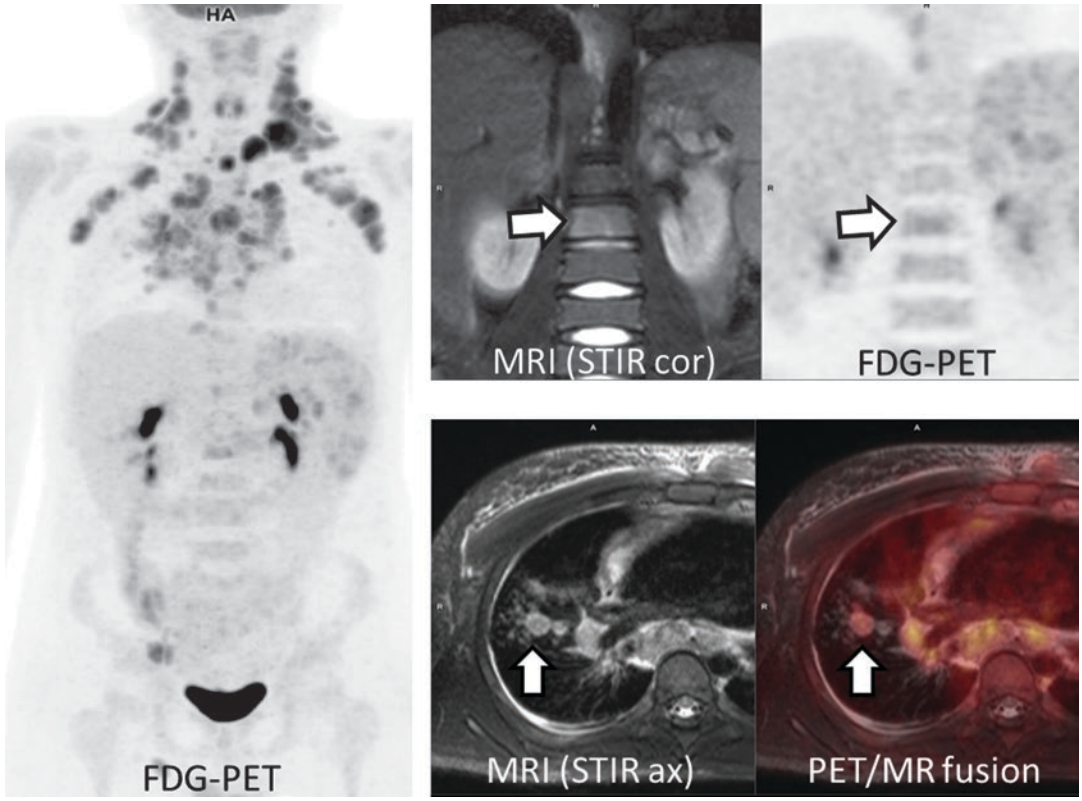

Fig. 4.5 PET/MR in lymphoma. Patient with Hodgkin lymphoma stage IV. MRI shows pulmonary and bone marrow involvement (arrows) also in areas with only subtle FDG uptake

that is relevant for surgical planning, has high sensitivity for the detection of distant metastases, and furthermore offers information about tumor biology using DWI. MIBG-negative neuroblastomas are associated with a generally better prognosis [21]. On the other hand, elevated FDG uptake in neuroblastoma may indicate poor prognosis [22] (Fig. 4.7). With the recent development and expected clinical translation of the PET analogue of 123I-MIBG—^{18}F-MFBG—PET/MR can become the comprehensive diagnostic tool in neuroblastoma assessing tumor spread and tumor biology in a single examination [23].

4.4.4 Neuroendocrine Tumors (NETs)

Staging as well as tumor characterization of NETs can be performed exceptionally well with PET using specific tracers such as somatostatin receptor (SSR) ligands (^{18}Ga DOMITATE and DOTATATE) (Fig. 4.4) in well-differentiated tumors or FDG in dedifferentiated tumors [24]. The degree of tracer uptake using receptor-specific tracers or FDG thus also provides information on tumor biology. PET/MR can be preferentially used over PET/CT in cases of soft-tissue involvement, e.g., for imaging small liver metastases [25].

4.4.5 Neurofibromatosis Type I

FDG-PET has been identified as a good marker for the prediction of malignant transformation of plexiform neurofibroma into a malignant peripheral nerve sheath tumor (MPNST) [26, 27]. MRI on the other hand allows for detailed anatomical depiction of soft-tissue lesions in these patients and is thus highly relevant for biopsy and surgical planning [28]. PET/MR combines both aspects and in addition enables dedicated imaging of

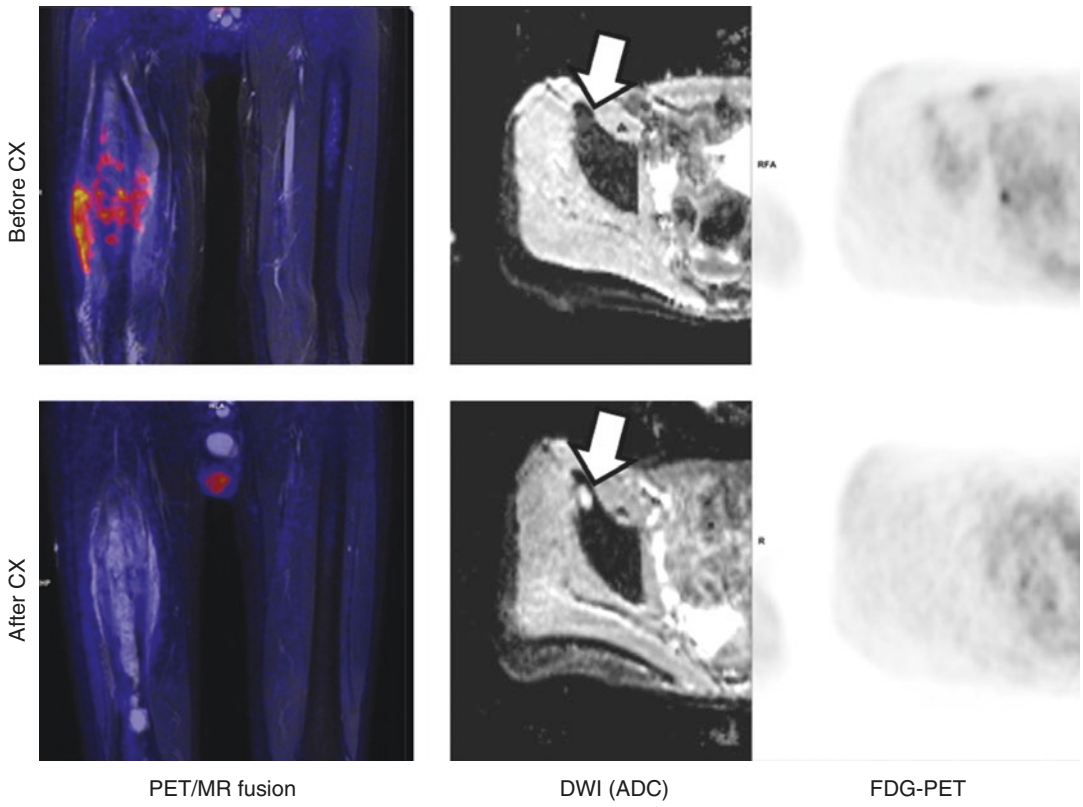

Fig. 4.6 FDG-PET/MR in sarcoma. This example shows PET/MR images of a patient with metastatic Ewing sarcoma of the right femur. Initial staging (top row) revealed a large mass with FDG uptake in the right femur and osseous metastases with marked diffusion restriction (arrow) but low FDG uptake. After chemotherapy (bottom row), therapy response of the primary tumor was established by reduced FDG uptake. In the metastases, however, DWI was the relevant marker demonstrating response to therapy, with increased diffusivity and high signal on the DWI (ADC) images

CNS changes that are often present in these patients. Furthermore, reduced radiation exposure of PET/MR compared to PET/CT is of relevance in these patients, who have an initially benign condition but who are imaged repeatedly during their lifetime.

4.4.6 Cancer Predisposition Syndromes

Similarly to patients with NF-1, numerous rare genetic syndromes with elevated risk for the development of malignant tumors are known and require close observation already in childhood. In these patients, MR may be the first modality of choice for screening. However, the addition of PET using combined PET/MR can potentially reduce the false-positive rate [29].

4.4.7 CNS Tumors

Pediatric CNS tumors are mostly diagnosed using multiparametric MRI. In certain clinical situations, i.e., poorly characterized brain tumors, prior to biopsy and after treatment, additional PET using dedicated tracers (amino acid tracers, e.g., methionine or FET for glioma) can provide information about tumor histology, tumor grade, and the presence of tumor recurrence [30] (Fig. 4.8). In these situations, PET and MRI can be performed in a single scan reducing total examination time and potentially the number of sedations.

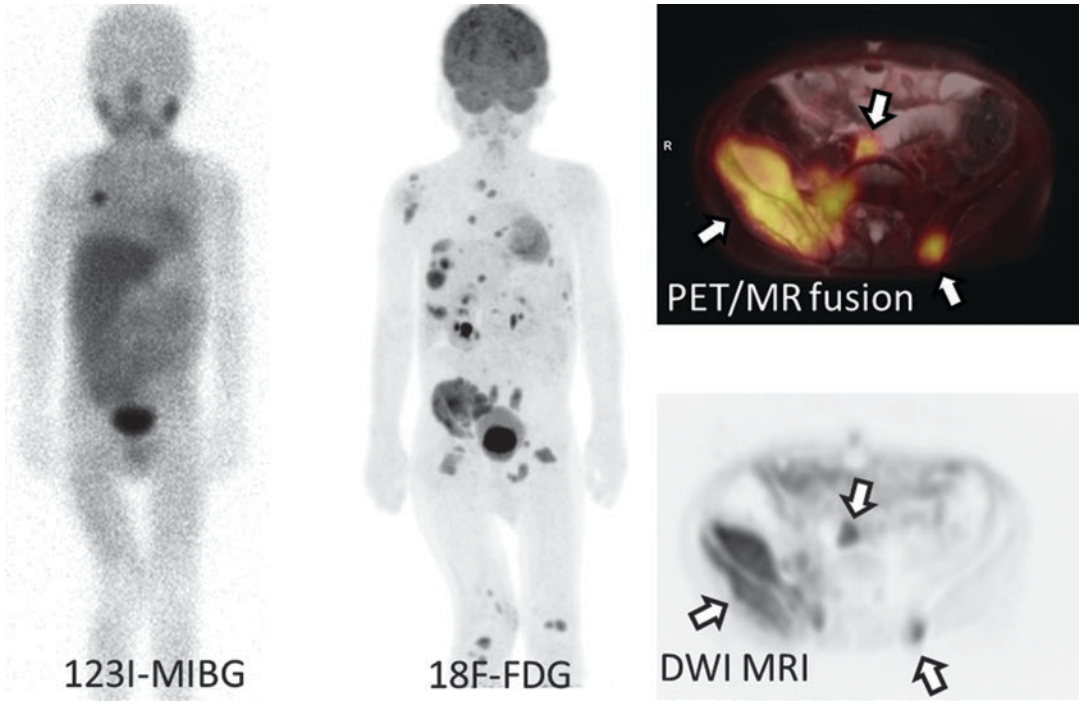

Fig. 4.7 PET/MR in neuroblastoma. Patient with recurrent neuroblastoma stage IV. 123I-MIBG scintigraphy (left figure) shows no pathologic uptake, while FDG-PET (middle figure) reveals disseminated metastases weeks later implying poor prognosis. DWI MRI (lower right figure) provides information very similar to FDG-PET (upper right figure)

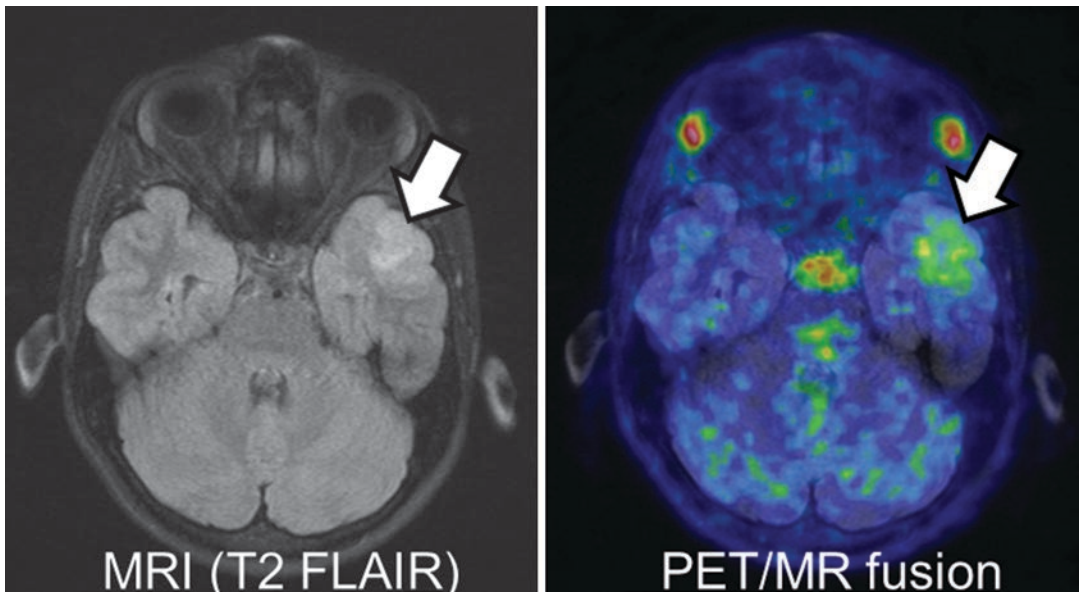

Fig. 4.8 PET/MR in neuro-oncology. Patient with ganglioglioma WHO grade 1. MRI (left figure) reveals a subtle lesion in the left temporal lobe. ^{11}C-Methionine PET (right figure) shows focal uptake establishing the likely diagnosis of a CNS tumor and enabling image-guided biopsy and resection

4.5 Research

Currently, the availability of PET/MR for imaging children, both in the US and Europe, is limited to a few major centers. Thus, despite the numerous potential advantages and applications stated above, PET/MR cannot yet be considered a standard modality in pediatric oncology. However, PET/MR is certainly an exceptional tool for preclinical and clinical research. The potential for functional and metabolic imaging using PET and MRI in a single scanner is unparalleled and can be used to gain insight into the pathophysiology of pediatric tumors, to better understand effects of oncologic therapies, and to validate novel developments in radiopharmacy and MR technology.

References

1. Delso G, Furst S, Jakoby B, Ladebeck R, Ganter C, Nekolla SG, Schwaiger M, Ziegler SI. Performance measurements of the Siemens mMR integrated whole-body PET/MR scanner. J Nucl Med. 2011;52(12):1914–22.
2. Schafer JF, Gatidis S, Schmidt H, Guckel B, Bezrukov I, Pfannenberg CA, Reimold M, Ebinger M, Fuchs J, Claussen CD, Schwenzer NF. Simultaneous whole-body PET/MR imaging in comparison to PET/CT in pediatric oncology: initial results. Radiology. 2014;273(1):220–31.
3. Gatidis S, Schmidt H, Gucke B, Bezrukov I, Seitz G, Ebinger M, Reimold M, Pfannenberg CA, Nikolaou K, Schwenzer NF, Schafer JF. Comprehensive oncologic imaging in infants and preschool children with substantially reduced radiation exposure using combined simultaneous (18)F-fluorodeoxyglucose positron emission tomography/magnetic resonance imaging: a direct comparison to (18)F-fluorodeoxyglucose positron emission tomography/computed tomography. Invest Radiol. 2016;51(1):7–14.
4. Pfluger T, Melzer HI, Mueller WP, Coppenrath E, Bartenstein P, Albert MH, Schmid I. Diagnostic value of combined (18)F-FDG PET/MRI for staging and restaging in paediatric oncology. Eur J Nucl Med Mol Imaging. 2012;39(11):1745–55.
5. Gatidis S, Bender B, Reimold M, Schafer JF. PET/MRI in children. Eur J Radiol. 2017;94:A64.
6. Levin CS, Maramraju SH, Khalighi MM, Deller TW, Delso G, Jansen F. Design features and mutual compatibility studies of the time-of-flight PET capable GE SIGNA PET/MR system. IEEE Trans Med Imaging. 2016;35(8):1907–14.
7. Bezrukov I, Schmidt H, Gatidis S, Mantlik F, Schafer JF, Schwenzer N, Pichler BJ. Quantitative evaluation of segmentation- and atlas-based attenuation correction for PET/MR on pediatric patients. J Nucl Med. 2015;56(7):1067–74.
8. Hofmann M, Pichler B, Scholkopf B, Beyer T. Towards quantitative PET/MRI: a review of MR-based attenuation correction techniques. Eur J Nucl Med Mol Imaging. 2009;36(Suppl 1):S93–104.
9. Brendle CB, Schmidt H, Fleischer S, Braeuning UH, Pfannenberg CA, Schwenzer NF. Simultaneously acquired MR/PET images compared with sequential MR/PET and PET/CT: alignment quality. Radiology. 2013;268(1):190–9.
10. Wurslin C, Schmidt H, Martirosian P, Brendle C, Boss A, Schwenzer NF, Stegger L. Respiratory motion correction in oncologic PET using T1-weighted MR imaging on a simultaneous whole-body PET/MR system. J Nucl Med. 2013;54(3):464–71.
11. Gatidis S, Schmidt H, la Fougere C, Nikolaou K, Schwenzer NF, Schafer JF. Defining optimal tracer activities in pediatric oncologic whole-body 18F-FDG-PET/MRI. Eur J Nucl Med Mol Imaging. 2016;43:2283.
12. Aghighi M, Pisani LJ, Sun Z, Klenk C, Madnawat H, Fineman SL, Advani R, Von Eyben R, Owen D, Quon A, Moseley M, Daldrup-Link HE. Speeding up PET/MR for cancer staging of children and young adults. Eur Radiol. 2016;26(12):4239–48.
13. Klenk C, Gawande R, Tran VT, Leung JT, Chi K, Owen D, Luna-Fineman S, Sakamoto KM, McMillan A, Quon A, Daldrup-Link HE. Progressing toward a cohesive pediatric 18F-FDG PET/MR protocol: is administration of gadolinium chelates necessary? J Nucl Med. 2016;57(1):70–7.
14. Gatidis S, Guckel B, la Fougere C, Schmitt J, Schafer JF. Simultaneous whole-body PET-MRI in pediatric oncology: more than just reducing radiation? Radiologe. 2016;56(7):622–30.
15. Asenbaum U, Nolz R, Karanikas G, Furtner J, Woitek R, Simonitsch-Klupp I, Raderer M, Mayerhoefer ME. Bone marrow involvement in malignant lymphoma: evaluation of quantitative PET and MRI biomarkers. Acad Radiol. 2017;25:453.
16. Tzeng CW, Smith JK, Heslin MJ. Soft tissue sarcoma: preoperative and postoperative imaging for staging. Surg Oncol Clin N Am. 2007;16(2):389–402.
17. Byun BH, Kong CB, Park J, Seo Y, Lim I, Choi CW, Cho WH, Jeon DG, Koh JS, Lee SY, Lim SM. Initial metabolic tumor volume measured by 18F-FDG PET/CT can predict the outcome of osteosarcoma of the extremities. J Nucl Med. 2013;54(10):1725–32.
18. Rauscher I, Eiber M, Furst S, Souvatzoglou M, Nekolla SG, Ziegler SI, Rummeny EJ, Schwaiger M, Beer AJ. PET/MR imaging in the detection and characterization of pulmonary lesions: technical and diagnostic evaluation in comparison to PET/CT. J Nucl Med. 2014;55(5):724–9.
19. Lee JW, Cho A, Yun M, Lee JD, Lyu CJ, Kang WJ. Prognostic value of pretreatment FDG PET in pediatric neuroblastoma. Eur J Radiol. 2015;84(12):2633–9.

20. Goo HW. Whole-body MRI of neuroblastoma. Eur J Radiol. 2010;75(3):306–14.
21. Dubois SG, et al. MIBG avidity correlates with clinical features, tumor biology, and outcomes in neuroblastoma: a report from the Children's Oncology Group. Pediatr Blood Cancer. 2017;64(11) https://doi.org/10.1002/pbc.26545.
22. Papathanasiou ND, Gaze MN, Sullivan K, Aldridge M, Waddington W, Almuhaideb A, Bomanji JB. 18F-FDG PET/CT and 123I-metaiodobenzylguanidine imaging in high-risk neuroblastoma: diagnostic comparison and survival analysis. J Nucl Med. 2011;52(4):519–25.
23. Zhang H, Huang R, Cheung NK, Guo H, Zanzonico PB, Thaler HT, Lewis JS, Blasberg RG. Imaging the norepinephrine transporter in neuroblastoma: a comparison of [18F]-MFBG and 123I-MIBG. Clin Cancer Res. 2014;20(8):2182–91.
24. Poeppel TD, Binse I, Petersenn S, Lahner H, Schott M, Antoch G, Brandau W, Bockisch A, Boy C. 68Ga-DOTATOC versus 68Ga-DOTATATE PET/CT in functional imaging of neuroendocrine tumors. J Nucl Med. 2011;52(12):1864–70.
25. Sawicki LM, Deuschl C, Beiderwellen K, Ruhlmann V, Poeppel TD, Heusch P, Lahner H, Fuhrer D, Bockisch A, Herrmann K, Forsting M, Antoch G, Umutlu L. Evaluation of (68)Ga-DOTATOC PET/MRI for whole-body staging of neuroendocrine tumours in comparison with (68)Ga-DOTATOC PET/CT. Eur Radiol. 2017;27(10):4091–9.
26. Warbey VS, Ferner RE, Dunn JT, Calonje E, O'Doherty MJ. [18F]FDG PET/CT in the diagnosis of malignant peripheral nerve sheath tumours in neurofibromatosis type-1. Eur J Nucl Med Mol Imaging. 2009;36(5):751–7.
27. Tsai LL, Drubach L, Fahey F, Irons M, Voss S, Ullrich NJ. [18F]-Fluorodeoxyglucose positron emission tomography in children with neurofibromatosis type 1 and plexiform neurofibromas: correlation with malignant transformation. J Neurooncol. 2012;108(3):469-75. https://doi.org/10.1007/s11060-012-0840-5.
28. Wasa J, Nishida Y, Tsukushi S, Shido Y, Sugiura H, Nakashima H, Ishiguro N. MRI features in the differentiation of malignant peripheral nerve sheath tumors and neurofibromas. AJR Am J Roentgenol. 2010;194(6):1568–74.
29. Kratz CP, Achatz MI, Brugieres L, Frebourg T, Garber JE, Greer MLC, Hansford JR, Janeway KA, Kohlmann WK, Mcgee R, Mullighan CG, Onel K, Pajtler KW, Pfister SM, Savage SA, Schiffman JD, Schneider KA, Strong LC, Evans DGR, Wasserman JD, Villani A, Malkin D. Cancer screening recommendations for individuals with Li-Fraumeni syndrome. Clin Cancer Res. 2017;23(11):E38–45.
30. Bisdas S, Ritz R, Bender B, Braun C, Pfannenberg C, Reimold M, Naegele T, Ernemann U. Metabolic mapping of gliomas using hybrid MR-PET imaging: feasibility of the method and spatial distribution of metabolic changes. Invest Radiol. 2013;48(5):295–301.

SPECT/CT in Pediatric Oncology

5

Helen Nadel and Lorenzo Biassoni

5.1 Background

Hybrid imaging scanners combining single-photon emission computed tomography (SPECT) imaging and computed tomography (CT) in one single imaging device have been commercially available since the beginning of the 2000s. These imaging techniques can combine tumor avidity provided by tumor-avid radiopharmaceuticals with the anatomical definition of CT [1]. Hybrid imaging with SPECT/CT has been shown to be superior to side-by-side reading of SPECT and CT scans [2] and has now become the state-of-the-art radionuclide imaging modality in several clinical conditions.

Although positron emission tomography (PET) has a significant advantage in sensitivity and a higher spatial resolution over conventional SPECT imaging, due mostly to the methods of collimation used in SPECT as compared to coincidence photon detection in PET, SPECT arguably has several advantages over PET. The physical half-lives for many SPECT radionuclides are generally longer and more aligned with the biologic half-lives of physiologic processes of interest; SPECT radiotracers are readily available and do not require the relatively close proximity to a medical cyclotron and a rapid distribution network; there is the potential for simultaneous multi-tracer studies with different radionuclides examining different biologic pathways in a single imaging session. The systems are also of lower cost and have a much greater installed base worldwide.

In pediatrics, similar to adults, SPECT/CT imaging is attractive because, if used at its full potential, it offers an opportunity to reduce the number of equivocal studies, the need for further diagnostic tests, and future hospital visits (scintigraphic multitasking) [3]. However, it is not without challenges, the main one being the additional radiation dose from the CT component of the study. Children are particularly sensitive to ionizing radiation, and any radiation exposure in a child should be justified to make sure that the clinical benefits outweigh the risks.

Previous published work has shown the superiority of SPECT/CT with a hybrid imaging device in diagnostic imaging interpretation [2, 4–7], with some reports also in pediatrics [1, 3].

Radionuclide imaging with SPECT/CT is now commonly used in adult nuclear medicine practice, with a wide variety of indications ranging from myocardial perfusion imaging, orthopedics,

H. Nadel
Department of Radiology, Lucile Packard Children's Hospital at Stanford, Stanford University School of Medicine, Stanford, CA, USA
e-mail: hnadel@stanford.edu

L. Biassoni (✉)
Department of Radiology, Great Ormond Street Hospital NHS Foundation Trust, London, UK
e-mail: Lorenzo.Biassoni@gosh.nhs.uk

S. D. Voss, K. McHugh (eds.), *Imaging in Pediatric Oncology*, Pediatric Oncology,
https://doi.org/10.1007/978-3-030-03777-2_5

cancer imaging (including post-radionuclide therapy scanning), brain imaging, and others. In pediatric radionuclide imaging, the SPECT/CT technique has been incorporated more slowly in clinical practice. We discuss some clinical applications of this imaging technique in pediatric oncology and present possible future developments.

5.2 Technical Considerations

When a request to perform a radionuclide imaging study with SPECT/CT is received in the nuclear medicine department, consideration must be given as to whether the study is indicated. The clinical history of the patient must be available, as well as the previous radiological examinations related to the clinical condition under investigation.

The amount of radiopharmaceutical activity to be administered is based on the patient's weight. The two most widely used methods to determine the injected activity are the North American consensus group recommendations and the European Association of Nuclear Medicine (EANM) pediatric dosage card [8, 9]; these have been updated and incorporated into a unified dosage card with recommendations for radiopharmaceutical use in pediatrics.

Following the injection of the radiopharmaceutical, usually the planar images are acquired first. The SPECT study follows and is centered on the body segments of interest, based on the clinical question, on the findings of the planar images, and on previous imaging studies.

The CT component of the study is planned in such a way that it will help answer the clinical question with the lowest possible administered radiation dose. Three options for CT imaging are available, depending on the logistics of the radiology department, on the patient's disease status and treatment-related considerations, and on the model of SPECT/CT scanner available [10]. These include a fully diagnostic CT scan with intravenous contrast, a low-dose unenhanced CT scan for anatomical localization and image fusion, and an ultralow-dose CT scan for attenuation correction only.

The use of a contrast-enhanced CT scan with fully diagnostic parameters in conjunction with a SPECT study is justified only if it can avoid another contrast-enhanced CT scan that would have been necessary to guide clinical management. In this case, i.v. access must be available at the time of the study. Usually, the contrast bolus is timed for portal venous opacification. The dose of IV contrast to be administered is weight-based; 2 mg/kg up to maximum of 100 mL contrast is typical although some variability will exist between institutions. Although CT contrast reactions in children are infrequent, nonionic contrast is preferred. Contraindications and allergies to contrast should be determined prior to the study being performed. In some institutions, confirmation of adequate renal function is required, based on correlation with laboratory values for BUN and creatinine (see Manual on Contrast Media by the American College of Radiology [11]).

In clinical conditions when the cross-sectional imaging modality of choice is an MRI, the CT component of a SPECT/CT study is usually acquired with parameters for anatomical localization and image fusion purposes, in order to significantly reduce the radiation dose to the patient. The scan will have lower resolution and greater noise content than a fully diagnostic CT, with possible streak artifacts. However, a low-dose unenhanced CT scan can provide images of diagnostic quality in the skeleton and therefore be of great clinical utility when combined with bone scintigraphy in the context of musculoskeletal conditions, waiving the need for another CT scan.

When a SPECT study only is needed, the CT component of the study can be planned with ultralow-exposure settings for attenuation correction only, reducing the CT dose to about 3% of a diagnostic CT dose [12]. This is often the case with brain scintigraphy examinations, when the imaging modality of choice is a brain MRI and the CT component is usually noncontributory from a diagnostic point of view. The attenuation-corrected SPECT images can be easily co-registered to the brain MRI on a processing workstation using one of the commercially available software packages.

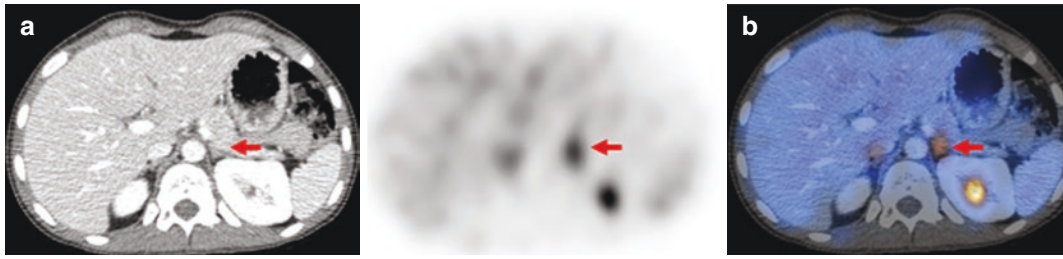

Fig. 5.1 Optimized SPECT/CT study showing contrast-enhanced CT of the abdomen (**a**) and ^{123}I-mIBG SPECT imaging (**b**), together with co-registered ^{123}I-mIBG SPECT /CT, demonstrating normal physiologic uptake of tracer in a normal appearing left adrenal gland (arrows). The CT component also shows normal contrast-enhanced abdominal viscera and normal opacification of the large vessels

The added value of obtaining the optimized post-contrast-enhanced CT study is an increased sensitivity for lesion detection, improved localization of lesions, and better activity delineation that can help distinguish between likely benign or physiologic activity and a pathologic process. In addition, incidental findings that can be significant may be detected when both SPECT and CT are combined and viewed as co-registered imaging versus their individual parts (Fig. 5.1).

An oncological radionuclide imaging examination is a lengthy procedure, requiring often more than 1 h, and it is essential—particularly for SPECT acquisitions—that the child keeps still during the exam. Children younger than 5–6 years of age may require sedation or general anesthesia (GA). If pediatric anesthetic support is available in the hospital, GA is usually preferable to sedation, as the effect of sedation can diminish before the end of the study, at which point providing additional sedation may not be effective or desirable. The child is usually assessed by an anesthesiologist prior to tracer administration to make sure that there are no contraindications for anesthesia. Sedated/anesthetized children are fully monitored during the procedure and are recovered by the anesthesiologist or nursing staff at the end of the examination.

Once the SPECT/CT examination has been acquired, the images are processed. The SPECT and the CT images are checked for motion and accuracy of co-registration. If a minor degree of misregistration is noted, this may be corrected with post-processing software; repeating the SPECT acquisition because of motion artifacts and misregistration is generally not necessary and should be avoided whenever possible, particularly if repeat imaging will prolong sedation/anesthesia. Once the images have been properly processed and fused, the SPECT/CT study is ready for clinical reporting by the radiologist.

While most SPECT/CT gamma cameras have sodium iodide detectors, the introduction of new solid-state detectors to full-field-of-view general-purpose SPECT/CT gamma cameras provides an option to develop different strategies to potentially reduce administered activity of radiopharmaceutical and/or reduce time to image for planar imaging and SPECT. The improved special resolution of the solid-state cadmium zinc telluride (CZT) detectors can potentially detect lesions as small as 2.5 mm compared to 4 mm for sodium iodide detectors. This is due to their direct conversion capability with reduced dead space time between detection events. There is also increased lesion conspicuity with sharpening of edges that can increase the certainty of a diagnosis. These detectors are optimized for ^{99m}Tc-based radiopharmaceuticals but in early studies are proving beneficial for imaging with ^{123}I-mIBG as well, with some manipulation of processing parameters [13] (Figs. 5.2, 5.3, and 5.9d).

The acquisition, processing, and review of images from SPECT/CT gamma cameras are dependent on specific hardware and software installations. Therefore, specific parameters for acquisition and processing are best optimized in the imaging department setting, and other than for conventional sodium iodide gamma camera systems listed below will not be specified here.

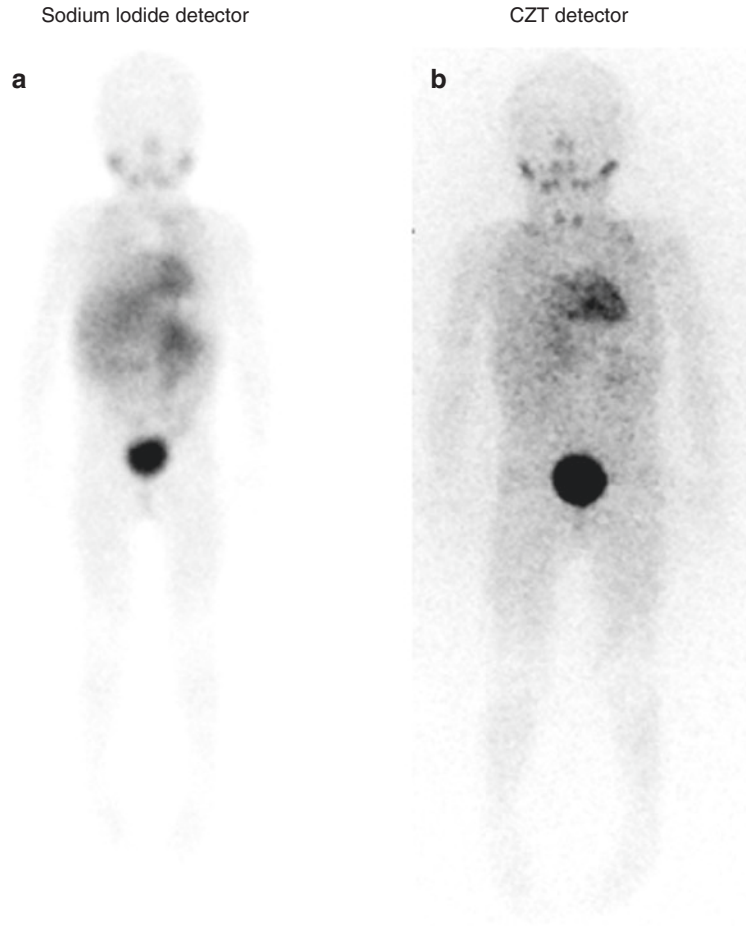

Fig. 5.2 Whole body ^{123}I-mIBG planar imaging of a 7-year-old patient with neuroblastoma. Imaging was performed at two different time intervals and on two different full field of view detector gamma camera systems. Images were acquired on a camera with conventional sodium iodide detectors (**a**) using a scan speed of 10 cm/min and a 15% energy window. Follow-up imaging was performed on a cadmium zinc telluride (CZT) solid-state detector, full field of view, gamma camera system (**b**) using a scan speed of 5 cm/min and an 11.5% energy window. While there is increased background activity on CZT system, there is sharper visualization of normal physiologic salivary gland, thyroid, and cardiac activity. By optimizing the energy window selection for CZT, there is improved spatial resolution with the CZT detector system, despite the shorter scan time

Table 5.1 identifies some general principles that can be applied to all SPECT/CT imaging systems with which oncologic imaging will be performed (Table 5.1).

Viewing of co-registered images can be performed on vendor-based nuclear medicine workstations. It is also possible to use third-party plug-in and dedicated systems to provide higher-level processing for the co-registered images and include software packages that can view multi-planar reformats of the co-registered images for multiple time-point studies. Co-registration of studies to other cross-sectional imaging including MR, CT, and PET/CT is possible. Higher-level processing of the CT studies for liver segmentation, tumor lesion tracking, RECIST, and WHO criteria are commercially available. Some programs are available for quantitation of activity based on SPECT imaging, similar to the standardized uptake values (SUV) commonly used with PET imaging. As yet, there is no baseline value or validation of the programs for pediatric studies available.

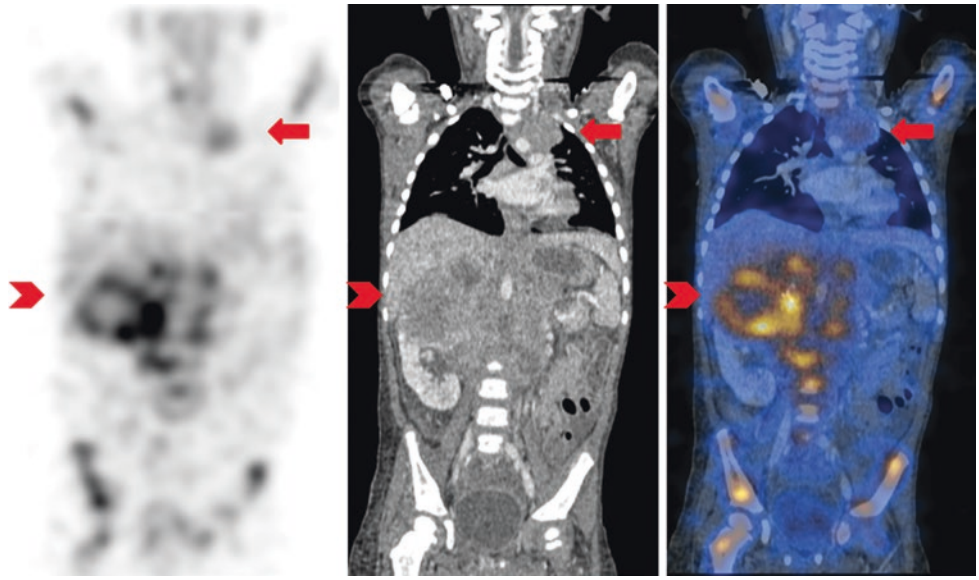

Fig. 5.3 ^{123}I-mIBG SPECT/CT in a 2-year-old child with stage 4 neuroblastoma. Coronal ^{123}I-mIBG SPECT/CT images show a large abdominal mass in the mid and right upper abdomen (chevron). The primary tumor is characterized by high mIBG avidity surrounding a central photopenic area, corresponding to regions of low attenuation on the accompanying CT and most likely due to necrosis. The SPECT/CT study also identifies a focal mIBG avid mass in the left upper thorax (arrow), indicating metastatic spread to a left supraclavicular (Virchow) lymph node. There is diffuse skeletal involvement, with mIBG avid lesions seen in the visualized arms, spine, and pelvis. The study was performed on CZT gamma camera detector system

Table 5.1 SPECT/CT imaging systems

	SPECT
SPECT reconstruction	Iterative
Resolution recovery	Utilized
	CT
Scout acquisition	80 kVp
CT scan acquisition	Per pediatric CT protocol: kVP range 70–110
Dose modulation	Applied
IV Contrast administration	2 mL/kg up to 100 mL maximum nonionic contrast; no oral bowel contrast
Phase of opacification	Portal venous; inject over 45 s; scan at 65–70 s
Acquisition slice thickness	– As thin as possible with optimized dose estimate – Scanner dependent, overlapping cuts
Scan reconstruction	– Iterative reconstruction applied if available – Soft tissue, bone, and lung reconstructions in 2–3 mm slice thickness for axial scans – Coronal and sagittal reconstruction

5.3 Clinical Applications of SPECT/CT in Pediatric Oncology

5.3.1 Neuroblastoma

Neuroblastic tumors are neuroendocrine tumors that arise in the developing sympathetic nervous system. They tend to occur in the adrenal glands and sympathetic ganglia. The median age at diagnosis is 18 months, with 40% diagnosed in infancy and 90% below 10 years of age [14]. Neuroblastic tumors are usually a very heterogeneous family of tumors from a biological point of view. These tumors present with different degrees of differentiation ranging from immature undifferentiated or poorly differentiated neuroblastic small round cells to differentiating neuroblastoma cells, ganglioneuroblastoma (composed of both immature cells and tumor cells with differentiation to ganglion cells), and ganglioneuroma (composed predominantly of tumor cells that show maturation to ganglion cells).

Contrast-enhanced CT and MRI are the cross-sectional imaging modalities of choice to stage the primary tumor and establish its relationships to surrounding structures such as vessels, organs, spine, and musculature: imaging-defined risk factors (IDRFs) have been described that define a particular neuroblastoma as localized and surgically resectable (L1) or locally advanced and unresectable (L2), requiring induction chemotherapy for tumor shrinkage [15].

The most frequent site of metastatic disease in neuroblastoma is the skeleton (bone marrow and cortical bone). The current gold standard imaging modality to define the presence and extent of skeletal metastatic disease is ^{123}I-meta-iodobenzylguanidine (^{123}I-mIBG) scintigraphy. mIBG imaging also allows for the semi-quantitative categorization of mIBG-avid disease burden using either the Curie or SIOPEN (International Society of Pediatric Oncology—Neuroblastoma) scoring systems, both of which have been validated and shown to provide prognostic information [16, 17].

5.3.2 Meta-iodobenzylguanidine in Neuroblastoma

5.3.2.1 Biodistribution

Meta-iodobenzylguanidine (mIBG) is a norepinephrine analog that is taken up by the norepinephrine transporter (NET) expressed in cells of neural crest origin and in neuroendocrine tumors and accumulates in the neurosecretory granules of adrenal chromaffin cells, similarly to norepinephrine [18]. Approximately 90% of neuroblastomas are mIBG-avid, due to the expression of the noradrenaline transporter. Iodine-123 (^{123}I) is preferred to ^{131}I for the radiolabeling of mIBG because it has a lower radiation dose and shorter half-life, produces better-quality images, and has lower thyroid toxicity than ^{131}I [19].

The ^{123}I-mIBG scan has an estimated sensitivity of 90% and a specificity of 99% and enables the assessment of both local and metastatic soft tissue and bone marrow disease [20].

5.3.2.2 Indications

mIBG can help to differentiate residual primary tumor from post-therapy changes [19]. It can also assess the response of bone marrow metastases to treatment, especially when the interpretation of an MRI scan is difficult due to post-therapy bone marrow changes [21].

Indications for radiolabeled mIBG imaging in neuroblastic tumors include the following:

- Confirmation of suspected neuroectodermally derived tumors, including neuroblastoma, pheochromocytoma, and ganglioneuroma
- Staging of disease
- Therapy planning and assessment of response evaluation
- Follow-up after treatment
- Before planning radionuclide therapy (selected theranostic indications)

The results of ^{123}I-mIBG imaging can have prognostic implications. At diagnosis, the extent of mIBG-avid disease may predict response to chemotherapy in children over 1 year of age who have metastatic disease [22]. After initial chemotherapy, persistence of ^{123}I-mIBG uptake in the cortical bone and bone marrow may be associated with poor prognosis [23]. Post-induction chemotherapy Curie scores of greater than 2 and SIOPEN scores of greater than 3 are associated with a poor prognosis and therefore can be used as a biomarker for response, providing referring clinicians with an early indication that a change in therapy may be indicated [16, 17].

5.3.2.3 Imaging Acquisition

Images are acquired 20–24 h after ^{123}I-mIBG injection. Early images (4–6 h post-injection) to avoid false-positive/false-negative and equivocal results are no longer routinely recommended [24]. Medium-energy collimator selection over low-energy parallel hole collimator choice has been recommended as more favorable to reduce septal penetration for ^{123}I-mIBG planar and SPECT imaging with sodium iodide detector gamma cameras [25]. Solid-state detector gamma camera systems do not currently have options to change collimators.

Images can be acquired as a whole-body sweep in the anterior and posterior projections, with a scan speed of 5 cm/min. Alternatively, spot views of the different body segments can also be

acquired. Each spot view is acquired for a maximum of 10 min (about 500,000 counts for spot views of the torso; 100,000 counts for the spot views of the lower limbs are sufficient) [24].

SPECT is an integral part of the ^{123}I-mIBG scintigraphy examination. The SPECT acquisition is usually centered to the area where further essential clinical information is required. Almost the entire body of small children can fit in the field of view of a SPECT acquisition. A SPECT acquisition can help to better define small lesions and normal variants. A SPECT acquisition protocol typically consists of 120 projections, in steps of 3 degrees each, in either continuous or step-and-shoot mode, 25–35 s/step, with a 128 × 128 matrix. Multiple SPECT acquisitions can be "stitched" together to provide, if necessary, a whole-body view. Usually, however, ^{123}I-mIBG SPECT imaging is performed either of the torso or of the abdomen and pelvis to delineate the most frequent sites of tumor. It is not usual to image the extremities specifically with SPECT for ^{123}I-mIBG imaging due to lack of significant counts in these areas, even in the presence of disease. This specific tailoring of the study is an important part of imaging with ^{123}I-mIBG to ensure the optimal study that will help the referring clinician. The determination of the field of view of SPECT for initial staging studies is confirmed by the nuclear medicine physician after the whole-body planar acquisition. Depending on the planar imaging results, SPECT imaging of the head and neck may be indicated to better delineate additional sites of disease, for example, in the setting of periorbital or skull base involvement. For follow-up studies, this can be specified at the time of booking the study depending on prior disease location.

SPECT/CT is increasingly available in many centers and should be routinely utilized where available to clarify the anatomical location of abnormal foci of mIBG uptake. In comparison to SPECT alone, SPECT/CT further improves the anatomical localization of mIBG uptake and the confidence of lesion detection [7].

There are several protocols for low-dose and ultralow-dose CT acquisitions. CT parameters may vary from one type of SPECT/CT scanner to the other. A possible low-dose CT acquisition may include a voltage around 80–100 kVp and a tube current of approximately 10–40 mAs. With a low-dose CT acquisition such as this, and with a CT scan limited to the region of interest, the radiation dose administered to the patient is very low, usually within a range of 0.2–0.5 mSv [10] (Fig. 5.4).

The CT scan acquisition optimization should occur after the SPECT is completed. The determination of field of view for the CT for SPECT/CT need not always include the entire field of view of the SPECT. This tailoring of the study requires physician input at the time of the study being acquired.

The CT scan imaging can also provide attenuation correction for the SPECT images. In some of the gamma camera systems, this is an automatic background process and cannot be modified. In the solid-state CZT detector system, this is mandatory to view the co-registered images, but non-attenuation-corrected images may be viewed as well, which is particularly important in the cases for which the SPECT field of view is larger than SPECT/CT field of view.

5.3.2.4 Added Value of 123I-mIBG SPECT/CT in Neuroblastic Tumors

SPECT/CT can add significant clinical value to the planar images of a ^{123}I-mIBG scintigraphy examination. It can improve the anatomical localization of mIBG-avid lesions, making the comparison with a recent MRI scan easier (Fig. 5.5); it can show the presence of mIBG non-avid portions of the primary tumor, which often demonstrate foci of calcification on the CT component of the SPECT/CT study (Fig. 5.6); it can also show soft tissue metastatic lesions, especially metastatic lymph nodes, with very-low-level or absent mIBG uptake (Fig. 5.7). In the case of mIBG-avid bone marrow metastases, the CT component of the study usually does not show a correlative abnormality, as the trabecular bone is usually not affected; however, it will help to more accurately identify the location of the bone marrow lesion. In the case of a cortical bone metastasis, a lytic lesion will be often demonstrated on CT, often with a sclerotic rim.

SPECT/CT can be very helpful in identifying mIBG-avid metastatic lymphadenopathy. As the primary neuroblastoma originates in the

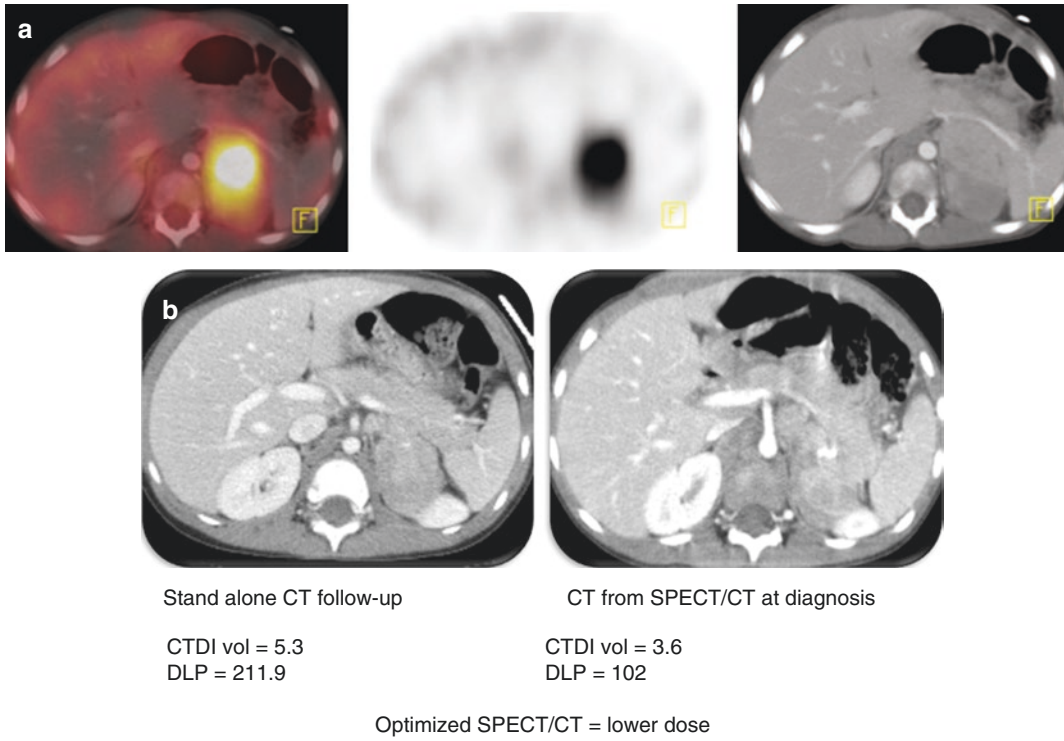

Fig. 5.4 (**a**) Optimized ^{123}I-mIBG SPECT/CT in child with abdominal neuroblastoma at diagnosis. (**b**) Comparison of CT from SPECT/CT with a stand-alone diagnostic CT in this patient. The anatomical detail shown by the contrast-enhanced SPECT/CT is very similar to the follow-up stand-alone contrast-enhanced CT, despite being acquired at approximately 50% lower CT dose (from EJNMMI with permission)

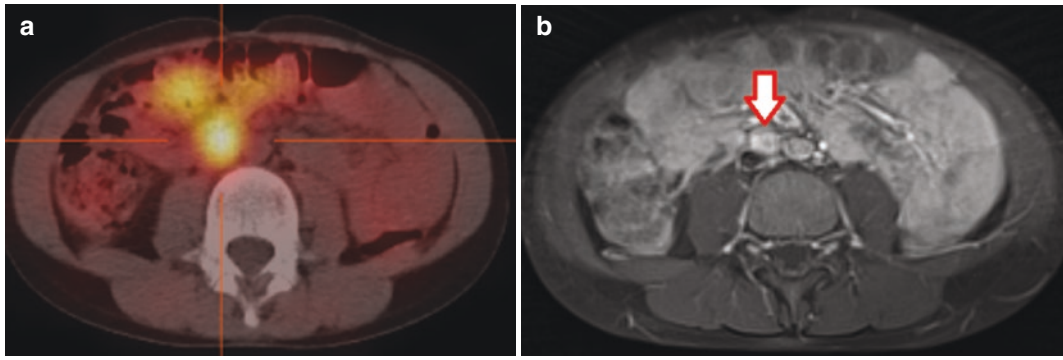

Fig. 5.5 ^{123}I-mIBG SPECT/CT (**a**) of the abdomen in a 5-year-old boy with relapsed neuroblastoma, showing recurrent disease in an aorto-caval lymph node, which is clearly confirmed on subsequent MRI (**b**)

sympathetic paravertebral ganglia and adrenal glands, metastatic lymphadenopathy can occur in the para-aortic, common iliac, external, and internal iliac lymph nodes, as well as in the retrocrural, mediastinal, and supraclavicular lymph nodes. Metastatic axillary lymph nodes from a primary neuroblastoma have also been described (Fig. 5.8).

Neuroblastoma can metastasize to the liver; however, ^{123}I-mIBG has poor sensitivity for liver metastases, owing to the normal tracer distribution in the liver parenchyma which gives a high background activity, thus making it difficult to identify hepatic metastatic lesions. MRI is usually the imaging modality of choice to

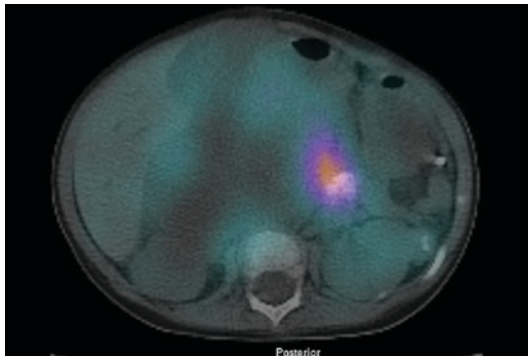

Fig. 5.6 ^{123}I-mIBG SPECT/CT of the abdomen in a 3-year-old boy with a primary poorly differentiated neuroblastoma at diagnosis. The primary neuroblastoma is mainly mIBG non-avid, with only some areas of high mIBG avidity

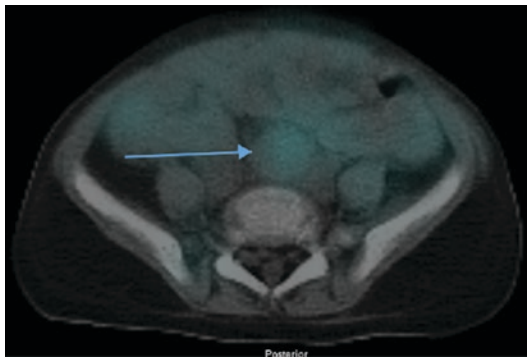

Fig. 5.7 ^{123}I-mIBG SPECT/CT in a child with a neuroblastoma of the lower abdomen and pelvis at diagnosis showing a large metastatic presacral lymph node with low-grade mIBG avidity. The primary neuroblastoma in the upper abdomen shows areas of intense mIBG uptake alternating to areas of absent uptake

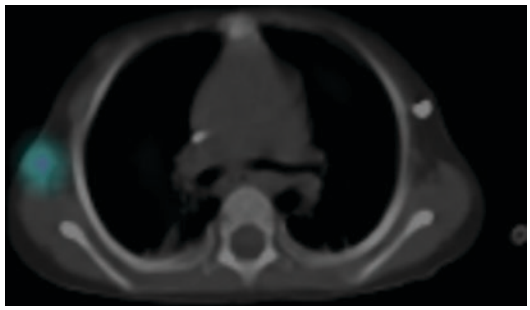

Fig. 5.8 ^{123}I-mIBG SPECT/CT of the chest in a 4-year-old girl with a primary intensely mIBG avid abdominal ganglioneuroblastoma intermixed. There is an enlarged mIBG avid right axillary lymph node, confirmed by ultrasonography and proven to be metastatic on excision biopsy

diagnose and follow up liver metastases (Fig. 5.9).

Lung metastases are uncommon in neuroblastoma; when they occur, they are often associated with a poor outcome. ^{123}I-mIBG SPECT/CT has poor sensitivity for detecting small metastatic lung lesions due to acquisition of both the SPECT and the CT components during free breathing. A chest CT has much higher sensitivity (with the latest CT scanners, the acquisition of the relevant images can occur in approximately 1 s), although the presence of associated chest infections, often fungal in origin, not uncommon during chemotherapy, can occasionally cause false positives.

The main pitfall with a SPECT/CT acquisition during a ^{123}I-mIBG scan in a child not under GA is related to motion artifacts. These can be difficult to correct, as an mIBG scan does not present many clear landmarks for co-registration with an unenhanced CT, the primary ones being the liver, the heart (if it is in the SPECT field of view), or the bladder (which may be filled with a different amount of urine relative to either CT or MRI exams). In the case of significant patient motion during the SPECT study, or between the SPECT and the CT, an accurate co-registration can be very difficult.

Optimized contrast-enhanced mIBG SPECT/CT has been shown to have significant added value and clinical impact for both staging and follow-up studies [26] (Fig. 5.3). These studies can obviate the need for additional separate stand-alone CT examinations, and improve the non-specificity and localization of mIBG uptake. When these optimized studies are performed, it is usual that the SPECT/CT report is a combined report or, if two reports are provided, these are done with direct consultation of the two physicians reporting the NM and CT studies.

5.3.3 Thyroid Cancer

Differentiated thyroid cancer (DTC) is an uncommon tumor type in children, but incidences of this cancer are increasing. This tumor type comprises 3.0% of all cancers in the USA. The median age at diagnosis is 51 years. DTC in patients less than 20 years of age comprises 1.3% of new cases of thyroid cancer [27].

While the mortality rate is very low for this tumor type in children, it is known that children often have more aggressive and advanced disease. Recent guidelines have been developed as to how to manage children with suspected thyroid cancer that include imaging and treatment recommendations [28].

Preoperative imaging with ^{123}I sodium iodide is not routinely recommended for children with thyroid nodules. The rare indication would be for a suspicious thyroid nodule in a patient who has a suppressed TSH nodule and hyperthyroidism. As with any scintigraphy, the addition of SPECT and possibly SPECT/CT may help with interpretation. Because of possible treatment of potential thyroid cancer with ^{131}I radioiodine therapy, any CT scan performed as part of a SPECT/CT study in patients with suspected DTC should avoid the use of intravenous iodinated contrast, as this can interfere with the ^{131}I therapy by saturating the iodine receptors in the thyroid gland and result in a delay in the initiation of the planned radioiodine therapy, potentially reducing the therapeutic benefit.

Routine postoperative evaluation with ^{123}I scintigraphy is not recommended for low-risk

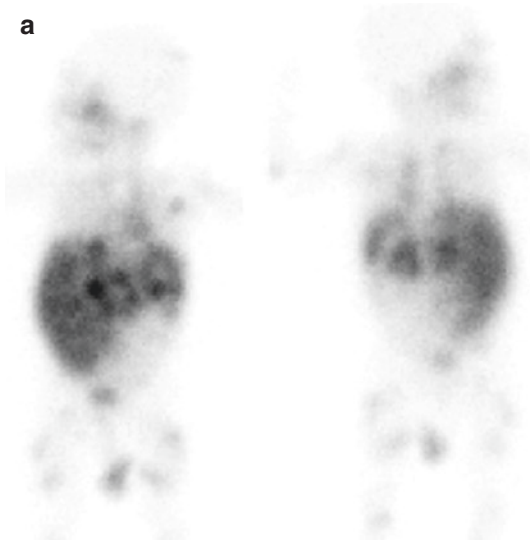

Fig. 5.9 (**a**) Anterior and posterior whole-body planar ^{123}I-mIBG images of a 12-month-old male infant with neuroblastoma; (**b**) MIP image from SPECT study. It is difficult to localize the activity to determine if this patient has bony disease versus only soft tissue disease; (**c**) select SPECT/CT images delineate the activity in focal lesions in enlarged liver, left adrenal area (green arrow), and within soft tissues in the left axilla (red arrow) and left lower chest wall (yellow arrow). SPECT/CT confirmed the extremity lesions to be within soft tissues and not in bone (not shown) (**d**) Follow-up imaging on CZT gamma camera system shows response with decrease in size of the left axillary lesion and resolution of liver enlargement and focal lesions. The left adrenal lesion is now better visualized on coronal imaging and on the axial optimized CT image from the SPECT/CT study. Lower extremity soft tissue lesions are better delineated and also have shown response

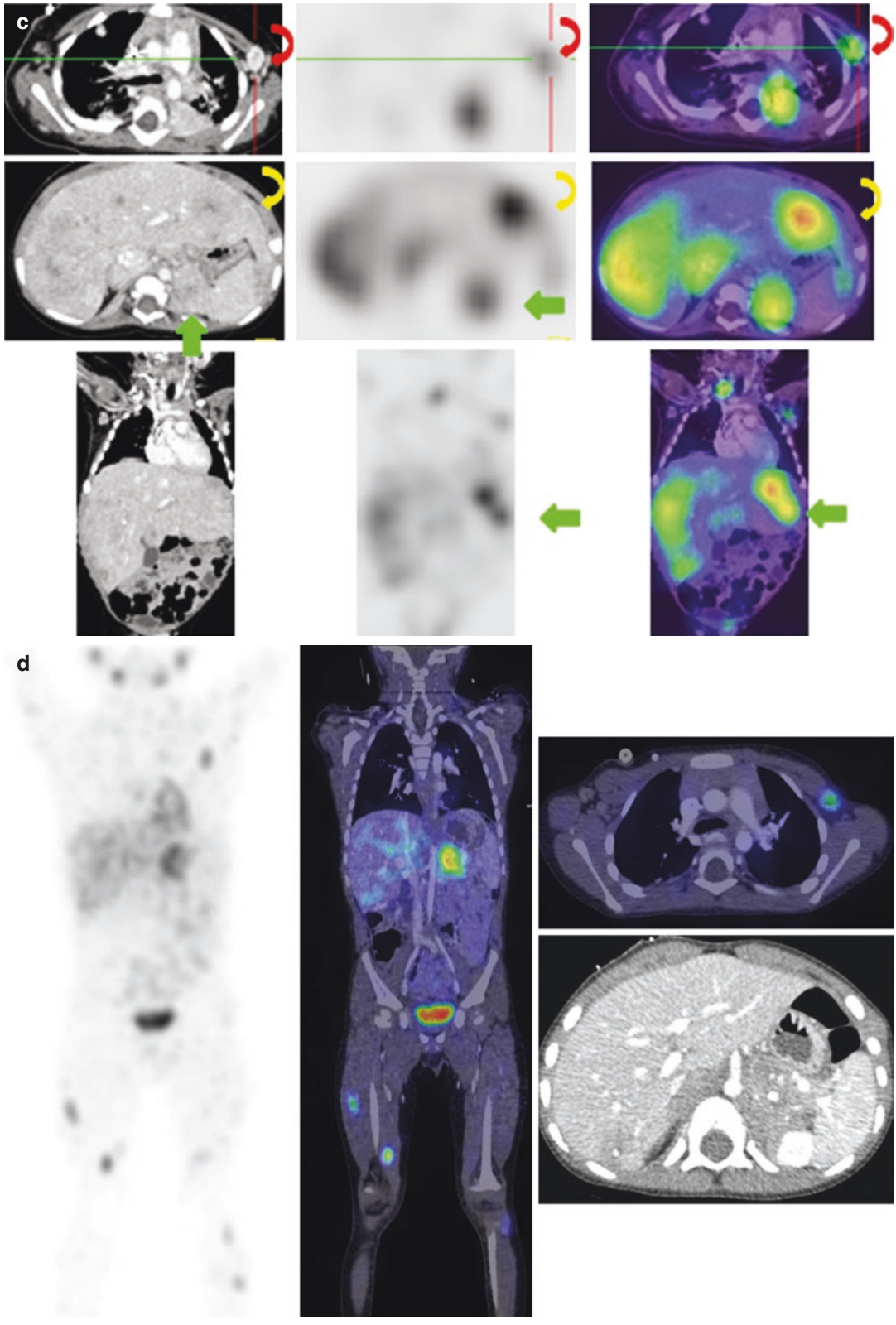

Fig. 5.9 (continued)

thyroid cancer according to the ATA guidelines [28]. Intermediate- and high-risk disease requires postoperative staging after thyroid hormone withdrawal or preferably TSH stimulation, for thyroglobulin level measurement and ^{123}I whole-body scintigraphy. The addition of SPECT/CT can again provide important information on residual thyroid tissue, nodal disease, and distant metastases including pulmonary metastases.

Preparation for these scans include withdrawal of levothyroxine (LT4) for 14 days or use of two doses of recombinant TSH given 24 h apart prior to administration of ^{123}I. Use of ^{123}I in an administered oral dose of 2–4 mCi (37–148 MBq) (min-max) scaled to body weight allows for whole-body anterior and posterior imaging, dedicated neck imaging with and without markers, and then non-contrast-enhanced SPECT/CT. The imaging is performed 24 h following radiopharmaceutical administration and on conventional sodium iodide detector system using either low-energy high-resolution or medium-energy collimators [29].

^{131}I scanning for staging purposes using a diagnostic dose of ^{131}I will not allow for optimal SPECT or SPECT/CT imaging. However, if therapeutic activity of ^{131}I is administered to a patient, then scanning at 7 days posttreatment with SPECT/CT may sometimes provide additional information to complement the planar whole-body acquisition. The CT for this hybrid study would again be performed without intravenous contrast to avoid potential interference with the ^{131}I therapy effect (Figs. 5.10 and 5.11).

Surveillance of children post ^{131}I treatment with stimulated thyroglobulin measurement and ^{123}I whole-body scan is recommended 1–2 years after treatment. Again in this instance, SPECT/CT may be performed as necessary depending on planar imaging findings, clinical symptoms, and laboratory results. In the absence of significant clinical concern, perhaps based on correlative ultrasonography, and in the absence of worrisome activity on the planar whole-body imaging, given the low counts present on the study, the addition of SPECT or SPECT/CT imaging may not be necessary.

A common site of physiologic activity on these scans is noted in the thymus in up to 25% of children imaged [29]. Co-registered SPECT/CT can be helpful for this assessment.

5.4 Future Developments

Work is in progress to make quantitation of tracer uptake available with SPECT/CT scanners routine [30], particularly given the success of quantitative PET imaging. Potential clinical

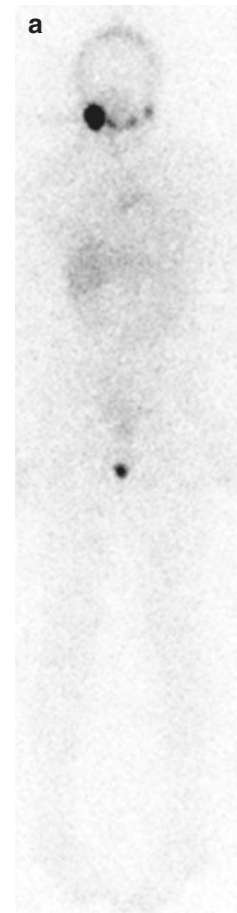

Fig. 5.10 A 14-year-old female who had total thyroidectomy and node dissection for metastatic papillary thyroid cancer. Post-thyroidectomy diagnostic ^{123}I thyroid scan was negative (not shown). She re-presented with rising thyroglobulin and ^{123}I whole body planar scintigraphy (**a**), and subsequent diagnostic thyroid SPECT/CT scan (**b**) identified increased activity in right neck node. Repeat surgery identified recurrent metastatic disease. The surgeon utilized the SPECT/CT for presurgical planning

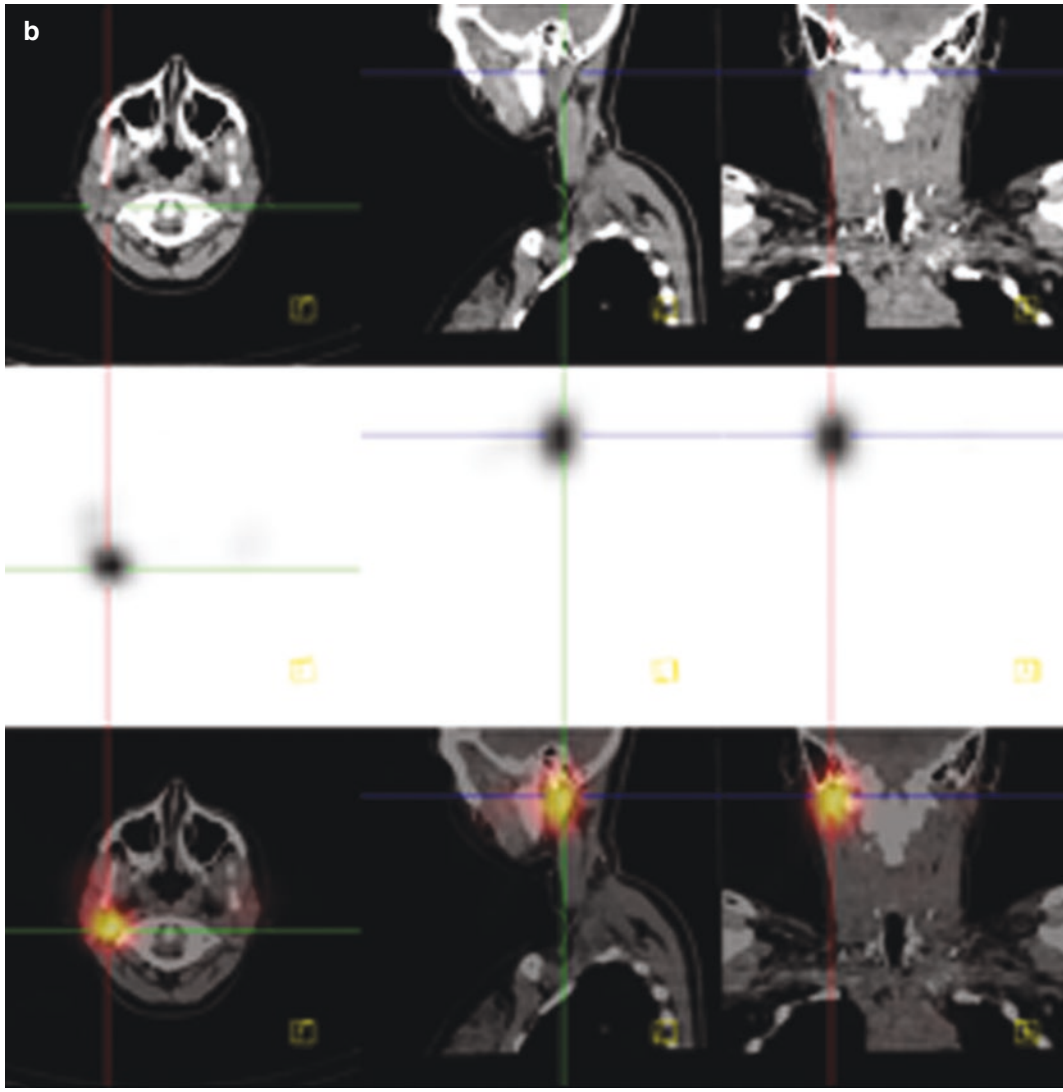

Fig. 5.10 (continued)

advantages include the measurement of radionuclide biodistribution and dosimetry prior to molecular radiotherapy, quantitative measurement of tracer uptake with bone scanning, response assessment to radionuclide therapy in thyroid cancer treated with ^{131}I, or, in general nuclear medicine imaging, the use of standardized uptake values (SUV) to assess disease response to therapy. Quantitative gamma camera imaging using SPECT/CT holds promise and is likely to find a useful role in clinical nuclear medicine.

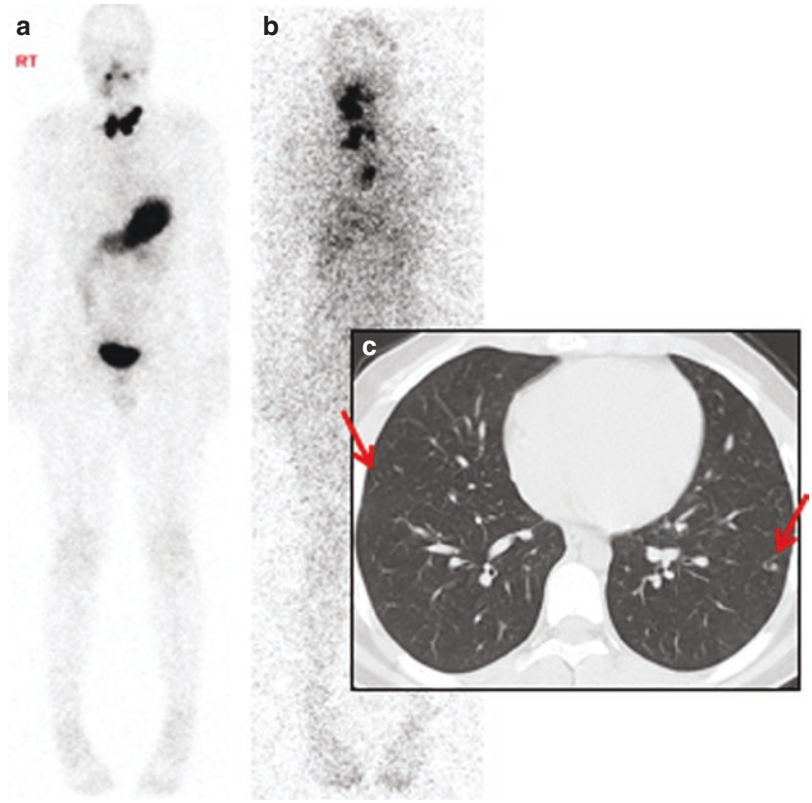

Fig. 5.11 Recurrent metastatic thyroid cancer. 16 year old, post I-131 radioiodine therapy, with rising thyroglobulin > 1000 ng/ml. Diagnostic ^{123}I thyroid whole body scan (**a**) and post-treatment I-131 whole body thyroid scan after treatment with 5550 MBq (150 mCi) (**b**). SPECT/CT study at time of diagnostic scan identified pulmonary metastases on the CT scan (**c**, arrows). The post-treatment scan did not show focal or diffuse activity

Hardware future development may include SPECT/MR. Currently this is being directed to small animal imaging, but the development of silicon photomultipliers (SiPMs) that have enabled technology for PET/MR may encourage this development for full-field-of-view gamma cameras.

References

1. Biermann M, Schwarzlmuller T, Fasmer KE, Reitan BC, Johnsen B, Rosendahl K. Is there a role for PET-CT and SPECT-CT in pediatric oncology? Acta radiologica. 2013;54:1037–45.
2. Pfannenberg AC, Eschmann SM, Horger M, Lamberts R, Vonthein R, Claussen CD, et al. Benefit of anatomical-functional image fusion in the diagnostic work-up of neuroendocrine neoplasms. Eur J Nucl Med Mol Imaging. 2003;30:835–43.
3. Nadel HR. SPECT/CT in pediatric patient management. Eur J Nucl Med Mol Imaging. 2014;41(Suppl 1):S104–14.
4. Even-Sapir E, Keidar Z, Sachs J, Engel A, Bettman L, Gaitini D, et al. The new technology of combined transmission and emission tomography in evaluation of endocrine neoplasms. J Nucl Med. 2001;42:998–1004.
5. Schillaci O, Danieli R, Manni C, Simonetti G. Is SPECT/CT with a hybrid camera useful to improve scintigraphic imaging interpretation? Nucl Med Commun. 2004;25:705–10.
6. Abikhzer G, Keidar Z. SPECT/CT and tumour imaging. Eur J Nucl Med Mol Imaging. 2014;41(Suppl 1):S67–80.
7. Rozovsky K, Koplewitz BZ, Krausz Y, Revel-Vilk S, Weintraub M, Chisin R, et al. Added value of SPECT/CT for correlation of MIBG scintigraphy and diagnostic CT in neuroblastoma and pheochromocytoma. AJR Am J Roentgenol. 2008;190:1085–90.
8. Gelfand MJ, Parisi MT, Treves ST. Pediatric radiopharmaceutical administered doses: 2010 North American consensus guidelines. J Nucl Med. 2011;52:318–22.

9. Lassmann M, Biassoni L, Monsieurs M, Franzius C, Jacobs F, Dosimetry E, et al. The new EANM paediatric dosage card. Eur J Nucl Med Mol Imaging. 2007;34:796–8.
10. Gelfand MJ, Lemen LC. PET/CT and SPECT/CT dosimetry in children: the challenge to the pediatric imager. Semin Nucl Med. 2007;37:391–8.
11. Manual on Contrast Media. https://www.acr.org/Clinical-Resources/Contrast-Manual. 2018.
12. Fahey FH, Palmer MR, Strauss KJ, Zimmerman RE, Badawi RD, Treves ST. Dosimetry and adequacy of CT-based attenuation correction for pediatric PET: phantom study. Radiology. 2007;243:96–104.
13. Peterson TE, Furenlid LR. SPECT detectors: the Anger Camera and beyond. Phys Med Biol. 2011;56:R145–82.
14. London WB, Castleberry RP, Matthay KK, Look AT, Seeger RC, Shimada H, et al. Evidence for an age cutoff greater than 365 days for neuroblastoma risk group stratification in the Children's Oncology Group. J Clin Oncol. 2005;23:6459–65.
15. Brisse HJ, McCarville MB, Granata C, Krug KB, Wootton-Gorges SL, Kanegawa K, et al. Guidelines for imaging and staging of neuroblastic tumors: consensus report from the International Neuroblastoma Risk Group Project. Radiology. 2011;261:243–57.
16. Ladenstein R, Lambert B, Potschger U, Castellani MR, Lewington V, Bar-Sever Z, et al. Validation of the mIBG skeletal SIOPEN scoring method in two independent high-risk neuroblastoma populations: the SIOPEN/HR-NBL1 and COG-A3973 trials. Eur J Nucl Med Mol Imaging. 2018;45:292–305.
17. Yanik GA, Parisi MT, Naranjo A, Nadel H, Gelfand MJ, Park JR, et al. Validation of postinduction curie scores in high-risk neuroblastoma: a Children's Oncology Group and SIOPEN Group report on SIOPEN/HR-NBL1. J Nucl Med. 2018;59:502–8.
18. Dubois SG, Geier E, Batra V, Yee SW, Neuhaus J, Segal M, et al. Evaluation of norepinephrine transporter expression and metaiodobenzylguanidine avidity in neuroblastoma: a report from the Children's Oncology Group. Int J Mol Imag. 2012;2012:250834.
19. Matthay KK, Shulkin B, Ladenstein R, Michon J, Giammarile F, Lewington V, et al. Criteria for evaluation of disease extent by (123)I-metaiodobenzylguanidine scans in neuroblastoma: a report for the International Neuroblastoma Risk Group (INRG) Task Force. Br J Cancer. 2010;102:1319–26.
20. Vik TA, Pfluger T, Kadota R, Castel V, Tulchinsky M, Farto JC, et al. (123)I-mIBG scintigraphy in patients with known or suspected neuroblastoma: results from a prospective multicenter trial. Pediatr Blood Cancer. 2009;52:784–90.
21. Taggart DR, Han MM, Quach A, Groshen S, Ye W, Villablanca JG, et al. Comparison of iodine-123 metaiodobenzylguanidine (MIBG) scan and [18F] fluorodeoxyglucose positron emission tomography to evaluate response after iodine-131 MIBG therapy for relapsed neuroblastoma. J Clin Oncol. 2009;27:5343–9.
22. Suc A, Lumbroso J, Rubie H, Hattchouel JM, Boneu A, Rodary C, et al. Metastatic neuroblastoma in children older than one year: prognostic significance of the initial metaiodobenzylguanidine scan and proposal for a scoring system. Cancer. 1996;77:805–11.
23. Lewington V, Lambert B, Poetschger U, Sever ZB, Giammarile F, McEwan AJ, et al. 123I-mIBG scintigraphy in neuroblastoma: development of a SIOPEN semi-quantitative reporting, method by an international panel. Eur J Nucl Med Mol Imaging. 2017;44:234.
24. Bombardieri E, Giammarile F, Aktolun C, Baum RP, Bischof Delaloye A, Maffioli L, et al. 131I/123I-metaiodobenzylguanidine (mIBG) scintigraphy: procedure guidelines for tumour imaging. Eur J Nucl Med Mol Imaging. 2010;37:2436–46.
25. Snay ER, Treves ST, Fahey FH. Improved quality of pediatric 123I-MIBG images with medium-energy collimators. J Nucl Med Technol. 2011;39:100–4.
26. Eksioglu A, Nadel H. Our experience of co-registered diagnostic CT scan for I-123-mIBG SPECT/CT in children with neuroblastoma. Reston, VA: Society of Pediatric Radiology; 2017.
27. Dinauer C, Francis GL. Thyroid cancer in children. Endocrinol Metab Clin North Am. 2007;36:779–806. vii.
28. Francis GL, Waguespack SG, Bauer AJ, Angelos P, Benvenga S, Cerutti JM, et al. Management guidelines for children with thyroid nodules and differentiated thyroid cancer. Thyroid. 2015;25:716–59.
29. Parisi MT, Eslamy H, Mankoff D. Management of differentiated thyroid cancer in children: focus on the American Thyroid Association Pediatric Guidelines. Semin Nucl Med. 2016;46:147–64.
30. Bailey DL, Willowson KP. An evidence-based review of quantitative SPECT imaging and potential clinical applications. J Nucl Med. 2013;54:83–9.

Functional MRI: DWI and DCE-MRI

6

Govind B. Chavhan and Paul D. Humphries

6.1 Introduction

In addition to providing images with exquisite anatomic detail from superior soft tissue contrast, magnetic resonance imaging (MRI) also provides an opportunity to functionally assess various disease processes. Oncologic imaging will likely benefit from the introduction of functional imaging. Most cancers are densely cellular tissue because of their high proliferative activity. The dense cellularity of the cancer can be assessed by diffusion-weighted imaging (DWI). Similarly, most cancerous tissues have neoangiogenesis and are more vascular than normal tissues, which can be assessed using dynamic contrast-enhanced (DCE) MRI. Various indices derived from these functional MRI techniques can serve as biomarkers for detection, differentiation, monitoring, and therapy response assessment of the tumors. Even though these techniques are well established in brain tumor assessment, their application to extracranial tumors, particularly in children, is new and challenging due to different tissue characteristics and different kinds of movements associated with body organs.

In this chapter we discuss DWI and DCE-MRI techniques in relation to pediatric body oncology imaging.

6.2 Diffusion-Weighted Imaging

6.2.1 Principles

Random motion of water molecules in tissues and structures is called diffusion. Water molecules constantly diffuse to dissipate their thermal energy. The variation in the diffusion of water molecules between different tissues forms the basis for contrast in DWI. Tissues with high mobility of water molecules will appear low in signal, while those with restricted mobility will appear high in signal on diffusion-weighted images. The degree and extent of water molecule diffusion can be affected by various factors including the compartment in which the water molecules are located (intravascular, extracellular, or intracellular spaces), cellularity, cell membrane integrity, and hindrances in the fluid such as large molecules [1–3]. Water molecule mobility is restricted in tissues with higher cellular density, intact cell membranes, and more complex fluid with hindrances (Fig. 6.1). The differing signal intensities on DW

G. B. Chavhan (✉)
Department of Diagnostic Imaging, The Hospital for Sick Children and Medical Imaging, University of Toronto, Toronto, ON, Canada
e-mail: govind.chavhan@sickkids.ca

P. D. Humphries
Department of Radiology, Great Ormond Street Hospital for Children, NHS Foundation Trust, London, UK
e-mail: paul.humphries5@nhs.net; Paul.Humphries@gosh.nhs.uk

S. D. Voss, K. McHugh (eds.), *Imaging in Pediatric Oncology*, Pediatric Oncology,
https://doi.org/10.1007/978-3-030-03777-2_6

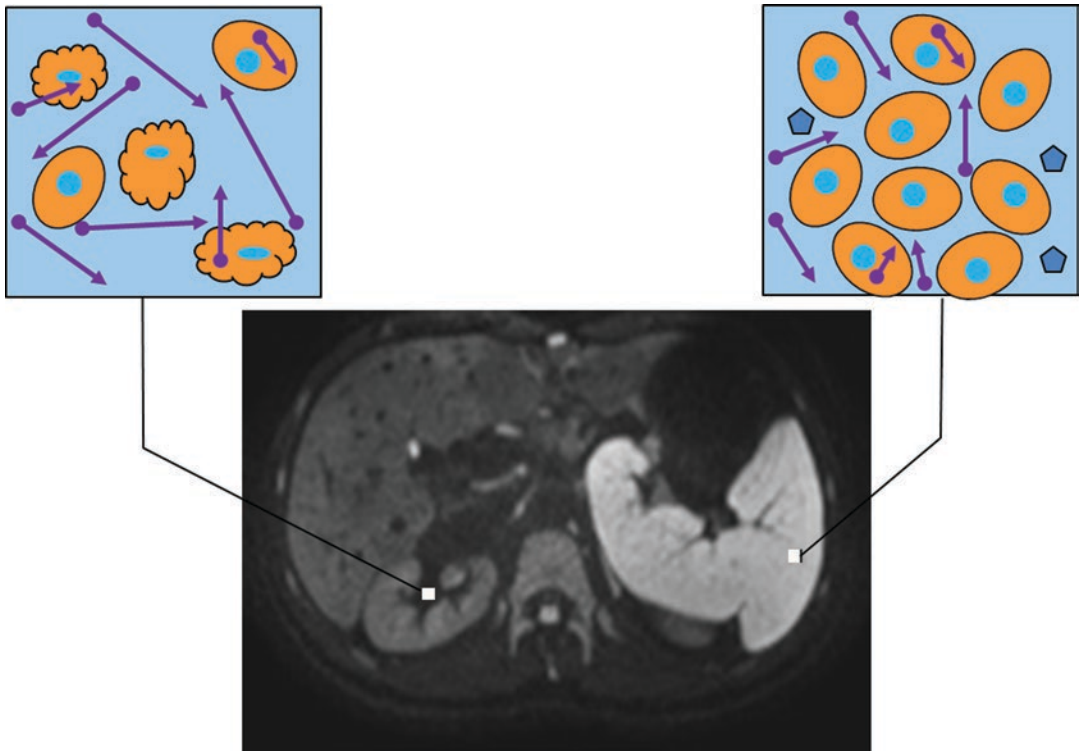

Fig. 6.1 Diagrammatic representation of increased versus restricted diffusion. The voxel on the left placed within the renal pelvis contains fewer cells, with resultant large extracellular space that allows free diffusion of water molecules. Also, this voxel has damaged cells that allow mobility of water molecules across cell membrane. There are no mobility hindrances like macromolecules in this voxel. Contrary to this the right voxel placed over the spleen contains a greater number of cells, all cells with intact cell membrane and macromolecules in the extracellular space. One or all of these factors are restricting mobility of water molecules in this voxel

images provide indirect information about the tissue microenvironment.

6.2.2 Technique

6.2.2.1 Diffusion Weighting

The process of making the sequences sensitive to the diffusion of water molecules is called diffusion weighting and is achieved by applying two diffusion gradients, one before and another after the 180-degree radiofrequency pulse, in a T2-weighted sequence. The degree of diffusion weighting of the sequence increases with the *b*-value (expressed in s/mm^2). The *b*-value is determined by and increases with the amplitude and duration of application of two diffusion gradients as well as how separate they are from each other. As the *b*-value increases, the signal from water molecules diminishes such that at a high *b*-value, only tissues with either restricted water molecule mobility or a very long T2 relaxation time will retain high signal.

6.2.2.2 Sequences

A single-shot fast-spin-echo echo-planar sequence is the most frequently used DWI sequence in body imaging and can be acquired with breath-hold, free-breathing, or respiratory triggering [1]. Free-breathing techniques take long acquisition times of about 4–5 min but provide better signal-to-noise ratio (SNR) and spatial resolution. Breath-hold imaging is quick and motion artifact-free but provides poorer SNR and lower spatial resolution. Breath-hold imaging also has the limitations of minimal slice thickness

and the number of *b*-values that can be used. A special DWI sequence used for whole-body imaging is diffusion-weighted whole-body imaging with background body signal suppression (DWIBS) [4]. DWIBS is acquired with free-breathing, heavy diffusion weighting (*b*-values 1000–1500 s/mm^2), and fat suppression by a prepulse [4].

6.2.2.3 Selection of *b*-Values

Three factors taken into consideration while choosing the appropriate *b*-value include organ of interest with its T2 relaxation time, the purpose of DWI (lesion detection versus characterization), and to a certain extent field strength. Lower "high *b*-values" than those typically found in neuroimaging are used for body DWI to counteract the low SNR from short T2 relaxation time of solid organs like the liver [5]. High field strength provides more SNR; hence, higher *b*-values can be used on 3 T scanner as compared to 1.5 T scanner. Typical high *b*-values used in pediatric body imaging include 500–600 s/mm^2 for liver imaging and 800–1000 s/mm^2 for kidney, bowel, and musculoskeletal imaging [1]. At least two *b*-values are required for calculation of ADC. A greater number of *b*-values are required for other quantitative models, as discussed below.

6.2.3 Qualitative Assessment of DW Images

Qualitative interpretation of DW images generally makes use of the images obtained at a maximum *b*-value (diffusion-weighted image) and the calculated ADC map (discussed below). Tissues or structures with restricted diffusion will appear bright on DW images and dark on an ADC map, whereas tissues with increased diffusion of water molecules will appear dark on DW images and bright on an ADC map. Tissues or lesions with a very high T2 relaxation time but without true restricted diffusion will appear bright on both the DW images and the ADC map, a phenomenon known as T2 shine-through. Some vendors also provide an exponential ADC map, which is derived by dividing high *b*-value images by an image in the same series obtained at $b = 0$ s/mm^2 at the pixel level. Truly diffusion-restricted tissues remain bright on an exponential ADC map. Some body tissues, including lymphoid tissues like the spleen and lymph nodes, spinal cord, ovarian and testicular stroma, neonatal kidneys, adrenal glands, and red bone marrow, normally demonstrate qualitative diffusion restriction [1] (Fig. 6.2). The spleen and spinal cord can serve as a reference tissue to judge diffusion restriction in other tissues and lesions.

6.2.4 Quantitative Assessment of DW Images

Currently, there are four common mathematical models used for quantitative assessment in DWI including mono-exponential ADC maps, intravoxel incoherent motion (IVIM), diffusion kurtosis imaging (DKI), and stretched-exponential model [6]. While ADC maps have been used for the last three decades in clinical practice, the other three models are largely in the research phase and not well established for clinical use.

6.2.4.1 Apparent Diffusion Coefficient (ADC) Maps

Parametric ADC maps are calculated from multiple *b*-value images. At least two *b*-values are required for calculation of an ADC map, but the accuracy of ADC measurement increases with the number of *b*-values. A graph of decreasing logarithm of signal intensity of tissues is plotted against increasing *b*-values (Fig. 6.3). The slope of the mono-exponential graph represents ADC [7]. ADC calculation takes into account all *b*-values and assumes that signal attenuation with increasing *b*-value is linear and has a Gaussian distribution. ADC values (mm^2/s) can be derived by drawing a region of interest on an ADC map. Diffusion-restricted tissue will have a lower ADC, whereas nonrestricted tissue will have a higher ADC. ADC maps are also used in qualitative assessment to differentiate between true diffusion restriction and T2 shine-through, as discussed above.

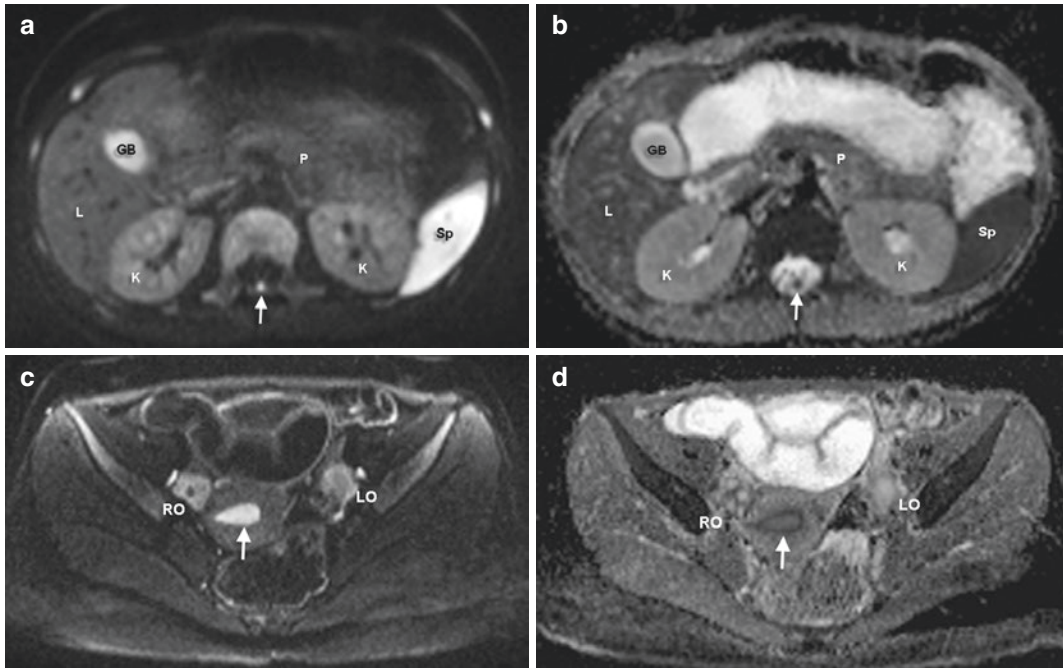

Fig. 6.2 (**a**, **b**) Normal diffusion signal intensities of upper abdominal organs in a 13-year-old girl. The spleen (*Sp*) and conus medullaris of the spinal cord (*arrow*) are normally restricted and appear hyperintense on diffusion-weighted image (**a**) and hypointense on apparent diffusion coefficient (ADC) map (**b**). The gallbladder (*GB*) and to a lesser extent kidneys (*K*) show T2 shine-through. The liver (*L*) and pancreas (*P*) show intermediate signal on both diffusion-weighted image and ADC map. (**c**, **d**) Normal diffusion signal intensities of pelvic structures in a 16-year-old girl. (**c**) Diffusion-weighted image (DWI) and (**d**) apparent diffusion coefficient (ADC) map demonstrating diffusion restriction of normal ovarian stroma in the right ovary (*RO*) and left ovary (*LO*). The endometrium (*arrow*) shows T2 shine-through, and the junctional zone is hypointense on both DWI and ADC images. Muscles show intermediate signal on DWI and slightly hyperintense signal on ADC map

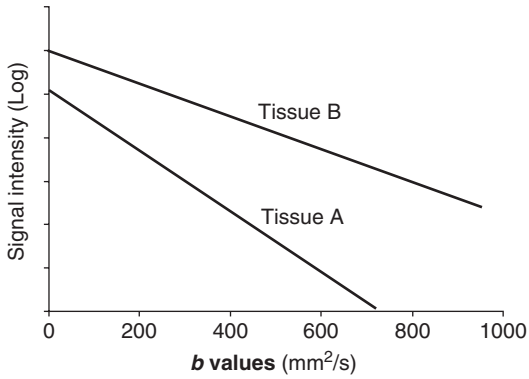

Fig. 6.3 Apparent diffusion coefficient (ADC) map. Logarithm of signal intensity of a tissue is plotted against increasing *b*-values. The slope of the mono-exponential line representing signal decay represents ADC. The slope of the signal decay line characterizing tissue B is more gradual and less than the slope of the line characterizing tissue A. This indicates a lower ADC and more restriction of water molecule mobility in tissue B, as compared to tissue A, which as a greater slope and hence a higher ADC

6.2.4.2 Intravoxel Incoherent Motion (IVIM) Model

IVIM model separates signal attenuation in DWI into two components: static tissue molecular diffusion (also called as true diffusion) and that related to perfusion (also called as pseudo-diffusion) [6, 8]. The signal attenuation seen on diffusion-weighted imaging, especially at low *b*-values (<200 s/mm^2), is caused by water diffusion in tissues (cellular and extracellular space) as well as microcirculation within the normal capillary network [7]. Routine ADC represents the slope of a mono-exponential graph of signal attenuation plotted against increasing *b*-values and takes into account all the *b*-values. In contrast, with the IVIM model, signal attenuation caused by capillary perfusion and tissue diffusion is represented by a bi-exponential graph in which the diffusion coefficient calculated from low *b*-values (<200 s/mm^2)

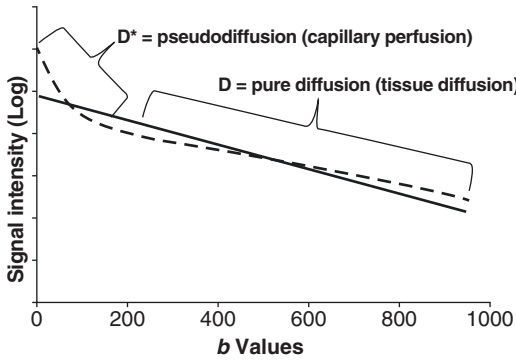

Fig. 6.4 Mono-exponential versus bi-exponential apparent diffusion coefficient (ADC) curves. Routine ADC represents the slope of a mono-exponential graph of signal attenuation plotted against increasing *b*-values (*solid line*) and takes into account all the *b*-values. The bi-exponential curve (*dashed line*) shows rapid attenuation of signal at lower *b*-values, below 150–200 s/mm^2, from capillary perfusion as compared to more gradual signal attenuation at higher *b*-values from true tissue diffusion. The ADC calculated from lower *b*-values is called pseudodiffusion (*D**), while ADC calculated from higher *b*-values (>200 s/mm^2) represents pure tissue diffusion (*D*). Perfusion fraction (f) is calculated from *D** and *D*. (*Reprinted with permission from Ref.* [3])

represents the perfusion component and is termed pseudodiffusion or "*D*" (Fig. 6.4). The diffusion coefficient calculated from higher *b*-values (>200 s/mm^2) represents true tissue diffusion of water protons and is termed "*D*" (Fig. 6.3). From these two, a perfusion fraction (f) is calculated [9].

6.2.4.3 Diffusion Kurtosis Imaging (DKI)

DKI model involves a more advanced curve fitting of the signal attenuation, which enables characterization of non-Gaussian water diffusion behavior [10]. Ultra-high *b*-values (>1000 s/mm^2, typically 1500–2000 s/mm^2 for body imaging) are used for DKI, values at which the signal contribution from water in the extracellular space is significantly reduced making the diffusion measurements more sensitive to intracellular compartment fluid [6]. Two quantitative parameters derived from DKI include D_{app} and K_{app}. D_{app} is the diffusion coefficient equivalent to ADC (measured in the same unit s/mm^2) but corrected to account for the observed non-Gaussian behavior. K_{app} (the apparent diffusional kurtosis, unitless) represents the more peaked distribution of tissue diffusivities occurring in the setting of non-Gaussian diffusion behavior [10]. It is proposed that increased kurtosis results from complexity of tissues and irregularity and heterogeneity of cellular microstructure, including the increased nuclear-cytoplasmic ratio of tumor cells [10]. Malignant tissues like prostate cancer (where DKI has been extensively studied) typically show low D_{app} and elevated K_{app}.

6.2.4.4 Stretched-Exponential Model (SEM)

Imaging voxels are typically at least a millimeter in size, while water molecules typically diffuse on the order of a few micrometers (μm) during a course of diffusion measurement, resulting in heterogeneity of diffusion coefficient estimates due to non-Gaussian processes within the voxel [6]. SEM takes into account this sub-voxel heterogeneity and provides a measure of the local distribution of diffusion coefficients [11]. This diffusion model considers water diffusion as combination of multiple Gaussian compartments with a wide distribution of diffusivities [10]. The two main parameters derived in the SEM model include α, a measure of heterogeneity in the intravoxel distribution of diffusion coefficient and distributed diffusion coefficient (DDC). The SEM model can be understood as an adjustment to the mono-exponential model by α, such that when $\alpha = 1$, DDC and ADC (determined by mono-exponential model) are equivalent [12].

6.2.5 Technical Challenges in DWI

DWI acquisition usually involves EPI to make it faster. EPI is prone to artifact and has low SNR. Reduced spatial resolution (larger voxel >2 mm and thicker slices >5 mm) and shorter TEs are typically used to improve SNR. Geometric distortions can occur from inhomogeneities in B0 as well as B1 fields and are especially problematic at higher field strengths [13]. Nonlinearity of diffusion-encoding gradients may also lead to errors in ADC measurements at the edges of large fields of

view typically used in body imaging. Multiple station acquisitions with each at the isocenter help to reduce this error and distortions at the edges [13]. Despite recent advancements in radiofrequency and gradient hardware resulting in improvement in DWI, variability and poor reproducibility of ADC measurement remain major issues in using ADC as a quantitative biomarker. ADC variability can result from multiple factors including operator-related factors, protocols, acquisition techniques, and algorithms to convert DWI to ADC. ADC variability could also relate to tissue intrinsic factors from non-Gaussian behavior. Advancements in hardware have improved our ability to acquire multiple *b*-values and higher *b*-values, allowing application of other mathematical models like IVIM, DKI, and SEM for more accurate analysis of diffusion behavior in complex tissues. However, these methods are still in their early phase of development, particularly for body imaging applications.

6.2.6 DWI Applications in Pediatric Oncologic Imaging

Diffusion-weighted imaging can indirectly provide information about the microenvironment of a tumor, and quantitative parameters derived from DWI can serve as biomarkers. In oncological imaging, DWI can be useful for detection, for characterization of tumors, for assessment of therapy response, and for whole-body screening and staging.

6.2.6.1 Tumor Detection

It is easier to detect a lesion with diffusion restriction or a lesion with high T2 relaxation time at most body locations because most of the other normal structures lose their signal on diffusion-weighted images (Fig. 6.5). DWI can reliably detect and delineate malignant tumors in children and adolescents [14]. This is particularly true for the solid organs like the liver. Diffusion-weighted images at lower *b*-values (50–100 s/mm^2) detect significantly more liver lesions as compared to T2-weighted images [3, 15, 16]. On low *b*-value images, vessels appear dark, while most lesions retain T2 signal and are easily detected. Some authors have proposed replacing routine T2-weighted images with low *b*-value DWI for lesion detection in liver imaging [17]. High *b*-value images alone cannot be reliably used for lesion detection in the liver because only restricted or very high T2 relaxation lesions

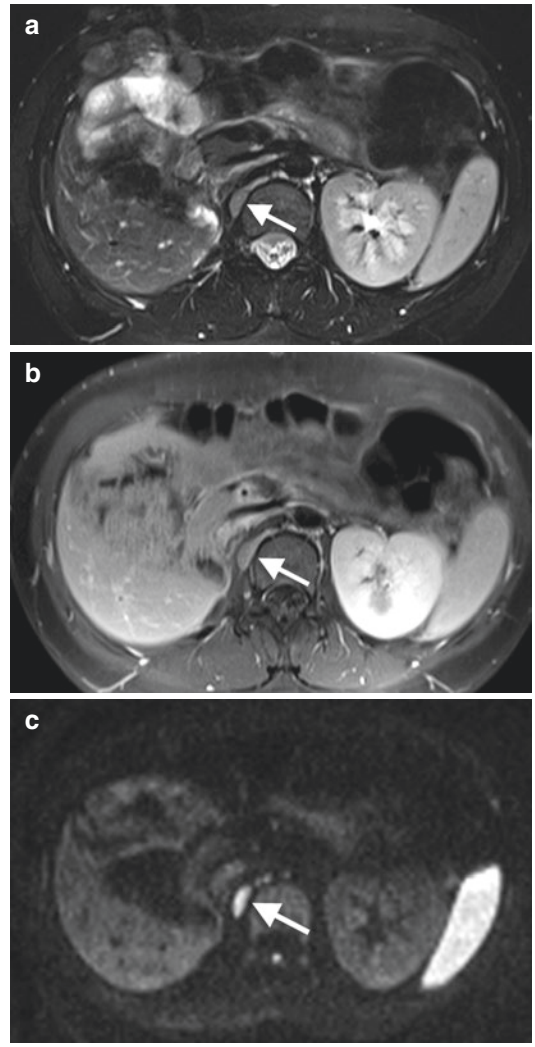

Fig. 6.5 Lesion detection by diffusion-weighted images. A 15-year-old girl with history of renal cell carcinoma requiring right nephrectomy. Follow-up MR images including T2W (**a**), post-contrast T1W fat-saturated (**b**), and *b* = 800 diffusion-weighted (**c**) images demonstrate recurrence in a retrocrural lymph node (arrows). The lymph node stands out on DW image and is easily appreciated as compared to other images

can be seen on high *b*-value images. DW images (high *b*-value) are useful for the detection of subtle peritoneal deposits from various cancers, including ovarian cancer [18, 19]. The small nodular and subtle linear peritoneal deposits are easily seen on DWI as compared to other sequences.

6.2.6.2 Tumor Characterization

Studies in adults and children have indicated that most malignant body tumors show diffusion restriction and tend to have lower ADC values [20–22]. DWI can potentially be used to differentiate benign from malignant tumors. In a pediatric study by Humphries et al. [20] evaluating various benign and malignant tumors in 19 children including neuroblastoma, Wilms tumor, rhabdomyosarcoma, and others, there was a significant relationship between cellularity and ADC. The major extracranial tumors in children including neuroblastoma, Wilms tumor, rhabdomyosarcoma, osteosarcoma, Ewing sarcoma (Fig. 6.6), and hepatoblastoma show qualitative diffusion restriction. Several studies have shown the ability of DWI to differentiate neuroblastoma from ganglioneuroma, which is not restricted (Fig. 6.7) [23–27]. However, there is no consensus regarding ADC cutoff values to reliably differentiate benign from malignant lesions.

There have been pediatric studies demonstrating that DWI and ADC values can help to differentiate between benign and malignant pediatric abdominal tumors using ADC cutoff values of 1.29×10^{-3} mm^2/s and 1.11×10^{-3} mm^2/s, respectively [21, 22]. In one recent study, for example, all pediatric malignant liver tumors showed qualitative diffusion restriction, while all of the benign lesions studied, with the exception of abscesses, did not show restriction [28]. A limitation common to several studies of this type is that the benign entities are also morphologically benign on standard anatomic imaging—for example, simple cystic lesions—and hence the DWI data does not add to the diagnostic pathway. More data is thus needed providing exceptions to this observation and on other benign neoplastic processes showing diffusion restriction. In our experience, for example, the fat/keratinous substance in ovarian germ cell tumors (mature or immature) shows diffusion restriction. Hence diffusion restriction in germ cell tumors alone cannot be used to differentiate benign and malignant tumors. Apart from differentiation of benign from malignant lesions, researchers have also attempted to differentiate histologic subtypes of certain pediatric body tumors like nephroblastoma and osteosarcoma [29–31].

Even though there is a significant relationship between cellularity and ADC, with malignant tumors showing lower ADC, currently ADC value is not a reliable method to unequivocally differentiate benign from malignant tumors. There is considerable overlap of ADC among malignant and benign lesions as noted in the above mentioned studies reporting different ADC cutoff values, probably related to technical factors, biological variation within tumors, and multiple other factors determining ADC apart from cellularity [20]. There is also significant variability and somewhat low reproducibility of ADC measurements [32, 33]. All these factors have hampered utilization of ADC values for tumor characterization in clinical practice. More recent studies have shown some improvement in intra- and interobserver variability and reproducibility of ADC in children [34, 35]. Advances and standardization of the technique in the future could make the routine use of ADC values more useful in clinical practice.

6.2.6.3 Therapy Response Assessment

An increased number of cells with an intact cell membrane are one of the causes of restricted diffusion seen in some malignant tumors. The ADC values are reduced in these tumors. Cancer therapy causes destruction of tumor cells and damage to cell membranes, increasing water molecule mobility and thereby increasing the ADC of the tumors (Fig. 6.8). Such increases in the ADC of the tumor following therapy can be used for assessing, monitoring, and predicting the response to therapy. Thus ADC value has potential to be used as a biomarker for therapy response. DWI and ADC values have been used for assessing therapy response, detecting residual

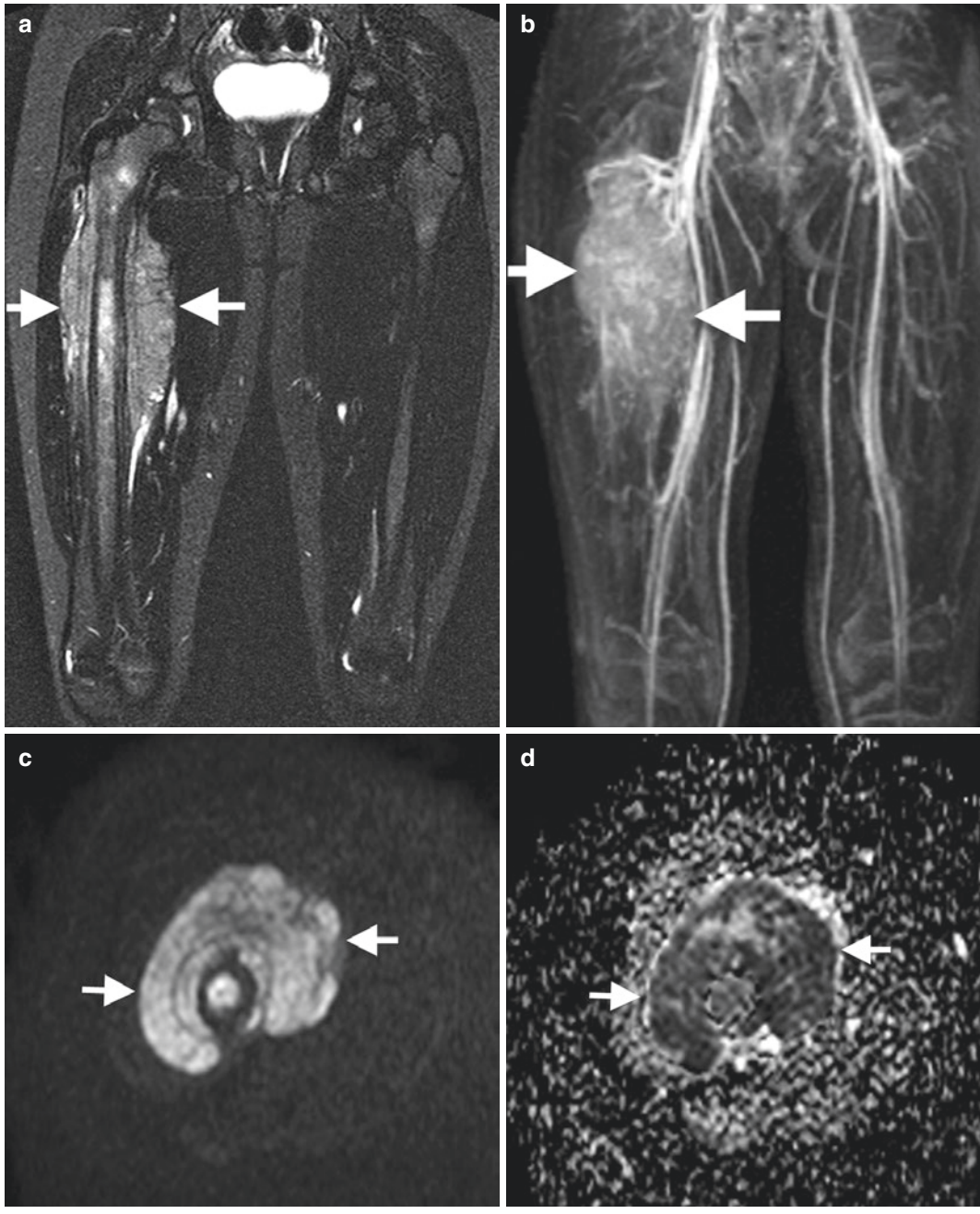

Fig. 6.6 Lesion characterization by diffusion-weighted images. A 10-year-old boy with Ewing sarcoma of the right femoral shaft. Coronal STIR image (**a**) shows a large lobulated hyperintense mass around the femoral shaft (arrows). The mass (arrow) shows avid enhancement on maximum intensity projection (MIP) image reconstructed from venous phase images of the MR angiogram (**b**). The mass (arrows) demonstrates hyperintense signal on b = 800 DW image (**c**) and turns dark on ADC map (**d**) consistent with diffusion restriction

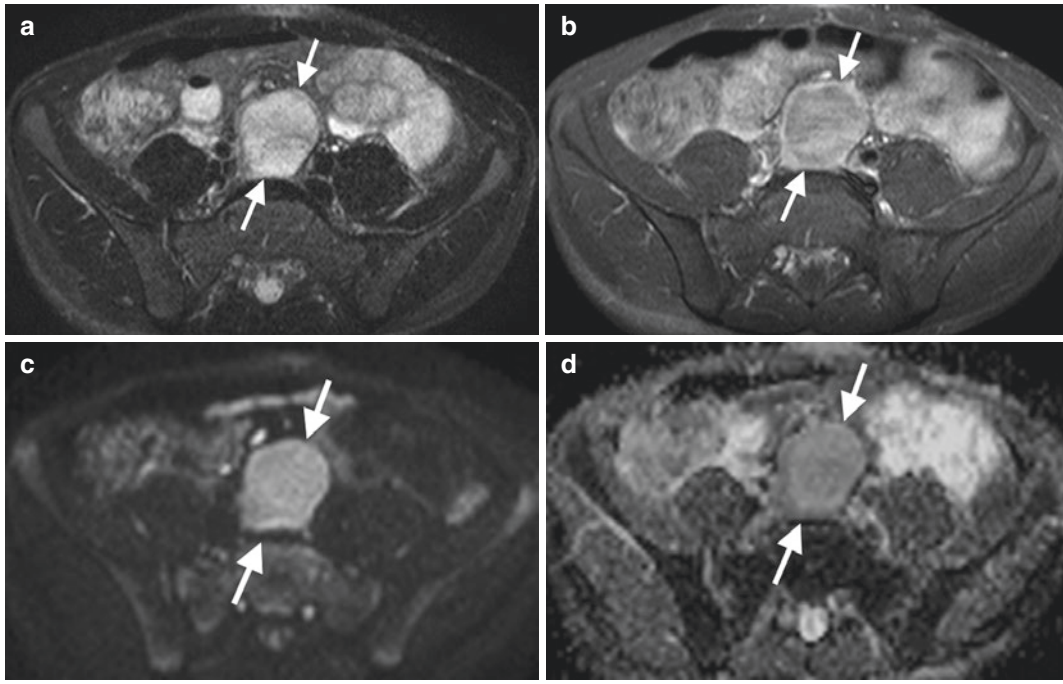

Fig. 6.7 Lesion characterization by diffusion-weighted images. A 9-year-old boy with ganglioneuroma just inferior to the aortic bifurcation (arrows). The mass is well circumscribed and hyperintense on T2W image (**a**) and shows enhancement on post-contrast T1W image (**b**). The mass (arrows) demonstrates hyperintense signal on $b = 600$ DW image (**c**) and remains hyperintense on ADC map (**d**) suggesting no diffusion restriction. ADC value was 2.32×10^{-3} mm^2/s

disease, and predicting response in various tumors, including lymphoma [36], prostate cancer [37], metastatic bone disease [38], nasopharyngeal carcinoma [39], and osteosarcoma [40, 41]. In a small pediatric study, treatment of hepatoblastoma and Wilms tumor resulted in a rise in ADC within tumor following chemotherapy [42]. In this same study, two rhabdomyosarcomas did not show an increase in ADC despite positive response to chemotherapy on histopathology. Recently, measurement of whole-tumor ADC values of Wilms tumor, excluding necrotic areas, was shown to be accurate for detection of chemotherapy-related change [34]. Despite these promising results, ADC remains an inconsistent and imperfect biomarker for assessment of therapy response for the reasons discussed above. The focus of investigation for DWI-derived biomarkers has now shifted to the newer quantitative models including IVIM, DKI, and SEM.

6.2.6.4 Staging and Whole-Body DWI

Most primary body malignant tumors have restricted diffusion, as do their metastases. Whole-body DWI has the potential to detect metastatic lesions and help in staging of the tumor. Whole-body DWI was comparable to PET in the assessment of early chemotherapeutic response in a small study of eight patients with large B-cell lymphoma [43]. Similarly, very good agreement was seen between whole-body DWI and PET/CT for nodal and extranodal sites for initial staging of lymphoma in 33 children [44]. Recently, visual whole-body DWI analysis and ADC values were found to have very good sensitivity for detection of viable residual disease after chemotherapy in lymphoma [36]. Even though these promising results demonstrate the potential of whole-body DWI to be a radiation-free alternative to positron emission tomography (PET) for lymphoma evaluation, there are some hindrances to its usefulness.

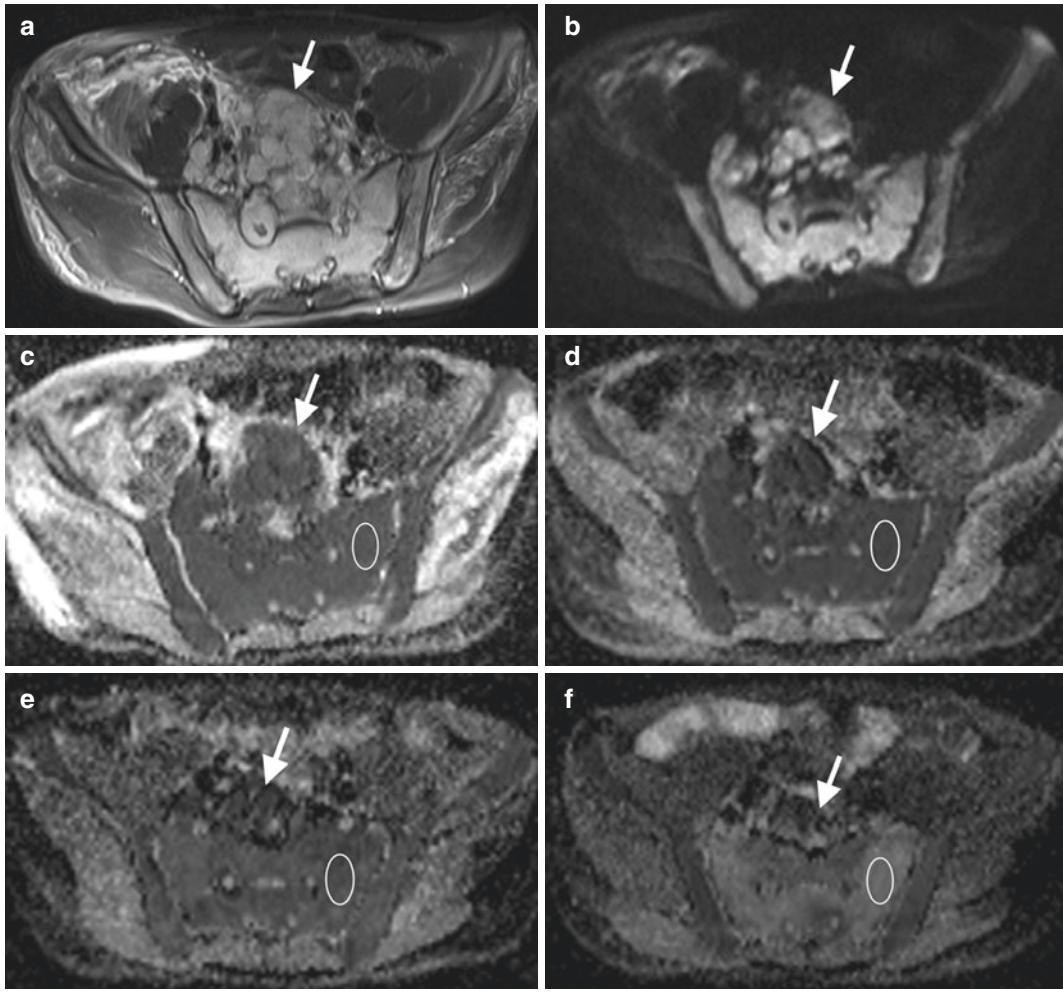

Fig. 6.8 Therapy response assessment by diffusion-weighted images. A 14-year-old boy with unusual stage IV neuroblastoma and widespread bony metastases. T2W image (**a**) demonstrates a lobulated presacral mass (arrows) and diffuse involvement of the sacrum. The mass (arrows) and the sacrum demonstrate hyperintense signal on $b = 800$ DW image (**b**) and turn dark on ADC map (**c**) consistent with diffusion restriction. The baseline ADC was 0.68×10^{-3} mm^2/s (oval region of interest (ROI) marked over the left sacral ala). ADC map after six cycles of chemotherapy (**d**) showed no significant improvement in ADC that remained at 0.68×10^{-3} mm^2/s. ADC maps 4 weeks after MIBG therapy (**e**) and subsequently 4 more weeks after addition on a new chemotherapeutic agent (**f**) demonstrate an increase in ADC to 1.027×10^{-3} mm^2/s and 1.68×10^{-3} mm^2/s, respectively. Note the associated decrease in the size of the presacral mass (arrows)

The usefulness of DWI for staging is hampered by potential poor sensitivity for lung lesions, in part secondary to susceptibility from air, and for marrow involvement due to the normal heterogeneity of cellular red marrow, which is normally restricted. A major limitation for using whole-body DWI in lymphoma assessment is the inability to differentiate between normal and abnormal lymph nodes because both show diffusion restriction. Whole-body MRI is used for screening children with cancer predisposition syndromes including Li-Fraumeni syndrome and hereditary paraganglioma-pheochromocytoma syndrome [45]. Whole-body DWI could potentially be used for this purpose given the better lesion detectability on diffusion-weighted images (Fig. 6.9).

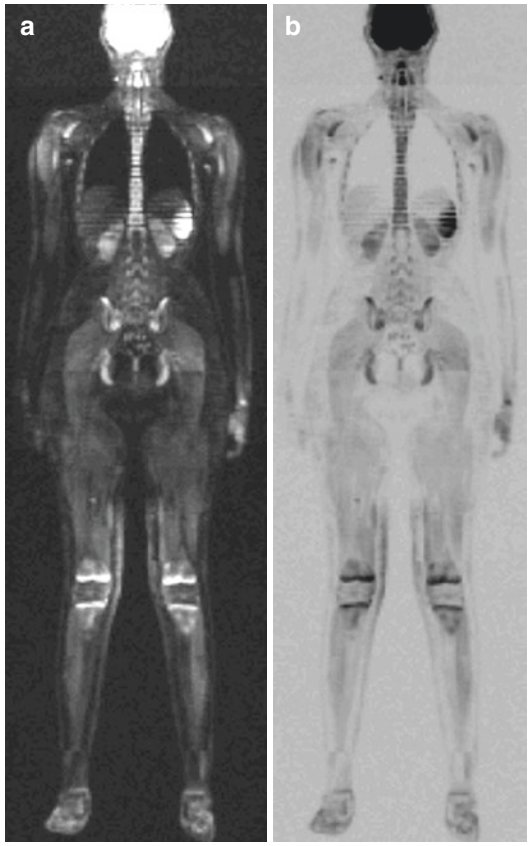

Fig. 6.9 Whole-body DWI for screening of cancer predisposition syndrome. A 12-year-old girl with hereditary paraganglioma-pheochromocytoma syndrome and history of previous resection of two pheochromocytomas. Coronal reformatted image from axially acquired diffusion-weighted images with b = 800 (**a**) and the inverted gray scale of the same image (**b**) performed during routine surveillance demonstrated no new lesion

6.3 Dynamic Contrast-Enhanced MRI

6.3.1 Principles

Changes in the microvascular circulation and new vessel development in neoplastic tissues alter the normal physiological parameters, and identifying these changes is an attractive target for functional imaging. There are several MR techniques that can be used to image tissue microvascular processes, where there is an exchange of oxygen and waste products between the capillary bed and extravascular space. As described above, IVIM/pseudodiffusion [7] reflects tissue perfusion, and other techniques such as arterial spin labelling [46] and blood oxygen level-dependent (BOLD) imaging [47] have also been described but are beyond the scope of this chapter.

Functional changes in tissue microvascular structure precede gross morphological changes, such as size change, and may therefore be a valuable early biomarker, potentially enabling DCE-MRI to identify neoplastic tissue, assess therapy response, and prognosticate.

DCE imaging uses an injection of contrast material followed by dynamic imaging of the tissue of interest [48] and may be evaluated qualitatively or quantitatively using software-derived mathematical models of tissue physiological parameters.

6.3.2 Physiological Parameters

There are many physiological parameters that can be assessed with DCE-MRI [49] and differences between normal and disease states investigated:

1. Tissue blood flow [F_t]—blood entering a volume of tissue (mL/min/100 mL of tissue)
2. Tissue blood volume [BV_t]/blood volume fraction [V_b]—volume of capillary blood contained in a volume of tissue (mL/100 mL of tissue or %)
3. Mean transit time [MTT]—mean time taken through the capillary network (s)
4. Permeability/surface area product [PS]—flow of molecules through capillary membranes in a certain volume of tissue (mL/min/100 mL of tissue)
5. Transfer constant [K_{trans}]—complex combination of PS and tissue blood flow, depending on circulation and measurement conditions
6. Extracellular and extravascular volume fraction [V_e]—interstitial volume (mL of extracellular/extravascular volume per 100 mL of tissue)

6.3.3 Technique

Dynamic enhanced MRI typically uses an intravenous contrast injection followed by repeated acquisitions over a limited tissue volume to assess the enhancement kinetics of the studied volume. There are several overlapping processes occurring during the acquisition, namely, microcirculation perfusion, accumulation of contrast within the interstitial space, and release from the interstitium via capillary leakage.

Pure tissue perfusion reflects the initial arterial input to capillary network entry, followed by circulation within the capillary bed, with subsequent exit from the capillary bed into the venous system. To image this, a rapid acquisition time is needed to accurately delineate the maximum peak contrast enhancement and the washout period during which contrast recirculates and is slowly eliminated by renal excretion.

Currently there is no standardized method for the application of DCE-MRI. There are several considerations that should be made when performing DCE-MRI, including:

1. The temporal resolution of the acquisition
2. The total measurement time
3. Whether to use a single slice, multiple slices, or a 3D dataset

The main challenges in pediatric imaging include DCE acquisition time, owing to rapid circulation of children; the overall examination time, which may be poorly tolerated if prolonged, leading to motion artifacts; and reduced signal-to-noise ratio in smaller voxels required to image children compared to adults. Strategies such as rigid or nonrigid motion correction techniques and noise filtering may be necessary to perform DCE-MRI reliably in children.

6.3.4 Analysis

DCE-MRI data can be analyzed qualitatively (visually), semiquantitatively, or quantitatively, with vendor system software packages increasingly available to readily facilitate this. Analysis may be based on region of interest analysis, on clusters of pixels with similar enhancement patterns, or voxel by voxel.

Qualitative assessment of enhancement curves derived from a lesion provides the most rapid method of evaluation, as used in breast MRI, with different enhancement curves suggesting a benign or malignant lesion, visually assessing the enhancement curve pattern [50].

Semiquantitative analyses perform calculations based on the enhancement curve, for example, calculating the area under the curve, and are often compared to a reference tissue such as skeletal muscle or an adjacent normal portion of an organ.

Quantitative analysis uses mathematical models based on tissue physiological parameters, requiring an arterial input function from the vessel supplying the tissue of interest. The most widely used and recommended model is the Tofts-Kety model [51, 52], which produces two measures, K_{trans} and V_e. The results obtained with the Tofts-Kety model are only comparable between different centers/systems if the conditions of acquisition are identical. In addition to the Tofts-Kety model, there are numerous other physiological models available; however, these are beyond the scope of this chapter.

6.3.5 Pediatric Applications of DCE-MRI

There is limited data currently regarding the use of DCE-MRI in pediatric oncology, with some emerging studies testing its use in pediatric tumors.

6.3.5.1 Therapy Response Assessment and Prognostication

The advent of anti-angiogenic agents has led to an additional therapeutic option for some cancers, specifically targeting neovascularization of tumors. The principle attraction of DCE-MR imaging is to be able to determine changes in the microvascular composition of tumors after therapy, before size change occurs (Fig. 6.10).

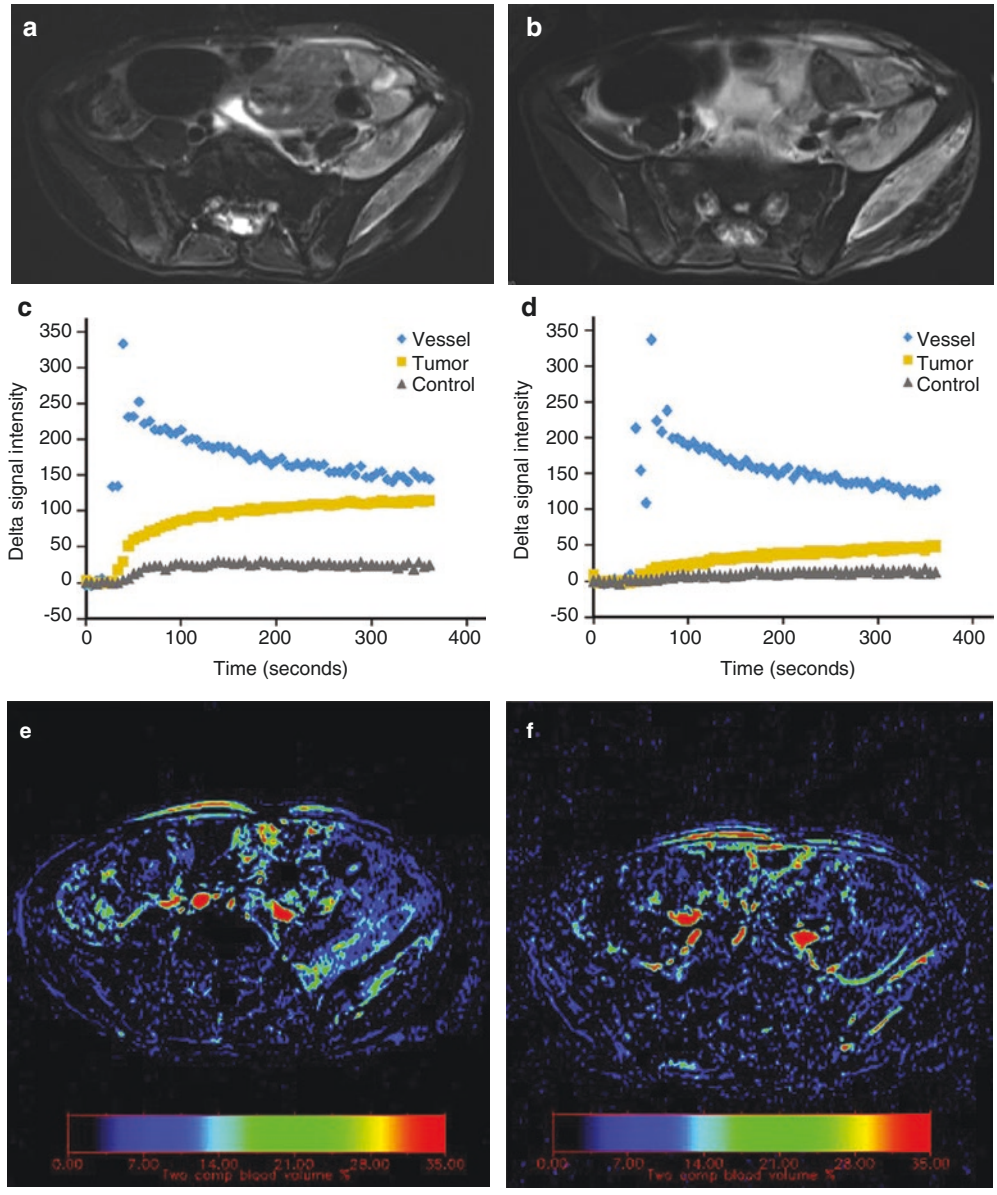

Fig. 6.10 Dynamic contrast-enhanced (DCE) MRI: representative images from a patient with clear-cell sarcoma being treated on COG ADVL0815, a phase 1 study of pazopanib, a multitargeted receptor tyrosine kinase inhibitor of vascular endothelial growth factor receptors (VEGFR) -1, -2, and -3, c-kit, and platelet-derived growth factor receptors, are shown. Conventional fat-saturated FSE T2 images at baseline (**a**) and following 15 days of pazopanib therapy (**b**) show no appreciable change in size or signal intensity of metastatic lesions surrounding the left iliac bone with infiltration of the left iliacus muscle anteriorly and the gluteus medius muscle posteriorly. DCE-MRI, obtained at baseline (**c**, **e**) and following 15 days of pazopanib therapy (**d**, **f**), using a dynamic, three-dimensional, T1-weighted gradient echo acquisition after bolus administration of a single dose of gadopentetic acid (0.1 mmol/kg), demonstrates a marked decrease in tumor enhancement, as shown on the time vs. signal intensity curve (yellow line: **c**, **d**) and the blood volume maps (**e**, **f**) from the area of the lesions. These results highlight the potential utility of DCE-MRI for demonstrating changes in tumor vascularity following treatment with targeted agents, such as anti-angiogenic drugs like pazopanib, even when conventional imaging techniques do not show any effect. With next-generation drug treatment trials placing greater emphasis on molecularly targeted therapies, techniques such as DCE-MRI have the potential to provide imaging biomarkers for drug activity, well before other clinical and imaging endpoints become evident. *Reproduced with permission* [57]

There is some evidence that DCE-MRI can detect microcirculation changes following anti-angiogenic treatment in pediatric osteosarcoma, with Guo et al. showing a change in plasma volume fraction and vascular leakage in a cohort of patients treated with bevacizumab [53]. This study also showed an association between lower K_{trans} and increased tumor necrosis and therefore longer event-free survival, which has been demonstrated by other pilot work [54]. The potential to identify patients with an inadequate tumor necrosis fraction pre-surgery could allow a more patient-centered risk-adaptive therapy, a central tenet of personalized cancer care.

Similar prognostication may also be possible in optic pathway glioma (OPG), with Jost et al. showing a higher mean permeability in clinically aggressive OPG compared to clinically stable disease [55].

Although there are no current clinical studies available, the effect of anti-angiogenic therapy in neuroblastoma has been studied in a murine model of aggressive MYC-N amplified neuroblastoma. Jamin et al. have shown a reduction in K_{trans} within tumors in a TH-*MYCN* mouse model following therapy with cediranib, an anti-angiogenic agent [56]. This not only demonstrates that DCE-MRI functional parameters may be useful in monitoring treatment responses but also facilitates the development of newer novel agents that target tumor vascularity, allowing their effect to be evaluated.

6.4 Conclusion

The use of functional MRI techniques such as DWI and DCE-MRI in pediatric oncology is promising, both for staging and lesion detection, as well as for assessing response to therapy. However, the clinical use of the elegant DWI and DCE-MRI techniques presented here remains primarily investigational at present. Nonetheless, as these techniques become more refined with greater reproducibility across a variety of platforms, and become more widely available for routine clinical use, the ability to interrogate tissue microstructure using functional MRI will inevitably lead to the development of newer anti-cancer agents and increasingly personalized cancer care for children in the future.

References

1. Chavhan GB, Alsabban Z, Babyn PS. Diffusion-weighted imaging in pediatric body MR imaging: principles, technique, and emerging applications. Radiographics. 2014;34(3):E73–88.
2. Koh DM, Collins DJ. Diffusion-weighted MRI in the body: applications and challenges in oncology. AJR Am J Roentgenol. 2007;188(6):1622–35.
3. Chavhan GB, Caro-Dominguez P. Diffusion-weighted imaging in pediatric body magnetic resonance imaging. Pediatr Radiol. 2016;46(6):847–57.
4. Takahara T, Imai Y, Yamashita T, Yasuda S, Nasu S, Van Cauteren M. Diffusion weighted whole body imaging with background body signal suppression (DWIBS): technical improvement using free breathing, STIR and high resolution 3D display. Radiat Med. 2004;22(4):275–82.
5. Taouli B, Koh DM. Diffusion-weighted MR imaging of the liver. Radiology. 2010;254(1):47–66.
6. Taouli B, Beer AJ, Chenevert T, Collins D, Lehman C, Matos C, et al. Diffusion-weighted imaging outside the brain: consensus statement from an ISMRM-sponsored workshop. J Magn Reson Imaging. 2016;44(3):521–40.
7. Le Bihan D, Breton E, Lallemand D, Grenier P, Cabanis E, Laval-Jeantet M. MR imaging of intravoxel incoherent motions: application to diffusion and perfusion in neurologic disorders. Radiology. 1986;161(2):401–7.
8. Le Bihan D, Breton E, Lallemand D, Aubin ML, Vignaud J, Laval-Jeantet M. Separation of diffusion and perfusion in intravoxel incoherent motion MR imaging. Radiology. 1988;168(2):497–505.
9. Koh DM, Collins DJ, Orton MR. Intravoxel incoherent motion in body diffusion-weighted MRI: reality and challenges. AJR Am J Roentgenol. 2011;196(6):1351–61.
10. Rosenkrantz AB, Padhani AR, Chenevert TL, Koh DM, De Keyzer F, Taouli B, et al. Body diffusion kurtosis imaging: basic principles, applications, and considerations for clinical practice. J Magn Reson Imaging. 2015;42(5):1190–202.
11. Bennett KM, Schmainda KM, Bennett RT, Rowe DB, Lu H, Hyde JS. Characterization of continuously distributed cortical water diffusion rates with a stretched-exponential model. Magn Reson Med. 2003;50(4):727–34.
12. Zhang G, Wang S, Wen D, Zhang J, Wei X, Ma W, et al. Comparison of non-Gaussian and Gaussian diffusion models of diffusion weighted imaging of rectal cancer at 3.0 T MRI. Sci Rep. 2016;6:38782.

13. Winfield JM, Payne GS, Weller A, deSouza NM. DCE-MRI, DW-MRI, and MRS in cancer: challenges and advantages of implementing qualitative and quantitative multi-parametric imaging in the clinic. Top Magn Reson Imaging. 2016;25(5):245–54.
14. Alibek S, Cavallaro A, Aplas A, Uder M, Staatz G. Diffusion weighted imaging of pediatric and adolescent malignancies with regard to detection and delineation: initial experience. Acad Radiol. 2009;16(7):866–71.
15. Soyer P, Boudiaf M, Placé V, Sirol M, Pautrat K, Vignaud A, et al. Preoperative detection of hepatic metastases: comparison of diffusion-weighted, T2-weighted fast spin echo and gadolinium-enhanced MR imaging using surgical and histopathologic findings as standard of reference. Eur J Radiol. 2011;80(2):245–52.
16. Parikh T, Drew SJ, Lee VS, Wong S, Hecht EM, Babb JS, et al. Focal liver lesion detection and characterization with diffusion-weighted MR imaging: comparison with standard breath-hold T2-weighted imaging. Radiology. 2008;246(3):812–22.
17. van den Bos IC, Hussain SM, Krestin GP, Wielopolski PA. Liver imaging at 3.0 T: diffusion-induced black-blood echo-planar imaging with large anatomic volumetric coverage as an alternative for specific absorption rate-intensive echo-train spin-echo sequences: feasibility study. Radiology. 2008;248(1):264–71.
18. Bozkurt M, Doganay S, Kantarci M, Yalcin A, Eren S, Atamanalp SS, et al. Comparison of peritoneal tumor imaging using conventional MR imaging and diffusion-weighted MR imaging with different b values. Eur J Radiol. 2011;80(2):224–8.
19. Satoh Y, Ichikawa T, Motosugi U, Kimura K, Sou H, Sano K, et al. Diagnosis of peritoneal dissemination: comparison of 18F-FDG PET/CT, diffusion-weighted MRI, and contrast-enhanced MDCT. AJR Am J Roentgenol. 2011;196(2):447–53.
20. Humphries PD, Sebire NJ, Siegel MJ, Olsen Ø. Tumors in pediatric patients at diffusion-weighted MR imaging: apparent diffusion coefficient and tumor cellularity. Radiology. 2007;245(3):848–54.
21. Gawande RS, Gonzalez G, Messing S, Khurana A, Daldrup-Link HE. Role of diffusion-weighted imaging in differentiating benign and malignant pediatric abdominal tumors. Pediatr Radiol. 2013;43(7):836–45.
22. Kocaoglu M, Bulakbasi N, Sanal HT, Kismet E, Caliskan B, Akgun V, et al. Pediatric abdominal masses: diagnostic accuracy of diffusion weighted MRI. Magn Reson Imaging. 2010;28(5):629–36.
23. Uhl M, Altehoefer C, Kontny U, Il'yasov K, Büchert M, Langer M. MRI-diffusion imaging of neuroblastomas: first results and correlation to histology. Eur Radiol. 2002;12(9):2335–8.
24. Gahr N, Darge K, Hahn G, Kreher BW, von Buiren M, Uhl M. Diffusion-weighted MRI for differentiation of neuroblastoma and ganglioneuroblastoma/ganglioneuroma. Eur J Radiol. 2011;79(3):443–6.
25. Serin HI, Gorkem SB, Doganay S, Cıracı S, Unal E, Guzel M, et al. Diffusion weighted imaging in differentiating malignant and benign neuroblastic tumors. Jpn J Radiol. 2016;34(9):620–4.
26. Wen Y, Peng Y, Duan XM, Zhang N. Role of diffusion-weighted imaging in distinguishing thoracoabdominal neuroblastic tumours of various histological types and differentiation grades. J Med Imaging Radiat Oncol. 2017;61:718.
27. Neubauer H, Li M, Müller VR, Pabst T, Beer M. Diagnostic value of diffusion-weighted MRI for tumor characterization, differentiation and monitoring in pediatric patients with neuroblastic tumors. Rofo. 2017;189(7):640–50.
28. Caro-Dominguez PGA, Chavhan GB. Can diffusion weighted imaging distinguish between benign and malignant pediatric liver tumors? Pediatr Radiol. 2018;48:85.
29. Littooij AS, Nikkels PG, Hulsbergen-van de Kaa CA, van de Ven CP, van den Heuvel-Eibrink MM, Olsen Ø. Apparent diffusion coefficient as it relates to histopathology findings in post-chemotherapy nephroblastoma: a feasibility study. Pediatr Radiol. 2017;47:1608.
30. Littooij AS, Sebire NJ, Olsen Ø. Whole-tumor apparent diffusion coefficient measurements in nephroblastoma: can it identify blastemal predominance? J Magn Reson Imaging. 2017;45(5):1316–24.
31. Wang J, Sun M, Liu D, Hu X, Pui MH, Meng Q, et al. Correlation between apparent diffusion coefficient and histopathology subtypes of osteosarcoma after neoadjuvant chemotherapy. Acta Radiol. 2017;58(8):971–6.
32. Braithwaite AC, Dale BM, Boll DT, Merkle EM. Short- and midterm reproducibility of apparent diffusion coefficient measurements at 3.0-T diffusion-weighted imaging of the abdomen. Radiology. 2009;250(2):459–65.
33. Miquel ME, Scott AD, Macdougall ND, Boubertakh R, Bharwani N, Rockall AG. In vitro and in vivo repeatability of abdominal diffusion-weighted MRI. Br J Radiol. 2012;85(1019):1507–12.
34. Littooij AS, Humphries PD, Olsen Ø. Intra- and interobserver variability of whole-tumour apparent diffusion coefficient measurements in nephroblastoma: a pilot study. Pediatr Radiol. 2015;45(11):1651–60.
35. Miyazaki K, Jerome NP, Collins DJ, Orton MR, d'Arcy JA, Wallace T, et al. Demonstration of the reproducibility of free-breathing diffusion-weighted MRI and dynamic contrast enhanced MRI in children with solid tumours: a pilot study. Eur Radiol. 2015;25(9):2641–50.
36. Littooij AS, Kwee TC, de Keizer B, Bruin MC, Coma A, Beek FJ, et al. Whole-body MRI-DWI for assessment of residual disease after completion of therapy in lymphoma: a prospective multicenter study. J Magn Reson Imaging. 2015;42(6):1646–55.
37. Liu L, Wu N, Ouyang H, Dai JR, Wang WH. Diffusion-weighted MRI in early assessment of tumour response

to radiotherapy in high-risk prostate cancer. Br J Radiol. 2014;87(1043):20140359.
38. Blackledge MD, Collins DJ, Tunariu N, Orton MR, Padhani AR, Leach MO, et al. Assessment of treatment response by total tumor volume and global apparent diffusion coefficient using diffusion-weighted MRI in patients with metastatic bone disease: a feasibility study. PLoS One. 2014;9(4):e91779.
39. Chen Y, Liu X, Zheng D, Xu L, Hong L, Xu Y, et al. Diffusion-weighted magnetic resonance imaging for early response assessment of chemoradiotherapy in patients with nasopharyngeal carcinoma. Magn Reson Imaging. 2014;32(6):630–7.
40. Wang CS, Du LJ, Si MJ, Yin QH, Chen L, Shu M, et al. Noninvasive assessment of response to neoadjuvant chemotherapy in osteosarcoma of long bones with diffusion-weighted imaging: an initial in vivo study. PLoS One. 2013;8(8):e72679.
41. Bajpai J, Gamnagatti S, Kumar R, Sreenivas V, Sharma MC, Khan SA, et al. Role of MRI in osteosarcoma for evaluation and prediction of chemotherapy response: correlation with histological necrosis. Pediatr Radiol. 2011;41(4):441–50.
42. McDonald K, Sebire NJ, Anderson J, Olsen OE. Patterns of shift in ADC distributions in abdominal tumours during chemotherapy-feasibility study. Pediatr Radiol. 2011;41(1):99–106.
43. Wu X, Kellokumpu-Lehtinen PL, Pertovaara H, Korkola P, Soimakallio S, Eskola H, et al. Diffusion-weighted MRI in early chemotherapy response evaluation of patients with diffuse large B-cell lymphoma--a pilot study: comparison with 2-deoxy-2-fluoro-D-glucose-positron emission tomography/computed tomography. NMR Biomed. 2011;24(10):1181–90.
44. Littooij AS, Kwee TC, Barber I, Granata C, Vermoolen MA, Enríquez G, et al. Whole-body MRI for initial staging of paediatric lymphoma: prospective comparison to an FDG-PET/CT-based reference standard. Eur Radiol. 2014;24(5):1153–65.
45. Villani A, Shore A, Wasserman JD, Stephens D, Kim RH, Druker H, et al. Biochemical and imaging surveillance in germline TP53 mutation carriers with Li-Fraumeni syndrome: 11 year follow-up of a prospective observational study. Lancet Oncol. 2016;17(9):1295–305.
46. Detre JA, Zhang W, Roberts DA, Silva AC, Williams DS, Grandis DJ, et al. Tissue specific perfusion imaging using arterial spin labeling. NMR Biomed. 1994;7(1-2):75–82.
47. Kwong KK, Belliveau JW, Chesler DA, Goldberg IE, Weisskoff RM, Poncelet BP, et al. Dynamic magnetic resonance imaging of human brain activity during primary sensory stimulation. Proc Natl Acad Sci U S A. 1992;89(12):5675–9.
48. Axel L. Cerebral blood flow determination by rapid-sequence computed tomography: theoretical analysis. Radiology. 1980;137(3):679–86.
49. Tofts PS, Brix G, Buckley DL, Evelhoch JL, Henderson E, Knopp MV, et al. Estimating kinetic parameters from dynamic contrast-enhanced T(1)-weighted MRI of a diffusable tracer: standardized quantities and symbols. J Magn Reson Imaging. 1999;10(3):223–32.
50. Schnall MD, Blume J, Bluemke DA, DeAngelis GA, DeBruhl N, Harms S, et al. Diagnostic architectural and dynamic features at breast MR imaging: multicenter study. Radiology. 2006;238(1):42–53.
51. Tofts PS, Kermode AG. Blood brain barrier permeability in multiple sclerosis using labelled DTPA with PET, CT and MRI. J Neurol Neurosurg Psychiatry. 1989;52(8):1019–20.
52. Leach MO, Brindle KM, Evelhoch JL, Griffiths JR, Horsman MR, Jackson A, et al. The assessment of antiangiogenic and antivascular therapies in early-stage clinical trials using magnetic resonance imaging: issues and recommendations. Br J Cancer. 2005;92(9):1599–610.
53. Guo J, Glass JO, McCarville MB, Shulkin BL, Daryani VM, Stewart CF, et al. Assessing vascular effects of adding bevacizumab to neoadjuvant chemotherapy in osteosarcoma using DCE-MRI. Br J Cancer. 2015;113(9):1282–8.
54. Guo J, Reddick WE, Glass JO, Ji Q, Billups CA, Wu J, et al. Dynamic contrast-enhanced magnetic resonance imaging as a prognostic factor in predicting event-free and overall survival in pediatric patients with osteosarcoma. Cancer. 2012;118(15):3776–85.
55. Jost SC, Ackerman JW, Garbow JR, Manwaring LP, Gutmann DH, McKinstry RC. Diffusion-weighted and dynamic contrast-enhanced imaging as markers of clinical behavior in children with optic pathway glioma. Pediatr Radiol. 2008;38(12):1293–9.
56. Jamin Y, Tucker ER, Poon E, Popov S, Vaughan L, Boult JK, et al. Evaluation of clinically translatable MR imaging biomarkers of therapeutic response in the TH-MYCN transgenic mouse model of neuroblastoma. Radiology. 2013;266(1):130–40.
57. Glade Bender JL, Lee A, Reid JM, Baruchel S, Roberts T, Voss SD, Wu B, Ahern CH, Ingle AM, Harris P, Weigel BJ, Blaney SM. Phase I pharmacokinetic and pharmacodynamic study of pazopanib in children with soft tissue sarcoma and other refractory solid tumors: a children's oncology group phase I consortium report. J Clin Oncol. 2013;31:3034–43. https://doi.org/10.1200/JCO.2012.47.0914.

7 Whole-Body MRI in Pediatric Oncology

Rutger A. J. Nievelstein and Annemieke S. Littooij

7.1 Introduction

Whole-body imaging is essential in pediatric oncology as tumor spread may involve different anatomical regions [1, 2]. Traditionally, ultrasonography (US) and computed tomography (CT) are used to detect tumors and to assess the extent of tumor spread before, during, and after therapy. But nowadays, there is an increasing interest in functional imaging techniques like positron emission tomography (PET) and single-photon emission computed tomography (SPECT) [3]. By combining these latter techniques with CT, it has become possible to acquire imaging data on the biological behavior of tumor as well as the anatomical localization and extent of tumor spread in one single examination throughout the body. A major disadvantage of these techniques is the use of ionizing radiation, which may be associated with induction of second cancers later during life. This small but not negligible health risk is of particular concern in children as their tissues are more radiosensitive than adults and they have more years ahead in which cancerous changes might occur. Magnetic resonance imaging (MRI) is a radiation-free imaging technique that allows for acquiring images with a high spatial resolution and excellent soft tissue contrast throughout the body. Due to recent technological advances in MRI such as moving table platforms, multichannel/multielement surface coils, and parallel imaging, it is now possible to cover the whole human body in a reasonable period of time [4–8]. This makes MRI an ideal imaging tool for the detection of pathology, especially in parenchymal and bone marrow locations. Moreover, with the introduction of new advanced MRI techniques like whole-body diffusion-weighted imaging (DWI), it has become possible to acquire functional information for better tumor characterization and therapy monitoring [9–13]. Although the feasibility of whole-body MRI in pediatric oncology has been proven in the literature over the past 10 years [14–21], several challenges remain including the frequent need for sedation or general anesthesia because of long scan times, artifacts from motion, as well as the suboptimal imaging of the lungs in the evaluation for pulmonary metastatic disease. Despite these challenges, whole-body MRI is nowadays being increasingly used in children to evaluate the extent of various oncologic entities at diagnosis and during therapy. In this chapter, the current status of the technique, major clinical applications, and future perspectives of whole-body MRI in children with cancer will be discussed.

R. A. J. Nievelstein (✉) · A. S. Littooij
University Medical Center Utrecht,
Utrecht, The Netherlands
e-mail: r.a.j.nievelstein@umcutrecht.nl

S. D. Voss, K. McHugh (eds.), *Imaging in Pediatric Oncology*, Pediatric Oncology,
https://doi.org/10.1007/978-3-030-03777-2_7

7.2 Technique

Until now, there is no standardized technique or protocol for performing whole-body MRI. In pediatric oncology, whole-body MRI is often restricted to the skull or skull base to groin region in line with most hybrid imaging techniques, but it can involve imaging of the entire body (from vertex to toes). Most modern MRI scanners are equipped with a moving table top for sequential movement of the patient through the magnet during imaging without the need for repositioning.

In whole-body MRI, the use of phased-array surface coils is preferred over the use of the quadrature body coil integrated in the magnet bore, because of the better spatial resolution and signal-to-noise ratio (SNR) of the former over the latter. This is especially true when functional imaging techniques like whole-body DWI are planned to be included in the imaging protocol. The way these coils can be used for a whole-body image acquisition depends on the type of MRI scanner available. A very practical and easy to implement approach, the so-called "sliding table and repositioning surface coil" approach, uses tabletop spacers to place an additional table platform on the original MR table allowing manipulation of the lower part of a non-integrated phased-array surface coil without repositioning the patient (Fig. 7.1) [22]. However, nowadays, on several modern MRI scanners, dedicated multichannel surface coil systems are available allowing for whole-body imaging without the need to reposition the coil at each station (Fig. 7.2) [5].

Until now, whole-body MRI is mainly performed on 1.5 T MRI equipment. MRI at 3 T has the intrinsic advantage of a higher signal-to-noise

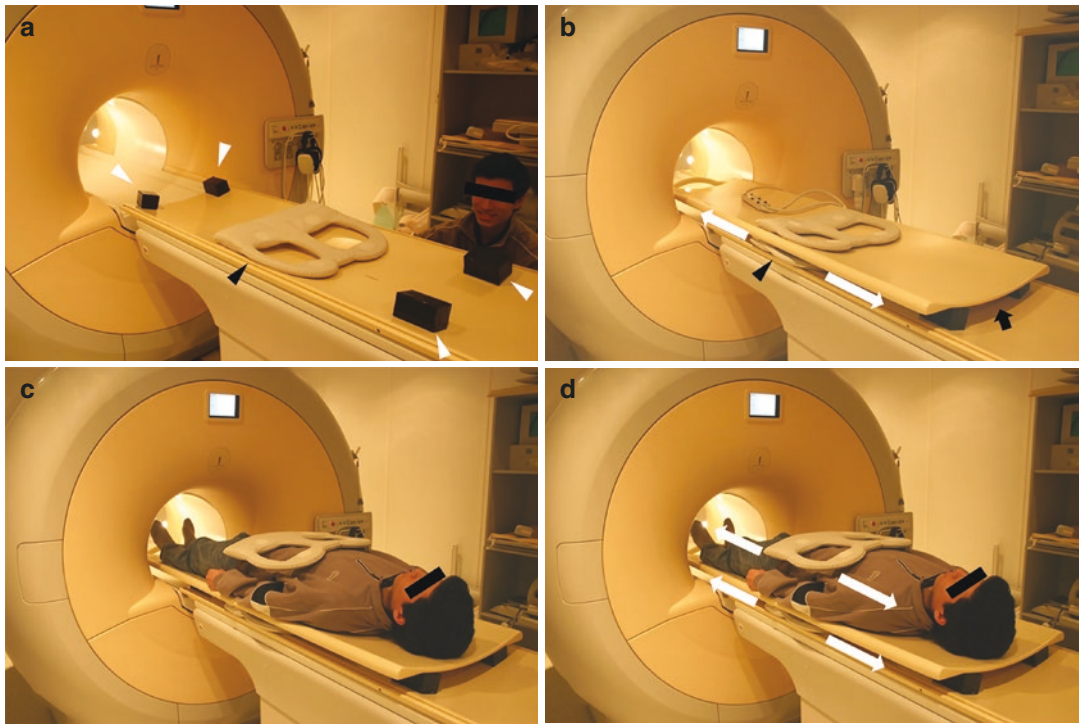

Fig. 7.1 Table preparation for whole-body MRI using a sliding surface coil approach. (**a**) Spacers (white arrowheads) are placed on top of the original patient table to create space for the lower part of the surface coil (black arrowhead). (**b**) An additional table platform is mounted on top of the spacers (black arrow). The lower part of the surface coil (black arrowhead) can be moved freely below the additional table platform (white arrows). (**c**, **d**) Patient is lying on top of the additional table platform; the surface coil can be moved freely without patient repositioning (white arrows) (adapted with permission from [22])

Fig. 7.2 Illustration of a dedicated multichannel surface coil system for whole-body MR imaging, consisting of multiple rows of coils covering large parts or the entire body of the patient (Courtesy of Royal Philips, Best, NL)

ratio (SNR) but remains challenging because of geometric distortion, image shearing, chemical shift, and ghosting artifacts, especially in case of larger fields of view. However, recent technical developments have improved whole-body imaging at 3 T, including the recently introduced dual-source radiofrequency transmission technology to reduce field non-homogeneities and the more robust suppression of fat by the slice-selection gradient reversal (SSGR) technique [10, 19, 23]. Furthermore, a recent study by Azzedine et al. in 23 adult patients has shown that 3 T whole-body DWI is feasible and yields accurate assessment and staging of lymphoma comparable to 1.5 T [24].

7.2.1 Sequences

The choice of sequences will depend largely on the type of tumor or clinical question, patient size, and the time available. Sequences that are typically used in whole-body MRI include short tau inversion recovery (STIR), T1-weighted fast spin-echo (FSE, TSE), and contrast material-enhanced (CE) T1-weighted three-dimensional gradient echo (VIBE, THRIVE, LAVA) sequences. Furthermore, with the introduction of diffusion-weighted whole-body imaging with background body signal suppression (DWIBS) in 2004 by Takahara et al., it became possible to perform whole-body DWI under free breathing within a clinically acceptable examination time [9].

7.2.1.1 Short Tau Inversion Recovery (STIR)

STIR is the most commonly used sequence in whole-body MRI. Due to the nulling of the fat signal and the fact that pathologic tissues are usually proton-rich (with prolonged T1 and T2 relaxation times), they will be highlighted on STIR images (Fig. 7.3) [5, 18, 19, 23, 25, 26]. Fat suppression on STIR images is more robust and homogeneous than on other types of T2-weighted fat-saturated images. Furthermore, the signal of other substances with a short T1 relaxation time (like blood, liquid protein, melanin, and gadolinium) will also be reduced. On STIR images, certain organs will have a physiological high signal, such as lymph nodes, spleen, thymus, Waldeyer's ring, and kidneys. In these organs, pathology will be more difficult to detect or appear as low signal lesions [25]. Furthermore, as normal and pathologic lymph nodes usually show similar high signal intensity, distinction of pathologic nodes is primarily based on size criteria. Finally, STIR is a highly sensitive technique to detect osteomedullary metastases, as in particular in young children hypercellular red marrow zones persist in large parts of the bone that will obscure metastatic disease on T1-weighted imaging (Fig. 7.3). Several studies have investigated the role of STIR in whole-body MRI [14, 17, 27, 28]. Although most studies did show that whole-body STIR is a sensitive technique to detect pathologic lesions, it is not specific for malignancy as inflammatory, infectious, traumatic, necrotic, and post-therapeutic changes, as well as benign lesions such as cysts and hemangiomas, can also present with high signal intensities. In addition, possible motion artifacts from respiration or vessel pulsation may obscure parenchymal lesions.

7.2.1.2 3D T2-Weighted Turbo Spin-Echo (T2-TSE)

Recent technological advances have made it possible to acquire 3D T2-weighted turbo or fast spin-echo images of large parts of the body within clinically acceptable examination times (Fig. 7.4). An important advantage of these sequences is the better anatomical delineation and higher signal-to-noise ratio when compared

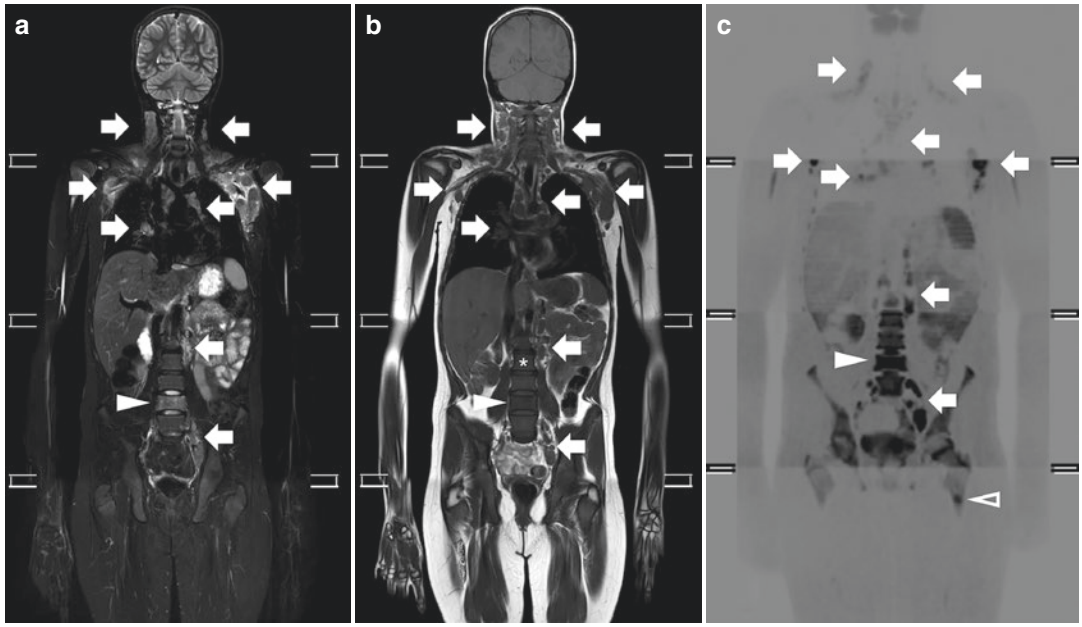

Fig. 7.3 Coronal whole-body short tau inversion recovery (STIR) (**a**), T1-weighted (**b**) and maximum intensity projection grayscale inverted diffusion-weighted (**c**) whole-body MRI images of a 16-year-old boy with stage IV B Hodgkin lymphoma, illustrating nodal involvement of cervical, axillary, mediastinal, hilar, para-aortic, and left para-iliac lymph nodes (arrows), as well as bone marrow involvement of vertebral body L4 (arrowhead). As illustrated in (**a**) and (**b**), bone marrow involvement is more easily detected on the STIR image when compared to the T1-weighted image, in this case due to diffuse bone marrow reconversion (asterisk in **b**) related to the lymphoma. On the maximum intensity projection grayscale inverted diffusion-weighted whole-body MRI image (**c**), an additional bone marrow lesion can be seen in the proximal femoral diaphysis (open arrowhead)

to STIR imaging. If fat suppression is required, the use of the (three point) Dixon technique is preferred over frequency-selective fat saturation techniques, as the former will result in a more uniform fat suppression especially in body regions such as the neck that suffer from main static magnetic field (B0) inhomogeneity [23, 29]. The Dixon technique allows generation of four sets of images with different image contrast in a single acquisition, i.e., fat-only, water-only, in-phase, and opposed-phase images. Due to its almost perfect fat suppression on the water-only images and the enhanced image contrast, this technique can be used to improve lesion detectability and characterization on pre- and post-contrast whole-body MRI [21, 23, 29–31]. Limitations of the Dixon technique include the fat-water separation or swapping error that sometimes occurs in one leg or around the thorax and the loss of signal around the heart due to cardiac pulsatility. However, as large-scale studies in children are still missing, it remains to be determined whether these promising new T2-weighted imaging techniques will become a mainstay in pediatric whole-body MRI beyond STIR imaging.

7.2.1.3 T1-Weighted Fast Spin-Echo (T1-FSE)

The T1-FSE sequence is especially helpful for anatomic delineation of lesions and to increase the specificity of the detection of bone marrow involvement in older children (Fig. 7.3) [18, 32, 33]. It is usually combined with whole-body STIR imaging. In our clinical experience, STIR is very useful for assessing the extent of disease at presentation but is less suitable for assessing response during treatment because the initial involved sites often show a decrease in T2 signal during treatment. Although not commonly used

Fig. 7.4 Coronal 3D T2-weighted turbo spin-echo (T2-TSE) image in a 3-year-old boy with stage IV neuroblastoma, illustrating the better anatomical delineation and higher signal-to-noise ratio when compared to STIR imaging. There is a left paravertebral tumor arising from the left adrenal region with involvement of the left renal hilar region (white arrows) and extension into the inferior mediastinum (arrowhead)

in whole-body imaging, the addition of 3D contrast-enhanced (CE) T1-weighted GRE sequence can improve the diagnostic accuracy of lesion delineation and characterization [4, 5, 18, 34]. In addition, it facilitates the combination of better local tumor staging and evaluation of metastatic disease. A disadvantage of this sequence is the suboptimal fat saturation. As mentioned before, the Dixon technique might be a good alternative for this as its almost perfect fat suppression on the water-only images and the increased image contrast will improve lesion detectability and characterization on pre- and post-contrast whole-body MRI [21, 23, 29–31].

7.2.1.4 Diffusion-Weighted Imaging (DWI)

With the introduction of diffusion-weighted whole-body imaging with background body signal suppression (DWIBS) in 2004 by Takahara et al., it became possible to perform whole-body DWI under free breathing within a clinically acceptable examination time [9, 10, 12, 13, 23]. Single-shot echo-planar imaging (EPI) is most commonly used in whole-body DWI in order to reduce motion artifacts. To optimize background body signal suppression and avoid image degradation due to severe chemical shift in EPI sequences, either a STIR pre-pulse or a frequency-selective (chemical shift selective, CHESS) pre-pulse is used for fat suppression. Although the selection of the method for fat suppression may depend on the organ/body region under examination, STIR usually results in the most robust fat suppression over an extended field of view, in particular in the neck/shoulder region and lower extremities. In addition, for bowel signal suppression in the abdominal region, STIR is the preferred method as well. When performing whole-body DWI at higher field strengths (e.g., 3 T), the recently reintroduced slice-selection gradient reversal (SSGR) technique allows for the most robust fat suppression without prolonging scan time or increasing SAR [10, 19]. Whole-body DWI is usually acquired in the axial plane with multiplanar reconstructions in the coronal and sagittal plane, as direct coronal or sagittal acquisitions are more vulnerable to image distortion. To facilitate optimal whole-body multiplanar reconstructions from different anatomic sections, it is important to ensure that data acquisition is performed in a way that minimizes voxel shifts between imaging stations for accurate stack alignment. For visual assessment of whole-body DWI high *b*-values up to 1000 s/mm^2 should be applied to improve lesion conspicuity. In case quantitative measurements of the diffusivity (apparent diffusion coefficient, ADC) in pathological tissues are required, the use of at least three *b*-values (including b0) is recommended. Besides b0 this should include two *b*-values at or above 100 s/mm^2 to reliably separate perfusion from bulk diffusion and allow for more accurate calculation of ADC values [35, 36]. Furthermore, to minimize the chance of misregistration, and thus incorrect ADC mapping, it is better to choose high *b*-values that maintain some background tissue signal, typically around 500 s/mm^2 up to 800 s/mm^2. This

background tissue visibility is also important when coregistration with conventional MRI sequences is foreseen and is especially important for free-breathing acquisitions. For a more in-depth discussion of the technique of DWI in the body, the reader is referred to Chapter 6 in this book and the recent literature [11, 13, 35–37].

By adding DWI to a whole-body imaging protocol, lesion detection can be improved, reading time can be decreased, and the functional information on water diffusivity can be of help to better characterize pathology and monitor therapy [10, 13, 36, 38–40]. For visual assessment an inverted gray scale image from the highest *b*-value acquisition is often used, with disease areas appearing as dark regions against a normal white background due to the restricted diffusion in these areas (Fig. 7.3). As mentioned above, the DWI images can be fused with other standard anatomic MRI sequences to further improve lesion localization (Fig. 7.5). In addition, whole-body DWI images should be reviewed in combination with conventional T1-weighted and T2-weighted MRI images to ensure accurate interpretation, as areas of diffusion restriction are not specific for malignancy and can be caused by normal red bone marrow or other disease processes, such as inflammation. Moreover, ADC maps should be used to ascertain the presence of diffusion restriction by excluding T2 shine through phenomena. Quantitative (ADC) measurements facilitate differentiation of benign versus malignant disease, although considerable overlap in ADC values does occur [18, 41, 42]. Furthermore, comparison of the mean or median ADC values of a lesion before and after treatment can be used to monitor tumor response as ADC values usually change (increase) after therapy. It should be mentioned, however, that reproducibility of ADC measurements obtained with whole-body DWI has not been established yet, particularly with regard to ADC variations across anatomic imaging stations.

Several normal structures do show diffusion restriction due to its high cellularity, including red marrow, brain, salivary glands, thymus, spleen, adrenals, prostate, and gonads (Fig. 7.6) [10, 13, 18, 37]. Moreover, lymphoid tissue also shows relative restricted diffusion and long T2 values, which limits the detection of pathology in lymph nodes, which are often involved in malignancies. Therefore, current criteria for diagnosing nodal involvement often rely on a combination of signs, including nodal signal intensity (on its own or compared with the primary tumor), ADC value, and size criteria. As the apparent size of lymph nodes on DWI images is dependent on the applied window level and width, these size measurements for prediction of nodal malignancy should be performed on conventional T1-weighted and T2-weighted sequences. The use of an ultrasmall superparamagnetic iron oxide (USPIO) contrast agent allows for a better delineation of malignant nodal (and bone marrow) infiltration, even in normal sized lymph nodes. USPIO nanoparticles are retained in the normal reticuloendothelial system of the lymph nodes, liver, spleen, and bone marrow with a resulting signal drop on T2, T2*, and DWI images, whereas malignant lesions lack uptake, thereby improving the tumor-to-background contrast effectively [20, 43]. In addition, USPIO nanoparticles result in long-lasting T1 shortening in vessels, which allows acquisition of enhanced T1-weighted images for anatomical localization. Unfortunately, USPIO nanoparticles are not approved by most (inter)national drug agencies, limiting their use in daily clinical practice. Furthermore, adverse reactions after intravascular USPIO administration do occur with hypersensitivity reactions in up to 3–7% and rare events of serious anaphylactic reactions in 0–2% in the adult population [20, 43]. For this reason the FDA has issued a black box warning regarding these risks, recommending clinicians to carefully consider the potential risks and benefits of administering USPIOs including careful screening for any history of allergies, in particular regarding dextran and iron compounds.

7.2.2 Scan Plane

The choice of scan plane will depend on the region of interest, type of malignancy, and diagnostic information required for optimal treatment planning and follow-up. However, because of time efficiency (less slices needed), the coronal plane is most often acquired and displayed in whole-body MRI, in particular when STIR and T1-weighted

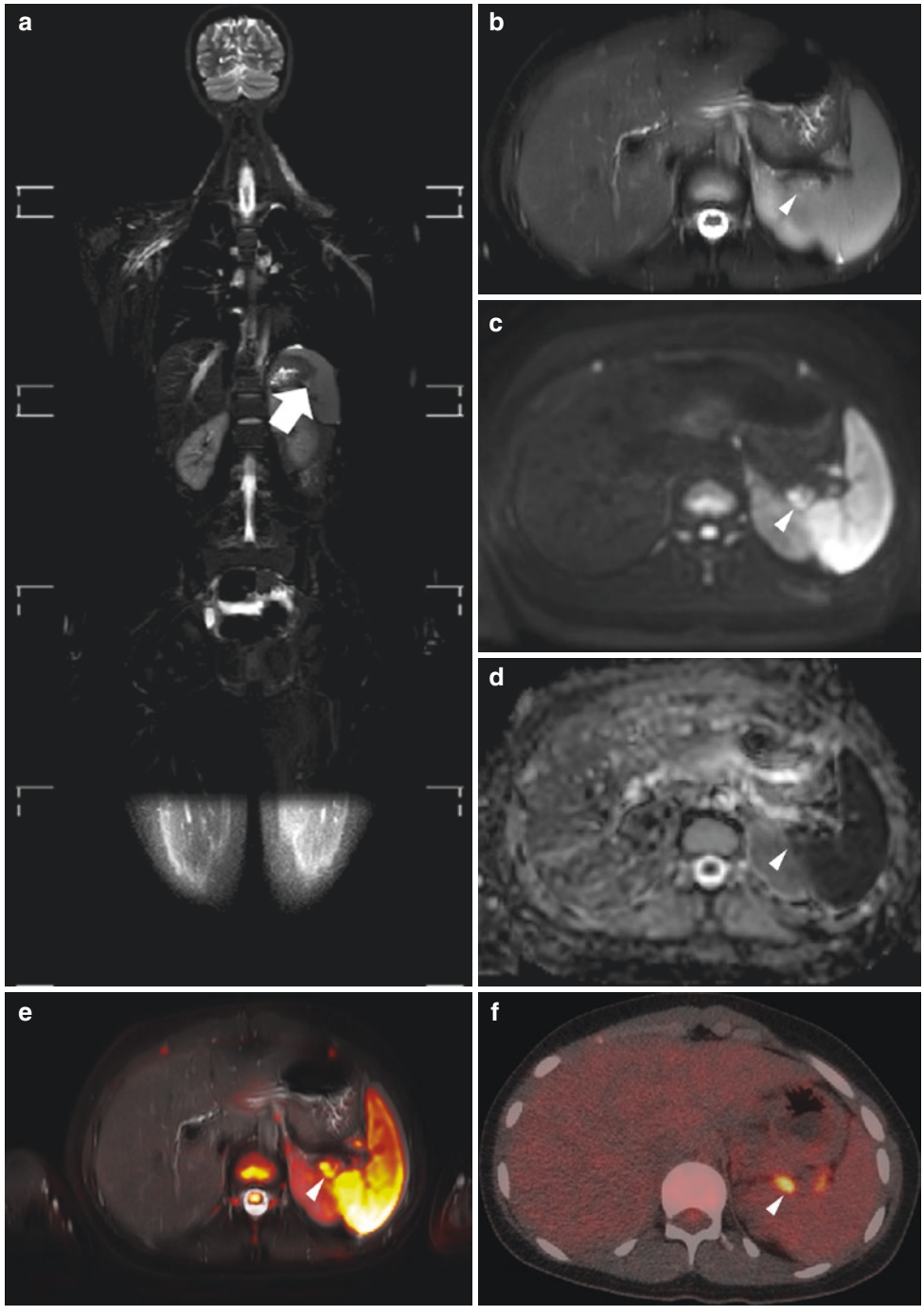

Fig. 7.5 Coronal whole-body short tau inversion recovery (STIR) (**a**), axial T2 spectral attenuated inversion recovery (SPAIR) (**b**), diffusion-weighted b800 (**c**), apparent diffusion coefficient (ADC) (**d**), and fused T2 SPAIR/DWI b800 images (**e**) in a 14-year-old girl with a stage III Hodgkin lymphoma, nicely illustrating the potential role of fusion of DWI/ADC images with other standard anatomic MRI sequences to further improve lesion localization. An additional pathologic lymph node region was detected in the splenic hilum, best appreciated on the fused T2 SPAIR/DWI b800 image (white arrow in **a**, white arrowhead in **b**–**e**). The corresponding PET/CT slice (**f**) shows increased tracer uptake in the same lymph node region suspicious of disease involvement (white arrowhead)

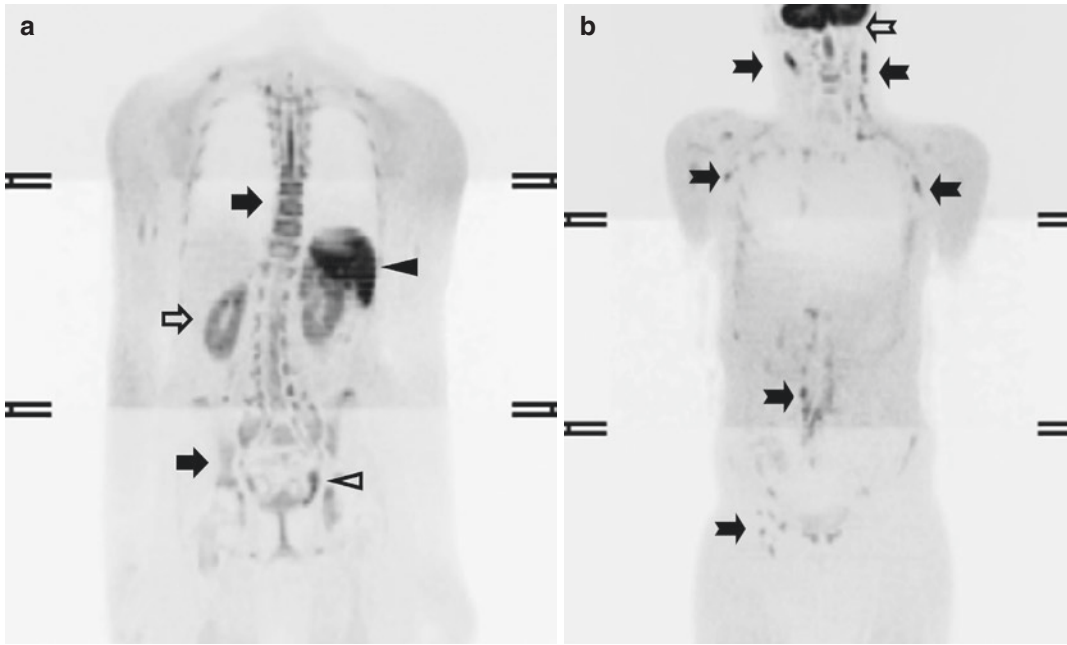

Fig. 7.6 Coronal maximum intensity projection gray-scale inverted diffusion-weighted whole-body MRI images of a 9-year-old girl who underwent a whole-body MRI for the follow-up of a lymphatic malformation (not shown). The images nicely illustrate the normal diffusion restriction seen in (**a**) bone marrow (black arrows), kidneys (open arrow), spleen (black arrowhead), left ovary (open arrowhead), and (**b**) the brain and spinal cord (squared open arrow) as well as normal lymph nodes (squared black arrows)

FSE sequences are used. The 3D contrast-enhanced T1-weighted GRE and DWIBS sequences are usually acquired in the axial plane, but the obtained images can be easily post-processed for multiplanar reconstruction (MPR) and maximum intensity projection (MIP). In addition, it has been shown that the axial plane is more sensitive, especially for lesions in the ribs, scapula, and skull/brain [4–6, 18, 44]. If there is a specific interest in disease involvement of the spine, a complementary sagittal plane is recommended because of its physiological curves [19]. Finally, a small overlap of 3–5 cm between adjacent stations during multi-station imaging is often indicated to compensate for signal loss at the periphery of each station and facilitate seamless whole-body reconstruction.

7.2.3 Reduction of Motion Artifacts

Several methods have been developed to reduce or correct for motion artifacts, each suitable for some tasks, but not for others. The methods for reduction of motion artifacts can roughly be divided into three groups: motion prevention (e.g., feed and wrap, training, breath hold, and sedation), artifact reduction (e.g., faster imaging, triggering, and gating), and motion correction (e.g., navigators, PROPELLER technique, retrospective correction) [45]. The PROPELLER (periodically rotated overlapping parallel lines with enhanced reconstruction) technique provides substantially reduced motion sensitivity due to strong oversampling of the k-space center. This technique collects data in concentric rectangular blades that rotate around the *k*-space center, which (a) allows for correction of spatial inconsistencies, (b) allows rejection of data based on a correlation measure indicating through-plane motion, and (c) further decreases motion artifacts through an averaging effect for low spatial frequencies. The PROPELLER imaging method is used by all major vendors (e.g., MultiVane (Philips), BLADE (Siemens), and PROPELLER (GE)). Imaging of the thorax and upper abdomen is usually obtained using respiratory compensation techniques,

whereas antiperistaltic agents can be considered if the abdomen is the site or predisposed area of the known or suspected malignancy. In children, we prefer the use of hyoscine butylbromide (scopolamine butylbromide; Buscopan™; not available in the USA) since the administration of glucagon is often associated with symptoms of nausea and vomiting and most contraindications for hyoscine butylbromide are rare in childhood.

7.2.4 Patient Preparation

As whole-body MRI scans are usually lengthy with anticipated examination times of 40–60 min, adequate patient preparation is essential to minimize movement and anxiety. Children should be warned that the scan could be noisy owing to the sequences used and vibrations of the MRI bed. The application of multiple surface coils to cover the whole body might provoke anxiety, and by leaving the head coil off (if not essential), patient tolerance can be improved. Furthermore, one or both parents should be asked to stay with their child in the MRI room, and listening to their own music or viewing a film can help to further reduce anxiety. The child should be offered the opportunity for bladder emptying before the examination to minimize discomfort during the scan. As with most lengthy MRI scans, children under the age of 6 years usually require sedation or general anesthesia.

In Tables 7.1 and 7.2, examples are given of two different whole-body MRI protocols for pediatric oncological indications used in the

Table 7.1 Whole-body MRI protocol—lymphoma (1.5 T, Ingenia, Philips Healthcare, Best, The Netherlands)

Parameter	Pulse sequence			
	T1-weighted TSE	STIR	DWI-STIR	T2-weighted SPAIR
Repetition time (ms)	583	5231	8046	1250
Echo time (ms)	18	65	67	80
Inversion time (ms)	–	165	180	–
Receiver bandwidth (Hz)	465.9	502.7	57.3	647.0
Slice orientation	Coronal	Coronal	Axial	Axial
Slice thickness (mm)	6.0	6.0	4.0	6.0
Slice gap (mm)	1.0	1.0	0	0.7
No. of slices per station	30	30	60	36
Cranio-caudal coverage per station	265	265	240	240
Field of view (mm^2)	530 × 265	530 × 265	450 × 365.625	450 × 366.4286
Acquisition matrix	208 × 287	336 × 133	128 × 82	280 × 202
b-values (s/mm^2)	–	–	0, 100, 800	–
No. of signal averaged	1	1	1	1
Echo-planar imaging factor	–	–	41	–
Respiratory motion compensation technique	Breath hold in thorax and abdomen	Breath hold in thorax and abdomen	Free breathing	Free breathing
Acquired voxel size (mm^3)	1.27 × 1.85 × 6.00	1.58 × 1.98 × 6.00	3.52 × 4.46 × 4.00	1.61 × 1.81 × 6.00
Reconstructed voxel size (mm^3)	1.04 × 1.04 × 6.00	1.04 × 1.04 × 6.00	2.01 × 1.99 × 4.00	0.94 × 0.93 × 6.00
Effective scan time per station	54 s	1 min 45 s	4 min	45 s
Total number of stations	5	5	4	4
Total effective scan time	4 min 30 s	8 min 45 s	16 min	3 min

Table 7.2 Whole-body MRI protocol—neuroblastoma (1.5 T, Ingenia, Philips Healthcare, Best, The Netherlands)

Parameter	Pulse sequence					
	3D T2W TSE	T1 THRIVE	DWI	T1 TSE (spine)	STIR (spine)	T1 THRIVE Gd
Repetition time (ms)	454	5.5	1341	550	2000	5.5
Echo time (ms)	90	2.7	73	8.0	60	2.7
Inversion time (ms)	–	–	–	–	180	–
Receiver bandwidth (Hz)	570.1	309.6	47.9	206.1	383.0	309.6
Slice orientation	Coronal	Axial	Axial	Sagittal	Sagittal	Axial
Slice thickness (mm)			4.0	3.0	3.0	
Slice gap (mm)	0		0	0.3	0.3	
No. of slices per station	139	85	26	15	15	85
Cranio-caudal coverage per station	400	127.5	130	449.1228	448	127.5
Field of view (mm^2)	400 × 354.023	250 × 189.2759	250 × 250	449.1228 × 160	448 × 160	250 × 189.2759
Acquisition matrix	348 × 308	232 × 185	88 × 70	228 × 494	160 × 381	232 × 185
b-values (s/mm^2)	–	–	0, 100, 1000	–	–	–
No. of signal averaged	1	4	1	2	2	4
Echo-planar imaging factor	–	–	35	–	–	–
Respiratory motion compensation technique	Respiratory triggered	Free breathing	Respiratory triggered	Free breathing	Free breathing	Free breathing
Acquired voxel size (mm^3)	1.15 × 1.15 × 1.15	1.08 × 1.07 × 3.00	2.84 × 3.57 × 5.00	0.70 × 0.91 × 3.00	1.00 × 1.17 × 3.00	1.08 × 1.07 × 3.00
Reconstructed voxel size (mm^3)	0.83 × 0.83 × 1.15	0.74 × 0.74 × 1.50	1.74 × 1.74 × 5.00	0.47 × 0.47 × 3.00	0.70 × 0.70 × 3.00	0.74 × 0.74 × 1.50
Effective scan time per station	4 min 09 s	2 min	1 min 48 s	5 min 10 s	4 min	2 min
Total number of stations	1	3	3	1	1	3
Total effective scan time	4 min 09 s	6 min	5 min 24 s	5 min 10 s	4 min	6 min

University Medical Center Utrecht, the Netherlands.

7.3 Current Applications

7.3.1 Bone Marrow Imaging

MRI is a sensitive method for assessing bone marrow, although it lacks specificity, especially in younger children. Normal bone marrow is composed of a combination of yellow (fatty) marrow and red (hematopoietic) marrow that together contribute to the signal seen in MRI. In children the distribution of red marrow and its cellular content varies with age. At birth, the bone marrow is entirely hematopoietic and then shortly after birth starts to become replaced by yellow marrow in an orderly and predictable sequence (Fig. 7.7) [46–48]. This transition from red to yellow marrow begins in the peripheral bones and progresses in a symmetrical manner to the central skeleton. Within the individual long bones, the marrow conversion occurs first in the diaphysis and then progresses to the metaphysis. The vertebral marrow remains predominantly hematopoietic during the first decade of life except for some yellow bone marrow around the central vertebral vein [49]. Good knowledge of this physiological marrow conversion as a function of age is required to be able to distinguish the areas of normal hematopoiesis from bone lesions.

On MRI, malignant infiltration of the bone marrow usually presents with low T1 and high T2 signal due to the combination of free water and edema in addition to replacement of the fatty content of normal marrow by malignant cells (Fig. 7.8) [33]. In children, the malignant bone marrow infiltration may be focal, such as in lymphoma (Figs. 7.3 and 7.9), but is often diffuse, e.g., in neuroblastomas and leukemias (Fig. 7.12) [18, 48, 50]. Especially in young patients it can be challenging to detect bone marrow disease, because the high cellularity of the normal red marrow can be misdiagnosed as diffuse bone marrow infiltration or mask tumor deposits, in particular on T1-weighted sequences. In these cases, the STIR sequence can be of use as the high signal intensity of the normal red marrow is frequently less distinct than that of malignant infiltration. On the other hand, it can be helpful to compare the signal intensity of the bone marrow

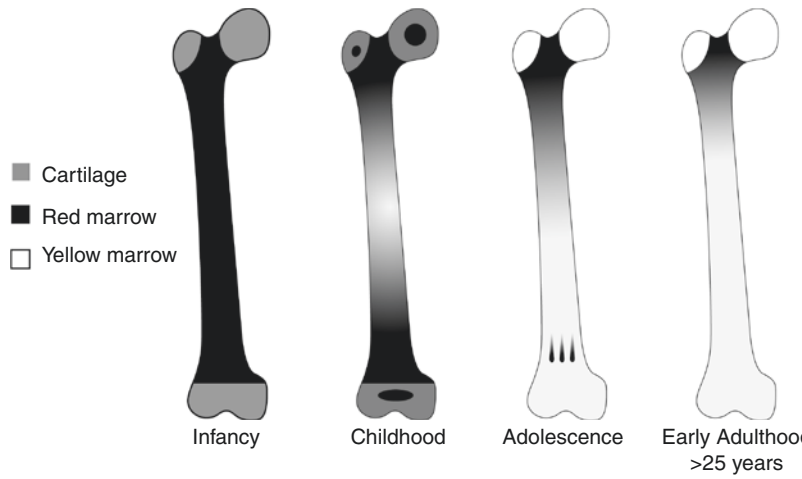

Fig. 7.7 Normal age-related bone marrow conversion within the long bone. Red to yellow marrow conversion occurs in a predictable manner throughout childhood and adolescence. The adult marrow pattern is reached around 25 years of age, characterized by red marrow confined to the axial skeleton and proximal femora and humeri. During infancy there is hematopoietic marrow (red marrow) throughout the long bones. The secondary ossification centers quickly convert from red to yellow marrow. In childhood, the marrow conversion starts in the center of the long bones and progresses proximally and distally toward the metaphysis

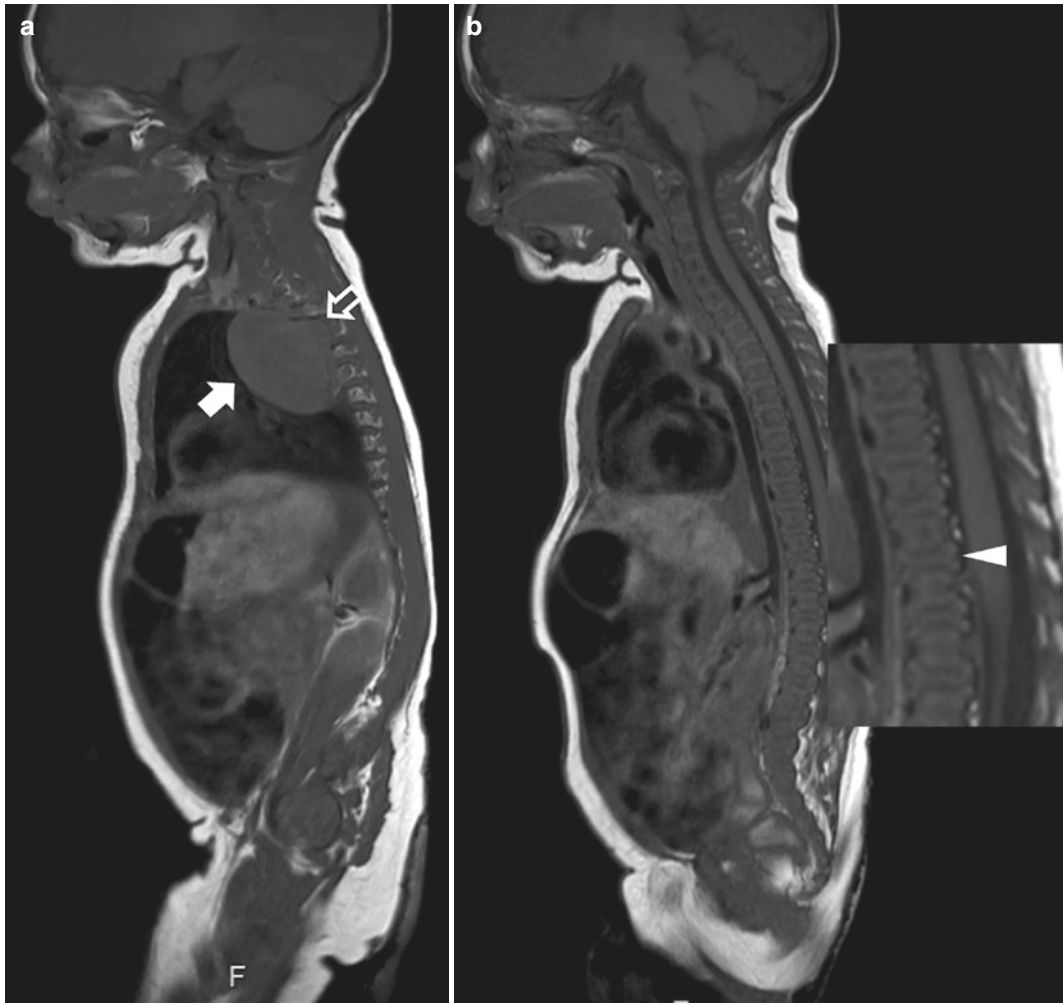

Fig. 7.8 3-month-old boy presenting with inspiratory stridor due to thoracic tumor (**a**; white arrow) located in the posterior mediastinum with extension in the neuroforamen Th3–Th4 (open arrow). With ultrasound-guided biopsy, a neuroblastoma, standard risk was diagnosed. The bone marrow biopsy appeared normal. At presentation diffuse low T1 signal of the bone marrow is seen, isointense compared to the intervertebral disc (**b** with zoomed insets; white arrowhead indicating the intervertebral disc) and muscles consistent with red bone marrow. Furthermore, the signal intensity of the bone marrow at the sagittal STIR is within normal limits (**c**). With watchful waiting spontaneous regression of the tumor was observed (**d**; white arrow) and no treatment was necessary. After 6 months, there is a marked decrease in size of the tumor (**d**; white arrow) with increased T1 signal intensity related to internal calcifications. Furthermore, the bone marrow signal showed an increase in signal intensity (**e** with zoomed insets), especially centrally within the vertebral body consistent with areas of fatty bone marrow. The signal intensity at the sagittal STIR of the spine is within normal limits (**f**)

on T1-weighted sequences with adjacent muscles or vertebral disc. Generally, after 1 year of age, the signal intensity of bone marrow should be iso- or hyperintense relative to the intervertebral disc or muscles. One should be cautious when evaluating bone marrow involvement during or after chemotherapy, as the post-therapeutic signal changes seen may be difficult to distinguish from active malignant bone lesions [46]. In addition, anemic or treatment-related medullary hyperplasia can obscure malignant infiltration. Finally, heterogeneous sharply demarcated linear areas or focal islands of red marrow can be encountered as normal variants in children [46, 51].

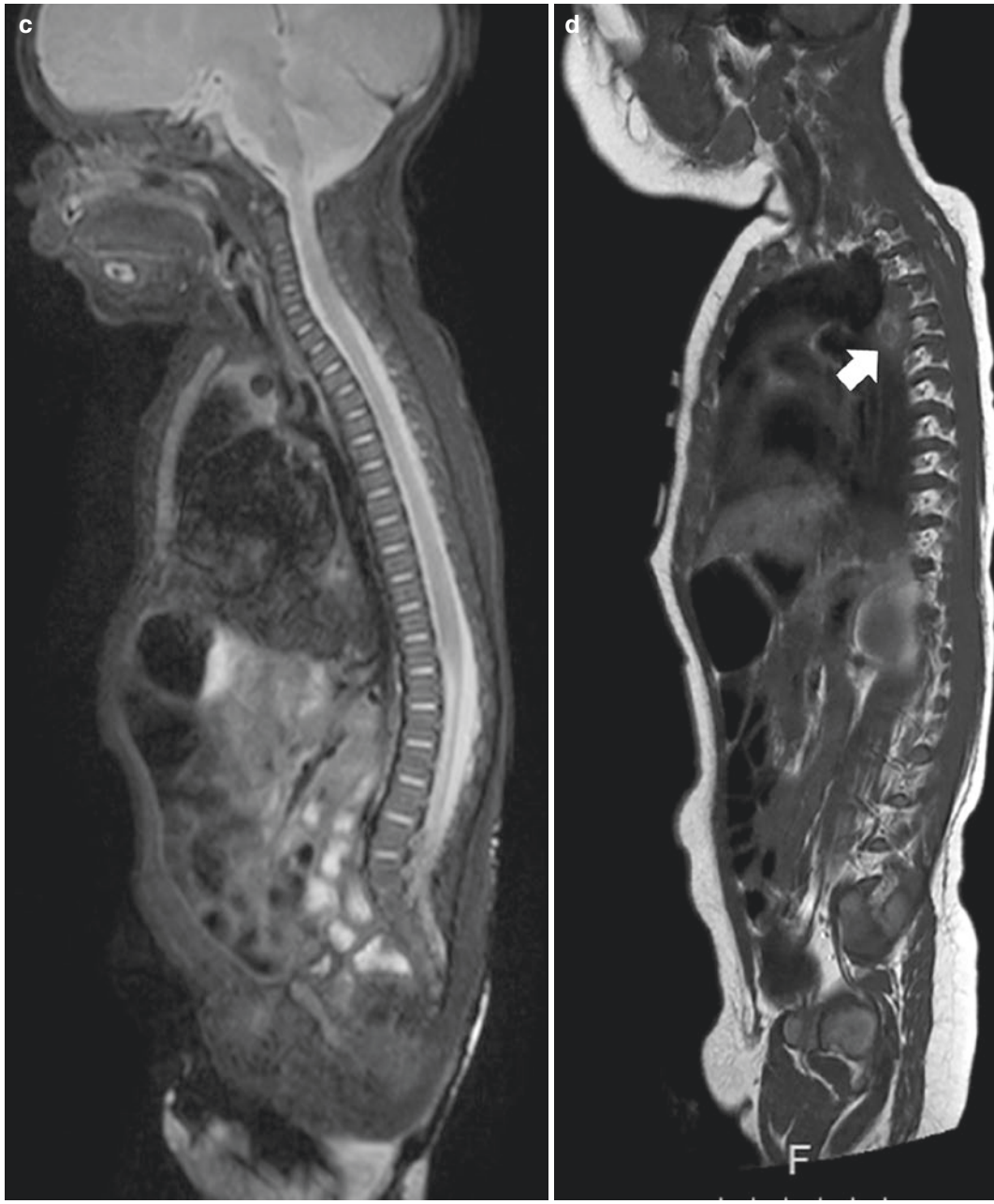

Fig. 7.8 (continued)

Although DWI is widely used for the assessment of bone marrow disease, it is of limited value due to the high cellular hematopoietic marrow that will exhibit impeded diffusion. This is especially true for young children. Ording-Müller et al. demonstrated that areas of restricted diffusion in the pelvic skeleton and lumbar spine are a normal finding in 48% of healthy children [52]. Therefore, DWI should not be used in isolation but in conjunction with T1- and T2-weighted images. Another technique that has been proposed as a complementary tool for the assessment of bone marrow disease in adults is chemical shift imaging (opposed-phase imaging) [53]. In

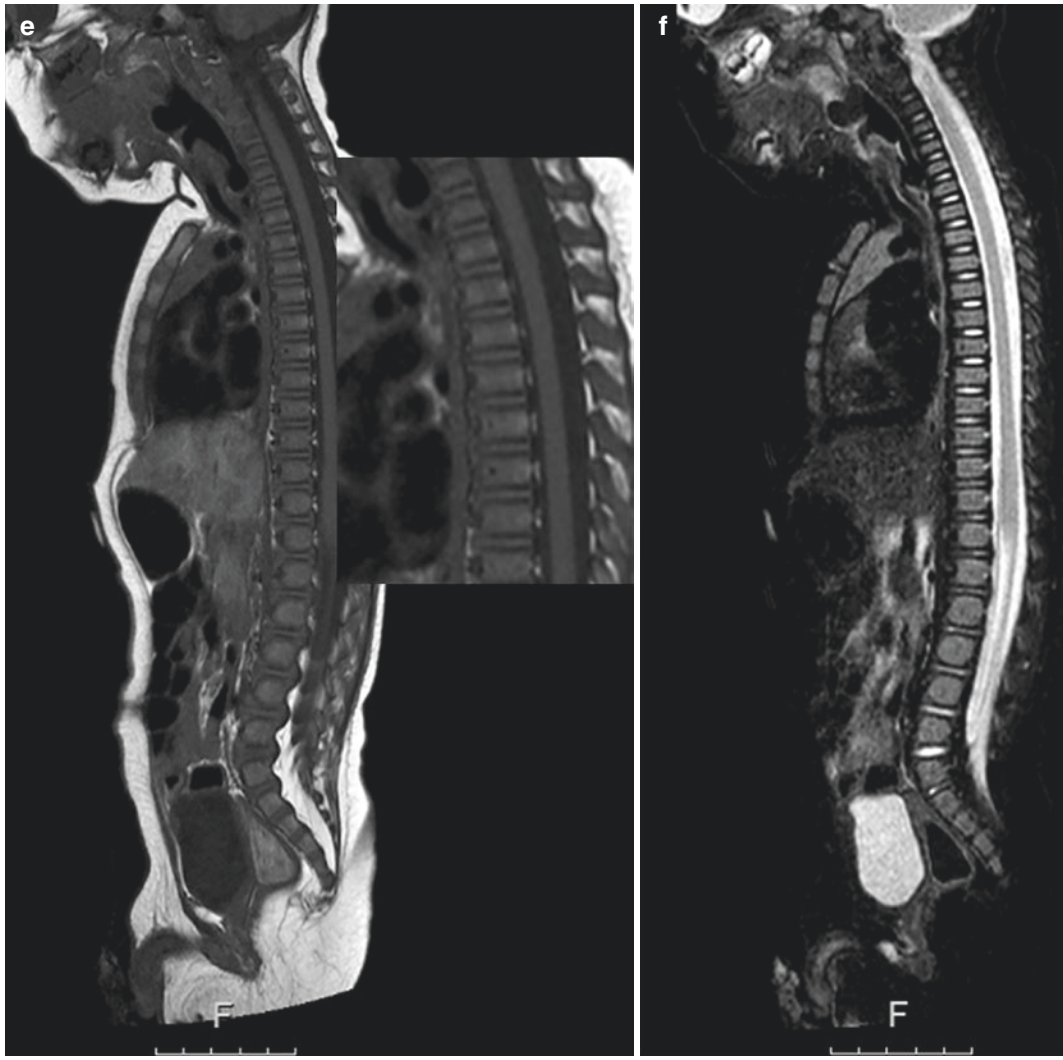

Fig. 7.8 (continued)

chemical shift imaging, the differentiation of malignant bone marrow infiltration from normal red marrow is based on the detection of small quantities of fat.

Meyer et al. tried to identify the best MRI sequence or imaging criteria for the diagnosis of bone marrow metastases in children with neuroblastoma [54]. They found that homogeneous low T1 signal had the highest sensitivity (88%), whereas a heterogeneous pattern on the post-gadolinium was highly specific (97%) but relatively insensitive (65%) for detecting metastasis.

7.3.2 Malignant Lymphoma

A pediatric malignancy for which whole-body MRI has been widely used already for many years is lymphoma. It is the third most common malignancy in children and includes Hodgkin lymphoma (HL) and non-Hodgkin lymphoma (NHL) [55]. NHL is most frequent in children younger than 15 years, whereas HL is predominantly diagnosed in teenagers. Pediatric lymphomas are staged using the modified Ann Arbor (Lugano) and Murphy classifications for HL and NHL, respectively [56, 57]. Recently, a new

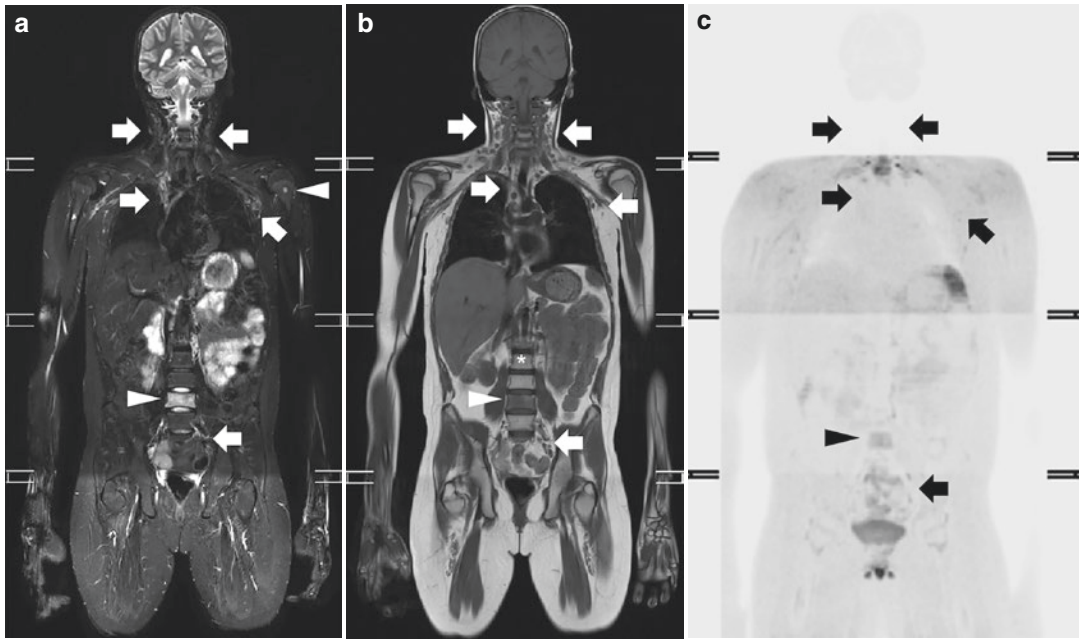

Fig. 7.9 Coronal whole-body short tau inversion recovery (STIR) (**a**), T1-weighted (**b**) and maximum intensity projection grayscale inverted diffusion-weighted (**c**) whole-body MRI images in the same patient as Fig. 7.3 after two cycles of chemotherapy. Almost all initially involved lymph node stations (cervical, axillary, mediastinal, para-aortic, para-iliac) are normalized in size (white arrows in **a** and **b**), and their restricted diffusion disappeared (black arrows in **c**). Several bone marrow localizations still show abnormal signal intensity on both the STIR and T1-weighted images (white arrowheads in **a** and **b**) as well as signs of diffusion restriction (black arrowhead in **c**). Bone marrow reconversion, as seen in Fig. 7.3, has disappeared as the signal intensity of the noninvolved vertebral bodies has returned to that of normal fatty marrow (asterisk in **b**)

revised International Pediatric Non-Hodgkin Lymphoma Staging System (IPNHLSS) has been developed incorporating new histologic entities, extranodal dissemination, improved diagnostic methods, and advanced imaging technology [58]. Accurate assessment of disease extent at diagnosis and response to treatment are essential to optimize therapy and prevent disease relapse while minimizing late therapy-related side effects.

Current guidelines encourage the use of FDG-PET/CT in staging and response assessment of FDG-avid lymphomas [56]. As both PET and CT involve substantial radiation exposure and children often undergo several PET/CT examinations during the course of treatment, there is an increasing interest in the use of whole-body MRI as a good radiation-free alternative for staging and follow-up. Several studies have shown that whole-body MRI is feasible in children (Fig. 7.3) [14, 28, 59]. In the study by Punwani et al., a very good agreement for nodal and extranodal disease involvement between whole-body MRI compared to an FDG-PET/CT reference standard was reported, despite only using STIR for whole-body MRI [28]. Due to the clear visualization of lymphoid tissue, DWI is a potentially interesting technique for the evaluation of lymphoma. Lin et al. showed an excellent agreement between whole-body DWI and FDG-PET/CT in 15 adult patients with diffuse large B-cell lymphomas [60]. Similar results have been reported by Gu et al. and Stephane et al. based on studies performed in adult patients with varying types of lymphoma [38, 61]. However, in other studies the additional value of DWI to conventional MRI sequences could not be demonstrated [59, 62]. This could be related to the fact that both benign and malignant nodes demonstrate restricted diffusion. Furthermore, there are no validated ADC values yet for discriminating involved from non-

involved sites [41]. Therefore, the determination of pathologic lymph node involvement in whole-body DWI is still mainly based on size criteria. An additional issue with DWI is that several normal extranodal structures that can be involved in lymphoma (including the brain, Waldeyer's ring, thymus, spleen, testes, ovaries, spinal cord, peripheral nerves, and bone marrow) may demonstrate restricted diffusion (Fig. 7.6). Consequently, pathology in any of these areas may be obscured.

Klenck et al. prospectively compared ferumoxytol-enhanced whole-body diffusion-weighted MRI to FDG-PET/CT in 22 children and young adults for staging lymphoma and sarcoma [20]. This ultrasmall superparamagnetic iron oxide (USPIO) contrast agent is thought to overcome the limitations of conventional whole-body MRI regarding detection of nodal, bone marrow, and splenic involvement. Ferumoxytol has been shown to discriminate normal lymphoid tissues, which take up the USPIO agent, from lymphoid malignancies, which do not. Thus the better detection of lymphomatous involvement in the reticuloendothelial system (RES) depends on the uptake of USPIO in the noninvolved reticuloendothelial system (RES) and the non-uptake by (metastatic) tumor deposits.

Assessment of response to therapy is important for determining treatment effectiveness and predicting clinical outcome. The concept of early response assessment with FDG-PET/CT in lymphoma has received considerable attention in the past few years, although it is still not officially recommended outside clinical trials [56]. In addition, the value of relying solely on interim and end-of-treatment FDG-PET/CT in predicting outcome was demonstrated to be unsatisfactory by recent meta-analyses [63, 64]. The role of whole-body MRI in response assessment in children with lymphoma is still under investigation (Fig. 7.9). Mayerhoefer et al. recently published the results of their prospective study in 64 adult lymphoma patients that showed that whole-body MRI with DWI could serve as a feasible alternative for FDG-PET/CT during follow-up and treatment response assessment [65]. Several, mostly pilot, studies compared the quantitative data from FDG-PET/CT (SUV) with DWI (ADC values) for interim response assessment with inconclusive results. They reported presence or absence of an inverse correlation between ADC and SUV [66–70].

7.3.3 Histiocytosis

Langerhans cell histiocytosis (LCH) is a rare disease with an incidence of approximately 5 cases per 1 million children under age 15 years (median age at presentation 30 months) and an equal distribution among boys and girls [71]. LCH can involve almost any organ, but the most common presentation includes skin rashes and/or painful bone lesions. Less frequently, children present with diabetes insipidus due to pituitary involvement or back pain caused by vertebra plana. Adequate staging at diagnosis is essential, first of all because the presence or absence of liver, spleen, and/or bone marrow involvement determines whether the patient belongs to the clinical "high-risk" or "low-risk" group. "High-risk" LCH patients have a more than 85% long-term survival rate, whereas the survival rate of "low-risk" LCH patients approaches 100%. Furthermore, the number and locations of lesions at diagnosis influence the choice of (chemo) therapy.

The standard approach to staging usually consists of a combination of laboratory tests and imaging [71, 72]. Traditionally, the imaging evaluation of patients with LCH includes chest radiography and a complete skeletal survey. More recently an abdominal ultrasound has been added to rule out/demonstrate intra-abdominal organ involvement. Skeletal involvement is the most common radiographic abnormality with the skull, ribs, spine (vertebra plana), pelvis, and scapula as the most common sites of involvement. In case of long bone involvement, the femora are the most commonly affected site. Extension of the primary bony lesion into the surrounding soft tissues and epidural space can be seen, especially with bone lesions in the skull, ribs, and spine. Bone scintigraphy has been used for the evaluation of LCH

with a lesion detection rate compared to the skeletal survey. However, the scintigraphic appearance of LCH may vary especially when the lesions are small or fail to incite a significant osteoblastic response [72, 73]. The use of ^{18}F-FDG-PET for the evaluation of pediatric LCH has been reported, with high sensitivity and specificity of this imaging technique that is superior to the skeletal survey and bone scintigraphy [74–76]. An advantage of ^{18}F-FDG-PET over the traditional techniques is the possibility of identifying extra-osseous localizations of LCH. Furthermore, ^{18}F-FDG-PET shows lesion response to therapy earlier than conventional radiography and CT.

Interestingly, a recent study by Mueller et al. also showed that the overall sensitivity of ^{18}F-FDG-PET was lower than whole-body MRI, especially for small bony infiltrates (mean diameter 12 mm) and central nervous system involvement [76]. As stated before, whole-body MRI is in particular well suited for the evaluation of bone marrow involvement, accompanying soft tissue masses, as well as other extra-osseous manifestations. In LCH, most bony lesions will show an intermediate to hypointense signal intensity on T1-weighted images and a hyperintense signal intensity on T2-weighted and STIR images (Fig. 7.10) [77, 78]. On post-contrast T1-weighted images, the LCH lesions usually show marked enhancement, although predominantly peripheral enhancement can be seen (Fig. 7.10e). Early-stage lesions usually show edema in the adjacent bone marrow, periosteum, and soft tissues. During treatment, healing lesions will show decrease in signal intensity on STIR imaging.

Unfortunately, large prospective studies on the diagnostic accuracy of whole-body MRI in pediatric LCH are missing. A small study in only nine children with LCH by Goo et al. compared the use of whole-body MRI to plain radiography and bone scintigraphy [77]. Additional skeletal lesions were identified by whole-body MRI in 38% of patients when compared with plain radiography and in 25% when compared with scintigraphy. Furthermore, whole-body MRI detected extra-osseous lesions in five of nine patients exclusively (56%). In a study of six children with LCH at diagnosis and during follow-up, Steinborn et al. showed that whole-body MRI also detected additional lesions in two patients when compared to the skeletal survey, which resulted in a change of therapy in both children [78]. On the other hand, Mueller et al. showed that, although whole-body MRI was more sensitive for the detection of LCH lesions when compared to ^{18}F-FDG-PET, specificity was significantly lower (sensitivity and specificity: 67% and 76% for PET vs. 81% and 47% for whole-body MRI, respectively) [76]. This lower specificity was mainly due to the detection of false-positive bone lesions by whole-body MRI. In addition, residual T2 hyperintense signal and contrast enhancement after treatment on whole-body MRI resulted in false-positive findings during follow-up. Similar findings have been described by Goo et al. in 2006 [77]. Interestingly, Mueller at al. also described that a combined analysis of ^{18}F-FDG-PET and whole-body MRI decreased the number of false-negative findings at primary staging, whereas no advantage over ^{18}F-FDG-PET alone was seen in terms of false-positive or false-negative results during follow-up [76]. In view of the limited available literature, it seems justified to conclude that the skeletal survey and skeletal scintigram can be replaced by whole-body MRI (preferably in combination with PET), although further research is needed to replicate the initial findings of Goo and Mueller in larger patient cohorts.

7.3.4 Neuroblastoma

Neuroblastoma is the most common solid extracranial tumor in children and infants, representing approximately 6% of all cases of childhood cancer [55]. The peak incidence of presentation of neuroblastoma is around 2–3 years of age, and 90% of patients are diagnosed before 6 years. It is an embryonic tumor arising from primordial neural crest cells that are the precursors of the sympathetic nervous system. The most common site of the primary tumor is within the abdomen (the adrenal medulla in 35%), but it can occur anywhere along the sympathetic chain from neck to

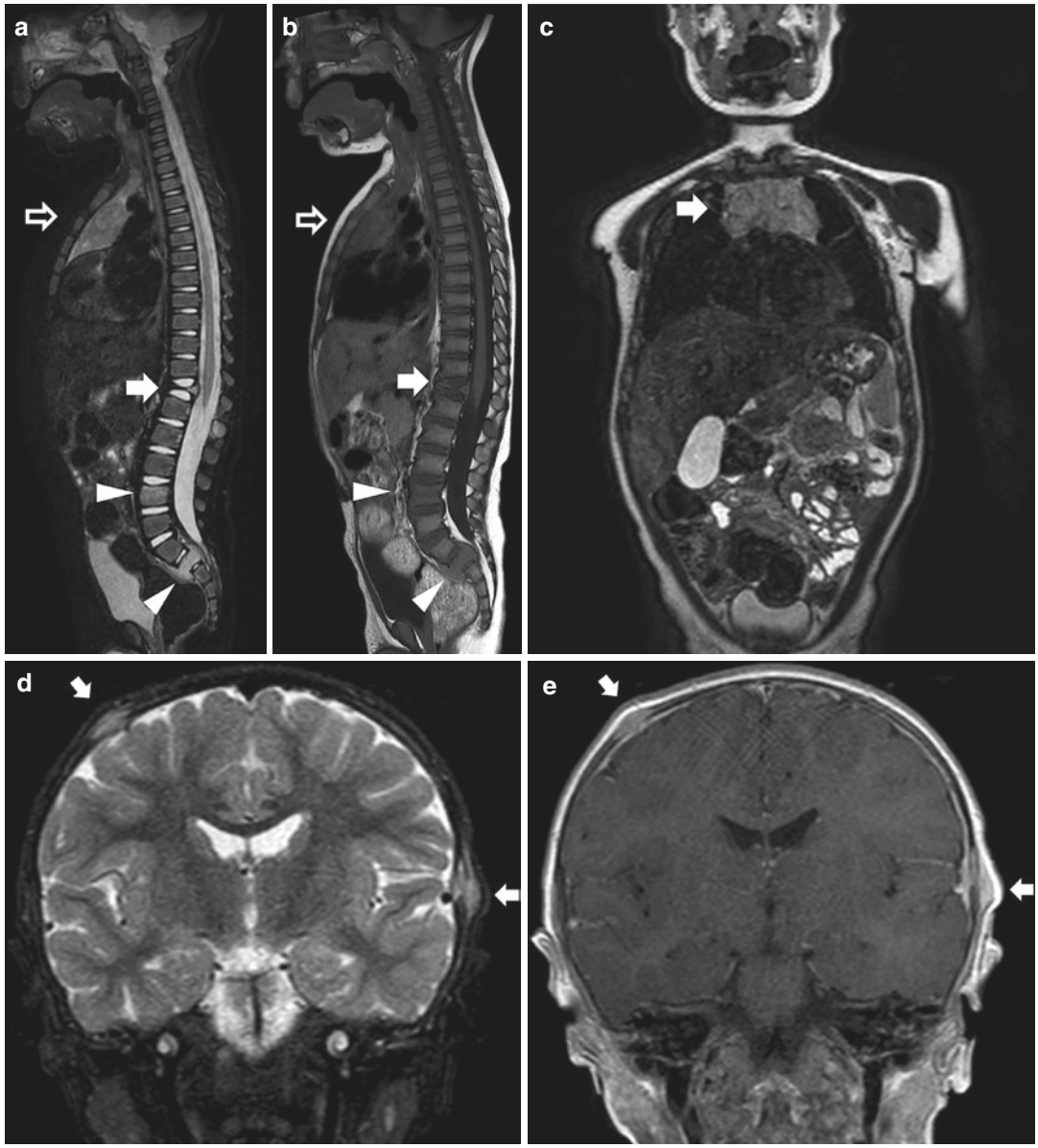

Fig. 7.10 Sagittal short tau inversion recovery (STIR) (**a**) and T1-weighted (**b**) images of the vertebral column in a 1.5-year-old boy with Langerhans cell histiocytosis (LCH), illustrating the typical vertebral plana at the level of Th12 (white arrow) as well as involvement of vertebral body L4 and S2 (white arrowheads). Furthermore, a heterogeneous enlarged thymus is present (open white arrow), suspicious of LCH involvement. Coronal 3D T2-weighted turbo spin-echo (T2-TSE) image (**c**) acquired to demonstrate/rule out intrathoracic and intra-abdominal organ involvement, once again showing the thymic involvement in LCH (white arrow). Coronal short tau inversion recovery (STIR) (**d**) and contrast-enhanced T1-weighted (**e**) images of the skull, showing two LCH lesions in the skull with epidural extension (white arrows)

pelvis [79]. Almost 70% of children with neuroblastoma will have metastatic disease at diagnosis in the bone marrow, lymph nodes, liver, and/or skin. The prognosis is variable with some tumors behaving aggressively, while others, usually in the younger age group, regress spontaneously. Overall, neuroblastoma accounts for 15% of cancer deaths in children.

In the past, staging of neuroblastoma was based on a postsurgical staging system, the International Neuroblastoma Staging System (INSS). However, in 2009, a new staging system was introduced, the International Neuroblastoma Risk Group Staging System (INRGSS), shifting focus to pre-treatment staging with identification of imaging defined risk factors (IDRF) [80, 81]. These IDRFs describe the relationship between the tumor and adjacent structures that ideally should not be injured during surgery (e.g., major vascular encasement, airway compression, nerve, plexus, or CNS infiltration). The evaluation of local and distant extent of disease at staging and during follow-up is usually based on a combination of cross-sectional imaging (either CT or MRI), I-123 MIBG scintigraphy, and bone marrow biopsy, although whole-body MRI is increasingly used for anatomic imaging instead of CT (Fig. 7.4) [79, 81, 82]. At presentation, neuroblastomas (and ganglioneuromas) usually occur as relatively hyperintense solid masses at T2-weighted imaging in the adrenal or paravertebral region from neck to pelvis (Fig. 7.11). They can be multifocal and present with areas of hemorrhage and/or necrosis, especially in case of extensive disease at diagnosis. Vascular encasement in the abdomen is common, and small calcifications are often seen, although the latter is usually difficult to appreciate on MRI. Another IDRF that is not infrequently seen in neuroblastoma is intraspinal extension of the primary tumor. Lymphadenopathy is a frequent finding at diagnosis with similar imaging appearances as the primary tumor. On DWI, neuroblastomas show diffusion restriction in the solid parts of the lesions. In addition, DWI can guide biopsy as more differentiated parts of lesions (ganglioneuroma/ganglioneuroblastoma) show relative higher ADC values [83]. Bone marrow involvement can be focal or diffuse with relatively low signal intensity on T1-weighted imaging compared to muscle or the intervertebral disc and increased signal intensity on STIR imaging (Fig. 7.12). Liver metastases usually present as T2 hyperintense lesions (Fig. 7.13).

As in many other pediatric oncological entities, the role of whole-body MRI in neuroblastoma has not yet been thoroughly evaluated. Pfluger et al. performed a retrospective study of 50 MRI and I-123 MIBG examinations in 28 patients acquired for the assessment of neuroblastoma lesions at presentation and follow-up [84]. They concluded that integrated imaging with I-123 MIBG scintigraphy and MRI increased the diagnostic accuracy. Goo et al. showed that in a group of 13 children with neuroblastoma, whole-body MRI had a higher sensitivity for detection of bone metastases than MIBG and CT (100%, 25%, and 10%, respectively) but poor positive predictive values for detection of skeletal and extraskeletal metastases in comparison with MIBG [15]. On the other hand, MIBG also has its limitations including failure to detect bone marrow involvement, lack of MIBG avidity in up to 10% of patients, loss of MIBG avidity at relapse, and suboptimal visualization of small lesions in the liver [18]. In the study by Gahr et al., the role of DWI in differentiating neuroblastoma, ganglioneuroblastoma, and ganglioneuroma was investigated in 15 patients with 16 histologically classified tumors [83]. They found that there was a significant difference in ADC between neuroblastoma and ganglioneuroblastoma/ganglioneuroma, although there was a considerable overlap between the two groups, and inter- and intraobserver variability of their applied method was not tested. Based on the above, it is suggested that a combination of nuclear medicine techniques (I-123 MIBG scintigraphy) and anatomical imaging will increase the diagnostic accuracy, both at staging and during follow-up, with whole-body MRI increasingly being preferred over CT.

7.3.5 Other Tumors

There is an increasing use of whole-body MRI for the staging (and follow-up) of other pediatric malignancies such as Ewing sarcoma, osteosarcoma, and rhabdomyosarcoma (Fig. 7.14) [17, 20, 27, 32, 85, 86]. Most studies focus on the detection of metastatic bone disease, with comparable or often increased sensitivity when compared to traditional imaging techniques. As the bony metastases can be seen anywhere in the skeleton, even the hands and feet, it is suggested that whole-body MRI should include the

Fig. 7.11 Whole-body MRI in a 3-year-old boy diagnosed with stage IV neuroblastoma (same patient as Fig. 7.4). Coronal 3D T2-weighted turbo spin-echo (T2-TSE) image (**a**) with sagittal reconstruction (**b**) demonstrates the primary tumor arising from the left adrenal gland with retroperitoneal extension (white arrows in **a**), vascular encasement (arrowheads in **a** and **b**), and lifting of the aorta (open arrow in **b**). The contrast-enhanced T1-weighted image (**c**) illustrates heterogeneous enhancement of the retroperitoneal tumor (white arrows) and the inferior mediastinal extension (white arrowhead). There is diffusion restriction seen as high signal at the b1000 image (**d**) with corresponding low signal at the ADC map (**e**)

entire body from vertex to toe. The main limitation of whole-body MRI in the context of staging is still its limited ability to detect small pulmonary nodules, although there is some recent literature on the detection of small pulmonary nodules of ≥4 mm in size, in particular when using ultrashort echo time MRI sequences [87, 88].

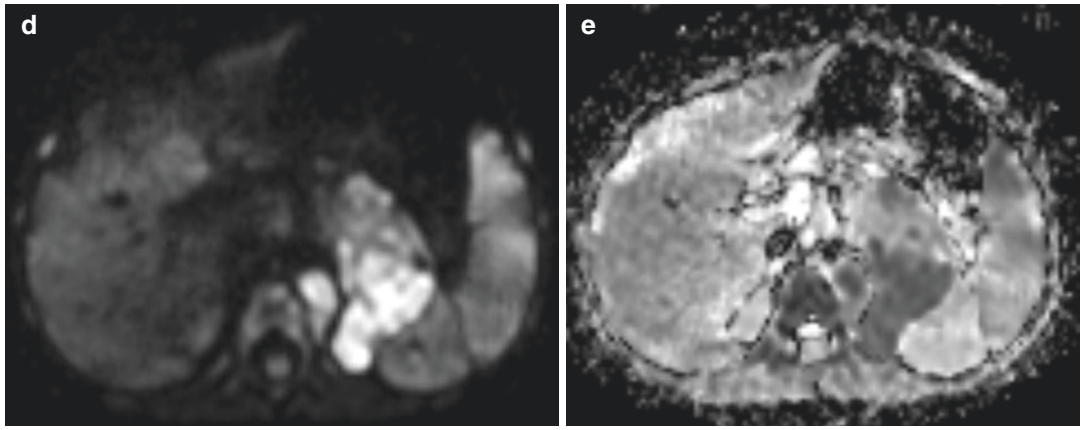

Fig. 7.11 (continued)

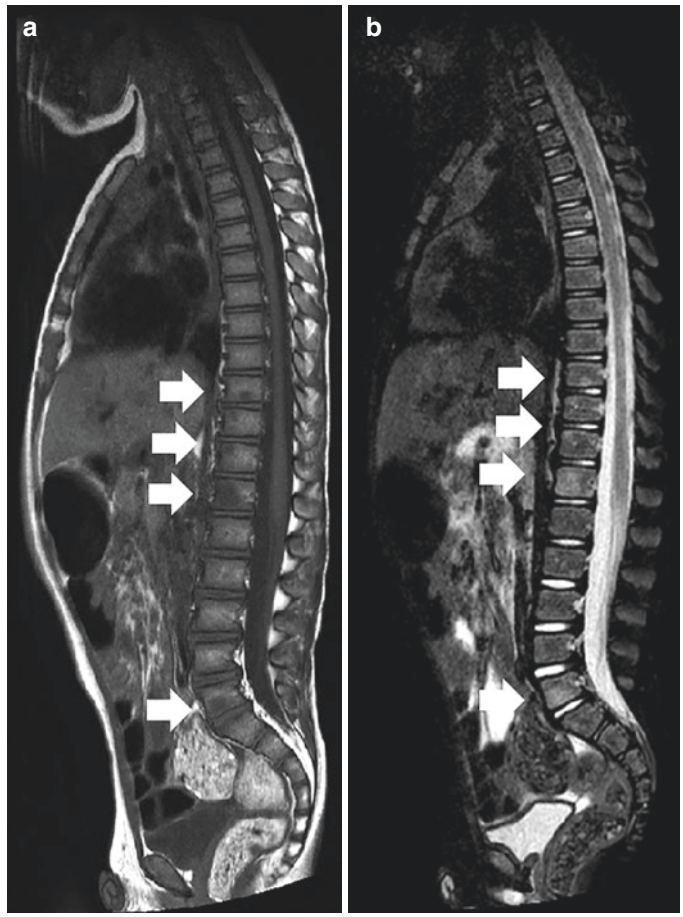

Fig. 7.12 Sagittal T1-weighted (**a**) and short tau inversion recovery (STIR) (**b**) in the same patient as Fig. 7.11, illustrating the bone marrow metastases in several thoracic and lumbar vertebral bodies (white arrows)

Several studies have investigated the role of whole-body MRI in patients with neurofibromatosis I (NF-1), as these patients have an increased risk of developing malignant peripheral nerve sheath tumors (MPNSTs) [89–91]. Both Mautner et al. and Nguyen et al. found a strong association

Fig. 7.13 Coronal whole-body 3D T2-weighted turbo spin-echo (T2-TSE) image in a 6-month-old boy diagnosed with a stage IVs neuroblastoma, illustrating the diffuse involvement of the liver (white arrows) as well as the retroperitoneal primary tumor mass (white arrowhead) which did arise from the left adrenal gland

between the benign whole-body tumor volume and the occurrence of MPNSTs in NF-1 patients younger than 30 years [89, 91]. Furthermore, MRI features like rapid growth, intratumoral lobulation, ill-defined margins, and irregular enhancement on post-contrast images can help to differentiate benign from malignant nerve sheath tumors. However, in the study by Derlin et al. evaluating the accuracy of whole-body MRI and ^{18}F-FDG PET/CT for detection of MPNSTs in 31 people with NF-1, PET/CT had a sensitivity of 100%, whereas whole-body MRI had a sensitivity of 66.7% for identifying malignant tumors [90]. From these studies, it can be concluded that whole-body MRI cannot replace FDG PET/CT for the detection of MPNSTs in this patient population but that the combination of PET and MRI might improve the diagnostic accuracy thereby diminishing the need for unnecessary biopsies or closer clinical follow-up.

7.3.6 Cancer Predisposition Syndromes

Whole-body MRI is a promising imaging tool for cancer surveillance and evaluation of genetic cancer predisposition syndromes (CPS), especially because of its lack of ionizing radiation [6, 92–96]. Children with CPS (including NF-1, Beckwith-Wiedemann, multiple endocrine neoplasia, Li-Fraumeni, von Hippel-Lindau, DICER1 syndrome, and rhabdoid tumor syndrome) are at a significantly increased risk of developing cancer. Whole-body screening on a regular basis is usually recommended in these children as it is difficult to predict in which organs tumors will develop. The frequency of imaging in this population depends on the specific syndrome and risk stratification. Although several publications have presented guidelines for the use of whole-body MRI as a screening method in CPS, studies on the performance of this technique in children are scarce. Friedman et al. retrospectively investigated the role of whole-body MRI as a screening tool in the follow-up of children and adolescents with hereditary retinoblastoma [92]. Whole-body MRI detected suspicious lesions in 5 of 25 patients during follow-up of which only two appeared to be malignant (osteosarcoma). One additional patient in this study was diagnosed with osteosarcoma 3 months after a normal MRI. They calculated that the sensitivity of whole-body MRI to detect subsequent malignant lesions in this specific patient group was 66.7% and the specificity 92.1%.

In another study by Jasperson et al., the role of screening whole-body MRI in a patient population with succinate dehydrogenase (SDH) mutation was investigated because of the increased risk of developing paragangliomas and pheochromocytomas related to this muta-

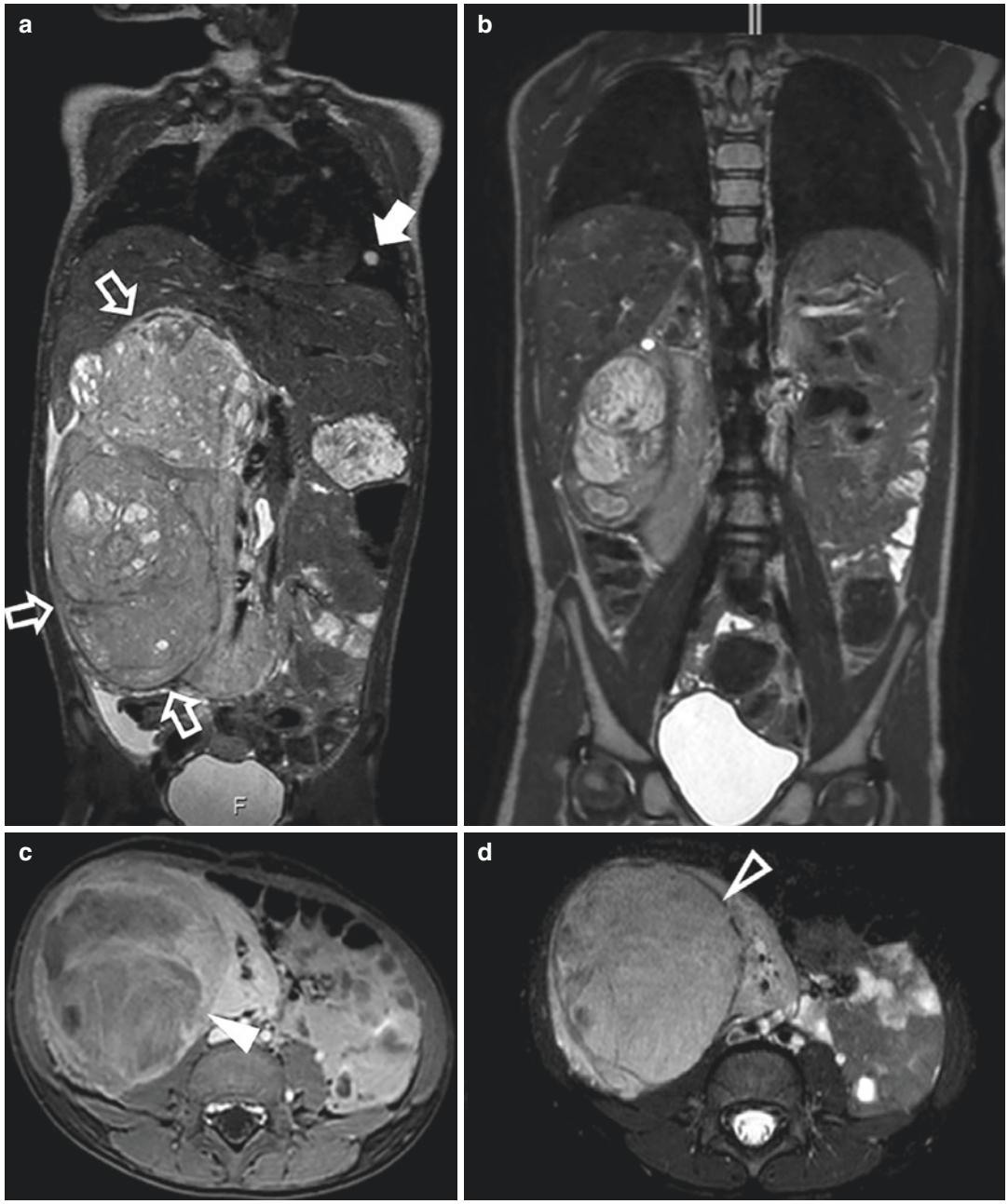

Fig. 7.14 A 3-year-old girl presenting with abdominal complaints was diagnosed with nephroblastoma stage IV, intermediate risk. Coronal 3D T2-weighted image shows a large tumor arising from the right kidney with few cystic areas (**a**; open arrows). Several metastases in the lungs are seen (**a**; white arrow). There is shrinkage of the tumor after preoperative treatment (**b**). The axial fat-suppressed T1-weighted image (**c**) after intravenous contrast shows a claw sign (arrowheads) indicating this lesion is arising from and not compressing upon the renal parenchyma. Axial T2-weighted image (**d**) shows the low T2 signal pseudo capsule (open arrowhead)

tion [93]. They evaluated 37 SDH mutation carriers as young as 10 years of age during a 4-year follow-up period using annual biochemical testing as well as biennial whole-body MRI including non-contrast axial and coronal half-Fourier acquisition single-shot fast spin-echo (HASTE) sequences performed with a 5-mm slice thickness from the skull base to pelvis. A total of six tumors were detected in this cohort, one by biochemical testing and five by whole-body MRI, the latter of which were negative by biochemical testing. In this study, the sensitivity of whole-body MRI was 87.5%, and the specificity was 94.7%, while the sensitivity of biochemical testing was 37.5% and the specificity was 94.9%.

Finally, in a recent retrospective study by Anupindi et al., which included 50 WB-MRI examinations in 24 children with genetic CPS, they found that whole-body MRI is a valuable screening tool with a high sensitivity of 100% (95% CI, 6–100%), specificity of 94% (82–98%), and negative predictive value of 94% (90–100%) [94]. Suspicious lesions were detected in 9 out of 50 whole-body MRI examinations, including two high-risk, two moderate-risk, and five low-risk lesions. However, of the four high- to moderate-risk lesions, only one lesion appeared to be malignant resulting in a positive predictive value of only 25% (95% CI, 1–78%). The other lesions and all low-risk lesions had a benign origin. Of interest, this study also showed that incidental findings were detected in 23 of 24 patients, most of which did not require imaging follow-up. All abnormalities were best detected on the fluid-sensitive STIR images. Based on their results, Anupindi et al. recommend that interpretation of these studies should be reserved to radiologists who are familiar with whole-body MRI to appropriately risk stratify abnormalities and minimize unnecessary interventions. None of the studies cited investigated the role of DWI as a screening technique. Based on the above, it can be concluded that, although whole-body MRI can be regarded as a valuable screening tool, larger cohort studies are needed to validate its role and cost-effectiveness in this specific group of patients.

7.4 Future Perspectives

As illustrated in this chapter, whole-body MRI is already widely used in pediatric oncology for diagnosis and follow-up, despite the fact that validation through large prospective cohort studies is still lacking. Although there are obvious technical advantages of whole-body MRI over other imaging modalities (including its high spatial resolution, excellent soft tissue contrast, and ability to acquire functional information), the main reason for this is our primary incentive to reduce radiation dose to children as much as possible.

Nevertheless, there is a strong need for large prospective cohort studies to better validate the role and cost-effectiveness of whole-body MRI in children with cancer, both for diagnosis and therapy response assessment and post-treatment surveillance. These studies should focus on further optimization of anatomic sequences (including reduction of scan duration), as well as on the introduction and validation of functional techniques such as DWI (including quantitative ADC measurements). In addition to the potential additional role of DWI in increasing sensitivity and establishing the extent of disease during staging, DWI could be of special interest in assessing response to treatment before size change can occur. Response to treatment is generally based on shrinkage of lesions. However, most often, this is a rather late marker of treatment-related changes, and sometimes volume change does not correspond to histopathological response; tumors that shrink can still contain considerable amounts of aggressive tumor cells. On the other hand, responding tumors can increase in size due to hemorrhage and necrosis or during differentiation as seen in nephroblastomas (Wilms tumor) and neuroblastomas. This increase in differentiation could be detected with an increase in ADC values [83, 97].

Other functional techniques that can play a role are dynamic contrast-enhanced MRI (DCE-MRI) and arterial spin labelling (ASL). Both techniques focus on tumor vascularization, with the major advantage of ASL over DCE-MRI that it does not need intravenous contrast material injection. In line with this, the potential role of

low *b*-value (<100 mm/s^2) perfusion fraction as a measure of tumor vascularization also needs further exploration. Magnetic resonance spectroscopy (MRS) allows for a noninvasive separation of the MRI signal from a given tissue into its different chemical components, which may further improve lesion characterization and prediction of clinical outcome. Although ASL and MRS are already established techniques in neuroradiology, their possible role in (pediatric) malignancies outside the brain has yet to be validated, in particular in a whole-body imaging setting. In this context, the recent development of integrated PET/MRI systems is very interesting, combining the superior structural imaging of whole-body MRI with the functional (molecular) information of both imaging techniques while decreasing the radiation dose. Although the first publications in children show promising results, it currently remains a technical challenge to construct and use these hybrid systems [98–100].

The major challenge will be to acquire enough data in children that will allow for definitive and statistically significant results. As most institutions will not have sufficient patient volume for this, due to the comparatively low incidence of most pediatric malignancies, an increasing international multi-institutional collaboration and establishment of multicenter clinical trials is needed [101].

7.5 Conclusion

Whole-body MRI is a very promising and already widely used imaging technique in pediatric oncology. The main reasons for this are the lack of ionizing radiation, its superior spatial resolution and soft tissue contrast, as well as its potential to noninvasively generate functional information on tumor biology. Whole-body MRI provides complementary information to the increasingly used molecular imaging techniques like PET/CT and SPECT/CT and can be a useful alternative to these techniques in patients in whom ionizing radiation is contraindicated and in regions with less availability. However, large-scale prospective cohort studies are still needed to better validate the role and cost-effectiveness of whole-body MRI in pediatric oncology.

References

1. Carty F, Shortt CP, Shelly MJ, Eustace SJ, O'Connell MJ. Whole-body imaging modalities in oncology. Semin Musculoskelet Radiol. 2010;14(1):68–85.
2. Goo HW. Regional and whole-body imaging in pediatric oncology. Pediatr Radiol. 2011;41(Suppl 1):S186–94.
3. Uslu L, Donig J, Link M, Rosenberg J, Quon A, Daldrup-Link HE. Value of 18F-FDG PET and PET/CT for evaluation of pediatric malignancies. J Nucl Med. 2015;56(2):274–86.
4. Darge K, Jaramillo D, Siegel MJ. Whole-body MRI in children: current status and future applications. Eur J Radiol. 2008;68:289–98.
5. Chavhan GB, Babyn PS. Whole body MR imaging in children: principles, technique, current applications, and future directions. Radiographics. 2011;31:1757–72.
6. Eutsler EP, Khanna G. Whole-body magnetic resonance imaging in children: technique and clinical applications. Pediatr Radiol. 2016;46:858–72.
7. Nievelstein RA, Littooij AS. Whole-body MRI in paediatric oncology. Radiol Med. 2016;121(5):442–53.
8. Smith EA, Dillman JR. Current role of body MRI in pediatric oncology. Pediatr Radiol. 2016;46(6):873–80.
9. Takahara T, Imai Y, Yamashita T, Yasuda S, Nasu S, Van Cauteren M. Diffusion weighted whole body imaging with background body signal suppression (DWIBS): technical improvement using free breathing, STIR and high resolution 3D display. Radiat Med. 2004;22(4):275–82.
10. Kwee TC, Takahara T, Vermoolen MA, Bierings MB, Mali WP, Nievelstein RA. Whole-body diffusion-weighted imaging for staging malignant lymphoma in children. Pediatr Radiol. 2010;40(10):1592–602.
11. Malayeri AA, El Khouli RH, Zaheer A, Jacobs MA, Corona-Villalobos CP, Kamel IR, Macura KJ. Principles and applications of diffusion-weighted imaging in cancer detection, staging, and treatment follow-up. Radiographics. 2011;31(6):1773–91.
12. Padhani AR, Koh DM, Collins DJ. Whole-body diffusion-weighted MR imaging in cancer: current status and research directions. Radiology. 2011;261:700–18.
13. Koh DM, Blackledge M, Padhani AR, Takahara T, Kwee TC, Leach MO, Collins DJ. Whole-body diffusion-weighted MRI: tips, tricks, and pitfalls. AJR Am J Roentgenol. 2012;199(2):252–62.
14. Kellenberger CJ, Miller SF, Khan M, Gilday DL, Weitzman S, Babyn PS. Initial experience with FSE STIR whole-body MR imaging for staging lymphoma in children. Eur Radiol. 2004;14(10):1829–41.

15. Goo HW, Choi SH, Ghim T, Moon HN, Seo JJ. Whole-body MRI of paediatric malignant tumours: comparison with conventional oncological imaging methods. Pediatr Radiol. 2005;35:766–73.
16. Ley S, Ley-Zaporozhan J, Schenk JP. Whole-body MRI in the pediatric patient. Eur J Radiol. 2009;70:442–51.
17. Siegel MJ, Acharyya S, Hoffer FA, Wyly JB, Friedmann AM, Snyder BS, et al. Whole-body MR imaging for staging of malignant tumours in pediatric patients: results of the American College of Radiology Imaging Network 6660 trial. Radiology. 2013;266:599–609.
18. Atkin KL, Ditchfield MR. The role of whole-body MRI in pediatric oncology. J Pediatr Hematol Oncol. 2014;36:342–52.
19. Canale S, Vilcot L, Ammari S, Lemery M, Bidault F, Balleyguier C, et al. Whole body MRI in paediatric oncology. Diagn Interv Imaging. 2014;95:541–50.
20. Klenck C, Gawande R, Uslu L, Khurana A, Qiu D, Quon A, et al. Ionising radiation-free whole-body MRI versus (18)F-fluorodeoxyglucose PET/CT scans for children and young adults with cancer: a prospective, non-randomised, single-centre study. Lancet Oncol. 2014;15(3):275–85.
21. Guimarães MD, Noschang J, Teixeira SR, Santos MK, Lederman HM, Tostes V, et al. Whole-body MRI in pediatric patients with cancer. Cancer Imaging. 2017;17:6–12.
22. Takahara T, Kwee TC, Kifune S, Ochiai R, Sakamoto T, Niwa T, et al. Whole-body MRI using a sliding table and repositioning surface coil approach. Eur Radiol. 2010;20:1366–73.
23. Goo HW. Whole-body MRI in children: current imaging techniques and clinical applications. Korean J Radiol. 2015;16(5):973–85.
24. Azzedine B, Kahina MB, Dimitri P, Christophe P, Alain D, Claude M. Whole-body diffusion-weighted MRI for staging lymphoma at 3.0T: comparative study with MR imaging at 1.5T. Clin Imaging. 2015;39:104–9.
25. Kellenberger CJ, Epelman M, Miller SF, Babyn PS. Fast STIR whole-body MR imaging in children. Radiographics. 2004;24:1317–30.
26. Merlini L, Carpentier M, Ferrey S, Anooshiravani M, Poletti PA, Hanquinet S. Whole-body MRI in children: would a 3D STIR sequence alone be sufficient for investigating common paediatric conditions? A comparative study. Eur J Radiol. 2017;88:155–62.
27. Mazumdar A, Siegel MJ, Narra V, Luchtman-Jones L. Whole-body fast inversion recovery MR imaging of small cell neoplasms in pediatric patients: a pilot study. AJR Am J Roentgenol. 2002;179(5):1261–6.
28. Punwani S, Taylor SA, Bainbridge A, Prakash V, Bandula S, De Vita E, et al. Pediatric and adolescent lymphoma: comparison of whole-body STIR half-Fourier RARE MR imaging with an enhanced PET/CT reference for initial staging. Radiology. 2010;255(1):182–90.
29. Costelloe CM, Madewell JE, Kundra V, Harrell RK, Bassett RL Jr, Ma J. Conspicuity of bone metastases on fast Dixon-based multisequence whole-body MRI: clinical utility per sequence. Magn Reson Imaging. 2013;31:669–75.
30. Ma J, Costelloe CM, Madewell JE, Hortobagyi GN, Green MC, Cao G, et al. Fast dixon-based multisequence and multiplanar MRI for whole-body detection of cancer metastases. J Magn Reson Imaging. 2009;29(5):1154–62.
31. Vasanawala SS, Madhuranthakam AJ, Venkatesan R, Sonik A, Lai P, Brau AC. Volumetric fat-water separated T2-weighted MRI. Pediatr Radiol. 2011;41(7):875–83.
32. Daldrup-Link HE, Franzius C, Link TM, Laukamp D, Sciuk J, Jürgens H, et al. Whole-body MR imaging for detection of bone metastases in children and young adults: comparison with skeletal scintigraphy and FDG PET. AJR Am J Roentgenol. 2001;177(1):229–36.
33. Schmidt GP, Schoenberg SO, Reiser MF, Baur-Melnyk A. Whole-body MR imaging of bone marrow. Eur J Radiol. 2005;55(1):33–40.
34. Manenti G, Cicciò C, Squillaci E, Strigari L, Calabria F, Danieli R, et al. Role of combined DWIBS/3D-CE-T1w whole-body MRI in tumor staging: comparison with PET-CT. Eur J Radiol. 2012;81(8):1917–25.
35. Kwee TC, Takahara T, Ochiai R, Nievelstein RAJ, Luijten PR. Diffusion-weighted whole-body imaging with background body signal suppression (DWIBS): features and potential applications in oncology. Eur Radiol. 2008;18:1937–52.
36. Attariwala R, Picker W. Whole body MRI: improved lesion detection and characterization with diffusion weighted techniques. J Magn Reson Imaging. 2013;38:253–68.
37. Parameswaran BK, Lau E, Ferris NJ. Recognising pitfalls in assessment of tumours by diffusion-weighted MRI: a pictorial essay. J Med Imaging Radiat Oncol. 2015;59(2):188–94.
38. Gu J, Chan T, Zhang J, Leung AYH, Kwong YL, Khong PL. Whole-body diffusion-weighted imaging: the added value to whole-body MRI at initial diagnosis of lymphoma. AJR Am J Roentgenol. 2011;197:W384–91.
39. Li B, Li Q, Nie W, Liu S. Diagnostic value of whole-body diffusion-weighted magnetic resonance imaging for detection of primary and metastatic malignancies: a meta-analysis. Eur J Radiol. 2014;83(2):338–44.
40. Toledano-Massiah S, Luciani A, Itti E, Zerbib P, Vignaud A, Belhadj K, et al. Whole-body diffusion-weighted imaging in Hodgkin lymphoma and diffuse large B-cell lymphoma. Radiographics. 2015;35:747–64.
41. Kwee TC, Takahara T, Luijten PR, Nievelstein RA. ADC measurements of lymph nodes: inter- and intra-observer reproducibility study and an overview of the literature. Eur J Radiol. 2010;75(2):215–20.

42. Vermoolen MA, Kwee TC, Nievelstein RAJ. Apparent diffusion coefficient measurements in the differentiation between benign and malignant lesions: a systematic review. Insights Imaging. 2012;3:395–409.
43. Daldrup-Link HE. Ten things you might not know about iron oxide nanoparticles. Radiology. 2017;284(3):616–29.
44. Hirsch W, Kluge R, et al. Preliminary results in whole body MRI in children - a prospective study [abstract]. Pediatr Radiol. 2005;35:S89.
45. Zaitsev M, Maclaren J, Herbst M. Motion artifacts in MRI: a complex problem with many partial solutions. J Magn Reson Imaging. 2015;42(4):887–901.
46. Burdiles A, Babyn PS. Pediatric bone marrow MR imaging. Magn Reson Imaging Clin N Am. 2009;17:391–409.
47. Murphy DT, Moynagh MR, Eustace SJ, Kavanagh EC. Bone marrow. Magn Reson Imaging Clin N Am. 2010;18:727–35.
48. Guillerman RP. Marrow: red, yellow and bad. Pediatr Radiol. 2013;43:S181–92.
49. Laor T, Jaramillo D. MR imaging insights into skeletal maturation: what is normal? Radiology. 2009;250(1):28–38.
50. Ryan SP, Weinberger E, White KS, Shaw DWW, Patterson K, Nazar-Stewart V, Miser J. MR imaging of bone marrow in children with osteosarcoma: effect of granulocyte colony-stimulating factor. AJR Am J Roentgenol. 1995;165:915–20.
51. Shabshin N, Schweitzer ME, Morrison WB, Carrino JA, Keller MS, Grissom LE. High-signal T2 changes of the bone marrow of the foot and ankle in children: red marrow or traumatic changes? Pediatr Radiol. 2006;36:670–6.
52. Ording-Müller LS, Avenarius D, Olsen OE. High signal in bone marrow at diffusion-weighted imaging with body background suppression (DWIBS) in healthy children. Pediatr Radiol. 2011;41(2):221–6.
53. Zajick DC, Morrison WB, Schweitzer ME, Parellada JA, Carrino JA. Benign and malignant processes: normal values and differentiation with chemical shift MR imaging in vertebral marrow. Radiology. 2005;237:590–6.
54. Meyer JS, Siegel MJ, Farooqui SO, Jaramillo D, Fletcher BD, Hoffer FA. Which MRI sequence of the spine best reveals bone-marrow metastases of neuroblastoma? Pediatr Radiol. 2005;35(8):778–85.
55. Siegel RL, Miller KD, Jemal A. Cancer statistics, 2015. CA Cancer J Clin. 2015;65(1):5–29.
56. Cheson BD, Fisher RI, Barrington SF, Cavalli F, Schwartz LH, Zucca E, et al. Recommendations for initial evaluation, staging, and response assessment of Hodgkin and non-Hodgkin lymphoma: the Lugano classification. J Clin Oncol. 2014;32(27):3059–68.
57. Johnson SA, Kumar A, Matasar MJ, Schöder H, Rademaker J. Imaging for staging and response assessment in lymphoma. Radiology. 2015;276(2):323–38.
58. Rosolen A, Perkins SL, Pinkerton CR, Guillerman RP, Sandlund JT, Patte C, et al. Revised international pediatric non-Hodgkin lymphoma staging system. J Clin Oncol. 2015;33(18):2112–8.
59. Littooij AS, Kwee TC, Barber I, Vermoolen MA, Enriquez G, Zsiros J, et al. Whole-body MRI for initial staging of paediatric lymphoma: prospective comparison to an FDG-PET/CT-based reference standard. Eur Radiol. 2014;24(5):1153–65.
60. Lin C, Luciani A, Itti E, El-Gnaoui T, Vignaud A, Beaussart P, et al. Whole-body diffusion-weighted magnetic resonance imaging with apparent diffusion coefficient mapping for staging patients with diffuse large B-cell lymphoma. Eur Radiol. 2010;20(8):2027–38.
61. Stéphane V, Samuel B, Vincent D, Joelle G, Remy P, Francois GG, Jean-Pierre T. Comparison of PET-CT and magnetic resonance diffusion weighted imaging with body suppression (DWIBS) for initial staging of malignant lymphomas. Eur J Radiol. 2013;82(11):2011–7.
62. Kwee TC, van Ufford HM, Beek FJ, Takahara T, Uiterwaal CS, Bierings MB, et al. Whole-body MRI, including diffusion-weighted imaging, for the initial staging of malignant lymphoma: comparison to computed tomography. Invest Radiol. 2009;44(10):683–90.
63. Sun N, Zhao J, Qiao W, Wang T. Predictive value of interim PET/CT in DLBCL treated with R-CHOP: meta-analysis. Biomed Res Int. 2015;2015:648572. https://doi.org/10.1155/2015/648572.
64. Adams HJ, Nievelstein RA, Kwee TC. Prognostic value of interim FDG-PET in Hodgkin lymphoma: systematic review and meta-analysis. Br J Haematol. 2015;170(3):356–66.
65. Mayerhoefer ME, Karanikas G, Kletter K, Prosch H, Kiesewetter B, Skrabs C, et al. Evaluation of diffusion-weighted magnetic resonance imaging for follow-up and treatment response assessment of lymphoma: results of an 18F-FDG-PET/CT-controlled prospective study in 64 patients. Clin Cancer Res. 2015;21(11):2506–13.
66. Punwani S, Prakash V, Bainbridge A, Taylor SA, Bandula S, Olsen OE, et al. Quantitative diffusion weighted MRI: a functional biomarker of nodal disease in Hodgkin lymphoma? Cancer Biomark. 2010;7(4):249–59.
67. Lin C, Itti E, Luciani A, Zegai B, Lin SJ, Kuhnowski F, et al. Whole-body diffusion-weighted imaging with apparent diffusion coefficient mapping for treatment response assessment in patients with diffuse large B-cell lymphoma: pilot study. Invest Radiol. 2011;46(5):341–9.
68. Punwani S, Taylor SA, Saad ZZ, Bainbridge A, Groves A, Daw S, et al. Diffusion-weighted MRI of lymphoma: prognostic utility and implications for PET/MRI? Eur J Nucl Med Mol Imaging. 2013;240(3):373–85.
69. Wu X, Pertovaara H, Dastidar P, Vornanen M, Paavolainen L, Järvenpää R, et al. ADC measure-

ments in diffuse large B-cell lymphoma and follicular lymphoma: a DWI and cellularity study. Eur J Radiol. 2013;82:e158–64.
70. Siegel MJ, Jokerst CE, Rajderkar D, Hildebolt CF, Goyal S, Dehdashti F, et al. Diffusion weighted MRI for staging and evaluating response in diffuse large B-cell lymphoma: a pilot study. NMR Biomed. 2014;27(6):681–91.
71. Allen CE, Kelly KM, Bollard CM. Pediatric lymphomas and histiocytic disorders of childhood. Pediatr Clin North Am. 2015;62:139–65.
72. Azouz EM, Saigal G, Rodriguez MM, Podda A. Langerhans' cell histiocytosis: pathology, imaging and treatment of skeletal involvement. Pediatr Radiol. 2005;35:103–15.
73. Van Nieuwenhuyse JP, Clapuyt P, Malghem J, Everarts P, Melin J, Pauwels S, et al. Radiographic skeletal survey and radionuclide bone scan in Langerhans cell histiocytosis of bone. Pediatr Radiol. 1996;26(10):734–8.
74. Binkovitz LA, Olshefski RS, Adler BH. Coincidence FDG-PET in the evaluation of Langerhans' cell histiocytosis: preliminary findings. Pediatr Radiol. 2003;33:598–602.
75. Phillips M, Allen C, Gerson P, McClain K. Comparison of FDG-PET scans to conventional radiography and bone scans in management of Langerhans cell histiocytosis. Pediatr Blood Cancer. 2009;52:97–101.
76. Mueller WP, Melzer HI, Schmid I, Coppenrath E, Bartenstein P, Pfluger T. The diagnostic value of 18F-FDG PET and MRI in paediatric histiocytosis. Eur J Nucl Med Mol Imaging. 2013;40:356–63.
77. Goo HW, Yang DH, Ra YS, Song JS, Im HJ, Seo JJ, et al. Whole-body MRI of Langerhans cell histiocytosis: comparison with radiography and bone scintigraphy. Pediatr Radiol. 2006;36:1019–31.
78. Steinborn M, Wörtler K, Nathrath M, Schöniger M, Hahn H, Rummeny EJ. Whole-body MRI in children with langerhans cell histiocytosis for the evaluation of the skeletal system. RoFo. 2008;180:646–53.
79. Papaioannou G, McHugh K. Neuroblastoma in childhood: review and radiological findings. Cancer Imaging. 2005;5:116–27.
80. Monclair T, Brodeur GM, Ambros PF, Brisse HJ, Cecchetto G, Holmes K, et al. The International Neuroblastoma Risk Group (INRG) staging system: an INRG Task Force report. J Clin Oncol. 2009;27(2):298–303.
81. Brisse HJ, McCarville MB, Granata C, Krug KB, Wootton-Gorges SL, Kanegawa K, et al. Guidelines for imaging and staging of neuroblastic tumors: consensus report from the International Neuroblastoma Risk Group Project. Radiology. 2011;261(1):243–57.
82. Goo HW. Whole-body MRI of neuroblastoma. Eur J Radiol. 2010;75:306–14.
83. Gahr N, Darge K, Hahn G, Kreher BW, von Buiren M, Uhl M. Diffusion-weighted MRI for differentiation of neuroblastoma and ganglioneuroblastoma/ganglioneuroma. Eur J Radiol. 2011;79(3):443–6.
84. Pfluger T, Schmied C, Porn U, Leinsinger G, Vollmar C, Dresel S, et al. Integrated imaging using MRI and 123I metaiodobenzylguanidine scintigraphy to improve sensitivity and specificity in the diagnosis of pediatric neuroblastoma. AJR Am J Roentgenol. 2003;181(4):1115–24.
85. Furth C, Amthauer H, Denecke T, Ruf J, Henze G, Gutberlet M. Impact of whole-body MRI and FDG-PET on staging and assessment of therapy response in a patient with Ewing sarcoma. Pediatr Blood Cancer. 2006;47:607–11.
86. Krohmer S, Sorge I, Krausse A, Kluge R, Bierbach U, Marwede D, et al. Whole-body MRI for primary evaluation of malignant disease in children. Eur J Radiol. 2010;74:256–61.
87. Gorkem SB, Coskun A, Yikilmaz A, Zurakowski D, Mulkern RV, Lee EY. Evaluation of pediatric thoracic disorders: a comparison of unenhanced fast imaging sequence 1.5T MRI and contrast-enhanced MDCT. AJR Am J Roentgenol. 2013;200:1352–7.
88. Burris NS, Johnson KM, Larson PE, Hope MD, Nagle SK, Behr SC, Hope TA. Detection of small pulmonary nodules with ultrashort echo time sequences in oncology patients by using a PET/MR system. Radiology. 2016;278:239–46.
89. Mautner VF, Asuagbor FA, Dombi E, Fünsterer C, Kluwe L, Wenzel R, et al. (2008) Assessment of benign tumor burden by whole-body MRI in patients with neurofibromatosis 1. Neuro Oncol. 2008;10:593–8.
90. Derlin T, Tornquist K, Munster S, Apostolova I, Hagel C, Friedrich RE, et al. Comparative effectiveness of 18F-FDG PET/CT versus whole-body MRI for detection of malignant peripheral nerve sheath tumors in neurofibromatosis type 1. Clin Nucl Med. 2013;38:e19–25.
91. Nguyen R, Jett K, Harris GJ, Cai W, Friedman JM, Mautner VF. Benign whole body tumor volume is a risk factor for malignant peripheral nerve sheath tumors in neurofibromatosis type 1. J Neurooncol. 2014;116:307–13.
92. Friedman DN, Lis E, Sklar CA, Oeffinger KC, Reppucci M, Fleischut MH, et al. Whole-body magnetic resonance imaging (WB-MRI) as surveillance for subsequent malignancies in survivors of hereditary retinoblastoma: a pilot study. Pediatr Blood Cancer. 2014;61(8):1440–4.
93. Jasperson KW, Kohlmann W, Gammon A, Slack H, Buchmann L, Hunt J, et al. Role of rapid sequence whole-body MRI screening in SDH-associated hereditary paraganglioma families. Fam Cancer. 2014;13:257–65.
94. Anupindi SA, Bedoya MA, Lindell RB, Rambhatla SJ, Zelley K, Nichols KE, Chauvin NA. (2015) Diagnostic performance of whole-body MRI as a tool for cancer screening in children with genetic cancer-predisposing conditions. AJR Am J Roentgenol. 2015;205:400–8.
95. Bueno MT, Martínez-Ríos C, la Puente GA, Ahyad RA, Villani A, Druker H, et al. Pediatric

imaging in DICER1 syndrome. Pediatr Radiol. 2017;47(10):1292–301.
96. Van Engelen K, Villani A, Wasserman JD, Aronoff L, Greer MC, Tijerin Bueno M, et al. DICER1 syndrome: approach to testing and management at a large pediatric tertiary care center. Pediatr Blood Cancer. 2018;65(1) https://doi.org/10.1002/pbc.26720.
97. Littooij AS, Nikkels PG, Hulsbergen-van Kaa CA, van de Ven CP, van den Heuvel-Eibrink MM, Olsen ØE. Apparent diffusion coefficient as it relates to histopathology findings in postchemotherapy nephroblastoma: a feasibility study. Pediatr Radiol. 2017;47(12):1608–14.
98. Hirsch FW, Sattler B, Sorge I, Kurch L, Viehweger A, Ritter L, et al. PET/MR in children. Initial clinical experience in paediatric oncology using an integrated PET/MR scanner. Pediatr Radiol. 2013;43:860–75.
99. Eiber M, Takei T, Souvatzoglou M, Mayerhoefer ME, Fürst S, Gaertner FC, et al. Performance of whole-body integrated 18F-FDG PET/MR in comparison to PET/CT for evaluation of malignant bone lesions. J Nucl Med. 2014;55:191–7.
100. Schäfer JF, Gatidis S, Schmidt H, Gückel B, Bezrukov I, Pfannenberg CA, et al. Simultaneous whole-body PET/MR imaging in comparison to PET/CT in pediatric oncology: initial results. Radiology. 2014;273:220–31.
101. Offiah AC, Andronikou S, Avni F, Daltro P, Donnelly LF, Jaramillo D, et al. Expert opinion: what are the greatest challenges and barriers to applying evidence-based and practical approaches to preclinical and clinical research in the field of pediatric radiology? Pediatr Radiol. 2014;44(10):1209–12.

8 Contrast-Enhanced Ultrasound: The Current State

M. Beth McCarville, Annamaria Deganello, and Zoltan Harkanyi

8.1 Introduction

Ultrasound (US) imaging in children has been a widely accepted and routinely used imaging modality for many decades. In fact, in many clinical scenarios, US is the preferred, first-line imaging modality to be performed. The attributes of US, particularly in pediatrics, are many; it is noninvasive, child-friendly, and portable, provides Doppler capabilities for vascular interrogation, does not require sedation, and most importantly does not expose the patient to the potentially harmful effects of ionizing radiation. The avoidance of radiation and sedation is particularly relevant in pediatric oncology because children with cancer undergo innumerable imaging examinations for diagnosis and staging, during therapy to monitor treatment response and to assess acute and chronic complications of therapy and then during surveillance for years after completion of therapy. A recent study from Great Britain showed an association between radiation exposure from CT scans and an increased risk of developing brain tumors and leukemia in children [1]. In that study the reported brain tumor risk was comparable to observed risk estimates for brain tumors following childhood radiation exposure in Japanese atomic bomb survivors. These findings underscore the importance of minimizing radiation exposure in children whenever possible.

Although US is often useful in identifying pathology in the abdomen, pelvis, pleural spaces, and extremities, image resolution of B-mode US is limited, and further cross-sectional imaging with CT or MRI may be required. In addition to radiation exposure and sedation, these additional tests add cost, can create anxiety, and frequently necessitate the administration of an intravenous contrast agent. There are risks associated with the iodinated contrast agents used for CT and gadolinium-based contrast agents used for MRI. Neither of these types of contrast agents can be safely administered in patients with renal insufficiency due to the risk of nephrotoxicity and nephrogenic systemic fibrosis, respectively. Recently, gadolinium contrast agents have come under increased scrutiny for the yet unknown, but potential, long-term effects associated with gadolinium deposition in the brain and other solid organs [2]. Unlike the very small molecules that

M. B. McCarville (✉)
Department of Diagnostic Imaging, St. Jude Children's Research Hospital, Memphis, USA
e-mail: beth.mccarville@stjude.org

A. Deganello
Department of Radiology, King's College Hospital, London, UK
e-mail: adeganello@nhs.net

Z. Harkanyi
Department of Radiology, Heim Pal Children's Hospital, Budapest, Hungary

S. D. Voss, K. McHugh (eds.), *Imaging in Pediatric Oncology*, Pediatric Oncology,
https://doi.org/10.1007/978-3-030-03777-2_8

constitute iodinated and gadolinium-based contrast agents, ultrasound contrast agents (UCAs) are comprised of microspheres approximating the size of red blood cells. Due to their size, UCAs remain in the vascular space and, because they are not metabolized by the kidneys, can be safely administered to patients with renal insufficiency. Numerous reports have shown that these contrast agents have a high safety profile in adults and there is a growing body of literature showing similar safety in children [3–9]. A position statement issued by the European Federation of Societies for Ultrasound in Medicine and Biology, published in 2016, stated: "The evidence to date suggests that the safety profile of UCA in adults is good, and comparable to contrast agents used in MR imaging, better than the contrast agents in CT imaging. The more limited safety data in children suggests that UCA are as safe in children as in the adult population" [10]. Importantly, in 2016 the United States Federal Drug Administration (FDA) approved the first UCA for intravenous use in children to evaluate liver lesions and intravesical administration to assess for vesicoureteral reflux.

The addition of a contrast agent to ultrasound imaging offers the opportunity to improve lesion conspicuity and diagnostic confidence and could obviate the need for additional cross-sectional imaging in some circumstances. The use of UCAs in adult practices is well established in Europe and is increasing in North America. The expansion of CEUS into pediatric applications has lagged behind, primarily because of the lack of regulatory approval and limited clinical experience outside of large academic centers. With the recent US FDA approval of a UCA for children, coupled with an increasing emphasis on medical cost containment and radiation reduction, the time is ripe for the development of this important alternative imaging modality in routine pediatric clinical practice. In this chapter we will discuss the essential technical and safety features that are vital to the successful performance of CEUS in children. Although the role of CEUS in pediatric oncology is currently somewhat limited, we will present examples illustrating the value of CEUS in this setting, particularly with regard to pediatric liver lesions. Finally, we will discuss future directions and potential applications of CEUS in the diagnosis and management of pediatric malignancies.

8.2 Safety Considerations of CEUS Studies

All current UCAs consist of a gas surrounded by a thin encapsulating shell. The most widely used UCA is sulfur hexafluoride with a phospholipid shell (SonoVue/Lumason®, Bracco, Milan, Italy), which was introduced in 2001 and approved by the US FDA for pediatric intravenous (IV) and intravesical use in 2016. In the United States, there are two additional UCAs that are approved only for adult cardiac studies: Definity® (Lantheus Medical Imaging, Billerica, MA), which is comprised of octafluoropropane encapsulated in a phospholipid shell, and Optison™ (GE Healthcare, Princeton, NJ), an octafluoropropane gas within an albumin shell. There are no data regarding pediatric applications of Sonazoid (GE Healthcare, Oslo, Norway), a hepatocyte-specific agent composed of perfluorobutane gas within a phospholipid shell, that is widely used in Asia [10, 11].

The safety profile of SonoVue/Lumason® UCA during intravenous administration has been documented in a large cohort of 23,188 adults with no fatal event encountered and only 29 adverse reactions noted (three severe, three moderate, and 23 mild) [12]. The overall rate of adverse events (0.0086%) was comparable to the administration of contrast media used in MR imaging (0.0088%) and lower than iodinated contrast media used in CT imaging (0.6%) [10]. The safety profile of UCAs in children is based on limited but growing information. Three dedicated safety studies have included vital signs monitoring, while using UCA containing a perfluorocarbon gas [5, 9, 13]. In a study of 13 children who underwent IV CEUS with escalating doses of Optison™ based on body surface area, three children experienced mild adverse events; two had altered taste and one mild tinnitus and light-headedness [13]. In a further study by the same group, 134 CEUS examinations in 34 children (median age 8.7 years) were evaluated, reporting a lower frequency of similar mild

adverse reactions [5]. In a study of 20 children (median age 15 years) receiving Optison™, four experienced adverse reactions; three developed a transient headache and one reported brief taste alteration [9]. A sulfur hexafluoride gas containing UCA was also evaluated in a dedicated safety study of 167 intravenous CEUS investigations in 137 children (median 10.2 years) [4]. In that study, a single patient (0.6%) suffered severe anaphylactic shock that was potentially life threatening and directly related to the IV UCA administration. Management consisted of oxygen, IV epinephrine, and fluids (0.9% NaCl) with resolution in 2 h. In a survey of radiologists from 29 European centers, there were 948 CEUS examinations performed in children with intravenous sulfur hexafluoride gas-filled UCA. Five minor adverse events were reported which included skin reaction, altered taste, and hyperventilation [14].

Ultrasound contrast agents are not metabolized by the kidneys, and there is no evidence of nephrotoxicity associated with their use. Therefore, unlike iodinated and gadolinium-based contrast agents, UCAs can be safely administered to patients with poor renal function. However, a drawback is that UCAs cannot be used to evaluate the renal collecting system when they are administered intravenously.

History of a hypersensitivity reaction to any of the ingredients in UCAs is a contraindication to their use. During CEUS studies one must always be prepared to manage an adverse reaction. Resuscitation facilities including appropriate drugs must be available in the examination room, and a second person must be present during the study.

8.3 Technical Considerations of CEUS Studies

The radiologist must clearly define the goal of the CEUS study before its performance. It is almost always a focused study in order to answer a specific diagnostic question. Basic training in B-mode and color Doppler techniques are essential prerequisites for those wishing to perform contrast studies.

8.3.1 Checklist for Performance of a CEUS Examination [11]

1. Examination and documentation of the region of interest with B-mode and color Doppler US.
2. Review of any prior imaging studies (US/CEUS/MR/CT). This is of utmost importance in long-term follow-up of pediatric oncology patients to better characterize the lesion of interest.
3. Determine whether a CEUS study is indicated for the diagnostic question.
4. Assess patient for any contraindication to CEUS.
5. Have a second person present during the CEUS study to inject and monitor the patient.
6. Ensure that treatment and life support are available for allergic reactions to UCA.
7. Obtain informed consent (verbal or written as per local institutional practice) from parents or patient as appropriate.
8. Determine dose of UCA and saline flush and verify contrast agent expiration date.
9. Use a needle of 20–24 gauge for IV. If the needle caliber is too small, it may result in microbubble destruction.
10. Ensure capability of US machine to record video clips during the CEUS study.
11. Be certain that the contrast-specific software within the US scanner is functional.
12. Select appropriate US probe and scanning parameters for CEUS study.
13. Start timer at the moment of injection.
14. Start recording cine loop after the arrival of the first bubbles for approximately 20–40 s, and then record in the venous and late phase using short clips while scanning the whole organ. Store images and video clips (e.g., picture archive and communication system [PACS], DVD, CD).
15. Review the study at a PACS workstation using stored images and cine clips and report the examination.

The dose of UCA generally can be determined by the patients' age or weight depending on the agent being used [3, 9]. When using SonoVue/Lumason® to perform a liver CEUS study on a

child, the following doses are suggested: between the age of 0 and 6 years, 0.6 mL; 6–12 years, 1.2 mL; and between 12 and 18 years, 2.4 mL. Recommended doses for Optison™ are 0.3 mL for patients less than 20 kg and 0.5 mL for others [9]. However, doses may need to be adjusted depending on the size and body habitus of the patient, depth of the lesion, underlying diffuse hepatic parenchymal disease, type of transducer (convex or linear), and the CEUS software version of the ultrasound system. In the case of multiple parenchymal lesions (liver, kidney) or when the characterization of a lesion remains questionable, repeat injections can be performed as needed after allowing the first dose to clear the circulation (generally about 10 min). The manufacturer's maximum cumulative dose recommendation can be found in the package insert and should be adhered to. The quality of CEUS studies has significantly improved with the introduction of contrast-specific software; however, the sensitivity to display microvascularity (presence of microbubbles at the capillary level) can vary between US systems.

Imaging parameters, such as the mechanical index (MI) and position of the focal zone, should be adjusted at the beginning of the CEUS study according to the diagnostic question. The use of a split screen, with a grayscale image on one side and the corresponding CEUS image on the other, is quite helpful to maintain the proper scanning plane during the study. In the later phase of imaging, the CEUS display alone may be sufficient to depict the lesion(s) and allows viewing of a larger area of anatomy. The average time required to perform a CEUS study in experienced hands is 15–25 min, including preparation of the UCA.

8.4 Contrast-Enhanced Ultrasound Imaging Features of Pediatric Malignancies

To be incorporated into the routine management of oncology patients, CEUS will need to demonstrate added value or improved diagnostic performance over existing imaging modalities. The added value of CEUS, and its accuracy relative to CT and MRI, has perhaps been best described in the assessment of liver lesions. In a study of 147 adult patients by D'Onofrio and colleagues, the late phase of CEUS was compared to the hepatobiliary phase of contrast-enhanced MRI for distinguishing benign from malignant liver lesions. Contrast-enhanced ultrasound had a sensitivity, specificity, positive predictive value (PPV), negative predictive value (NPV), and accuracy of 90%, 93%, 97%, 80%, and 91% compared to 91%, 93%, 97%, 81%, and 92%, respectively, by MRI and rose to 98%, 98%, 99%, 95%, and 98%, respectively, when findings from both modalities were considered concurrently [15]. Similar findings were reported by Quaia et al., who compared CEUS to contrast-enhanced CT (CE-CT) in 46 non-cirrhotic adults with 55 liver lesions. In that study, the sensitivity, specificity, PPV, NPV, and accuracy for two reviewers were superior for CEUS compared to CE-CT and improved when CEUS and CE-CT images were reviewed concurrently [16]. In a study of 134 adult patients with focal liver lesions (FLLs) who underwent CEUS and contrast-enhanced CT and/or MRI, Trillaud and colleagues found that CEUS had a sensitivity, specificity, and accuracy of 98%, 88%, and 93% compared to 69%, 79%, and 72%, respectively, for CT/MRI. Thirty patients in their study underwent biopsy; compared to pathology CEUS had a sensitivity, specificity, and accuracy of 96%, 75%, and 90% compared to 73%, 38%, and 63% for CT and 82%, 43%, and 67% for MRI [17].

There are a small number of studies dedicated to the role of CEUS in focal liver lesion (FLL) characterization in pediatrics [4, 6, 8, 18, 19]. In a study of 44 children with indeterminate FLLs on grayscale ultrasound, investigators compared CEUS with consensus cross-sectional imaging or histology as the gold-standard method and showed agreement in 85% of cases [6]. A more recent dedicated pediatric study compared CEUS to CT and MR of 60 liver lesions and anomalies of portal vein perfusion. CEUS was able to differentiate accurately between benign and malignant lesions and could characterize 45 out of 49 FLLs; MRI and CEUS findings were concordant

in 84% of the cases and CT and CEUS were concordant in five out of eight cases. In 21 lesions CEUS was the only imaging modality used to characterize the lesions and was deemed sufficient to achieve a diagnosis [19].

A study by Smith et al. showed that the incidence of new focal liver lesions in 273 children treated for a solid malignancy who were followed with abdominal imaging was 17% [20]. When such lesions arise in a child with a history of underlying malignancy, there is always a concern for metastatic recurrence. Given the body of evidence supporting the use of CEUS to distinguish benign from malignant liver lesions, in conjunction with the recent FDA approval of a UCA for assessment of the liver in children, this modality should be given high priority in the management of these patients. Taken together, the high spatial resolution of ultrasonography and the accuracy of CEUS in determining the nature of a FLL, CEUS could become the modality of choice to identify and characterize small liver lesions [21].

The assessment of pediatric FLLs with CEUS does not differ from the adult population. The purely intravascular nature of the UCA gives the examiner the opportunity to visualize in real time the vascular enhancement of a lesion during the arterial, portal venous, and late phases. During the arterial phase, it is important to establish the position of initial enhancement within the lesion (central, eccentric, or peripheral) and the pattern of vascularization (uniform, stellate/spoke wheel, haphazard, globular, or peripheral rim). During the portal venous and late phases, the examiner needs to establish whether the lesion fills in or retains contrast or, conversely, if there is washout of contrast from the lesion. Contrast washout is a feature that is usually indicative of malignancy [15]. Some benign lesions, such as focal nodular hyperplasia (FNH) and hemangiomas (Fig. 8.1), have specific patterns of enhancement in the arterial phase (spoke wheel, centrifugal, or globular peripheral, respectively). Benign lesions typically remain iso- or hyperenhancing (Fig. 8.2) or continue to fill in during the portal venous and late phases (Fig. 8.1). Focal nodular hyperplasia may exhibit a central, non-enhancing scar (Fig. 8.3). Therefore, the enhancement patterns of these lesions can be established readily allowing a quick and accurate diagnosis. This is especially desirable in examining a child because it obviates the need for radiation exposure, sedation, and iodinated or gadolinium-based contrast infusion. An added, important benefit is that this approach allows immediate feedback to the patient/caregiver, thus alleviating the anxiety associated with additional imaging and a delayed diagnosis.

Primary liver tumors are uncommon in children, and the majority are benign [22, 23]. Benign lesions can, nevertheless, undergo malignant transformation. The most common primary malignant liver tumor in children is hepatoblastoma. Others include hepatocellular carcinoma (HCC), embryonal sarcoma, and rhabdomyosarcoma. In children with chronic liver disease, the progression toward cirrhosis increases the risk of developing HCC, and these patients require close follow-up [11, 24].

On CEUS primary liver malignancies such as HCC and hepatoblastoma both display early disorganized vessels and hyperenhancement (Fig. 8.4) in the arterial phase. During the portal venous phase, hepatoblastoma tends to have rapid washout of contrast, whereas HCC (Fig. 8.5) may show hypoenhancement or slow washout only during delayed phase imaging depending on the degree of differentiation of the tumor. Undifferentiated embryonal sarcoma (UES) of the liver is a rare mesenchymal tumor of childhood but represents the third most common primary hepatic neoplasm after hepatoblastoma and HCC [25]. On CEUS, UES (Fig. 8.6) may display a hyperenhancing rim (thought to represent a fibrous pseudocapsule on pathology), with lack of internal enhancement during the arterial phase, followed by heterogeneous internal nodular enhancement in the late phase and late, faint washout of the peripheral rim.

Rhabdomyosarcoma of the liver is another rare malignant tumor but represents the most common biliary tract tumor in children; it often arises from the common bile duct (but can arise anywhere along the biliary tree) and, on B-mode ultrasound, presents as a solid mass occupying the bile duct lumen (Fig. 8.7), with or without

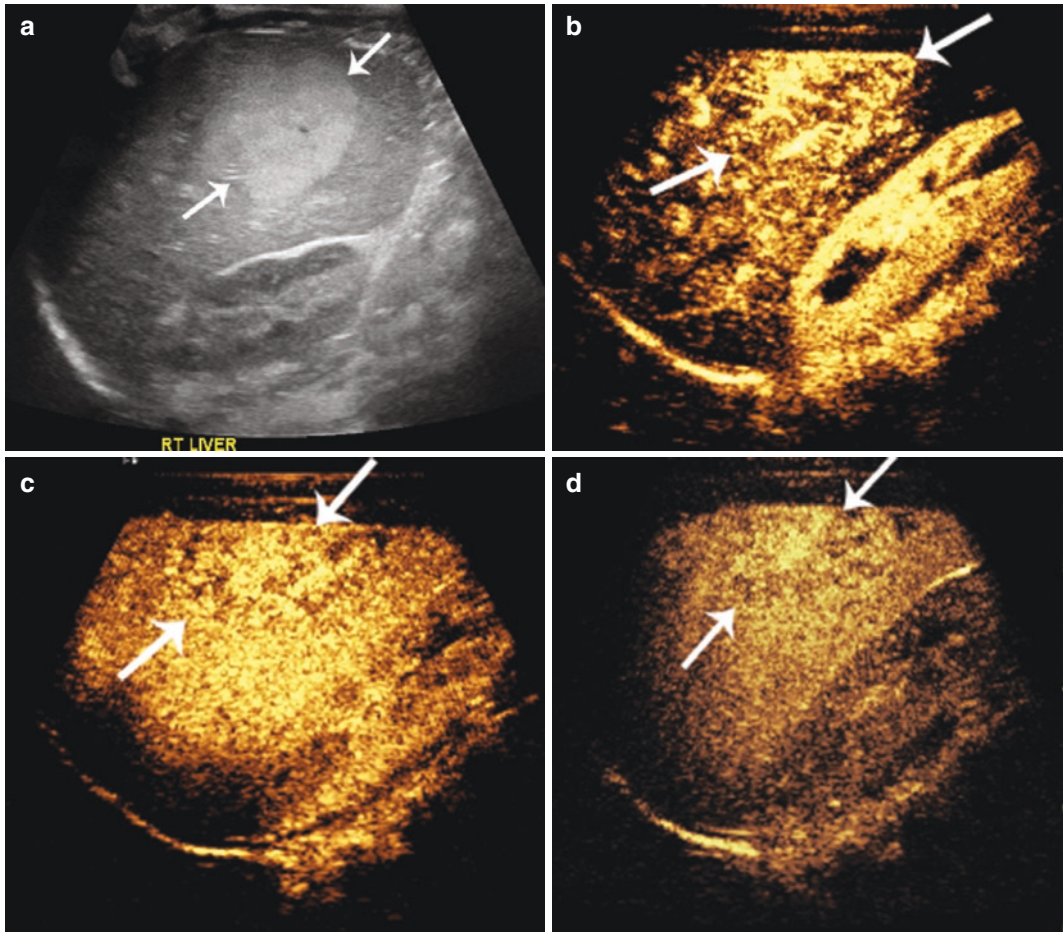

Fig. 8.1 A 3-month-old boy underwent an ultrasound to assess for pyloric stenosis and was incidentally found to have a liver lesion. (**a**) Sagittal grayscale ultrasound shows a large hyperechoic lesion in segments 5 and 6 of the liver (arrows). (**b**) Sagittal contrast-enhanced ultrasound (CEUS) image obtained in early arterial phase shows peripheral, globular enhancement of the lesion (arrows). (**c**) Sagittal portal venous phase CEUS shows centripetal enhancement of the lesion (arrows). (**d**) Sagittal delayed phase CEUS shows persistent, somewhat globular, central hyperenhancement of the lesion (arrows). These CEUS features are typical of hemangioma

extension into the liver parenchyma. On CEUS, like other imaging modalities, this lesion does not have specific features [26]. In our limited experience, this lesion has CEUS features similar to other liver malignancies, with variable arterial contrast enhancement and early washout in the portal venous phase (Fig. 8.7).

Metastases can either be hypoenhancing in all phases, hyperenhancing in the arterial phase, or hypoenhancing in the portal venous and late phases (Fig. 8.8) or show a rim of arterial enhancement followed by washout in the portal venous and late phases.

When assessing liver lesions, it is crucial to continue intermittent scanning for at least 4 min, to avoid missing late washout and misdiagnosing a malignant lesion as benign. Hyperenhancing metastases, some malignant mesenchymal primaries, and well-differentiated HCC may not demonstrate washout until 4–5 min after injection [27–29]. Therefore, caution and technique tuning (such as image freezing and intermittent scanning) must be applied to avoid microbubble destruction caused by the insonating sound waves and artifactual loss of enhancement that could precede contrast washout. It should be

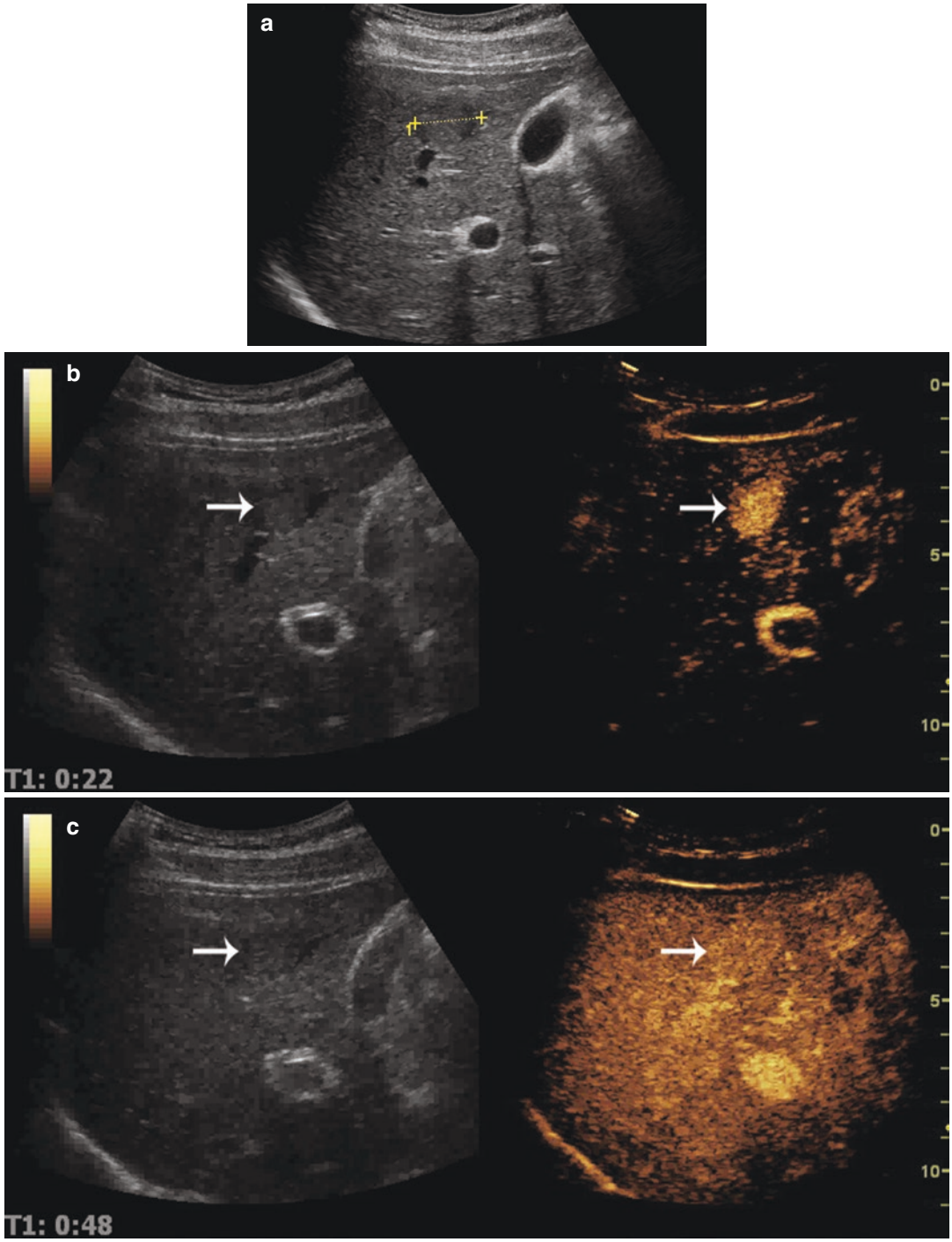

Fig. 8.2 An 18-year-old boy with cystic fibrosis. (**a**) Sagittal grayscale ultrasound image of the liver shows a mass in segment 5 (cursors). Sagittal CEUS images (right side of panels) (**b**) show the mass to be hyperenhancing in the arterial phase (arrows) (**c**) and isoenhancing in the delayed phase (arrows) with no evidence of washout. Clinical follow-up and MR imaging (not shown) were suggestive of hepatic adenoma

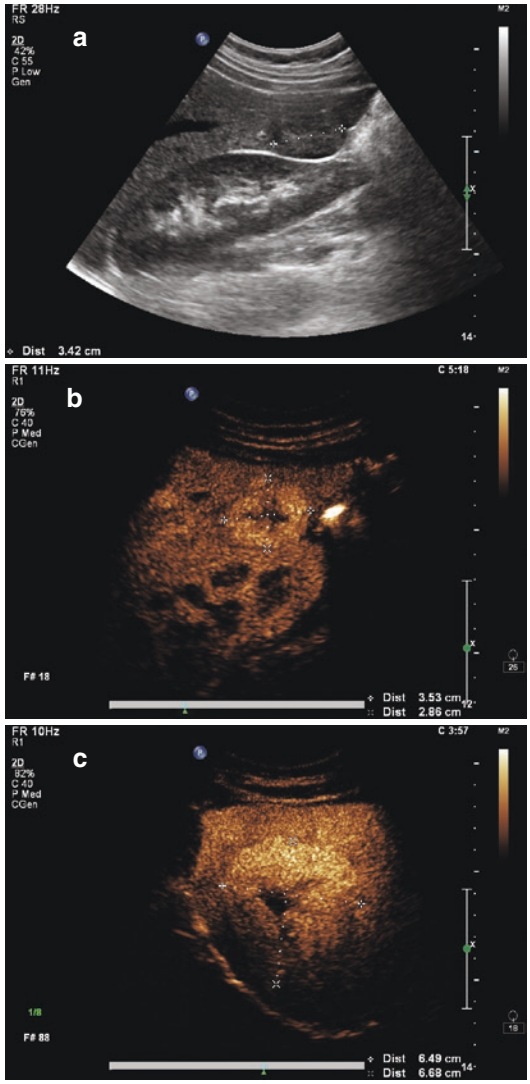

Fig. 8.3 A 17-year-old girl with history of treated neuroblastoma and multiple focal nodular hyperplasia (FNH) nodules. (**a**) Conventional sagittal grayscale ultrasound image shows a hypoechoic solid nodule in segment 6 of the liver (cursors). (**b**) Sagittal contrast-enhanced ultrasound (CEUS) image obtained during the portal venous phase shows the nodule is hyperenhancing and has a central scar (cursors). (**c**) A second, larger FNH in segments 7 and 8 (cursors) shows similar enhancement features. The lesions did not wash out on delayed phase imaging. These CEUS features are typical of FNH

remembered that no imaging modality is 100% accurate all of the time. There are reported cases of benign lesions, including adenomas and FNH, showing hypoenhancement in the late phase which was due to scarring or inflammation [6, 30]. Therefore, CEUS findings must be correlated with the clinical scenario and the index of suspicion for malignancy. When the CEUS and clinical findings are equivocal or conflicting early follow-up, alternative imaging modalities or biopsy may be needed as clinically indicated.

Non-hepatic oncology applications of pediatric CEUS is an expanding field with only a limited number of publications that are mainly focused on its safety profile [3, 5]. There are only sporadic case reports of the value of CEUS to aid the diagnosis of solid tumors [31]. An important, potential application of CEUS in pediatric oncology is establishing solid tumor resectability by defining tumor margins and identifying possible local vascular invasion [13]. The optimal spatial and temporal resolution of CEUS may make it the ideal tool for this purpose, especially in cases where CT and MRI are ambiguous. Likewise, CEUS can identify viable tissue within a solid lesion, to target biopsy and facilitate accurate sampling. Intravenous renal applications of CEUS have been evaluated in adults and can be applied to the pediatric population. These include differentiation between benign and malignant lesions and characterization of complex renal cysts [32]. CEUS has also proved to be useful in the evaluation of testicular lesions. Preliminary studies focused on CEUS time-intensity curves show its potential in discriminating Leydig cell tumors from seminomas on the basis of differing vascularity [33]. This could prove extremely useful in adolescent boys with the aim of testis sparing surgery.

8.5 Future Directions

The role of CEUS in oncology is rapidly expanding and evolving. There are a wide variety of potential applications of CEUS in the management of adult and pediatric oncology patients. Due to the relative rarity of pediatric malignancies, much of the clinical research in this area is occurring in the adult population. In addition to the malignancies already discussed, investigators have reported the value of CEUS in distinguishing benign from malignant thyroid nodules,

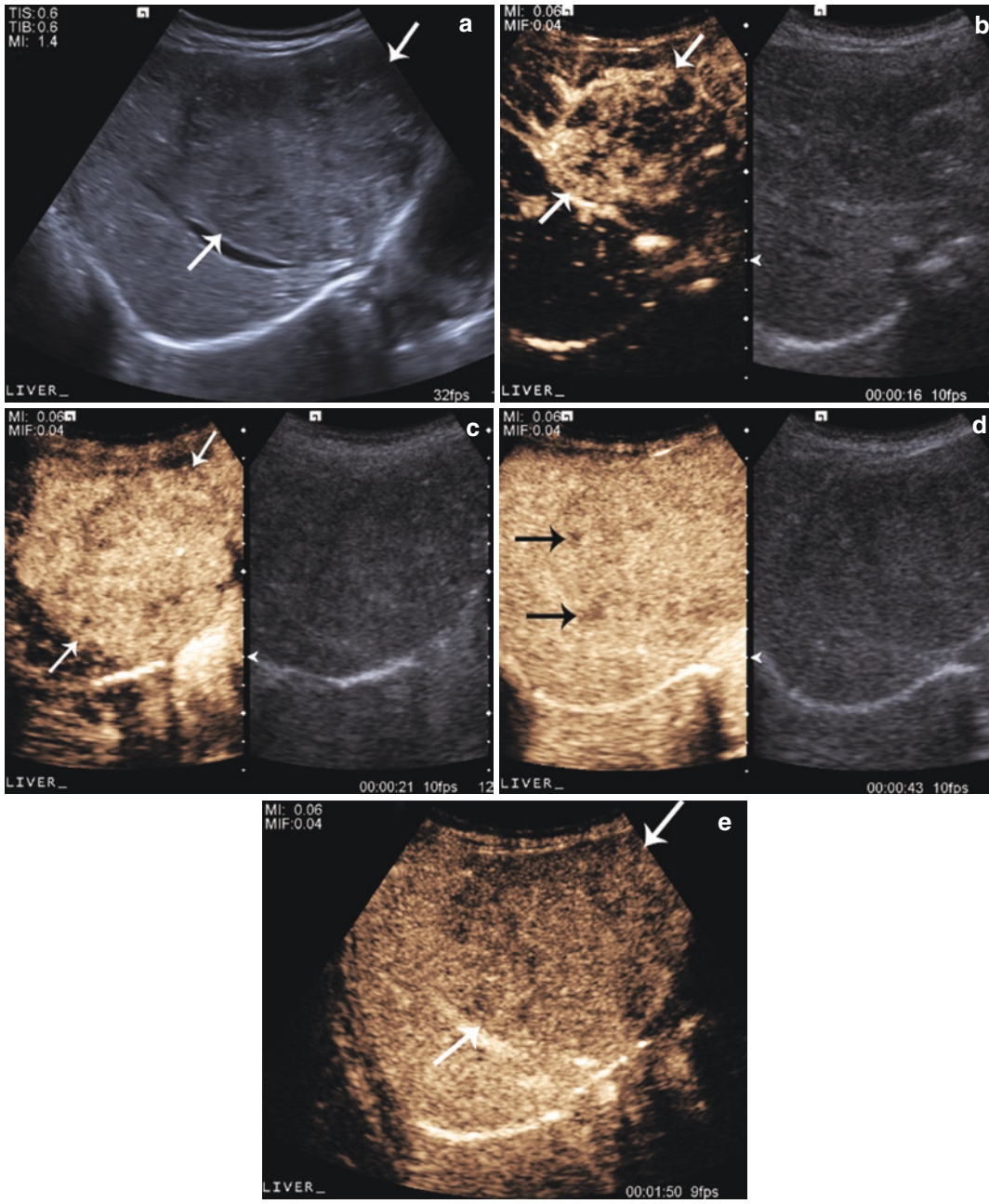

Fig. 8.4 A 2-year-old girl with hepatoblastoma. (**a**) Transverse grayscale ultrasound image showing primary tumor in segments 8 and 4A of the liver (arrows). (**b**) Transverse CEUS image (left side of panel) obtained in the early arterial phase shows hyperenhancement of tumor (arrows) with disorganized feeding vessels. (**c**) Transverse CEUS image (left side of panel) obtained in the late arterial phase shows diffuse hyperenhancement of tumor (arrows). (**d**) Transverse CEUS image (left side of panel) obtained at 43 s after injection shows early washout of contrast in some areas of the tumor (arrows). (**e**) At approximately 2 min after injection, there is continued washout of contrast throughout the tumor (arrows). These features are consistent with a malignant lesion

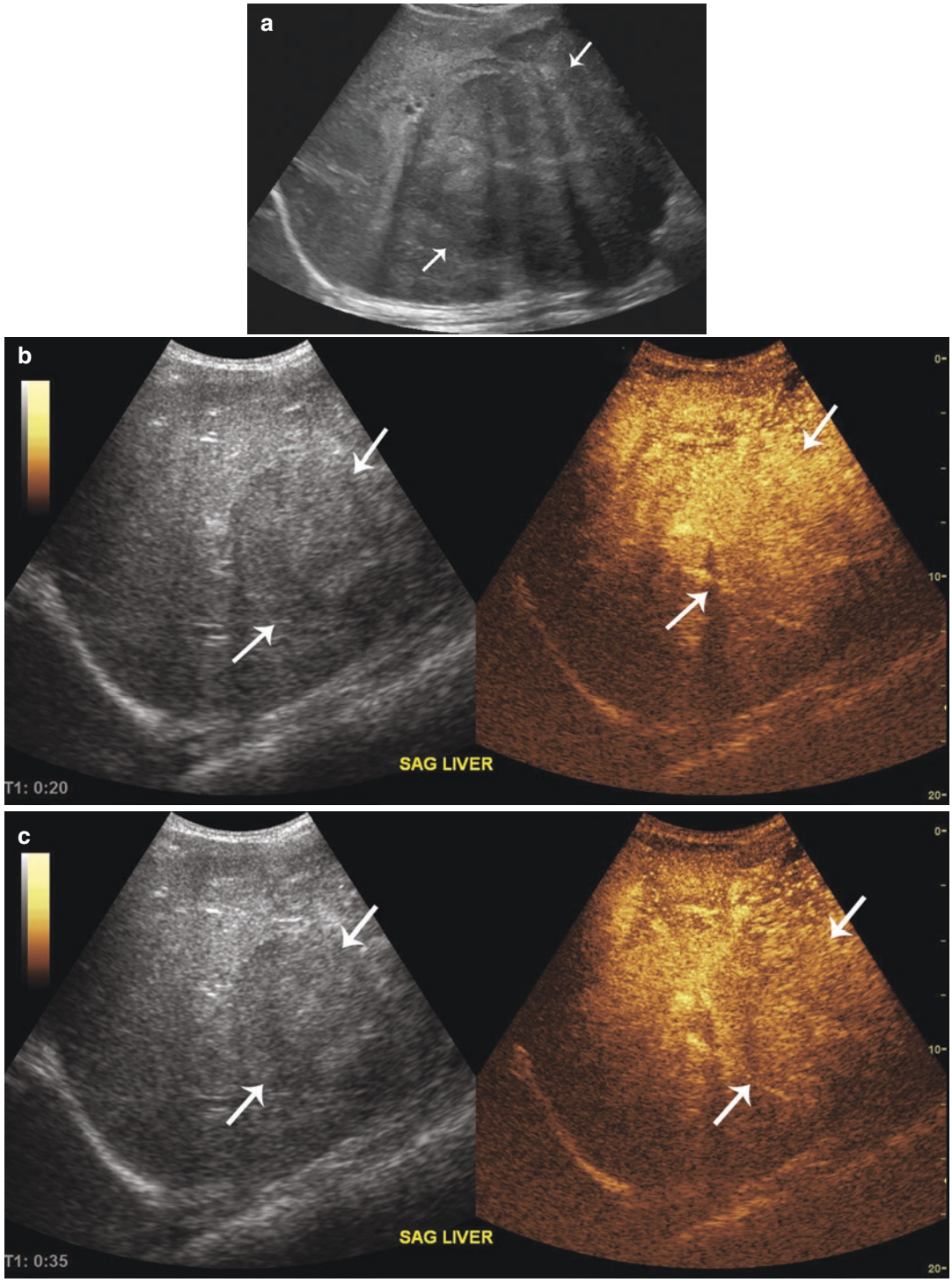

Fig. 8.5 A 15-year-old boy with palpable right upper quadrant mass proven by biopsy to be fibrolamellar hepatocellular carcinoma (HCC). (**a**) Transverse grayscale image shows large intrahepatic tumor (arrows). Transverse CEUS images (right side of panels) in the (**b**) early arterial phase shows hyperenhancement of the tumor (arrows). (**c**) In the portal venous phase, the tumor is isoenhancing (arrows), and (**d**) 1 min after injection, the tumor shows washout of contrast agent (arrows). These CEUS features are typical of HCC

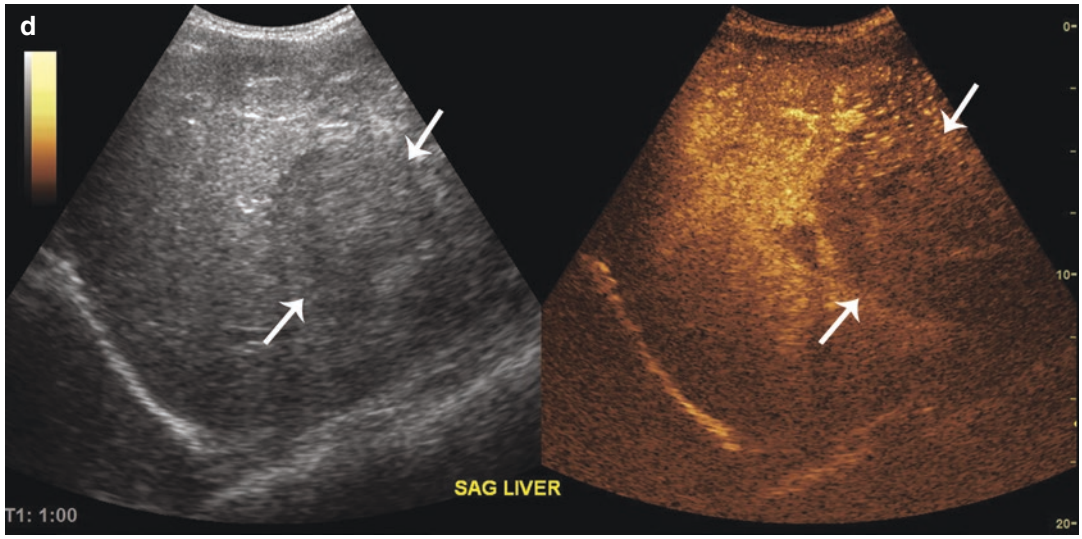

Fig. 8.5 (continued)

distinguishing endometrial hyperplasia from neoplasms, distinguishing benign from malignant soft tissue masses, differentiating low- from high-grade bladder carcinoma, distinguishing benign from malignant lymph nodes, distinguishing prostate carcinoma from benign prostatic hypertrophy and to monitor response to therapy in breast cancer, liver metastases, and liver tumors treated with transarterial chemoembolization and radiofrequency ablation [15–17, 34–53]. Clearly there is substantial interest in the development of CEUS to diagnose and assess treatment response in the oncology population.

It is widely accepted that angiogenesis (the development of new blood vessels) is essential for tumor development, growth, and metastasis [54, 55]. Subsequently, accurate imaging and quantitation of tumor vascularity is an important area of investigation. Contrast-enhanced ultrasound is emerging as a reliable method of measuring tumor vascularity and assessing therapy response in a variety of adult malignancies [56–66]. Ultrasound contrast agents can be given in very small doses, remain in the vascular space (due to their size), and are detectable at the capillary level. With contrast-specific software programs, several CEUS time-intensity curve parameters, such as peak enhancement intensity (PI), rise time (RT), mean transit time (MTT), and area under the curve (AUC), can be quantitated. CEUS has unique attributes that make it more appealing for measuring tumor blood flow than other imaging modalities. Because UCAs remain in the vascular space, the pharmacodynamics are less complex than for CT and MR contrast agents that freely diffuse across the vascular membrane. It is less expensive than contrast-enhanced CT and MRI, can be performed at the bedside, does not require sedation, and, most importantly in the pediatric population, does not expose the patient to the potentially harmful effects of ionizing radiation.

In one study of 13 children receiving Phase 1 anti-angiogenic therapy, investigators performed quantitative, dynamic CEUS in children with recurrent solid tumors to monitor the effect of anti-angiogenic therapy. In that study a target lesion (primary or metastatic) that was amenable to ultrasound visualization was chosen for baseline and follow-up imaging. A contrast compatible transducer was placed over the largest diameter of the target lesion in either the transverse or longitudinal plane. The study subject was administered an intravenous bolus of a UCA and dynamic contrast imaging was obtained for 60 s after the injection. Using the ultrasound machine contrast-specific software, a region of interest was drawn just inside the tumor margins, and time-intensity curves were

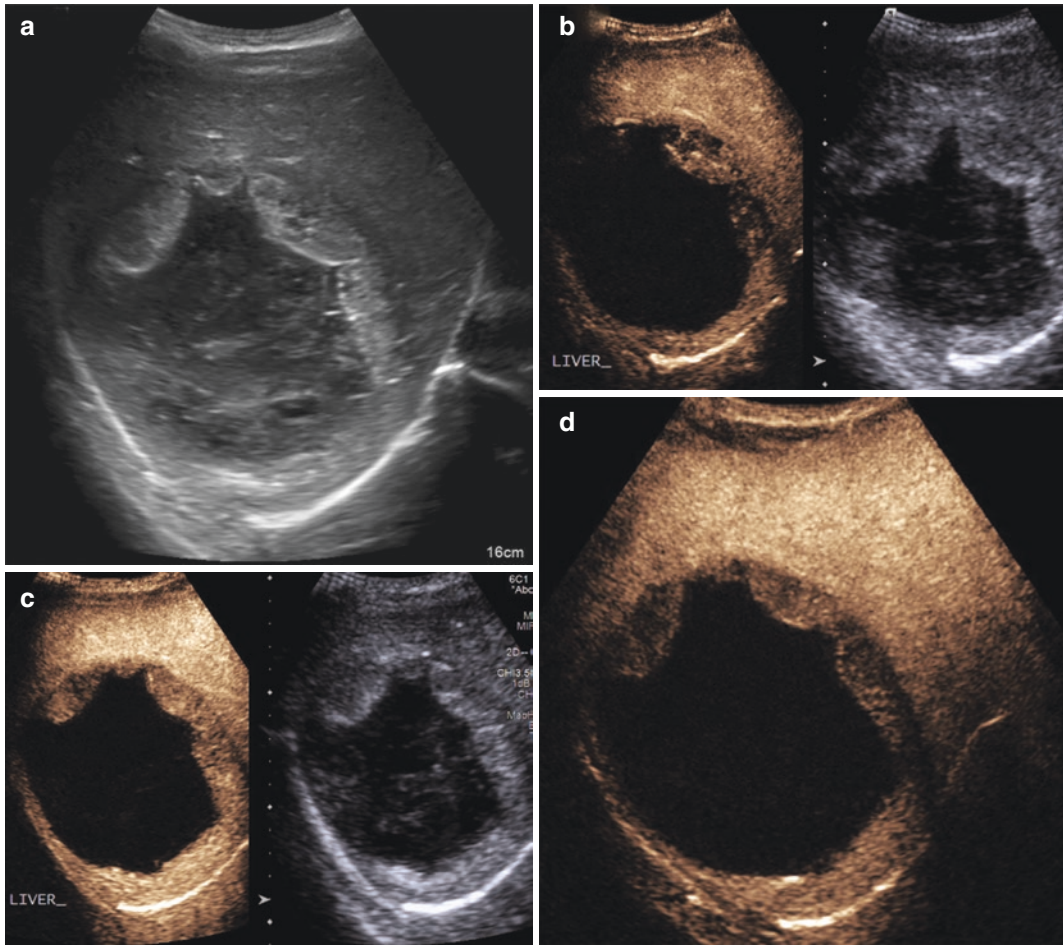

Fig. 8.6 A 10-year-old girl with undifferentiated embryonal sarcoma of the liver. (**a**) Sagittal grayscale ultrasound image shows the largely cystic primary tumor. Sagittal CEUS images (left side of panels) obtained in the (**b**) arterial phase show enhancement of the solid rim of tumor. (**c**) In the portal venous phase, there is further globular enhancement toward the center of the lesion with lack of internal enhancement. (**d**) At about 3 min after injection, there is faint, late washout in the peripheral rim. These imaging features are typical of embryonal sarcoma of the liver

obtained (Fig. 8.9). The investigators were careful to include an anatomic landmark within the field of view in order to ensure similar placement of the transducer at follow-up imaging time points (Figs. 8.10 and 8.11). From each time-intensity curve, six parameters were derived including peak enhancement (PE), rate of enhancement (RE), time to peak enhancement (TTP), total area under the curve (AUC), AUC during the first 10 s of enhancement (wash-in, AUC_1), and AUC during the second 10 s of enhancement (washout, AUC_2) (Fig. 8.9). The investigators found that the PE, RE, and AUC_1 were significantly associated with time to progression such that greater reductions in those parameters from baseline to the end of course one predicted a longer time to progression. Figures 8.10 and 8.11 show the difference in enhancement patterns between a patient with a long time to progression and a patient with a short time to progression [67]. These results are promising and warrant validation in larger clinical trials. Recent reports from the adult oncology community show that this approach is useful not only in assessing response to anti-angiogenic therapy, but to assess response to conventional chemotherapy as well [59–63, 68].

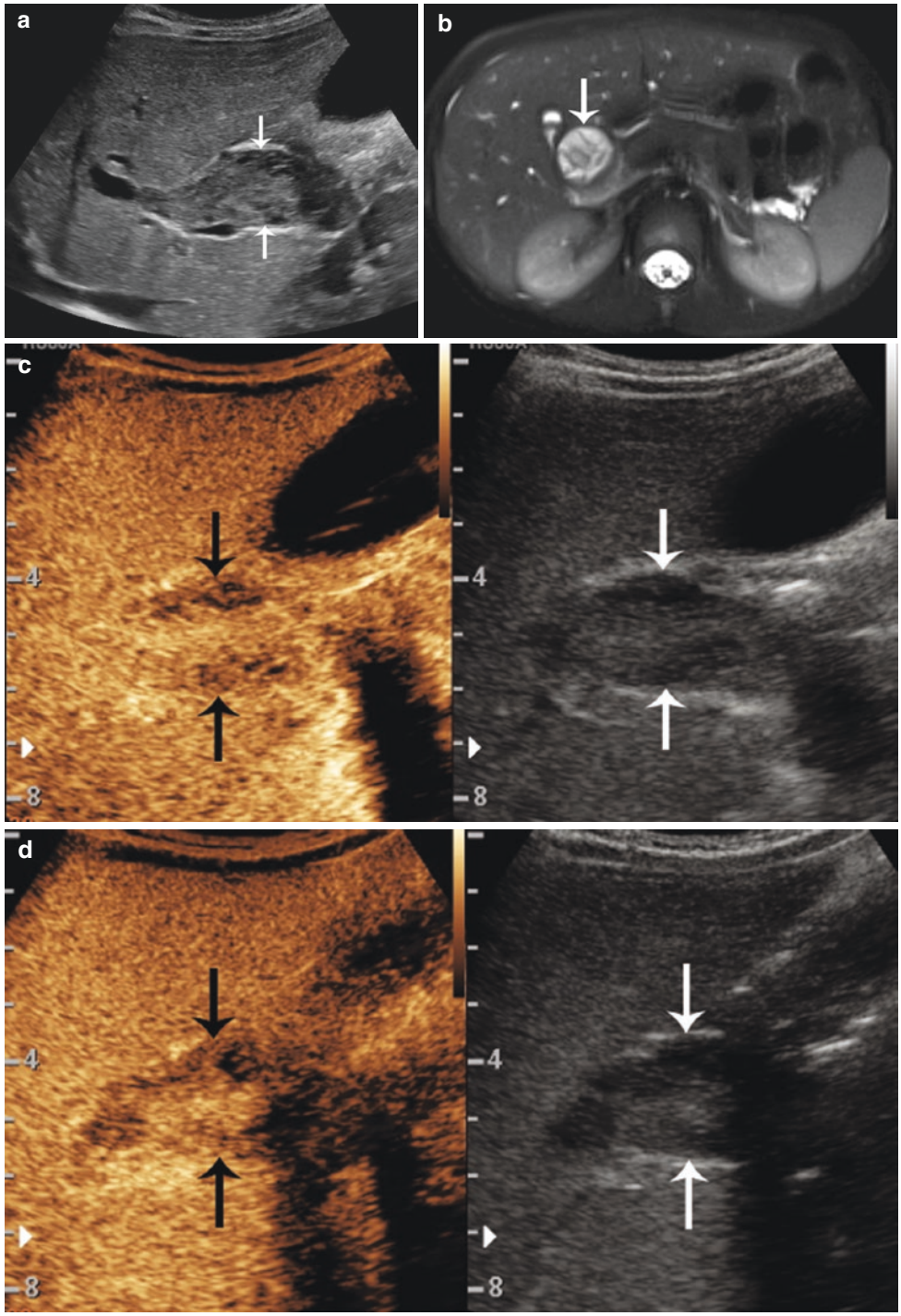

Fig. 8.7 A 5-year-old boy with rhabdomyosarcoma of the biliary tree. (**a**) Transverse grayscale ultrasound image shows tumor arising from the common bile duct (arrows). Transverse CEUS images (left side of panels) show (**b**) Transverse T2W MR image shows the tumor occupying and expanding the lumen of the common bile duct (arrows). (**c**) heterogeneous enhancement in the early arterial phase (arrows). (**d**) Early washout of contrast material at 32 s after injection (arrows)

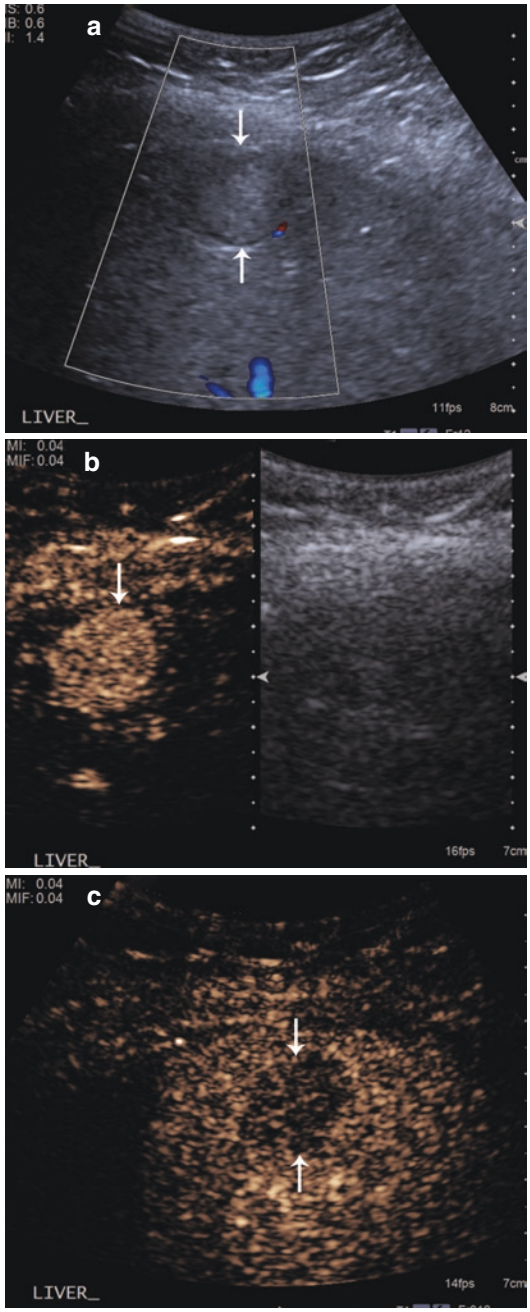

Fig. 8.8 An 11-year-old girl with metastatic pancreatic neuroendocrine tumor. (**a**) Transverse grayscale ultrasound image shows a slightly hyperechoic subcapsular lesion with a hypoechoic halo and no visible internal vascularity (arrows). (**b**) Transverse CEUS image (left side of panel) obtained in the arterial phase shows the lesion to be hyperenhancing. (**c**) This CEUS image obtained in the portal venous phase shows frank washout of the lesion (arrows). These features are consistent with a liver metastasis

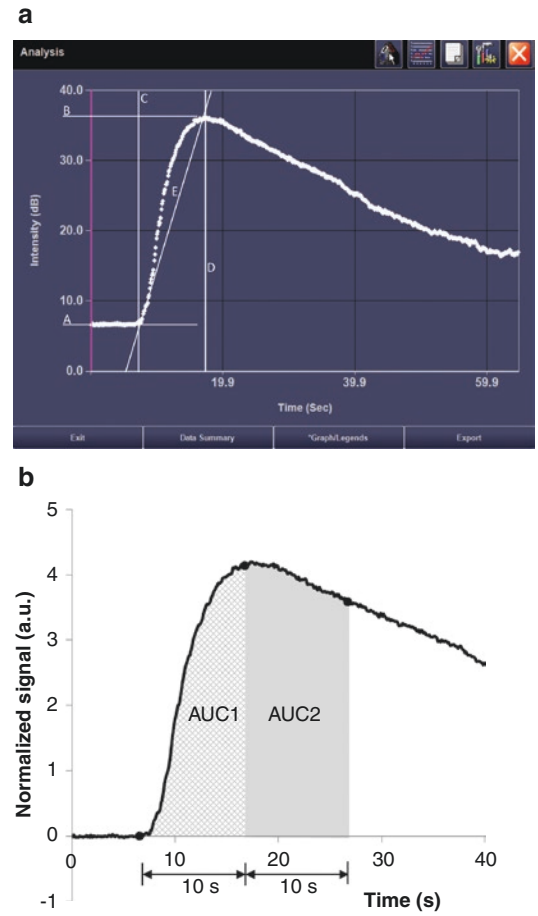

Fig. 8.9 (**a**) Time-intensity curve and parameters generated from a region of interest within the tumor shown in Fig. 8.10. (**b**) This normalized time-intensity curve for measurement of the area under the curve (AUC) was created off-line from exported raw data for the same tumor (reprinted with permission from reference [67]). *A* = baseline, pre-contrast signal (dB). *B* = maximal enhancement: peak enhancement (PE) = *B* − *A* in dB. *C* = time of arrival of contrast agent into region of interest (s). *D* = time of maximal enhancement (s): time to peak (TTP) = *D* − *C* (s). *E* = rate of change in enhancement (RE) calculated as PE/TTP in dB/s

The role of CEUS in oncology is extending beyond diagnosis and treatment monitoring into the realm of molecular imaging and targeted therapy. Numerous methods of UCA-mediated drug delivery are under investigation in preclinical and clinical trials. These include the use of microbubble contrast agents for direct and indirect drug

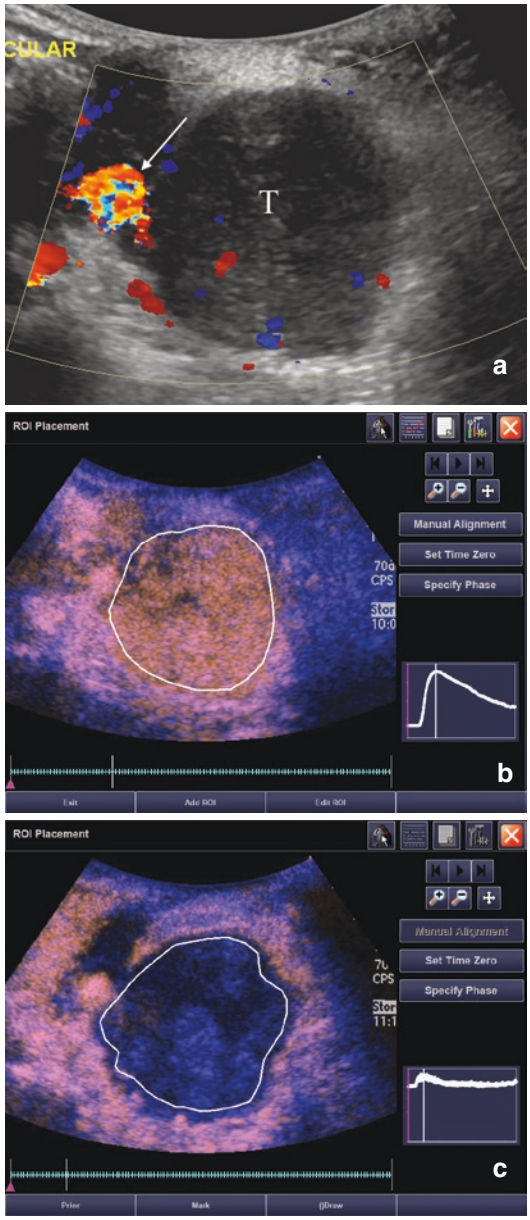

Fig. 8.10 A 15-year-old girl with recurrent synovial sarcoma. (**a**) Transverse color Doppler grayscale sonogram of the largest transverse area of a left supraclavicular tumor (T). Common carotid artery (arrow) was used as a landmark to insure similar transducer placement on follow-up studies. (**b**) Baseline CEUS with region of interest (ROI, solid line) drawn just inside tumor margins. Vertical line in the inset time-intensity curve indicates that this image was obtained at peak enhancement (PE) of 28.9 dB. (**c**) Day 7 after initiation of therapy, image obtained at PE of 2.0 dB giving a 93% reduction compared to baseline. This subject's time to progression was 242 days after initiation of therapy (reprinted with permission from reference [67])

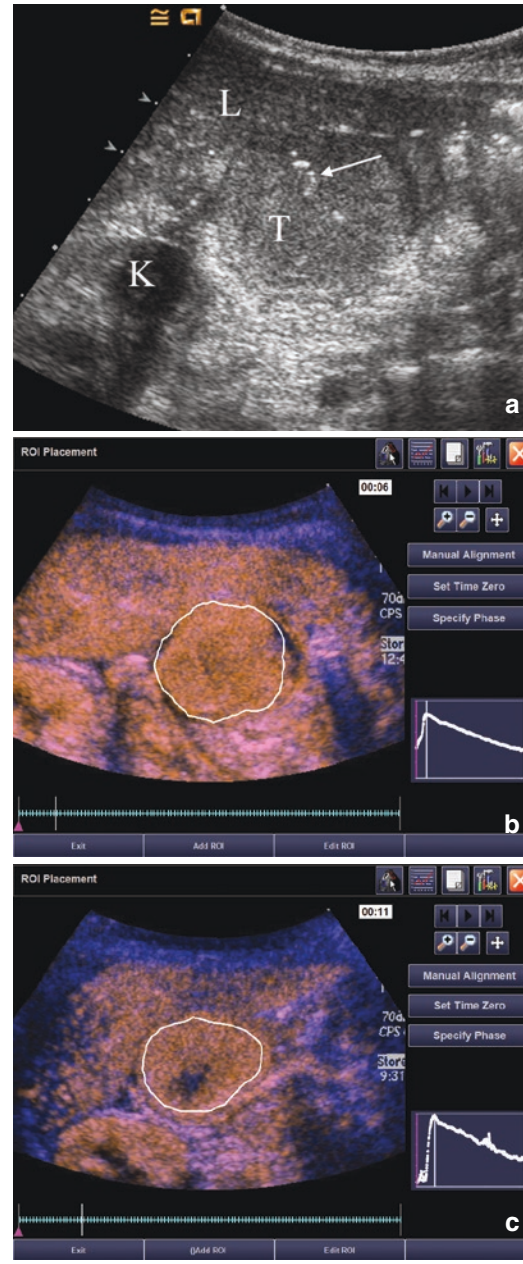

Fig. 8.11 A 21-month-old girl with recurrent rhabdoid tumor. (**a**) Transverse grayscale sonogram shows a peritoneal tumor (T) located posterior to the liver (L) and medial to the right kidney (K). Tumoral calcification (arrow) and adjacent organs were used as landmarks for transducer placement. (**b**) Baseline CEUS image with ROI inside tumor margins, obtained at PE of 33.5 dB. (**c**) Day 7 after initiation of therapy, CEUS image obtained at PE of 30.6 dB giving an 8.7% reduction compared to baseline. This subject progressed at 22 days after initiation of therapy (reprinted with permission from reference [67])

delivery and nanoscaled UCAs. Using an ultrasound pulse microbubble, UCAs can be destroyed to create micro-jets or excited to oscillate and physically massage the vascular wall to create pores in the vascular membrane. The resultant enhanced vessel permeability allows for the extravasation of co-administered drugs (indirect drug delivery). Alternatively, the microbubble shell itself can be loaded with a drug to be released during microbubble destruction which can then extravasate through the US-mediated, permeabilized vascular membrane (direct drug delivery). A limitation of this technique is the difficulty in achieving high enough doses of the therapeutic agent. The use of nanoscaled UCAs capitalizes on the fact that tumor vasculature has disorganized architecture and wider, leakier, endothelial fenestrations than normal vessels. Despite this, the relatively large UCA microbubbles cannot pass through the endothelial openings. This has led to the development of nanobubble, nanoparticle, and nanodroplet UCAs that are capable of passing through the damaged endothelium and accumulate in the extracellular space. Once in the extracellular space, they can be manipulated to coalesce and form microbubbles which can be further induced to cause tissue cavitation and to release drugs directly into the tumor. This approach could be especially advantageous in treating brain tumors by allowing the drug to pass through the blood-brain barrier. A variety of nanoscaled UCAs are currently under investigation. Although some of these agents have a short shelf life and handling difficulties, they provide promising clinical directions and exciting research opportunities [69].

8.6 Conclusions

Contrast-enhanced ultrasound is especially well suited for pediatric use because the contrast agents are safe in children, the equipment is portable, and the technique does not require prescreening laboratory testing or sedation and most importantly does not expose the patient to the harmful effects of ionizing radiation. The latter point is particularly relevant to the pediatric oncology population because these children undergo innumerable radiological examinations during diagnosis and staging, throughout treatment and during surveillance after the completion of therapy. We have presented pediatric safety data and clinical applications that support and promote the use of this modality in pediatric oncology patients. There is active ongoing research investigating the value of CEUS to quantitatively monitor the effect of therapy and as a theranostic tool in cancer treatment. We believe that these developments will significantly expand the role and increase the impact of CEUS in the management of pediatric oncology patients in the near future.

References

1. Berrington de Gonzalez A, Salotti JA, McHugh K, et al. Relationship between paediatric CT scans and subsequent risk of leukaemia and brain tumours: assessment of the impact of underlying conditions. Br J Cancer. 2016;114(4):388–94.
2. Tibussek D, Rademacher C, Caspers J, et al. Gadolinium brain deposition after macrocyclic gadolinium administration: a pediatric case-control study. Radiology. 2017;285:223.
3. Yusuf GT, Sellars ME, Deganello A, Cosgrove DO, Sidhu PS. Retrospective analysis of the safety and cost implications of pediatric contrast-enhanced ultrasound at a single center. AJR Am J Roentgenol. 2017;208(2):446–52.
4. Piskunowicz M, Kosiak W, Batko T, Piankowski A, Polczynska K, Adamkiewicz-Drozynska E. Safety of intravenous application of second-generation ultrasound contrast agent in children: prospective analysis. Ultrasound Med Biol. 2015;41(4):1095–9.
5. Coleman JL, Navid F, Furman WL, McCarville MB. Safety of ultrasound contrast agents in the pediatric oncologic population: a single-institution experience. AJR Am J Roentgenol. 2014;202(5):966–70.
6. Jacob J, Deganello A, Sellars ME, Hadzic N, Sidhu PS. Contrast enhanced ultrasound (CEUS) characterization of grey-scale sonographic indeterminate focal liver lesions in pediatric practice. Ultraschall Med. 2013;34(6):529–40.
7. Valentino M, Serra C, Pavlica P, et al. Blunt abdominal trauma: diagnostic performance of contrast-enhanced US in children--initial experience. Radiology. 2008;246(3):903–9.
8. Bonini G, Pezzotta G, Morzenti C, Agazzi R, Nani R. Contrast-enhanced ultrasound with SonoVue in the evaluation of postoperative complications in pediatric liver transplant recipients. J Ultrasound. 2007;10(2):99–106.

9. McMahon CJ, Ayres NA, Bezold LI, et al. Safety and efficacy of intravenous contrast imaging in pediatric echocardiography. Pediatr Cardiol. 2005;26(4):413–7.
10. Sidhu PS, Cantisani V, Deganello A, et al. Reply: role of contrast-enhanced ultrasound (CEUS) in paediatric practice: an EFSUMB position statement. Ultraschall Med. 2017;38:33.
11. Harkanyi Z. Potential applications of contrast-enhanced ultrasound in pediatric patients. Ultrasound Clin. 2013;2013(3):403–22.
12. Piscaglia F, Bolondi L. The safety of Sonovue in abdominal applications: retrospective analysis of 23188 investigations. Ultrasound Med Biol. 2006;32(9):1369–75.
13. McCarville MB, Kaste SC, Hoffer FA, et al. Contrast-enhanced sonography of malignant pediatric abdominal and pelvic solid tumors: preliminary safety and feasibility data. Pediatr Radiol. 2012;42(7):824–33.
14. Riccabona M. Application of a second-generation US contrast agent in infants and children--a European questionnaire-based survey. Pediatr Radiol. 2012;42(12):1471–80.
15. D'Onofrio M, Crosara S, De Robertis R, et al. Malignant focal liver lesions at contrast-enhanced ultrasonography and magnetic resonance with hepatospecific contrast agent. Ultrasound. 2014;22(2):91–8.
16. Quaia E, De Paoli L, Angileri R, Cabibbo B, Cova MA. Indeterminate solid hepatic lesions identified on non-diagnostic contrast-enhanced computed tomography: assessment of the additional diagnostic value of contrast-enhanced ultrasound in the non-cirrhotic liver. Eur J Radiol. 2014;83(3):456–62.
17. Trillaud H, Bruel JM, Valette PJ, et al. Characterization of focal liver lesions with SonoVue-enhanced sonography: international multicenter-study in comparison to CT and MRI. World J Gastroenterol. 2009;15(30):3748–56.
18. Stenzel M. Intravenous contrast-enhanced sonography in children and adolescents - a single center experience. J Ultrason. 2013;13(53):133–44.
19. Pschierer K, Grothues D, Rennert J, et al. Evaluation of the diagnostic accuracy of CEUS in children with benign and malignant liver lesions and portal vein anomalies. Clin Hemorheol Microcirc. 2015;61(2):333–45.
20. Smith EA, Salisbury S, Martin R, Towbin AJ. Incidence and etiology of new liver lesions in pediatric patients previously treated for malignancy. AJR Am J Roentgenol. 2012;199(1):186–91.
21. Dietrich CF, Maddalena ME, Cui XW, Schreiber-Dietrich D, Ignee A. Liver tumor characterization--review of the literature. Ultraschall Med. 2012;33(Suppl 1):S3–10.
22. Weinberg AG, Finegold MJ. Primary hepatic tumors of childhood. Hum Pathol. 1983;14(6):512–37.
23. Chiorean L, Cui XW, Tannapfel A, et al. Benign liver tumors in pediatric patients - review with emphasis on imaging features. World J Gastroenterol. 2015;21(28):8541–61.
24. Meyers RL. Tumors of the liver in children. Surg Oncol. 2007;16(3):195–203.
25. Yikilmaz A, George M, Lee EY. Pediatric hepatobiliary neoplasms: an overview and update. Radiol Clin North Am. 2017;55(4):741–66.
26. Roebuck DJ, Yang WT, Lam WW, Stanley P. Hepatobiliary rhabdomyosarcoma in children: diagnostic radiology. Pediatr Radiol. 1998;28(2):101–8.
27. Mork H, Ignee A, Schuessler G, Ott M, Dietrich CF. Analysis of neuroendocrine tumour metastases in the liver using contrast enhanced ultrasonography. Scand J Gastroenterol. 2007;42(5):652–62.
28. Trojan J, Hammerstingl R, Engels K, Schneider AR, Zeuzem S, Dietrich CF. Contrast-enhanced ultrasound in the diagnosis of malignant mesenchymal liver tumors. J Clin Ultrasound. 2010;38(5):227–31.
29. Liu GJ, Xu HX, Lu MD, et al. Correlation between enhancement pattern of hepatocellular carcinoma on real-time contrast-enhanced ultrasound and tumour cellular differentiation on histopathology. Br J Radiol. 2007;80(953):321–30.
30. Dietrich CF, Averkiou MA, Correas JM, Lassau N, Leen E, Piscaglia F. An EFSUMB introduction into dynamic contrast-enhanced ultrasound (DCE-US) for quantification of tumour perfusion. Ultraschall Med. 2012;33(4):344–51.
31. Al Bunni F, Deganello A, Sellars ME, Schulte KM, Al-Adnani M, Sidhu PS. Contrast-enhanced ultrasound (CEUS) appearances of an adrenal phaeochromocytoma in a child with Von Hippel-Lindau disease. J Ultrasound. 2014;17(4):307–11.
32. Ragel M, Nedumaran A, Makowska-Webb J. Prospective comparison of use of contrast-enhanced ultrasound and contrast-enhanced computed tomography in the Bosniak classification of complex renal cysts. Ultrasound. 2016;24(1):6–16.
33. Drudi FM, Valentino M, Bertolotto M, et al. CEUS time intensity curves in the differentiation between leydig cell carcinoma and seminoma: a multicenter study. Ultraschall Med. 2016;37(2):201–5.
34. Zhang Y, Luo YK, Zhang MB, Li J, Li J, Tang J. Diagnostic accuracy of contrast-enhanced ultrasound enhancement patterns for thyroid nodules. Med Sci Monit. 2016;22:4755–64.
35. Defortescu G, Cornu JN, Bejar S, et al. Diagnostic performance of contrast-enhanced ultrasonography and magnetic resonance imaging for the assessment of complex renal cysts: a prospective study. Int J Urol. 2017;24(3):184–9.
36. Wei SP, Xu CL, Zhang Q, et al. Contrast-enhanced ultrasound for differentiating benign from malignant solid small renal masses: comparison with contrast-enhanced CT. Abdom Radiol (NY). 2017;42:2135.
37. Sanz E, Hevia V, Gomez V, et al. Renal complex cystic masses: usefulness of contrast-enhanced ultrasound (CEUS) in their assessment and its agreement with computed tomography. Curr Urol Rep. 2016;17(12):89.
38. Barr RG, Peterson C, Hindi A. Evaluation of indeterminate renal masses with contrast-enhanced

US: a diagnostic performance study. Radiology. 2014;271(1):133–42.
39. Edenberg J, Gloersen K, Osman HA, Dimmen M, Berg GV. The role of contrast-enhanced ultrasound in the classification of CT-indeterminate renal lesions. Scand J Urol. 2016;50(6):445–51.
40. Putz FJ, Erlmeier A, Wiesinger I, et al. Contrast-enhanced ultrasound (CEUS) in renal imaging at an interdisciplinary ultrasound centre: possibilities of dynamic microvascularisation and perfusion. Clin Hemorheol Microcirc. 2017;66:293.
41. Liu Y, Xu Y, Cheng W, Liu X. Quantitative contrast-enhanced ultrasonography for the differential diagnosis of endometrial hyperplasia and endometrial neoplasms. Oncol Lett. 2016;12(5):3763–70.
42. Gruber L, Loizides A, Luger AK, et al. Soft-tissue tumor contrast enhancement patterns: diagnostic value and comparison between ultrasound and MRI. AJR Am J Roentgenol. 2017;208(2):393–401.
43. Guo S, Xu P, Zhou A, et al. Contrast-enhanced ultrasound differentiation between low and high-grade bladder urothelial carcinoma and correlation with tumor microvessel density. J Ultrasound Med. 2017;36:2287.
44. Cantisani V, Bertolotto M, Weskott HP, et al. Growing indications for CEUS: the kidney, testis, lymph nodes, thyroid, prostate, and small bowel. Eur J Radiol. 2015;84(9):1675–84.
45. Knieling F, Strobel D, Rompel O, et al. Spectrum, applicability and diagnostic capacity of contrast-enhanced ultrasound in pediatric patients and young adults after intravenous application - a retrospective trial. Ultraschall Med. 2016;37(6):619–26.
46. Seitz K, Strobel D. A milestone: approval of CEUS for diagnostic liver imaging in adults and children in the USA. Ultraschall Med. 2016;37(3):229–32.
47. Seitz K, Strobel D, Bernatik T, et al. Contrast-enhanced ultrasound (CEUS) for the characterization of focal liver lesions - prospective comparison in clinical practice: CEUS vs. CT (DEGUM multicenter trial). Parts of this manuscript were presented at the Ultrasound Dreilandertreffen 2008, Davos. Ultraschall Med. 2009;30(4):383–9.
48. Mori N, Mugikura S, Takahashi S, et al. Quantitative analysis of contrast-enhanced ultrasound imaging in invasive breast cancer: a novel technique to obtain histopathologic information of microvessel density. Ultrasound Med Biol. 2017;43(3):607–14.
49. Tai CJ, Huang MT, Wu CH, et al. Contrast-enhanced ultrasound and computed tomography assessment of hepatocellular carcinoma after transcatheter arterial chemo-embolization: a systematic review. J Gastrointestin Liver Dis. 2016;25(4):499–507.
50. Ishii T, Numata K, Hao Y, et al. Evaluation of hepatocellular carcinoma tumor vascularity using contrast-enhanced ultrasonography as a predictor for local recurrence following radiofrequency ablation. Eur J Radiol. 2017;89:234–41.
51. Bartolotta TV, Taibbi A, Picone D, Anastasi A, Midiri M, Lagalla R. Detection of liver metastases in cancer patients with geographic fatty infiltration of the liver: the added value of contrast-enhanced sonography. Ultrasonography. 2017;36(2):160–9.
52. Pandey P, Lewis H, Pandey A, et al. Updates in hepatic oncology imaging. Surg Oncol. 2017;26(2):195–206.
53. Granata V, Fusco R, Catalano O, et al. Diagnostic accuracy of magnetic resonance, computed tomography and contrast enhanced ultrasound in radiological multimodality assessment of peribiliary liver metastases. PLoS One. 2017;12(6):e0179951.
54. Maj E, Papiernik D, Wietrzyk J. Antiangiogenic cancer treatment: the great discovery and greater complexity (Review). Int J Oncol. 2016;49(5):1773–84.
55. Hendry SA, Farnsworth RH, Solomon B, Achen MG, Stacker SA, Fox SB. The role of the tumor vasculature in the host immune response: implications for therapeutic strategies targeting the tumor microenvironment. Front Immunol. 2016;7:621.
56. Lee SC, Grant E, Sheth P, et al. Accuracy of contrast-enhanced ultrasound compared with magnetic resonance imaging in assessing the tumor response after neoadjuvant chemotherapy for breast cancer. J Ultrasound Med. 2017;36(5):901–11.
57. Lassau N, Bonastre J, Kind M, et al. Validation of dynamic contrast-enhanced ultrasound in predicting outcomes of antiangiogenic therapy for solid tumors: the French multicenter support for innovative and expensive techniques study. Invest Radiol. 2014;49(12):794–800.
58. Atri M, Hudson JM, Sinaei M, et al. Impact of acquisition method and region of interest placement on inter-observer agreement and measurement of tumor response to targeted therapy using dynamic contrast-enhanced ultrasound. Ultrasound Med Biol. 2016;42(3):763–8.
59. Amioka A, Masumoto N, Gouda N, et al. Ability of contrast-enhanced ultrasonography to determine clinical responses of breast cancer to neoadjuvant chemotherapy. Jpn J Clin Oncol. 2016;46(4):303–9.
60. Saracco A, Szabo BK, Tanczos E, Bergh J, Hatschek T. Contrast-enhanced ultrasound (CEUS) in assessing early response among patients with invasive breast cancer undergoing neoadjuvant chemotherapy. Acta Radiol. 2017;58(4):394–402.
61. Matsui S, Kudo M, Kitano M, Asakuma Y. Evaluation of the response to chemotherapy in advanced gastric cancer by contrast-enhanced harmonic EUS. Hepatogastroenterology. 2015;62(139):595–8.
62. Peng C, Liu LZ, Zheng W, et al. Can quantitative contrast-enhanced ultrasonography predict cervical tumor response to neoadjuvant chemotherapy? Eur J Radiol. 2016;85(11):2111–8.
63. Jia WR, Tang L, Wang DB, et al. Three-dimensional contrast-enhanced ultrasound in response assessment for breast cancer: a comparison with dynamic contrast-enhanced magnetic resonance imaging and pathology. Sci Rep. 2016;6:33832.
64. Ohno N, Miyati T, Yamashita M, Narikawa M. Quantitative assessment of tissue perfusion in

hepatocellular carcinoma using perflubutane dynamic contrast-enhanced ultrasonography: a preliminary study. Diagnostics. 2015;5(2):210–8.
65. Mogensen MB, Hansen ML, Henriksen BM, et al. Dynamic contrast-enhanced ultrasound of colorectal liver metastases as an imaging modality for early response prediction to chemotherapy. Diagnostics. 2017;7(2)
66. Wu Z, Yang X, Chen L, et al. Anti-angiogenic therapy with contrast-enhanced ultrasound in colorectal cancer patients with liver metastasis. Medicine. 2017;96(20):e6731.
67. McCarville MB, Coleman JL, Guo J, et al. Use of quantitative dynamic contrast-enhanced ultrasound to assess response to antiangiogenic therapy in children and adolescents with solid malignancies: a pilot study. AJR Am J Roentgenol. 2016;206(5):933–9.
68. Ueda N, Nagira H, Sannomiya N, et al. Contrast-enhanced ultrasonography in evaluation of the therapeutic effect of chemotherapy for patients with liver metastases. Yonago Acta Med. 2016;59(4):255–61.
69. Guvener N, Appold L, de Lorenzi F, et al. Recent advances in ultrasound-based diagnosis and therapy with micro- and nanometer-sized formulations. Methods. 2017;130:4.

9 Tumor Response Assessment: RECIST and Beyond

Kieran McHugh and Simon Kao

9.1 Introduction

Objective assessment of the change in tumor burden and size is known to be important for evaluating the response of tumors to anticancer drugs and is generally regarded as a surrogate for symptomatic response. In addition, objective response has been shown to be closely correlated with prolonged survival in adult patients with solid tumors. To quote from Eisenhauer et al., 'agents which produce tumor shrinkage in a proportion of patients have a reasonable (albeit imperfect) chance of subsequently demonstrating an improvement in overall survival or other time to event measures in randomised phase III studies' [1]. Despite the increasing number of functional imaging techniques at our disposal today, the use of objective response based on change in tumor size is supported by a body of evidence greater than any other biomarker. The Response Evaluation Criteria in Solid Tumors (RECIST) guidance was introduced in 2000 [2] and later became known as RECIST version 1.0 in 2009 [1]. RECIST was put together by a task force set up by the European Organization for Research and Treatment of Cancer (EORTC), the National Cancer Institute of the United States, and the National Cancer Institute of Canada, with the goal of standardising and simplifying tumor response criteria. The important role of imaging in response assessment was recognised, and specific imaging guidelines were included.

The key features of RECIST 1.0 (Table 9.1) included definition of minimum size of measurable lesions on computed tomography (CT), instructions on how many lesions to follow (then up to 10, with a maximum of 5 lesions per organ), and the use of unidimensional CT measures for overall evaluation of tumor burden [2, 3] (Fig. 9.1). RECIST rapidly became accepted in adult oncology practice as the standard measure of tumor response, especially in clinical trials where the primary end points were objective response or time to progression. However, over the subsequent decade, limitations with the universal application of RECIST 1.0 to all tumor types, and other technological developments such as multi-detector CT (MDCT) and positron emission tomography-CT (PET/CT), pointed to a need for further revisions to the original RECIST criteria.

In January 2009, a revised RECIST guideline (version 1.1, Table 9.1) was published by the RECIST working group, based in part on

K. McHugh (✉)
Radiology Department, Great Ormond Street Hospital for Children, London, UK
e-mail: Kieran.McHugh@gosh.nhs.uk

S. Kao
Department of Radiology, Carver College of Medicine, The University of Iowa, Iowa City, IA, USA
e-mail: simon-kao@uiowa.edu

S. D. Voss, K. McHugh (eds.), *Imaging in Pediatric Oncology*, Pediatric Oncology,
https://doi.org/10.1007/978-3-030-03777-2_9

Table 9.1 Comparison of WHO, RECIST, and RECIST 1.1 response criteria

Characteristics	WHO 1976	RECIST 2000	RECIST 1.1 2009
Lesion measurability LD = longest diameter CT = computed tomography	1. *Measurable*: bidirectional (product of LD and largest perpendicular diameter) 2. *Non-measurable* (such as pulmonary lymphangitic metastases)	1. *Measurable*: unidimensional (LD only: size ≥20 mm with conventional CT and ≥10 mm for spiral CT) 2. *Non-measurable*: all other lesions, such as small lesions; not recommended to be evaluable	1. *Measurable*: unidimensional (LD only, size ≥20 mm with conventional CT and ≥10 mm for spiral CT; lymph nodes, target short axis ≥15 mm, non-target 10–15 mm, and normal <10 mm) 2. *Non-measurable*: all other lesions, such as small lesions; not recommended to be evaluable
Objective response **CR** = complete response **PR** = partial response **PD** = progressive disease **SD** = stable disease **NC** = no change **PET** = positron emission tomography	1. *Measurable* (change in sum of products of LD and largest perpendicular diameters without specifying maximal number of lesions): **CR** = disappearance of all known disease, confirmed at ≥4 weeks **PR** = ≥50% decrease from baseline, confirmed at ≥4 weeks **PD** = 25% increase of one or more lesions or appearance of new lesion **NC** = neither PR nor PD 2. *Non-measurable*: **CR** = disappearance of all known disease, confirmed at ≥4 weeks **PR** = estimated decrease of ≥50%, confirmed at ≥4 weeks **PD** = estimated increase of ≥25% or appearance of new lesion **NC** = neither PR nor PD	*Target* lesions (change in sum of LD, maximum of 5 per organ and up to 10 total (multi-organ)): **CR** = disappearance of all target lesions, confirmed at ≥4 weeks **PR** = ≥30% decrease from baseline, confirmed at ≥4 weeks **PD** = ≥20% increase over smallest sum observed or appearance of new lesion **SD** = neither PR nor PD 2. *Non-target* lesions: **CR** = disappearance of all non-target lesions and normalisation of tumor markers, confirmed at ≥4 weeks **PD** = unequivocal progression of non-target lesions or appearance of new lesion **Non-PD** = persistence of one or more non-target lesions or tumor markers above normal limit	*Target* lesions (change in sum of LD, maximum of 2 per organ and up to 5 total (multi-organ)): **CR** = disappearance of all target lesions, confirmed at ≥4 weeks **PR** = ≥30% decrease from baseline, confirmed at 4 weeks **PD** = ≥20% increase over smallest sum observed and over 5 mm net increase or appearance of new lesion **SD** = neither PR nor PD 2. *Non-target* lesions: **CR** = disappearance of all non-target lesions and normalisation of tumor markers, confirmed at ≥4 weeks **PD** = unequivocal progression of non-target lesions or appearance of new lesion; must be unequivocal; can be new PET+ve scan with confirmed anatomic progression. Stable PET+ve is not PD if it corresponds to anatomic non-PD **Non-PD** = persistence of one or more non-target lesions or tumor markers above normal limit
Overall response	1. Best response is recorded in measurable disease 2. NC in non-measurable lesions will make CR in measurable lesions to overall PR 3. NC in non-measurable lesions will not reduce PR in measurable lesions	1. Best response is recorded in measurable disease from start of treatment to recurrence or progression of disease 2. Non-PD in non-target lesions will reduce CR in target lesions to overall PR 3. Non-PD in non-target lesions will not reduce PR in target lesions 4. Unequivocal new lesions are PD regardless of response in target and non-target lesions	1. Best response is recorded in measurable disease from start of treatment to recurrence or progression of disease 2. Non-PD in non-target lesions will reduce CR in target lesions to overall PR 3. Non-PD in non-target lesions will not reduce PR in target lesions 4. Unequivocal new lesions are PD regardless of response in target and non-target lesions

(continued)

Table 9.1 (continued)

Duration of response	1. CR: from date CR are first met to date PD is first noted 2. Overall response: from date of start of treatment to date PD is first noted 3. In patients achieving only PR, only period of overall response is recorded	1. Overall CR: from date CR first met to date recurrence first noted 2. Overall response: from date of CR or PR first met (whichever comes first) to date of recurrence first noted 3. SD: from date of start of treatment to date PD first noted	1. Overall CR: from date CR first met to date recurrence first noted 2. Overall response: from date of CR or PR first met (whichever comes first) to date of recurrence first noted 3. SD: from date of start of treatment to date PD first noted

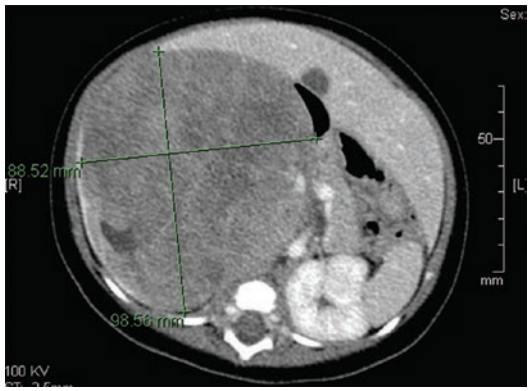

Fig. 9.1 Axial CT section post-intravenous contrast enhancement through the mid-abdomen in a 1-year-old child shows a large right renal tumor which turned out to be an intra-renal neuroblastoma at histopathology. The lesion has been measured in its longest axial diameter (anteroposterior in this case, as per RECIST), and to illustrate the old WHO lesion area approach, a second caliper at right angles to the first (transverse here) is also included. Measurement in the *Z* (cranio-caudal) axis was not included in RECIST 1.0, but is allowed in RECIST 1.1. It is good practice to select the image which was chosen to be representative of a tumor's maximal diameter with calipers added and archive this image to PACS. This archived image then aids the next reporting radiologist to know at what level to measure the tumor at follow-up. The RECIST guidance recommends the same cross-sectional imaging modality should be used for all follow-ups, although this can be impractical in children (CT at diagnosis followed by MRI later can in reality be acceptable)

investigations using a database consisting of more than 6500 patients with more than 18,000 target lesions [1, 3]. The significant imaging-related changes in RECIST 1.1 in comparison to RECIST 1.0 included a reduction in the number of lesions to be addressed, from a maximum of 10 to a maximum of 5 and from 5 lesions per organ to 2 per organ; assessment of lymph node size (lymph nodes ≥15 mm in short axis are considered abnormal and measurable and evaluable as target lesions; and the lymph node's short axis measurement should be included in the sum of lesions in the calculation of tumor response); clarification of what constituted disease progression (in addition to a 20% increase in unidimensional measurement, a 5 mm absolute increase is now required as a minimum); and inclusion of FDG PET/CT assessment exclusively in the section on detection of new lesions [1].

The RECIST guidelines were originally formulated to simplify and document change in tumor size and to monitor treatment response in oncological imaging [1]. Prior to RECIST 1.0, the World Health Organisation (WHO), in its 1979 WHO handbook, recommended the use of four specific criteria (Table 9.1) for the codification of response evaluation in solid tumors [4, 5]. These categories, namely, complete response (CR), partial response (PR), stable disease (SD) (also termed 'no change', NC), and progressive disease (PD), came to be used widely both in adult and paediatric oncology practice. However, the WHO criteria did not address the minimal lesion size, the number of lesions to be measured in patients with multiple lesions, and the type of imaging modality to be utilised. The WHO response categories have been retained with the RECIST criteria. However, in order to appreciate the evolution in tumor response criteria that has taken place over the past four decades, it is important to note four major problems with the WHO classifications of response that had become apparent

over time: (1) methods of integrating the change in tumor size into response assessments varied between research groups; (2) the minimum lesion size and number of lesions to be documented varied both between studies and reviewers; (3) disease progression was based on the change in size of a single lesion by some authors and a change in the overall tumor burden, including measurements of all lesions, by others; and (4) new technologies, notably CT and magnetic resonance imaging (MRI), further complicated matters with regard to the relevance of volumetric and 3D measurements in response assessments [2]. Consequently, a situation arose whereby the WHO response criteria were no longer comparable between research organisations—the very circumstance that the original WHO publication had set out to avoid [2]. To address these limitations in the WHO criteria, the international RECIST working group convened and developed a set of new guidelines presented as RECIST 1.0. The RECIST guidelines originally came in two parts: the RECIST definitions of response and associated guidance on imaging techniques (Table 9.1). RECIST 1.0 relied heavily on repeated CT, which was worrisome from a paediatric perspective, in part because of concerns that frequent CT scanning carries an increased radiation burden and also because some paediatric solid tumors (e.g. soft tissue sarcomas) are better evaluated by MRI [6, 7]. With RECIST 1.1, this problem has been addressed as good quality multiplanar MRI is permitted within RECIST 1.1 and this guidance now also allows tumor assessment in any plane. The single longest diameter (LD) can be taken from any orthogonal plane on CT or MRI, but it is important that this same plane and imaging modality should also be used for later response assessment whenever possible [1, 5], noting that the longest diameter of the lesion should always be measured even if the actual axis differs from the one used to measure the lesion at baseline (e.g. AP/oblique vs. AP at baseline).

While the four categories of response assessment were retained within RECIST 1.0 and 1.1, there has been slight alteration in their determination [8]. CR and SD remain essentially the same under RECIST as with the older WHO system. It was agreed that no major difference in the meaning and the concept of partial response (PR) should exist between the old and the new guidelines, but measurement criteria would be different [1, 2, 9]. To achieve PR, the RECIST guidelines require that at least a 30% decrease in the sum of the longest diameters must be evident. This is roughly equivalent to the previous WHO 50% reduction in the product of the two maximal perpendicular diameters [1, 9]. These criteria are equivalent if one assumes tumors have a spherical shape and that the longest diameter (LD) and the diameter perpendicular to the LD (although the latter was not measured in the original RECIST assessment) both decrease by at least 30% [10]. The only truly significant change in definition has occurred with the progressive disease (PD) category in that greater volume increases are necessary to establish disease progression, in comparison to the old WHO recommendations. RECIST 1.1 requires a 20% increase in longest dimension for a single lesion or in the sum of the LDs of multiple masses to establish PD. An absolute increase in target lesion size of ≥5 mm is now required to avoid small changes in size of very small lesions being over-interpreted as disease progression. The need for greater tumor burden to define PD came about as concerns had been raised regarding the ease with which a patient could have been mistakenly considered to have disease progression by the WHO criteria. Furthermore, incorrectly designating a patient as having PD could also lead to the inappropriate cessation of a treatment that was having an anticancer effect.

9.2 Definitions Within RECIST

The RECIST guidelines define in detail whether tumour lesions should be classified as *measurable* or *non-measurable*, *target* or *non-target* lesions (Table 9.1). These concepts and terms were new to imaging in paediatric oncology in the year 2000 [6, 7]. They had greatest applicability in the setting of adult phase II clinical trials in metastatic malignancies but are now widely employed in many pharmaceutically sponsored phase I, II, and III oncologic trials in children. A *measurable* lesion is defined as one that can be accurately and reproducibly measured in at least one dimension and measures 10 mm or more on CT or MRI. *Non-measurable* lesions are lesions

smaller than 10 mm, as well as bone metastases, leptomeningeal secondaries, malignant ascites, pleural or pericardial effusions, and lymphatic spread, all of which are termed 'truly' *non-measurable* [2]. Lesions in bone are generally considered *non-measurable* unless there is an associated soft tissue mass (>1 cm in diameter).

In RECIST 1.0, cystic lesions were considered non-measurable, which posed a big problem in paediatric oncology [6, 7]. Many solid tumors in children are cystic or necrotic at first presentation, and these apparently necrotic masses do frequently shrink with chemotherapy. These necrotic masses are probably pseudo-necrotic, accounting for their change in response to treatment. Cystic lesions if >1 cm are considered measurable in RECIST 1.1, although if non-cystic (thus more solid) lesions or metastases are present in the same patient, these are preferred for selection as target lesions.

After establishing that measurable disease is present, it is necessary to document *target* and *non-target* lesions. Up to five measurable lesions per organ and ten measurable lesions in total, representative of all involved organs, were originally required as *target* lesions within RECIST 1.0. In RECIST 1.1, only five lesions in total and two per organ system are now required to characterise measurable disease. The sum of the diameter of all *target* lesions constitutes the 'baseline sum longest diameter'. All other lesions (or sites of disease) should be identified as *non-target* lesions and should also be recorded at baseline. Measurements of these non-target lesions are not required, but their presence or absence should be noted and documented throughout follow-up. *Non-target* lesions may therefore be in the *measurable* (>10 mm) or in the *non-measurable* range. Pathological nodes of insufficient size to be defined as target lesions, which thus measure ≥10 mm but <15 mm in short axis, are considered non-target lesions.

CR and SD designations are possible with both *non-target* and *target* lesions. As an entity, PR with *non-target* lesions is not possible because they are not measured. However, PD may be documented—if one or more new lesions are seen or if there is an unequivocal progression of existing *non-target* lesions with a minimum absolute size increase of 5 mm (Table 9.1).

9.2.1 RECIST and Paediatric Solid Tumors

Paediatric oncology trials have traditionally used three-dimensional volumetric assessments for tumor response evaluation. However, nowadays most, if not all, pharma-sponsored phase I–III trials have switched to the RECIST criteria. In addition, there has been some limited research into the applicability of RECIST in paediatric tumors [11–13]. In all three papers, two studying rhabdomyosarcomas and one neuroblastoma, one-dimensional assessments were equivalent to three-dimensional (volumetric) tumor response assessments with no method clearly superior to the other. In the next iteration of the International Neuroblastoma Response Criteria (INRC), the formal recommendations will include adopting RECIST 1.1 for neuroblastoma tumor response assessments, thus abandoning the need for 3D volumetric evaluations of the tumor mass or masses at each time point. It is also very likely that for the next European pediatric Soft Tissue Sarcoma (EpSSG) trial, a similar recommendation to switch to the simpler RECIST guidelines will be made also.

To better understand the RECIST guidelines in paediatric drug development, Carceller et al. evaluated a cohort of 61 children and adolescents treated in 11 phase I trials from 2006 to 2015 in two paediatric and adolescent drug development units [14]. This group demonstrated that the degree of radiological response assessed according to RECIST correlated with the overall survival (OS), which is as anticipated. More importantly those patients who achieved disease stabilisation, which historically had not been considered as an objective criteria of response, also had a survival advantage [14]. As most targeted therapies being tested nowadays have a cytostatic rather than a cytotoxic effect, this finding is relevant as it supports the hypothesis that cessation of tumor growth is also associated with improved survival. Therefore sustained disease stabilisation should also be considered evidence of both pharmacologic and antitumor activity in early phase trials of targeted agents in children. For these reasons the immune response criteria mentioned below are more relevant to the newer targeted therapies.

In a more recent retrospective study aimed at assessing response to therapy in primary Ewing sarcoma [15], authors compared the agreement of three-dimensional (3D) measurements (using manual tracing of tumor perimeters) to the Children's Oncology Group (COG) (3D measurements taking into account all diameters in *x*, *y*, and *z* axes), the RECIST (longest diameter only), and WHO (taking into account the *x* and *y* axes only) criteria. It was found that the agreement with the reference standard (by 3D using manual trace method) was significantly better using COG (3D) than for RECIST (1D) and WHO (2D) measurements on the basis of therapeutic thresholds. Moreover, higher dimensional measurements were significantly better predictors of overall survival. Whether this conclusion and the additional time and effort required for accurate 3D measurements can or should be applied to other paediatric tumor types remains to be studied.

9.2.2 Other Tumor Response Criteria

RECIST was never intended to be used for response evaluation in malignant brain tumors or for lymphomas [1]. There are adult and paediatric neuro-oncology response criteria and also recently revised adult and paediatric lymphoma response assessments [16–19]. The ongoing development of the Response Assessment in Pediatric Neuro-Oncology (RAPNO) criteria illustrates the efforts being made to address some of the unique issues relating to radiological response assessment of brain tumors in children [17]. Non-Hodgkin lymphoma (NHL) in children and adolescents involves different histologies, dissimilar primary sites of disease, patterns of metastatic spread, approaches to therapy, and responses to treatment compared with adult NHL [19]. International paediatric NHL response criteria were developed with the goal of incorporating both contemporary diagnostic imaging and pathology techniques, including novel molecular and flow cytometric technologies used for the determination of minimal residual disease (MRD), as MRD is essentially beyond the resolution of standard diagnostic radiologic techniques. The PET response criteria in solid tumors (PERCIST, Table 9.2) and the Lugano classification for adult lymphoma are now well established, and both incorporate data from PET studies as the basis for response evaluation [18, 20]. Detailed description regarding

Table 9.2 PET response criteria in solid tumors (PERCIST 1.0)

Characteristics	PERCIST 1.0 2009
Lesion measurability at baseline SUL = SUV normalised to lean body mass TLG = total lesion glycolysis	1. *Measurable*: *target* lesion refers to the hottest single tumor lesion SUL of maximal 1.2 cm diameter volume ROI in tumor (SUL peak). SUL peak is ≥1.5× greater than liver SUL mean + 2 SDs (in 3 cm spherical ROI in normal right lobe of the liver). If the liver is abnormal, primary tumor should have >2× SUL mean of blood pool in a 1 cm diameter ROI in descending thoracic aorta over 2 cm *z*-axis 2. Tumor with maximal SUL peak is assessed after treatment. Although this is typically in the same region of tumor as that of the highest SUL peak at baseline, it need not be 3. Uptake measurements should be made for the peak and maximal single-voxel tumor SUL. Other SUV metrics, including SUL mean at 50% or 70% of SUV peak, can be collected as exploratory data. TLG can be collected ideally on basis of voxels more intense than 2 SDs above the liver mean SUL (see below) 4. These parameters can be recorded as exploratory data on up to five measurable target lesions (typically the five hottest lesions), which are typically the largest, and no more than 2 per organ. Tumor size of these lesions is determined by RECIST 1.1
Uptake normalisation	Normal liver SUL must be within 20% (and <0.3 SUL mean units) for baseline and follow-up study to be assessable. If the liver is abnormal, blood-pool SUL must be within 20% (and <0.3 SUL mean units) for baseline and follow-up study to be assessable. Uptake time of baseline study and follow-up study 2 must be within 15 min of each other to be assessable. Typically, these are ≥60 min after injection but not <50 min after injection. The same scanner, or the same scanner model at the same site, injected dose, acquisition protocol (two- vs. three-dimensional), and software for reconstruction should be used. Scanners should provide reproducible data and be properly calibrated

Table 9.2 (continued)

Objective response **CMR** = complete metabolic response **PMR** = partial metabolic response **SMD** = stable metabolic disease **PMD** = progressive metabolic disease **CR** = complete remission **PR** = partial remission **PD** = progressive disease **NC** = no change	**CMR** = complete resolution of 18-F-FDG uptake within measurable target lesion so that it is less than liver activity and indistinguishable from surrounding background blood-pool levels. Disappearance of all other lesions to background blood-pool levels. % decline in SUL should be recorded from measurable region, as well as time in weeks after treatment was begun. No new 18-F-FDG-avid lesions in pattern typical of cancer. If progression by RECIST, must verify with follow-up **PMR** = at least 30% decrease in measurable target tumor 18-F-FDG SUL peak. Absolute decrease in SUL must be at least 0.8 SUL units as well. Measurement is commonly in the same lesion as baseline but can be another lesion if that lesion was previously present and is the most active lesion after therapy. ROI is usually in the same area as baseline. No more than 30% increase in SUL or size of target or non-target lesions. Reduction in extent of tumor uptake is not a requirement for PMR. Percentage decline in SUL should be recorded as well as time in weeks after therapy was begun. No new lesions **SMD** = not CMR, PMR, or PMD. Record SUL peak in metabolic target lesion and time from start of therapy **PMD** = >30% increase in 18-F-FDG SUL peak, with >0.8 SUL unit increase in tumor SUV peak from baseline scan in pattern typical of tumor and not of infection or therapy effect, *or* visible increase in extent of 18-F-FDG tumor uptake (75% in TLG volume with no decline in SUV), *or* new 18-F-FDG-avid lesions that are typical of cancer and not related to therapy effect or infection. PMD other than new visceral lesions should be confirmed on follow-up study within 1 month unless PMD also is clearly associated with progressive disease by RECIST 1.1. PMD should be reported to include % change in SUV peak, time after therapy, whether new lesions are present/absent, and their number. Because SUL is a continuous variable, dividing response criteria also limited number of somewhat arbitrary response categories loses much data. For this reason, PERCIST preserves % declines in SUV peak in each reported category. Because rapidity with which scan normalises is important, PERCIST asks for time from start of therapy as part of reporting. More than one measurement of PET response may be needed at different times, and it may be treatment type-dependent. PERCIST 1.0 evaluates SUL peak of only the hottest tumor. This is a possible limitation of approach, but lesions and their responses are highly correlated, in general. Additional data are required to determine how many lesions should be assessed over 1. A suggested option is to include the five hottest lesions or the five observed on RECIST 1.1 that are most measurable. % change in SUL can be reported for single lesion with largest increase in uptake or smallest decline in uptake. Additional studies will be needed to define how many lesions are optimal for assessment *Non-target* lesions: **CMR** = disappearance of all 18-F-FDG-avid lesions, **PMD** = unequivocal progression of 18-F-FDG-avid non-target lesions or appearance of new 18-F-FDG-avid lesions typical of cancer, **non-PMD** = persistence of one or more non-target lesions or tumor markers above normal limits
Overall response	1. Best response is recorded in measurable disease from start of treatment to recurrence or progression of disease 2. Non-PMD in measurable or non-measurable non-target lesions will reduce CR in target lesions to overall PMR 3. Non-PMD in non-target lesions will not reduce PR in target lesions
Duration of response	1. Overall CMR: from date CMR criteria first met to date recurrence first noted 2. Overall response: from date of CMR or PMR first met (whichever come first) to date of recurrence first noted 3. SMD: from date of start of treatment to date PMD first noted

response criteria for both NHL and Hodgkin lymphoma is beyond the scope of this chapter. Readers can refer to references included here [21–23]. Other response criteria relating to adult cancers also exist. Gastrointestinal stromal tumors (GISTs) do occur rarely in children. The Choi criteria (Table 9.3) for adult GISTs rely on repeated CT to assess tumor density and size [19, 20]. This poses many problems for paediatric GIST patients as these are typically indolent tumors and MRI or contrast-enhanced ultrasound (CEUS) may be a better alternative in young patients [24–26]. Modifications of Choi criteria have also been proposed in adult metastatic renal cell carcinomas to take into account size and CT attenuation changes after therapy [27–29], such as SACT criteria [27]

Table 9.3 Choi tumor response criteria in gastrointestinal stromal tumors (GISTs) based on CT

Response	Choi 2007
Complete response (CR)	Disappearance of all target lesions, no new lesions
Partial response (PR)	≥10% decrease in tumor size or ≥15% decrease in tumor attenuation (Hounsfield Units) at CT; no new lesions; no obvious progression of non-measurable disease
Progressive disease (PD)	≥10% increase in sum of longest diameter (SLD) of lesions, does not meet the criteria for PR by virtue of tumor attenuation (HU), new intratumoural nodules, or an increase in the size of existing intratumoral nodules
Stable disease (SD)	None of the above; no symptomatic deterioration attributed to tumor progression

and the MASS criteria [28]. However, these criteria have not been studied in children, and the repeated use of CT for ongoing response assessment may be problematic, particularly when other imaging methodologies exist.

9.2.3 Immune Response Assessment and iRECIST

In recent years there has been a paradigm shift towards biology-driven early clinical trials with molecularly targeted agents [30]. As a result of this, biomarkers (which can be predictive, prognostic, or pharmacodynamic) have become an indispensable part of drug development. RECIST does not take into account the mechanism of action and therapeutic intent for many of these newer anticancer agents, particularly the targeted non-cytotoxic drugs, whose main aim may be to provide improved survival via prolonged stable disease. For example, with new immunotherapeutic agents, SD is viewed as a meaningful therapeutic effect [31]. In studies with cytokines, cancer vaccines, and monoclonal antibodies (such as ipilimumab for melanoma), CR, PR, and SD have been seen to occur after an initial increase in tumor burden, an increase that would be incorrectly designated as PD by RECIST. The apparent increases in tumor burden that sometimes precede responses in patients receiving immune therapy may result from either continued tumor growth until a sufficient tumor response develops or transient immune-cell infiltrate with or without oedema. Examination of tumor biopsies from ipilimumab-treated patients with radiographic PD before response is consistent with both hypotheses [32, 33]. T-cell infiltration into radiographically undetectable lesions may easily be misinterpreted as PD due to the development of small new lesions (tumor flare reaction). This so-called pseudoprogression with immune therapies is now well recognised such that separate immune-related response criteria (irRECIST and iRECIST) have been developed [31, 34]. With regard to immune therapies, these points are worth noting: (a) measurable antitumor activity may take longer to achieve than for cytotoxic therapies; (b) responses to immune therapies may occur after apparent radiographic PD; (c) discontinuation of immune therapies after initial progression may be inappropriate; (d) insignificant PD with a few new small lesions may also occur; and (e) durable SD represents antitumor activity [31].

Of note also, the initial immune response criteria (irRC) had reverted to measuring tumor area similar to the old WHO approach [31]. However, a recent update by Seymour et al. has been published as consensus guidelines—iRECIST—by the RECIST working group [34]. This is in effect a modified RECIST 1.1 for immune-based therapeutics. Their approach again utilises unidimensional measurements of tumor size, and this method is likely to be adopted into most new pharmaceutical trials involving immunotherapeutic agents in the future [34]. According to Seymour et al., the earlier irRECIST had not been consistently applied leading to concerns regarding the comparability of data and results across trials [34]. Because of the need to standardise and validate response criteria, the RECIST working group put together a committee of clinical, statistical, and imaging experts in methodology and immunotherapeutics, representatives from pharmaceutical companies developing immunotherapeutics, and key regulatory

authorities. The major change to iRECIST is aimed at dealing with the possibility of pseudoprogression and the concept of resetting the bar if what appears to be progression by RECIST 1.1 is followed at the next assessment by tumor shrinkage. This approach allows atypical responses, such as delayed responses that occur after pseudoprogression, to be identified. It should be noted, however, that most patients being treated with these new agents have considerable disease burdens refractory to conventional therapies. As a result, most of the apparent episodes of progression with immunotherapies still represent actual PD, with pseudoprogression occurring in a minority (approximately 10%) of the patients.

iRECIST now incorporates a category of unconfirmed progressive disease (iUPD). Responses assigned using iRECIST have a prefix 'i' (for immune) [34]. Thus there is immune complete response (iCR), partial response (iPR), and confirmed progressive disease (iCPD). iRECIST defines iUPD on the basis of RECIST 1.1 principles. However, iUPD requires confirmation of disease progression, which may happen at the next assessment with either a further increase in size of the lesion category measured, with a minimum size increase of 5 mm, or further new lesions elsewhere, indicating that iCPD has occurred [34]. If progression is not confirmed at the next assessment, however, but instead tumor shrinkage occurs (compared with baseline), then either iCR, iPR, or iSD are possible, and, assuming the patient remains well, the patient would continue to take that particular immunotherapeutic agent. Finally, iUPD can be assigned multiple times during treatment as long as iCPD is not confirmed at the next assessment [34].

9.2.4 Limitations to RECIST

Some weaknesses inherent to RECIST have already been mentioned. As tumor response is only assessed via anatomical imaging, RECIST has many limitations. Situations exist in paediatrics where no tumour shrinkage may be evident on radiological follow-up but a clear histological response can be seen, e.g. ganglioneuromatous change in neuroblastoma or rhabdomyomatous change in bilateral Wilms tumour. In one Wilms tumor study, a volume change following preoperative chemotherapy did not correlate with histopathological risk group [35]. It is well recognised that changes in tumor cellularity as measured by differences in diffusion restriction on follow-up MRI can occur without a corresponding change in tumor size. Conversely, tumour progression can be inferred when a rise in a serum tumour marker occurs, e.g. rising alpha-foetoprotein levels in a child with a teratoma or hepatoblastoma, possibly with no objective evidence on imaging of tumour size change.

RECIST does not take functional imaging into account. Functional imaging, however, is now seen as a useful tool in the pipeline of drug development that can inform on the mechanism of drug action (Fig. 9.2), early treatment response, potentially the prediction of treatment outcomes, and disease prognostication [37]. It is becoming increasingly clear from nuclear medicine functional imaging, notably positron emission tomography (PET), that metabolic and physiologic changes antecede tumour size change [38]. Hence responses based on changes in FDG uptake as measured by either PET/CT or PET/MRI may be a better surrogate for assessing treatment efficacy than making complex tumour volume measurements. In addition, functional imaging will increasingly have a role in quantitating drug effects on tumor perfusion, cellularity, hypoxia, and metabolism. Although RECIST does not account for the contribution of functional imaging techniques in staging and response assessment for most paediatric malignancies (the criteria are primarily concerned with tumour size change), metaiodobenzylguanidine (MIBG) scintigraphy, for example, remains crucial for accurate staging and assessment of response in metastatic neuroblastoma for the foreseeable future and is used in concert with RECIST criteria for characterising response to treatment in neuroblastoma [39].

Current RECIST guidelines state that the frequency of tumour re-evaluation while on treatment should be protocol specific and adapted to the type and schedule of treatment [1]. Although

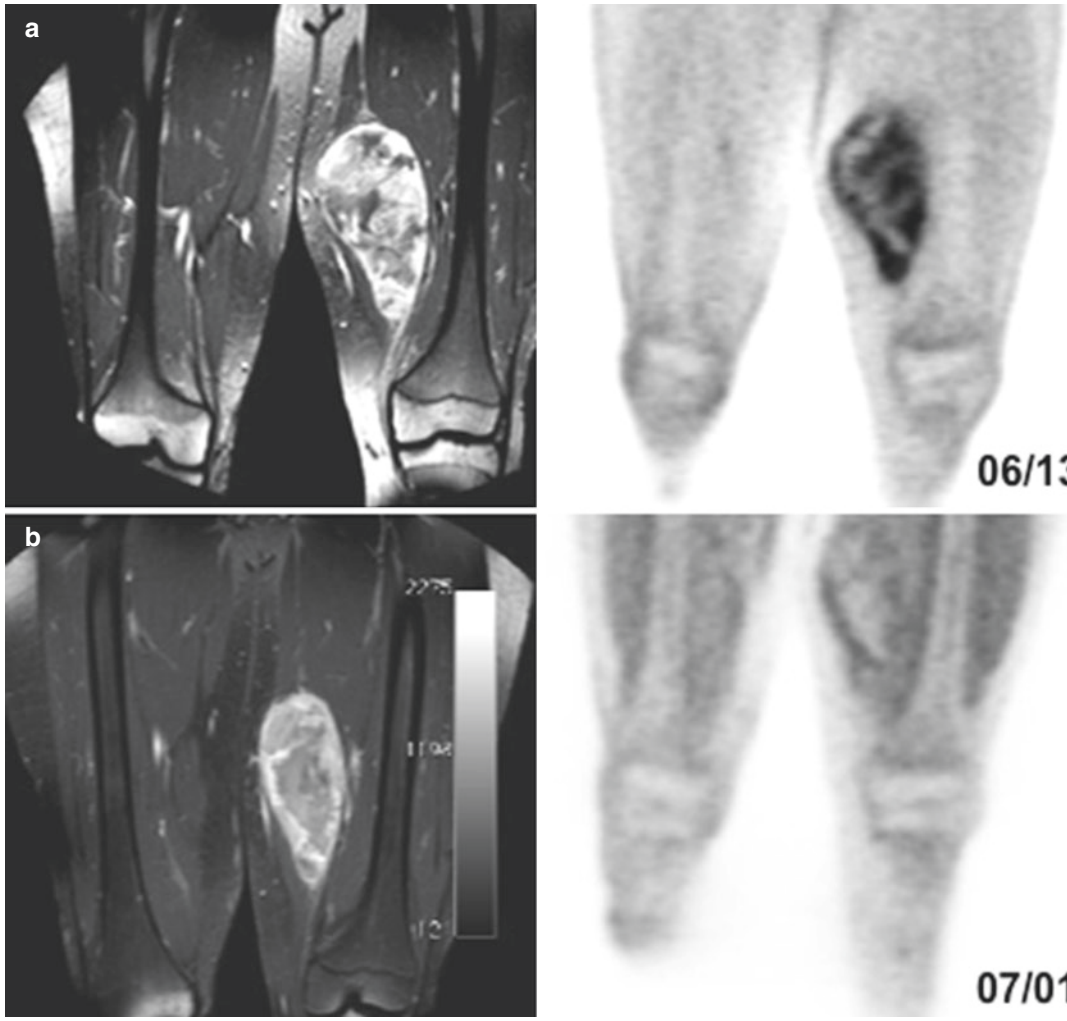

Fig. 9.2 Reduction in FDG PET activity following treatment with the insulin-like growth factor-I receptor (IGF-IR) targeted agent, cixutumumab [36]. Coronal contrast-enhanced MRI and FDG PET images in a patient with IGFR-I+ fibrosarcoma, obtained at baseline (**a**) and following 2 weeks of cixutumumab therapy (**b**), show intense FDG baseline uptake in the primary thigh tumor. Following just 2 weeks of cixutumumab therapy, there was a significant reduction in FDG uptake at the primary left thigh site, confirming activity of the IGFR-IR-targeted agent, despite little apparent change in size of the tumor (Image courtesy of Dr Stephan Voss)

it is recommended that CR and PR should always be confirmed with a follow-up study 4 weeks later, the need to confirm response may only need to be adhered to closely in the context of formal phase I–III trials of pharmaceutical agents. Many children with metastatic tumours have a good prognosis, and thus the suggested frequency of repeated CT may be problematic for paediatric trials. For example, in metastatic Wilms tumour, survival approaches 50%. In particular, for good prognosis tumours such as localised or favourable histology abdominal Wilms tumor, repeated CT at four-weekly intervals is not justifiable. Perhaps herein lies an opportunity for paediatric radiologists to insist that either an overall reduction in the frequency of follow-up imaging together with a shift away from CT to MRI for these tumors is the way forward, a notion that is supported by a recent COG report recommending a dramatic reduction in surveillance CT imaging

in patients with favourable histology Wilms tumor [40]. Not all protocols demand four-weekly follow-up, of course, but when there is a formal requirement to confirm CR or PR by repeating a study 4 weeks later, then upfront MRI must be strongly recommended whenever possible, taking into account the requirements for sedation or anaesthesia.

A perfect system for measuring response in each type of paediatric malignancy, including the brain, is difficult to envisage for a number of reasons. Outcomes and treatment in paediatric oncology are constantly changing. Paediatric tumors encompass a variety of very different cancers, with differing biology even within the same tumor groups. MRI (or ultrasound or CT) may not be the best modality to objectively document tumour size change 20 years from now. New functional imaging parameters that reflect the degree of tumour vascularity and cellular metabolism will undoubtedly become more widely available and will increase the need for functional imaging assessments in the future.

9.3 Conclusion

RECIST has become widely accepted by investigators, cooperative groups, industry, and regulatory authorities and serves as the current yardstick of reference in the assessment of response rate as an intermediate endpoint in clinical trials of anticancer agents for patients with extra-cranial solid tumors. The same method of assessment and the same technique should be used at baseline and follow-up ideally. As this may lead to repeated CT in young patients with cancer, it is important to consider, whenever possible, whether MRI of the primary site should be used either as the optimal or as an alternative imaging technique both for initial baseline and follow-up response assessments.

The significance of functional imaging, such as MIBG in neuroblastoma and FDG PET imaging in other paediatric solid tumors, should not be forgotten as the accuracy of tumour volume estimations is not always the most important radiological response criterion in an individual patient. The paradigm of conventional radiological assessments of drug efficacy remains particularly attractive in oncology, however, because tumour size can be monitored easily and serially [41]. Hence the RECIST criteria are likely to endure for the foreseeable future. Finally, the authors of RECIST 1.1 named it thus, acknowledging that the fundamental approach to tumor response assessment remained grounded in the anatomical approach [1]. If and when functional imaging is an integral component of RECIST, that iteration of RECIST will likely be called RECIST 2.0.

References

1. Eisenhauer EA, Therasse P, Bogaerts J, Schwartz LH, Sargent D, Ford R, et al. New response evaluation criteria in solid tumours: revised RECIST guideline (version 1.1). Eur J Cancer. 2009;45(2):228–47.
2. Therasse P, Arbuck S, Eisenhauer EA, et al. New guidelines to evaluate the response to treatment in solid tumours. J Natl Cancer Inst. 2000;92:205–16.
3. Nishino M, Jackman DM, Hatabu H, Yeah BY, Cioffredi L-A, Yap JT, et al. New response evaluation criteria in solid tumors (RECIST) guidelines for advanced non–small cell lung cancer: comparison with original RECIST and impact on assessment of tumor response to targeted therapy. AJR Am J Roentgenol. 2010;195(3):W221–8.
4. WHO. Handbook for reporting results of cancer treatment, No. 48. Geneva: World Health Offset Organization; 1979.
5. Suzuki C, Jacobson H, Hatschek T, Torkzad MR, Bodén K, Eriksson-Alm Y, et al. Radiologic measurements of tumor response to treatment: practical approaches and limitations. Radiographics. 2008;28:329–44.
6. McHugh K, Kao SCS. Response evaluation criteria in solid tumors (RECIST): problems and need for modifications in paediatric oncology? Br J Radiol. 2003;76:433–6.
7. McHugh K, Kao SCS. Can paediatric radiologists resist RECIST (response evaluation criteria in solid tumors)? Pediatr Radiol. 2003;33(11):739–43.
8. Chalian H, Tore HG, Horowitz MH, Salem R, Miller FH, Yaghmai V. Radiologic assessment of response to therapy: comparison of RECIST versions 1.1 and 1.0. Radiographics. 2011;31:2093–105.
9. Padhani AR. The RECIST criteria: implications for diagnostic radiologists. Br J Radiol. 2001;74:983–6.
10. Gehan EA, Tefft MC. Will there be resistance to RECIST (Response Evaluation Criteria in Solid Tumours)? J Natl Cancer Inst. 2000;92:179–81.
11. Ferrari A, Miceli R, Meazza C, Casanova M, Favini F, Morosi C, et al. Comparison of the prognostic

value of assessing tumor diameter versus tumor volume at diagnosis or in response to initial chemotherapy in rhabdomyosarcoma. J Clin Oncol. 2010;28(8):1322–8.
12. Schoot RA, McHugh K, van Rijn RR, Kremer LC, Chisholm JC, Caron HN, et al. Response assessment in pediatric rhabdomyosarcoma: can Response Evaluation Criteria in Solid Tumors replace three-dimensional volume assessments? Radiology. 2013;269(3):870–8.
13. Bagatell R, McHugh K, Naranjo A, Van Ryn C, Kirby C, Brock P, et al. Assessment of primary site response in children with high-risk neuroblastoma: an international multicenter study. J Clin Oncol. 2016;34(7):740–6.
14. Carceller F, Bautista FJ, Fowkes LA, Marshall LV, Sirvent SI, Chisholm JC, et al. Response assessment in pediatric phase I trials according to RECIST guidelines: survival outcomes, patterns of progression and relevance of changes in tumor measurements. Pediatr Blood Cancer. 2016;63:1400–6.
15. Aghighi M, Boe J, Rosenberg J, Von Eyben R, Gawande RS, Petit P, et al. Three-dimensional radiologic assessment of chemotherapy response in Ewing sarcoma can be used to predict clinical outcome. Radiology. 2016;280:905–15.
16. MacDonald DR, Cascino TL, Schold SC Jr, Cairncross JG. Response criteria for phase II studies of supratentorial malignant glioma. J Clin Oncol. 1990;8:1277–80.
17. Warren KE, Poussaint TY, Vezina G, Hargrave D, Packer RJ, Goldman S, et al. Challenges with defining response to antitumor agents in pediatric neuro-oncology: a report from the response assessment in pediatric neuro-oncology (RAPNO) working group. Pediatr Blood Cancer. 2013;60:1397–401.
18. Cheson BD, Fisher RI, Barrington SF, Cavalli F, Schwartz LH, Zucca E, et al. Recommendations for initial evaluation, staging and response assessment in Hodgkin and non-Hodgkin lymphoma: the Lugano classification. J Clin Oncol. 2014;32:3059–68.
19. Sandlund JT, Guillerman RP, Perkins SL, Pinkerton CR, Rosolen A, Patte C, et al. International pediatric non-Hodgkin lymphoma response criteria. J Clin Oncol. 2015;33(18):2106–11.
20. Wahl RL, Jacene H, Kasamon Y, Lodge MA. From RECIST to PERCIST: evolving considerations for PET response criteria in solid tumors. J Nucl Med. 2009;50(S1):1225–50.
21. Tirkes T, Hollar MA, Tann M, Kohli MD, Akisik F, Sandrasegaran K. Response criteria in oncologic imaging: review of traditional and new criteria. Radiographics. 2013;33:1323–41.
22. Cheson BD, Horning SJ, Coiffier B, Shipp MA, Fisher RI, Connors JM, et al. Report of an international workshop to standardize response criteria for non-Hodgkin's lymphomas. NCI sponsored International Working Group. J Clin Oncol. 1999;17(4):1244.
23. Cheson BD, Pfistner B, Juweid ME, Gascoyne RD, Specht L, Horning SJ, et al. Revised response criteria for malignant lymphoma. J Clin Oncol. 2007;25(5):579–86.
24. Choi H, Charnsangavej C, Faria SC, Macapinlac HA, Burgess MA, Patel SR, et al. Correlation of computed tomography and positron emission tomography in patients with metastastic gastrointestinal stromal tumor treated at a single institution with imatinib mesylate: proposal of new computed tomography response criteria. J Clin Oncol. 2007;25:1753–9.
25. Choi H. Response evaluation of gastrointestinal stromal tumors. Oncologist. 2008;13(Suppl 2):4–7.
26. Dietrich C, Hartung E, Ignee A. The use of contrast-enhanced ultrasound in patients with GIST metastases that are negative in CT and PET. Ultraschall Med. 2008;29(Suppl 5):276–7.
27. Smith AD, Lieber ML, Shah SN. Assessment tumor response and detecting recurrence in metastatic renal cell carcinoma on targeted therapy: importance of size and attenuation on contrast-enhanced CT. AJR Am J Roentgenol. 2010;194(1):157–65.
28. Smith AD, Shah SN, Rini BI, Liber ML, Remer EM. Morphology attenuation, size, and structure (MASS) criteria: assessing response and predicting clinical outcome in metastatic renal cell carcinoma on antiangiogenic targeted therapy. AJR Am J Roentgenol. 2010;194(6):1470–8.
29. Vancini C, Alfano DF, Abousiam RN, Totaro M, Diago NMD, Giganti M. Comparison of radiological criteria (RECIST – MASS – SACT – Choi) in anti-angiogenic therapy of renal cell carcinoma. Univ J of Public Health. 2016;4(5):239–43.
30. Tan D, Thomas GV, Garrett MD, Banerji U, de Bono J, Kaye SB, et al. Biomarker-driven early clinical trials in oncology: a paradigm shift in drug development. Cancer J. 2009;15:406–20.
31. Wolchok JD, Hoos A, O'Day S, Weber JS, Hamid O, Lebbé C, et al. Guidelines for the evaluation of immune therapy activity in solid tumors: immune-related response criteria. Clin Cancer Res. 2009;15(23):7412–20.
32. Hodi FS, Butler M, Oble DA, Seiden MV, Haluska FG, Kruse A, et al. Immunologic and clinical effects of antibody blockade of cytotoxic T lymphocyte-associated antigen 4 in previously vaccinated cancer patients. Proc Natl Acad Sci U S A. 2008;105:3005–10.
33. Hodi FS, Oble DA, Drappatz J, Velazquez EF, Ramaiya N, Ramakrishna N, et al. CTLA-4 blockade with ipilimumab induces significant clinical benefits in a female with melanoma metastases to the CNS. Nat Clin Pract Oncol. 2008;5:557–61.
34. Seymour L, Boggaerts J, Perrone A, Ford R, Schwartz LH, Mandrekar S, et al. iRECIST: guidelines for response criteria for use in trials testing immunotherapeutics. Lancet Oncol. 2017;18:e143–51.
35. Olsen ØE, Jeanes AC, Sebire NJ, Roebuck DJ, Michalski AJ, Risdon RA, et al. Changes in computed tomography features following preoperative chemotherapy for nephroblastoma: relation to histopathological classification. Eur Radiol. 2004;14:990–4.

36. Malempati S, Weigel B, Ingle AM, Ahern CH, Carroll JM, Roberts CT, Reid JM, Schmechel S, Voss SD, Cho SY, Chen HX, Krailo MD, Adamson PC, Blaney SM. Phase I/II trial and pharmacokinetic study of cixutumumab in pediatric patients with refractory solid tumors and Ewing sarcoma: a report from the Children's Oncology Group. J Clin Oncol. 2012;30(3):256–62. https://doi.org/10.1200/JCO.2011.37.4355.
37. Fowkes LA, Koh DM, Collins DJ, Jerome NP, MacVicar D, Chua SC, et al. Childhood extracranial neoplasms: the role of imaging in drug development and clinical trials. Pediatr Radiol. 2015;45:1600–15.
38. Smith TA. FDG uptake, tumour characteristics and response to therapy: a review. Nucl Med Commun. 1998;19:97–105.
39. Park JR, Bagatell R, Cohn SL, Pearson AD, Villablanca JG, Berthold F, et al. Revisions to the international neuroblastoma response criteria (INRC): a consensus statement from the NCI-clinical trials planning meeting. J Clin Oncol. 2017;35(22):2580–7.
40. Mullen EA, Chi YY, Hibbitts E, Anderson JR, Steacy KJ, Geller JI, Green DM, Khanna G, Malogolowkin MH, Grundy PE, Fernandez CV, Dome JS. Impact of surveillance imaging modality on survival after recurrence in patients with favorable-histology Wilms Tumor: a report from the children's oncology group. J Clin Oncol. 2018:JCO1800076. https://doi.org/10.1200/JCO.18.00076. [Epub ahead of print].
41. Saini S. Radiologic measurement of tumor size in clinical trials: past, present, and future. AJR Am J Roentgenol. 2001;176:333–4.

10 Neuro-oncology: Assessing Response in Paediatric Brain Tumours

Felice D'Arco, Kshitij Mankad, Marvin Nelson, and Benita Tamrazi

10.1 Part I: Assessment of Size and Use of Structural MRI Sequences

10.1.1 Introduction

In comparison to adults, paediatric patients show unique challenges in application of the Response Assessment in Neuro-Oncology (RANO) criteria. This is why in 2013 the Response Assessment in Paediatric Neuro-Oncology (RAPNO) Working Group was established to address specific issues in paediatric neuro-oncology [1].

In adults the majority of brain tumours are gliomas and particularly high-grade gliomas (HGGs), and conversely in children most of the tumours are low-grade gliomas (LGGs) which do not enhance homogeneously and have very slow growth over time. For these neoplasms, response to therapy (with cytostatic agents) can be achieved, even when a tumour does not change significantly in size over time, while a significant reduction in size is necessary for response in the adult population [1].

Moreover, there are profound differences in paediatric tumours when compared to their adult counterparts relating to location, histology, molecular biology and imaging characteristics.

The recent World Health Organization (WHO) classification of tumours of the central nervous system identified specific molecular characteristics of paediatric tumours related to different biological behaviours and thus differences in terms of methods of response assessment [2, 3].

Further, the fact that tumours like an optic pathway glioma or diffuse midline gliomas (formerly called Diffuse Intrinsic Pontine Glioma (DIGP)) cannot be resected and would not undergo biopsy in the majority of cases makes molecular subgrouping impossible.

For these reasons our ability to translate adult methods for tumour assessment in children is considered suboptimal, and it is unlikely that in children a single method for assessment of tumour response will be applicable. At the moment, there is no agreement on standards to define response or progression for paediatric brain tumours in clinical trials and, consequently, in clinical practice. As a result, most of paediatric neuro-oncology trials are still based on the same methods used in adults.

In summary, paediatric brain tumours are unique entities that require the use of specific imaging

F. D'Arco (✉) · K. Mankad
Department of Radiology, Great Ormond Street Hospital for Children, NHS Foundation Trust, London, UK
e-mail: felice.d'arco@gosh.nhs.uk; Kshitij.Mankad@gosh.nhs.uk

M. Nelson · B. Tamrazi
Department of Radiology, Children's Hospital Los Angeles, Los Angeles, CA, USA
e-mail: mdnelson@chla.usc.edu; btamrazi@chla.usc.edu

S. D. Voss, K. McHugh (eds.), *Imaging in Pediatric Oncology*, Pediatric Oncology,
https://doi.org/10.1007/978-3-030-03777-2_10

criteria; a "one-size-fits-all" strategy may not be the right approach for all paediatric brain tumour types.

In the first part of this chapter, we will summarize current proposed methods, challenges and controversies in assessing tumour response to therapy in paediatric patients using structural (conventional) MRI techniques. Mostly the evidence presented is based on recommendations for clinical trials from specialized international groups. In the second part we will explore the use of advanced MRI techniques.

10.1.2 Role of Contrast Enhancement

In adults response assessment of high-grade gliomas is based on measurement of the enhancing lesion (Macdonald and RANO criteria) [4]. In the case of paediatric tumours, particularly low-grade gliomas, this method is difficult and often not possible since most of the paediatric CNS tumours do not enhance or enhance inhomogeneously because of their characteristic vasculature, presence of cysts or areas of necrosis (Fig. 10.1).

Some authors have previously included cysts (nonenhancing components) in clinical trials for the evaluation of tumour size, while others have not, and it is not clear at this point whether or not reduction in the cystic aspect of a tumour, without changes in the solid part, can be confidently labelled as response to therapy [1].

Furthermore, tumoural enhancement can vary even without treatment and without changes in overall tumour size; thus an increase or reduction in enhancement should not be considered as a sign of definite tumour progression/response unless associated with a clear increase in tumoural volume, particularly in the case of pilocytic astrocytomas [5]. On the other hand, it is to be noted that interval development of new areas of contrast enhancement may correspond to new areas of tumour, thereby increasing the sensitivity of the study for diagnosing tumour progression (Fig. 10.2). Changes in the contrast characteristics can also vary for the same patient in different scans due to technical reasons (i.e. sequences used) and in the same scan between consecutive sequences due to differences in timing of the sequence acquisition after contrast injection.

Another important fact is that in cases where changes in contrast enhancement reflect real modification of the overall tumour volume, there is not always a clear correlation between the

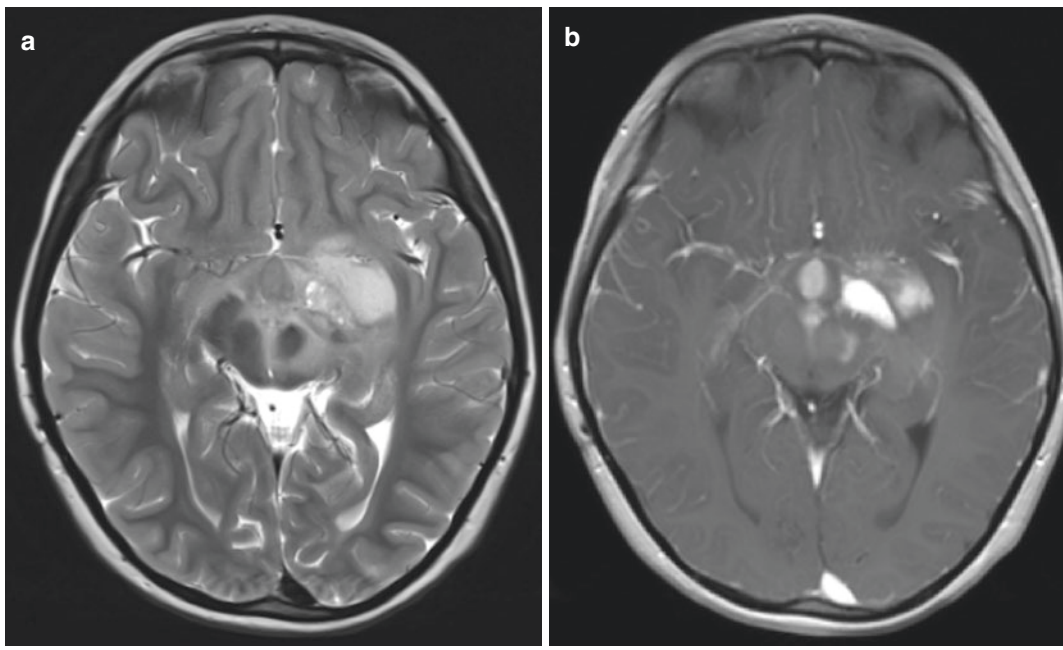

Fig. 10.1 Low-grade glioma (LGG) in a child with NF1. Axial T2 WI (**a**) shows infiltrative tumour involving hypothalamus, optic tracts, midbrain and left mesio-temporal lobe. Axial post-contrast T1 WI (**b**) shows patchy areas of enhancement not corresponding entirely to the area of abnormal signal noted on T2 WI

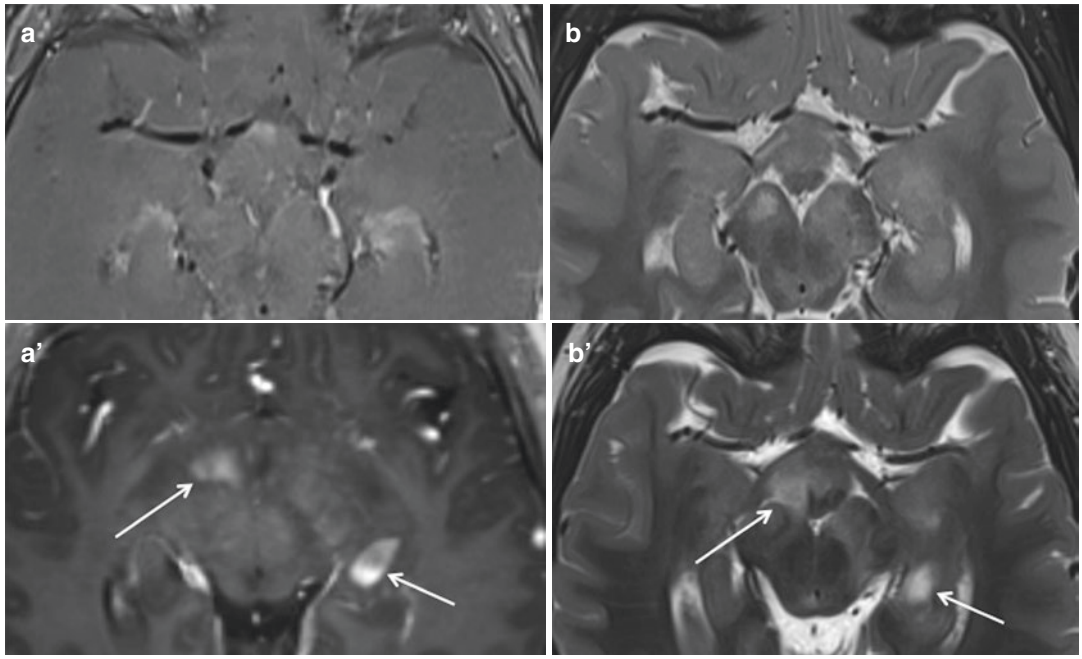

Fig. 10.2 (**a**, **a**′) axial T1 WI post-contrast sequences. (**b**, **b**′) axial T2 WI sequences in patient with LGG. First scan (upper row) shows only minimal areas of enhancement and abnormal T2 signal in hypothalamus, optic tracts and midbrain. Follow-up scan (bottom row) demonstrates two new areas of enhancement in the right hypothalamus and left hippocampus (arrows in **a**′) corresponding to increased tumour size clearly evident on T2 WI (arrows in **b**′)

reduction in volume and improved survival. In fact, several studies on paediatric LGGs demonstrate that stable disease (i.e. no reduction in tumoural size under treatment) correlates with increased progression-free survival (PFS) and indicates response to treatment [6].

Finally, significant interobserver variability in measurements of the enhancing tumoural components has been shown for both adult and paediatric patients because assessment is difficult in the case of invasive lesions with ill-defined borders and variable patterns of enhancement.

10.1.3 Assessment of Paediatric High-Grade Gliomas (HGGs): RANO Criteria, Pseudoprogression and Pseudoresponse

The Macdonald criteria were established in 1990 to assess the response to first line of treatment in adult glioblastomas and were based on the bidimensional measurement of the tumour in post-contrast CT or MRI scans [7].

These criteria have several weaknesses relating to the fact that only contrast enhancement was used to assess the tumour. The known phenomena of pseudoresponse and pseudoprogression were not taken into account, as well as the other causes of variation in enhancement already mentioned in the previous paragraphs. This is why they were subsequently replaced by Response Assessment in Neuro-Oncology Criteria (RANO) published in 2010 [4].

The RANO criteria were initially proposed to assess the effect of anti-angiogenic agents and radiotherapy in the treatment of HGGs in adults. The main changes in comparison to the Macdonald criteria were incorporation of T2/FLAIR sequences and use of corticosteroids in the evaluation of the response to therapy. Subsequently RANO criteria were adapted for response assessment in paediatric HGGs [8]. The RANO criteria are summarized in Table 10.1 and Fig. 10.3. To better understand the rationale of RANO criteria, it is important to be familiar with the definitions of pseudoprogression and pseudoresponse [8]:

Table 10.1 RANO criteria modified from [9]

Criterion	Complete response (CR)	Partial response (PR)	Stable disease (SD)	Progressive disease (PD)
T1 weighted post-Gd measurable disease[a]	None	at least 50% reduction in the sum of the products of perpendicular diameters of the contrast-enhancing lesions	All others	At least 25% increase in the sum of the products of perpendicular diameters of the contrast-enhancing lesions
T2/FLAIR	Stable or reduced	Stable or reduced	Stable or reduced	increase
New lesions	None	None	None	Present
Non measurable lesions	None	No progression	No progression	Significant progression
Corticosteroids	None	Stable or reduced	Stable or reduced	N/A
Clinical	Stable or improved	Stable or improved	Stable or improved	worsened
Requirement for response	All	All	All	Any

[a]Measurable disease: lesion showing contrast enhancement, clear margins, visible in two or more slices (preferably <5 mm thickness), at least 10 mm thickness or 2 × slice thickness if slices >5 mm

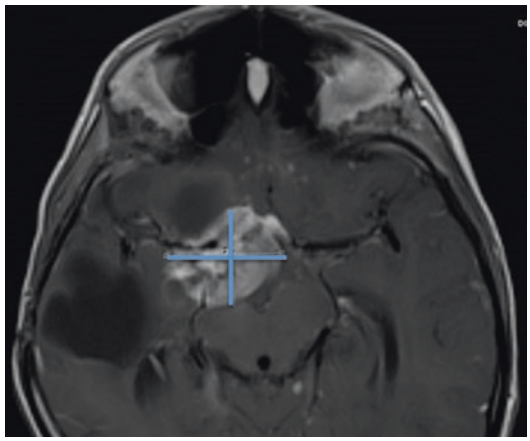

Fig. 10.3 Axial post-contrast T1 WI in patient with optic pathway glioma (OPG). Example of RANO bidimensional assessment: products of perpendicular diameters are used as baseline for tumour assessment on follow-up

- **Pseudoprogression** is an increase in lesion enhancement and/or T2 signal related to treatment rather than true progression. This will be discussed separately later in this chapter.
- **Pseudoresponse** is a reduction in tumour-related contrast enhancement and oedema-simulating response to therapy, while the lesion has actually remained stable in size or even progressed. Pseudoresponse can be observed shortly after administration of anti-angiogenic therapy [9] (i.e. bevacizumab, aflibercept and cediranib) that affects vascular permeability and thus reduces gadolinium enhancement of the tumour. Reduction in contrast enhancement needs to last for more than 30 days to be called a true response. A quantitative and qualitative evaluation of the mass on T2/FLAIR sequences can help in diagnosis of pseudoresponse when the solid tumour is clearly stable in size despite reduction of the enhancement [10].

Current international guidelines suggest follow-up in high-grade tumours: (a) 1–2 days after surgery and (b) after 12 weeks. However to date, there have been no studies on evaluation of pseudoresponse/pseudoprogression in paediatric high-grade tumours, and extrapolation of results from adults to children is not appropriate. Consideration of advanced techniques such as perfusion and diffusion is suggested to help in differentiating between these entities [11]. Interestingly, a new trial for assessment of response in paediatric HGGs defined criteria for tumour response and progression, for the first time including the combined use of structural MRI techniques (i.e. RANO criteria) and advanced functional

sequences (diffusion and perfusion sequences) to provide more comprehensive assessment of response. This is promising for future inclusion of diffusion and perfusion in standardized scanning criteria [8].

In conclusion, due to the limited information available, at present there are no universally accepted standards in use for evaluating tumour response in children.

10.1.4 Assessment of Optic Pathway Gliomas

Optic pathway gliomas (OPGs) are low-grade neoplasms that grow in the optic nerves, chiasm tracts, optic radiations and can also involve the hypothalamus. OPGs are often associated with neurofibromatosis type 1 (NF1) and are more frequent in young children than in adolescents or adults. These tumours have irregular and unpredictable growth which causes challenges and controversies in their clinical management and in assessment of tumour response to therapy [12]. OPGs are histologically grade I juvenile pilocytic astrocytomas and pilomyxoid astrocytomas or grade II diffuse fibrillary astrocytomas. The diagnosis is made based on a combination of radiological and clinical features.

Imaging protocols for OPGs should include imaging of the brain, along with thin slices through the orbits with fat-saturated T2 WI and post-contrast T1 WI. As general rule these tumours appear T2 hyperintense (sometimes isointense) and T1 isointense to grey matter; they also show variable degree of enhancement. Typically, involved optic nerves and chiasm show diffuse tubular enlargement with associated optic nerve kinking due to distortion and mass effect of the tumour (Fig. 10.4). Cystic components may be present, which can sometimes be relatively large with prominent mass effect on the surrounding brain structures and may further complicate assessment during therapy.

MRI measurements for OPGs are non-standardized to date, although prospective studies have demonstrated that these tumours can remain stable, grow or regress irrespective of the therapy and independently from the visual acuity [1, 13]. Of note, there is an increasing interest in advanced MRI techniques such as diffusion tensor imaging (DTI) in the study of white matter involvement in OPGs. [14].

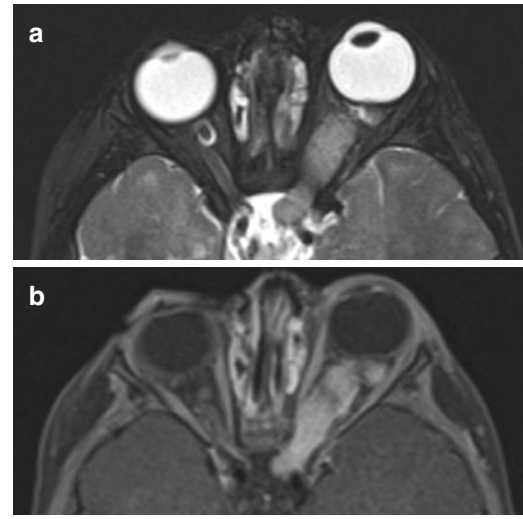

Fig. 10.4 Axial T2 WI fat-sat (**a**) and axial post-contrast T1 WI fat-sat (**b**) of the orbits showing typical MR appearances of OPG involving the left optic nerve

The first step in the assessment of OPG is to look for other radiological signs in keeping with NF1, i.e. foci of abnormal signal intensity (FASI), neurofibromas, etc. and the extension of the OPG (pre- vs. post-chiasmatic). Studies on both NF1 and sporadic patients with OPGs show that there is no single MRI criterion predictive of tumour growth and prognosis; moreover there is no correlation between tumour enhancement, internal structure and the tumour clinical course [15, 16]. Finally, it is important to keep in mind that both NF1-related and sporadic OPGs have shown spontaneous regression on rare occasions [17]. Interestingly, it is possible that an OPG is growing while vision improves or is stable or alternatively to have deteriorating vision in a radiologically stable tumour.

Despite these controversies and pitfalls, the literature data show that involvement of the posterior visual pathway is associated with poorer visual outcomes and thus the radiologic assessment of these pathways can help in predicting prognosis and guiding management [18].

10.1.4.1 Radiological Approach to Children with OPGs

NF1 patients should not be routinely screened with MRI looking for OPGs unless unexplained visual symptoms are present [19]. For newly diagnosed OPGs, a follow-up scan is suggested every 3 months for the first year and then every 6 months. New or progressive visual loss and increase in the size of the tumour indicates need for more frequent follow-up. If NF1 patients with OPGs are asymptomatic for 8 years, they can then be scanned every year.

There is no consensus about percentage of volume change to identify tumour progression; generally stable disease without new clinical symptoms is considered tumour response. Given the fact that radiotherapy is no longer recommended for treatment of these tumours (due to increased risk of visual or hormonal deficit and development of vasculopathy), in our institution we use linear measurements on T2/FLAIR sequences, including cystic areas. The RANO working group proposed response criteria for LGGs that are similar to that for HGG, but the recommendation is to measure T2/FLAIR signal instead of contrast enhancement. In addition, because responses are often relatively modest, minor response criteria were introduced: decrease in T2/FLAIR tumour of 25–50% [20].

Due to the association between location and prognosis, it is important to clearly define the anatomical location of OPGs, reporting tumours as involving either the optic nerves alone, the chiasm with or without nerve involvement and the hypothalamus or other adjacent structures (Dodge classification) [21].

10.1.5 Medulloblastomas (MLBs) and Other Leptomeningeal Seeding Tumours

An international working group has recently proposed recommendations for response assessment of patients with medulloblastomas (MLBs) and other leptomeningeal seeding tumours [22].

MLBs have variable appearance and location on images, depending on the molecular subtypes recently included in the WHO classification of CNS tumours [3]. One radiological feature almost found universally in MLBs is relative diffusion restriction due to their high cellularity—this is why it is important to look for new areas of diffusion restriction when assessing for the presence of recurrent/residual tumour. The presence of metastatic deposits at diagnosis is associated with a poor prognosis and needs to be carefully evaluated on images [23].

Figure 10.5 summarizes the proposed differences in location for different MLBs subtypes (WNT, SHH and non-WNT/non-SHH).

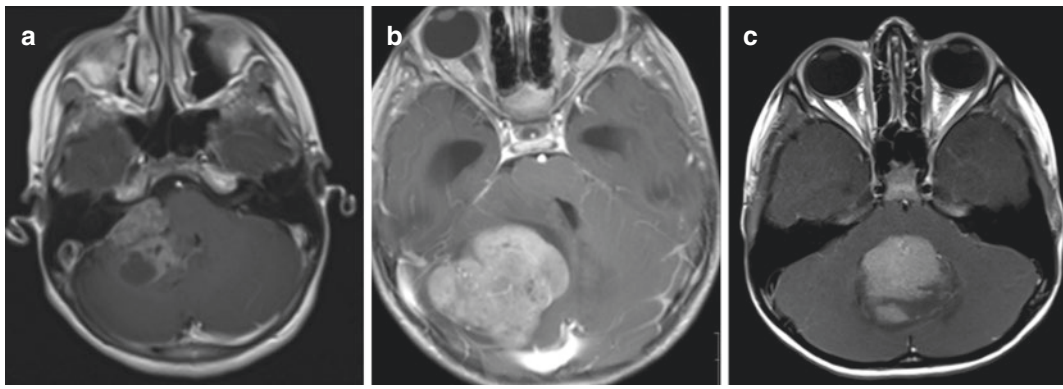

Fig. 10.5 Axial T1 post contrast showing three different subgroups of medulloblastoma (MLB). (**a**) Wingless (WNT)-MLB typical location in ponto-cerebellar angle. (**b**) Sonic hedgehog (SHH) MLB typical location centred in the periphery of the cerebellum with centripetal extension. (**c**) Non-WNT/non-SHH type in typical midline location. An overlap between radiological appearances has been described. For details see references [24, 25]

10.1.5.1 Issues on Assessment of MLBs

One problem in the assessment of MLBs is related to the different histological and molecular subgroups which have been associated with separate risk categories [26]. Specific molecular types can have distinctive imaging characteristics (particularly based on location), and preliminary results suggest that the MRI findings may differ by subgroup, although more studies are needed [24]. Therefore for response assessment, it may be useful to try to diagnose the specific MLB category, although currently there is no strong evidence that different response criteria should apply to different types of MLBs.

The other issue is the low sensitivity of detecting leptomeningeal metastases on T1 post-contrast images of the spine. The sensitivity can increase when radiological assessment is used together with CSF cytology.

The definition of the baseline scan is particularly important: gold standard treatment for MLBs is surgical resection so, in contrast to LGGs, pre-operative size of the tumour cannot be used as baseline for clinical trials; however, it is important to carefully evaluate the imaging characteristics of the original tumour (e.g. degree of enhancement and restriction) because metastatic deposits would have (often, but not always) similar MRI features as compared to the original tumour.

10.1.5.2 Specific Recommendations [22]

Given the current scientific evidence, these recommendations apply to all the types of MLBs and other CNS seeding tumours such as pineoblastoma, atypical teratoid rhabdoid tumour (ATRT), other embryonal tumours (previously defined as PNET), choroid plexus tumours and germ cells tumours.

- Brain and spine MRI pre and post contrast is mandatory. DWI sequence of the brain should always be performed.
- Pre- and post-contrast T1-weighted image acquisition utilizing isotropic volume (3D) MRI sequences should be obtained. These sequences allow for high resolution and better detection of small lesions.
- Alternatively or in addition, 2D T1-weighted images can be acquired in at least two planes.
- Maximum 2D slice thickness acquisition should be 4 mm; a small interslice gap (of 10% of the slice thickness) can be introduced to minimize any cross-talk artefacts if a consecutive image acquisition order is used.
- T2 FLAIR-weighted images should be preferably acquired post contrast because of the high sensitivity to leptomeningeal metastases.
- As for other CNS tumours, postoperative MRI should be done within 72 h.
- If any large postsurgical parenchymal change is noted that can obscure residual tumour, an early follow-up scan is suggested (2–3 weeks postsurgery).
- The timing of follow-up varies depending on the institution, risk and age of patients. In our institutions in cases of high-risk MLBs, we scan 4–6 weeks for the first five scans and then every 3 months.
- No strong data are available regarding timing of spinal images; therefore the committee recommends that surveillance spine imaging should be done together with brain imaging.
- Response to treatment follows RANO criteria (for both brain and spine). The size of measurable lesions should be at least two times the thickness of the slices (adding the gap between slices).
- Confirmed objective responses must be evident in both the spine and brain, while for progressive disease, showing disease progression in either the brain and/or the spine is necessary.
- CSF cytology, neurological status of the patient and steroid administration are included in the evaluation.

10.1.6 Diffuse Midline Gliomas (DMGs)

Diffuse midline glioma is a recently described entity characterized by H3 K27 M histone mutation that includes most of the diffuse intrinsic pontine gliomas (DIPG) [2]. DMGs can be found in both infra- and supratentorial compartments along the midline.

These tumours are very difficult to treat, no surgical option is available and radio-/chemotherapy effects are minimal and temporary. Diagnosis of brainstem DMGs is based on characteristic image findings: tumour centred in the pons, expansion of the brainstem and encasement of the basilar artery. Although typically most of these tumours do not enhance, localised areas of enhancement can be seen and have been interpreted as possible anaplastic areas [27]. Furthermore, the presence of foci of haemorrhage is possible, as well as necrosis surrounded by an enhancing rim.

10.1.6.1 Current Concepts of Radiological Assessment in DMG/DIPG

There are a number of problems when trying to apply radiological response criteria (i.e. RANO) to patients with DMG/DIPG. These criteria were developed primarily for enhancing high-grade supratentorial gliomas, and lack of homogeneous enhancement in DMGs, together with their invasive nature and indistinct borders, makes use of RANO criteria unreliable. Consequently, significant interobserver variability is expected when using standard tumour measurement criteria in DMGs [28].

When clearly defined rim-enhancing lesions are present, these can be used for the assessment of the tumour according to RANO; however the overall size of T2-weighted changes should also be considered [29].

The criteria used for determining percent change in size of enhancing lesions to establish partial response, progressive disease or stable disease are the same as described for adults. However, as mentioned previously, the presence of discrete enhancing lesions is not common. Of note adult GBMs are completely different tumour entities. Currently, most of the response assessment is based on clinical data, in fact, even though the tumour size may be reduced under therapy, this is generally not sustained and does not translate confidently to improved survival.

The limitation of structural MRI in assessing tumours has been highlighted by several studies in the last years. Lobel et al. demonstrated that focal areas of T2 hypointensity (which do not represent spared white matter bundles) are associated with areas of lower ADC, higher CBV and variable enhancement in comparison to the rest of the tumour which is T2-hyperintense [27] and may represent areas of anaplasia. These patterns highlight the importance of analysis of these areas, rather than all the tumour, as a radiological marker of tumour response to therapy. In DMGs, it is likely that whole tumour volume suffers the confounding effect of the treatment since the therapy can reduce the intrinsic oedema of the lesion without acting on the cellular component and without influencing the survival. On the contrary new enhancement months after radiation therapy may represent treatment effect (e.g. radiation necrosis), tumour progression or both.

In another recent study, the authors correlated volumetric changes in radiologically visible tumour (using T2/FLAIR) with changes in total brain volume [30]. They normalized the reduction in volume of the tumour with the reduction over time of the nonirradiated brain (supratentorial white matter) and concluded that most of the volumetric changes may be due to adjuvant non-tumour targeted therapy, although some effect of the therapy on the tumour volume is still appreciable after normalization. Therefore, those changes likely develop in response to systemic medication used during treatment, particularly corticosteroids, which cause reversible changes in the brain parenchyma. The implication of this finding is that tumour volume reduction induced by corticosteroids may be misinterpreted as response to therapy. This is probably another reason why structural MRI changes can be unreliable for appreciating a real antitumour effect (or absence of it) and changes in size often have poor correlation with clinical status of the patient and are in many cases inadequate for assessment of partial response or progressive disease.

Another study comparing volumetric changes in the T2 hyperintense area and the MRS metabolic profile in 31 children with pontine DMGs showed a discrepancy between the two, with volume reduction but stable metabolic profile of the tumour [31].

In conclusion assessing response to treatment in DMGs by using linear or volume-based

response criteria is challenging because the "lesion" seen on structural MRI does not necessarily correspond to the "real tumour". Future implementation and standardization of advanced techniques in the assessment of DMGs is necessary and desirable.

10.1.7 Leptomeningeal Dissemination

Response assessment in leptomeningeal dissemination based on imaging can be very difficult because radiological findings often do not correlate with clinical status of the patient and it is problematic to measure leptomeningeal metastases [20]. The leptomeningeal metastasis (LM) RANO working group recommends the assessment of LM using neurological exam, CSF examination and imaging [32].

LM is defined radiologically as presence of pathological enhancement of cranial nerves, spinal nerve roots, brain or spinal surface and within the ventricles. Because of the small volume and/or complex geometry, LM are often not measurable with the current level of technology [33]. The current definition of measurable disease for LM is 5 × 10 mm on orthogonal planes, and the LM RANO working group recommends high-resolution T1 post contrast of the brain and spine as the method of choice for assessment; other techniques such as PET, perfusion and diffusion have no defined role at the moment. One important element introduced in the LM assessment guidelines is that only changes in size and extent of disease are considered. Changes in the intensity of enhancement are not emphasized in the guidelines.

T2 and FLAIR abnormalities without enhancement should also be considered with caution because of the possibility of false-positive findings and are not part of the suggested criteria of assessment in clinical trials [33]. Radiological evaluation should focus on the presence of nodular metastases (easier to be measured and/or subjectively evaluated), their evolution over time, cranial nerve or nerve root enhancement and the presence of hydrocephalus secondary to CSF dissemination.

These guidelines have not been validated yet for paediatric leptomeningeal disease and should be considered as work in progress.

10.1.8 Volumetrics

A few studies in children have compared linear and volumetric measurements and have found generally good concordance between the two methods; however, these focus on either high-grade tumours [34] or have a small number of patients [35]. In low-grade gliomas, a volumetric analysis is intuitively more reliable due to their slow growth, infiltrative nature and irregular margins. Hence there is increasing interest in application of volumetry to assess tumour response which is supported by several publications showing that volume and growth measurements based on semiautomated segmentation are reproducible and sensitive to minimal volume changes [36, 37].

Despite multidimensional measurements that would best capture subtle and anisotropic growth or response of LGGs, there is limited availability of software for automated segmentation and volumetric assessment. Linear two-dimensional or three-dimensional assessments remain the cornerstone for objective response assessment in clinical trials. At present, due to technical limitation, manual segmentation with dedicated software seems to be the only reliable method, although it is time-consuming.

Nevertheless, in NF1 patients with schwannomas or neurofibromas in the body, MRI with volumetric analysis is now recommended to evaluate changes in tumour size in clinical trials due to their complex irregular shape which makes uni- or bidimensional assessment inaccurate. Volumetric analysis requires adherence to specific imaging recommendations; 20% volume change was chosen to indicate a decrease or increase in tumour size [38].

Currently, there are no cut-off values available for volumetric changes in tumour response or progression for brain tumours. When mathematically extrapolating volumetry from Macdonald criteria, the definition of tumour progression

becomes >40% volume increase and tumour response as at least 65% volume reduction [39] which is too big a variation to be applied confidently in clinical practice. Despite this caveat, when comparing volumetry with 2D measurements in 70 paediatric patients with LGGs, substantial differences were found in defining tumour response using these two different methods [40].

Additional studies will be required to establish reference values to be used clinically and to evaluate the feasibility of additional cost and complexity associated with making volumetric measurements.

10.2 Part II: Role of Diffusion-Weighted Imaging Techniques

In this section, we will evaluate the expanding role of diffusion-weighted imaging techniques in the evaluation of paediatric brain tumours. We shall also highlight some potential pitfalls that the reading radiologist needs to be aware of.

As diffusion-weighted imaging (DWI) provides information on the biology of the tumour and its surrounding environment, DWI provides added value in the estimation of tumour response in comparison with mere assessment of gadolinium contrast-enhanced T1-weighted sequences. This concept has been supported in recent studies on response assessment in paediatric neuro-oncology, and it has been proposed to expand the current RANO criteria to incorporate diffusion and perfusion metrics in the assessment of tumour response [8].

This section introduces and discusses the following practical applications of diffusion-weighted imaging techniques:

1. Qualitative and quantitative assessment of apparent diffusion coefficient (ADC)
2. ADC at high *b*-values
3. Diffusion tensor imaging (DTI)
4. Diffusion kurtosis imaging (DKI)

10.2.1 Standard Diffusion Imaging Protocol

Diffusion-weighted imaging (DWI) should be routinely performed in the initial evaluation and surveillance of all brain tumours. We recommend:

At 1.5 T:

Two-dimensional echo-planar imaging in three orthogonal planes at *b*-values 0, 500 and 1000 s/mm^2.

At 3.0 T:

Two-dimensional echo-planar imaging with higher SNR and reduced susceptibility with quicker scan times, again at three *b*-values

DTI protocol:

Sixty directions at *b*-value 1000 s/mm^2 with echo-planar imaging read-out against a spin echo preparation

10.2.2 Utility of Serial ADC Monitoring: Pearls and Pitfalls

ADC is a measure of the diffusion of water molecules within a tissue. In neuro-oncology ADC values are reduced in high-grade neoplasms because of the high cellular concentration, whereas low-grade tumours show higher ADC values. Lysis or apoptosis of neoplastic cells, expected during therapy, may result in an increase of the ADC values in comparison to the baseline scan [41].

For quantitative analysis a region of interest (ROI) should initially be placed on the entire tumour volume being assessed. Separate ROIs should be considered for what is judged to represent peritumoral oedema. Subsequently a more focused evaluation of areas of internal tumour heterogeneity should also be considered and documented, as this may assist with targeting initial biopsy, as well as facilitate follow-up of more

focal areas of anaplasia to monitor treatment response [27].

We advocate that the minimum ADC values in the ROI should be used for surveillance monitoring, rather than the average reading.

ADC within a tumour should always be compared with the grey and white matter of the "normal" appearing surrounding brain: ADC value of normal white matter being approximately 0.705 ± 0.014 mm^2/ms [42] and that of normal grey matter being 0.75 ± 0.3 mm^2/ms [43].

A potential pitfall is that most intracranial tumours (particularly low-grade gliomas) will actually have ADC values higher than that of the normal brain parenchyma which may be a reflection of the degree of internal oedema [44]. Then, during treatment, ADC values may drop on serial monitoring as the tumour mass responds to therapy (Fig. 10.6). In fact, as therapy is initiated, areas within the tumour that show early response may manifest as decreased diffusion values due to transient swelling of tumour cells or secondary to ischemic injury (cytotoxic oedema). Over time, tumour showing response to therapy will show increased diffusion (i.e. increase of ADC values) due to cell lysis or apoptosis. However areas resistant to therapy may not show any appreciable change in their diffusion coefficients. These concepts are extremely useful in the early prediction of tumour response and in avoiding premature change in management strategy [45].

Furthermore, with predominantly cystic tumours, the absence of cellular complexity with intact cell membranes can lead to higher ADC values due to unrestricted diffusion; similarly the destruction of cells with loss of cellular membrane integrity in the context of tumour necrosis can be associated with increased diffusivity and

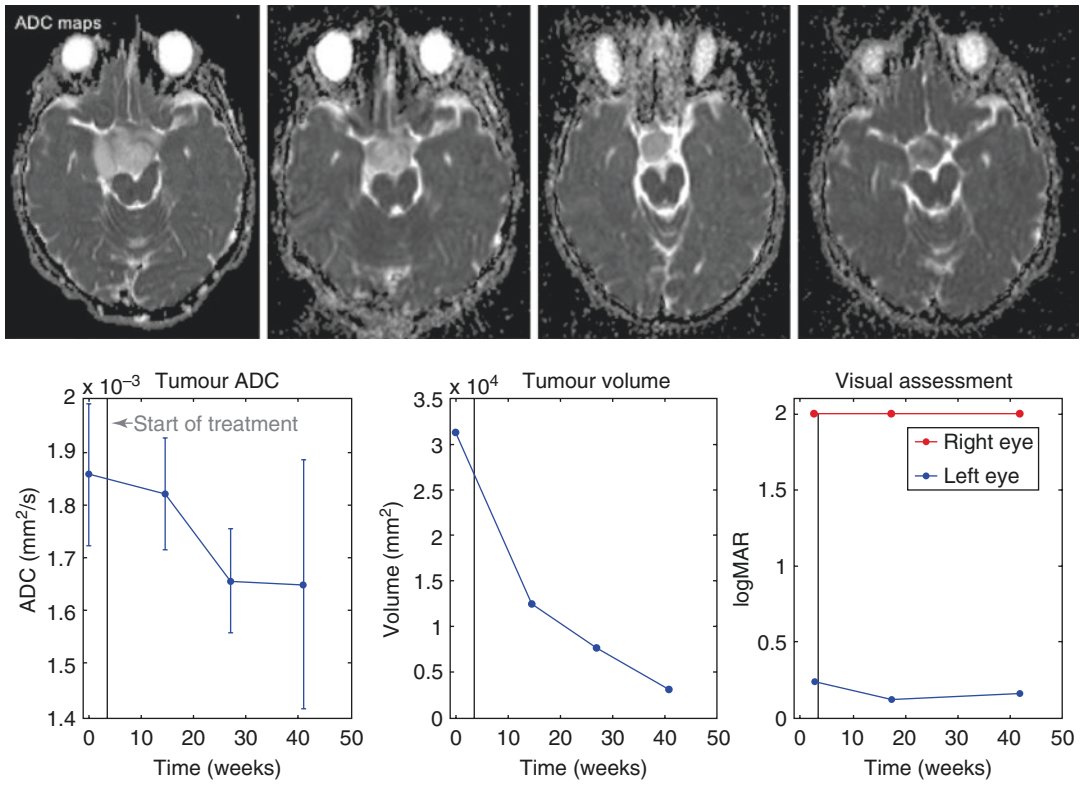

Fig. 10.6 Case of optic pathway glioma. Serial apparent diffusion coefficient (ADC) measurements on standard treatment reveal a stepwise decrement in ADC with a concomitant tumour response to therapy in terms of volume reduction

higher ADC values [46]. On the other hand, the presence of dense calcification and/or haemorrhage even in low-grade tumours can restrict diffusion and result in lower than expected ADC values. Thus changes of ADC values during therapy need to be evaluated in conjunction with other conventional and advanced sequences to avoid misinterpretation.

Diffusion changes observed at a later stage in treatment can also be used to differentiate radiation-induced injury from tumour recurrence with ADC values significantly smaller in recurrence than in radiation necrosis [45, 47].

Certain studies have also compared the utility of higher *b*-value diffusion-weighted imaging (over 3000 s/mm^2) with standard *b*-values at 1000 s/mm^2. Higher *b*-value has been shown to improve the delineation of tumour from normal brain tissue with stronger inverse correlation between the minimum ADC values and tumour cellularity. This technique is particularly useful on 3 Tesla systems [48], but, when using high *b*-values, radiologists should be aware of the higher rate of artefacts and of false positives.

In summary, apart from differentiating between normal and abnormal tissues, the diffusion coefficient measure is a powerful tool as it can evaluate alterations in the intra- and extracellular fluid volume shifts as a tumour responds to chemotherapy, radiotherapy as well as immunotherapy and/or gene therapy. At the moment, there is no standardized ADC cut-off available to differentiate active tumour from non-tumoural tissue. Furthermore, the use of DWI/ADC in clinical trials is not standardized, and DWI findings should always be interpreted together with standard MRI sequences and other advanced MRI techniques (e.g. perfusion) [49, 50].

10.2.3 Diffusion Tensor Imaging (DTI)

Diffusion tensor imaging provides a direction-dependent assessment of how movement of water molecules is affected along fibre tracts in the brain. Magnetic field gradients when applied in multiple directions/orientations allow the assessment of integrity of white matter bundles in the brain. These microstructural changes cannot be visualized on conventional DWI.

It is to be remembered that the primary application of diffusion tensor imaging is to assess the integrity of the structure of the white matter fibres surrounding the lesion, rather than within the tumour.

DTI allows measurement of fractional anisotropy (FA) and mean diffusivity (MD) index which represent an index of integrity of the white matter tracts. Impairment of the tracts will result in increased MD and reduced FA.

Tumour tissue typically shows low anisotropy within its matrix, and therefore there may be little benefit in evaluating or following up diffusion anisotropy within tumours; nevertheless the internal structural changes of the tumour matrix may be evaluated with DTI using ADC, as described with DWI, with the advantage of increased resolution [51].

Four patterns of relationship between tumour and white matter tracts can be described:

1. Normal signal with tract displacement. This is caused by the mass effect and/or peritumoral oedema (Fig. 10.7). The tract is not infiltrated.
2. Decreased but present signal with normal direction which corresponds to vasogenic oedema within the tract.
3. Decreased signal with tract disruption corresponding to tumour infiltration.
4. Loss of anisotropic signal representing tract disruption or destruction by the lesion.

To recognize these different patterns is important in baseline evaluation of the tumour, particularly in order to assess the prognosis before surgical treatment [52].

This information can also be used for radiotherapy planning to map the exact extent of the tumour, especially when more focused radiotherapy is planned and the dose distribution can thus be optimized focusing on the area of higher tumour density [53].

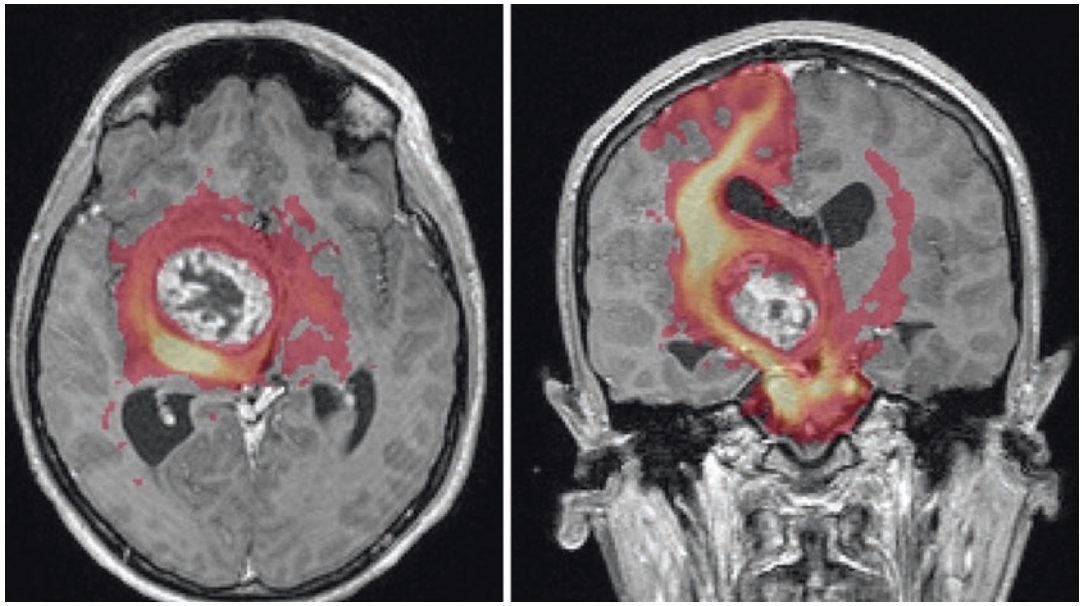

Fig. 10.7 Case of pilocytic astrocytoma (WHO grade 1). Note the right cortico-spinal tract being displaced by the tumour laterally and posteriorly on these diffusion tensor imaging (DTI)-derived track density colour maps

10.2.4 Diffusion Kurtosis Imaging (DKI)

Traditional DWI and DTI are based on a simplified assumption that the diffusion of water molecules follows a Gaussian distribution. The reality however is that the complexity of intracellular and extracellular environments makes the diffusion of these molecules non-Gaussian rather than Gaussian.

DKI attempts to analyse and measure this variation and allows a more realistic evaluation of the heterogeneous internal structure of the tumour [54].

The relatively long acquisition time limits the use of this technique in regular clinical practice. This is an important opportunity for research and further development, however, particularly because the information generated by DKI can provide more comprehensive insights about the microstructure of the tumour environment as it relates to its molecular and histological subtype. Several studies have shown usefulness of DKI in differentiating high- and low-grade gliomas in adults [55], and a few recent papers showed the usefulness of DKI in assessment of tumour response in gastrointestinal or hepatic cancers [56, 57]. Hence a future role of this technique in the evaluation of response in paediatric brain tumours is promising, although DKI will require validation in clinical trial settings [58].

In conclusion, diffusion-weighted sequences represent a useful technique to assess response to therapy, especially in high-grade brain neoplasms where internal structure is expected to change in the case of tumour response (higher ADC values representing cell lysis/apoptosis). More advanced diffusion techniques (DTI and DKI) have the potential to improve sensitivity in future assessment of response to therapy and can be used for preoperative planning. It is important to remember that DWI information needs to be always evaluated together with other MRI sequences.

10.3 Part III: Advanced Imaging Assessment of Pseudoprogression

10.3.1 Definition

The term pseudoprogression was first used in 2007 to describe the phenomenon mimicking

tumour progression [59]. In brain tumour imaging, specifically gliomas, it has been defined as a treatment-related process characterized by changes in tumour radiographic appearance, with or without clinical symptoms that are suggestive of disease progression and that subsequently resolve or stabilize without additional treatment [60, 61]. Radiographically, pseudoprogression demonstrates a transient increase in the size/extent of contrast enhancement, mimicking tumour growth. It is considered part of a continuum of treatment-related change that is histologically distinct from both true tumour progression and other more delayed changes related to treatment such as radiation necrosis, the latter specifically associated with the combination of chemotherapy and radiation. This is a phenomenon that has been almost exclusively described in the adult glioma population.

Treatment-related changes have been categorized based on timing after radiation therapy. In the acute phase, there is often oedema, which is mostly transient and reversible. In the subacute or early delayed phase, occurring a few weeks to 3 months after radiation, there is characteristically an increase in the size/extent of enhancement, often referred to as pseudoprogression, with improvement in the changes within 6 weeks (Fig. 10.8). In the late phase, occurring greater than 3 months to years after radiation therapy, there is irreversible, progressive and possibly lethal injury, often referred to as radiation necrosis [62]. Pseudoprogression can be considered a pathologic continuum between acute postradiation therapy changes and radiation necrosis.

In adults, 20–30% of patients undergoing concurrent chemoradiation therapy show a size increase in an enhancing lesion within the first 3 months. In children, the rates of pseudoprogression are similar, with 21% reported incidence, and in children with diffuse midline glioma (formerly DIPG) receiving radiation therapy and temozolomide or immunotherapy, the pseudoprogression rate is reported at 19–24% [63–65]. Additionally, patients who developed pseudoprogression have been described as having improved survival secondary to a favourable correlation with methylguanine methyltransferase (MGMT) promoter status [66].

10.3.2 Imaging Analysis

10.3.2.1 Perfusion MRI

In order to understand the various imaging techniques used to assess progressive disease versus pseudoprogression, the physiological/histological differences between tumour and treatment-related changes must be discussed. Although treatment-related changes including pseudoprogression and radiation necrosis could be indistinguishable from progressive high-grade tumour on conventional MR sequences, as both can present with an enlarging, enhancing mass, the underlying histology is distinct. Recurrent glioblastoma multiforme (GBM) and other high-grade gliomas are characterized by vascular proliferation, whereas radiation necrosis results in decreased microvascular density and capillary perfusion secondary to endothelial and small vessel injury [67]. Additionally, recurrent/progressive tumour is further characterized by increased cellularity, whereas treatment-related changes are not [66]. Pseudoprogression results from a robust inflammatory response to radiation therapy that temporarily increases the blood-brain barrier permeability with increased contrast enhancement seen on MRI.

Advanced imaging techniques such as perfusion imaging can be used to differentiate treatment-related response from progressive disease by identifying tumour angiogenesis and increased microvascular density as is seen in high-grade glial tumours. The types of perfusion imaging used include dynamic susceptibility contrast perfusion (DSC) and dynamic contrast-enhanced perfusion (DCE), as well as arterial spin labelling (ASL).

Dynamic susceptibility contrast perfusion (DSC) is a functional imaging technique used to assess tumour angiogenesis. DSC is a technique that essentially estimates vascular density with vascular volume and flow [68]. DSC perfusion exploits the susceptibility-induced

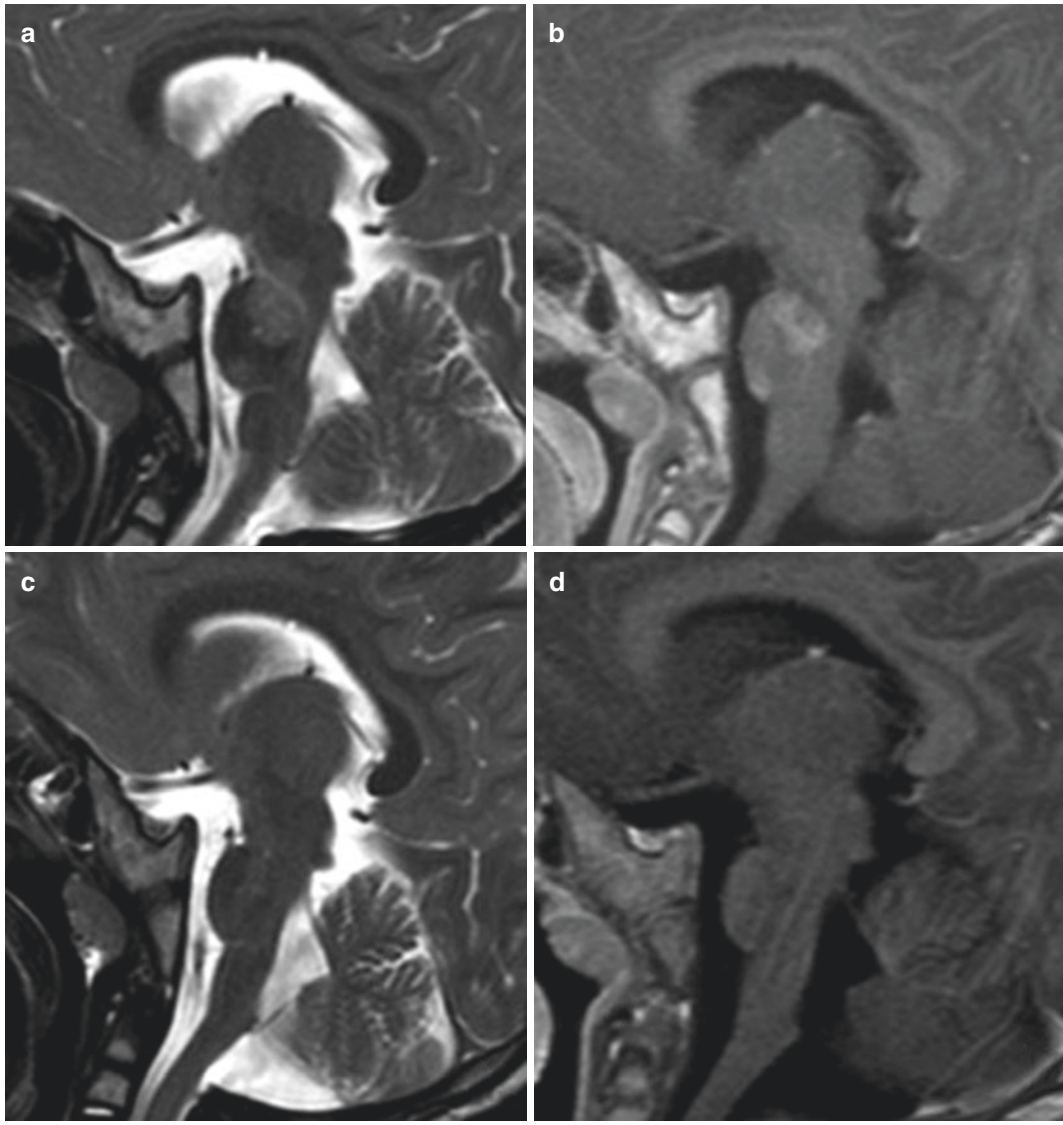

Fig. 10.8 Pseudoprogression after proton radiotherapy. (**a**, **b**) Sagittal T2 and sagittal T1 post-contrast images demonstrate signal abnormality and enhancement in a patient with history of ependymoma status post resection who received proton radiotherapy. (**c**, **d**) 4-month follow-up demonstrates resolution of signal abnormality and enhancement consistent with pseudoprogression

signal loss caused by paramagnetic contrast agents on T2-weighted images. Gadolinium-containing contrast is injected intravenously, and rapid repeated imaging of the brain is performed during the first pass. This leads to a series of images with the signal in each voxel representing intrinsic tissue T2/T2* signal attenuated by susceptibility-induced signal loss proportional to the amount of contrast primarily in the microvasculature. A signal intensity-time curve is then generated, from which perfusion parameters including relative cerebral blood volume and flow can be calculated [69, 70].

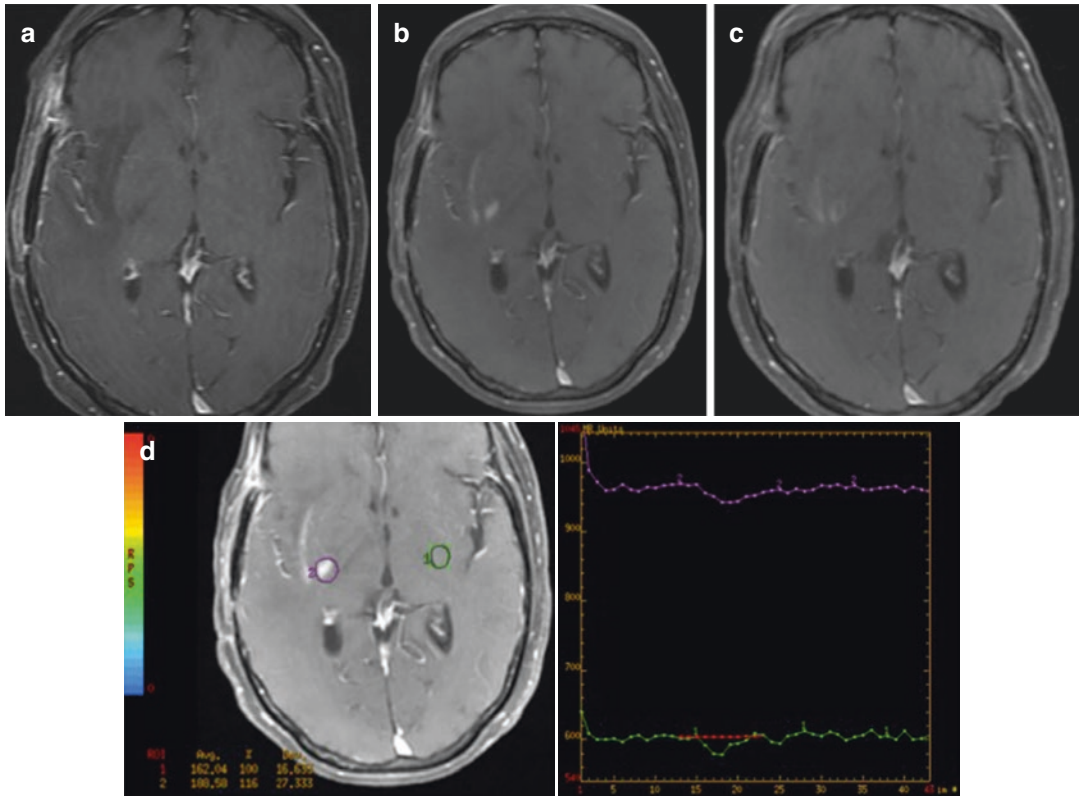

Fig. 10.9 Dynamic susceptibility contrast (DSC) perfusion and pseudoprogression. (**a**–**c**) Axial T1 post-contrast sequence with fat saturation demonstrating appearance of enhancing nodule in the posterior limb of the internal capsule on the right as well as enhancement of the subinsular cortex in a patient with GBM after completion of chemoradiation. There was decreased conspicuity on 4-month follow-up (**c**). (**d**) DSC perfusion demonstrating no corresponding elevation of rCBV in the enhancing nodule consistent with pseudoprogression

Relative cerebral blood volume (rCBV) is used to measure contrast confined to the tissue vasculature under interrogation and provides information regarding vascular density. It is a technique often used clinically to monitor angiogenesis and response to treatment. Multiple prior studies in high-grade glial neoplasms have reported higher levels of rCBV within contrast-enhanced regions of recurrent GBM as compared to areas of radiation necrosis [11, 71, 72]. Although these studies predominantly focus on adult GBM patients, similar findings of elevated rCBV have been reported in children with progressive high-grade tumour, specifically pertaining to differences in permeability of the tissue as predicted by DSC perfusion in cases of angiogenesis and anti-angiogenic agents [72]. The development and progression of high-grade gliomas is dependent on the promotion of angiogenesis (angiogenic switch), which ultimately helps produce vessels that are leakier than normal brain vasculature. Thus imaging, including DSC, can be used to track changes in permeability and vascular density of progressive tumour in the setting of anti-angiogenic treatment [73–75]. Both pseudoprogression and radiation necrosis have similar findings on DSC with lower rCBV as opposed to progressive tumour [66] (Fig. 10.9). DSC is not without limitations however. In the paediatric population, there are technical issues with gadolinium-based perfusion methods in that they require power injection with large-bore intravenous access, which is difficult in children. Additionally, the DSC technique is more sensitive to susceptibility effects, which can become problematic in hemorrhagic tumours or in

patients with dental hardware, often more commonly seen in the paediatric population. Taking these limitations into consideration, the sensitivity and specificity for differentiating pseudoprogression from tumour recurrence is still quite high and is estimated at 80–90% [76].

Dynamic contrast-enhanced perfusion (DCE) technique is used to estimate vascular permeability by measuring contrast leakage through the blood-brain barrier. DCE is dependent on T1-shortening effects of gadolinium-based contrast agents. An intravenous contrast bolus is injected and rapid repeated T1 imaging is obtained. Regional increased signal occurs due to gadolinium concentration that ultimately depends on intravascular gadolinium and accumulation of gadolinium in the extravascular space. DCE relies on pharmacokinetic modelling which helps derive regional values that include *k*-trans (transfer constant), rate constant, fractional volume of extravascular-extracellular space and fractional volume of the plasma space [69].

The two values that are often used to assess treatment response versus recurrent tumour with DCE perfusion are the vascular transfer constant, *k*-trans and the initial area under the curve (iAUC). *K*-trans is dependent on blood flow and endothelial permeability which helps predict the neoangiogenic nature of tumour microvasculature and vascular density [68]. In recurrent tumour, both *k*-trans and iAUC are elevated as compared to treatment-related changes [68]. DCE is often used in the setting of anti-angiogenic therapy such as in patients with high-grade gliomas receiving bevacizumab. In the paediatric population, clinical trials of patients with recurrent ependymoma and gliomas, DCE-derived *k*-trans demonstrated decreased permeability in patients that were on anti-angiogenic therapy such as bevacizumab [74]. During response to therapy, there is a presumed decrease in tumour neovasculature, reflected by decreased vascular permeability seen on DCE. Alternatively, if there is lack of response to treatment with progressive tumour, the permeability will increase as a reflection of increased tumour neoangiogenesis, and the *k*-trans will be increased [77]. The main disadvantage of DCE perfusion technique over DSC is a longer scan time. Additionally, as with all contrast-based perfusion techniques, large-bore IV access is required for power injection of the gadolinium contrast agent, a limitation that can be a problem in the paediatric population.

In addition to perfusion techniques that require an exogenous contrast agent such as DSC and DCE perfusion, arterial spin labelling (ASL) is a perfusion-based MRI technique that does not require an exogenous contrast agent. ASL can be used for evaluation of cerebral blood flow (CBF), where arterial blood water is used as an endogenous tracer. This perfusion technique is particularly useful in the paediatric population, as it does not require intravenous access, which is a major technical limitation with both DSC and DCE perfusion. Prior studies have demonstrated the utility of ASL in differentiating high-grade from low-grade tumours [78, 79]. Yeom et al. demonstrated that elevated CBF was seen in high-grade paediatric brain tumours [79]. Furthermore, Choi et al. explored the utility of ASL in the assessment of treatment-related changes [80]. Progressive tumour demonstrated elevated CBF as compared to pseudoprogression/treatment-related change [80]. Therefore ASL can be a potential tool to not only assess tumour grade at initial presentation but also to follow patients after chemoradiation to decipher treatment-related changes from true progressive disease, especially in the paediatric brain tumour population.

10.3.2.2 Diffusion MRI

Diffusion-weighted imaging (DWI) is an MRI technique that maps the motion of water molecules in tissue. Water molecules in theory are relatively more restricted in their movement within cells and less restricted in extracellular space, and therefore, the apparent diffusion coefficient (ADC) as measured by DWI reflects tumour cellularity. It is well known that ADC values are inversely correlative with tumour cellularity, with hypercellular, high-grade tumour demonstrating lower ADC values [81–83]. Prior studies have examined the role of DWI and ADC values in deciphering between posttreatment changes and tumour. Recurrent high-grade tumours have been shown to decrease ADC values as compared to

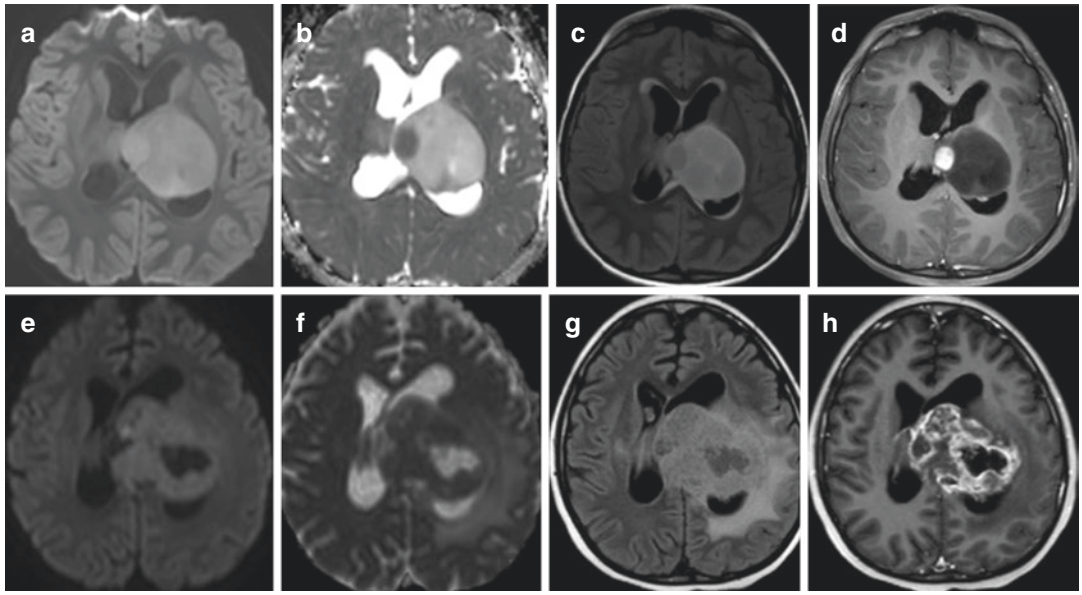

Fig. 10.10 Diffusion-weighted imaging (DWI) and progressive disease. (**a**–**d**) Axial DWI, ADC, T2 FLAIR and T1 post-contrast images demonstrating infiltrative mass in the left thalamus with an enhancing, hypercellular component. (**e**–**h**) Enlargement of the hypercellular tumour as seen on DWI/ADC with corresponding increase in size and extent on T2 FLAIR and post-contrast T1W images consistent with progressive disease

radiation necrosis [47, 84–86] (Fig. 10.10). This is thought to be due to degradation of cellular integrity and treatment-related changes with inflammation and necrosis, which ultimately increase diffusivity and ADC values. Lee et al. compared patients with true progressive disease to those with pseudoprogression and found higher signal intensity on DWI with lower ADC values in the truly progressive disease group and either a rim of high signal intensity or no increased signal intensity on DWI in the pseudoprogression group on imaging performed within 2 months of chemoradiation [87] (Fig. 10.11).

10.3.2.3 Multiparametric MRI

Multiparametric MRI sequences have also been utilized for the assessment of progressive disease versus treatment-related changes. As perfusion techniques are used to assess tumour vascular density and diffusion techniques are used for the assessment of tumour cellularity, combining these two sequences can potentially differentiate recurrent-progressive tumour from treatment-related changes. Prager et al. demonstrated increased specificity in deciphering progressive disease from pseudoprogression and radiation necrosis when both ADC and CBV values were examined concurrently [66]. Furthermore, Cha et al. also endorsed the utility of multiparametric MRI analysis of post chemoradiation therapy patients to determine true progression versus pseudoprogression [88]. The subtracted histogram mode with a multiparametric approach was higher than the single parametric MR approach with a sensitivity of 81.8% and a specificity of 100% [88]. Additionally, a high mode of rCBV on the subtracted histogram was found to be the best predictor of true progression [88]. Park et al. demonstrated similar findings with multiparametric volume-weighted voxel-based clustering over single parametric methods to decipher true progressive disease from pseudoprogression [89].

10.3.2.4 Emerging MRI Techniques

Additional MR techniques have been described in the literature as potentially useful for the evaluation of pseudoprogression. Dual-contrast perfusion MRI in a single imaging session using ferumoxytol has been described in the evaluation of paediatric brain tumours. Ferumoxytol is an

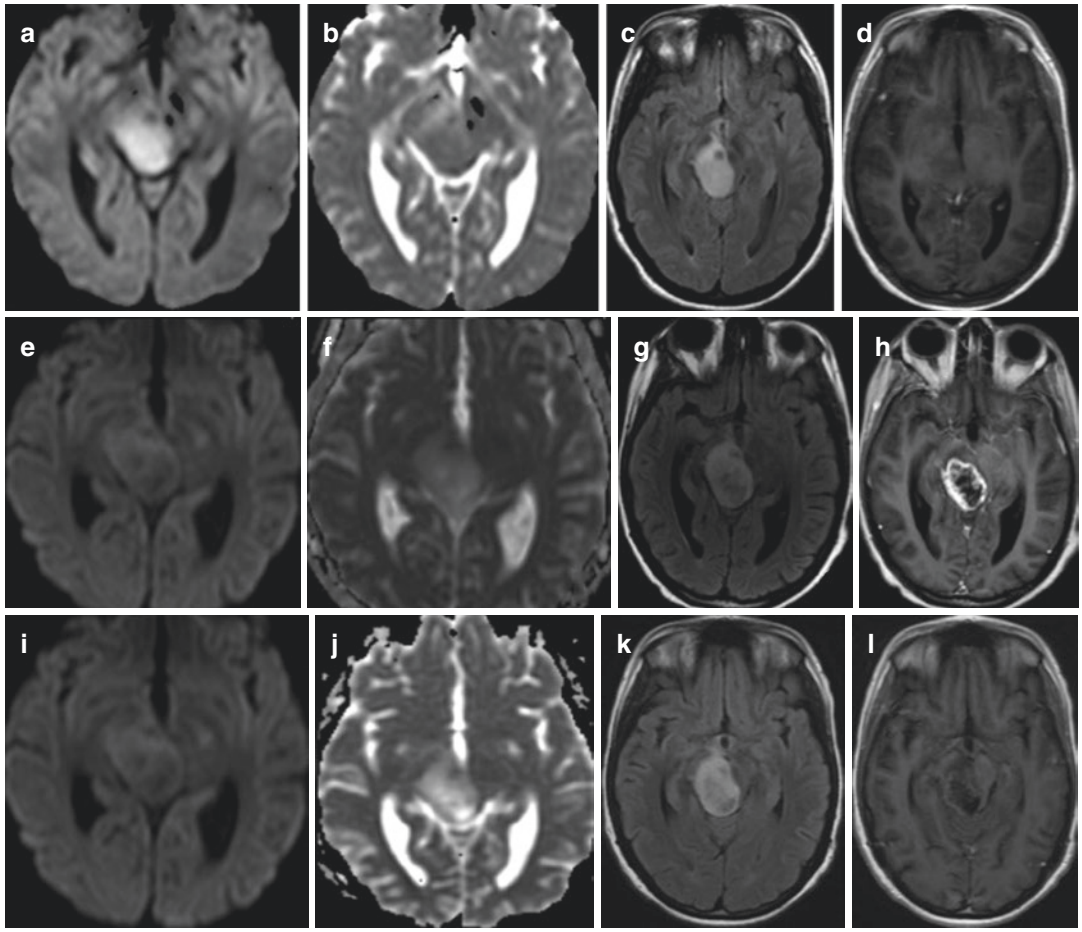

Fig. 10.11 DWI and pseudoprogression. (**a**–**d**) Axial DWI, ADC, T2 FLAIR and T1 post-contrast sequences demonstrating a hypercellular, nonenhancing, expansile mass of the brainstem (anaplastic astrocytoma). Over time after chemoradiation, there is progressive increased enhancement (**h**) that resolved (**l**). The follow-up ADC demonstrate increased diffusivity (**e**, **f**, **i**, **j**) and stable size (**g**, **k**) suggestive of pseudoprogression

ultrasmall superparamagnetic iron oxide (USPIO) nanoparticle that remains intravascular at early time points and therefore has advantages over gadolinium-based contrast agents in identifying active tumour [75]. This agent can potentially be helpful in perfusion imaging to differentiate pseudoprogression from progressive disease. An additional MRI-based technique known as applied parametric response mapping (PRM), formerly known as functional diffusion mapping, has also been described in the paediatric brain tumour population as a tool to differentiate progressive disease from pseudoprogression. PRM is used to characterize temporal diffusion profiles with higher specificity for true tumour progression than mean ADC measurements or tumour volume measurements [65]. This advantage is based on the concept that treatment-related changes cause heterogeneity of tissue with areas of oedema and necrosis mixed in with viable tumour. PRM helps minimize the heterogeneity encountered to better detect true progressive disease [65].

10.3.3 Nuclear Medicine

Multiple prior studies have examined the role of nuclear medicine techniques for the evaluation of progression versus pseudoprogression in brain tumour patients. Hatzoglou et al. found that

^{18}F-FDG PET/CT had similar predictive capabilities as compared to MR DSC perfusion in differentiating posttreatment changes from progressive tumour [67].

Pseudoprogression and radiation necrosis reportedly demonstrate decreased FDG avidity on PET/CT as compared to tumour [90]. PET/MR is also being used increasingly in this regard. There are studies that report the limitations of FDG PET/CT, demonstrating the lack of specificity for this technique as there are false positives with increased uptake, which can be seen in inflammatory processes and are not specific for progressive tumour [62]. Furthermore, the use of amino acid tracers in nuclear medicine has also been described as a potentially helpful technique to differentiate treatment-related changes from progressive disease. Terakawa et al. reported that ^{11}C-Methionine is better than FDG-PET in differentiating radiation necrosis from tumour recurrence [91]. Others have also reported the utility of amino acid tracers in differentiating between pseudoprogression and recurrent high-grade glial tumours in patients, including L-Tyrosine PET techniques [92]. ^{18}F-DOPA PET has been used more recently and is reported to show an increased conspicuity of tumour compared with normal surrounding tissue [93].

10.4 Part IV: MR Spectroscopy for the Evaluation of Treatment Response

MRS is a widely available noninvasive imaging tool that provides information regarding the biochemistry and metabolism of tissue. Often obtained in conjunction with conventional MR imaging, MRS can play an important diagnostic role in the multiparametric MR imaging assessment of brain tumours. ^{1}H-MRS has often been used to provide a specific diagnosis for brain tumours in conjunction with conventional MRI. Information gained from MRS has also been used to guide biopsies, predict histologic aggressiveness/grade and assess response to treatment [94]. The MRS hallmark of brain tumours relative to normal tissue is increased choline (Cho) and decreased *N*-acetylaspartate (NAA) levels. In general, decrease in NAA and creatine (Cr) levels with a simultaneous increase in Cho, lactate and lipids corresponds to increase in histologic grade. Very aggressive, malignant tumours typically demonstrate high metabolic activity, which translates to depletion of energy stores resulting in a decrease/absence of Cr, high levels of Cho, high levels of lipids/lactate due to necrosis and utilization of glycolytic pathways as well as lower levels of NAA.

MRS is often used in combination with diffusion-weighted imaging as well as perfusion imaging as part of a multiparametric MRI approach to evaluate progression and treatment-related changes. For example, in the setting of increased enhancement, if there is no significant change in the metabolites, pseudoprogression is favoured over true progression [95]. Furthermore, the increase in Cho/Cr or Cho/NAA ratios and decrease of NAA/Cr ratio in the treated area are highly suggestive of tumour recurrence/progressive disease rather than treatment-related change [96, 97] (Fig. 10.12). Paediatric brain tumour metabolic profiles typically do not change significantly from diagnosis to first relapse and thus can aid in the confirmation of recurrent/progressive disease [94].

Posttreatment changes can have characteristic metabolic profiles. Walecki et al. described elevation of the myoinositol-to-creatine ratio as one of the first indicators of postradiation changes [98]. Furthermore, prior studies have demonstrated that late radiation necrosis changes cause an overall decrease in all metabolites with the exception of lipids [99]. Ultimately, the assessment of treatment response and treatment-related changes depend on serial MRS throughout the patient's treatment course. Alexander et al. reported an evolving metabolite pattern identified at week 4 of radiation therapy with normalization of the choline-to-creatine ratio and lactate to NAA as a marker for early treatment response [100]. Quon also endorsed serial MRS for the evolution of posttreatment related changes in high-grade glioma patients, demonstrating that changes in normalized choline levels at 2 months postradiation therapy are prognostic of overall survival. Specifically, they reported that patients with greater than 40% reduction in normalized

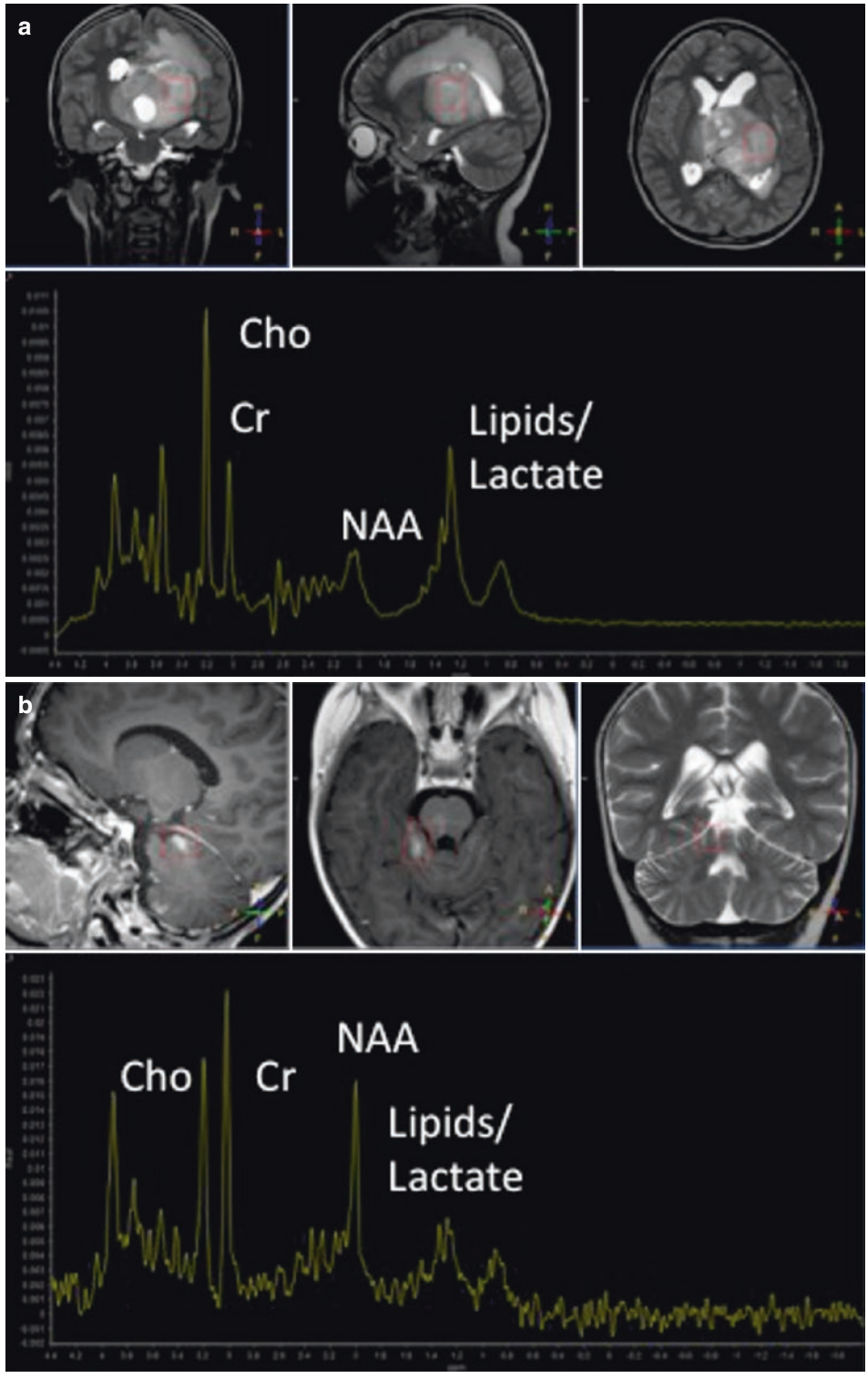

Fig. 10.12 MR spectroscopy (MRS) of true tumour progression and pseudoprogression. (**a**) Progressive tumour with elevated choline (Cho), decreased creatine (Cr), decreased *N*-acetyl-aspartate (NAA) and elevated lipids and lactate consistent with progressive disease. (**b**) Pseudoprogression with minimally decreased NAA, relatively normal Cho and minimal lipids/lactate

choline levels from week 4 to 2 months postradiation therapy had a worse overall survival than the patients without such a change [101].

10.5 Conclusion

Pediatric brain tumors are unique when compared to their adult counterparts, and as such require a careful and systematic approach when assessing response to therapy. As we have outlined here, different tumor types necessitate a tailored approach to imaging that takes into account tumor type and location, characteristic pathways for disease spread, and history of both ongoing and prior therapies, including surgery, radiation and chemotherapy. These considerations are essential when determining which of the many anatomic and functional imaging techniques available will provide the most accurate and reproducible assessment of treatment response.

Acknowledgements Miss Jess Cooper, MRI Superintendent Radiographer, Great Ormond Street Hospital, London

References

1. Warren KE, Poussaint TY, Vezina G, Hargrave D, Packer RJ, Goldman S, et al. Challenges with defining response to antitumor agents in pediatric neuro-oncology: a report from the response assessment in pediatric neuro-oncology (RAPNO) working group. Pediatr Blood Cancer. 2013;60(9):1397–401.
2. Louis DN, Perry A, Reifenberger G, von Deimling A, Figarella-Branger D, Cavenee WK, et al. The 2016 World Health Organization Classification of Tumors of the Central Nervous System: a summary. Acta Neuropathol. 2016;131(6):803–20.
3. Chhabda S, Carney O, D'Arco F, Jacques TS, Mankad K. The 2016 World Health Organization Classification of tumours of the Central Nervous System: what the paediatric neuroradiologist needs to know. Quant Imaging Med Surg. 2016;6(5):486–9.
4. Wen PY, Macdonald DR, Reardon DA, Cloughesy TF, Sorensen AG, Galanis E, et al. Updated response assessment criteria for high-grade gliomas: response assessment in neuro-oncology working group. J Clin Oncol. 2010;28(11):1963–72.
5. Gaudino S, Quaglio F, Schiarelli C, Martucci M, Tartaglione T, Gualano MR, et al. Spontaneous modifications of contrast enhancement in childhood non-cerebellar pilocytic astrocytomas. Neuroradiology. 2012;54(9):989–95.
6. Gnekow AK, Kortmann RD, Pietsch T, Emser A. Low grade chiasmatic-hypothalamic glioma-carboplatin and vincristine chemotherapy effectively defers radiotherapy within a comprehensive treatment strategy -- report from the multicenter treatment study for children and adolescents with a low grade glioma -- HIT-LGG 1996 -- of the Society of Pediatric Oncology and Hematology (GPOH). Klin Padiatr. 2004;216(6):331–42.
7. Macdonald DR, Cascino TL, Schold SC, Cairncross JG. Response criteria for phase II studies of supratentorial malignant glioma. J Clin Oncol. 1990;8(7):1277–80.
8. Jaspan T, Morgan PS, Warmuth-Metz M, Sanchez Aliaga E, Warren D, Calmon R, et al. Response assessment in pediatric neuro-oncology: implementation and expansion of the RANO criteria in a randomized phase II trial of pediatric patients with newly diagnosed high-grade gliomas. AJNR Am J Neuroradiol. 2016;37(9):1581–7.
9. Chinot OL, Macdonald DR, Abrey LE, Zahlmann G, Kerloëguen Y, Cloughesy TF. Response assessment criteria for glioblastoma: practical adaptation and implementation in clinical trials of antiangiogenic therapy. Curr Neurol Neurosci Rep. 2013;13(5):347.
10. Brandsma D, van den Bent MJ. Pseudoprogression and pseudoresponse in the treatment of gliomas. Curr Opin Neurol. 2009;22(6):633–8.
11. Barajas RF, Chang JS, Segal MR, Parsa AT, McDermott MW, Berger MS, et al. Differentiation of recurrent glioblastoma multiforme from radiation necrosis after external beam radiation therapy with dynamic susceptibility-weighted contrast-enhanced perfusion MR imaging. Radiology. 2009;253(2):486–96.
12. Avery RA, Mansoor A, Idrees R, Biggs E, Alsharid MA, Packer RJ, et al. Quantitative MRI criteria for optic pathway enlargement in neurofibromatosis type 1. Neurology. 2016;86:2264.
13. Avery RA, Ferner RE, Listernick R, Fisher MJ, Gutmann DH, Liu GT. Visual acuity in children with low grade gliomas of the visual pathway: implications for patient care and clinical research. J Neurooncol. 2012;110(1):1–7.
14. Ge M, Li S, Wang L, Li C, Zhang J. The role of diffusion tensor tractography in the surgical treatment of pediatric optic chiasmatic gliomas. J Neurooncol. 2015;122:357.
15. Kornreich L, Blaser S, Schwarz M, Shuper A, Vishne TH, Cohen IJ, et al. Optic pathway glioma: correlation of imaging findings with the presence of neurofibromatosis. AJNR Am J Neuroradiol. 2001;22(10):1963–9.
16. Chateil JF, Soussotte C, Pédespan JM, Brun M, Le Manh C, Diard F. MRI and clinical differences between optic pathway tumours in children with and without neurofibromatosis. Br J Radiol. 2001;74(877):24–31.

17. Zuccoli G, Ferrozzi F, Sigorini M, Virdis R, Bassi P, Bellomi M. Early spontaneous regression of a hypothalamic/chiasmatic mass in neurofibromatosis type 1: MR findings. Eur Radiol. 2000;10(7):1076–8.
18. Dodgshun AJ, Elder JE, Hansford JR, Sullivan MJ. Long-term visual outcome after chemotherapy for optic pathway glioma in children: site and age are strongly predictive. Cancer. 2015;121:4190.
19. Listernick R, Ferner RE, Liu GT, Gutmann DH. Optic pathway gliomas in neurofibromatosis-1: controversies and recommendations. Ann Neurol. 2007;61(3):189–98.
20. Wen PY, Chang SM, Van den Bent MJ, Vogelbaum MA, Macdonald DR, Lee EQ. Response assessment in neuro-oncology clinical trials. J Clin Oncol. 2017;35(21):2439–49.
21. Taylor T, Jaspan T, Milano G, Gregson R, Parker T, Ritzmann T, et al. Radiological classification of optic pathway gliomas: experience of a modified functional classification system. Br J Radiol. 2008;81(970):761–6.
22. Warren KE, Vezina G, Poussaint TY, Warmuth-Metz M, Chamberlain MC, Packer RJ, et al. Response assessment in medulloblastoma and leptomeningeal seeding tumors: recommendations from the response assessment in Pediatric Neuro-Oncology Committee. Neuro Oncol. 2018;20:13.
23. Packer RJ, Gajjar A, Vezina G, Rorke-Adams L, Burger PC, Robertson PL, et al. Phase III study of craniospinal radiation therapy followed by adjuvant chemotherapy for newly diagnosed average-risk medulloblastoma. J Clin Oncol. 2006;24(25):4202–8.
24. Perreault S, Ramaswamy V, Achrol AS, Chao K, Liu TT, Shih D, et al. MRI surrogates for molecular subgroups of medulloblastoma. AJNR Am J Neuroradiol. 2014;35(7):1263–9.
25. D'Arco F, Khan F, Mankad K et al. Differential diagnosis of posterior fossa tumours in children: new insights. Pediatr Radiol. 2018;48(13):1955–63.
26. Gajjar A, Bowers DC, Karajannis MA, Leary S, Witt H, Gottardo NG. Pediatric brain tumors: innovative genomic information is transforming the diagnostic and clinical landscape. J Clin Oncol. 2015;33(27):2986–98.
27. Löbel U, Sedlacik J, Reddick WE, Kocak M, Ji Q, Broniscer A, et al. Quantitative diffusion-weighted and dynamic susceptibility-weighted contrast-enhanced perfusion MR imaging analysis of T2 hypointense lesion components in pediatric diffuse intrinsic pontine glioma. AJNR Am J Neuroradiol. 2011;32(2):315–22.
28. Warren KE. Diffuse intrinsic pontine glioma: poised for progress. Front Oncol. 2012;2:205.
29. Burzynski SR, Janicki TJ, Burzynski GS, Marszalek A. The response and survival of children with recurrent diffuse intrinsic pontine glioma based on phase II study of antineoplastons A10 and AS2-1 in patients with brainstem glioma. Childs Nerv Syst. 2014;30(12):2051–61.
30. Svolos P, Reddick WE, Edwards A, Sykes A, Li Y, Glass JO, et al. Measurable supratentorial white matter volume changes in patients with diffuse intrinsic pontine glioma treated with an anti-vascular endothelial growth factor agent, steroids, and radiation. AJNR Am J Neuroradiol. 2017;38(6):1235–41.
31. Löbel U, Hwang S, Edwards A, Li Y, Li X, Broniscer A, et al. Discrepant longitudinal volumetric and metabolic evolution of diffuse intrinsic Pontine gliomas during treatment: implications for current response assessment strategies. Neuroradiology. 2016;58:1027.
32. Chamberlain M, Soffietti R, Raizer J, Rudà R, Brandsma D, Boogerd W, et al. Leptomeningeal metastasis: a response assessment in neuro-oncology critical review of endpoints and response criteria of published randomized clinical trials. Neuro Oncol. 2014;16(9):1176–85.
33. Chamberlain M, Junck L, Brandsma D, Soffietti R, Rudà R, Raizer J, et al. Leptomeningeal metastases: a RANO proposal for response criteria. Neuro Oncol. 2017;19(4):484–92.
34. Warren KE, Patronas N, Aikin AA, Albert PS, Balis FM. Comparison of one-, two-, and three-dimensional measurements of childhood brain tumors. J Natl Cancer Inst. 2001;93(18):1401–5.
35. Kilday J-P, Branson H, Rockel C, Laughlin S, Mabbott D, Bouffet E, et al. Tumor volumetric measurements in surgically inaccessible pediatric low-grade glioma. J Pediatr Hematol Oncol. 2015;37(1):e31–6.
36. Rees J, Watt H, Jäger HR, Benton C, Tozer D, Tofts P, et al. Volumes and growth rates of untreated adult low-grade gliomas indicate risk of early malignant transformation. Eur J Radiol. 2009;72(1):54–64.
37. Connor SEJ, Gunny R, Hampton T, O'gorman R. Magnetic resonance image registration and subtraction in the assessment of minor changes in low grade glioma volume. Eur Radiol. 2004;14(11):2061–6.
38. Dombi E, Ardern-Holmes SL, Babovic-Vuksanovic D, Barker FG, Connor S, Evans DG, et al. Recommendations for imaging tumor response in neurofibromatosis clinical trials. Neurology. 2013;81(21 Suppl 1):S33–40.
39. Henson JW, Ulmer S, Harris GJ. Brain tumor imaging in clinical trials. AJNR Am J Neuroradiol. 2008;29(3):419–24.
40. D'Arco F, O'Hare P, Dashti F et al. Volumetric assessment of tumor size changes in pediatric low grade gliomas: feasability and comparison with linear measurements. Neuroradiology. 2018;60(4):427–36.
41. Weber M-A, Giesel FL, Stieltjes B. MRI for identification of progression in brain tumors: from morphology to function. Expert Rev Neurother. 2008;8(10):1507–25.
42. Maier SE, Gudbjartsson H, Patz S, Hsu L, Lovblad KO, Edelman RR, et al. Line scan diffusion imaging: characterization in healthy subjects and stroke patients. AJR Am J Roentgenol. 1998;171(1):85–93.
43. Helenius J, Soinne L, Perkiö J, Salonen O, Kangasmäki A, Kaste M, et al. Diffusion-weighted

MR imaging in normal human brains in various age groups. AJNR Am J Neuroradiol. 2002;23(2):194–9.
44. Steen RG. Edema and tumor perfusion: characterization by quantitative 1H MR imaging. AJR Am J Roentgenol. 1992;158(2):259–64.
45. Maier SE, Sun Y, Mulkern RV. Diffusion imaging of brain tumors. NMR Biomed. 2010;23(7):849–64.
46. Lyng H, Haraldseth O, Rofstad EK. Measurement of cell density and necrotic fraction in human melanoma xenografts by diffusion weighted magnetic resonance imaging. Magn Reson Med. 2000;43(6):828–36.
47. Asao C, Korogi Y, Kitajima M, Hirai T, Baba Y, Makino K, et al. Diffusion-weighted imaging of radiation-induced brain injury for differentiation from tumor recurrence. AJNR Am J Neuroradiol. 2005;26(6):1455–60.
48. Han C, Zhao L, Zhong S, Wu X, Guo J, Zhuang X, et al. A comparison of high b-value vs standard b-value diffusion-weighted magnetic resonance imaging at 3.0 T for medulloblastomas. Br J Radiol. 2015;88(1054):20150220.
49. Mardor Y, Roth Y, Lidar Z, Jonas T, Pfeffer R, Maier SE, et al. Monitoring response to convection-enhanced taxol delivery in brain tumor patients using diffusion-weighted magnetic resonance imaging. Cancer Res. 2001;61(13):4971–3.
50. Mardor Y, Pfeffer R, Spiegelmann R, Roth Y, Maier SE, Nissim O, et al. Early detection of response to radiation therapy in patients with brain malignancies using conventional and high b-value diffusion-weighted magnetic resonance imaging. J Clin Oncol. 2003;21(6):1094–100.
51. Sinha S, Bastin ME, Whittle IR, Wardlaw JM. Diffusion tensor MR imaging of high-grade cerebral gliomas. AJNR Am J Neuroradiol. 2002;23(4):520–7.
52. Jellison BJ, Field AS, Medow J, Lazar M, Salamat MS, Alexander AL. Diffusion tensor imaging of cerebral white matter: a pictorial review of physics, fiber tract anatomy, and tumor imaging patterns. AJNR Am J Neuroradiol. 2004;25(3):356–69.
53. van der Heide UA, Houweling AC, Groenendaal G, Beets-Tan RGH, Lambin P. Functional MRI for radiotherapy dose painting. Magn Reson Imaging. 2012;30(9):1216–23.
54. Steven AJ, Zhuo J, Melhem ER. Diffusion kurtosis imaging: an emerging technique for evaluating the microstructural environment of the brain. AJR Am J Roentgenol. 2014;202(1):W26–33.
55. Van Cauter S, De Keyzer F, Sima DM, Sava AC, D'Arco F, Veraart J, et al. Integrating diffusion kurtosis imaging, dynamic susceptibility-weighted contrast-enhanced MRI, and short echo time chemical shift imaging for grading gliomas. Neuro Oncol. 2014;16(7):1010–21.
56. Goshima S, Kanematsu M, Noda Y, Kondo H, Watanabe H, Bae KT. Diffusion kurtosis imaging to assess response to treatment in hypervascular hepatocellular carcinoma. AJR Am J Roentgenol. 2015;204(5):W543–9.
57. Hu F, Tang W, Sun Y, Wan D, Cai S, Zhang Z, et al. The value of diffusion kurtosis imaging in assessing pathological complete response to neoadjuvant chemoradiation therapy in rectal cancer: a comparison with conventional diffusion-weighted imaging. Oncotarget. 2017;8:75597.
58. Hyare H, Thust S, Rees J. Advanced MRI techniques in the monitoring of treatment of gliomas. Curr Treat Options Neurol. 2017;19(3):11.
59. Taal W, Brandsma D, de Bruin HG, Bromberg JE, Swaak-Kragten AT, Smitt PAES, et al. Incidence of early pseudo-progression in a cohort of malignant glioma patients treated with chemoirradiation with temozolomide. Cancer. 2008;113(2):405–10.
60. Brandsma D, Stalpers L, Taal W, Sminia P, van den Bent MJ. Clinical features, mechanisms, and management of pseudoprogression in malignant gliomas. Lancet Oncol. 2008;9(5):453–61.
61. Verma N, Cowperthwaite MC, Burnett MG, Markey MK. Differentiating tumor recurrence from treatment necrosis: a review of neuro-oncologic imaging strategies. Neuro Oncol. 2013;15(5):515–34.
62. Meyzer C, Dhermain F, Ducreux D, Habrand J-L, Varlet P, Sainte-Rose C, et al. A case report of pseudoprogression followed by complete remission after proton-beam irradiation for a low-grade glioma in a teenager: the value of dynamic contrast-enhanced MRI. Radiat Oncol. 2010;5:9.
63. Negretti L, Blanchard P, Couanet D, Kieffer V, Goma G, Habrand JL, et al. Pseudoprogression after high-dose busulfan-thiotepa with autologous stem cell transplantation and radiation therapy in children with brain tumors: impact on survival. Neuro Oncol. 2012;14(11):1413–21.
64. Chassot A, Canale S, Varlet P, Puget S, Roujeau T, Negretti L, et al. Radiotherapy with concurrent and adjuvant temozolomide in children with newly diagnosed diffuse intrinsic pontine glioma. J Neurooncol. 2012;106(2):399–407.
65. Ceschin R, Kurland BF, Abberbock SR, Ellingson BM, Okada H, Jakacki RI, et al. Parametric response mapping of apparent diffusion coefficient as an imaging biomarker to distinguish pseudoprogression from true tumor progression in peptide-based vaccine therapy for pediatric diffuse intrinsic pontine glioma. AJNR Am J Neuroradiol. 2015;36(11):2170–6.
66. Prager AJ, Martinez N, Beal K, Omuro A, Zhang Z, Young RJ. Diffusion and perfusion MRI to differentiate treatment-related changes including pseudoprogression from recurrent tumors in high-grade gliomas with histopathologic evidence. AJNR Am J Neuroradiol. 2015;36:877.
67. Hatzoglou V, Ulaner GA, Zhang Z, Beal K, Holodny AI, Young RJ. Comparison of the effectiveness of MRI perfusion and fluorine-18 FDG PET-CT for differentiating radiation injury from viable brain tumor: a preliminary retrospective analysis with pathologic correlation in all patients. Clin Imaging. 2013;37(3):451–7.

68. Shin KE, Ahn KJ, Choi HS, Jung SL, Kim BS, Jeon SS, et al. DCE and DSC MR perfusion imaging in the differentiation of recurrent tumour from treatment-related changes in patients with glioma. Clin Radiol. 2014;69:e264.
69. Essig M, Shiroishi MS, Nguyen TB, Saake M, Provenzale JM, Enterline D, et al. Perfusion MRI: the five most frequently asked technical questions. AJR Am J Roentgenol. 2013;200(1):24–34.
70. Petrella JR, Provenzale JM. MR perfusion imaging of the brain: techniques and applications. AJR Am J Roentgenol. 2000;175(1):207–19.
71. Barajas RF, Chang JS, Sneed PK, Segal MR, McDermott MW, Cha S. Distinguishing recurrent intra-axial metastatic tumor from radiation necrosis following gamma knife radiosurgery using dynamic susceptibility-weighted contrast-enhanced perfusion MR imaging. AJNR Am J Neuroradiol. 2009;30(2):367–72.
72. Carceller F, Fowkes LA, Khabra K, Moreno L, Saran F, Burford A, et al. Pseudoprogression in children, adolescents and young adults with non-brainstem high grade glioma and diffuse intrinsic pontine glioma. J Neurooncol. 2016;129(1):109–21.
73. Gururangan S, Chi SN, Young Poussaint T, Onar-Thomas A, Gilbertson RJ, Vajapeyam S, et al. Lack of efficacy of bevacizumab plus irinotecan in children with recurrent malignant glioma and diffuse brainstem glioma: a Pediatric Brain Tumor Consortium study. J Clin Oncol. 2010;28(18):3069–75.
74. Gururangan S, Fangusaro J, Young Poussaint T, Onar-Thomas A, Gilbertson RJ, Vajapeyam S, et al. Lack of efficacy of bevacizumab + irinotecan in cases of pediatric recurrent ependymoma--a Pediatric Brain Tumor Consortium study. Neuro Oncol. 2012;14(11):1404–12.
75. Thompson EM, Guillaume DJ, Dósa E, Li X, Nazemi KJ, Gahramanov S, et al. Dual contrast perfusion MRI in a single imaging session for assessment of pediatric brain tumors. J Neurooncol. 2012;109(1):105–14.
76. Patel P, Baradaran H, Delgado D, Askin G, Christos P, John Tsiouris A, et al. MR perfusion-weighted imaging in the evaluation of high-grade gliomas after treatment: a systematic review and meta-analysis. Neuro Oncol. 2017;19(1):118–27.
77. Yoo R-E, Choi SH. Recent application of advanced MR imaging to predict pseudoprogression in high-grade glioma patients. Magn Reson Med Sci. 2016;15(2):165–77.
78. Noguchi T, Yoshiura T, Hiwatashi A, Togao O, Yamashita K, Nagao E, et al. Perfusion imaging of brain tumors using arterial spin-labeling: correlation with histopathologic vascular density. AJNR Am J Neuroradiol. 2008;29(4):688–93.
79. Yeom KW, Mitchell LA, Lober RM, Barnes PD, Vogel H, Fisher PG, et al. Arterial spin-labeled perfusion of pediatric brain tumors. AJNR Am J Neuroradiol. 2014;35(2):395–401.
80. Choi YJ, Kim HS, Jahng G-H, Kim SJ, Suh DC. Pseudoprogression in patients with glioblastoma: added value of arterial spin labeling to dynamic susceptibility contrast perfusion MR imaging. Acta Radiol. 2013;54(4):448–54.
81. Guo AC, Cummings TJ, Dash RC, Provenzale JM. Lymphomas and high-grade astrocytomas: comparison of water diffusibility and histologic characteristics. Radiology. 2002;224(1):177–83.
82. Hayashida Y, Hirai T, Morishita S, Kitajima M, Murakami R, Korogi Y, et al. Diffusion-weighted imaging of metastatic brain tumors: comparison with histologic type and tumor cellularity. AJNR Am J Neuroradiol. 2006;27(7):1419–25.
83. Herneth AM, Guccione S, Bednarski M. Apparent diffusion coefficient: a quantitative parameter for in vivo tumor characterization. Eur J Radiol. 2003;45(3):208–13.
84. Hein PA, Eskey CJ, Dunn JF, Hug EB. Diffusion-weighted imaging in the follow-up of treated high-grade gliomas: tumor recurrence versus radiation injury. AJNR Am J Neuroradiol. 2004;25(2):201–9.
85. Matsusue E, Fink JR, Rockhill JK, Ogawa T, Maravilla KR. Distinction between glioma progression and post-radiation change by combined physiologic MR imaging. Neuroradiology. 2010;52(4):297–306.
86. Zeng Q-S, Li C-F, Liu H, Zhen J-H, Feng D-C. Distinction between recurrent glioma and radiation injury using magnetic resonance spectroscopy in combination with diffusion-weighted imaging. Int J Radiat Oncol Biol Phys. 2007;68(1):151–8.
87. Lee WJ, Choi SH, Park C-K, Yi KS, Kim TM, Lee S-H, et al. Diffusion-weighted MR imaging for the differentiation of true progression from pseudoprogression following concomitant radiotherapy with temozolomide in patients with newly diagnosed high-grade gliomas. Acad Radiol. 2012;19(11):1353–61.
88. Cha J, Kim ST, Kim HJ, Kim BJ, Kim YK, Lee JY, et al. Differentiation of tumor progression from pseudoprogression in patients with posttreatment glioblastoma using multiparametric histogram analysis. AJNR Am J Neuroradiol. 2014;35(7):1309–17.
89. Park JE, Kim HS, Goh MJ, Kim SJ, Kim JH. Pseudoprogression in patients with glioblastoma: assessment by using volume-weighted voxel-based multiparametric clustering of MR imaging data in an independent test set. Radiology. 2015;275(3):792–802.
90. Caroline I, Rosenthal MA. Imaging modalities in high-grade gliomas: pseudoprogression, recurrence, or necrosis? J Clin Neurosci. 2012;19(5):633–7.
91. Terakawa Y, Tsuyuguchi N, Iwai Y, Yamanaka K, Higashiyama S, Takami T, et al. Diagnostic accuracy of 11C-methionine PET for differentiation of recurrent brain tumors from radiation necrosis after radiotherapy. J Nucl Med. 2008;49(5):694–9.
92. Galldiks N, Dunkl V, Stoffels G, Hutterer M, Rapp M, Sabel M, et al. Diagnosis of pseudoprogression in patients with glioblastoma using O-(2-[^{18}F]

fluoroethyl)-L-tyrosine PET. Eur J Nucl Med Mol Imaging. 2015;42(5):685–95.
93. Morana G, Piccardo A, Tortora D, Puntoni M, Severino M, Nozza P, et al. Grading and outcome prediction of pediatric diffuse astrocytic tumors with diffusion and arterial spin labeling perfusion MRI in comparison with 18F-DOPA PET. Eur J Nucl Med Mol Imaging. 2017;44:2084.
94. Zarifi M, Tzika AA. Proton MRS imaging in pediatric brain tumors. Pediatr Radiol. 2016;46(7):952–62.
95. Martín Noguerol T, Sánchez-González J, Martínez Barbero JP, García-Figueiras R, Baleato-González S, Luna A. Clinical imaging of tumor metabolism with ^{1}h magnetic resonance spectroscopy. Magn Reson Imaging Clin N Am. 2016;24(1):57–86.
96. Smith EA, Carlos RC, Junck LR, Tsien CI, Elias A, Sundgren PC. Developing a clinical decision model: MR spectroscopy to differentiate between recurrent tumor and radiation change in patients with new contrast-enhancing lesions. AJR Am J Roentgenol. 2009;192(2):W45–52.
97. Elias AE, Carlos RC, Smith EA, Frechtling D, George B, Maly P, et al. MR spectroscopy using normalized and non-normalized metabolite ratios for differentiating recurrent brain tumor from radiation injury. Acad Radiol. 2011;18(9):1101–8.
98. Walecki J, Sokól M, Pieniazek P, Maciejewski B, Tarnawski R, Krupska T, et al. Role of short TE 1H-MR spectroscopy in monitoring of post-operation irradiated patients. Eur J Radiol. 1999;30(2):154–61.
99. Dhermain FG, Hau P, Lanfermann H, Jacobs AH, van den Bent MJ. Advanced MRI and PET imaging for assessment of treatment response in patients with gliomas. Lancet Neurol. 2010;9(9):906–20.
100. Alexander A, Murtha A, Abdulkarim B, Mehta V, Wheatley M, Murray B, et al. Prognostic significance of serial magnetic resonance spectroscopies over the course of radiation therapy for patients with malignant glioma. Clin Invest Med. 2006;29(5):301–11.
101. Quon H, Brunet B, Alexander A, Murtha A, Abdulkarim B, Fulton D, et al. Changes in serial magnetic resonance spectroscopy predict outcome in high-grade glioma during and after postoperative radiotherapy. Anticancer Res. 2011;31(10):3559–65.

Complications of Therapy

11

Eline E. Deurloo and Anne M. J. B. Smets

11.1 Multisystem

11.1.1 Infections

Cancer therapy-related suppression of the bone marrow and immune system and disruption of the natural barriers of the body make patients more vulnerable to infections. Infections are the most important cause of morbidity and mortality during cancer treatment and a common cause of hospital admission. Neutropenia is the most important risk factor (absolute count <500 cells/mm^3). Yet remarkably, only 20–30% of patients with febrile neutropenia have positive blood cultures [1]. Of the proven bloodstream infections, about 70% are caused by gram-positive bacteria (e.g., staphylococci, enterococci, streptococci), 23% by gram-negative bacteria (e.g., *E. coli*, klebsiella, pseudomonas, serratia, proteus), and 7% by fungi or viruses (e.g., candida, aspergillus, CMV, varicella zoster, adenovirus, *Pneumocystis jirovecii*). Fungal infections typically occur in patients with severe and prolonged neutropenia. A higher incidence of invasive fungal infections is reported in patients with a hematologic malignancy (acute myeloid leukemia (AML) and acute lymphoblastic leukemia (ALL)), than in patients with a solid tumor: 13.6% (AML) versus 5.9% (ALL) versus 1.6% (solid tumors), respectively [2]. If there is an intracranial fungal infection, in up to 90% of patients, there is a concomitant pulmonary infection or an infection elsewhere.

Besides neutropenia, other predisposing factors for multisystemic fungal infection are the presence of a central venous catheter, a high intensity of treatment score, and corticosteroid treatment [2].

Infections are also the commonest cause of death after relapse/progression [3] with mortality rates between 1% and 3% in episodes of febrile neutropenia.

Early diagnosis of invasive aspergillosis is important, as it has been shown to improve treatment success significantly [4].

In the 2017 update of the guideline for the management of fever and neutropenia in children with cancer and hematopoietic stem cell transplantation (HSCT) recipients, imaging recommendations are formulated [7]. A large systematic review showed that the rate of pneumonia in asymptomatic children is <3%, and therefore chest X-ray should only be performed in patients with respiratory signs or symptoms [4–6]. In patients with prolonged (≥96 h) neutropenic fever, chest CT and abdominal ultrasound are strongly recommended in search for signs of fungal disease [7]. CT of the paranasal sinus is often abnormal in patients with prolonged fever and neutropenia and does not distinguish fungal

E. E. Deurloo (✉) · A. M. J. B. Smets
Department of Radiology, Amsterdam UMC, University of Amsterdam, Meibergdreef 9, Amsterdam, The Netherlands
e-mail: e.e.deurloo@amc.uva.nl; a.m.smets@amc.uva.nl

S. D. Voss, K. McHugh (eds.), *Imaging in Pediatric Oncology*, Pediatric Oncology,
https://doi.org/10.1007/978-3-030-03777-2_11

infection from another cause in many instances. It should therefore not be performed routinely in children with neutropenic fever [1, 7].

Finally, the systemic distribution of fungal infection (lungs, paranasal sinuses, muscles, liver, spleen, kidneys) renders these patients candidates for WB-MRI [1, 8].

11.2 Central Nervous System (CNS)

Acute complications of the central nervous system can be divided into infections, treatment toxicity, and vascular complications.

11.2.1 Infection

The incidence of central nervous system infections in children treated for cancer is reported to be 2–14% [9]. CNS infections can be due to disease- or treatment-related immunosuppression, e.g., steroid therapy, chemotherapy, and radiation therapy [8], but occur most frequently in patients undergoing neurosurgical procedures or hematopoietic stem cell transplantation. Life-threatening infections are mainly caused by viruses (herpesvirus, CMV) or fungi (*Aspergillus*, *Candida*, and less commonly *Zygomycetes*, *Trichosporon*, *Fusarium*).

CNS imaging is indicated to establish the diagnosis of a CNS infection, to detect complications of the infection and to monitor response to treatment [8]. On imaging studies, CNS infection can present as focal cerebral lesions, invasive sinusitis, cerebral infarction, demyelination, encephalitis, or meningitis.

CT of CNS infection shows nonspecific areas of hypoattenuation with no or minimal mass effect [10] but often yields false-negative results, particularly in the early stages. Therefore, children suspected of having a CNS infection should undergo MRI rather than CT.

11.2.1.1 Fungal

In immunosuppressed pediatric cancer patients, fungi are the major causative organisms of brain abscesses, in contrast to bacteria in immune-competent children [10]. In the majority of cases, CNS infections are caused by *Aspergillus* [9]. The main clinical symptom of fungal CNS infections is headache.

Imaging findings of fungal infections are nonspecific. The age and the immune status of the patient likely play a role in the distribution of the lesions and the imaging characteristics, but this has not been fully understood [11]. On CT hypodense lesions with little or no mass effect are found in the basal ganglia and the juxtacortical white matter, typically showing no enhancement (Fig. 11.1). On MRI the lesions are of intermediate or high signal intensity on T2-weighted images, with surrounding hyperintense perilesional edema (Fig. 11.2) [12]. They are hypointense on T1-weighted images and may show rim enhancement after gadolinium injection. However, in severe immune-compromised patients, lesions from angioinvasive aspergillus are often non-enhancing (Fig. 11.2) [11].

At times, there is a hemorrhagic component, and infarction may secondarily occur due to occlusion of vessels by hyphae. As a result of the paramagnetic effect within the hyphae, susceptibility artifacts may surround the aspergillus collections (Fig. 11.2) mimicking calcifications or hemorrhage.

Importantly, infectious lesions are most of the time much more conspicuous on diffusion-weighted imaging (DWI) than on conventional T1- or T2-weighted images: DWI is the most sensitive sequence with respect to the presence of a fungal abscess within the brain. Fungal cerebral abscesses typically show central restricted diffusion similar to bacterial abscesses, most likely because it contains highly proteinaceous fluid and because there is cellular infiltration (Fig. 11.3) [8]. However, the pattern of diffusion restriction may be different, or diffusion restriction may even be absent with certain organisms [11].

Invasive fungal sinusitis is usually caused by aspergillus or mucormycosis. If sinus disease is associated with brain lesions, *Aspergillus* infection should be included in the differential diagnosis. CT then shows nonspecific signs with an opaque paranasal sinus without a fluid level [9].

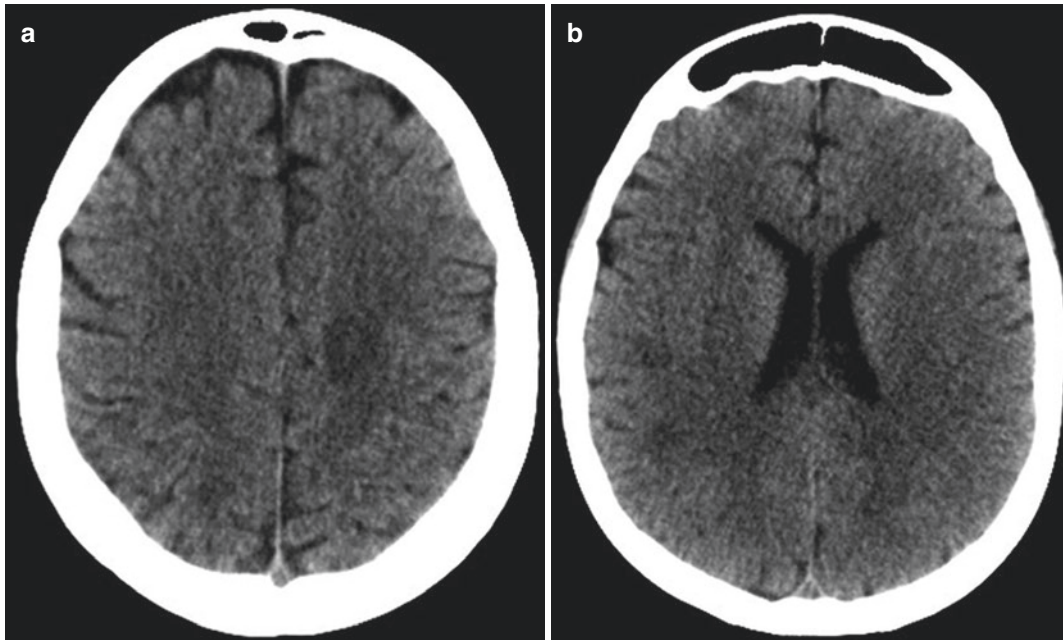

Fig. 11.1 Cerebral aspergillosis in a 15-year-old boy with AML and chloroma; neutropenic fever since 2 weeks and recent signs of meningitis, change in behavior, and diplopia. Axial CT images (**a**, **b**) show hypodense cerebral lesions

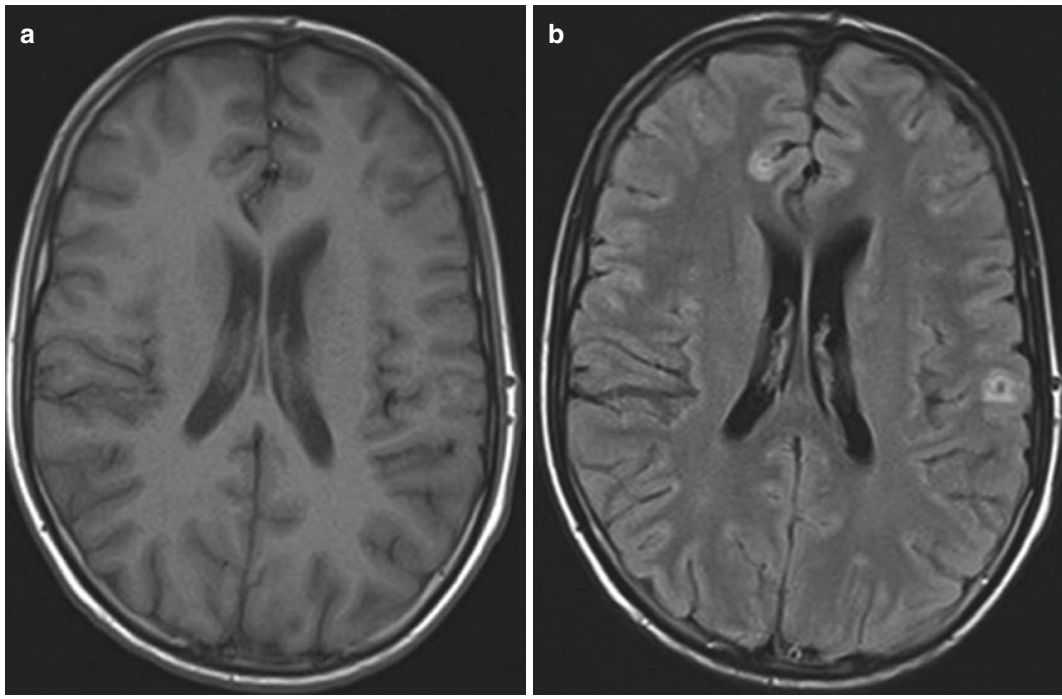

Fig. 11.2 Cerebral aspergillosis in the same patient as in Fig. 11.1. Multiple small cerebral lesions, only some enhancing and with artifacts on susceptibility-weighted imaging (SWI). Axial MRI: (**a**) T1-W, (**b**) FLAIR, (**c**) T2-W, (**d**) SWI, (**e**) gadolinium-enhanced T1-W, (**f**) DWI, (**g**) ADC, (**h**) gadolinium-enhanced T1-W, (**i**) FLAIR

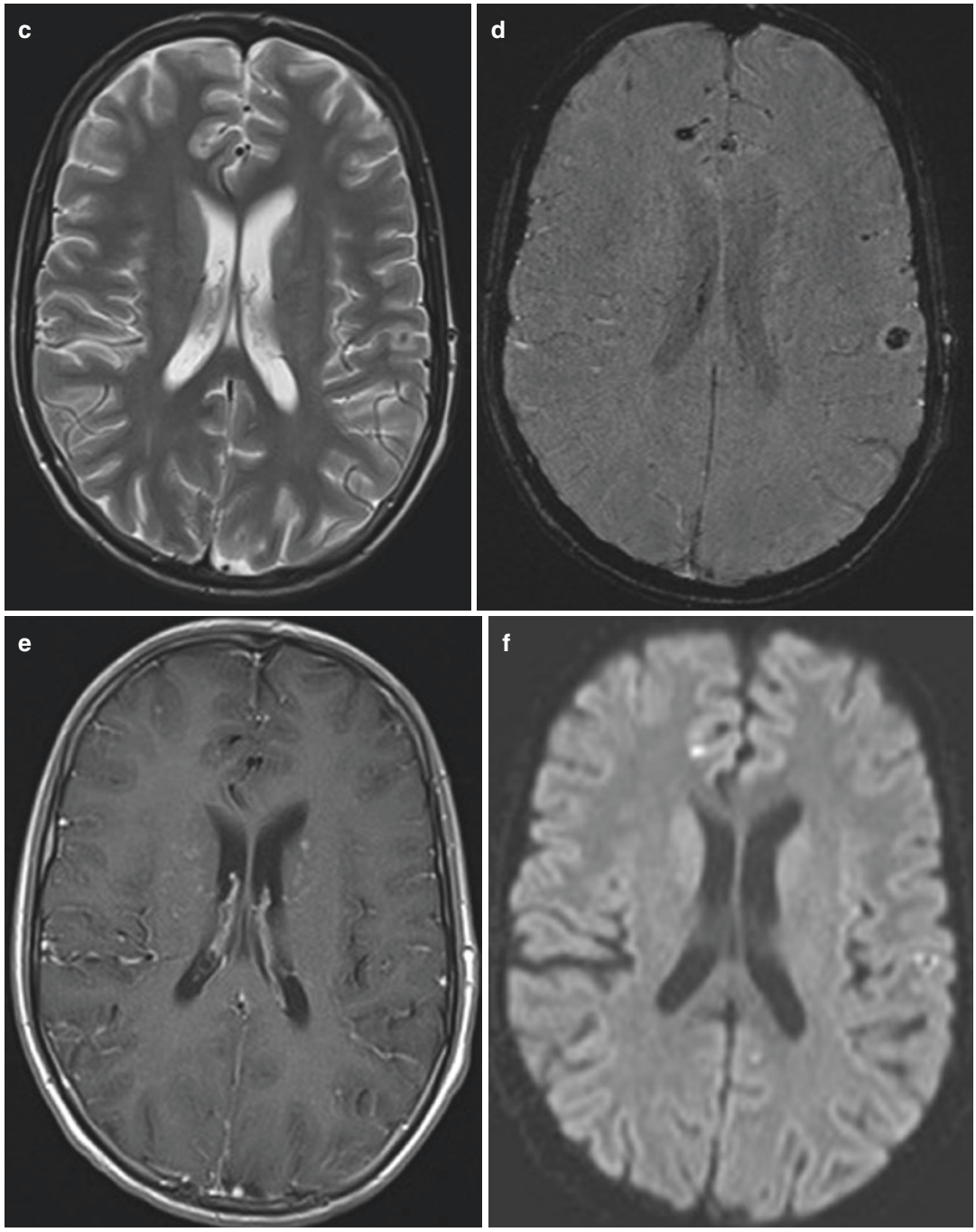

Fig. 11. 2 (continued)

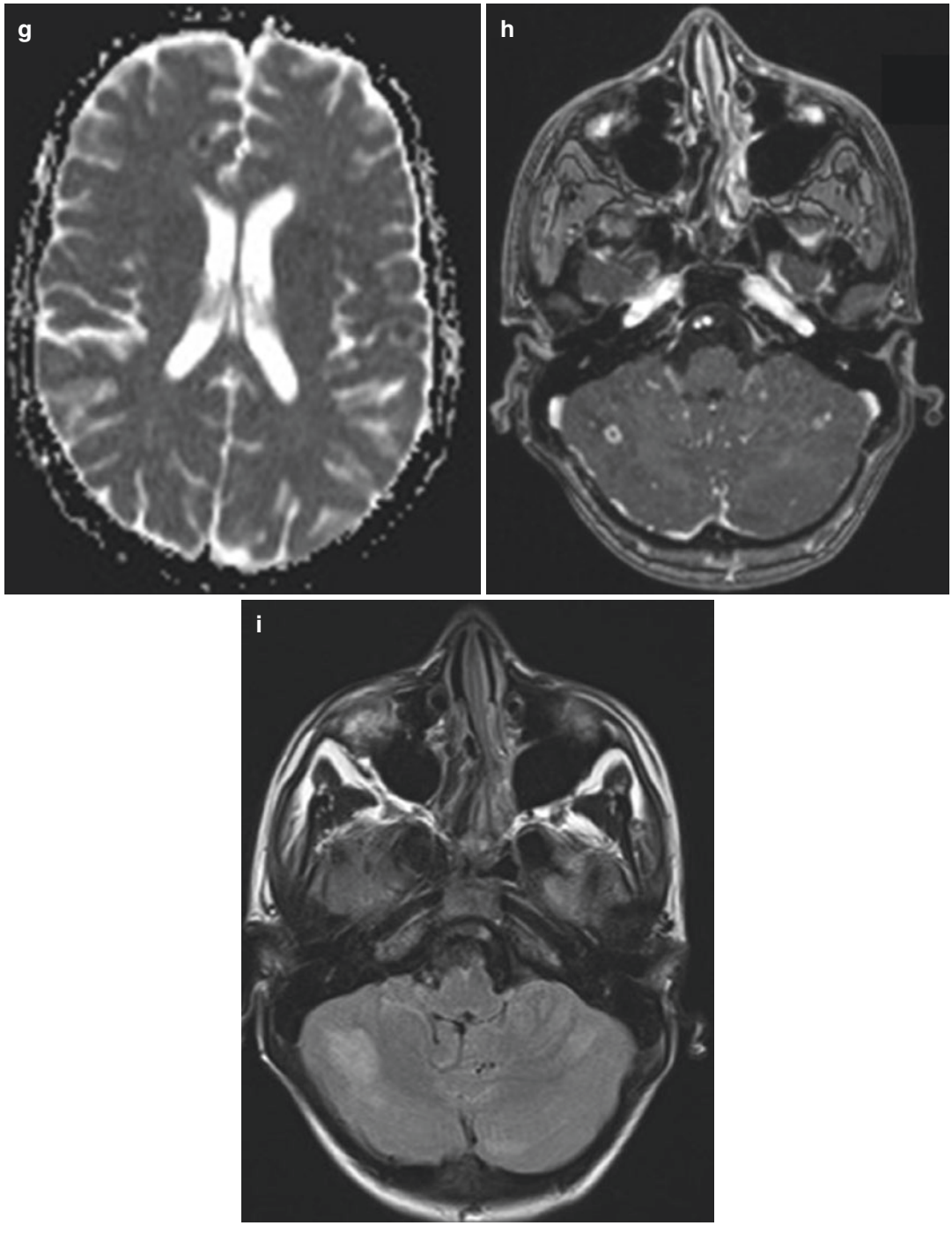

Fig. 11. 2 (continued)

11.2.1.2 Viral

Patients with a viral CNS infection may show a variety of presentations, ranging from infarction secondary to vasculitis (herpes zoster) to encephalitis (herpes, EBV more often than CMV) and progressive multifocal leukoencephalopathy (JC virus) [9]. Reactivation of a latent herpes virus occurs in 50% of patients who have undergone bone marrow transplantation. In a minority of patients, subsequent encephalopathy may occur [8]. CT is relatively insensitive for the detection of viral encephalitis: the

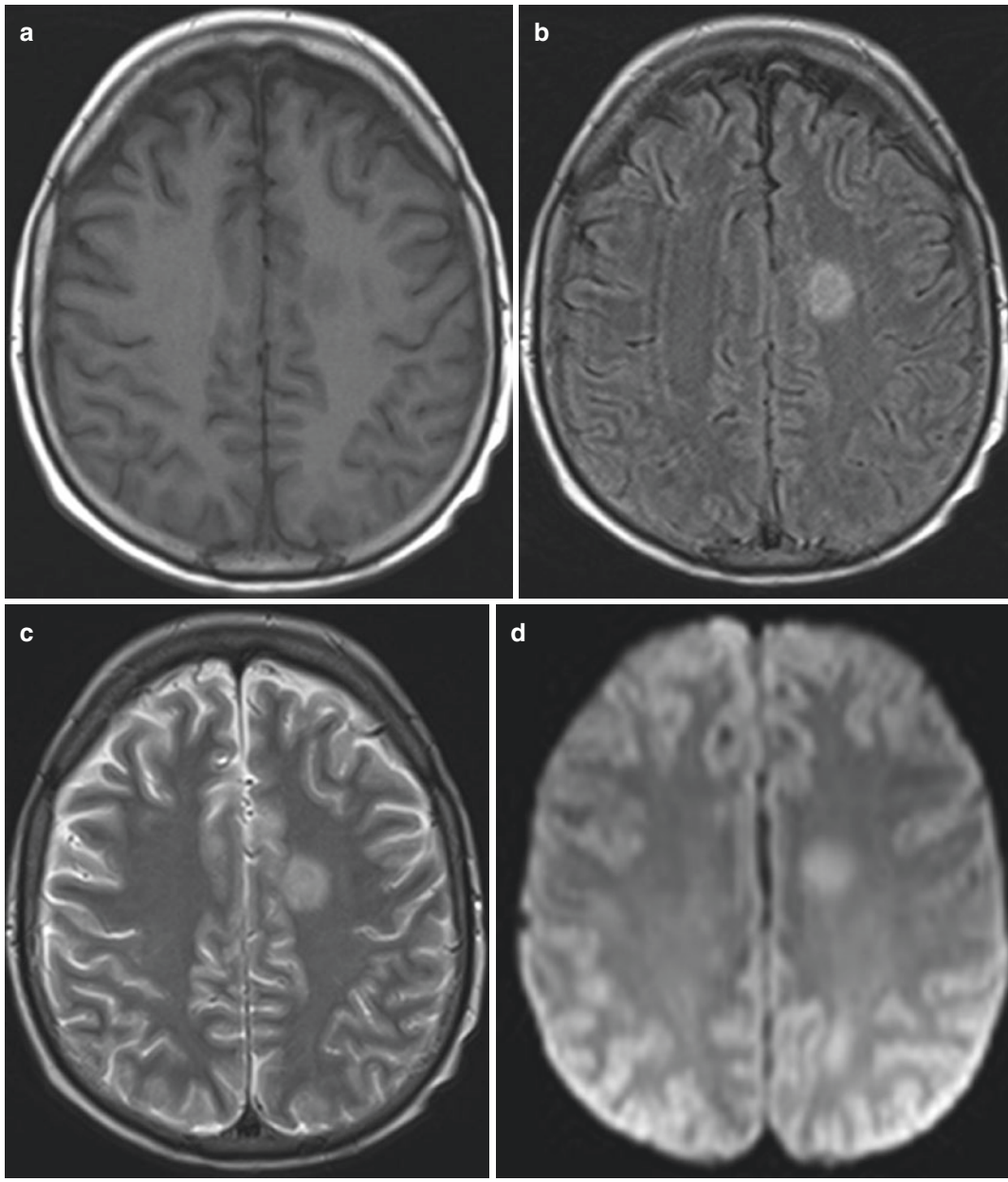

Fig. 11.3 Cerebral aspergillosis in a 16-year-old boy with ALL with neutropenic fever, severe headache, and altered mental status. Cerebral lesions showing restricted diffusion and rim enhancement. (**a**) T1-W, (**b**) FLAIR, (**c**) T2-W, (**d**) DWI, (**e**) ADC, (**f**–**h**) gadolinium-enhanced T1-W

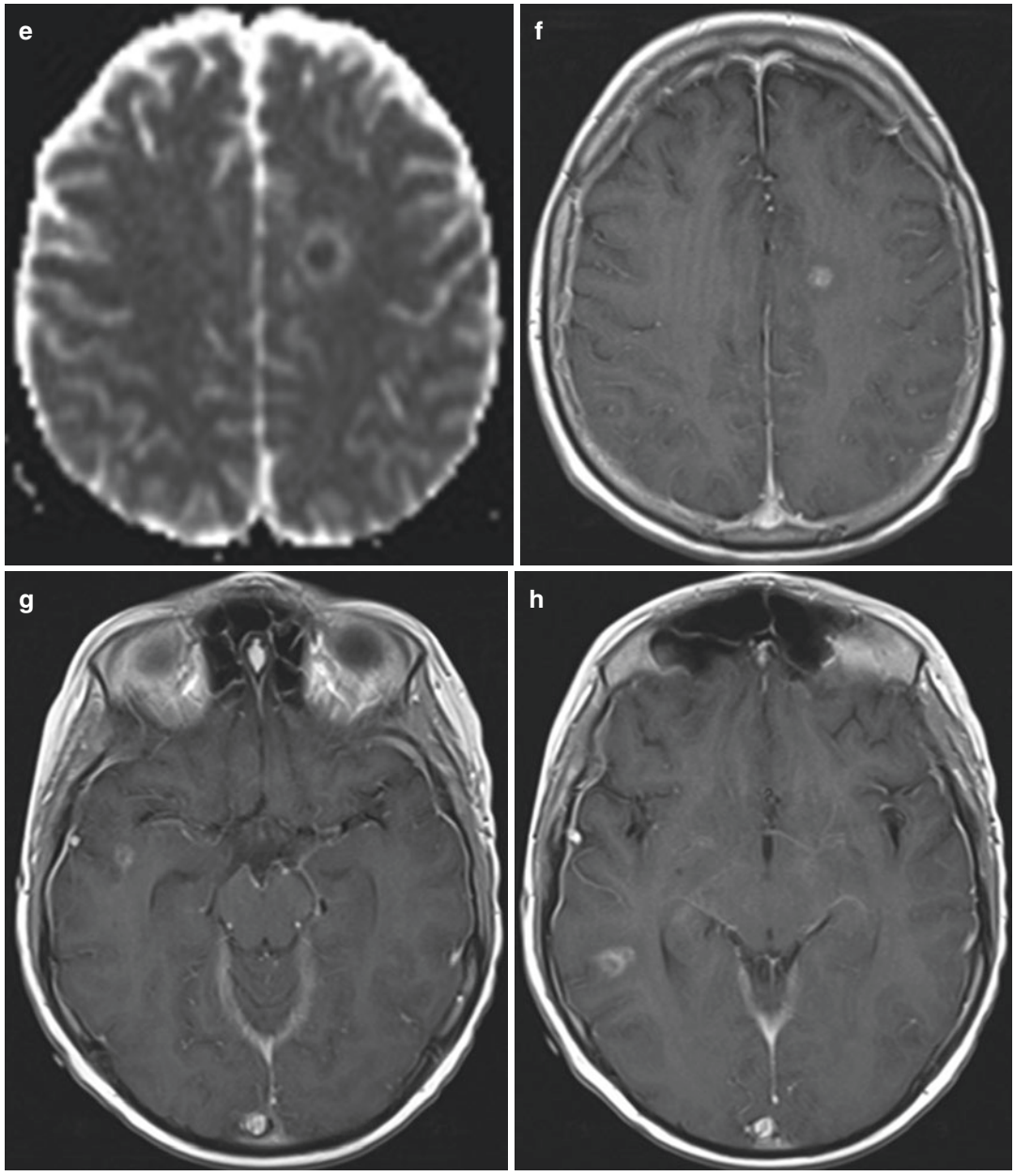

Fig. 11.3 (continued)

lesions are subtle and of low density, blurring the junction between gray and white matter and showing minimal contrast enhancement. MRI shows unilateral or bilateral areas of high signal intensity in the hippocampi, amygdalae, or parahippocampal gyri, on T2-weighted and FLAIR imaging, usually without diffusion restriction.

If a CMV infection affects the ependymal and subependymal tissue, decreased signal intensity is seen on T1-weighted imaging, increased ependymal signal intensity on FLAIR, periventricular

enhancement after administration of gadolinium, and ventriculomegaly.

11.2.2 Posterior Reversible Encephalopathy Syndrome (PRES)

Posterior reversible encephalopathy syndrome (PRES) is a clinico-neuroradiologic disease, i.e., a combination of clinical neurologic alterations with characteristic MRI findings. PRES occurs in patients treated for a variety of tumor types but predominantly in leukemia patients (in up to 1.6% of patients). It is also the most frequent neurologic complication of oncologic therapy in patients with ALL [13, 14]. Patients present with headache, altered mental status, seizures, visual disorders, and/or loss of consciousness [8, 15].

The cause of PRES is probably multifactorial and related to hypertension, high-dose poly-chemotherapy, transplantation, infection or sepsis, graft-versus-host disease, immunosuppressive agents (e.g., cyclosporine, tacrolimus, and corticosteroids), and autoimmune disorders [8, 16, 17].

One of the proposed theories is that oncologic therapy may lead to a direct toxic effect on the cerebrovascular endothelium. Injury to the endothelium leads to local vasoconstriction followed by hypoperfusion of the brain bordering the involved vessels. Consequently, the blood-brain barrier will be disrupted with subsequent vasogenic edema. Another hypothesis involves acute hypertension or hyperperfusion, leading to a breakdown of the blood-brain barrier, and extravasation of fluid, potentially containing blood or macromolecules, resulting in reversible vasogenic edema [8, 16]. If the condition is left untreated, cytotoxic edema may follow and result in sequelae, such as epilepsy [8].

MRI is the imaging modality of choice when PRES is suspected. It typically shows vasogenic edema: non-enhancing hyperintense areas on T2-weigthed imaging and ADC maps (Fig. 11.4) [8, 13, 16, 17]. PRES is predominantly located in the occipital lobes but can occur in any cerebral lobe, as well as in the cerebellum (Fig. 11.4) [8, 13, 16, 17]. Atypical features are hemorrhage, contrast enhancement, and restricted diffusion [8]. In the majority of patients, the lesions disappear at follow-up imaging, but laminar necrosis, micro-hemorrhage, and focal atrophy can be seen as sequelae from PRES [15].

11.2.3 Toxic Effects to the White Matter and Spinal Cord

Treatment-induced leukoencephalopathy (toxic leukoencephalopathy (TE)) is a frequent complication, especially in patients receiving methotrexate (MTX) in a high dose or intrathecally, in young children, and when associated with cranial radiation therapy. In patients with ALL, the incidence of TE is reported to be as high as 18% [18]. In addition to MTX, 5-fluorouracil, fludarabine, cyclosporine, and tacrolimus are also reported to be causative agents [8, 17].

Clinically, TE may vary from completely reversible to irreversible severe neurological damage. Patients present within the first 2 weeks of treatment with a wide range of neurologic symptoms, including headache, lethargy, altered mental status, seizures, transient ischemic attacks, encephalopathy, ataxia, and myelopathy [15].

In the acute stage, areas of diffusion restriction in the periventricular white matter, usually showing no contrast enhancement, suggest cytotoxic edema. The abnormalities are typically symmetrical and located bilaterally in the centrum semiovale and the corona radiata. Signal changes at DWI may precede the corresponding abnormalities on FLAIR or T2-weighted imaging. The acute cellular swelling is not necessarily irreversible, and patients often recover spontaneously. In a chronic setting, imaging may show gliosis and encephalomalacia.

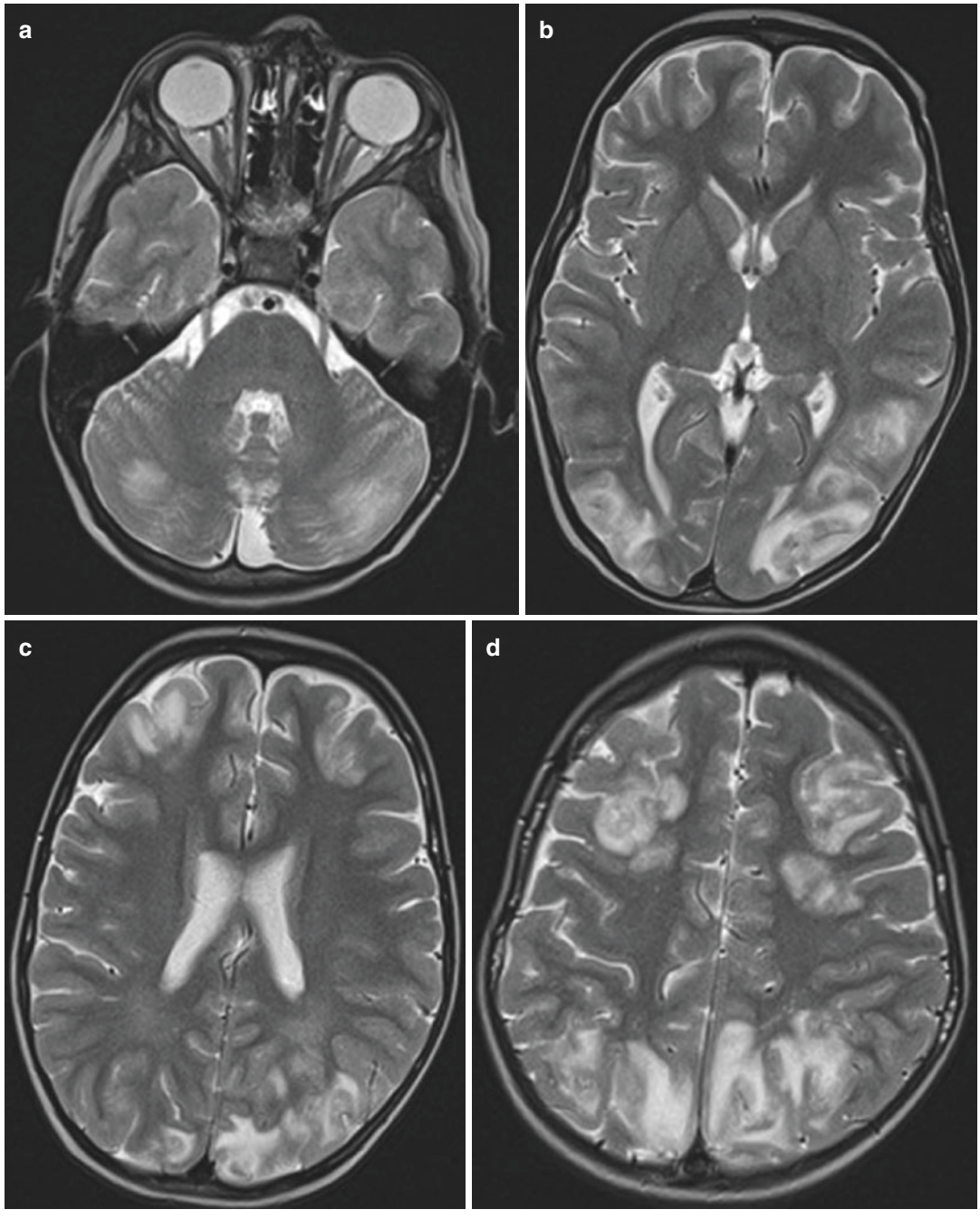

Fig. 11.4 PRES in a 6-year-old boy treated with chemotherapy for ALL presenting with hypertension. Multiple hyperintense areas on T2-W, images localized not only in the occipital lobes but also in the frontal lobes and cerebellum; no diffusion restriction on the corresponding ADC images. (**a**–**d**) T2-W, (**e**–**h**) FLAIR, (**i**–**j**) ADC

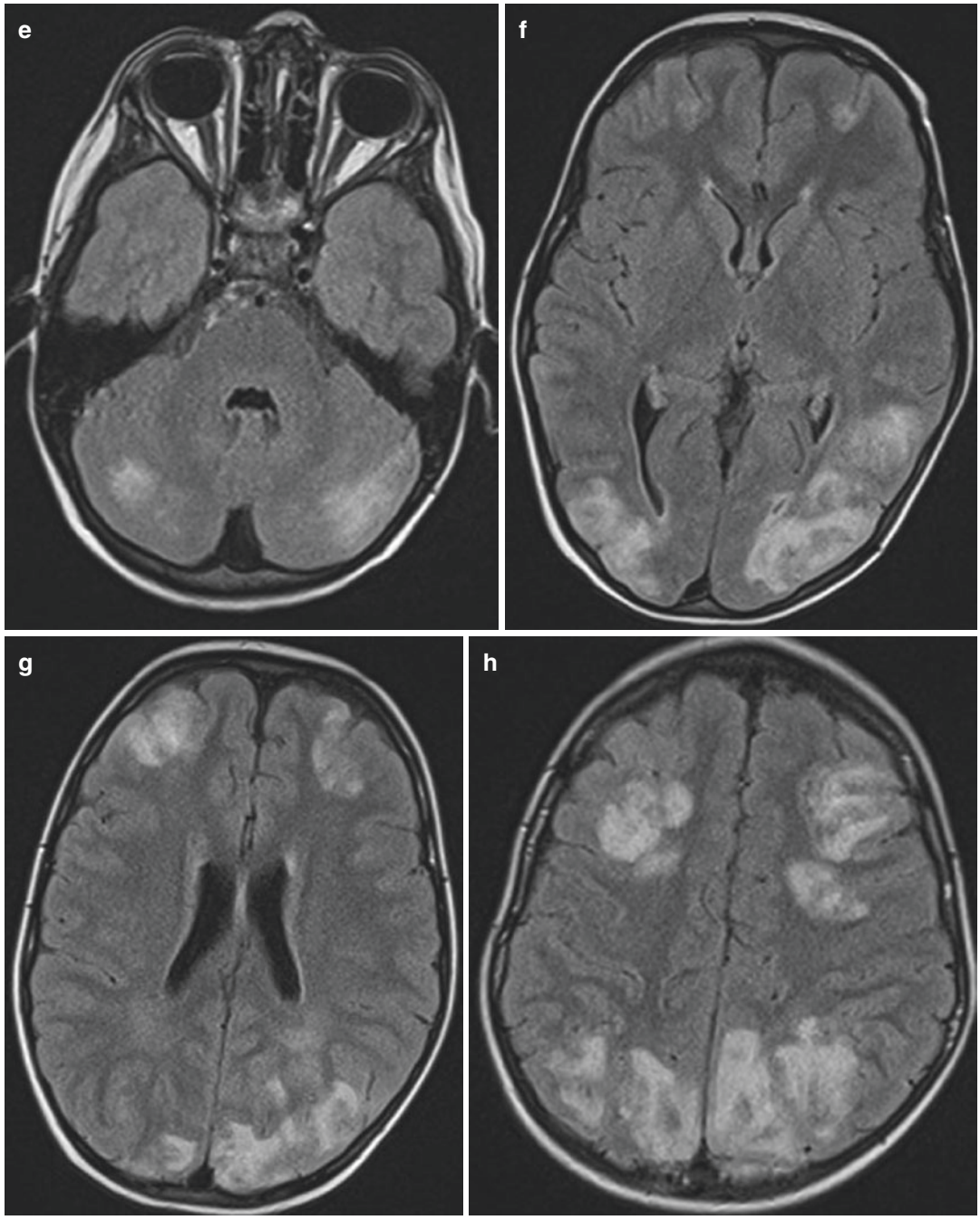

Fig. 11. 4 (continued)

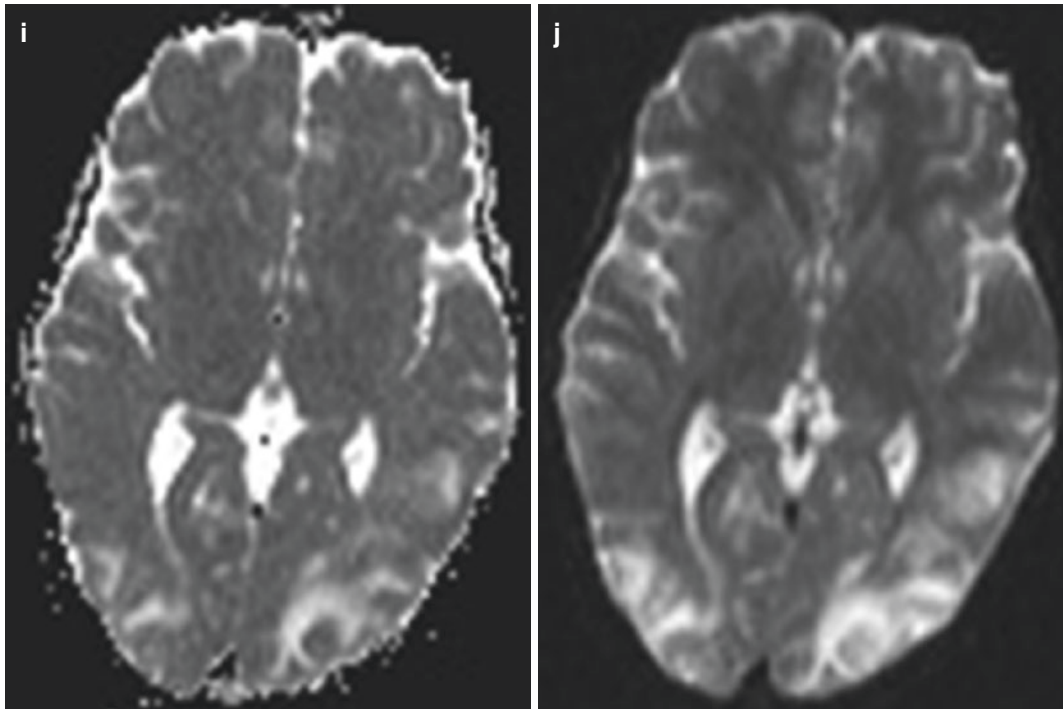

Fig. 11.4 (continued)

The main imaging differential diagnosis of TE is PRES. Both entities have the same clinical symptoms at onset, but cognitive dysfunction can be more severe in acute TE [17]. On MRI the distribution of abnormalities is different: TE causes damage to the deep white matter, whereas PRES causes signal changes to the cortex or subcortical white matter. The prognosis of TE is slightly worse than that of PRES.

Ascending polyradiculoneuropathy after intrathecal MTX therapy is a rare complication. At MRI lumbosacral ventral root enhancement is shown that correlates with nerve conduction and EMG abnormalities.

11.2.4 Cerebrovascular Complications

Cerebrovascular treatment complications can be divided into hemorrhagic and ischemic complications.

Risk factors for acute intracranial hemorrhage are a platelet count less than 10×10^9/L (10,000/μL), when the patient has a coagulopathy or when drugs such as prednisone or asparaginase are administered [8, 17].

Cerebral venous thrombosis is a serious complication encountered in patients with hematologic malignancies. Risk factors are increased thrombin generation related to leukemia, administration of asparaginase (leading to alterations in the clotting system) and corticosteroids, infections, and an inherited prothrombotic state [8]. It typically occurs in the third and fourth week of therapy [10]. Clinical presentation is variable, ranging from isolated headache to severe and often multifocal neurologic deficits, seizures, or even coma.

On CT venous thrombosis typically presents as hyperdense lines in the deep veins and cortical veins. Contrast-enhanced CT has a sensitivity of 60%; the sensitivity of MRI is higher [17]. On T1-weighted images, a hyperintense thrombus is seen, and T2* allows identification of the thrombosed vein (Fig. 11.5). MR venography shows a flow void.

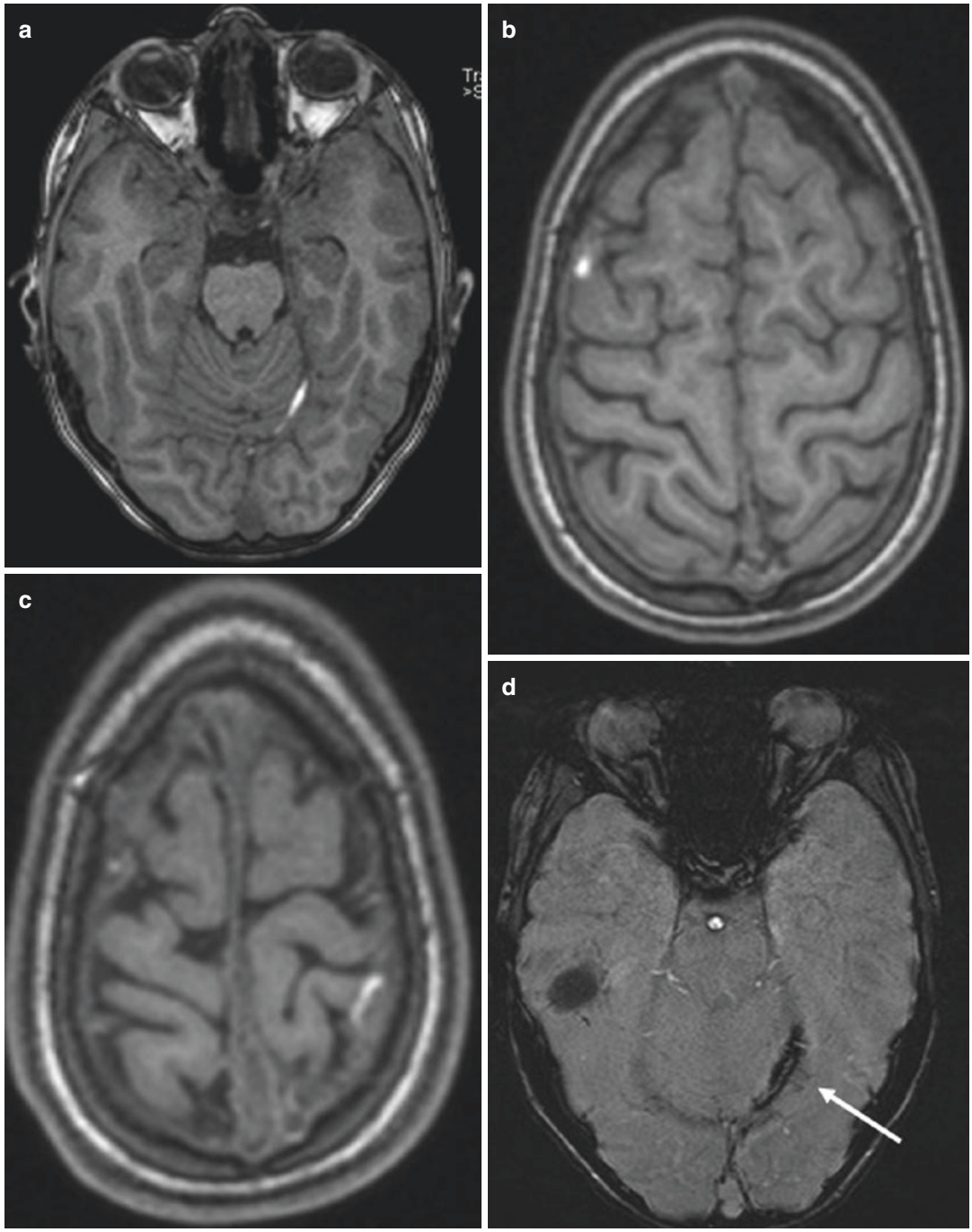

Fig. 11.5 Cortical vein thrombosis in a 12-year-old boy with ALL presenting with hypertension and sudden onset of headache. Hyperintense linear foci on T1-W (**a**–**c**) and blooming artifact (arrow) on SWI (**d**)

11.2.5 Spinal Epidural Lipomatosis

Spinal epidural lipomatosis, or encapsulated overgrowth of adipose tissue in the spinal canal, is a rare complication that can develop in children with leukemia or lymphoma who are treated with systemic or intrathecal corticosteroids [15]. Epidural thickening may impede repeated lumbar punctures. Difficult lumbar puncture may be the first sign. MRI shows accumulation of fat tissue in the epidural space.

11.3 Chest

11.3.1 Infection

Risk factors for pulmonary infection in pediatric oncologic patients are bone marrow aplasia due to chemotherapy (mainly gram-positive or gram-negative bacteria, less frequently *Mycoplasma*, *Chlamydia*, *M. tuberculosis*, or fungi), the presence of a central venous catheter (candida), and therapy with steroids and calcineurin inhibitors (*Aspergillus* or other fungi) [19].

In children with neutropenic fever and pulmonary infection, chest radiographs can initially be normal due to their weak inflammatory response [20]. In a large pediatric study, 73% of the patients with proven pulmonary fungal infection initially had a normal chest X-ray [4]. Chest radiograph abnormalities are generally nonspecific (e.g., segmental consolidation, multilobar consolidation, perihilar infiltrate, single or multiple nodules, masses and pleural effusions, ground-glass pattern, and cavitation), which increases the risk of a delay in diagnosis and treatment [19, 21, 22].

As mentioned before, chest CT is the recommended imaging test in pediatric patients with prolonged (>96 h) febrile neutropenia despite broad-spectrum antibiotics [1, 7], because of its higher sensitivity for the detection of pulmonary infection. The drawback of chest CT is of course the radiation exposure. Results on the value of MRI of the lungs in neutropenic adult patients are promising [23–26], and a few studies have been performed in (neutropenic febrile) children, showing technical feasibility [27, 28]. Furthermore, the correlation with HRCT was high, and sensitivity and specificity to HRCT are comparable [28]. However, more research is needed to confirm the value of MRI of the lungs as a diagnostic tool in these patients.

Patients with pulmonary aspergillus infection present with fever, cough, chest pain, and hemoptysis or pneumothorax. Invasive pulmonary aspergillosis can be divided into angioinvasive and airway invasive aspergillosis, each entity with its corresponding CT features.

The CT findings of angioinvasive pulmonary aspergillosis depend on the immune response of the patient and are nonspecific: nodules of varying size, irregular areas of consolidation, and tree-in-bud and/or ground-glass opacities are described [9, 22]. In neutropenic patients, a nodule or consolidation surrounded by an area of ground-glass attenuation can be seen, forming the typical halo sign (Fig. 11.6) [19]. The central nodule represents necrosis and fungi invading pulmonary blood vessels, leading to thrombosis, hemorrhagic infarction, and intra-alveolar

Fig. 11.6 Angioinvasive aspergillosis in an 11-year-old girl with AML and neutropenic fever. A typical presentation with consolidation surrounded by ground-glass changes

hemorrhage, which in turn leads to ground-glass changes in the surrounding lung parenchyma. The halo sign is an early sign of infection, occurring within 5 days from the onset of fever and lasting 5 days. Despite effective therapy, increase in lesion size and number of lesions may be observed for 7–10 days, followed by a plateau for a few days. When the patient recovers from neutropenia, in about half of the patients, the air crescent sign will develop after 2–3 weeks, representing retraction of the necrotic nodule from viable lung parenchyma. Cavitation is also a late finding, in the recovery phase of neutropenia [22], and usually appears in large areas of the consolidation [19] (Fig. 11.7).

Nevertheless, the typical halo sign, air crescent sign, and cavitation are less common in children than in adult patients, and this lower incidence is not completely understood [1]. Also, none of these signs is pathognomonic for angioinvasive aspergillosis: other fungi and mycobacteria, bacterial pneumonia (e.g., *S. aureus*, *Nocardia*, gram-negatives), and some viral infections (e.g., herpes) may cause similar radiological signs [19].

Airway invasive aspergillosis is caused by invasion of the basement membrane of the bronchial tree by *Aspergillus*, leading to exudative bronchiolitis and air space infiltration. Chest X-ray can be normal or show patchy consolidation (usually in the lower lobes) or ill-defined nodules. At chest CT, peribronchiolar consolidation, lobar consolidation, centrilobular nodules, and areas of ground-glass attenuation can be present [19].

Pneumocystis pneumonia is caused by *Pneumocystis jirovecii*. Patients present with dyspnea, nonproductive cough, fever, and rarely chest pain. Chest X-ray typically shows bilateral progressively coalescing interstitial infiltrates with a perihilar distribution (Fig. 11.8). However, the infiltrates may be unilateral; there may be consolidations, nodules or cavitation, or no abnormalities

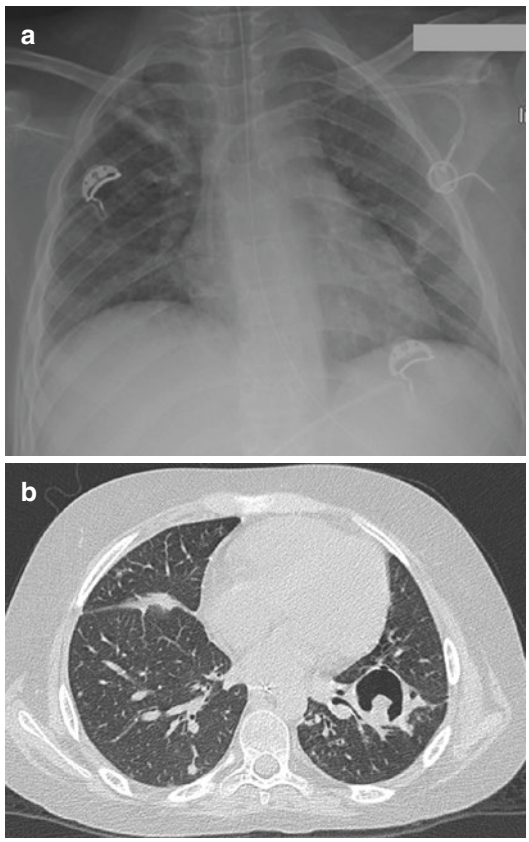

Fig. 11.7 Invasive pulmonary aspergillosis in a 12-year-old girl with ALL. Chest X-ray (**a**) and non-contrast chest CT (**b**) show a cavitating pulmonary lesion

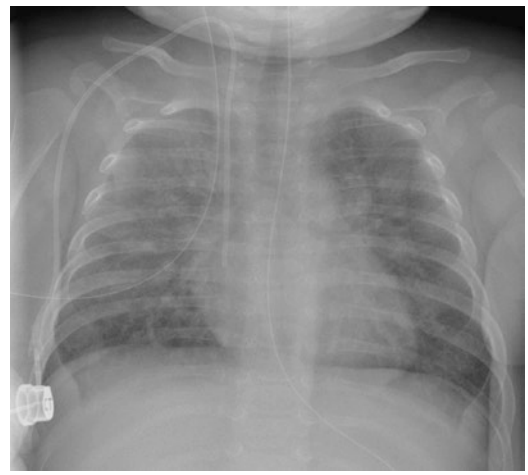

Fig. 11.8 *Pneumocystis jirovecii* (PJ) infection in a 4-month-old boy with localized neuroblastoma receiving chemotherapy; he presented with dyspnea. Chest x-ray shows bilateral coalescing interstitial opacity with a perihilar distribution

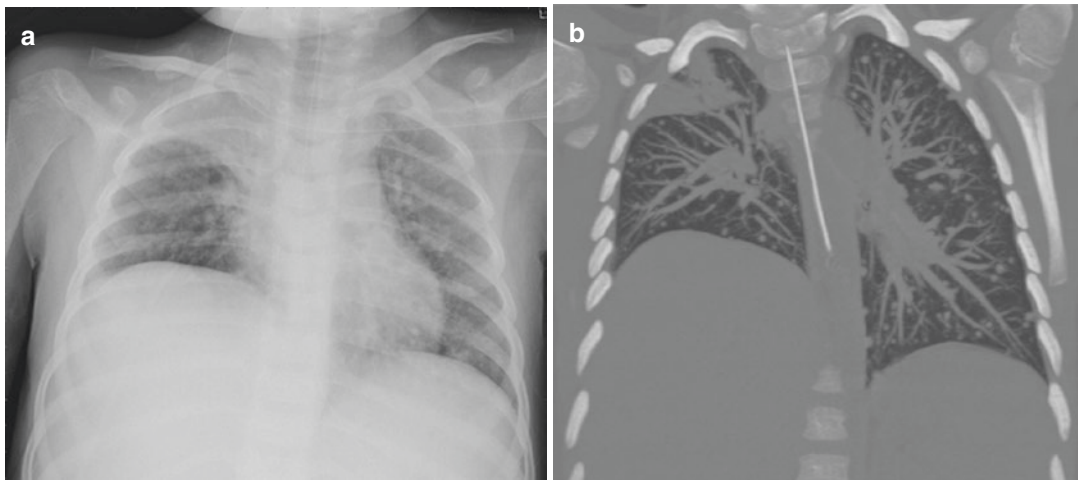

Fig. 11.9 Pulmonary candida infection in a 6-year-old boy with recurrent neuroblastoma with multiple nodules on chest X-ray (**a**) and chest CT (**b**, MIP reconstruction)

at all. Pneumothorax and pneumomediastinum are possible late complications [19].

Candida involvement of the lung is rare and most often related to hematological dissemination from another location [19]. Findings at chest CT are nonspecific, mainly consisting of bilateral nodules and areas of consolidation (Fig. 11.9).

11.3.2 Pneumothorax Caused by Cavitation of Lung Lesions During Chemotherapy

Pneumothorax can be a complication in patients with a pulmonary malignancy treated with chemotherapy, radiation therapy, targeted biological agents, or after radio-frequency ablation (RFA) of a pulmonary nodule (Fig. 11.10).

The incidence of pneumothorax has been reported to be 5–33% in patients with pulmonary abnormalities [29]. The phenomenon is not completely understood, but necrosis of a subpleural tumor leading to formation of a fistula between the lung parenchyma and the pleural space, infarction and necrosis of tumor emboli, overdistension and subsequent rupture of alveoli due to tumor progression, and increased intrathoracic pressure following emetogenic chemotherapy are all possible causes (Fig. 11.11) [29].

11.4 Abdomen

11.4.1 Infection/Abscesses

Fungal abscesses typically present as round hypoechoic lesions in the liver and spleen that may progressively calcify (Fig. 11.12).

11.4.2 Pancreatitis

Several chemotherapeutic agents are known to induce pancreatitis in children, particularly drugs used in the treatment of acute lymphoblastic leukemia: doxorubicin, vincristine, prednisolone, and particularly L-asparaginase. Pancreatitis, at times severe necrotic pancreatitis [30], complicates 5–18% of patients treated with asparaginase [1]. Pancreatitis typically occurs early in the course of treatment, but it can complicate every treatment phase [31]. There is a high risk of recurrent pancreatitis when the patient is rechallenged with the inciting chemotherapy drug.

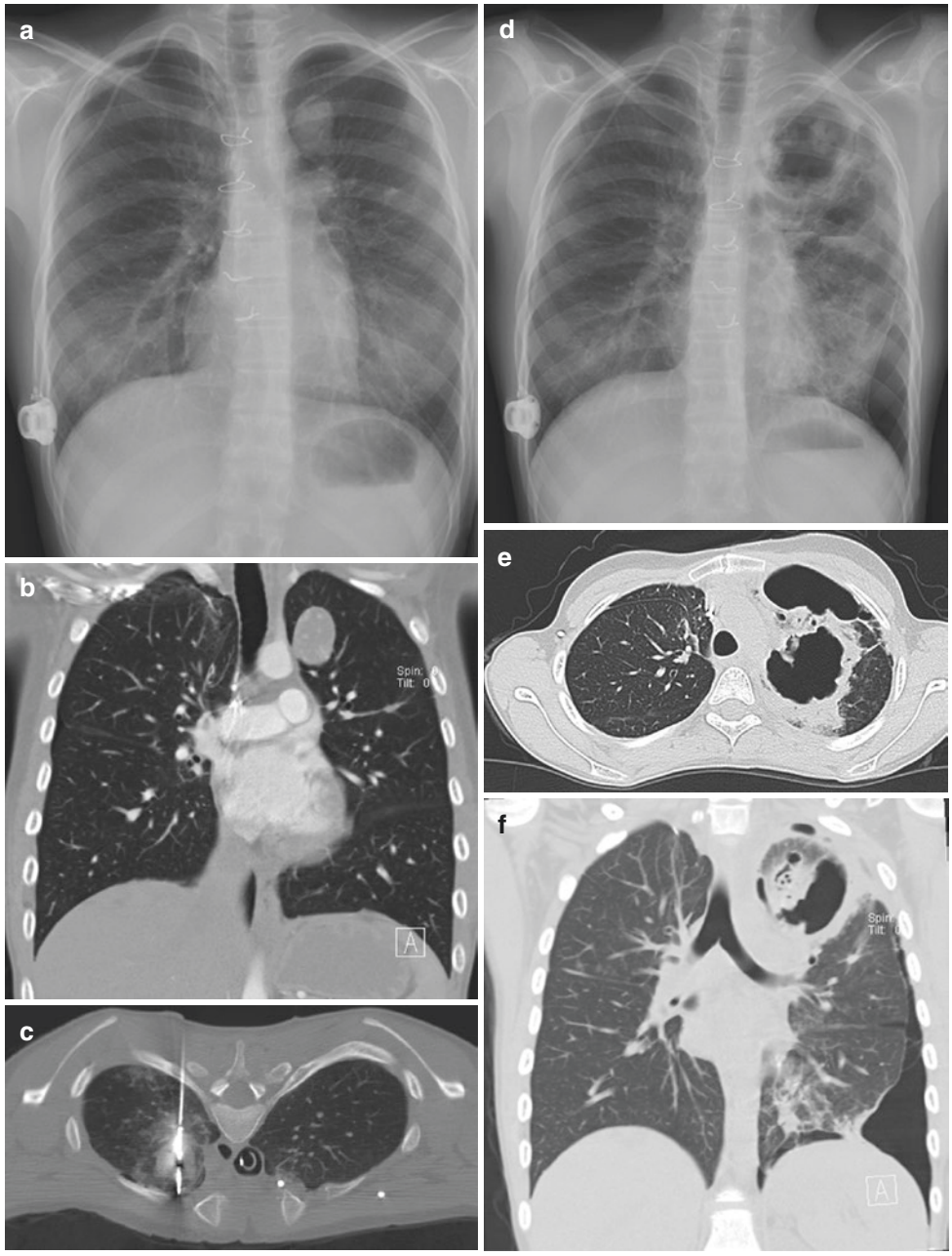

Fig. 11.10 Pneumothorax in a 13-year-old girl with osteosarcoma with a pulmonary metastasis in the left upper lobe during follow-up ((**a**) chest X-ray, (**b**) chest CT). Radio-frequency ablation (RFA) was performed (**c**), resulting in cavitation of the lesion and subsequent pneumothorax (**d**–**f**)

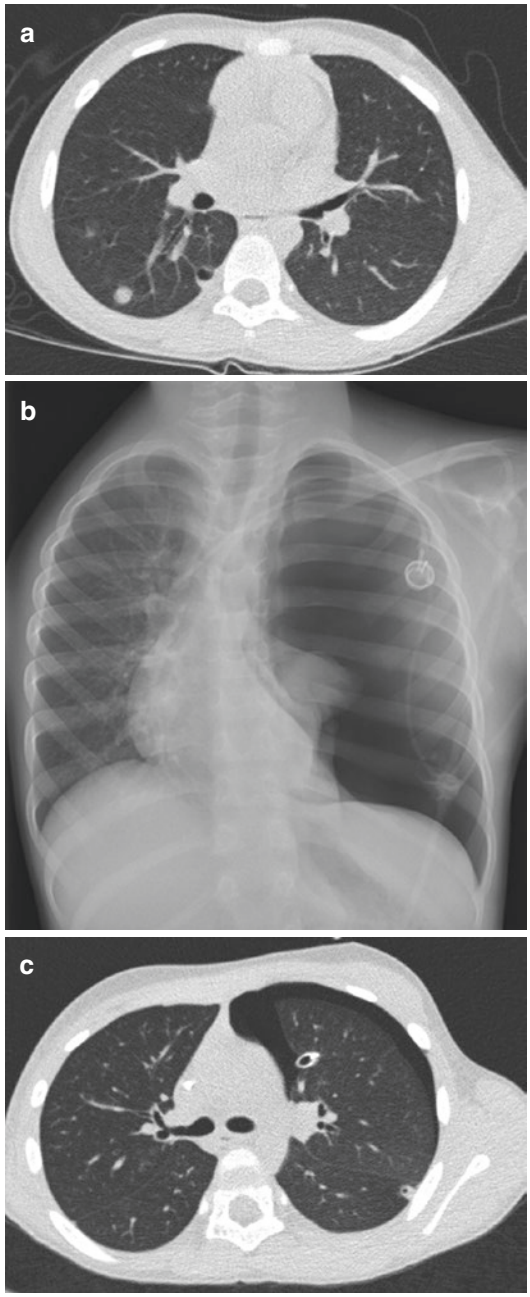

Fig. 11.11 Cavitating pulmonary metastases from osteosarcoma in a 9-year-old boy at chest CT (**a**). He developed fever and coughing during chemotherapy and presented with hypersonorous percussion due to secondary pneumothorax; (**b**) chest X-ray and (**c**) CT

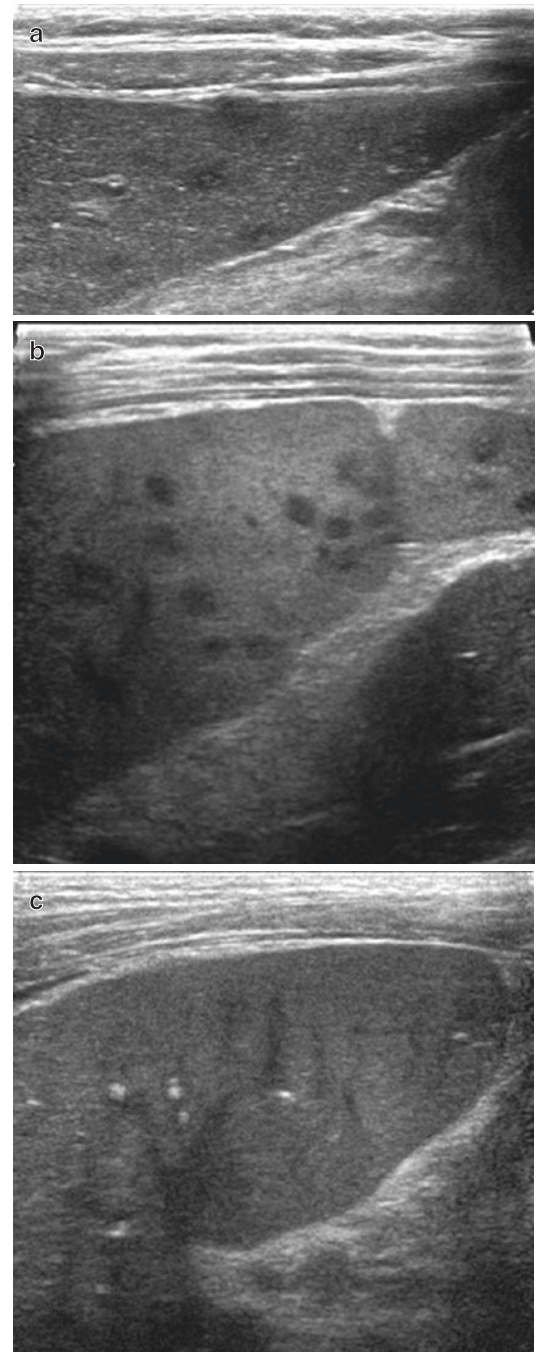

Fig. 11.12 Systemic candida infection in a 6-year-old boy with recurrent neuroblastoma (same patient as in Fig. 11.9). Ultrasound shows multiple hypoechoic lesions in both the liver and spleen, optimally visualized with a high-frequency transducer. (**a**) Liver, (**b**) spleen; (**c**) calcification of the splenic lesions on follow-up examination

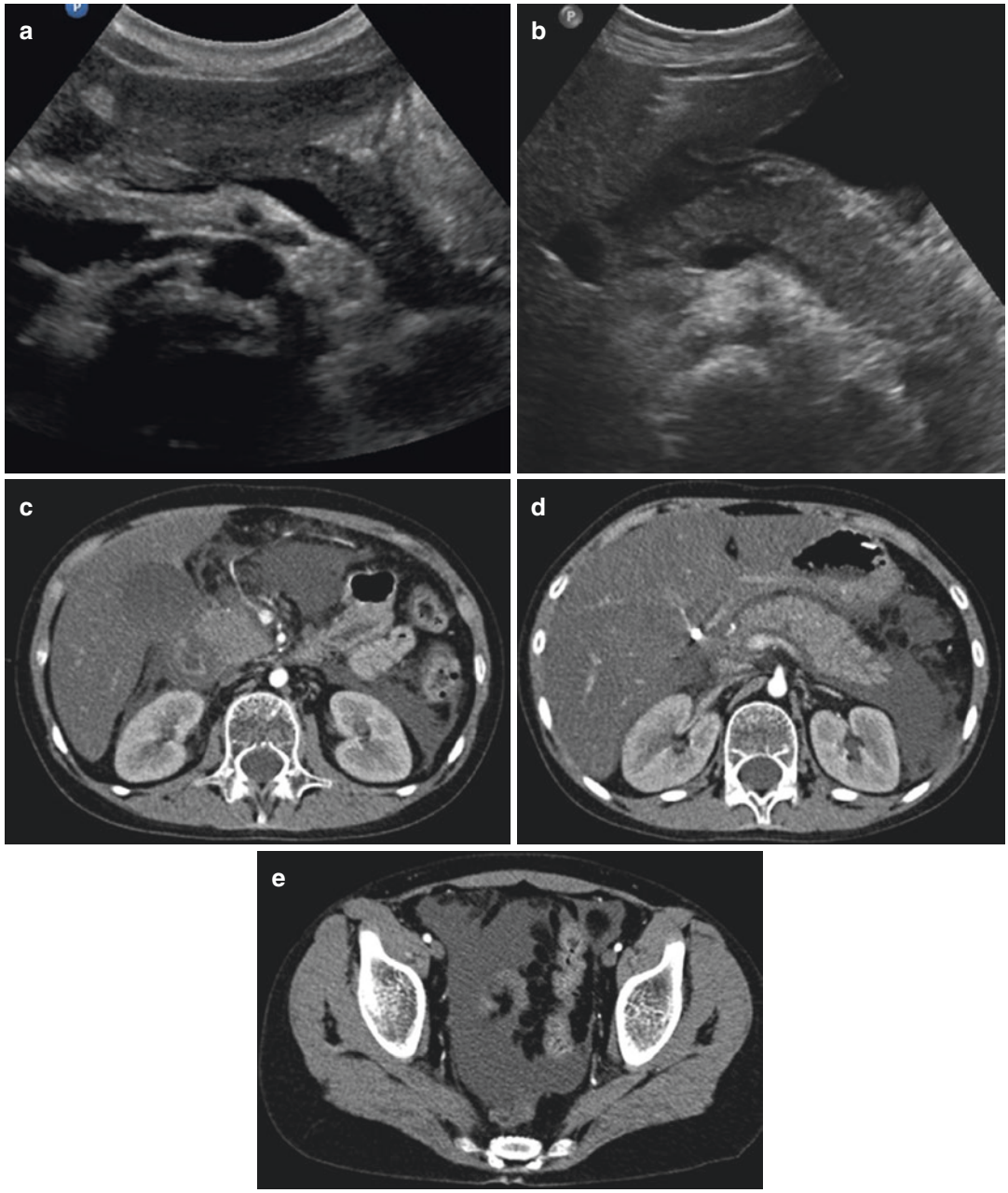

Fig. 11.13 Pancreatitis in a 13-year-old boy with ALL. Ultrasound image of the pancreas at the time of ALL diagnosis (**a**) and when the patient presented with pancreatitis (**b**, edematous pancreas). Abdominal CT scan (**c**–**e**) shows the edematous pancreas, peripancreatic fluid, and pelvic ascites

Patients present with nausea and vomiting or abdominal or back pain. On all imaging modalities, diffuse enlargement of the pancreas, peripancreatic fat streaking, and fluid collections can be seen (Fig. 11.13) [15, 30]. High blood levels of amylase and lipase confirm the diagnosis. In severe cases, pseudocysts may form (Fig. 11.14), and pancreatic necrosis may occur.

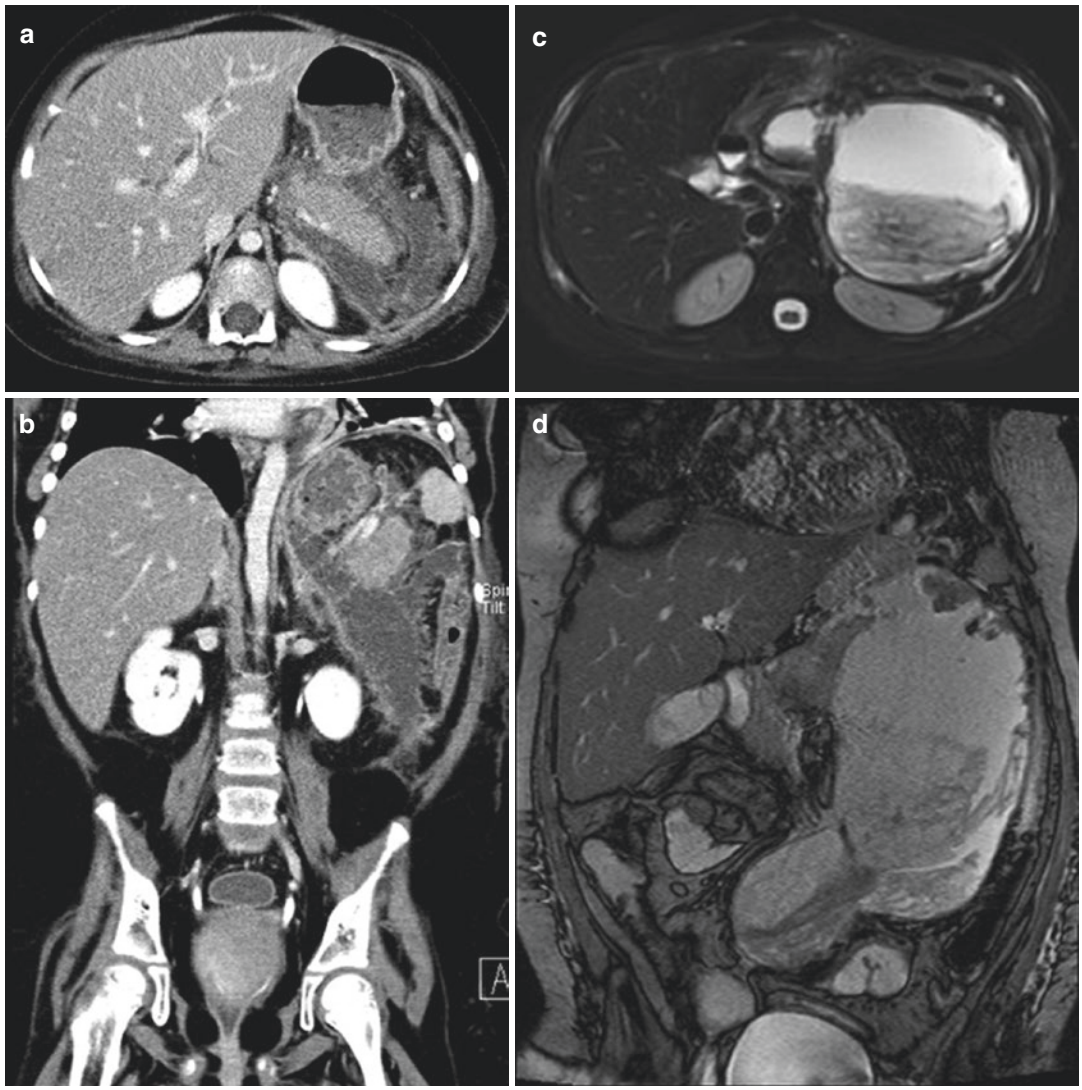

Fig. 11.14 Pancreatitis in a 6-year-old girl with ALL due to asparaginase treatment. CT (**a**, **b**) shows an edematous pancreas and peripancreatic fluid. MRI (**c**, **d**) demonstrated pseudocyst formation during follow-up

11.4.3 Hepatic Sinusoidal Obstruction Syndrome (Veno-occlusive Disease)

Hepatic sinusoidal obstruction syndrome (HSOS), formerly known as veno-occlusive disease (VOD), is a serious, potentially life-threatening complication of chemotherapy. In children it occurs with an incidence of 10–20% [32]. The most common risk factor is high-dose chemotherapy in a context of hematopoietic stem cell transplantation (HSCT). Less frequently, patients receiving conventional chemotherapy may present with HSOS although in a milder form which usually resolves spontaneously [33–35]. The cause of HSOS is damage to the hepatic venous microvasculature leading to obliteration and a decreased liver outflow, causing portal hypertension. Symptoms are weight gain, fluid reten-

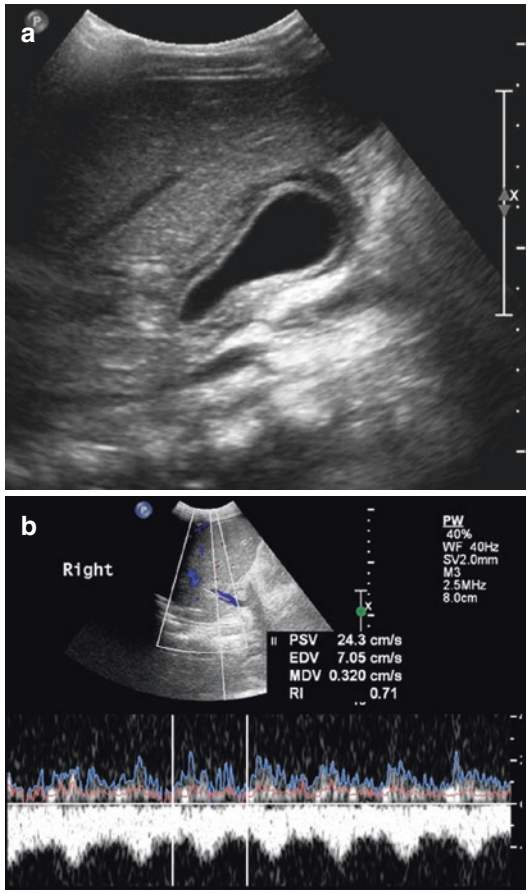

Fig. 11.15 Hepatic sinusoidal obstruction syndrome during chemotherapy in a 3-year-old boy with biliary rhabdomyosarcoma. Ultrasound shows a thickened gallbladder wall (**a**) and hepatofugal flow in the main portal vein (**b**)

tion and ascites, painful hepatomegaly, and jaundice. Laboratory and imaging findings are nonspecific: hepatomegaly, periportal edema, ascites, diminished or reversed portal venous flow, high resistive index of the hepatic artery, attenuated but patent hepatic veins, gallbladder wall edema, and splenomegaly may be present (Fig. 11.15) [1, 9, 30].

A reliable predictive diagnostic test is lacking, although according to recent publications, an increase in maximum systolic velocity of the hepatic artery and an increase in liver stiffness evaluated by transient elastography might be early findings of HSOS in children [36–38].

11.4.4 Portal Vein Thrombosis

A rare complication of chemotherapeutic treatment is portal vein thrombosis. In pediatric patients on intensive chemotherapy with autologous stem cell support, it occurs with an incidence of 0.7% [39]. Clinical symptoms are nonspecific abdominal distension and ascites. There may be thrombocytopenia and a moderate elevation of bilirubin. The diagnosis is based on imaging, and ultrasound is a highly sensitive and specific modality in this context. In the majority of patients, portal venous thrombosis is preceded by HSOS [39].

11.4.5 Neutropenic Enterocolitis/ Typhlitis

Neutropenic enterocolitis or typhlitis is an inflammatory syndrome of the bowel wall in neutropenic patients. At histology, bowel wall edema with ulceration and necrosis of the mucosa with (almost) absent inflammatory infiltrates are seen [40, 41].

It is most commonly encountered in patients with acute leukemia, probably due to a combination of corticosteroid exposure, long periods of neutropenia, frequent administration of antibiotics, and recurrent infections [42–45]. However, any neutropenic patient is at risk. The precise pathogenesis and etiology are unclear, but the association of immunosuppression, mucosal injury, and bacterial invasion may be responsible [41, 42, 46] with a significant association with *C. difficile* infection [46]. Antibiotic treatment during more than 10 days before the administration of chemotherapy also seems to be a risk factor [47], and iatrogenic vincristine-induced hypomotility of the bowel wall might also play a role [41].

Interestingly typhlitis may also occur before the initiation of treatment, supposedly as a result of leukemic bowel wall infiltration [42, 48].

The incidence of typhlitis in pediatric patients with cancer is strongly dependent on the criteria used and has been reported between 0.2% and 9% [1, 41, 42, 46, 49]. If only patients on chemotherapy were included, the incidence increased to

11% [41]. Several studies reported a mortality rate of 8–11% in patients with typhlitis, but in the last 10 years, it seems to have decreased to 2.5–5% [30, 41, 46].

Patients typically present with the clinical triad of fever, abdominal pain, and neutropenia. Fever may be absent in the early stage. Other common symptoms are abdominal tenderness, often localized in the right iliac fossa, vomiting, nausea, and constipation [15, 30, 41, 45]. Uncommon signs are prolonged anorexia, intestinal hemorrhage, or a palpable mass due to abscess formation [45]. Typhlitis most commonly occurs in the terminal ileum or cecum but can affect any part of the digestive tract [30].

Imaging is indicated whenever typhlitis is clinically suspected. The findings typically consist of circumferential bowel wall thickening of the cecum (≥0.3–0.4 cm) extending into the terminal ileum and ascending colon, but other parts of the bowel can be involved as well. Since bowel wall thickness can accurately be evaluated with high-frequency ultrasound transducers, it is a reliable technique for diagnosing typhlitis (Fig. 11.16). Other imaging findings are pneumatosis intestinalis and perintestinal fluid and inflammatory changes [1, 30, 50].

In children CT is less suitable because of the lack of intra-abdominal fat and its lower resolution compared to ultrasound. Moreover, radiation in children should be kept as low as possible. Only occasionally, in large patients or when bowel gas is preventing ultrasound examination of the bowel, CT might be necessary (Fig. 11.17). Radiographs are only indicated when perforation is suspected.

The differential diagnosis of typhlitis is appendicitis. Differentiation is important because the therapeutic approach is obviously different.

Treatment regimens of typhlitis consist of broad-spectrum antibiotics, total parenteral nutrition, bowel rest, granulocytic colony-stimulating factor, and/or antifungal agents [41, 45, 46, 51], depending on the extent and severity of the disease. However, no controlled trials have been performed on the treatment of typhlitis. Typhlitis can be complicated by ulcerations, hemorrhage, fistula formation, perforation, or abscess formation. Surgery is required in case of perforation, uncontrolled

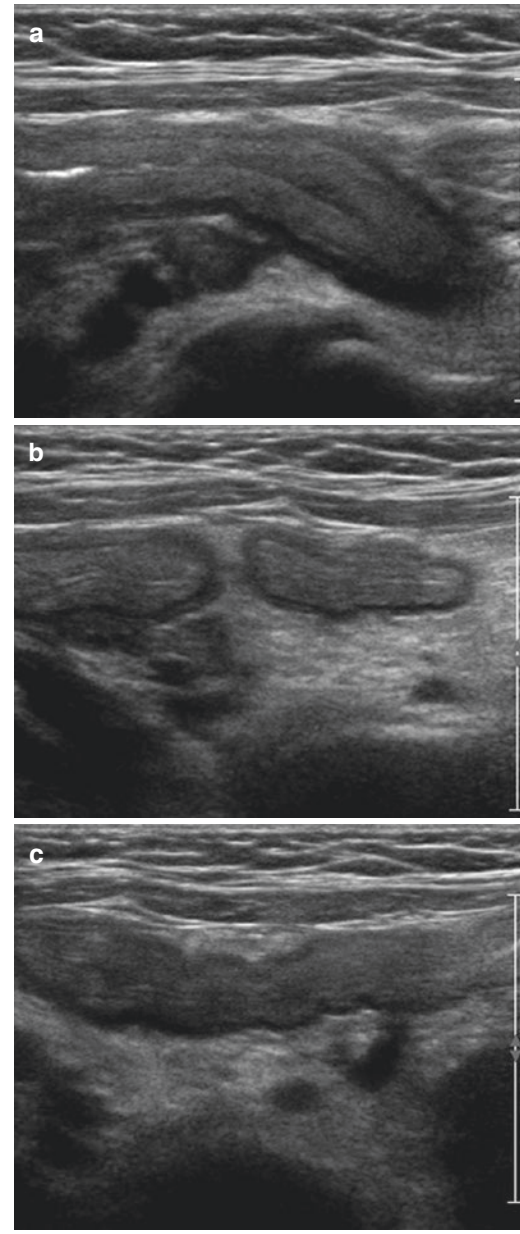

Fig. 11.16 Typhlitis in a 1-year-old girl with stage 4 neuroblastoma after stem cell reinfusion. She presented with neutropenic fever and bloody diarrhea. Abdominal ultrasound shows bowel wall thickening of the terminal ileum and stranding of the surrounding fat (**a**–**c**)

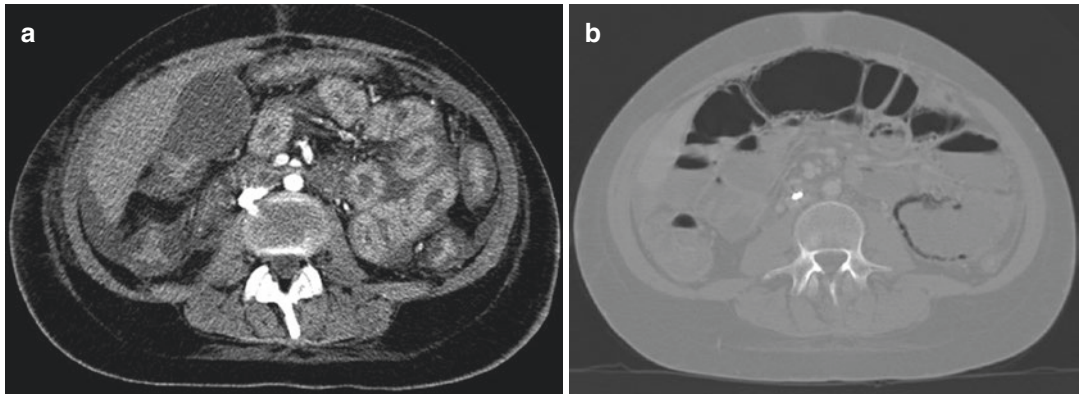

Fig. 11.17 Typhlitis in a 14-year-old girl with leukemia treated with chemotherapy presenting with neutropenic fever and abdominal pain. Abdominal CT shows thickened small bowel walls (**a**) and pneumatosis intestinalis (**b**)

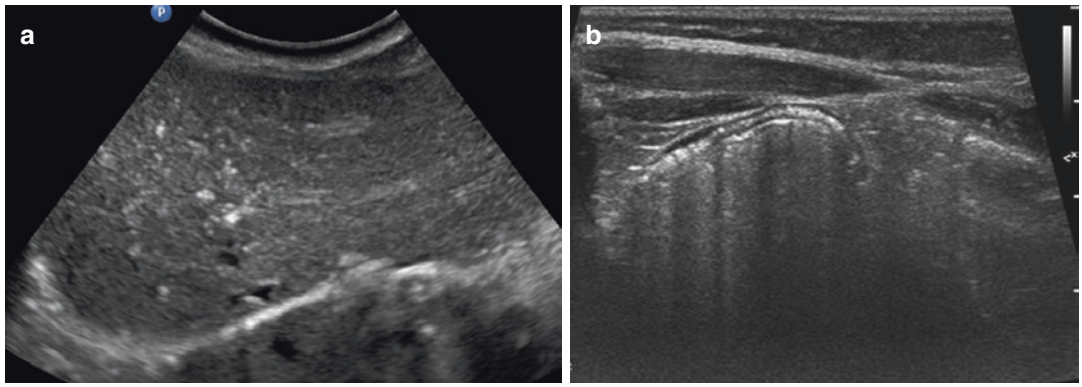

Fig. 11.18 Benign pneumatosis intestinalis without clinical symptoms in a 2-year-old boy with stage 4 neuroblastoma after stem cell reinfusion and during chemotherapy. Portal venous air (**a**) and intestinal pneumatosis of the colon (**b**) on ultrasound

sepsis, and GI bleeding [41, 45]. In the latter, an interventional radiology procedure can also be attempted [52].

11.4.6 Benign Pneumatosis Intestinalis

Pneumatosis intestinalis can be discovered incidentally as an isolated finding in a pediatric cancer patient during therapy, in the absence of clinical signs or symptoms. Risk factors are immunosuppression and bone marrow transplantation [53]. It is thought to be due to loss of bowel wall integrity and mucosal disruption as a result of chemotherapy facilitating intramural intestinal gas (Fig. 11.18) [54]. It is a self-limiting entity [55]. However, soft-tissue bowel wall thickening, free peritoneal fluid, extensive pneumatosis intestinalis, and peribowel soft-tissue stranding are alarming features [55] and should prompt further investigation.

11.4.7 Hemorrhagic Cystitis

Oncological treatment (chemotherapy, radiotherapy, bone marrow transplantation) and infections may damage the transitional epithelium and blood vessels of the urinary tract, with diffuse

mucosal bleeding as a consequence [56]. Although the bladder is the most susceptible organ, the entire urothelial surface is at risk, including the renal pelvis and ureter [1].

The reported incidence of hemorrhagic cystitis in oncologic pediatric patients is about 6% [56]. However, children who have undergone HSCT have an increased risk of up to 25%. Risk factors are cyclophosphamide, pelvic irradiation, ALL, BK virus positivity, and total body irradiation [56, 57]. Hemorrhagic cystitis can occur within a few weeks to even several years after completion of therapy. Severe cystitis occurs more often in older children (>5 years), after HSCT, and in patients with BK virus in their urine. Patients with severe cystitis have an increased risk of complications such as bladder perforation, hydronephrosis due to reflux or obstruction, and renal impairment.

Ultrasound is the imaging modality of choice and may show diffuse or focal bladder wall thickening (>3 mm for a distended bladder, >5 mm for a non-distended bladder) with hypervascularity and intraluminal clots (Fig. 11.19) [57].

The majority of patients are treated noninvasively with hyperhydration, anticholinergic drugs, and antiviral medication as indicated [56].

Fig. 11.19 Hemorrhagic cystitis in a 17-year-old girl treated with chemotherapy and radiation therapy for a pelvic Ewing sarcoma; during cyclophosphamide therapy, she presented with hematuria. Ultrasound shows focal bladder wall thickening up to 1.3 cm

11.5 Conclusion

Complications related to oncologic treatment can present significant diagnostic and management challenges in pediatric oncology patients. For this reason, it is essential that the interpreting radiologist has an understanding of the imaging features' characteristic of specific treatment-related complications. The aim of this chapter was to present an overview of the imaging findings seen in commonly encountered complications of therapy and to suggest strategies for selecting the appropriate imaging technique to provide a safe and effective approach to managing these complex patients.

References

1. Chavhan GB, Babyn PS, Nathan PC, Kaste SC. Imaging of acute and subacute toxicities of cancer therapy in children. Pediatr Radiol. 2016;46(1):9–20. quiz 6–8.
2. Mor M, Gilad G, Kornreich L, Fisher S, Yaniv I, Levy I. Invasive fungal infections in pediatric oncology. Pediatr Blood Cancer. 2011;56(7):1092–7.
3. MCG S, Caron HN, Biondi A. Cancer in children. Clinical management. 6th ed. New York, NY: Oxford University Press; 2012.
4. Roberts SD, Wells GM, Gandhi NM, York NR, Maron G, Razzouk B, et al. Diagnostic value of routine chest radiography in febrile, neutropenic children for early detection of pneumonia and mould infections. Support Care Cancer. 2012;20(10):2589–94.
5. Cox JA, DeMasi J, McCollom S, Jackson G, Scothorn D, Aquino VM. The diagnostic utility of routine chest radiography in the evaluation of the initial fever in patients undergoing hematopoietic stem cell. Pediatr Blood Cancer. 2011;57(4):666–8.
6. Phillips RS, Lehrnbecher T, Alexander S, Sung L. Updated systematic review and meta-analysis of the performance of risk prediction rules in children and young people with febrile neutropenia. PLoS One. 2012;7(5):e38300.
7. Lehrnbecher T, Robinson P, Fisher B, Alexander S, Ammann RA, Beauchemin M, et al. Guideline for the management of fever and neutropenia in children with cancer and hematopoietic stem-cell transplantation recipients: 2017 update. J Clin Oncol. 2017;35(18):2082–94.
8. Vazquez E, Delgado I, Sanchez-Montanez A, Barber I, Sanchez-Toledo J, Enriquez G. Side effects of oncologic therapies in the pediatric central nervous system: update on neuroimaging findings. Radiographics. 2011;31(4):1123–39.

9. Zerizer I, Humphries PD. Imaging 'the lost tribe': a review of adolescent cancer imaging. Part 2: imaging of complications of cancer treatment. Cancer Imaging. 2009;9:82–8.
10. Chu WC, Lee V, Howard RG, Roebuck DJ, Chik KW, Li CK. Imaging findings of paediatric oncology patients presenting with acute neurological symptoms. Clin Radiol. 2003;58(8):589–603.
11. Nickerson JP, Richner B, Santy K, Lequin MH, Poretti A, Filippi CG, et al. Neuroimaging of pediatric intracranial infection--Part 2: TORCH, viral, fungal, and parasitic infections. J Neuroimaging. 2012;22(2):e52–63.
12. Orlowski HLP, McWilliams S, Mellnick VM, Bhalla S, Lubner MG, Pickhardt PJ, et al. Imaging spectrum of invasive fungal and fungal-like infections. Radiographics. 2017;37(4):1119–34.
13. Khan RB, Sadighi ZS, Zabrowski J, Gajjar A, Jeha S. Imaging patterns and outcome of posterior reversible encephalopathy syndrome during childhood cancer treatment. Pediatr Blood Cancer. 2016;63(3):523–6.
14. Baytan B, Evim MS, Guler S, Gunes AM, Okan M. Acute central nervous system complications in pediatric acute lymphoblastic leukemia. Pediatr Neurol. 2015;53(4):312–8.
15. Averill LW, Acikgoz G, Miller RE, Kandula VV, Epelman M. Update on pediatric leukemia and lymphoma imaging. Semin Ultrasound CT MR. 2013;34(6):578–99.
16. Tavares M, Arantes M, Chacim S, Junior AC, Pinto A, Mariz JM, et al. Posterior reversible encephalopathy syndrome in children with hematologic malignancies. J Child Neurol. 2015;30(12):1669–75.
17. Rossi Espagnet MC, Pasquini L, Napolitano A, Cacchione A, Mastronuzzi A, Caruso R, et al. Magnetic resonance imaging patterns of treatment-related toxicity in the pediatric brain: an update and review of the literature. Pediatr Radiol. 2017;47(6):633–48.
18. Lo Nigro L, Di Cataldo A, Schiliro G. Acute neurotoxicity in children with B-lineage acute lymphoblastic leukemia (B-ALL) treated with intermediate risk protocols. Med Pediatr Oncol. 2000;35(5):449–55.
19. Toma P, Bertaina A, Castagnola E, Colafati GS, D'Andrea ML, Finocchi A, et al. Fungal infections of the lung in children. Pediatr Radiol. 2016;46(13):1856–65.
20. Muller FM, Trusen A, Weig M. Clinical manifestations and diagnosis of invasive aspergillosis in immunocompromised children. Eur J Pediatr. 2002;161(11):563–74.
21. Patsios D, Maimon N, Chung T, Roberts H, Disperati P, Minden M, et al. Chest low-dose computed tomography in neutropenic acute myeloid leukaemia patients. Respir Med. 2010;104(4):600–5.
22. Thomas KE, Owens CM, Veys PA, Novelli V, Costoli V. The radiological spectrum of invasive aspergillosis in children: a 10-year review. Pediatr Radiol. 2003;33(7):453–60.
23. Attenberger UI, Morelli JN, Henzler T, Buchheidt D, Fink C, Schoenberg SO, et al. 3 Tesla proton MRI for the diagnosis of pneumonia/lung infiltrates in neutropenic patients with acute myeloid leukemia: initial results in comparison to HRCT. Eur J Radiol. 2014;83(1):e61–6.
24. Yan C, Tan X, Wei Q, Feng R, Li C, Wu Y, et al. Lung MRI of invasive fungal infection at 3 Tesla: evaluation of five different pulse sequences and comparison with multidetector computed tomography (MDCT). Eur Radiol. 2015;25(2):550–7.
25. Nagel SN, Wyschkon S, Schwartz S, Hamm B, Elgeti T. Can magnetic resonance imaging be an alternative to computed tomography in immunocompromised patients with suspected fungal infections? Feasibility of a speed optimized examination protocol at 3 Tesla. Eur J Radiol. 2016;85(4):857–63.
26. Rieger C, Herzog P, Eibel R, Fiegl M, Ostermann H. Pulmonary MRI--a new approach for the evaluation of febrile neutropenic patients with malignancies. Support Care Cancer. 2008;16(6):599–606.
27. Peltola V, Ruuskanen O, Svedstrom E. Magnetic resonance imaging of lung infections in children. Pediatr Radiol. 2008;38(11):1225–31.
28. Sodhi KS, Bhatia A, Khandelwal N. Rapid lung magnetic resonance imaging in children with pulmonary infection. Pediatr Radiol. 2017;47(6):764–5.
29. Interiano RB, McCarville MB, Wu J, Davidoff AM, Sandoval J, Navid F. Pneumothorax as a complication of combination antiangiogenic therapy in children and young adults with refractory/recurrent solid tumors. J Pediatr Surg. 2015;50(9):1484–9.
30. Khoury NJ, Kanj V, Abboud M, Muwakkit S, Birjawi GA, Haddad MC. Abdominal complications of chemotherapy in pediatric malignancies: imaging findings. Clin Imaging. 2009;33(4):253–60.
31. Flores-Calderon J, Exiga-Gonzalez E, Moran-Villota S, Martin-Trejo J, Yamamoto-Nagano A. Acute pancreatitis in children with acute lymphoblastic leukemia treated with L-asparaginase. J Pediatr Hematol Oncol. 2009;31(10):790–3.
32. Cesaro S, Pillon M, Talenti E, Toffolutti T, Calore E, Tridello G, et al. A prospective survey on incidence, risk factors and therapy of hepatic veno-occlusive disease in children after hematopoietic stem cell transplantation. Haematologica. 2005;90(10):1396–404.
33. Choi A, Kang YK, Lim S, Kim DH, Lim JS, Lee JA. Severe hepatic sinusoidal obstruction syndrome in a child receiving vincristine, actinomycin-D, and cyclophosphamide for rhabdomyosarcoma: successful treatment with defibrotide. Cancer Res Treat. 2016;48(4):1443–7.
34. Mohty M, Malard F, Abecassis M, Aerts E, Alaskar AS, Aljurf M, et al. Sinusoidal obstruction syndrome/veno-occlusive disease: current situation and perspectives-a position statement from the European Society for Blood and Marrow Transplantation (EBMT). Bone Marrow Transplant. 2015;50(6):781–9.
35. Cesaro S, Spiller M, Sartori MT, Alaggio R, Peruzzo M, Saggiorato G, et al. Veno-occlusive disease in pediatric patients affected by Wilms tumor. Pediatr Blood Cancer. 2011;57(2):258–61.

36. McCarville MB, Hoffer FA, Howard SC, Goloubeva O, Kauffman WM. Hepatic veno-occlusive disease in children undergoing bone-marrow transplantation: usefulness of sonographic findings. Pediatr Radiol. 2001;31(2):102–5.
37. Kaya N, Erbey F, Atay D, Akcay A, Bozkurt C, Ozturk G. The diagnostic value of hepatic arterial velocity in venoocclusive disease after pediatric hematopoietic stem cell transplantation. J Pediatr Hematol Oncol. 2017;39:249.
38. Colecchia A, Marasco G, Ravaioli F, Kleinschmidt K, Masetti R, Prete A, et al. Usefulness of liver stiffness measurement in predicting hepatic veno-occlusive disease development in patients who undergo HSCT. Bone Marrow Transplant. 2017;52(3):494–7.
39. Brisse H, Orbach D, Lassau N, Servois V, Doz F, Debray D, et al. Portal vein thrombosis during antineoplastic chemotherapy in children: report of five cases and review of the literature. Eur J Cancer. 2004;40(18):2659–66.
40. Dosik GM, Luna M, Valdivieso M, McCredie KB, Gehan EA, Gil-Extremera B, et al. Necrotizing colitis in patients with cancer. Am J Med. 1979;67(4):646–56.
41. Mullassery D, Bader A, Battersby AJ, Mohammad Z, Jones EL, Parmar C, et al. Diagnosis, incidence, and outcomes of suspected typhlitis in oncology patients--experience in a tertiary pediatric surgical center in the United Kingdom. J Pediatr Surg. 2009;44(2):381–5.
42. Shafey A, Ethier MC, Traubici J, Naqvi A, Sung L. Incidence, risk factors, and outcomes of enteritis, typhlitis, and colitis in children with acute leukemia. J Pediatr Hematol Oncol. 2013;35(7):514–7.
43. Rizzatti M, Brandalise SR, de Azevedo AC, Pinheiro VR, Aguiar Sdos S. Neutropenic enterocolitis in children and young adults with cancer: prognostic value of clinical and image findings. Pediatr Hematol Oncol. 2010;27(6):462–70.
44. Urbach DR, Rotstein OD. Typhlitis. Can J Surg. 1999;42(6):415–9.
45. Gray TL, Ooi CY, Tran D, Traubici J, Gerstle JT, Sung L. Gastrointestinal complications in children with acute myeloid leukemia. Leuk Lymphoma. 2010;51(5):768–77.
46. El-Matary W, Soleimani M, Spady D, Belletrutti M. Typhlitis in children with malignancy: a single center experience. J Pediatr Hematol Oncol. 2011;33(3):e98–100.
47. Reyna-Figueroa J, Garcia-Beristain JC, Galindo-Delgado P, Limon-Rojas AE, Madrid-Marina V. Antibiotic use before chemotherapy: a risk factor for developing neutropenic colitis in children with leukemia. J Pediatr Hematol Oncol. 2015;37(2):121–7.
48. Capria S, Vitolo D, Cartoni C, Dessanti L, Micozzi A, Mandelli F, et al. Neutropenic enterocolitis in acute leukemia: diagnostic and therapeutic dilemma. Ann Hematol. 2004;83(3):195–7.
49. McCarville MB, Adelman CS, Li C, Xiong X, Furman WL, Razzouk BI, et al. Typhlitis in childhood cancer. Cancer. 2005;104(2):380–7.
50. Parisi MT, Fahmy JL, Kaminsky CK, Malogolowkin MH. Complications of cancer therapy in children: a radiologist's guide. Radiographics. 1999;19(2):283–97.
51. Cardona Zorrilla AF, Reveiz Herault L, Casasbuenas A, Aponte DM, Ramos PL. Systematic review of case reports concerning adults suffering from neutropenic enterocolitis. Clin Transl Oncol. 2006;8(1):31–8.
52. de Lijster MS, Smets AM, van den Berg H, Reekers JA. Embolisation for caecal bleeding in a child with typhlitis. Pediatr Radiol. 2015;45(2):283–5.
53. Fenton LZ, Buonomo C. Benign pneumatosis in children. Pediatr Radiol. 2000;30(11):786–93.
54. McCarville MB, Whittle SB, Goodin GS, Li CS, Smeltzer MP, Hale GA, et al. Clinical and CT features of benign pneumatosis intestinalis in pediatric hematopoietic stem cell transplant and oncology patients. Pediatr Radiol. 2008;38(10):1074–83.
55. Olson DE, Kim YW, Ying J, Donnelly LF. CT predictors for differentiating benign and clinically worrisome pneumatosis intestinalis in children beyond the neonatal period. Radiology. 2009;253(2):513–9.
56. Johnston D, Schurtz E, Tourville E, Jones T, Boemer A, Giel D. Risk factors associated with severity and outcomes in pediatric patients with hemorrhagic cystitis. J Urol. 2016;195(4 Pt 2):1312–7.
57. McCarville MB, Hoffer FA, Gingrich JR, Jenkins JJ III. Imaging findings of hemorrhagic cystitis in pediatric oncology patients. Pediatr Radiol. 2000;30(3):131–8.

Non-neurologic Late Effects of Therapy

12

Sue C. Kaste and Anurag Arora

12.1 Introduction

Improved diagnostic techniques and contemporary therapy have led to an increase in 5-year overall survival of patients diagnosed with pediatric cancers to over 80%. As of 2010, the number of living individuals in the United States, who had been diagnosed with a childhood cancer, was estimated at nearly 380,000 [1, 2]. By the year 2020, there may be as many as 500,000 survivors of childhood cancer living in the United States [1]. Concurrently, the growing population of survivors of childhood cancers is burdened with adverse late toxicities that may compromise quality and length of survival [3, 4]. Bhakta et al., from the St. Jude Lifetime Cohort Study of over 5500 patients treated at St. Jude Children's Research Hospital, who survived for at least 10 years from initial cancer diagnosis [5], found that the cumulative incidence for developing a chronic health condition as defined by the Common Terminology Criteria of Adverse Events was 99.9% (95% confidence interval 99.9 to 99.9), by age 50 years and 96% for severe chronic health condition. Each survivor developed an average of 17 chronic health conditions by age 50 years as opposed to 9.2 in matched community controls [5].

Therapy for childhood cancer is administered during the time of most active patient development and maturation, thereby contributing to disruption of normal growth and leading to long-term adverse sequelae. A chronic medical condition will develop in approximately 73% of survivors of childhood cancers, with 40% being a life-threatening or serious condition [4]. Thus, it is paramount that radiologists and other healthcare providers be familiar with late effects of treatment that may alter and compromise the health of this growing population.

12.2 Therapy

Although radiotherapy is well-recognized as an effective therapeutic modality, exposure to radiation therapy significantly increases the risk for later treatment-related mortality [3]. Radiotherapy

This work was supported in part by grant number P30CA021765-38 from the National Institutes of Health, a Center of Excellence grant from the State of Tennessee, and the American Lebanese Syrian Associated Charities (ALSAC).

S. C. Kaste (✉)
Department of Oncology, St. Jude Children's Research Hospital, Memphis, TN, USA

Department of Diagnostic Imaging, St. Jude Children's Research Hospital, Memphis, TN, USA

Department of Radiology, University of Tennessee Health Science Center, Memphis, TN, USA
e-mail: Sue.Kaste@STJUDE.ORG

A. Arora
Department of Radiology, University of Tennessee Health Science Center, Memphis, TN, USA

S. D. Voss, K. McHugh (eds.), *Imaging in Pediatric Oncology*, Pediatric Oncology,
https://doi.org/10.1007/978-3-030-03777-2_12

damages tumor cell DNA thereby reducing tumor volume by inhibiting rapidly dividing cells with high mitotic rates. The type and dose of the radiation source also determine the type of late effects. As the effects of radiotherapy are local, the severity and extent of late effects reflect the radiotherapy field and dose [6, 7]. The tissue response to radiotherapy depends on the tissue type. Atrophy results from damage to epithelial tissue, while fibrosis results from damage to stromal tissue. The process of tissue fibrosis is complex involving multiple pathways; investigations of the interaction and roles of pathways leading to inflammatory response, cell activation, oxidative stress, and genetics are ongoing [7–10]. Chemotherapy is typically given systemically. As such, its effects are generalized and affect normal as well as malignant cells. Since many children receive both chemotherapy and radiation therapy, distinguishing between effects caused by one therapy versus the other may be difficult, and the interaction between radiation therapy and chemotherapy may be synergistic [11].

As the population of survivors of childhood cancer has increased, guidelines have been developed for monitoring late effects, based upon patient exposures to therapy and subsequent risk for developing various toxicities [12]. This chapter highlights many of the common late effects of pediatric cancer therapy and the role of imaging in their detection and monitoring based upon several decades of experience. The impact of current disease- and patient-specific therapeutic regimens on long-term outcomes and sequelae will undoubtedly be assessed in the future as will the impact on the approach to imaging of these patients [13–15].

Craniofacial late effects: The effect of radiation on growing facial bones and cranium has been reported in 35–100% of children who receive high-dose radiotherapy, and many incur craniofacial abnormalities [16–18]. Younger age at treatment and increased radiotherapy volume and dose contribute to the extent and severity. Patients treated with both chemotherapy and radiation doses in excess of 24 Gy when younger than 5 years of age developed the most severe craniofacial abnormalities [16].

Dysodontogenesis, salivary gland dysfunction, trismus, oral graft-versus-host disease, and oral malignancies are among the radiation-related late effects [19, 20]. Denys et al. found that, although similar chemoradiation therapy was given to patients with nasopharyngeal carcinoma and nasopharyngeal rhabdomyosarcoma, disrupted craniofacial growth was significantly more severe in those with rhabdomyosarcoma [21]. The main difference between these two cohorts was the median age at diagnosis: those with rhabdomyosarcoma being diagnosed at an age about 10 years younger than those with nasopharyngeal carcinoma, 5.7 years versus 16.7 years, respectively [21].

Dental late effects: Mitosis of odontoblasts is directly inhibited by radiation. Children in whom odontoblasts are rapidly dividing are at risk for disrupted odontogenesis [18, 22]. Radiation-induced damage to the tooth buds may lead to hypodontia, anondontia, altered eruption pattern, root stunting, deficient enamel formation, and caries [16, 23] (Figs. 12.1, 12.2, and 12.3). A radiation dose of 10 Gy damages mature ameloblasts and 30 Gy arrests dental development at the phase of maturation at which the dentition is irradiated [24] (Fig. 12.1).

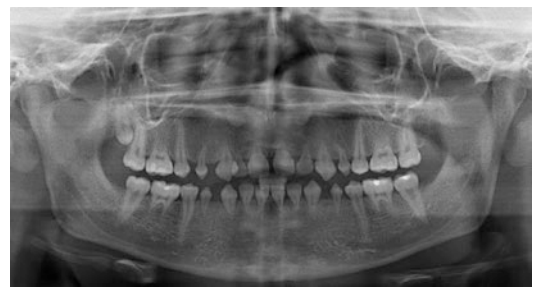

Fig. 12.1 Therapy-induced dysodontogenesis: A 15-year-old underwent allogeneic bone marrow transplantation at age 10 years for hemophagocytic lymphohistiocytosis. The severity and distribution of the abnormally formed teeth reflect the patient's age at the time of therapy. Panoramic radiograph demonstrates severe microdontia of all first premolars, severe root stunting of all central dentition, and all first molars. First premolars and second molars are nearly normal. Of third molars, only the right maxillary third molar has developed. The second primary molars and second molars had already developed at the time of therapy

Fig. 12.2 Dysodontogenesis: A 15-year-old boy, diagnosed with bilateral retinoblastoma at 1 month of age. Treatments included chemotherapy, 45 Gy radiation therapy to both eyes, and unilateral enucleation. Panoramic radiograph shows root stunting of all first permanent molars, over-retained left mandibular, and bilateral maxillary second primary molars. Also note foreshortened roots of central dentition

Fig. 12.3 Radiation-induced caries: A 21-year-old patient treated at the age of 9 years for Hodgkin lymphoma stage IIIB with chemotherapy and mantle (22 Gy), lower mediastinal (2 Gy), and para-aortic splenic (15.5 Gy) irradiation. He ultimately underwent complete extraction of teeth. Panoramic radiograph demonstrates extensive carious destruction of all teeth. Periapical lucency surrounding the roots of the right mandibular first molar, left mandibular second premolar, and minimally around the roots of the left mandibular second molar is indicative of multiple dental abscesses. Note severe radiation-induced root stunting of mandibular canines, premolars, and second molars, sparing the maxillary dentition

Abnormal teeth may contribute to malocclusion, subsequent temporomandibular joint dysfunction, and decreased growth of facial bones [23]. Variables which determine the late effects of radiation upon dental health include patient age and degree of dental development at the time of treatment, total radiation dose, daily radiation fraction, preexisting dental health, and interaction with specific chemotherapeutic agents [19, 25, 26]. Standard orthodontic interventions may require modification in survivors of childhood cancer due to abnormally short dental roots [26–28] (Figs. 12.1 and 12.2).

The affected dentition directly reflects the radiation field (Fig. 12.1). Thus, in the cases of mantle radiation therapy for Hodgkin lymphoma, mandibular dentition may be affected, while maxillary dentition is spared [29]. With total body irradiation, extensive dysodontogenesis may occur [30]. A retrospective study found that prior to dental maturation, 43% of 73 patients with acute lymphoblastic leukemia had treatment-related alteration of dental development [31]. Children who undergo bone marrow transplantation are also at risk for dysodontogenesis [32, 33]. However, many of the dental abnormalities may reflect therapy-induced changes that predate bone marrow transplantation [34].

From the Childhood Cancer Survivor Study, a report on approximately 9300 survivors found that dose-dependent exposure to alkylating agents significantly increased the likelihood of dental abnormalities in patients who were younger than 5 years at the time of treatment. The investigators also found that treatment with ≥20 Gy to the teeth was associated with altered dental development [25].

Based upon these sequelae, rigorous dental care is advised. Survivors of a childhood cancer should obtain at least annual dental follow-up. Those who received radiation therapy that included the head and neck may warrant more frequent evaluation to maintain oral-dental health [35].

12.3 Musculoskeletal Late Effects

The common long-term effects of oncotherapy on the skeleton include pathologic fractures, bone mineral density deficits (Fig. 12.4), limb length discrepancy (Figs. 12.5 and 12.6), slipped capital femoral epiphyses (Figs. 12.6 and 12.7), hemiatrophy (Fig. 12.8), osteonecrosis (Fig. 12.9), radiation osteitis (Fig. 12.10), short stature, osteochondromas (Figs. 12.6, 12.7, and 12.11), and scoliosis (Figs. 12.8, 12.12, and 12.13). While radiation therapy, chemotherapy, and surgery all independently contribute to late musculoskeletal

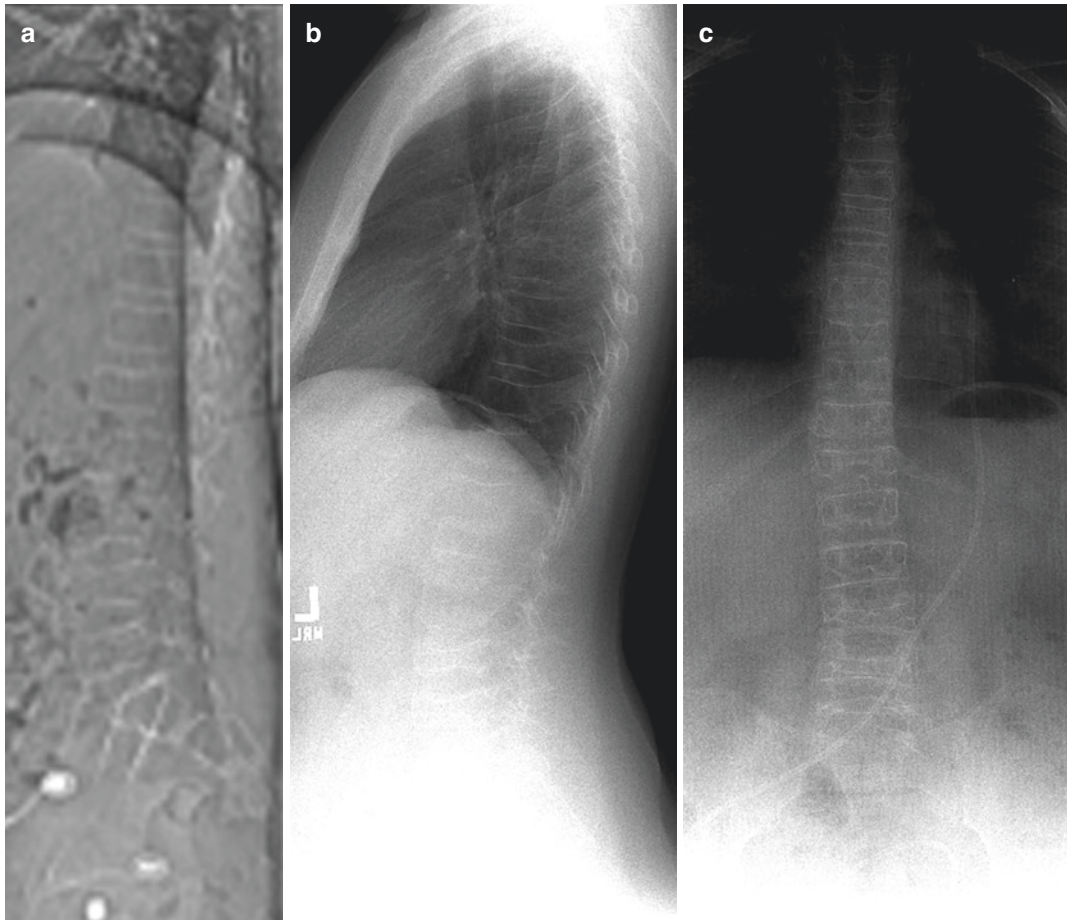

Fig. 12.4 A 11-year-old girl was diagnosed with a nongerminomatous germ cell tumor of the third ventricle and treated with chemotherapy and radiation therapy. She developed multiple endocrinopathies contributing to severe bone mineral density deficit (*Z*-score of −5.49) and multiple compression fractures of the thoracolumbar spine, 1 year from diagnosis. (**a**) Lateral scout image from the quantitative computed tomography study performed 1 year from diagnosis shows multiple compression fractures. Bone mineral density *Z*-score at this time was more than 5 standard deviations below the mean. (**b**, **c**). Lateral and frontal views from the corresponding scoliosis series show severe demineralization throughout the skeleton, numerous compression fractures, and severe thinning of vertebral cortices

sequelae, treatment with both radiation therapy and chemotherapy may enhance toxicities affecting the musculoskeletal system [36, 37].

Radiotherapy directly affects bone length, bone volume, and bone mineral density in the area irradiated due to disruption of not only osteoclast and osteoblast balance but also a decrease in hematopoietic stem cells, destruction of chondrocytes, and induction of apoptosis in relevant cell lines [18]. The resultant imbalance between osteoblastic and osteoclastic activity contributes to a decrease in bone mineral deposition and altered remodeling and growth [18, 38]. Vertebral body height may be stunted by radiation therapy [39–42] as well as by deficiency in growth hormone [43] and chemotherapy-induced skeletal growth aberrations [40, 44], contributing individually and collectively to short stature.

Indirect effects of radiotherapy on bone may occur from hormonal imbalance, such as seen in patients treated with cranial irradiation affecting the hypothalamic-pituitary axis, and hormonal

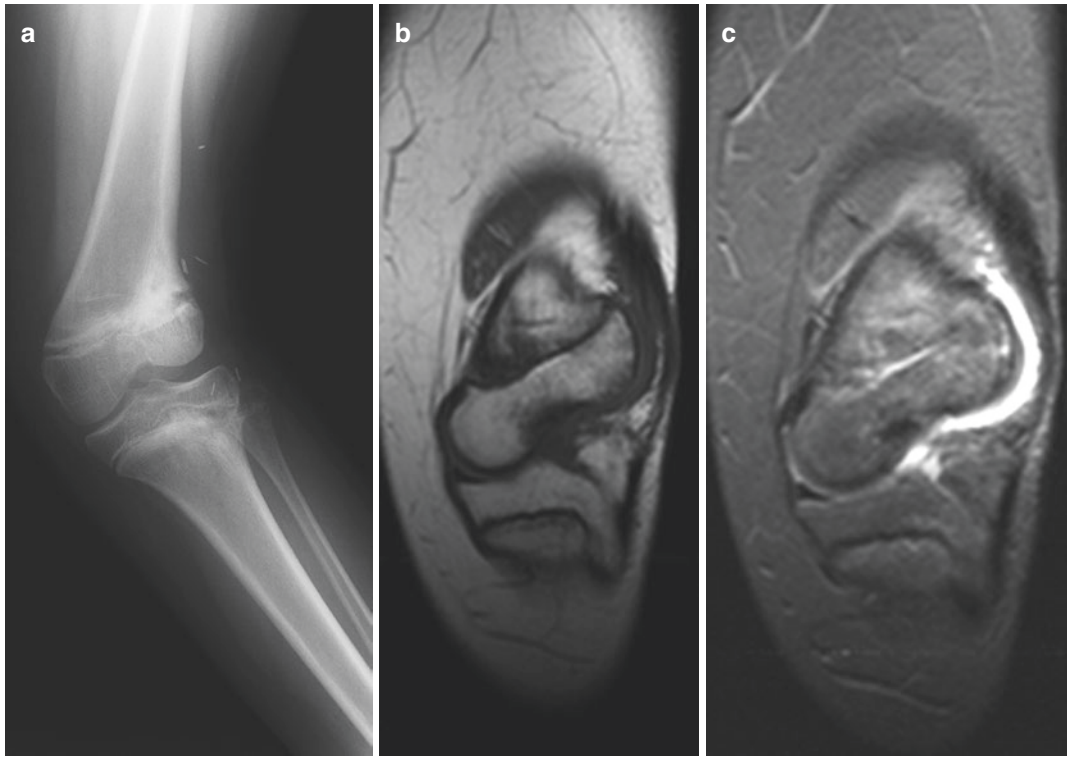

Fig. 12.5 Post-radiation growth disturbance: At the age of 9 years, the patient was diagnosed with synovial sarcoma left knee. She underwent surgical resection and radiation therapy comprised of 24.8 Gy brachytherapy and 50.4 Gy external beam. She developed progressive varus deformity of her left leg and leg length discrepancy of 6 cm, ultimately requiring corrective osteotomy. (**a**) Anteroposterior radiograph of the left knee showing severe varus deformity and asymmetric physeal fusion. (**b**, **c**) Corresponding coronal T1-weighted (**b**) and STIR (**c**) images of the left knee showing marked asymmetric growth of the distal femur with asymmetric physeal fusion

imbalance, such as seen with pelvic irradiation where the ovaries are included in the radiation portals [45, 46]. High radiation dose, younger patient age at the time of treatment, and asymmetric radiation volume to bone contribute to the overall late radiation therapy effects on the developing skeleton [36].

Chemotherapeutic agents, alone, can alter bone metabolism through systemic and organ-specific effects, contributing to decreased bone mineral density. Glucocorticoids, a mainstay of antileukemia therapy, primarily affect trabecular bone through an imbalance between osteoclasts and osteoblasts [45, 47]. The effects of ifosfamide- and platinum-derived therapies on bone metabolism result from their associated nephrotoxicity [45]. Cyclophosphamide and doxorubicin have both direct and indirect effects on bone turnover, the latter secondary to drug-induced ovarian failure [45, 48, 49] (Fig. 12.4).

Bone mineral density: Risk factors for deficits in bone mineral density are male sex, Caucasian race, treatment with cranial radiation in excess of 18 Gy, high doses of steroids, and methotrexate [46, 50, 51]. Hypogonadism has also been associated with decreased bone mineral density [46, 52] (Fig. 12.4). Patients receiving high doses of antimetabolites have a tendency for lower bone mineral density, though not reaching statistical significance [53].

A long-term follow-up study of 845 patients (median age at follow-up of 31 years) from the St. Jude Lifetime Cohort found that 6% of young adult survivors of childhood acute lymphoblastic

Fig. 12.6 Therapy-induced leg length inequality: This 10-year-old who underwent bone marrow transplantation at the age of 4 months for infant leukemia (also shown in Fig. 12.7). Anteroposterior long scanogram demonstrates bilateral slipped capital femoral epiphyses, a mild rightward pelvic tilt, multiple osteochondromas with resultant leg length inequality of greater than 1 cm

leukemia had a deficit in bone mineral density determined by quantitative computed tomography (QCT) of at least 2 standard deviations (*Z*-score) below the mean for age- and gender-matched QCT controls. Approximately 24% had a *Z*-score falling between −1 and −2. However, for a subset of 400 participants for whom at least one prior QCT was available, obtained a median of 8.5 years earlier, the BMD *Z*-scores in 67% of those had either improved or remained stable [54].

Bone mineral density may be assessed using quantitative computed tomography (QCT) or dual energy X-ray absorptiometry (DXA) scans. An initial assessment of BMD with entry into long-term follow-up is recommended by the Children's Oncology Group Long-Term Follow-up Guidelines for patients who have received therapy known to be associated with BMD deficits (e.g., glucocorticoids, methotrexate, radiation therapy, hematopoietic stem cell transplantation) and those with endocrinopathies predisposing them to BMD deficits [12, 46].

Osteonecrosis is a common therapy-related toxicity of leukemia therapy largely attributed to prolonged therapeutic exposure to high-dose glucocorticoids and reported in up to 74% of pediatric patients treated for acute lymphoblastic leukemia [55]. In addition to patients having been treated for childhood acute lymphoblastic leukemia, other high-risk survivor populations include those who have undergone hematopoietic stem cell transplantation and patients receiving high-dose glucocorticoids for other reasons [56–58].

Osteonecrosis may progress to a debilitating chronic condition ultimately leading to joint collapse and secondary arthritis [36, 59–64]. The clinical factor most strongly and consistently associated with the patient developing osteonecrosis is adolescent age at the time of therapy [58, 59, 65, 66]. Unlike osteonecrosis developing after trauma or radiation therapy, the systemic effect of glucocorticoid therapy places all joints at risk for its development; survivors of childhood cancer typically develop multi-joint involvement [Fig. 12.9]. The hips have been most often evaluated and are seen to be associated with greatest functional morbidity. Large lesions of the femoral heads portend a high likelihood of collapse; 80% of femoral head lesions involving at least 30% of the articular surface collapse within 2 years [67]. Though the hips are most often evaluated, the knees are more commonly involved than the hips [57, 68]. Involvement of shoulders and ankles may be underestimated [69, 70].

MR is the most sensitive imaging method to diagnosis osteonecrosis. Radiographs are insensitive for detecting osteonecrotic involvement

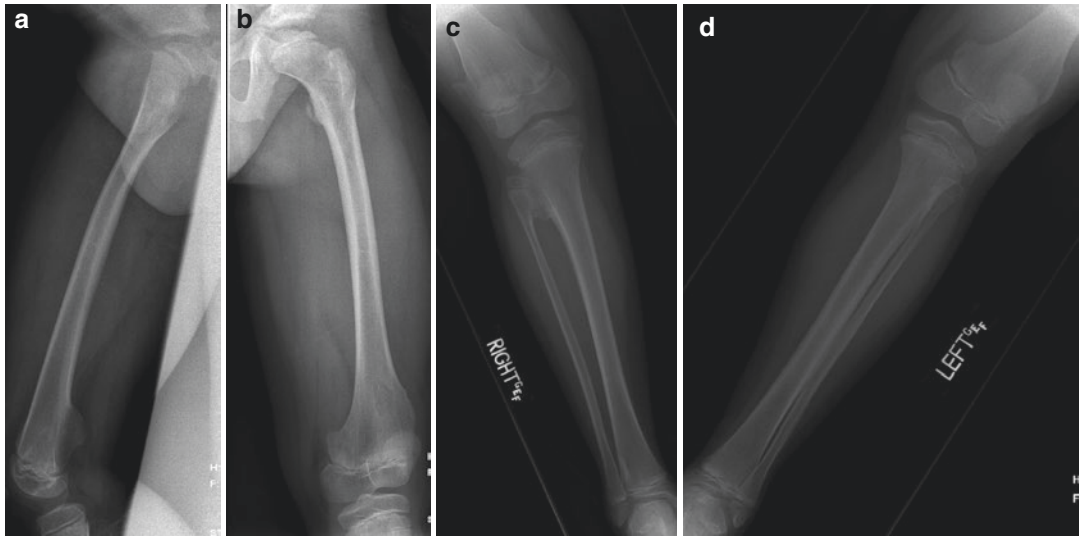

Fig. 12.7 Post-bone total body irradiation: At the age of 4 months, the patient was diagnosed with infant acute lymphoblastic leukemia and underwent hematopoietic stem cell transplantation. He developed a 1 cm leg length discrepancy, mild right-sided genu valgus. Radiographs obtained approximately 10 years later demonstrate multiple exostoses, chronic right-sided slipped capital femoral epiphysis, and fragmentation left capital femoral epiphysis. (**a**, **b**) Anteroposterior radiographs of the femurs demonstrate a right-sided slipped capital femoral epiphysis, fragmentation of the left capital femoral epiphysis, and multiple osteochondromas of the distal femoral metaphyses, bilaterally. (**c**, **d**) Anteroposterior radiographs of the lower legs show multiple exostoses involving the knees

early in its phase of development (Fig. 12.9) [55]. Patients are often asymptomatic until collapse of the articular surface occurs, at which time, conservative methods of management have limited efficacy [63, 71, 72].

Scoliosis: Historically, scoliosis developed after unilateral or asymmetric radiation therapy that included the developing spine (Figs. 12.8, 12.12, and 12.13). However, contemporary treatment portals are designed to provide symmetrical exposure of developing vertebral bodies in order to offset potential development of scoliosis [39].

A recent study of long-term survivors of childhood sarcoma treated between 1964 and 2002 identified scoliosis in 27% (100 of 367) of young adults followed for more than 10 years. Risk factors found to be identified with the development of scoliosis were radiation to the chest and rib resection. The authors found scoliosis to be associated with decreased pulmonary function as well as self-reported pain and impaired function [73]. Lucas et al. also found that the extent of surgical resection, including the number and location of resected ribs, was associated with the severity and extent of scoliosis but found no association between radiation dose and tumor size and scoliosis in a group of 23 consecutive patients treated for chest wall sarcomas [74].

Cardiovascular sequelae: Treatment toxicities place survivors of childhood cancers at considerably increased risk of cardiovascular disease and cardiac deaths compared with the general population. Recent estimates indicate that by the age of 50 years, survivors will suffer from more than twice the number of chronic and almost five times the number of severe cardiovascular conditions compared to the general population [5]. Risk correlates to specific treatment exposures which reflected the era in which the patient was treated [75]. Development of congestive heart failure, valvular disease, and cardiomyopathy may have a delayed onset but, once initiated, are progressive and have irreversible conditions [76–78].

Approximately 60% of childhood cancer survivors have been exposed to anthracycline therapy or chest irradiation. As a result, these patients

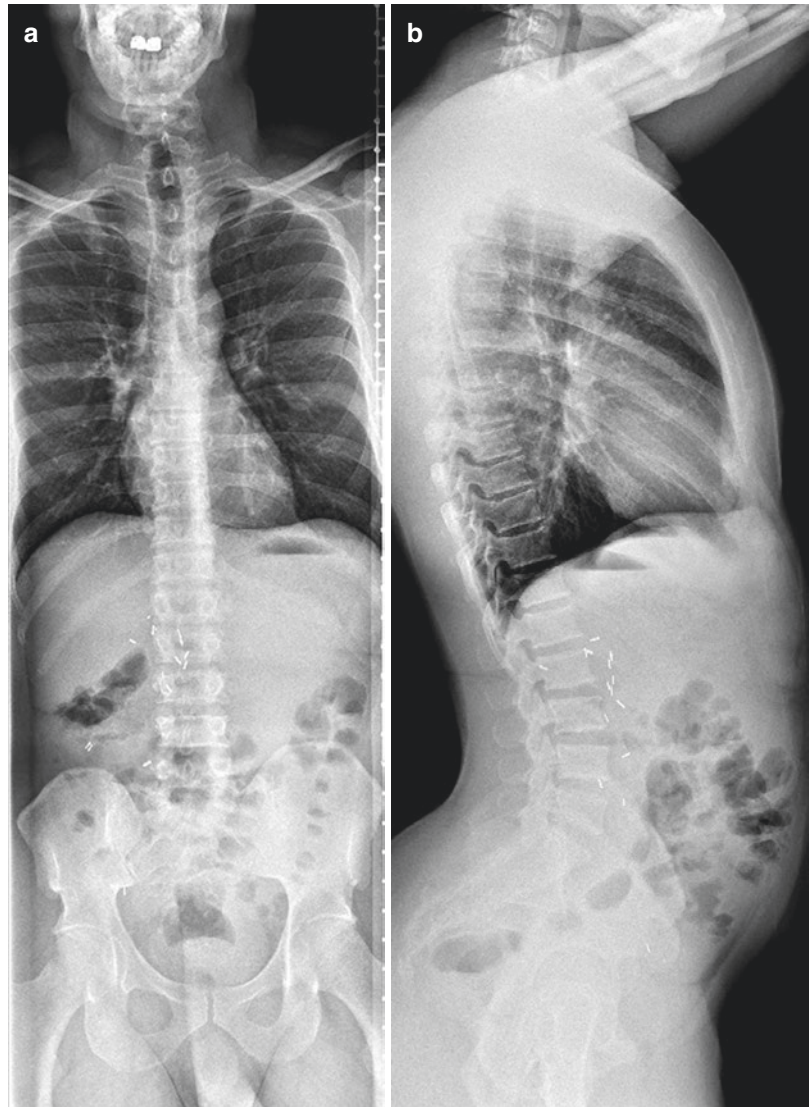

Fig. 12.8 (**a**, **b**) A 36-year-old man diagnosed at age 10 months with right renal Wilms tumor treated with chemotherapy, unilateral nephrectomy, and hemiabdominal radiation therapy. Scoliosis series demonstrates dysplastic changes in the right hemipelvis with associated mild rotoscoliosis. Surgical staples in the right retroperitoneum indicate prior nephrectomy

are at 15-fold risk of cardiac complications particularly heart failure [4, 77, 79]. A report from the Childhood Cancer Survivor Study indicated that radiation therapy to the chest, spine, or total body was associated with a greater than threefold increased risk of cardiac death [3]. Patients who received therapy that included greater than 300 mg/m^2 anthracycline had a nearly 12-fold increased risk of developing clinically apparent heart failure, compared with those treated with lower doses [80, 81].

Although echocardiography has internationally been recommended to evaluate late cardiovascular complications, high-quality cardiac MR is evolving as a valuable method for screening survivors of childhood cancer who received cardiotoxic therapy, superseding 2-D echocardiography in the detection of cardiomyopathy [82, 83]. As cardiac decompensation typically lies dormant for a variable number of years, the first indication of cardiovascular deterioration may be seen on chest radiography obtained for other reasons [76]. Cardiac CT may also be useful for estimation of coronary artery disease, which Kupeli et al. found in 16% of survivors of childhood Hodgkin lymphoma [84]. Patients, who received

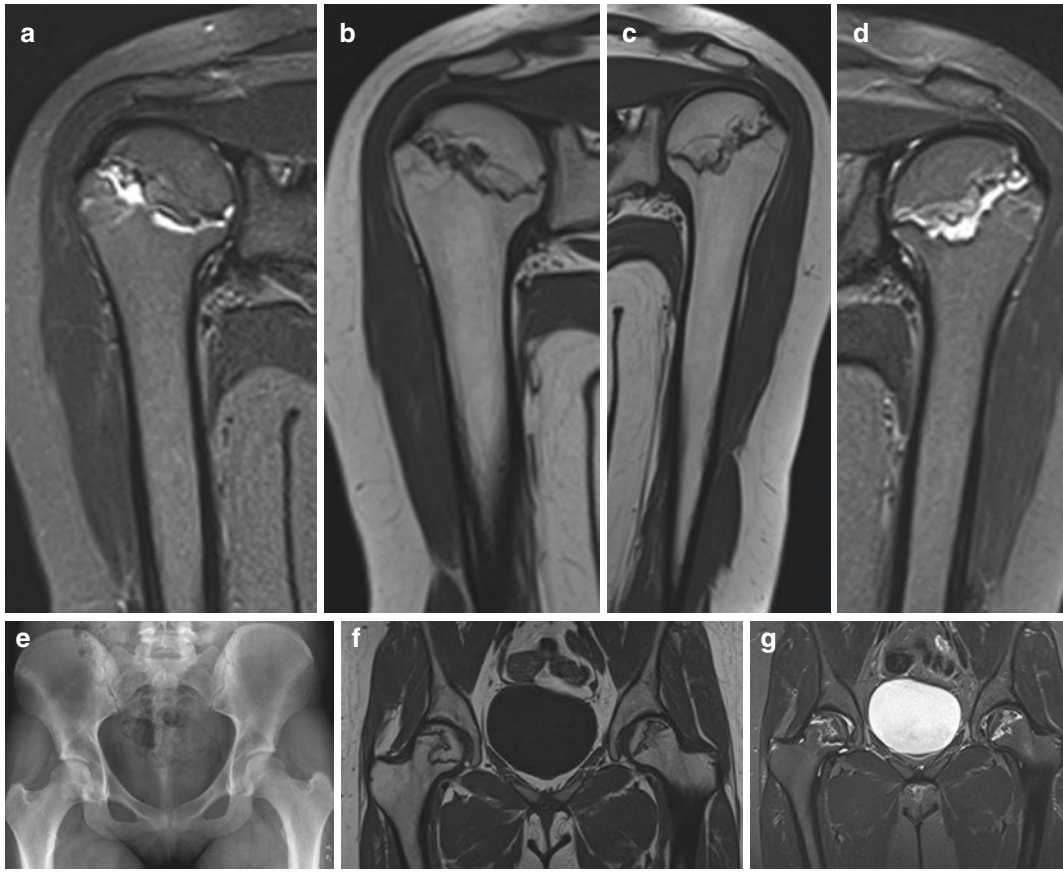

Fig. 12.9 Chemotherapy-induced osteonecrosis: Diagnosed at age 17 years with lymphoblastic lymphoma, this patient was treated with chemotherapy, total body irradiation, and bone marrow transplantation for multiple disease relapses. Among multiple late toxicities, the patient developed advanced osteonecrosis involving her shoulders, hips, and knees. (**a**–**d**) Coronal non-contrast T1 (**b**, **c**) and STIR (**a**, **d**) images of the proximal humeri show extensive involvement of both humeral heads by osteonecrosis. (**e**) Anteroposterior radiograph of the pelvis is normal and specifically shows no evidence of osteonecrosis. (**f**, **g**) Coronal non-contrast T1 (**f**) and STIR (**g**) imaging of the pelvis and hips show extensive involvement of both femoral heads, despite the normal appearance on the radiograph obtained 1 month earlier. (**h**, **i**) Coronal non-contrast T1 (**h**) and STIR (**i**) imaging of the knees show extensive osteonecrotic involvement of both distal femoral diametaphyses, as well as involvement of both proximal tibial diametaphyses

mediastinal radiation therapy in addition to chemotherapy, had a nearly sevenfold increased risk of coronary artery disease compared with those not treated with mediastinal irradiation.

Pulmonary late effects: The risk for developing pulmonary complications from therapy varies with treatment exposures and doses of chemotherapy and radiation therapy, age at the time of treatment, and smoking history [85].

Reported from the Childhood Cancer Survivor Study, the cumulative risk for development of pulmonary radiation fibrosis was approximately 3.5% at 20 years from exposure, with chest irradiation being statistically associated with its development (RR = 4.3; P = 0.001) [86]. Recurrent pneumonia (RR = 2.2; P = 0.001) and chronic cough (RR = 2.0; $P < 0.001$) have been reported in children surviving 5 years or more post cancer therapy [86]. Radiation-induced injury to type II pneumocytes and endothelial cells may progress over time to pulmonary fibrosis as evidenced by a cumulative incidence of 3.5% of patients 20 years after chest radiation [86–88]. Though not reaching statistical signifi-

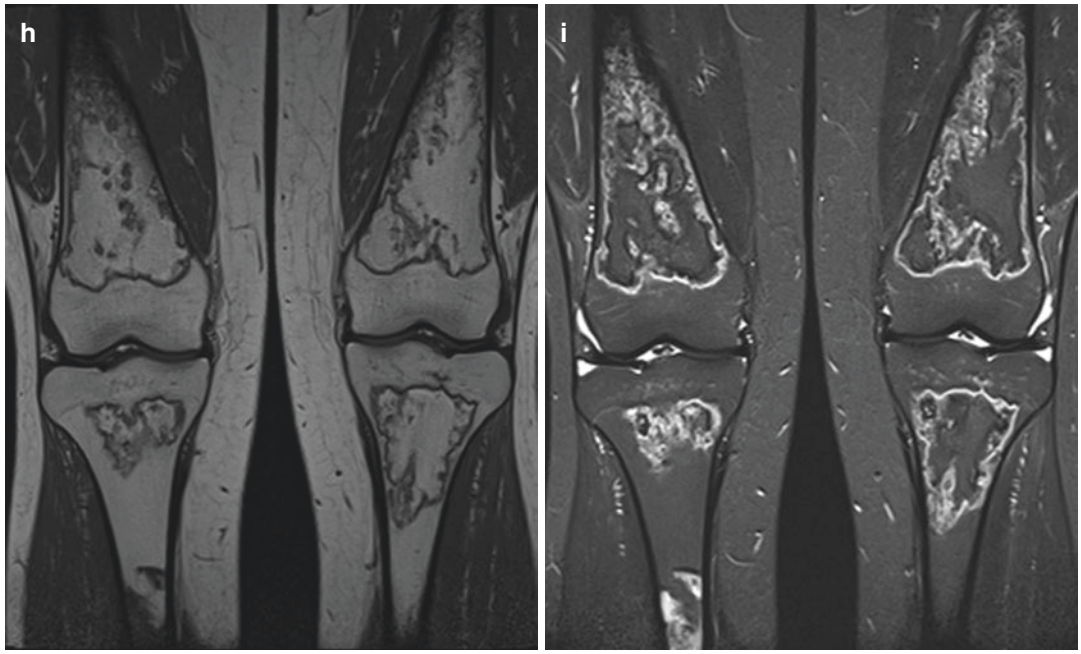

Fig. 12. 9 (continued)

cance, patients treated with total body irradiation or radiation to the chest or spine have been reported to be at increased risk for pulmonary death [89].

However, some chemotherapeutic agents such as busulfan, bleomycin, carmustine, and lomustine can incite pulmonary fibrosis, chronic cough, and dyspnea in the absence of radiation therapy [86]. Chemotherapy also compounds the pulmonary toxic effects of radiation therapy. Children receiving both radiation and chemotherapy suffer long-term pulmonary dysfunction in up to 72% cases [90].

Chest radiography or CT is useful for detecting pulmonary fibrosis, indicated by pleural thickening, retraction, and scarring of the hila or focally within the lung parenchyma (Fig. 12.14). Post-radiation changes may extend beyond the radiation portals [87]. The demonstration of pulmonary interstitial or alveolar infiltrates without infection by high-resolution chest CT is associated with decreased pulmonary function when compared with pulmonary function studies of patients with normal high-resolution chest CT. Conversely, approximately 36% of studied patients with normal chest CT had abnormal pulmonary function tests [91]. Bronchiolitis obliterans and bronchiolitis obliterans organizing pneumonia (BOOP) may also be seen [92].

12.4 Gastrointestinal and Hepatobiliary Late Effects

Survivors of childhood cancer are at significantly increased risk for the development of gastrointestinal and hepatic diseases compared with the general population [93, 94]. At 20 years after diagnosis of a malignancy, the cumulative incidence of adverse late effects affecting the gastrointestinal system is estimated to be 38% [94]. The gastrointestinal effects of cancer therapy can be further subcategorized into enteric and hepatobiliary complications [92]. Combination therapy typically imparts more frequent and severe toxicities.

Enteric complications: Ionizing radiation compromises the integrity of the mucosal epithelium of the gastrointestinal tract [95]. Chronic radiation-induced bowel disease occurs in 0.5–16.9% of patients receiving abdominopelvic irradiation, usually manifesting 6–24 months after

Fig. 12.10 Radiation osteitis: This 15-year-old boy was diagnosed at age 2 years with rhabdomyosarcoma of the prostate and treated with chemotherapy and 50.4 Gy radiation therapy to the prostate. Radiographs obtained approximately 11 years later show extensive post-radiation skeletal changes and growth disturbance. (**a**) Anteroposterior radiograph of the pelvis shows diffusely thickened trabeculae of midline pelvic bones and femoral heads and necks in distribution of the radiation portals. Note also the foreshortened femoral necks and thickening of the acetabula. (**b**) Corresponding coronal T1-weighted MR through the pelvis demonstrates heterogeneous mineralization with irregularity of the articular surface of the right capital femoral epiphysis, worrisome for developing osteonecrosis. (**c**, **d**) Lateral (**c**), and anteroposterior (**d**), radiographs of the lumbar spine, sacrum, and coccyx show growth disturbance defining the radiation portal. The vertebral bodies within the radiation portal are small compared to those outside of the treatment field

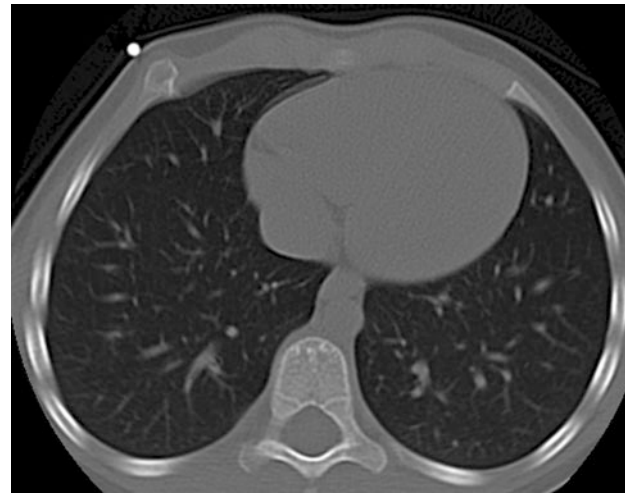

Fig. 12.11 Post-radiation osteochondroma: At the age of 3 years, this patient was diagnosed with chronic myelogenous leukemia and treated with chemotherapy, total body irradiation of 12 Gy, and allogeneic bone marrow transplantation. She returned for routine follow-up and complained of a lump in her right anterior chest wall. Axial CT image with bone windows through the level of the lower thorax showing a small exostosis projecting from the right anterior fourth rib, subjacent to the skin marker

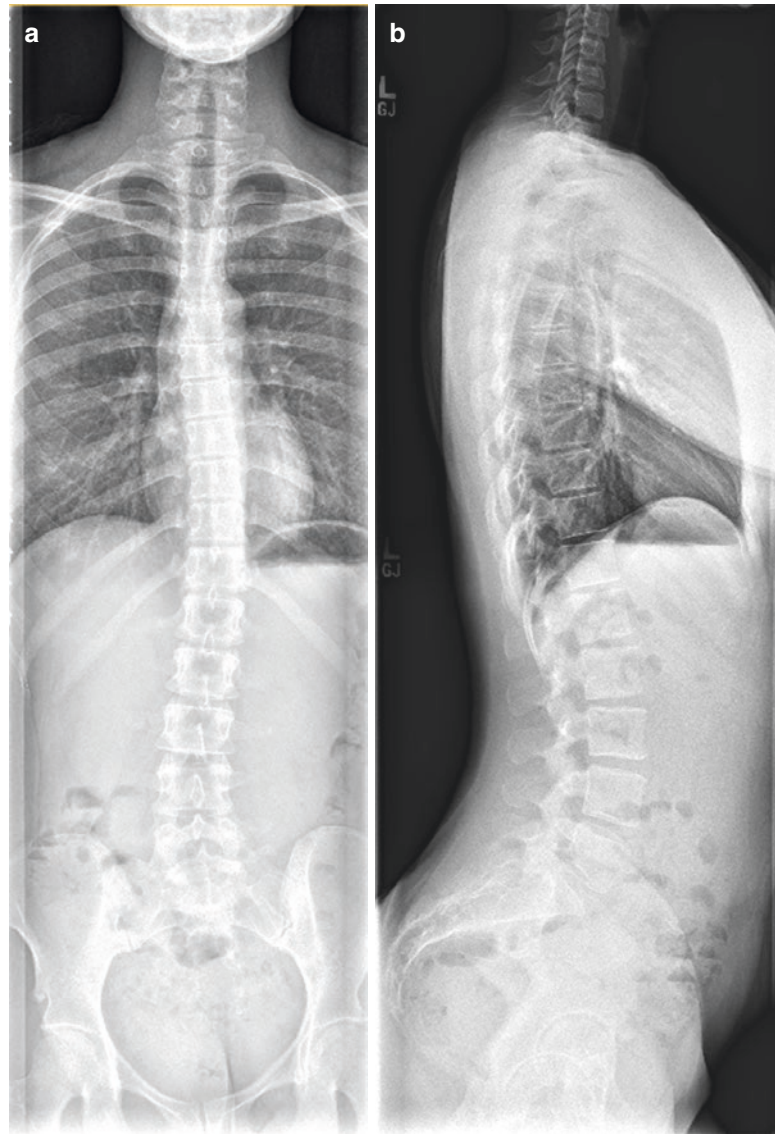

Fig. 12.12 (**a**, **b**) Therapy-related scoliosis: A 37-year-old treated for osteosarcoma of the foot at age 14 years that included chemotherapy and below-knee amputation. Scoliosis series, anteroposterior and lateral views, shows a mild S-shaped thoracolumbar scoliosis; note subtle rightward pelvic tilt, ipsilateral to the side of amputation

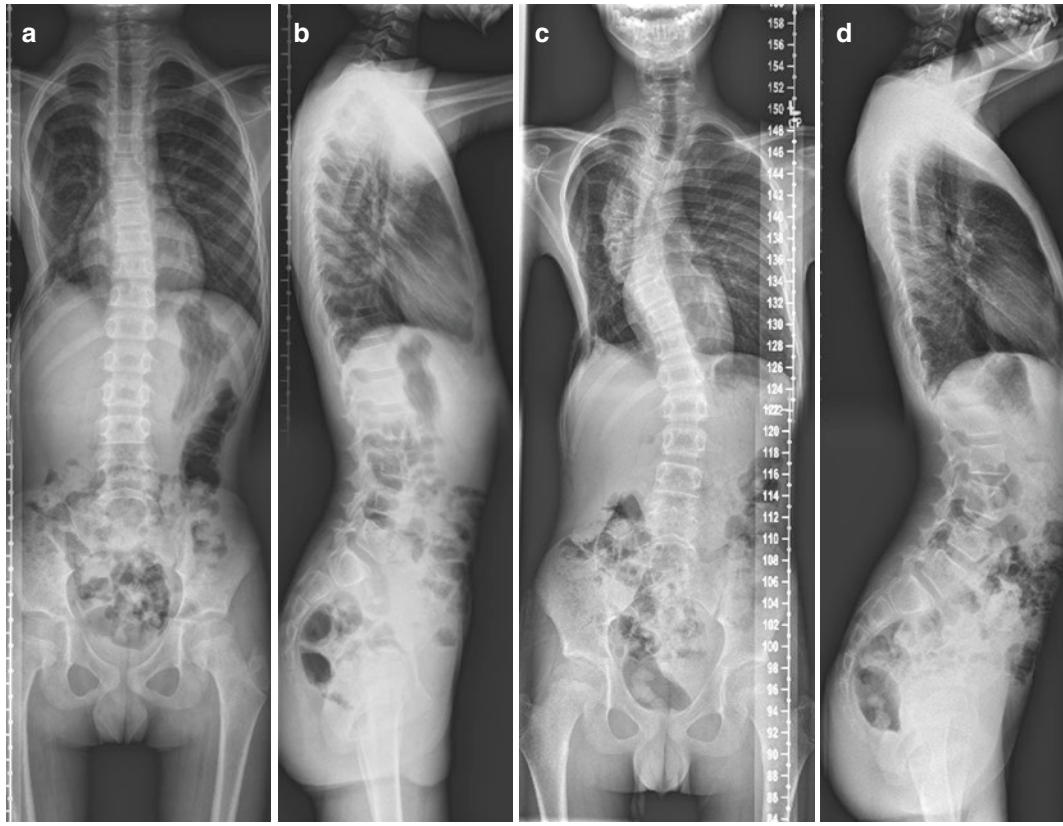

Fig. 12.13 Severe therapy-induced scoliosis: At the age of 6 years, this patient was diagnosed with Ewing sarcoma in the right sixth to eighth ribs. Treatment included chemotherapy, multiple rib resection, and 50.4 Gy radiation therapy. Scoliosis series performed 5 (**a**, **b**) years and 8 (**c**, **d**) years, respectively, after completion of therapy. (**a**, **b**) Lateral and anteroposterior scoliosis images demonstrate surgical changes of the right lateral and posterior chest wall resection. A minimal lower thoracic *D*-convex curve is suggested on the anteroposterior image, with apex at T11. (**c**, **d**) Repeat scoliosis series 3 years later shows marked progression of the thoracic component, now with flattening of the normal thoracic curve and progression of radiation-induced right thoracic hypoplasia

radiotherapy [95, 96]. The long-term effects of radiotherapy are thought to be due an admixture of occlusive vasculitis, inflammation, collagen deposition and fibrosis, and alteration of intestinal flora [97–100]. Collagen deposition and fibrosis account for the chronic complications [98]. Usually, chronic radiation-induced small bowel disease develops between 18 months and 6 years from completion of radiation therapy but has been reported as early as 2 months and as late as 30 years following radiation therapy involving the colon [99–105]. Due to its rapid cell turnover, the small bowel mucosa is the most radiosensitive tissue in the gastrointestinal tract [106]. Symptoms of radiation-induced small bowel disease may develop after as little as fractionated 5–12 Gy, although usually symptoms develop after higher doses [99].

Mucosal ulcerations, strictures, bowel obstruction, and malabsorption are common enteric complications in children surviving cancer therapy [95, 107]. Bowel obstruction from stenosis or adhesions has been reported in 36% of survivors [20, 108]. Surgery-related late complications result from formation of dense adhesions, a high incidence of anastomotic dehiscence, re-obstruction, and mortality after resection of previously irradiated bowel [98, 101, 103]. Strictures, bowel obstruction, and enteric fistulae are common late enteric complications in chil-

dren surviving cancer therapy [107]. Therapy-related adhesions could lead to bowel obstruction and intussusception.

Bowel obstruction requiring surgery has been reported to occur with a cumulative incidence at 35 years in 5.8% of survivors of childhood cancer (95% confidence interval, 4.4–7.3%) treated for an abdominopelvic tumor and in 1.0% (95% confidence interval, 0.7–1.4%) of those without a tumor in the abdomen or pelvis. Intestinal

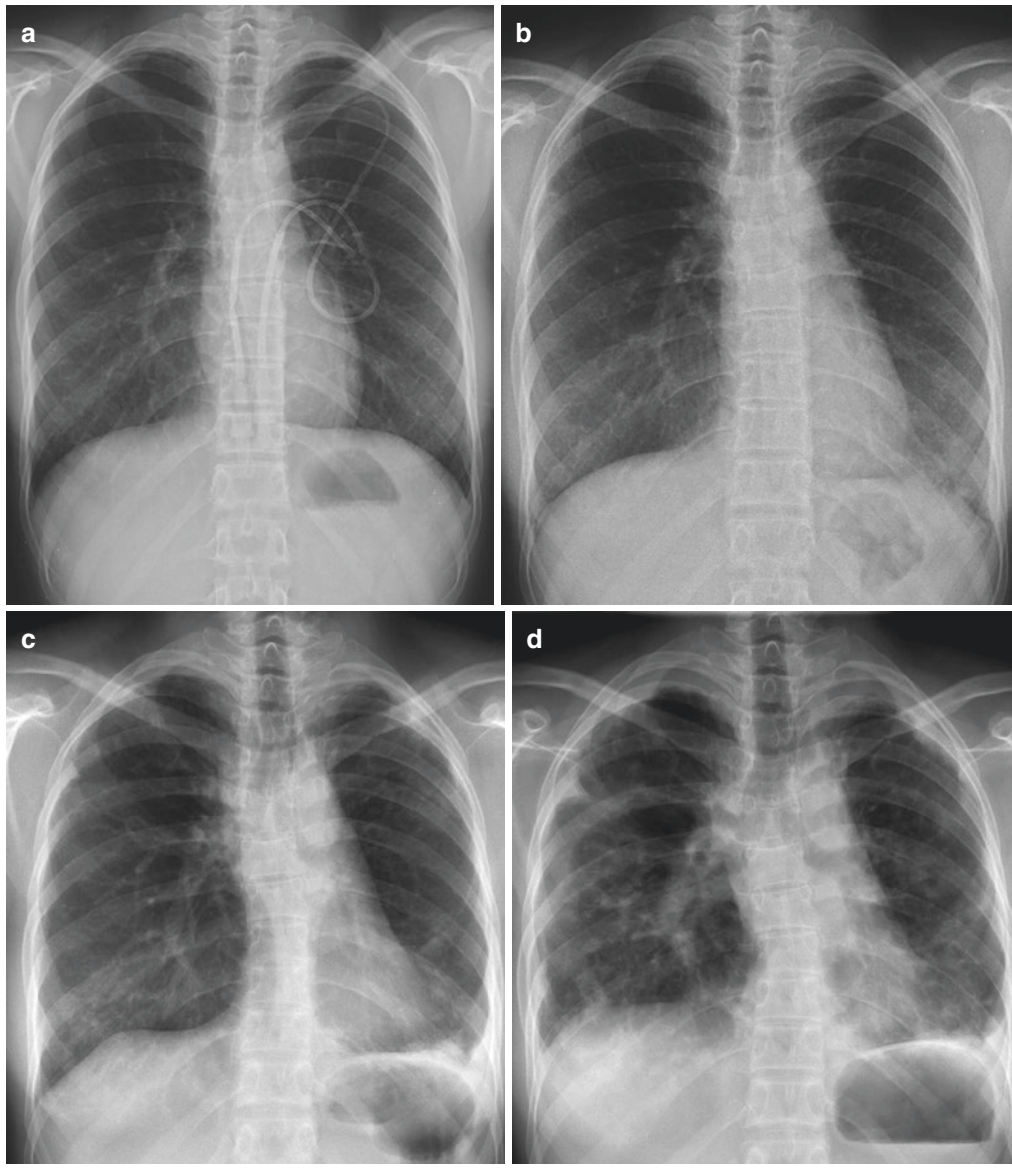

Fig. 12.14 Pulmonary fibrosis: A 17-year-old girl diagnosed with nodular sclerosing Hodgkin lymphoma and treated with chemotherapy and modified mantle irradiation of 25.5 Gy. She relapsed with Hodgkin disease 2 years later and underwent bone marrow transplantation with irradiation to sites of relapse. She developed progressive pulmonary fibrosis ultimately leading to her demise. (**a**) Posteroanterior chest radiograph at the time of relapse showed normal appearance of the mediastinum and lungs. (**b**) Posteroanterior chest radiograph 1 year after completion of relapse therapy shows development of left lower lobe pleural thickening with straightening of the left mediastinal margin and left lower lobe scarring. Note subtle coarsened interstitial markings in the right lower lobe. (**c**, **d**) Posteroanterior chest radiographs obtained 4 years and 5 years, respectively, after completion of therapy show progressive and extensive pulmonary fibrosis with thickened septa, scarring, retraction of mediastinal tissues, and biapical pleural thickening

obstruction occurred with an adjusted rate ratio of 3.6 (95% confidence interval, 1.9–6.8, $P < 0.001$) in those with an abdominopelvic tumor and in those receiving radiation therapy doses exceeding 50 Gy within 5 years of initial diagnosis of cancer (adjusted rate ratio of 2.4; 95% confidence interval, 1.6–3.7; $P < 0.001$) when compared with their siblings [109]. Development of an intestinal obstruction was associated with increased mortality [109].

Imaging findings of radiation-related bowel disease vary widely and include ileus, bowel obstruction, ulceration, dysmotility, tubulation, bowel wall thickening, fistulae formation, abscess, or perforation [100, 110–113]. Approximately 15% of patients with chronic radiation-related bowel disease have normal imaging studies [101, 114]. As many of the imaging findings are non-specific, correlation of the clinical history of radiation therapy to the abdomen and/or pelvis with imaging findings is key to making the correct diagnosis of radiation-related bowel disease.

A report from the Childhood Cancer Survivor Study of over 14,000 childhood cancer survivors, median age at the time of post-therapy assessment of 23 years (range, 7–49 years), revealed that survivors self-reported sequelae nearly twice as frequently as their siblings for the upper gastrointestinal tract (ratio rate 1.8; 95% confidence interval 1.6–2.0), liver (ratio rate 2.1; 95% confidence interval, 1.8–2.5), and lower gastrointestinal tract (ratio rate 1.9; 95% confidence interval, 1.7–2.2). Increased risk of development of some of the late sequelae included older age at the time of therapy, radiation therapy to the abdomen, and abdominal surgery [94]. Asdahl et al. reported in a similar long-term follow-up study of over 31, 000 survivors a 60% increased relative risk in survivors of childhood cancer for the development of gastrointestinal or hepatic disease (risk ratio, 1.6; 95% confidence interval 1.6–1.7) at a median follow-up of 10 years (range, 0–42 years) after therapy completion [93]. An unexpected finding in this report was the prevalence of esophageal stricture (risk ratio, 13; 95% confidence interval 9.2–20), notably in survivors of childhood acute lymphoblastic leukemia. The authors attribute candida esophagitis as the likely explanation [93].

Fluoroscopy-assisted contrast studies like loopogram, esophagram, and upper GI studies with small bowel follow-through are useful tools for imaging of strictures, bowel obstruction, and fistulae [107]. More recently, CT and MR enterography have been shown to play a valuable role in diagnosing radiation-related bowel sequelae [110, 112]. CT findings that may indicate post-therapy bowel disease include bowel wall thickening, increase in pelvic fat, soft tissue stranding, and formation of strictures and fistulae [112]. Algin et al. using MR enterography found that the most valuable information obtained with this technique was identification of an abnormal loop of bowel within the radiation field [110]. Other reported findings from this adult case series included bowel wall thickening, contrast enhancement of the bowel wall, small bowel wall thickening, narrowed bowel lumen, and stranding of the mesentery [110]. MR enterography is reportedly well-tolerated by pediatric patients [115].

12.5 Hepatobiliary Complications

There is limited information regarding long-term hepatic insufficiency in survivors of childhood cancer. However, the reported incidence of such is low without associated coexistent morbidities such as infection [116]. Chemotherapy, radiation therapy, and hepatic resections can independently and additively lead to hepatic injury [39, 116–120].

Focal nodular hyperplasia (FNH) is the most common entity seen within 2–12 years of cancer therapy. Pediatric cases of FNH account for only 7% of all reported cases. FNH are the most common benign hepatic tumors within 2–12 years of cancer therapy with a median interval of 6.7 years [121]. It is seen with increasing frequency after treatment with chemotherapy and radiotherapy [122]. FNH in cancer survivors may be atypical, small, and multiple with lack of central scar [123]. Pillon et al. found FNH to develop in 5.2% (17 of 324) of patients who underwent hematopoietic stem cell transplantation, 94% of

those with FNH being younger than 12 years at the time of transplantation [124].

FNH is a hepatocellular proliferation that is induced by vascular injuries such as thrombosis, intimal hyperplasia, high sinusoidal pressure, or increased flow [122, 125] and in cancer survivors is thought to be a manifestation of injury to the vascular endothelium caused by chemotherapy or radiotherapy.

The definitive diagnosis of FNH is based upon specific imaging criteria. On CT scan a classic FNH is a homogenous hypo-attenuating mass enhancing avidly on arterial phase with a non-enhancing central scar [122]. Ultrasound examination for screening and contrast-enhanced CT scan or MRI may be used for definitive diagnosis of FNH [92, 124, 126]. More recently, the use of contrast-enhanced ultrasound has been shown to be a valuable modality for differentiating FNH from other hepatic lesions [126–130] (Fig. 12.15). Please see Chap. 8, dedicated to contrast-enhanced US as it relates to pediatric oncologic imaging. Hepatocyte-specific MR contrast agents are useful to characterize hepatic lesions and differentiate focal nodular hyperplasia from other lesions [127, 131, 132].

Hemochromatosis: Hepatic iron overload, which can contribute to the development of endocrine and cardiac complications as well as being associated with hepatic fibrosis and cirrhosis, is common in patients who have received multiple blood cell transfusions [133–137]. Based upon serum ferritin levels and liver histology, 14–70% of children treated for acute lymphoblastic leukemia develop histologically positive siderosis [92, 136, 137]. From 26% to 93% of children who have undergone hematopoietic stem cell transplantation have been reported to have hepatic iron deposition [134, 135]. MR quantification of hepatic iron content provides accurate noninvasive assessment of hepatic iron deposition [138–140].

Steatosis: Fatty infiltration (steatosis) of the liver results from deposition of triglycerides in hepatocytes and is commonly seen in survivors of acute lymphocytic leukemia [111, 136]. Other patients in whom steatosis may be seen include those with hepatoblastoma who were treated with liver transplantation and those with metabolic syndrome related to insulin resistance caused by whole body irradiation and from immunosuppressive chemotherapy [92, 141]. Ultrasound examination demonstrates increased echogenicity of liver parenchyma [39, 43]. In and out of phase imaging on MRI is an accurate method of diagnosis [92].

Fibrosis: Though seen less commonly than hemosiderosis, hepatic fibrosis may occur with variable frequency in patients treated for acute lymphoblastic leukemia [136]. Portal hypertension, cirrhosis, and hepatocellular carcinoma are potential fibrosis-related complications in children [116, 135, 136].

Ultrasound assessment of liver stiffness, fibrosis, and steatosis and MR elastography are gaining interest as adjunct methods for assessing hepatic toxicity, though the experience of their use in pediatric and young adult patient populations is not as robust as in adult populations [142–149].

12.6 Genitourinary Late Effects

Renal atrophy and urinary bladder fibrosis are the prime manifestation of cancer therapy diagnosed on imaging [106].

Renal: Chemotherapy and radiation-induced nephropathy can present as focal or diffuse renal parenchymal volume loss and end-stage renal disease [106] (Fig. 12.16).

Renal late effects are usually manifested within 6–12 months after therapy [92]. Radiation oncologists seek to minimize renal radiation as kidneys are very radiosensitive. As the ureters are relatively resistant to radiation-induced changes, radiation-induced ureteral strictures are rare late complications [106, 150]. Hypophosphatemic rickets may result from ifosfamide-induced renal disease [59, 151].

In patients who have undergone unilateral nephrectomy, compensatory hypertrophy of the remaining kidney is commonly seen, reported in 83% of survivors of Wilms tumor [152]. Contemporary nephron-sparing techniques contribute to disease cure while decreasing therapy-related renal morbidity [153, 154]. Ultrasound

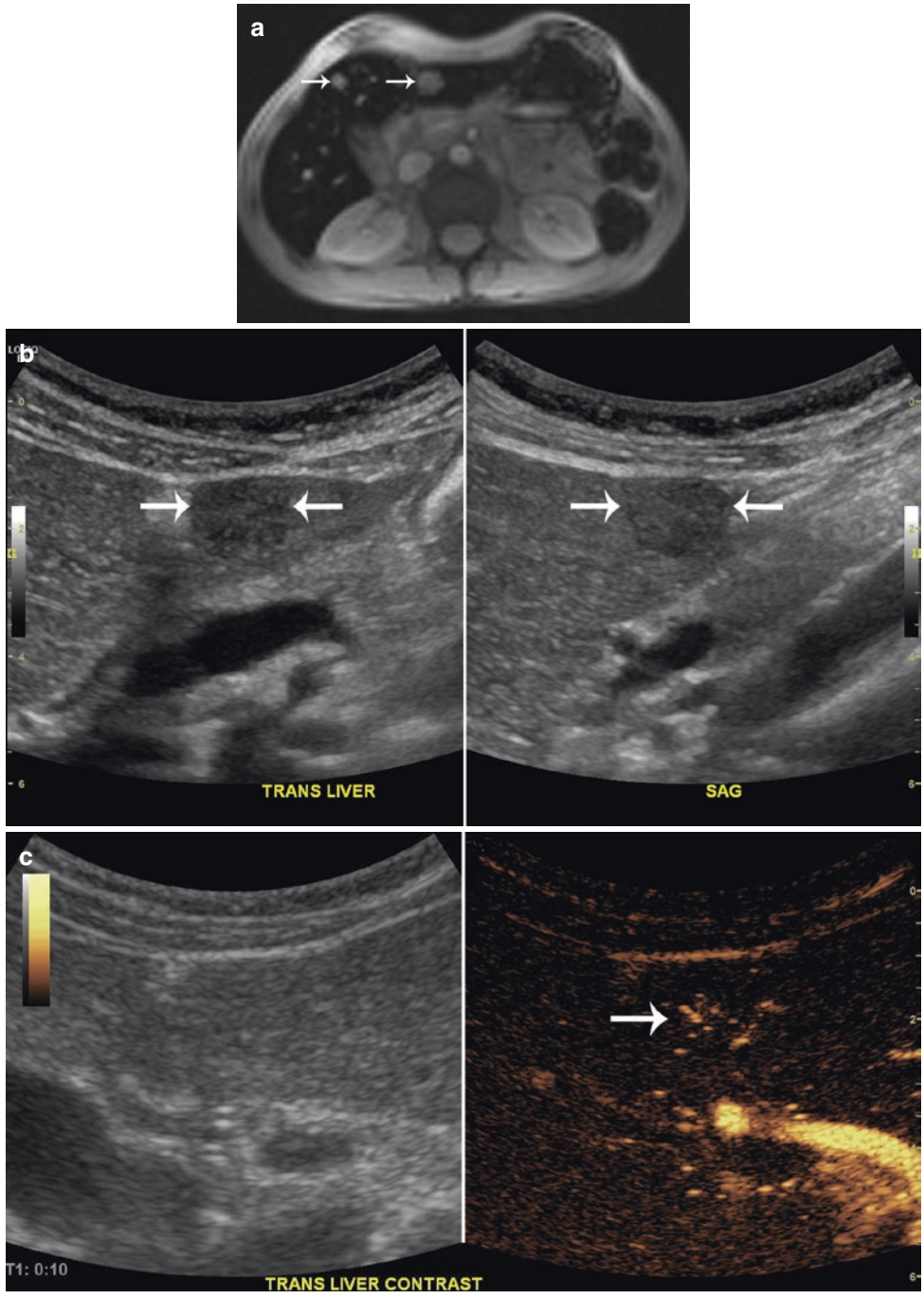

Fig. 12.15 Post-therapy focal nodular hyperplasia: A 27-year-old male treated during childhood for leukemia developed transfusional iron overload. Incidentally found to have focal liver lesions on an MRI performed for liver iron estimation (Courtesy, Dr. M. Beth McCarville). (**a**) Axial T2W gradient echo image demonstrates two focal liver lesions (arrows). (**b**) Grayscale transverse (left-hand side) and sagittal (right-hand side) ultrasound images show the lesion to be slightly hypoechoic. (**c**–**f**) Transverse contrast-enhanced ultrasound images of the larger lesion shown, obtained in (**c**) the early arterial phase, show feeding arteries within the focal liver lesion (arrows). (**d**) During the late arterial phase, there is centrifugal hyperenhancement of the lesion (arrows). (**e**) During the portal venous phase, there is continued hyperenhancement of the lesion (straight arrows). Note enhancement of the main portal vein (curved arrow). (**f**) During delayed phase imaging there is iso- to hyperenchancement of the lesion (arrows). There was no washout of the lesion on further delayed imaging. These features are consistent with focal nodular hyperplasia

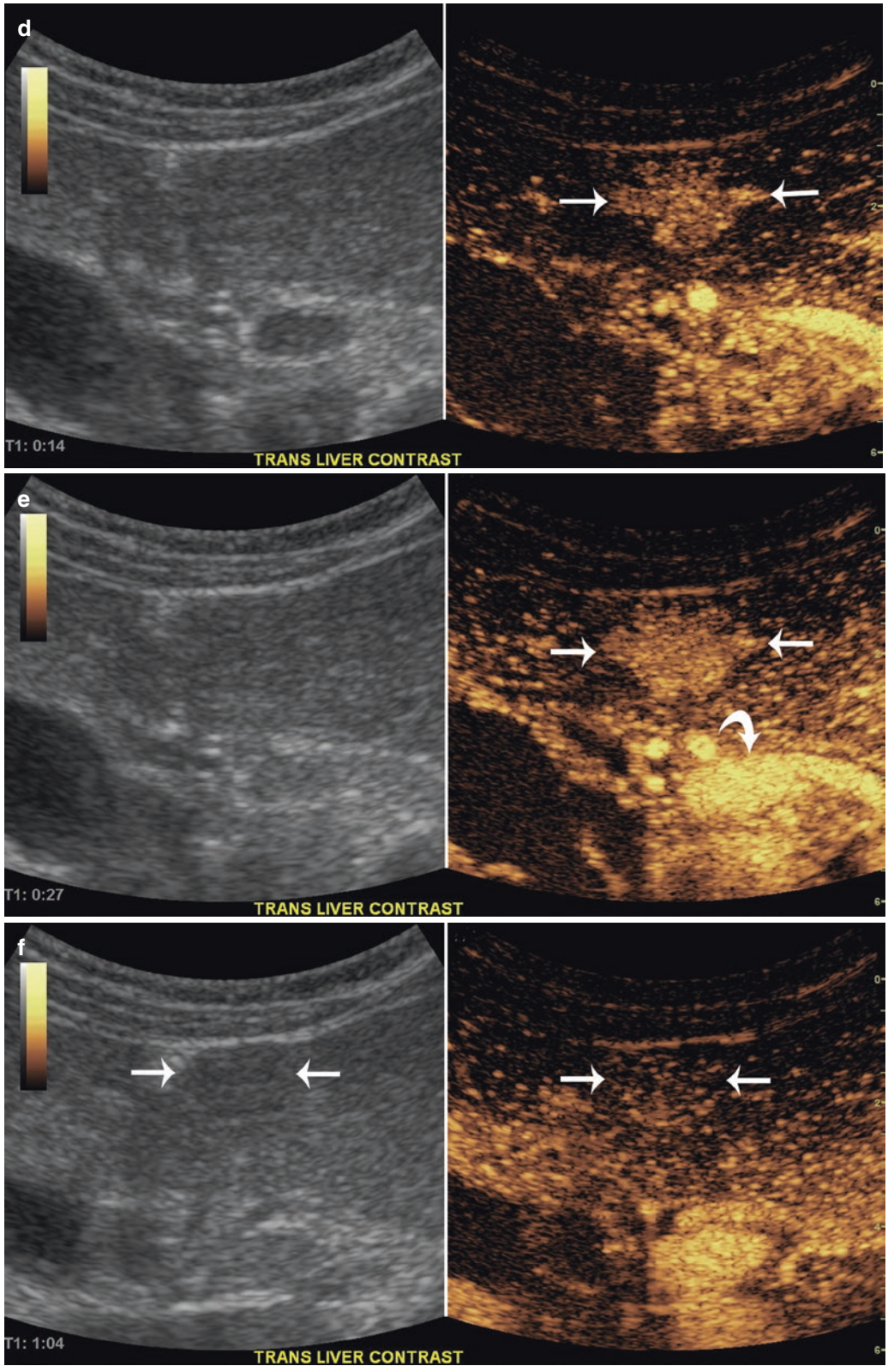

Fig. 12.15 (continued)

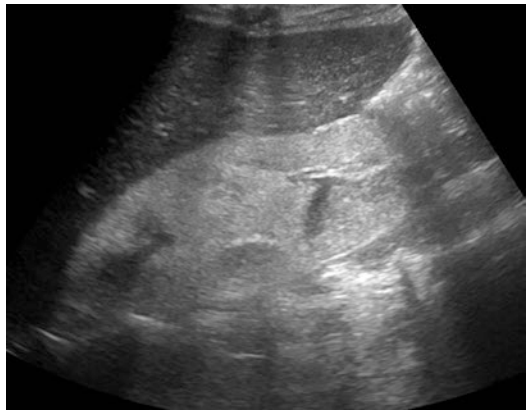

Fig. 12.16 Therapy-induced renal failure: Diagnosed at age 11 years with acute myelogenous leukemia, this teen was treated with multi-agent chemotherapy and allogeneic bone marrow transplantation. Her recovery was complicated by renal failure, ultimately requiring renal transplantation. Longitudinal ultrasound image of the right kidney shows marked homogeneous hyperechogenicity throughout the renal parenchyma

serves as a frontline modality for monitoring disease recurrence without patient exposure to ionizing radiation. MR urography can provide quantitative assessment of renal function [155] and is increasingly being used to evaluate renal function in cancer survivors.

Urinary bladder: Urinary bladder fibrosis exhibited as a contracted and poorly distended bladder on imaging is most often seen as a late effect of cancer therapy. It may also be accompanied by hydronephrosis [156]. Decreased bladder distensibility and bladder fibrosis are long-term complications of cancer therapy usually seen when a large portion of the bladder lies within a high-dose radiation field [106]. Bladder fibrosis is particularly seen as a late complication of cyclophosphamide therapy-induced interstitial fibrosis of the bladder wall [92]. Urinary bladder fibrosis, exhibited as a contracted and poorly distended bladder on ultrasound and cystogram, may also be accompanied by hydronephrosis [156].

Rectovesical and rectovaginal fistulae occasionally occur as complications of radiation-induced cystopathy, commonly seen with brachytherapy in adults [106, 156]. Enterocystic fistulae may also develop.

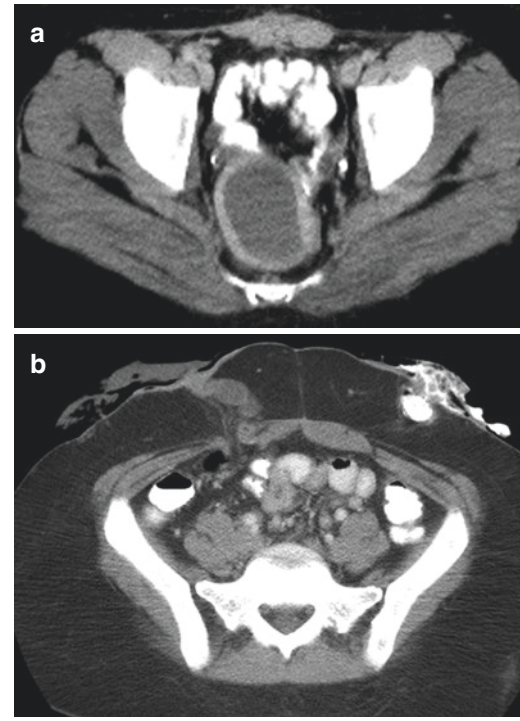

Fig. 12.17 Acquired vaginal occlusion: A 15-year-old girl diagnosed at age 2 years for vaginal alveolar rhabdomyosarcoma was treated with chemotherapy but subsequently required vaginal brachytherapy for local disease control. She complained of amenorrhea and abdominal pain. Due to repeated urinary tract infections, urinary incontinence, and multiple colovaginal and urovaginal fistulas, she ultimately underwent cystectomy, hysterectomy, bilateral salpingo-oophorectomy, colostomy, and ileal loop diversion. (**a**) Axial CT image through the pelvic after intravenous and oral contrast administration shows a well-defined low-density midline pelvic mass with enhancing thickened wall indicative of hematocolpos. (**b**) Axial CT image through the lower abdomen showing the presence of colostomy and ileal loop diversion

Other late complications of oncotherapy resulting from local tissue damage such as seen with acquired vaginal occlusion are induced by chemotherapy and/or radiation therapy [157, 158]. This entity may be unsuspected and can mimic local disease recurrence (Fig. 12.17).

Ultrasound examinations are especially valuable for assessing late effects on the kidneys and bladder but may be limited in assessing non-dilated urinary tracts and in patients

with large body habitus [155]. Both MR and CT urography have the potential to provide comprehensive assessment of renal parenchyma, urinary collecting system, as well as surrounding structures. MR urography on the other hand provides a method of disease detection without exposing the patient to ionizing radiation [159].

The role of these modalities is especially important in diagnosing urinary tract obstructions unrelated to urolithiasis such as radiotherapy-related ureteric strictures [155, 159], although as noted earlier these are relatively uncommon. Post contrast MR urography is effective in diagnosing focal scarring and diffuse renal parenchymal loss as a late effect of cancer therapy [155].

12.7 Endocrine Late Effects

In long-term survivors of pediatric malignancies, endocrine toxicities may result from local or central insults.

Thyroid: As irradiation of the thyroid gland is inevitable when treating children with head, neck, or mediastinal tumors, children are at risk for developing thyroid disorders such as hypothyroidism, hyperthyroidism, thyroid nodules, and thyroid malignancies [160]. Histologic features of long-term radiation on the thyroid gland include atrophy of thyroid stroma, degeneration of thyroid follicles, and obliteration of underlying vasculature [96].

In a comprehensive literature review of 4012 survivors who were treated for Hodgkin lymphoma during childhood, 40% of the study population were reported to have developed thyroid disorders [161]. Hypothyroidism is the most common condition seen in survivors who undergo radiotherapy [92]. Hancock et al. reported an actuarial risk of developing abnormalities of the thyroid gland of 52% at 20 years after radiation therapy that included the thyroid gland [162]. They also found an increased incidence of hypothyroidism in children who were treated at an older age with the greatest risk during the first 5 years of treatment. The risk for hypothyroidism was most closely related to an increasing relative risk accompanying increasing radiation dose [162]. In the presence of hypothyroidism, the thyroid gland is usually normal by ultrasound [92].

From the Childhood Cancer Survivor Study, Sklar et al. reported on 1791 survivors treated with irradiation that included the thyroid gland [160]. Of the study cohort, the most common abnormality found in 456 patients was hypothyroidism. However 146 patients developed thyroid nodules, of which 11 were malignant; 82 developed hyperthyroidism representing an eightfold greater incidence than in their siblings [160].

In comparison to the healthy population, there is significant risk of developing thyroid malignancies (Fig. 12.18) in cancer therapy survivors. Sklar et al. studied 1700 lymphoma survivors and reported 20 cases of thyroid carcinomas [160]. The overall incidence of thyroid cancers in cancer survivors who underwent neck radiotherapy ranges from 2% to 65% [160, 163]. According to the literature, the majority of cancers were well differentiated and predominantly papillary carcinomas with a latency period of 5–26 years from the time of therapy for childhood malignancy [160].

As clinical examination and thyroid function tests are insensitive, ultrasound serves as the primary imaging modality for detecting thyroid abnormalities and is particularly applicable as a sensitive, inexpensive, versatile modality that does not expose patients to ionizing radiation [96, 163, 164].

A variety of sonographic findings related to late effects from cancer therapy on the thyroid gland have been described and include solitary or multiple nodules (benign or malignant), diffuse thyroid atrophy, and cysts (simple or complex) [164]. The most common sonographic findings in long-term survivors are thyroid volume loss, atrophy, single or multiple echogenic or hypoechoic nodules, and cysts (Fig. 12.19). Soberman et al. studied 18 long-term survivors of Hodgkin disease of whom 16 patients were found to have a variety of findings on ultrasound [164]. Six patients exhibited diffuse atrophy of the thyroid gland, five patients demonstrated multiple nodules, solitary nodules were noted in four of them, and one patient had thyroid gland heterogeneity with calcifications [164].

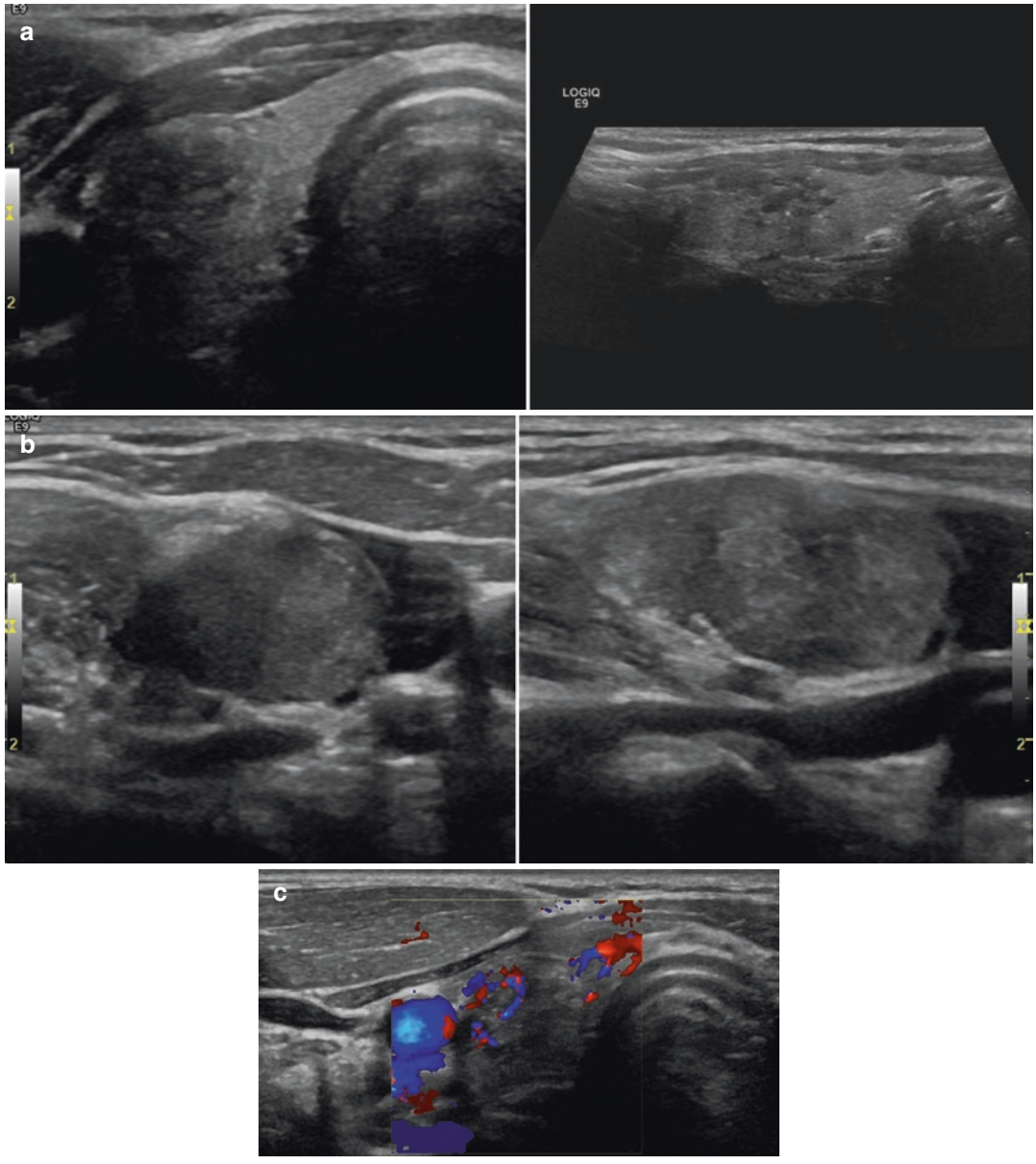

Fig. 12.18 Secondary thyroid cancer: A 17-year-old boy diagnosed and treated 6 years earlier for posterior fossa medulloblastoma. Treatment included gross total resection of the mass, chemotherapy, cranial-spinal irradiation, and autologous bone marrow transplantation. At the time of his first screening thyroid ultrasound, a right-sided mass was palpable. A total thyroidectomy and lymph node dissection was performed. Histologic evaluation revealed a 2 cm dominant nodule with many microscopic foci of papillary thyroid carcinoma distributed throughout both lobes, extracapsular extension and positive lymph nodes. Screening ultrasound shows a poorly marginated heterogeneous right thyroid lobe mass (**a**, transverse and longitudinal grayscale images) with punctate calcifications (**b**) and hypervascularity (**c**). Panel (**b**), obtained with higher resolution technique, shows to better advantage the heterogeneously solid mass with punctate calcifications. Transverse and longitudinal images of the left thyroid lobe showed tiny calcifications without discrete mass. Microscopic foci of carcinoma were found

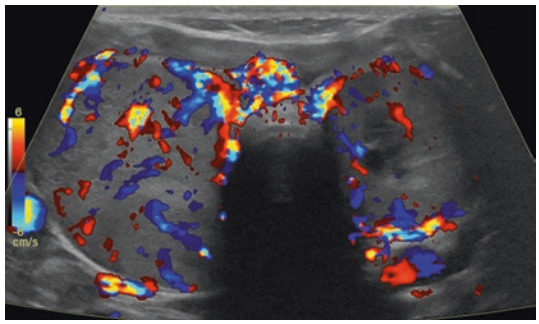

Fig. 12.19 Multinodular goiter: A 44-year-old woman treated at age 18 years for Hodgkin lymphoma with chemotherapy and 19.6 Gy mantle field irradiation. Notably, the patient subsequently also developed breast cancer

Malignant thyroid nodules can demonstrate microcalcifications, irregular outline, and heterogeneous echo texture [165] (Fig. 12.18). Though nodules vary widely in size and most nodules are benign, malignancy may still be found in small, millimetric lesions. Thus, routine periodic monitoring of patients at risk for radiation-induced thyroid malignancy is justified to assess for potential change in size or ultrasound appearance [165].

Gonads: Alkylating agents and pelvic radiotherapy affect the gonads severely with significant long-term gonadal dysfunction [92, 161]. Local effects may mimic or be compounded by central long-term effects of irradiation to the hypothalamic-pituitary axis and may manifest as growth hormone delayed or advanced skeletal age [41].

12.8 Second Malignant Neoplasms

Second malignant tumors represent a significant added health burden to survivors of childhood cancer and vary by primary disease, treatment exposures, and patient age at the time of therapy [166–169]. At 30-year follow-up from therapy for the first malignancy, the estimated cumulative incidence of developing any second malignancy was 20.5% (95% confidence interval = 19.1–21.8%) and, excluding non-melanoma skin cancer, was 7.9% (95% confidence interval = 7.2–8.5%). From the Childhood Cancer Survivor Study, the median time to development of any second malignancy was 17.8 years (range, 5.0–35.3 years). The investigators found a median time between diagnosis of the primary malignancy and secondary leukemia to be 8.9 years (range, 5.0–31.1 years). The longest time interval from primary to second malignancy was for development of secondary bowel malignancy with a median time to development of 23.1 years (range, 7.0–29.4 years) [167].

Primary malignancies associated with the highest risk for development of a second malignant neoplasm were Hodgkin lymphoma (standardized incidence ratio = 8.7, 95% confidence interval = 7.7–9.8) and Ewing sarcoma (standardized incidence ratio = 8.5, 95% confidence interval = 6.2–11.7) [167]. Patients who received combined radiation and chemotherapy are at greater risk for the development of secondary neoplasms than those treated with either radiation or chemotherapy alone [170]. Breast, thyroid, brain, and bone tumors are strongly associated with radiation therapy; a greater risk of developing second malignant tumors is associated with higher radiation dose and younger age at the time of therapy [92, 171].

Perhaps the best studied survivor cohort are those treated for Hodgkin lymphoma. Compared to the general population, these survivors have a 10% increased risk of any second malignancy at 20 years and 26% increased risk at 30 years of age. The most common solid second malignant neoplasm is breast cancer with a standardized risk ratio of 56.7 [170].

Metayer et al. studied 5925 pediatric patients treated for Hodgkin disease and found a total of 157 solid tumors and 26 acute leukemia [171]. The cumulative risk of developing solid tumors was 6.5%, persisting for 20 years after cancer therapy and increasing to almost 12% by 25 years. The most common solid tumors observed in survivors of radiation therapy were the thyroid, breast, connective tissue, stomach, and esophagus. Children treated before age 10 had a 50 times increased risk of tumors of the thyroid and respiratory tract. The second

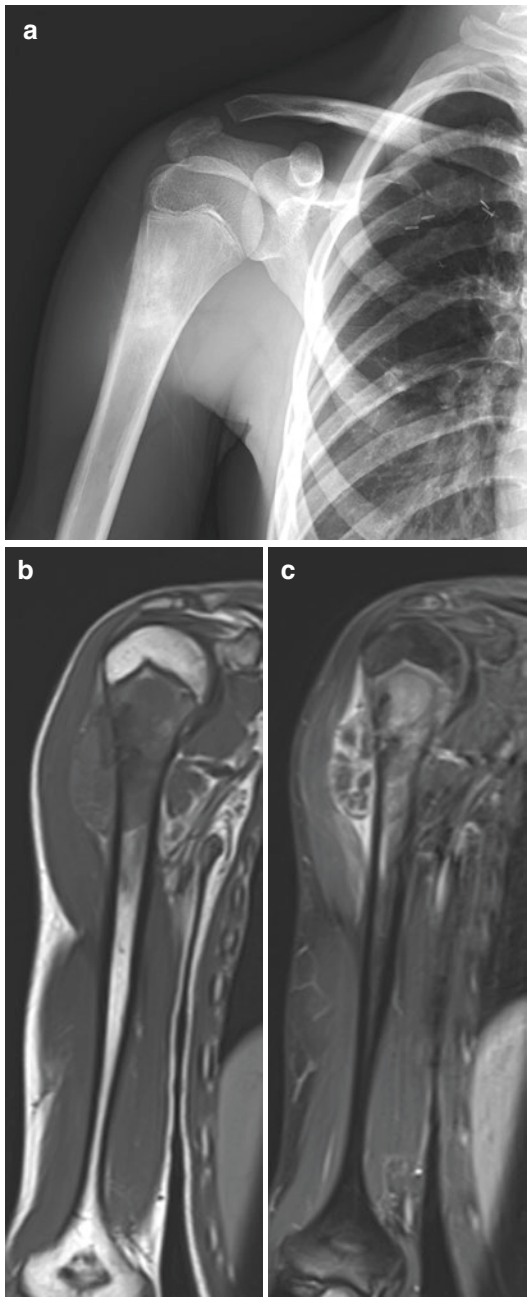

Fig. 12.20 Radiation-induced secondary malignancy: A 15-year-old complained of right shoulder pain. He had been treated at age 3 years for rhabdomyosarcoma of the right fifth posterior rib with chemotherapy, surgical resection, and radiation therapy. (**a**) Anteroposterior radiograph of the right shoulder showing aggressive periosteal reaction, Codman's triangles, and poorly defined sclerosis of the proximal right humeral neck. (**b**, **c**) Coronal non-contrast T1-weighted (**b**) and post-contrast T1-weighted with fat saturation (**c**) MR images better demonstrate the histologically proven osteosarcoma proximal humerus with extracortical extension and brisk heterogeneous enhancement. A skip lesion was identified on other images in the mid-diaphysis

greatest number of malignancies occurred in the digestive tract and breast in children older than 10 years at the time of exposure to radiotherapy [171].

Based upon the significantly elevated risk for developing breast cancer in young patients receiving radiation therapy that includes the chest and breast tissue, the Children's Oncology Group recommends MRI or mammography beginning at age 25 or 8 years after radiation therapy to the chest to screen for breast cancers [92, 172, 173]. Similarly, ultrasound screening coupled with clinical examination is recommended as screening for thyroid cancer as discussed above.

Secondary bone tumors [benign tumors, such as osteochondromas (Fig. 12.11), and malignant tumors, such as bone sarcomas (Fig. 12.20)] may develop and are strongly associated with prior radiation therapy [36, 169, 174–176]. The mean latency period to development of radiation-related bone tumors is 10 years. Myelodysplasia and acute myeloid leukemia are strongly associated with prior chemotherapy and develop within a shorter latency period from the primary malignancy than do solid tumors [169, 170].

12.9 Summary

Survivors of childhood cancers have a lifetime risk for developing late effects that may affect a variety of organ systems and compromise quality and length of life. Knowledge of adverse treatment effects, populations at risk, and time to expression of such effects helps guide follow-up care and proper diagnosis.

Acknowledgments The authors are grateful to Vella Laws-Bell for manuscript preparation and to Cynthia Lyle for critical review.

References

1. Robison LL, Hudson MM. Survivors of childhood and adolescent cancer: life-long risks and responsibilities. Nat Rev Cancer. 2014;14:61–70.
2. Mariotto AB, Rowland JH, Yabroff KR, Scoppa S, Hachey M, Ries L, Feuer EJ. Long-term survivors

of childhood cancers in the United States. Cancer Epidemiol Biomarkers Prev. 2009;18:1033–40.
3. Armstrong GT, Plana JC, Zhang N, Srivastava D, Green DM, Ness KK, Daniel Donovan F, Metzger ML, Arevalo A, Durand JB, Joshi V, Hudson MM, Robison LL, Flamm SD. Screening adult survivors of childhood cancer for cardiomyopathy: comparison of echocardiography and cardiac magnetic resonance imaging. J Clin Oncol. 2012;30:2876–84.
4. Oeffinger KC, Mertens AC, Sklar CA, Kawashima T, Hudson MM, Meadows AT, Friedman DL, Marina N, Hobbie W, Kadan-Lottick NS, Schwartz CL, Leisenring W, Robison LL, Childhood Cancer Survivor S. Chronic health conditions in adult survivors of childhood cancer. N Engl J Med. 2006;355:1572–82.
5. U.S. Department of Health and Human Services. Common Terminology Criteria for Adverse Events (CTCAE) Version 5.0. Published: Nov 27, 2017. https://ctep.cancer.gov/protocoldevelopment/electronic_applications/docs/CTCAE_v5_Quick_Reference_5x7.pdf.
6. Bakta N, Liu Q, NEss KK, Baassiri M, Eissa H, Yeo F, Chematilly W, Ehrhardt MJ, Bass J, Bishop MW, Shelton K, Lu L, Huang S, Li Z, et al. The cumulative burden of surviving childhood cancer: an initial report from the St. Jude Lifetime Cohort Study (SJLIFE). Lancet 2017; 390(10112):2569–2582. https://doi.org/10.1016/SO140-6736(17)31610-0. Epub 2017 Sep 8. PMID:28890157.
7. Lind MJ. Principles of cytotoxic chemotherapy. Medicine. 2008;36:19–23.
8. Yarnold J, Brotons MC. Pathogenetic mechanisms in radiation fibrosis. Radiother Oncol. 2010;97:149–61.
9. Hojan K, Milecki P. Opportunities for rehabilitation of patients with radiation fibrosis syndrome. Rep Pract Oncol Radiother. 2014;19:1–6.
10. Tsoutsou PG, Koukourakis MI. Radiation pneumonitis and fibrosis: mechanisms underlying its pathogenesis and implications for future research. Int J Radiat Oncol Biol Phys. 2006;66:1281–93.
11. Rajan Radha R, Chandrasekharan G. Pulmonary injury associated with radiation therapy - assessment, complications and therapeutic targets. Biomed Pharmacother. 2017;89:1092–104.
12. Gawade PL, Hudson MM, Kaste SC, Neglia JP, Constine LS, Robison LL, Ness KK. A systematic review of dental late effects in survivors of childhood cancer. Pediatr Blood Cancer. 2014;61:407–16.
13. COG. Long-term follow-up guidelines for survivors of childhood, adolescent, and young adult cancers, v.4.0. http://www.survivorshipguidelines.org [Online]. Children's Oncology Group. 2014. Available: http://www.survivorshipguidelines.org/pdf/LTFUGuidelines_40. Accessed 24 Aug 2017.
14. Carroll WL, Raetz E, Meyer J. State of the art discovery with tumor profiling in pediatric oncology. Am Soc Clin Oncol Educ Book. 2015:e601–7.
15. Glade Bender J, Verma A, Schiffman JD. Translating genomic discoveries to the clinic in pediatric oncology. Curr Opin Pediatr. 2015;27:34–43.
16. Biermann M, Schwarzlmuller T, Fasmer KE, Reitan BC, Johnsen B, Rosendahl K. Is there a role for PET-CT and Spect-CT in pediatric oncology? Acta Radiol. 2013;54:1037–45.
17. Sonis AL, Tarbell N, Valachovic RW, Gelber R, Schwenn M, Sallan S. Dentofacial development in long-term survivors of acute lymphoblastic leukemia. A comparison of three treatment modalities. Cancer. 1990;66:2645–52.
18. Gevorgyan A, La Scala GC, Neligan PC, Pang CY, Forrest CR. Radiation-induced craniofacial bone growth disturbances. J Craniofac Surg. 2007;18:1001–7.
19. Jegoux F, Malard O, Goyenvalle E, Aguado E, Daculsi G. Radiation effects on bone healing and reconstruction: interpretation of the literature. Oral Surg Oral Med Oral Pathol Oral Radiol Endod. 2010;109:173–84.
20. Vesterbacka M, Ringden O, Remberger M, Huggare J, Dahllof G. Disturbances in dental development and craniofacial growth in children treated with hematopoietic stem cell transplantation. Orthod Craniofac Res. 2012;15:21–9.
21. Paulino AC, Simon JH, Zhen W, Wen BC. Long-term effects in children treated with radiotherapy for head and neck rhabdomyosarcoma. Int J Radiat Oncol Biol Phys. 2000;48:1489–95.
22. Denys D, Kaste SC, Kun LE, Chaudhary MA, Bowman LC, Robbins KT. The effects of radiation on craniofacial skeletal growth: a quantitative study. Int J Pediatr Otorhinolaryngol. 1998;45:7–13.
23. Ash MM, Nelson SJ. Wheeler's dental anatomy, physiology and occlusion. St. Louis, MO: W.B. Saunders Company; 2002.
24. Nwoku AL, Koch H. Effect of radiation injury on the growing face. J Maxillofac Surg. 1975;3:28–34.
25. Jaffe N, Toth BB, Hoar RE, Ried HL, Sullivan MP, McNeese MD. Dental and maxillofacial abnormalities in long-term survivors of childhood cancer: effects of treatment with chemotherapy and radiation to the head and neck. Pediatrics. 1984;73:816–23.
26. Kaste SC, Goodman P, Leisenring W, Stovall M, Hayashi RJ, Yeazel M, Beiraghi S, Hudson MM, Sklar CA, Robison LL, Baker KS. Impact of radiation and chemotherapy on risk of dental abnormalities: a report from the Childhood Cancer Survivor Study. Cancer. 2009;115:5817–27.
27. Zarina RS, Nik-Hussein NN. Dental abnormalities of a long-term survivor of a childhood hematological malignancy: literature review and report of a case. J Clin Pediatr Dent. 2005;29:167–74.
28. Dahllof G, Jonsson A, Ulmner M, Huggare J. Orthodontic treatment in long-term survivors after pediatric bone marrow transplantation. Am J Orthod Dentofacial Orthop. 2001;120:459–65.
29. Neill CC, Migliorati C, Trojan T, Kaste S, Karydis A, Rowland C, Parris W. Experience and expertise regarding orthodontic management of childhood and adolescent cancer survivors. Am J Orthod Dentofacial Orthop. 2015;148:765–70.
30. Kaste SC, Hopkins KP, Jenkins JJ 3rd. Abnormal odontogenesis in children treated with radiation

and chemotherapy: imaging findings. AJR Am J Roentgenol. 1994;162:1407–11.
31. Dahllof G, Barr M, Bolme P, Modeer T, Lonnqvist B, Ringden O, Heimdahl A. Disturbances in dental development after total body irradiation in bone marrow transplant recipients. Oral Surg Oral Med Oral Pathol. 1988;65:41–4.
32. Martin MB, Li CS, Rowland CC, Howard SC, Kaste SC. Correlation of bone age, dental age, and chronological age in survivors of childhood acute lymphoblastic leukaemia. Int J Paediatr Dent. 2008;18:217–23.
33. Vaughan MD, Rowland CC, Tong X, Srivastava DK, Hale GA, Rochester R, Kaste SC. Dental abnormalities after pediatric bone marrow transplantation. Bone Marrow Transplant. 2005;36:725–9.
34. Tanaka M, Kamata T, Yanagisawa R, Morita D, Saito S, Sakashita K, Shiohara M, Kurita H, Koike K, Nakazawa Y. Increasing risk of disturbed root development in permanent teeth in childhood cancer survivors undergoing cancer treatment at older age. J Pediatr Hematol Oncol. 2017;39:e150–4.
35. Vaughan MD, Rowland CC, Tong X, Srivastava DK, Hale GA, Rochester R, Kaste SC. Dental abnormalities in children preparing for pediatric bone marrow transplantation. Bone Marrow Transplant. 2005;36:863–6.
36. Hudson MM, Oeffinger K. Future health of survivors of adolescent and young adult cancer. In: Schwartz CL, Hobbie W, Constine LS, Ruccione KS, editors. Survivors of childhood and adolescent cancer; a multidisciplinary approach. 2nd ed. New York, NY: Springer; 2005.
37. Gawade PL, Hudson MM, Kaste SC, Neglia JP, Wasilewski-Masker K, Constine LS, Robison LL, Ness KK. A systematic review of selected musculoskeletal late effects in survivors of childhood cancer. Curr Pediatr Rev. 2014;10:249–62.
38. McVay CS, Klei TR, Coleman SU, Bosshardt SC. A comparison of host responses of the Mongolian jird to infections of Brugia malayi and B. pahangi. Am J Trop Med Hyg. 1990;43:266–73.
39. Zhang J, Wang Z, Wu A, Nie J, Pei H, Hu W, Wang B, Shang P, Li B, Zhou G. Differences in responses to X-ray exposure between osteoclast and osteoblast cells. J Radiat Res. 2017;58:791–802.
40. Mackenzie JR. Complications of treatment of paediatric malignancies. Eur J Radiol. 2001;37:109–19.
41. Shalet SM, Crowne EC, Didi MA, Ogilvy-Stuart AL, Wallace WH. Irradiation-induced growth failure. Baillieres Clin Endocrinol Metab. 1992;6:513–26.
42. Shalet SM, Gibson B, Swindell R, Pearson D. Effect of spinal irradiation on growth. Arch Dis Child. 1987;62:461–4.
43. Clayton PE, Shalet SM. The evolution of spinal growth after irradiation. Clin Oncol (R Coll Radiol). 1991;3:220–2.
44. Parisi MT, Fahmy JL, Kaminsky CK, Malogolowkin MH. Complications of cancer therapy in children: a radiologist's guide. Radiographics. 1999;19:283–97.
45. Siebler T, Shalet SM, Robson H. Effects of chemotherapy on bone metabolism and skeletal growth. Horm Res. 2002;58(Suppl 1):80–5.
46. D'Oronzo S, Stucci S, Tucci M, Silvestris F. Cancer treatment-induced bone loss (CTIBL): pathogenesis and clinical implications. Cancer Treat Rev. 2015;41:798–808.
47. Wasilewski-Masker K, Kaste SC, Hudson MM, Esiashvili N, Mattano LA, Meacham LR. Bone mineral density deficits in survivors of childhood cancer: long-term follow-up guidelines and review of the literature. Pediatrics. 2008;121:e705–13.
48. Mori G, D'Amelio P, Faccio R, Brunetti G. Bone-immune cell crosstalk: bone diseases. J Immunol Res. 2015;2015:108451.
49. Pfeilschifter J, Diel IJ. Osteoporosis due to cancer treatment: pathogenesis and management. J Clin Oncol. 2000;18:1570–93.
50. Rana T, Chakrabarti A, Freeman M, Biswas S. Doxorubicin-mediated bone loss in breast cancer bone metastases is driven by an interplay between oxidative stress and induction of TGFbeta. PLoS One. 2013;8:e78043.
51. Mandel K, Atkinson S, Barr RD, Pencharz P. Skeletal morbidity in childhood acute lymphoblastic leukemia. J Clin Oncol. 2004;22:1215–21.
52. Den Hoed MA, Klap BC, Te Winkel ML, Pieters R, Van Waas M, Neggers SJ, Boot AM, Blijdorp K, Van Dorp W, Pluijm SM, Van Den Heuvel-Eibrink MM. Bone mineral density after childhood cancer in 346 long-term adult survivors of childhood cancer. Osteoporos Int. 2015;26:521–9.
53. Siegel DA, Claridy M, Mertens A, George E, Vangile K, Simoneaux SF, Meacham LR, Wasilewski-Masker K. Risk factors and surveillance for reduced bone mineral density in pediatric cancer survivors. Pediatr Blood Cancer. 2017;64(9)
54. Porosnicu M, Nimmanapalli R, Nguyen D, Worthington E, Perkins C, Bhalla KN. Co-treatment with As2O3 enhances selective cytotoxic effects of STI-571 against Brc-Abl-positive acute leukemia cells. Leukemia. 2001;15:772–8.
55. Gurney JG, Kaste SC, Liu W, Srivastava DK, Chemaitilly W, Ness KK, Lanctot JQ, Ojha RP, Nottage KA, Wilson CL, Li Z, Robison LL, Hudson MM. Bone mineral density among long-term survivors of childhood acute lymphoblastic leukemia: results from the St. Jude Lifetime Cohort Study. Pediatr Blood Cancer. 2014;61:1270–6.
56. Ippolito D, Masetto A, Franzesi CT, Bonaffini PA, Sala A, Biondi A, Sironi S. Lower-limb MRI in the staging and re-staging of osteonecrosis in paediatric patients affected by acute lymphoblastic leukaemia after therapy. Skeletal Radiol. 2016;45:495–503.
57. Sharma S, Leung WH, Deqing P, Yang J, Rochester R, Britton L, Neel MD, Ness KK, Kaste SC. Osteonecrosis in children after allogeneic hematopoietic cell transplantation: study of prevalence, risk factors and longitudinal changes using MR imaging. Bone Marrow Transplant. 2012;47:1067–74.

58. Sharma S, Yang S, Rochester R, Britton L, Leung WH, Yang J, Neel MD, Ness KK, Kaste SC. Prevalence of osteonecrosis and associated risk factors in children before allogeneic BMT. Bone Marrow Transplant. 2011;46:813–9.
59. Kadan-Lottick NS, Dinu I, Wasilewski-Masker K, Kaste S, Meacham LR, Mahajan A, Stovall M, Yasui Y, Robison LL, Sklar CA. Osteonecrosis in adult survivors of childhood cancer: a report from the childhood cancer survivor study. J Clin Oncol. 2008;26:3038–45.
60. Kunstreich M, Kummer S, Laws HJ, Borkhardt A, Kuhlen M. Osteonecrosis in children with acute lymphoblastic leukemia. Haematologica. 2016;101:1295–305.
61. Kaste SC, Karimova EJ, Neel MD. Osteonecrosis in children after therapy for malignancy. AJR Am J Roentgenol. 2011;196:1011–8.
62. Fan C, Foster BK, Wallace WH, Xian CJ. Pathobiology and prevention of cancer chemotherapy-induced bone growth arrest, bone loss, and osteonecrosis. Curr Mol Med. 2011;11:140–51.
63. Diller L. Clinical practice. Adult primary care after childhood acute lymphoblastic leukemia. N Engl J Med. 2011;365:1417–24.
64. Kaste SC, Pei D, Cheng C, Neel MD, Bowman WP, Ribeiro RC, Metzger ML, Bhojwani D, Inaba H, Campbell P, Rubnitz JE, Jeha S, Sandlund JT, Downing JR, Relling MV, Pui CH, Howard SC. Utility of early screening magnetic resonance imaging for extensive hip osteonecrosis in pediatric patients treated with glucocorticoids. J Clin Oncol. 2015;33:610–5.
65. Girard P, Auquier P, Barlogis V, Contet A, Poiree M, Demeocq F, Berbis J, Herrmann I, Villes V, Sirvent N, Kanold J, Chastagner P, Chambost H, Plantaz D, Michel G. Symptomatic osteonecrosis in childhood leukemia survivors: prevalence, risk factors and impact on quality of life in adulthood. Haematologica. 2013;98:1089–97.
66. Relling MV, Yang W, Das S, Cook EH, Rosner GL, Neel M, Howard S, Ribeiro R, Sandlund JT, Pui CH, Kaste SC. Pharmacogenetic risk factors for osteonecrosis of the hip among children with leukemia. J Clin Oncol. 2004;22:3930–6.
67. Burger B, Beier R, Zimmermann M, Beck JD, Reiter A, Schrappe M. Osteonecrosis: a treatment related toxicity in childhood acute lymphoblastic leukemia (ALL)--experiences from trial ALL-BFM 95. Pediatr Blood Cancer. 2005;44:220–5.
68. Karimova EJ, Kaste SC. MR imaging of osteonecrosis of the knee in children with acute lymphocytic leukemia. Pediatr Radiol. 2007;37:1140–6.
69. Karimova EJ, Rai SN, Howard SC, Neel M, Britton L, Pui CH, Kaste SC. Femoral head osteonecrosis in pediatric and young adult patients with leukemia or lymphoma. J Clin Oncol. 2007;25:1525–31.
70. Kaste SC, Defeo BM, Neel MD, Weiss KS, Fernandez-Pineda I, Ness KK. Osteonecrosis of the shoulders in pediatric patients treated for leukemia or lymphoma: single-institutional experience. J Pediatr Orthop. 2017;
71. Chollet CT, Britton L, Neel MD, Hudson MM, Kaste SC. Childhood cancer survivors: an at-risk cohort for ankle osteonecrosis. Clin Orthop Relat Res. 2005;(430):149–55.
72. Karimova EJ, Rai SN, Ingle D, Ralph AC, Deng X, Neel MD, Howard SC, Pui CH, Kaste SC. MRI of knee osteonecrosis in children with leukemia and lymphoma: Part 2, clinical and imaging patterns. AJR Am J Roentgenol. 2006;186:477–82.
73. Te Winkel ML, Pieters R, Wind EJ, Bessems JH, Van Den Heuvel-Eibrink MM. Management and treatment of osteonecrosis in children and adolescents with acute lymphoblastic leukemia. Haematologica. 2014;99:430–6.
74. Interiano RB, Kaste SC, Li C, Srivastava DK, Rao BN, Warner WC Jr, Green DM, Krasin MJ, Robison LL, Davidoff AM, Hudson MM, Fernandez-Pineda I, Ness KK. Associations between treatment, scoliosis, pulmonary function, and physical performance in long-term survivors of sarcoma. J Cancer Surviv. 2017;11:553.
75. Lucas JT Jr, Fernandez-Pineda I, Tinkle CL, Bishop MW, Kaste SC, Heda R, Davidoff AM, Krasin MJ. Late toxicity and outcomes following radiation therapy for chest wall sarcomas in pediatric patients. Pract Radiat Oncol. 2017;7:411.
76. Fidler MM, Reulen RC, Henson K, Kelly J, Cutter D, Levitt GA, Frobisher C, Winter DL, Hawkins MM, British Childhood Cancer Survivor Study Steering, G. Population-based long-term cardiac-specific mortality among 34 489 five-year survivors of childhood cancer in Great Britain. Circulation. 2017;135:951–63.
77. Mulrooney DA, Armstrong GT, Huang S, Ness KK, Ehrhardt MJ, Joshi VM, Plana JC, Soliman EZ, Green DM, Srivastava D, Santucci A, Krasin MJ, Robison LL, Hudson MM. Cardiac outcomes in adult survivors of childhood cancer exposed to cardiotoxic therapy: a cross-sectional study. Ann Intern Med. 2016;164:93–101.
78. Lipshultz SE, Adams MJ, Colan SD, Constine LS, Herman EH, Hsu DT, Hudson MM, Kremer LC, Landy DC, Miller TL, Oeffinger KC, Rosenthal DN, Sable CA, Sallan SE, Singh GK, Steinberger J, Cochran TR, Wilkinson JD, American Heart Association Congenital Heart Defects Committee of The Council on Cardiovascular Disease in the Young, C. O. B. C. S. C. O. C. & Stroke Nursing, C. O. C. R. Long-term cardiovascular toxicity in children, adolescents, and young adults who receive cancer therapy: pathophysiology, course, monitoring, management, prevention, and research directions: a scientific statement from the American Heart Association. Circulation. 2013;128:1927–95.
79. Lipshultz SE, Cochran TR, Franco VI, Miller TL. Treatment-related cardiotoxicity in survivors of childhood cancer. Nat Rev Clin Oncol. 2013;10:697–710.
80. Spichev VP. A comprehensive assessment of the medical and prophylactic support for the troops of

a military district and the ways to enhance its efficiency. Voen Med Zh. 1990; 34–7.
81. Kremer LC, Van Dalen EC, Offringa M, Ottenkamp J, Voute PA. Anthracycline-induced clinical heart failure in a cohort of 607 children: long-term follow-up study. J Clin Oncol. 2001;19:191–6.
82. Maeda M. Late effects of childhood cancer: life-threatening issues. J Nippon Med Sch. 2008;75:320–4.
83. Armenian SH, Hudson MM, Mulder RL, Chen MH, Constine LS, Dwyer M, Nathan PC, Tissing WJ, Shankar S, Sieswerda E, Skinner R, Steinberger J, Van Dalen EC, Van Der Pal H, Wallace WH, Levitt G, Kremer LC, International Late Effects of Childhood Cancer Guideline Harmonization, G. Recommendations for cardiomyopathy surveillance for survivors of childhood cancer: a report from the International Late Effects of Childhood Cancer Guideline Harmonization Group. Lancet Oncol. 2015;16:e123–36.
84. Armstrong GT, Stovall M, Robison LL. Long-term effects of radiation exposure among adult survivors of childhood cancer: results from the childhood cancer survivor study. Radiat Res. 2010;174:840–50.
85. Kupeli S, Hazirolan T, Varan A, Akata D, Alehan D, Hayran M, Besim A, Buyukpamukcu M. Evaluation of coronary artery disease by computed tomography angiography in patients treated for childhood Hodgkin's lymphoma. J Clin Oncol. 2010;28:1025–30.
86. Liles A, Blatt J, Morris D, Wardrop R III, Sharma A, Sznewajs A, Goldsby R, Children's Oncology G. Monitoring pulmonary complications in long-term childhood cancer survivors: guidelines for the primary care physician. Cleve Clin J Med. 2008;75:531–9.
87. Mertens AC, Yasui Y, Liu Y, Stovall M, Hutchinson R, Ginsberg J, Sklar C, Robison LL, Childhood Cancer Survivor S. Pulmonary complications in survivors of childhood and adolescent cancer. A report from the Childhood Cancer Survivor Study. Cancer. 2002;95:2431–41.
88. Friedman DL, Constine LS. Late effects of cancer treatment. In: Halperin EC, Constine LS, Tarbell NJ, Kun LE, editors. Pediatric radiation oncology. 5th ed. Philadelphia, PA: Wolters Kluwer Health/Lippincott Williams & Wilkins; 2011.
89. Rubin P, Casarett GW. Clinical radiation pathology. Philadelphia, PA: W.B. Saunders; 1968.
90. Cardous-Ubbink MC, Heinen RC, Langeveld NE, Bakker PJ, Voute PA, Caron HN, Van Leeuwen FE. Long-term cause-specific mortality among five-year survivors of childhood cancer. Pediatr Blood Cancer. 2004;42:563–73.
91. Bhatia S, Sklar C. Second cancers in survivors of childhood cancer. Nat Rev Cancer. 2002;2:124–32.
92. Taylor GI, Doyle M, McCarten G. The Doppler probe for planning flaps: anatomical study and clinical applications. Br J Plast Surg. 1990;43:1–16.
93. Shelmerdine SC, Chavhan GB, Babyn PS, Nathan PC, Kaste SC. Imaging of late complications of cancer therapy in children. Pediatr Radiol. 2017;47:254–66.
94. Asdahl PH, Winther JF, Bonnesen TG, De Fine Licht S, Gudmundsdottir T, Holmqvist AS, Malila N, Tryggvadottir L, Wesenberg F, Dahlerup JF, Olsen JH, Hasle H, Group, A. L. S. Gastrointestinal and liver disease in adult life after childhood cancer in Scandinavia: a population-based cohort study. Int J Cancer. 2016;139:1501–11.
95. Goldsby R, Chen Y, Raber S, Li L, Diefenbach K, Shnorhavorian M, Kadan-Lottick N, Kastrinos F, Yasui Y, Stovall M, Oeffinger K, Sklar C, Armstrong GT, Robison LL, Diller L. Survivors of childhood cancer have increased risk of gastrointestinal complications later in life. Gastroenterology. 2011;140:1464–71.e1.
96. Macnaughton WK. Review article: new insights into the pathogenesis of radiation-induced intestinal dysfunction. Aliment Pharmacol Ther. 2000;14:523–8.
97. Friedman DL, Constine LS. Late effects of cancer treatment. In: Halperin EC, Constine LS, Tarbell NJ, Kun LE, editors. Pediatric radiation oncology. Philadelphia, PA: Lippincott Williams & Wilkins; 2005.
98. Touchefeu Y, Montassier E, Nieman K, Gastinne T, Potel G, Bruley Des Varannes S, Le Vacon F, De La Cochetiere MF. Systematic review: the role of the gut microbiota in chemotherapy- or radiation-induced gastrointestinal mucositis - current evidence and potential clinical applications. Aliment Pharmacol Ther. 2014;40:409–21.
99. Sher ME, Bauer J. Radiation-induced enteropathy. Am J Gastroenterol. 1990;85:121–8.
100. Theis VS, Sripadam R, Ramani V, Lal S. Chronic radiation enteritis. Clin Oncol (R Coll Radiol). 2010;22:70–83.
101. Harb AH, Abou Fadel C, Sharara AI. Radiation enteritis. Curr Gastroenterol Rep. 2014;16:383.
102. Kennedy GD, Heise CP. Radiation colitis and proctitis. Clin Colon Rectal Surg. 2007;20:64–72.
103. Griffiths JB, Cameron DR, Looby D. A comparison of unit process systems for anchorage dependent cells. Dev Biol Stand. 1987;66:331–8.
104. Decosse JJ, Rhodes RS, Wentz WB, Reagan JW, Dworken HJ, Holden WD. The natural history and management of radiation induced injury of the gastrointestinal tract. Ann Surg. 1969;170:369–84.
105. Libotte F, Autier P, Delmelle M, Gozy M, Pector JC, Van Houtte P, Gerard A. Survival of patients with radiation enteritis of the small and the large intestine. Acta Chir Belg. 1995;95:190–4.
106. Kountouras J, Zavos C. Recent advances in the management of radiation colitis. World J Gastroenterol. 2008;14:7289–301.
107. Maturen KE, Feng MU, Wasnik AP, Azar SF, Appelman HD, Francis IR, Platt JF. Imaging effects of radiation therapy in the abdomen and pelvis: evaluating "innocent bystander" tissues. Radiographics. 2013;33:599–619.

108. Lal DR, Foroutan HR, Su WT, Wolden SL, Boulad F, La Quaglia MP. The management of treatment-related esophageal complications in children and adolescents with cancer. J Pediatr Surg. 2006;41:495–9.
109. Donaldson SS, Jundt S, Ricour C, Sarrazin D, Lemerle J, Schweisguth O. Radiation enteritis in children. A retrospective review, clinicopathologic correlation, and dietary management. Cancer. 1975;35:1167–78.
110. Madenci AL, Fisher S, Diller LR, Goldsby RE, Leisenring WM, Oeffinger KC, Robison LL, Sklar CA, Stovall M, Weathers RE, Armstrong GT, Yasui Y, Weldon CB. Intestinal obstruction in survivors of childhood cancer: a report from the childhood cancer survivor study. J Clin Oncol. 2015;33:2893–900.
111. Algin O, Turkbey B, Ozmen E, Algin E. Magnetic resonance enterography findings of chronic radiation enteritis. Cancer Imaging. 2011;11:189–94.
112. Khoury NJ, Kanj V, Abboud M, Muwakkit S, Birjawi GA, Haddad MC. Abdominal complications of chemotherapy in pediatric malignancies: imaging findings. Clin Imaging. 2009;33:253–60.
113. Horton KM, Corl FM, Fishman EK. CT evaluation of the colon: inflammatory disease. Radiographics. 2000;20:399–418.
114. Haddad MC, Khouzami RA, Saad HA, Azzi MC. Imaging findings of radiation enteritis. J Med Liban. 2004;52:55–7.
115. Den Hartog Jager FC, Cohen P, Van Haastert M. Late radiation injury of the rectum and sigmoid colon: barium enema findings in 92 patients. Br J Radiol. 1989;62:807–12.
116. Cronin CG, Lohan DG, Browne AM, Roche C, O'Keeffe D, Murphy JM. MR small-bowel follow-through for investigation of suspected pediatric small-bowel pathology. AJR Am J Roentgenol. 2009;192:1239–45.
117. Castellino S, Muir A, Shah A, Shope S, McMullen K, Ruble K, Barber A, Davidoff A, Hudson MM. Hepato-biliary late effects in survivors of childhood and adolescent cancer: a report from the Children's Oncology Group. Pediatr Blood Cancer. 2010;54:663–9.
118. Ingold JA, Reed GB, Kaplan HS, Bagshaw MA. Radiation Hepatitis. Am J Roentgenol Radium Ther Nucl Med. 1965;93:200–8.
119. Fellows KEJ, Vawter GF, Tefft M. Hepatic effects following abdominal irradiation in children: detection by Au198 scan and confirmation by histologic examination. Am J Roentgenol Radium Ther Nucl Med. 1968;103:422–31.
120. Tefft M, Mitus A, Das L, Vawter GF, Filler RM. Irradiation of the liver in children: review of experience in the acute and chronic phases, and in the intact normal and partially resected. Am J Roentgenol Radium Ther Nucl Med. 1970;108:365–85.
121. Kun LE, Camitta BM. Hepatopathy following irradiation and adriamycin. Cancer. 1978;42:81–4.
122. Masetti R, Colecchia A, Rondelli R, Martoni A, Vendemini F, Biagi C, Prete A, Festi D, Lima M, Pession A. Benign hepatic nodular lesions after treatment for childhood cancer. J Pediatr Gastroenterol Nutr. 2013;56:151–5.
123. Bouyn CI, Leclere J, Raimondo G, Le Pointe HD, Couanet D, Valteau-Couanet D, Hartmann O. Hepatic focal nodular hyperplasia in children previously treated for a solid tumor. Incidence, risk factors, and outcome. Cancer. 2003;97:3107–13.
124. Chavhan GB, Mann E, Kamath BM, Babyn PS. Gadobenate-dimeglumine-enhanced magnetic resonance imaging for hepatic lesions in children. Pediatr Radiol. 2014;44:1266–74.
125. Pillon M, Carucci NS, Mainardi C, Carraro E, Zuliani M, Chemello L, Calore E, Tumino M, Varotto S, Toffolutti T, Destro R, Gazzola MV, Alaggio R, Basso G, Messina C. Focal nodular hyperplasia of the liver: an emerging complication of hematopoietic SCT in children. Bone Marrow Transplant. 2015;50:414–9.
126. Kumagai H, Masuda T, Oikawa H, Endo K, Endo M, Takano T. Focal nodular hyperplasia of the liver: direct evidence of circulatory disturbances. J Gastroenterol Hepatol. 2000;15:1344–7.
127. Burgio MD, Ronot M, Salvaggio G, Vilgrain V, Brancatelli G. Imaging of hepatic focal nodular hyperplasia: pictorial review and diagnostic strategy. Semin Ultrasound CT MR. 2016;37:511–24.
128. Ronot M, Vilgrain V. Imaging of benign hepatocellular lesions: current concepts and recent updates. Clin Res Hepatol Gastroenterol. 2014;38:681–8.
129. Bertin C, Egels S, Wagner M, Huynh-Charlier I, Vilgrain V, Lucidarme O. Contrast-enhanced ultrasound of focal nodular hyperplasia: a matter of size. Eur Radiol. 2014;24:2561–71.
130. D'Onofrio M, Crosara S, De Robertis R, Canestrini S, Mucelli RP. Contrast-enhanced ultrasound of focal liver lesions. AJR Am J Roentgenol. 2015;205:W56–66.
131. Chiorean L, Cui XW, Tannapfel A, Franke D, Stenzel M, Kosiak W, Schreiber-Dietrich D, Jungert J, Chang JM, Dietrich CF. Benign liver tumors in pediatric patients - review with emphasis on imaging features. World J Gastroenterol. 2015;21:8541–61.
132. Mohajer K, Frydrychowicz A, Robbins JB, Loeffler AG, Reed TD, Reeder SB. Characterization of hepatic adenoma and focal nodular hyperplasia with gadoxetic acid. J Magn Reson Imaging. 2012;36:686–96.
133. Huppertz A, Haraida S, Kraus A, Zech CJ, Scheidler J, Breuer J, Helmberger TK, Reiser MF. Enhancement of focal liver lesions at gadoxetic acid-enhanced MR imaging: correlation with histopathologic findings and spiral CT--initial observations. Radiology. 2005;234:468–78.
134. Trovillion EM, Schubert L, Dietz AC. Iron overload in survivors of childhood cancer. J Pediatr Hematol Oncol. 2018;40:396.
135. Schempp A, Lee J, Kearney S, Mulrooney DA, Smith AR. Iron overload in survivors of childhood cancer. J Pediatr Hematol Oncol. 2016;38:27–31.

136. Chotsampancharoen T, Gan K, Kasow KA, Barfield RC, Hale GA, Leung W. Iron overload in survivors of childhood leukemia after allogeneic hematopoietic stem cell transplantation. Pediatr Transplant. 2009;13:348–52.
137. Halonen P, Mattila J, Suominen P, Ruuska T, Salo MK, Makipernaa A. Iron overload in children who are treated for acute lymphoblastic leukemia estimated by liver siderosis and serum iron parameters. Pediatrics. 2003;111:91–6.
138. Halonen P, Mattila J, Ruuska T, Salo MK, Makipernaa A. Liver histology after current intensified therapy for childhood acute lymphoblastic leukemia: microvesicular fatty change and siderosis are the main findings. Med Pediatr Oncol. 2003;40:148–54.
139. McCarville MB, Hillenbrand CM, Loeffler RB, Smeltzer MP, Song R, Li CS, Hankins JS. Comparison of whole liver and small region-of-interest measurements of MRI liver R2* in children with iron overload. Pediatr Radiol. 2010;40:1360–7.
140. Hankins JS, McCarville MB, Loeffler RB, Smeltzer MP, Onciu M, Hoffer FA, Li CS, Wang WC, Ware RE, Hillenbrand CM. R2* magnetic resonance imaging of the liver in patients with iron overload. Blood. 2009;113:4853–5.
141. Vag T, Kentouche K, Krumbein I, Reichenbach JR, Lopatta E, Renz DM, Stenzel M, Beck J, Kaiser WA, Mentzel HJ. Noninvasive measurement of liver iron concentration at MRI in children with acute leukemia: initial results. Pediatr Radiol. 2011;41:980–4.
142. Nobili V, Alisi A, De Ville De Goyet J. Metabolic syndrome and nonalcoholic steatohepatitis recurrence after liver transplantation in children. Liver Transpl. 2011;17:620–1.
143. Karanjia RN, Crossey MM, Cox IJ, Fye HK, Njie R, Goldin RD, Taylor-Robinson SD. Hepatic steatosis and fibrosis: non-invasive assessment. World J Gastroenterol. 2016;22:9880–97.
144. Assimos DG. Re: four of the most common mutations in primary hyperoxaluria type 1 unmask the cryptic mitochondrial targeting sequence of alanine: glyoxylate aminotransferase encoded by the polymorphic minor allele. J Urol. 2013;189:1769.
145. Lazo M, Hernaez R, Bonekamp S, Kamel IR, Brancati FL, Guallar E, Clark JM. Non-alcoholic fatty liver disease and mortality among US adults: prospective cohort study. BMJ. 2011;343:d6891.
146. Costa AF, Tremblay St-Germain A, Abdolell M, Smoot RL, Cleary S, Jhaveri KS. Can contrast-enhanced MRI with gadoxetic acid predict liver failure and other complications after major hepatic resection? Clin Radiol. 2017;72:598–605.
147. Joshi M, Dillman JR, Towbin AJ, Serai SD, Trout AT. MR elastography: high rate of technical success in pediatric and young adult patients. Pediatr Radiol. 2017;47:838–43.
148. Joshi M, Dillman JR, Singh K, Serai SD, Towbin AJ, Xanthakos S, Zhang B, Su W, Trout AT. Quantitative MRI of fatty liver disease in a large pediatric cohort: correlation between liver fat fraction, stiffness, volume, and patient-specific factors. Abdom Radiol (NY). 2018;43:1168.
149. Xanthakos SA, Podberesky DJ, Serai SD, Miles L, King EC, Balistreri WF, Kohli R. Use of magnetic resonance elastography to assess hepatic fibrosis in children with chronic liver disease. J Pediatr. 2014;164:186–8.
150. Litwiller DV, Mariappan YK, Ehman RL. Magnetic resonance elastography. Curr Med Imaging Rev. 2012;8:46–55.
151. Addley HC, Vargas HA, Moyle PL, Crawford R, Sala E. Pelvic imaging following chemotherapy and radiation therapy for gynecologic malignancies. Radiographics. 2010;30:1843–56.
152. Loebstein R, Atanackovic G, Bishai R, Wolpin J, Khattak S, Hashemi G, Gobrial M, Baruchel S, Ito S, Koren G. Risk factors for long-term outcome of ifosfamide-induced nephrotoxicity in children. J Clin Pharmacol. 1999;39:454–61.
153. Neu MA, Russo A, Wingerter A, Alt F, Theruvath J, El Malki K, Kron B, Dittrich M, Lotz J, Stein R, Beetz R, Faber J. Prospective analysis of long-term renal function in survivors of childhood Wilms tumor. Pediatr Nephrol. 2017;32:1915.
154. Millar AJW, Cox S, Davidson A. Management of bilateral Wilms tumours. Pediatr Surg Int. 2017;33:737–45.
155. Patel HD, Pierorazio PM, Johnson MH, Sharma R, Iyoha E, Allaf ME, Bass EB, Sozio SM. Renal functional outcomes after surgery, ablation, and active surveillance of localized renal tumors: a systematic review and meta-analysis. Clin J Am Soc Nephrol. 2017;12:1057–69.
156. Dickerson EC, Dillman JR, Smith EA, Dipietro MA, Lebowitz RL, Darge K. Pediatric MR urography: indications, techniques, and approach to review. Radiographics. 2015;35:1208–30.
157. Wong-You-Cheong JJ, Woodward PJ, Manning MA, Davis CJ. From the archives of the Afip: inflammatory and nonneoplastic bladder masses: radiologic-pathologic correlation. Radiographics. 2006;26:1847–68.
158. Kaste SC, Gronemeyer SA, Muram D. Vaginal occlusion induced by cancer therapy. Pediatr Radiol. 1993;23:369–70.
159. Muram D, CL G. Acquired vaginal occlusion. J Pediatr Adolesc Gynecol. 1990;3:141–5.
160. Leyendecker JR, Barnes CE, Zagoria RJ. MR urography: techniques and clinical applications. Radiographics. 2008;28:23–46. discussion 46–7.
161. Sklar C, Whitton J, Mertens A, Stovall M, Green D, Marina N, Greffe B, Wolden S, Robison L. Abnormalities of the thyroid in survivors of Hodgkin's disease: data from the Childhood Cancer Survivor Study. J Clin Endocrinol Metab. 2000;85:3227–32.
162. Van Dorp W, Van Beek RD, Laven JS, Pieters R, De Muinck Keizer-Schrama SM, Van Den Heuvel-Eibrink MM. Long-term endocrine side effects of

childhood Hodgkin's lymphoma treatment: a review. Hum Reprod Update. 2012;18:12–28.
163. Hancock SL, Cox RS, McDougall IR. Thyroid diseases after treatment of Hodgkin's disease. N Engl J Med. 1991;325:599–605.
164. Crom DB, Kaste SC, Tubergen DG, Greenwald CA, Sharp GB, Hudson MM. Ultrasonography for thyroid screening after head and neck irradiation in childhood cancer survivors. Med Pediatr Oncol. 1997;28:15–21.
165. Soberman N, Leonidas JC, Cherrick I, Schiff R, Karayalcin G. Sonographic abnormalities of the thyroid gland in longterm survivors of Hodgkin disease. Pediatr Radiol. 1991;21:250–3.
166. Hoang JK, Lee WK, Lee M, Johnson D, Farrell S. US Features of thyroid malignancy: pearls and pitfalls. Radiographics. 2007;27:847–60. discussion 861–5.
167. Bhakta N, Liu Q, Ness KK, Baassiri M, Eissa H, Yeo F, Chemaitilly W, Ehrhardt MJ, Bass J, Bishop MW, Shelton K, Lu L, Huang S, Li Z, Caron E, Lanctot J, Howell C, Folse T, Joshi V, Green DM, Mulrooney DA, Armstrong GT, Krull KR, Brinkman TM, Khan RB, Srivastava DK, Hudson MM, Yasui Y, Robison LL. The cumulative burden of surviving childhood cancer: an initial report from the St Jude Lifetime Cohort Study (SJLIFE). Lancet. 2017;390:2569.
168. Friedman DL, Whitton J, Leisenring W, Mertens AC, Hammond S, Stovall M, Donaldson SS, Meadows AT, Robison LL, Neglia JP. Subsequent neoplasms in 5-year survivors of childhood cancer: the Childhood Cancer Survivor Study. J Natl Cancer Inst. 2010;102:1083–95.
169. Turcotte LM, Liu Q, Yasui Y, Arnold MA, Hammond S, Howell RM, Smith SA, Weathers RE, Henderson TO, Gibson TM, Leisenring W, Armstrong GT, Robison LL, Neglia JP. Temporal trends in treatment and subsequent neoplasm risk among 5-year survivors of childhood cancer, 1970-2015. JAMA. 2017;317:814–24.
170. Neglia JP, Friedman DL, Yasui Y, Mertens AC, Hammond S, Stovall M, Donaldson SS, Meadows AT, Robison LL. Second malignant neoplasms in five-year survivors of childhood cancer: childhood cancer survivor study. J Natl Cancer Inst. 2001;93:618–29.
171. Bhatia S, Yasui Y, Robison LL, Birch JM, Bogue MK, Diller L, Delaat C, Fossati-Bellani F, Morgan E, Oberlin O, Reaman G, Ruymann FB, Tersak J, Meadows AT, Late Effects Study G. High risk of subsequent neoplasms continues with extended follow-up of childhood Hodgkin's disease: report from the Late Effects Study Group. J Clin Oncol. 2003;21:4386–94.
172. Metayer C, Lynch CF, Clarke EA, Glimelius B, Storm H, Pukkala E, Joensuu T, Van Leeuwen FE, Van't Veer MB, Curtis RE, Holowaty EJ, Andersson M, Wiklund T, Gospodarowicz M, Travis LB. Second cancers among long-term survivors of Hodgkin's disease diagnosed in childhood and adolescence. J Clin Oncol. 2000;18:2435–43.
173. Villani A, Tabori U, Schiffman J, Shlien A, Beyene J, Druker H, Novokmet A, Finlay J, Malkin D. Biochemical and imaging surveillance in germline TP53 mutation carriers with Li-Fraumeni syndrome: a prospective observational study. Lancet Oncol. 2011;12:559–67.
174. Marina N. Long-term survivors of childhood cancer. The medical consequences of cure. Pediatr Clin North Am. 1997;44:1021–42.
175. Pacheco R, Stock H. Effects of radiation on bone. Curr Osteoporos Rep. 2013;11:299–304.
176. Murphey MD, Choi JJ, Kransdorf MJ, Flemming DJ, Gannon FH. Imaging of osteochondroma: variants and complications with radiologic-pathologic correlation. Radiographics. 2000;20:1407–34.
177. Paulino AC. Late effects of radiotherapy for pediatric extremity sarcomas. Int J Radiat Oncol Biol Phys. 2004;60:265–74.

13 Complications and Pitfalls in Neuro-oncology Imaging

Stavros Michael Stivaros, John-Paul Kilday, Bruno P. Soares, and Thierry A. G. M. Huisman

13.1 Introduction

The identification of a neoplastic lesion in the paediatric neuro-axis is the primary step in a complex multidisciplinary process that leads from primary diagnosis, through treatment, assessment of treatment response and on to short- and long-term follow-up. In the paediatric cohort, this follow-up may either relate to complete response to treatment and total disease freedom, identification of local or metastatic disease relapse and in some tumour types, monitoring of residual disease for both early and late progressions. There exist potential pitfalls in each step of this pathway. This chapter aims to identify these potential complications and highlight imaging and reporting strategies that may be used to minimise (as far as is practicable and possible) the potential risk of such errors arising.

We will consider pitfalls and complications related to the imaging process itself, where the radiologist must be aware of possible normal variants specific to paediatric imaging, such as the technical and practical aspects of imaging assessment (e.g. timing of imaging). Whilst previous work has been published focusing on tumour mimics [1], in this chapter we will highlight where care must be taken to avoid either erroneous imaging interpretation of a neoplastic lesion or the potential for missing such a diagnosis as related to imaging technique.

S. M. Stivaros (✉)
Academic Unit of Paediatric Radiology, Royal Manchester Children's Hospital, Manchester Academic Health Sciences Centre, Manchester University, NHS Foundation Trust, Manchester, UK

Division of Informatics, Imaging and Data Sciences, School of Health Sciences, Faculty of Biology, Medicine and Health, Manchester Academic Health Science Centre, University of Manchester, Manchester, UK
e-mail: Stavros.Stivaros@manchester.ac.uk

J.-P. Kilday
Children's Brain Tumour Research Network (CBTRN), Royal Manchester Children's Hospital, Manchester, England, UK

Division of Cancer Sciences, The Centre for Paediatric, Teenage and Young Adult Cancer, The University of Manchester, Manchester, England, UK

B. P. Soares
Division of Pediatric Radiology and Pediatric Neuroradiology, The Johns Hopkins University School of Medicine, Baltimore, MD, USA
e-mail: bruno.soares@jhmi.edu

T. A. G. M. Huisman
Edward B. Singleton Department of Pediatric Radiology, Texas Children's Hospital, Houston, TX, USA
e-mail: huisman@texaschildrens.org

S. D. Voss, K. McHugh (eds.), *Imaging in Pediatric Oncology*, Pediatric Oncology,
https://doi.org/10.1007/978-3-030-03777-2_13

13.2 Technique-Related Pitfalls and Complications

13.2.1 Changes to the Imaging Paradigm

Even in the recent past extending back only a decade or so, imaging assessment of the paediatric brain generated studies numbering in the tens of images. These CT- and MRI-based studies mainly provided anatomical information followed by the addition of contrast to assess the integrity of the blood-brain barrier. We are now generating imaging studies comprised of thousands of images per examination, as we acquire not only anatomical but also physiological, functional and molecular data as part of routine paediatric neuro-oncology imaging assessment. This so-called multi-parametric imaging assessment is being increasingly assessed by novel techniques such as texture analysis [2–4]. It is incumbent on the reporting radiologist to interpret this increased imaging dataset in the context of changes in the pathological assessment of paediatric neuro-axis tumours given that the updated WHO tumour definitions include, for the first time, the molecular subtypes of these lesions [5, 6].

The previous approach to imaging study assessment was heavily reliant on the recognition of a characteristic radiological phenotype to aid radiological diagnosis, in effect a form of pattern recognition. This is now no longer recommended or indeed feasible given the complexity of imaging studies (as we enter the age of multi-parametric imaging). Hence it is now incumbent on radiologists to determine what the imaging discloses not only from an anatomical context but also incorporating both physiological and metabolic imaging findings and how this additional information impacts on both initial diagnoses (informing on tumour biology) as well as predicting both treatment response and longer-term outcome. This is of particular importance as we move towards an era of personalised medicine in which imaging will continue to play a pivotal and expanded role.

13.2.2 Imaging Technique

13.2.2.1 Imaging Dataset

Any MRI-based imaging assessment of the paediatric brain should maximise the available data presented to the reporting physician. Consensus recommendations from the Childhood Cancer and Leukaemia Group (CCLG) as well as the International Society of Paediatric Oncology Europe (SIOPE) on brain tumour imaging propose a standardised imaging dataset of "standard" (Table 13.1) as well as "additional" (Table 13.2) imaging sequences desirable in the context of paediatric neuro-oncology.

Table 13.1 Essential brain MRI sequences

Sequence	Technique	Plane
1–1.5 T scanner		
T_1W	2D SE, TSE/FSE	Axial (along AC-PC axis)
T_2W	2D SE, TSE/FSE	Axial
FLAIR	2D TSE/FSE	Axial or coronal
T_1W + contrast	2D SE, TSE/FSE	Axial, coronal and sagittal
DWI with ADC	2D EPI	Axial
3 T scanner		
T_1W	3D gradient echo	Axial or sagittal
T_2W	2D SE, TSE/FSE	Axial
FLAIR	2D TSE/FSE	Axial or coronal
T_1W + contrast	2D SE, TSE/FSE	Axial
T_1W + contrast	3D gradient echo	Axial or sagittal
DWI with ADC	2D EPI	Axial

Additional Notes

3D gradient echo (GRE) sequence is the inversion recovery GRE sequence (MPRAGE/IR SPGR/Fast SPGR/3D TFE/3D FFE).

2D sequences: Slice thickness ≤4 mm, and slice gap ≤1 mm (10% of slice thickness is desirable). For very small lesions, consider a slice thickness of 3 mm or less.

3D sequence: Slice thickness ≤1 mm with no slice gap. An isotropic voxel resolution of 1 mm × 1 mm × 1 mm is desirable depending on scanner capability.

Resolution parameters: Field of view, 230 mm (range 220–250 mm depending on head size); matrix size, minimum 256 (512 is desirable for better resolution; 96–128 for EPI sequences).

Some centres perform T1 FLAIR, T1 inversion recovery (IR) or T1 gradient echo instead of T1 SE sequence due to its suboptimal quality on 3 T scanners. This is acceptable as long as the diagnostic quality of the imaging is not compromised and the same sequence is used consistently for the individual patient.

There are increasing concerns of long-term gadolinium deposition, and the use of macrocyclic gadolinium-based contrast agents is recommended.

Table 13.2 Recommended brain MRI sequences (1.5 T or 3 T) that may provide additional information

Sequence	Technique	Plane
T_1W	3D gradient echo (on 1.5 T)	Axial or sagittal
FLAIR	3D gradient echo[a]	Axial or sagittal
Heavily weighted T_2W	2D or 3D CISS/B FFE/FIESTA[b]	Axial or coronal or sagittal
Advanced MRI	DTI, perfusion and spectroscopy[c]	

Slice thickness for 3D sequences ≤1 mm with no slice gap. An isotropic voxel resolution of 1 mm × 1 mm × 1 mm is desirable depending on scanner capability

[a]3D FLAIR can be used instead of 2D FLAIR but not if 2D sequences have been used for the same individual on previous occasions

[b]The heavily weighted T2 W sequence localised to a region of interest is useful in assessment of lesions (in particular poorly/non-enhancing) within the extra-axial space or along the parenchymal surface

[c]Please see Table 13.3 below

Failure to adopt and adhere to these suggested guidelines can lead to several potential pitfalls. The first obviously relates to primary diagnosis where often tumours can show little or no enhancement, and as such FLAIR and T2-weighted imaging and multi-parametric data gain even more significance on an individual case basis. Secondly failure to standardise imaging on follow-up will lead to errors in the comparison between imaging assessment time points. Finally patients being considered and then enrolled into clinical trials require a minimum imaging dataset for recruitment, and standardising imaging for all patients makes it more likely that cases will not "fall through the gaps" and receive suboptimal assessment at any particular assessment point.

The addition of further physiological assessment including perfusion imaging and spectroscopy will need to be based on local expertise and physics support. The SIOPE recommendations for such imaging are detailed below (Table 13.3), and as we shall see, such additional techniques can significantly improve lesion characterisation and follow-up.

For the sake of completeness, the corresponding spinal recommendations are also included in Table 13.4.

13.2.2.2 Incomplete Imaging Assessment

Once an imaging protocol for neuro-axis assessment has been established, it becomes imperative that the standard operating procedures are adhered to. Deviation from such, whilst often for the best of intentions, can lead to missed opportunities for diagnosis or to incorrect phenotyping. Spinal imaging assessment should be included in this regard, both in terms of neuro-axis assessment for metastasis from suspected brain tumours and to primary spinal lesions. A good example of this is the child referred for vague lower limb neurological symptoms referred from community paediatrics for spinal imaging, which identified the syrinx shown in Fig. 13.1. The identification of the syrinx should not be the endpoint of the imaging assessment. Indeed, this should include an attempt to ascertain why this syrinx has developed ensuring that the radiologist is satisfied that the imaging assessment is complete. In this case there was no evidence of any structural abnormality to account for the syrinx, e.g. a Chiari malformation. Imaging in cases such as this should include post-contrast assessment which was not performed until a later assessment. In this case assessment only included a sagittal post-contrast T1 sequence which identified a seemingly innocuous enhancing region thought to be vascular. It was not until a formal neuro-oncology assessment was obtained when trans-axial post-contrast imaging was performed. This revealed the enhancing nodule to be intrinsic to the spine and was proven at biopsy to be a pilocytic astrocytoma.

Similar pitfalls can ensue when the imaging assessment of a lesion within the brain is not fully characterised using all available imaging techniques as appropriate. As imaging physicians, radiologists have a suite of imaging tools available to them for lesion assessment. These include multimodality imaging (ultrasound, MRI, PET) as well as specific intra-modality techniques such as differing MRI sequences. The next example given here illustrates a common pitfall resulting from both search satisfaction and incomplete imaging assessment. A 6-year-old child presented with a de novo recent history of seizures to their local

Table 13.3 SIOPE recommendations for functional brain imaging

Multimodal Protocol					22/09/2016			Version 2.3	SIOPE Brain Imaging Group		
Core Multimodal Protocol (Brain)											
Modality		MRS			Diffusion			Perfusion			
Description		SVS (short-TE)			DTI			DSC—T2*			
		PRESS			EPI			GRE			
Sequence		Param	Value	Value	Param	Value	Param	Value	Param	Value	Param	Value
Fixed		Field	1.5 T	3 T	Field	1.5 T	Field	3 T	Field	1.5 T	Field	3 T
		TR (ms)	1500	2000	FOV (mm)	240	FOV (mm)	211	FOV (mm)	240 × 240 × 95	FOV (mm)	240 × 240 × 105
		Vector length	2048	2048	Acq matrix	96 × 96	Acq matrix	96 × 96	Acq matrix	96 × 96 × 19	Acq matrix	96 × 96 × 30
		TE (ms)	30		Resolution	2.5 isotropic	Resolution (mm)	2.2 isotropic	Orientation	axial	Orientation	axial
					Coverage	whole brain	Coverage	whole brain	Sense	2	Sense	2
					b factor	1000	*b* factor	1000	Temp resoln	1.49s × 60	Temp resoln	1.86s × 60
Variable		TE (ms)		30–35	TR (ms)	min	TR (ms)	min	Sequence	FE-EPI	Sequence	FE-EPI
		VOI (mL)	3.4–8 (to fit tumour)	2.2–8 (to fit tumour)	TE (ms)	min (fix BW?)	TE (ms)	min (fix BW?)	TE (ms)	40 ms	TE(ms)	40 ms
		BW (kHz)	2 or 2.5 kHz	2 or 2.5 kHz	Grad dirs	15+	Grad dirs	15+	TR (ms)	min	TR(ms)	min
		Aves (WS)	128–256	64–196	NSA ($b = 0$)	1 (3)	NSA ($b = 0$)	1 (3)	flip angle	20°	flip angle	20°
		Aves (W)	8–16	8–16	Speed-up	×2	Speed-up	×2	Injection rate	3 mL/s	Injection rate	3 mL/s
					Partial Fourier		Partial Fourier		Gd-DTPA	0.1 mmol/kg 50% as pre bolus	Gd-DTPA	0.1 mmol/kg 50% as pre bolus
Time (min)	Set-up		3	3					2		2	
	Acq		3.4–6.6	2.3–6.7					2		2	
	Total		6.4–9.6	5.3–9.7	5		3		4		4	
	Total	Minimum at 3 T—8.3 min + DSC										

Table 13.4 Recommended MRI sequences for spine imaging

Essential			
Sequence	**Technique**	**Parameter**	**Plane**
T1W + contrast	2D SE/TSE	Slice thickness ≤3 mm Slice gap <0.5 mm	Sagittal whole spine (entire dural sac)
T1W + contrast	2D SE/TSE or 3D gradient	Slice thickness 4–5 mm No slice gap	Axial—suspicious areas[a]
Sequences that may provide additional information			
Sequence	**Technique**		**Plane**
T2W	2D SE/TSE		Sagittal whole spine
T2W	2D SE/TSE		Axial—suspicious areas
Heavily weighted T2W	2D or 3D CISS/B FFE/FIESTA[b]		Sagittal ± axial

[a]Physiological veins over the surface of the cord can be mistaken for nodules of dissemination, and therefore *axial slices* without gaps (slice thickness should be 4 or 5 mm) are essential *for all suspicious areas*
1.5 T is preferred to 3 T for spinal imaging as the quality on older 3 T systems is often inferior and more unpredictable. More recent generation 3 T scanners now enable good, diagnostic quality spinal imaging, but there must be a low threshold to reimage the spine on a 1.5 T scanner if it is of a suboptimal quality
As fat suppression often leads to artefacts and is not necessary for the delineation of meningeal disease, it should not be used routinely
[b]The heavily T2 weighted sequence, localised to a region of interest, can be useful in the assessment of spinal lesions also. In particular non enhancing/nodular lesions on the surface of the cord or within the extra-axial but intradural space

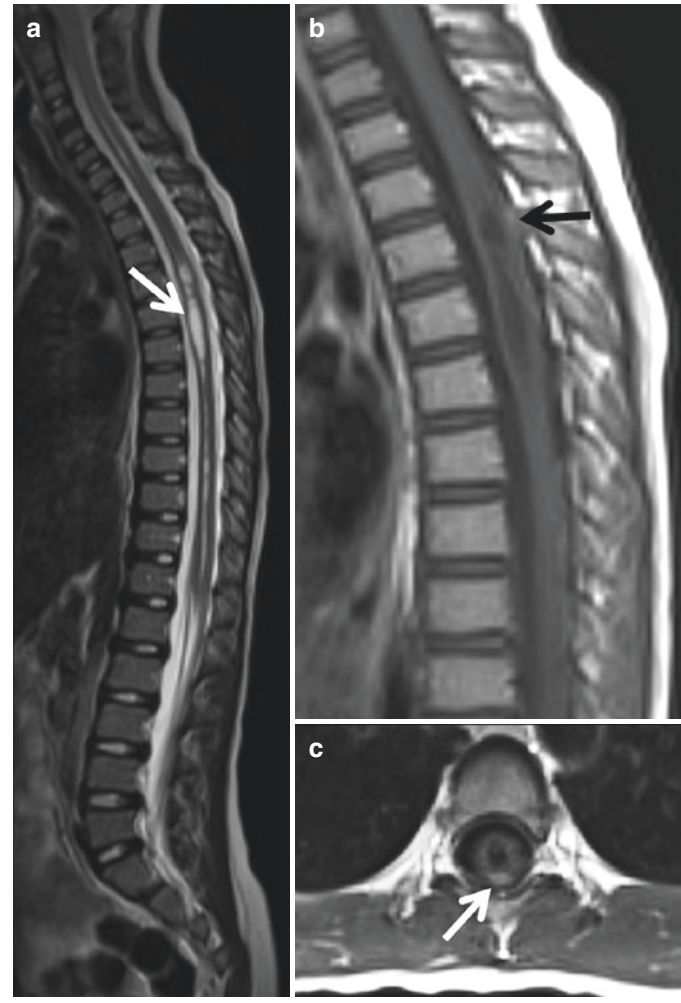

Fig. 13.1 Patient presented with vague lower limb neurological symptoms and imaging of the spine showed a syrinx that was high signal on T2 (arrow, panel **a**). Initial sagittal T1 post-contrast imaging only showed some vague enhancement (panel **b**, black arrow). Transaxial imaging is vital as this more clearly shows an enhancing nodule (panel **c**, white arrow), which at biopsy was a pilocytic astrocytoma

emergency department. Urgent CT of the brain was performed and reported as showing a haemorrhagic lesion in the left temporal lobe, most likely representative of an underlying tumour mass. Referral to the local neurosurgical unit was undertaken, and disclosure of this underlying tumour diagnosis was made to both patient and parents on the basis of a left temporal haemorrhagic lesion with intrinsic areas of enhancement (Fig. 13.2). Upon arrival at the paediatric tertiary level neuro-

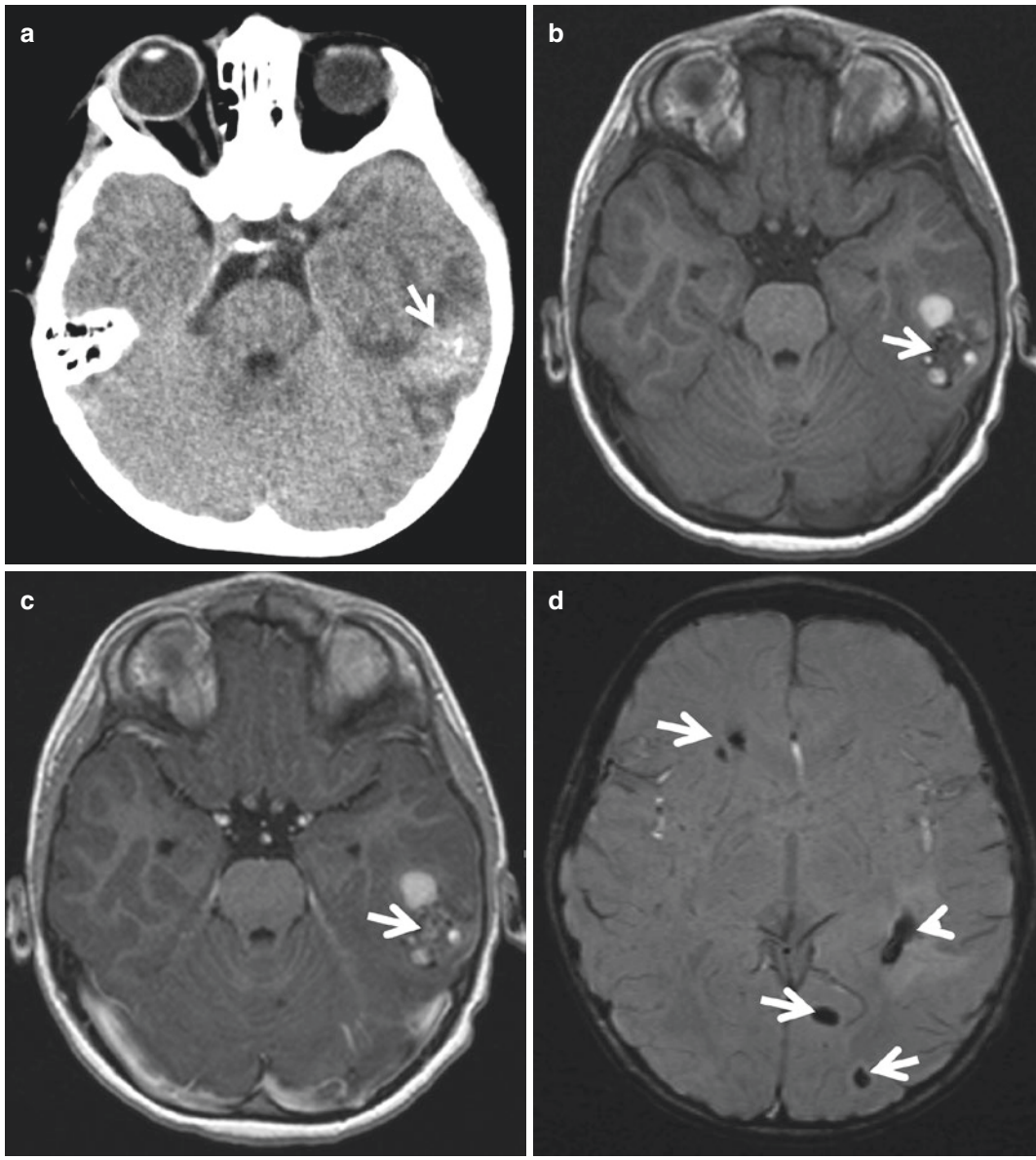

Fig. 13.2 (Panel **a**) initial post-contrast CT shows a mass lesion in the left temporal lobe (white arrow) with features of presumed haemorrhage and surrounding oedema. The axial T1 images (pre-contrast (panel **b**) and post-contrast (panel **c**)) show high-signal foci in the lesion in keeping with haemorrhage as well as some vague solid component showing contrast enhancement. The presence of haemorrhage mandated further imaging sequence assessment. In this instance, a susceptibility-weighted study was performed (panel **d**) which showed haemorrhage relating to the primary lesion (white arrow head) and multiple haemorrhagic lesions scattered throughout the brain (white arrows). The findings were in keeping with multiple cavernomas

surgical unit, repeat imaging was performed including susceptibility-weighted imaging (SWI), given the haemorrhagic nature of the primary mass. This clearly demonstrates multiple SWI lesions throughout the brain not identified on other sequences. A diagnosis of multiple cavernomatous lesions was made with a referral for genetic testing confirming an underlying CMC1 abnormality. This cautionary tale illustrates that imaging assessment is not complete until consideration has been made to all imaging modalities and sequences necessary for a thorough assessment on an individual patient basis.

With regard to search satisfaction, the reporting radiologist must always remain vigilant when attributing imaging findings to an apparently obvious oncological abnormality and thereby failing to recognise paediatric-specific developmental mimics. The case represented in Fig. 13.3 is such an example. A 3-year-old child presented from an outside hospital with a diagnosis of a posterior fossa tumour. Multiparametric assessment of the tumour and tumour resection confirmed a medulloblastoma. Initial assessment had only included a post-contrast sagittal T1 sequence of the spine and the filum terminale and showed a T1 bright lesion near the filum which had been interpreted as an enhancing metastatic lesion given the primary diagnosis. Repeat spinal imaging, in combination with awareness of developmental abnormalities of the spine, demonstrated that the lesion had increased T1 signal on pre-contrast non-fat-suppressed images, with complete suppression of the T1 signal on the fat saturation assessment, findings that are keeping with a lipoma. It is therefore apparent that a non-metastatic benign filum terminale lipoma has significant importance to the patient and to the clinical treating physicians and as such one should always beware of such potential errors.

13.2.2.3 Timing

Pitfalls in neuro-oncological imaging in children relating to temporal considerations fall into two main categories: the imaging assessment as related to the timing of the disease process which will be discussed in Sect. 13.2.4 below and imaging timing as related to diagnosis, treatment and imaging follow-up.

In general terms once a mass lesion has been identified and is being assessed neuroradiologically, it becomes incumbent on the imaging team to ensure that the whole neuro-axis has been assessed adequately. In some instances this will require additional scanning as the patient may have been transferred from an outside unit with a presumptive diagnosis but incomplete imaging assessment, and in some cases the accepting neuro-oncology unit will be undertaking the complete imaging assessment de novo. If the baseline MRI does not conform to the previously stated requirements, it should either be repeated preoperatively, or the post-operative imaging should be performed in a way (e.g. additional sequences to the standard protocol) that will ensure comparability with the preoperative MRI recommendations. However, this latter approach can introduce a complication in assessment, underscoring the importance of completing a full neuro-axis assessment prior to therapy. This is vital in ensuring that errors relating to intervention (surgery) are not misinterpreted as disease dissemination.

An example of such (Fig. 13.4) is a 4-year-old international referral in whom initial imaging demonstrated an intrinsic fourth ventricular tumour. No spinal imaging was performed prior to initial tumour resection surgery, with spinal imaging being undertaken 2 weeks following surgical clearance. Once the cranial vault had been breached during neurosurgery, the normal cerebrospinal fluid and haemodynamic homeostatic mechanisms within the neuro-axis will be disrupted. This can then lead to abnormal enhancement around the spinal cord, which in this case was wrongly identified as disseminated spinal disease. Follow-up imaging 6 weeks later confirmed this to be the case.

Similar consideration must be given to the immediate post-operative imaging assessment following tumour resection. The current recommendation is for such assessment to be undertaken within 48 h of surgery (and certainly within 72 h) to ensure that abnormal enhancement due to postsurgical granulation tissue, breakdown of

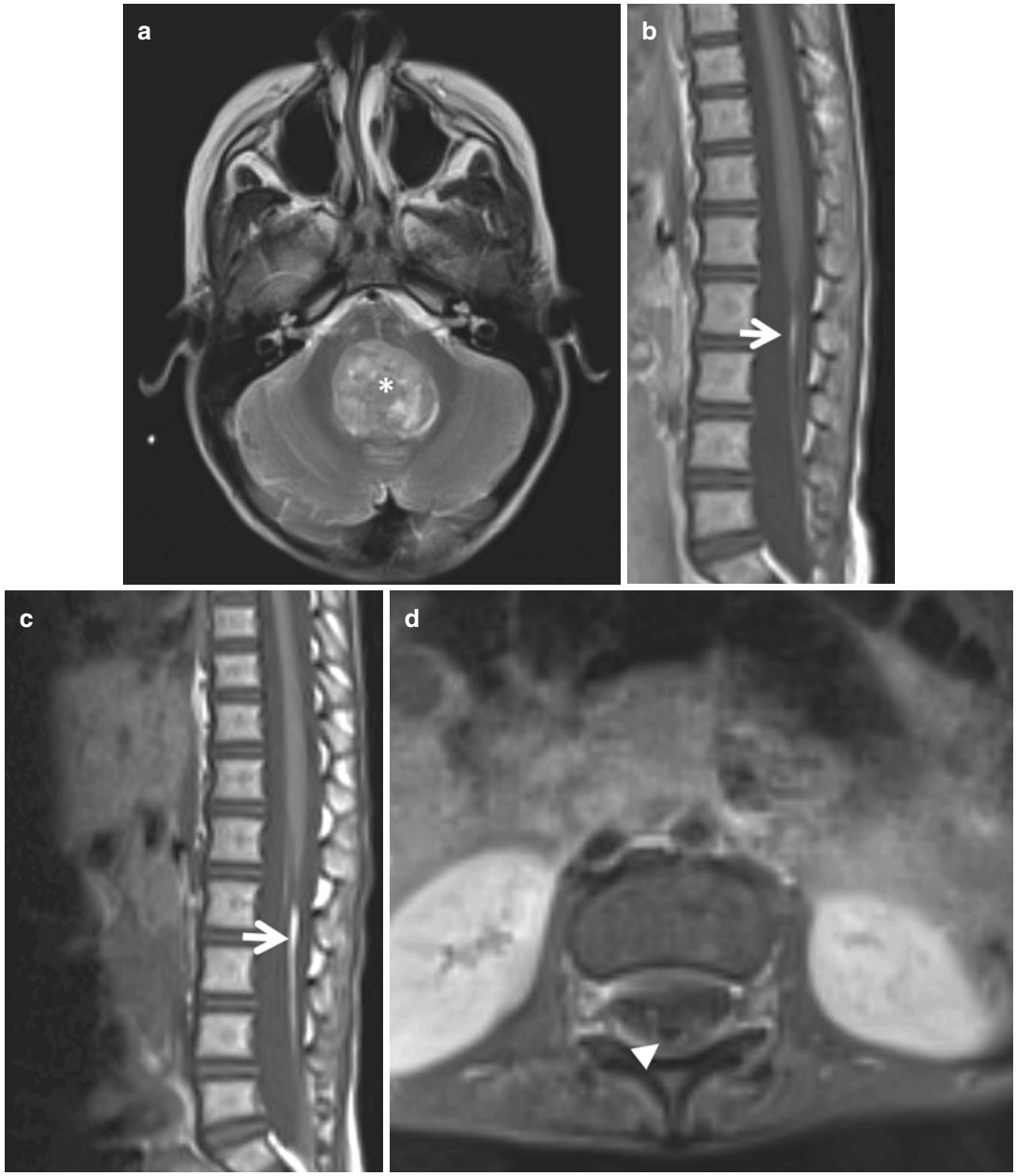

Fig. 13.3 (Panel **a**) axial T2 brain image at presentation, shows the primary lesion in the posterior fossa (white asterisk), which was on imaging assessment and histology confirmed as representing a medulloblastoma. At presentation there was increased signal on the post-contrast T1 sagittal image of the spine (panel **b**) in the filum terminale. This raised concerns regarding a possible metastasis. Further imaging assessment was performed which confirmed this lesion to have high T1 signal pre-contrast (panel **c**, white arrow) which fully suppressed on the post-contrast fat saturation axial imaging (panel **d**, white arrow head), thereby confirming a filum terminale lipoma and not a metastasis

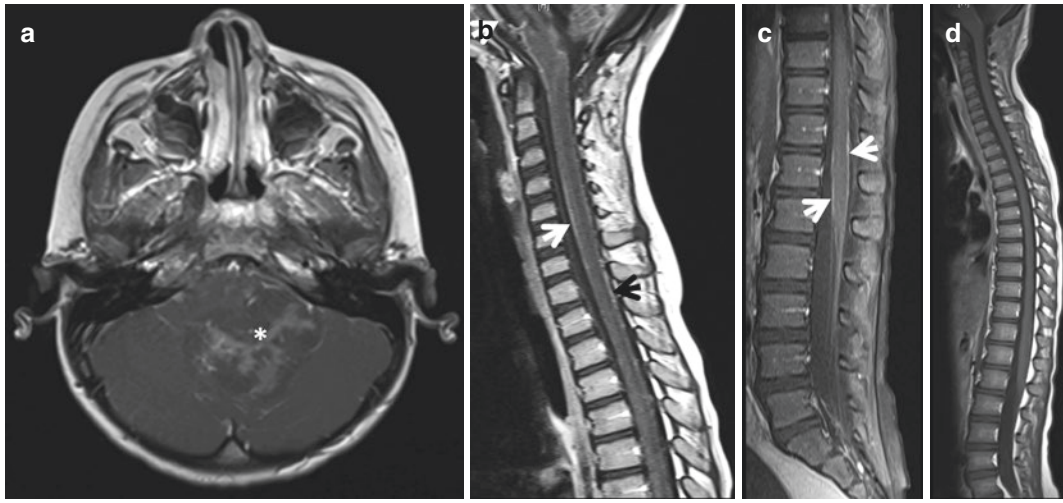

Fig. 13.4 Patient presentation scan showed a posterior fossa tumour with some scattered contrast enhancement (panel **a**, asterisk). Spinal imaging was not performed until 2 weeks following surgery, and this showed extensive leptomeningeal enhancement over the surface of the brainstem, pons, medulla and cord extending down to the conus. This was interpreted as metastatic leptomeningeal disease (panels **b** and **c**, white arrows). (**d**) Follow-up imaging 6 weeks later showed complete resolution of the leptomeningeal enhancement, confirming that the initial interpretation was erroneous and related to the previous surgical intervention

the normal CSF/haemodynamic homeostasis, iatrogenic material left at the surgical site, electrocoagulation or post-operative bleeding does not mask residual disease or mimic residuum when in fact none exists. However, even within this time window, it must be noted that nodular enhancement can be seen, and it is vital to ensure careful evaluation of the pre- and post-contrast T1-weighted images in combination with the signal intensities on the T2-weighted and FLAIR sequences.

We refer the reader to the other neuroradiology chapter within this work (Chap. 10) on assessing tumour response to therapy, but it is worth mentioning at this point the increasing use of intra-operative MRI assessment (ioMRI) in paediatric neuro-oncology. It is becoming more apparent that such scanning has significant benefit on obtaining gross tumour resection and maximising surgical efficacy [7, 8]. Recently completed work has shown that at the end of the procedure, ioMRI may be used to replace a standard post-operative assessment following tumour resection surgery [9]. If further studies confirm no difference between the two time points in identifying tumour residuum and the degree of related enhancement, then such errors relating to timing following surgery will be minimised. Indeed such early imaging may actually show reduced perioperative diffusion and oedema changes on the ioMRI scan compared with the immediate post-operative scan suggesting that such imaging, if available at the neurosurgical centre, is preferable and as such may reduce the burden on the imaging department by reducing the duplication of post-operative assessments.

13.2.3 Anatomical Considerations

It remains true that one of the primary imaging assessments of any intracranial mass lesion is the anatomical location of the mass itself. The differential assessment of a mass varies on the basis of its intra-/extra-axial and supra-/infratentorial location, and as such close attention with regard to the compartment in which a lesion lies is a vital first step in tumour assessment.

Until recent times improvements in radiological imaging have focused mainly on increased anatomical resolution, with the result that radiological analyses of imaging studies have relied

primarily on pattern recognition and the association of imaging patterns with recognised radiological phenotypes. Such approaches have had significant yield in our understanding of disease processes, such as high-resolution imaging of the vestibular-cochlear nerves in neurofibromatosis type 2 in children, informing on the multifocal origin of vestibular schwannomas in these children and hence the difference in tumour treatment response compared to sporadic tumours.

A classic pitfall in paediatric brain assessment is the study in which slice thickness and inter-slice distance is not adequate enough to delineate lesions potentially amenable to treatment. Consider the case shown in Fig. 13.5, in which a 7-year-old boy with severe intractable epilepsy has been referred for consideration for vagal nerve stimulation in what was considered lesion-negative epilepsy. The referral imaging had not revealed any lesional cause for his epilepsy, but it became clear once high-resolution imaging was employed that there was a cortically based lesion which following successful surgical resection was proven to be a dysembryoplastic neuroepithelial tumour. This case serves to illustrate that in an era where volume and thin slice imaging is readily available on the majority of clinical scanners, failing to optimise scan protocols to achieve such will only lead to false-negative imaging studies. Avoiding this outcome has the potential to speed up time to diagnosis and hence treatment. Indeed, for the case shown in Fig. 13.5, improved accuracy would have resulted in earlier surgery, reducing the patient's seizure burden and increasing his developmental trajectory.

Whilst optimising anatomical resolution and correct localisation of a mass lesion to a specific anatomical location is obviously paramount, one must also be aware of using anatomy as the sole radiological discriminator of a lesion, as potential pitfalls exist in such approaches.

For example, the case presented in Fig. 13.6 illustrates a 12-year-old child referred with a bilateral hearing impairment. He was noted on imaging to have loss of signal with both of his

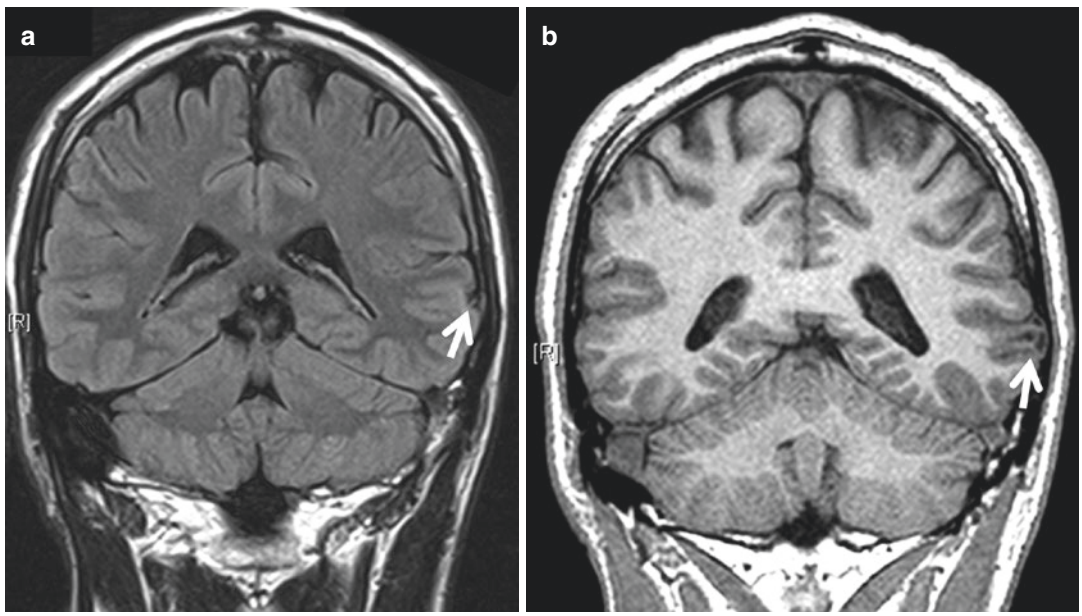

Fig. 13.5 Initial assessment imaging did not include high-resolution imaging and was reported normal. An exemplar of this is the coronal FLAIR sequence acquired at 5 mm slice thickness, shown in panel (**a**). Prior to vagal nerve stimulation, a comprehensive epilepsy protocol scan was performed including a high-resolution (sub 1 mm^3) volume T1 (panel **b**) which clearly showed a cortical-based lesion (white arrow), which cannot be seen on the thick slice imaging (panel **a**, white arrow)

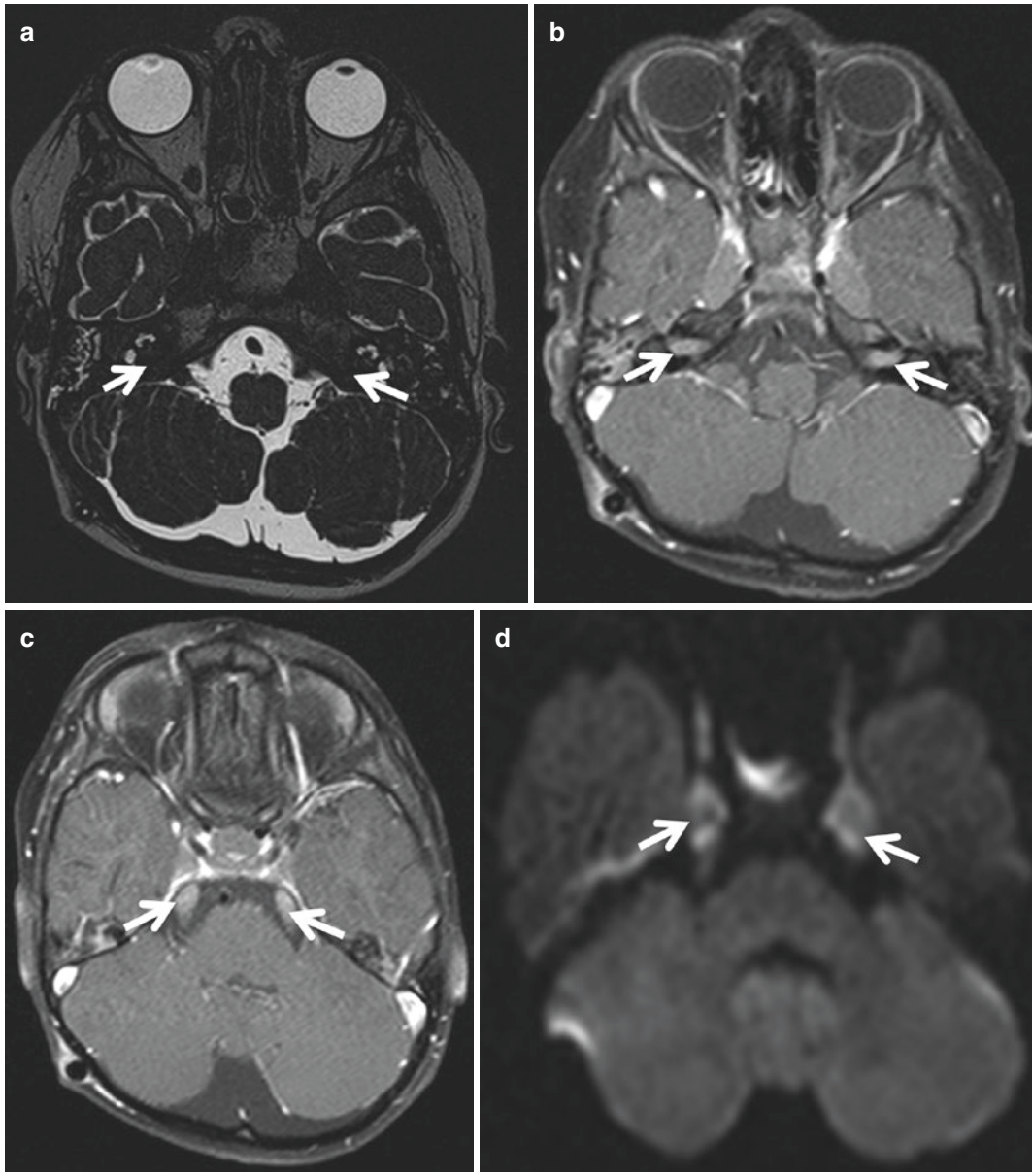

Fig. 13.6 Initial high-resolution T2-weighted imaging (panel **a**) shows complete "filling" of the IAMs bilaterally (white arrows), with loss of normal T2 signal. This filling shows contrast enhancement (panel **b**). Assessment of this post-contrast T1 sequence shows further thickening and enhancement of multiple cranial nerves including the fifth nerves bilaterally (panel **c**, white arrows). At this point a diagnosis of neurofibromatosis type 2 was considered. However the diffusion-weighted sequences showed these thickened nerves to have diffusion restriction (panel **d**, white arrows). This suggested increased cellular density along the nerves, a finding that is not in keeping with the expected diffusivity profile for cranial nerve schwannomas. CSF analysis confirmed this to be granulomatous disease

internal auditory meatii on standard internal auditory meatus heavily T2-weighted high-resolution imaging. A referral to the neurofibromatosis service ensued on the basis of this anatomical assessment and a presumptive diagnosis of neurofibromatosis type 2. Post-contrast imaging confirmed enhancing masses related to not only the IAMs but also involving multiple

cranial nerves. This seemingly confirmed the diagnosis. However, this was incongruous to the relative rapidity of the child's hearing loss and diffusion-weighted imaging which demonstrated increased cellular density relating to the cranial nerve thickening. A cellular diagnosis of granulomatous disease was eventually made following CSF analysis. This is an example of how the multi-parametric evolution of paediatric imaging enables the diagnostic process to overcome the limitations of purely anatomical assessment.

A further example of how anatomical location coupled with the radiologist focusing on limited imaging parameters can become a tumour assessment pitfall includes tumour mimics, in which imaging suggests a particular phenotype, but close consideration must be made to all the imaging correlates in a case to avoid being misguided. Consider a cerebello-pontine (CP) mass and the radiological phenotypes this may suggest [10]. In this example (Fig. 13.7), a right CP angle mass lesion was identified which demonstrated increased density on CT. The mass was intermediate to low signal on post-contrast T1 and had a high-signal homogenous pattern on FLAIR. There was significant diffusion restriction within the mass. The location and diffusion restriction, along with the lack of enhancement, led to an initial diagnosis of an epidermoid or a radiological "benign do not touch lesion" being made. However close attention to detail shows that this lesion was not similar to CSF on any sequence. Despite no interval change over a 2-month period, a decision to operate was made, and histologically this was then proven to represent a medulloblastoma.

13.2.4 Scanning in Relation to the Temporal Evolution of the Disease Process

As discussed above the timing of an imaging study must always be considered in relation to treatment or other iatrogenic interventions. However the radiological assessor must also remember to consider temporal evolution of a disease process. It is clear that as a disease process evolves, so too do the imaging characteristics of the pathology. Radiologists often refer to diseases as being representative of an "Aunt Minnie", in that the imaging phenotype is characteristic of a disease process, and as such their recognition of the pathology is absolute, just like their ability to recognise their parental sibling. However in many situations, the radiological differential is derived through the radiological equivalent of a surgical sieve. In these cases one is often left with a differential list that includes neoplastic causes as well as inflammatory, infectious or demyelinatory origins, and it becomes incumbent on the treating clinicians and allied health professionals to help refine and order the imaging differential. These considerations are discussed in further detail below, but it is important to remember that as one images later in the disease, the radiological phenotype will also evolve, potentially refining the differential list. Being aware of the pitfall of having potentially imaged early in a disease process before "characteristic findings" have declared themselves is therefore of paramount importance.

An example of this is shown in Fig. 13.8, with a child who presented with new onset seizures and little other clinical history. Initial imaging demonstrated multifocal non-enhancing T2 hyperintensity involving both grey and white matter leading to a wide differential. The spectroscopic profile, as detailed in other chapters, was not indicative of a typical tumour spectrum but did reveal a mildly elevated myo-inositol peak and slightly reduced NAA, suggesting a loss of neuronal density but of uncertain aetiology. This mimicked a similar case from several years earlier in which the myo-inositol peak rise was the only spectral abnormality seen, a finding that was dismissed as of little diagnostic importance, resulting in a delay in diagnosis until the imaging findings progressed and a diagnosis of a high-grade glial tumour was made. In this current instance, a recommendation was made for early biopsy, and the diagnosis of a glioblastoma multiforme was made histologically at the earliest possible

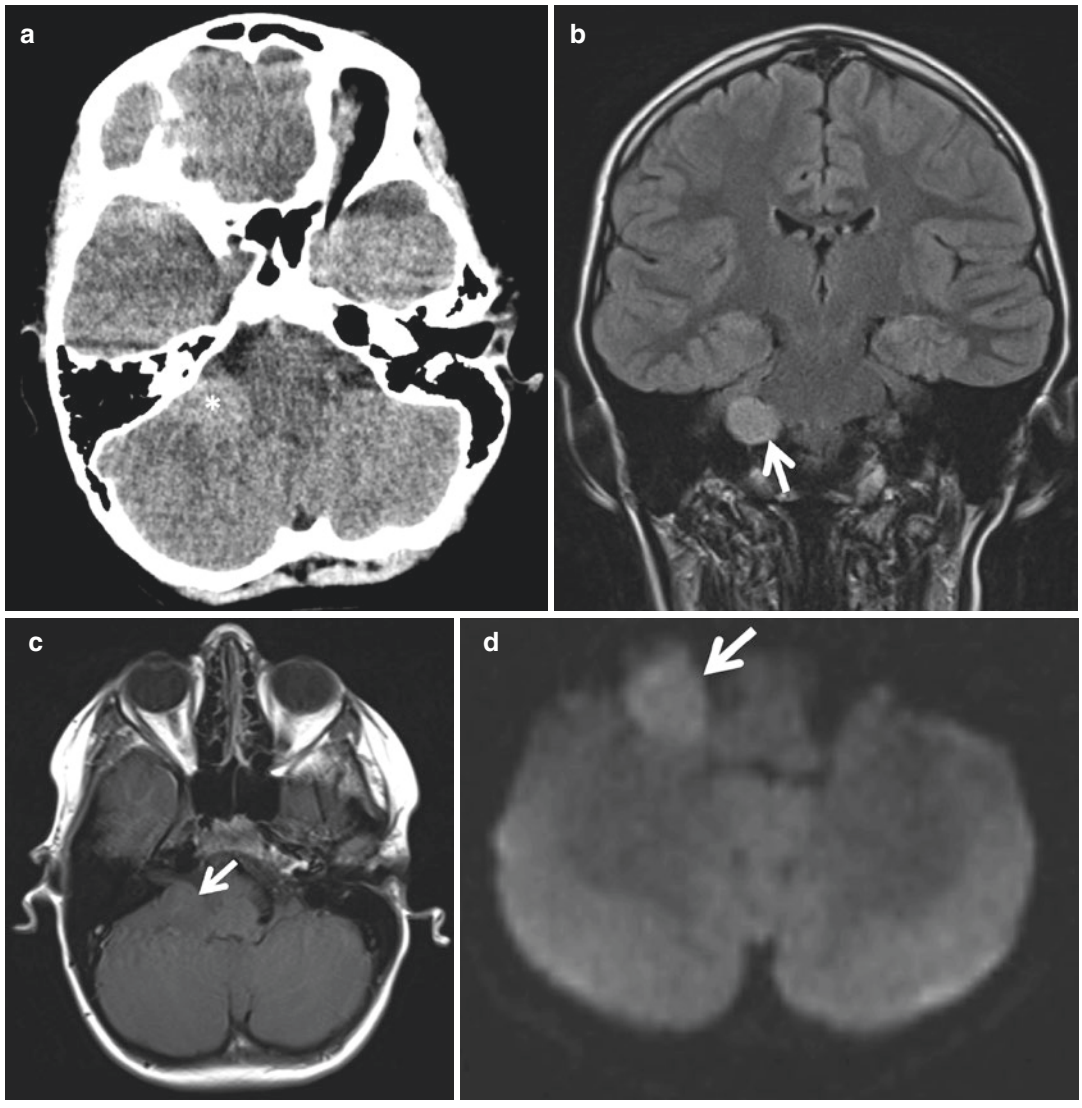

Fig. 13.7 Initial presentation CT scan (non-contrast) showed a right CP angle mass (panel **a**, asterisk). This lesion was high signal on FLAIR (panel **b**, white arrow) and did not enhance on T1 imaging (panel **c**). The mass had diffusion restriction within it (panel **d**) and as a result was erroneously interpreted as representing an epidermoid lesion. Beware of search satisfaction based on lesion location and selective bias to specific imaging sequences, with failure to pursue an appropriate interpretation of the other imaging findings. This lesion was histologically proven to represent a medulloblastoma

imaging time point. Further imaging assessment only 4 weeks later clearly now demonstrates a rapidly increasing myo-inositol peak despite the lack of a more characteristic tumour spectral profile and no enhancing lesion. This clearly indicates, therefore, that just as the standard imaging appearances on T1 and T2 and post-contrast imaging can evolve over time, so too can the multi-parametric imaging parameters, noting that sampling errors may also lead to a falsely reassuring imaging assessment when performing complex multi-parametric exams.

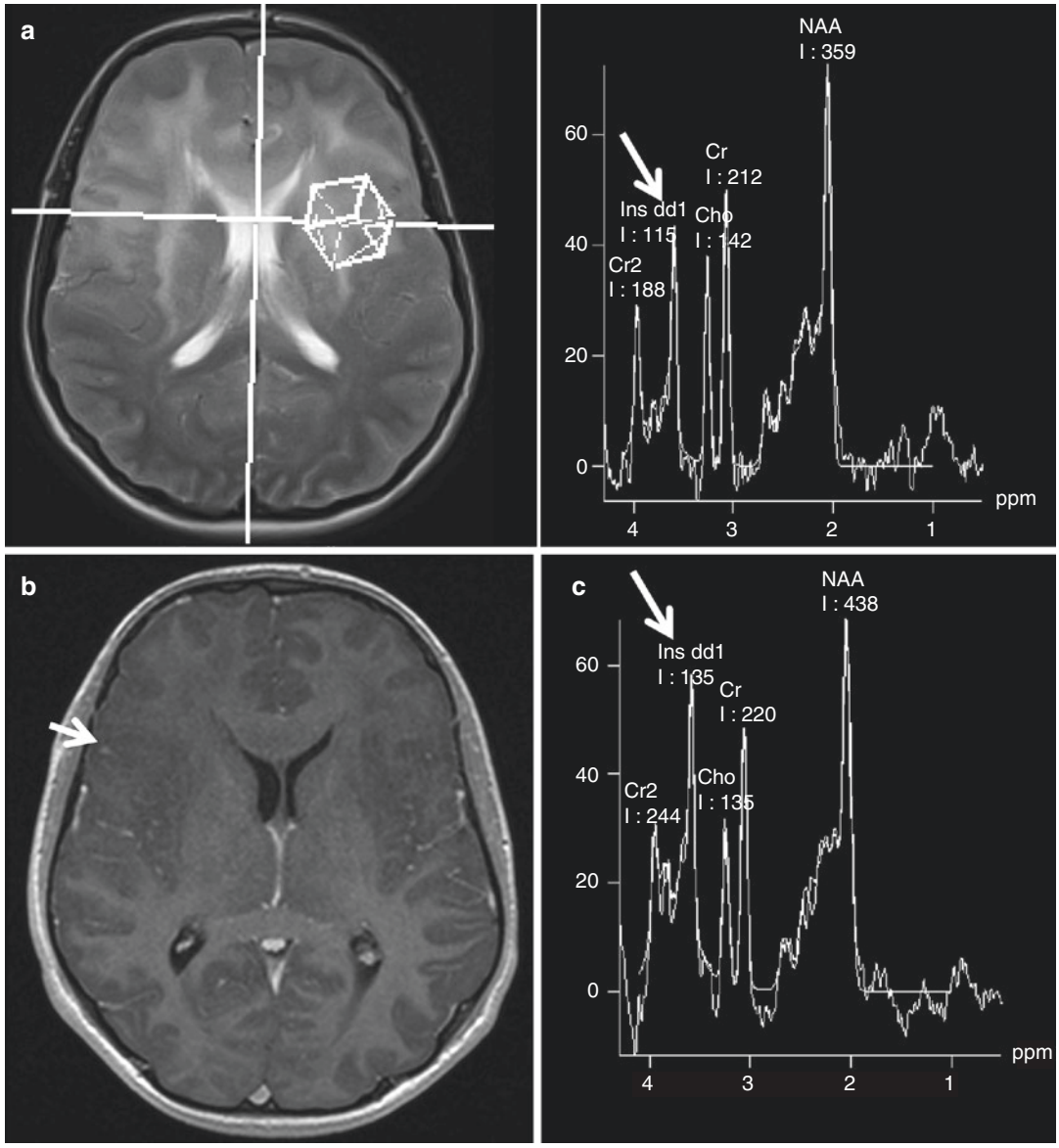

Fig. 13.8 Initial presentation scan showed T2 hyperintensity bilaterally with both cortical grey and white matter involvement. No significant contrast enhancement was seen, and the spectroscopy was relatively reassuring showing minor myo-inositol increase (panel **a** white arrow). Imaging 4 weeks later shows again no significant enhancement (panel **b**, white arrow) but with a clearly increasing myo-inositol peak (panel **c**, white arrow). Biopsy at that time confirmed glioblastoma multiforme

Whilst we may be reassured by an initial spectral profile that does not point to an oncological cause, this may indeed change over time, and in both of the cases presented, the need to biopsy early and confirm the diagnosis was vital, as the imaging profile early in the disease process was not able to provide diagnostic confirmation. One should also be aware that the myo-inositol peak is now thought of as being a precursor to the more traditional finding of NAA reduction and choline/creatine peak reversal as a spectroscopic marker for neoplastic disease.

13.2.5 Consideration of Advanced Imaging Metrics

13.2.5.1 Spectroscopy

The previous section discussed the evolution of spectroscopic imaging assessment over time as a correlate to the evolution of an aggressive neoplastic process. The correlate to this is the fact that within a specific disease type, imaging features may be identified that cannot be differentiated on standard imaging but require spectroscopic assessment if imaging pitfalls are to be avoided. An excellent example of this is the child with neurofibromatosis type I (NF1). As well as having an increased risk of developing optic nerve/chiasm/optic radiation gliomas, this disease process results in myelin vacuolation changes throughout the neuro-axis characterised by T2 signal hyperintensities that may wax and wane over time. These signal alterations may also present with minor mass effect and peripheral subtle contrast enhancement. Given that NF1 is a genetic tumour predisposition syndrome, problems arise in cases where T2 signal alteration is identified and differentiation between tumour and myelin vacuolation will have significant import in regard to follow-up and monitoring of the patient. Previous work has illustrated that the myelin vacuolation spectral profile deviates little from normal, with our own experience clearly demonstrating that low-grade tumour lesions in NF1 have a similar characteristic spectroscopic appearance to an expected tumour profile. As such, therefore, this is a condition in which a comprehensive imaging assessment requires the inclusion and understanding of characteristic spectroscopic findings, in addition to the conventional anatomic imaging sequences. Indeed such an assessment can also be used to track changes within a tumour during and following treatment. The case shown in Fig. 13.9 illustrates this point, with a child aged 11 years, whose tumour appears

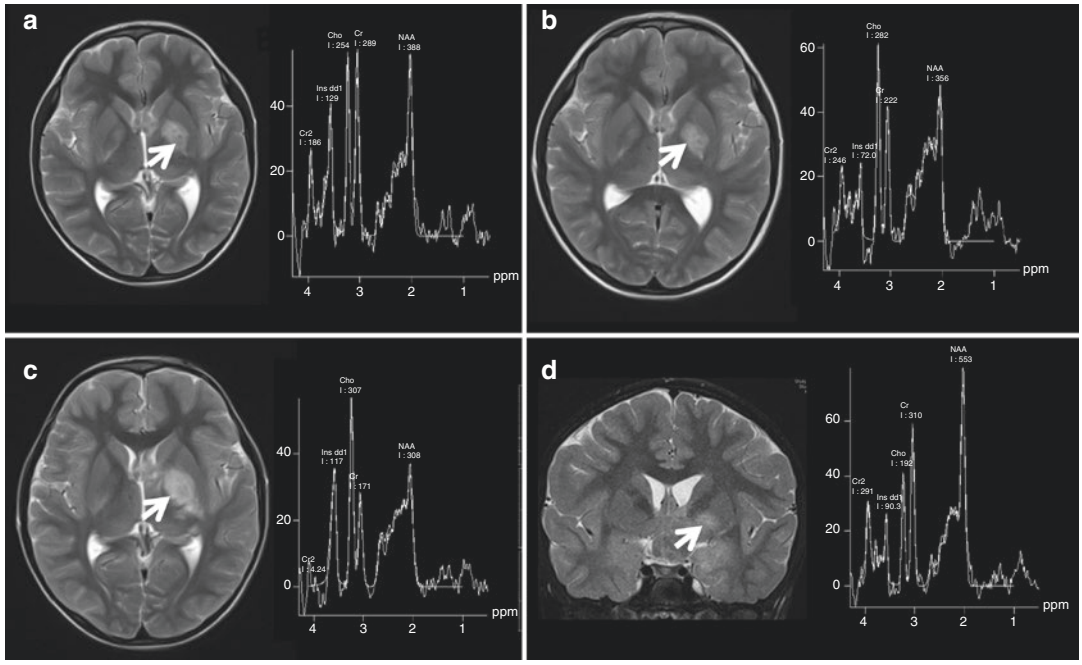

Fig. 13.9 Case 5: Left globus pallidus T2 signal change (panel **a**, white arrow) has a spectral profile with flattening of the major metabolite peaks (e.g. NAA) which is concerning for early tumour infiltration. Follow-up MRI 6 months later is unchanged on T2 (panel **b**), but there is now a clear tumour spectral pattern, with elevated Cho and further decrease in the NAA peak. Follow-up imaging again after 6 further months (panel **c**) now shows T2 signal progression as well as worsening of the spectroscopy profile. After chemotherapy the T2 signal change shows marked resolution on the coronal T2 (panel **d**) with normalisation of the spectral profile. Note there was no evidence of any contrast enhancement relating to the lesion at any time

stable on routine imaging assessment but clearly is worsening on spectroscopy. Decision to treat is therefore made on the spectroscopic assessment, and follow-up during and following therapy clearly shows normalisation of this spectroscopic profile, a radiologic feature that was more sensitive for worsening disease than the T2 signal changes alone.

13.2.5.2 Diffusion-Weighted Imaging

Diffusion-weighted imaging (DWI) is now a mainstay in paediatric neuro-oncological imaging and as such is not strictly an advanced imaging metric. However the inclusion of DWI imaging in the initial diagnostic and post-treatment setting is vital to prevent both diagnostic and follow-up complications. We have already discussed the relevance of diffusion-weighted imaging earlier in this chapter in the context of completing the imaging assessment of a child with multiple cranial nerve lesions (case 6), which was a good example of the importance of assessing cellular density at presentation and how this might affect the initial diagnostic differential. Diffusion-weighted imaging is also of importance in differentiation between tumour mimics and primary neoplasia. However even at the time of primary diagnosis, the failure to perform a complete diffusion assessment, which includes both DWI and ADC maps, can potentially contribute to a pitfall in imaging diagnostic accuracy. Consider the patients shown in Fig. 13.10, with two identical tumours as assessed on T2, FLAIR, T1 and T1 post-contrast imaging. There is a definite difference in the DWI pattern, with one lesion having free diffusivity within the tumour and the other having significant diffusion restriction. This is informing the radiologist that the tumour type shown in Fig. 13.10a is of a cellular dense nature and as such more likely to represent a medulloblastoma, rather than a less cellular dense tumour such as the pilocytic astrocytoma shown in Fig. 13.10b.

When considering diffusion assessment, one must be aware of complicating one's imaging assessment by failing to examine the ADC map during interpretation of the DWI study. T2 shine through is a common phenomenon seen on diffusion-weighted images and can be misinterpreted as restricted diffusion, with the result that differential considerations are incorrectly skewed towards tumour types with increased cellular packing such as medulloblastoma or lymphoma erroneously. This potential pitfall is easily avoided by reviewing both the DWI and ADC images together.

Similarly adequate consideration must be given to the inclusion of a DWI assessment in imaging follow-up, especially when this relates to the assessment of a patient in whom their primary diagnosis was a cellular dense tumour such as a medulloblastoma. Studies have shown that in certain instances DWI will represent the most sensitive imaging modality with regard to detecting tumour relapse or metastatic disease [11]. An example of just such a case is represented in Fig. 13.11. A 6-year-old child in whom the primary diagnosis was medulloblastoma, with complete surgical clearance and no initial disseminated disease, was under imaging surveillance. At 2 years post-surgery, DWI imaging identified a solitary right peri-Sylvian focus of diffusion restriction, with no enhancement and subtle FLAIR signal change. No other imaging metric abnormality was identified. The lesion was resected and histologically proven to be metastatic. This clearly illustrates the sensitivity of DWI sequences in such cases.

13.2.5.3 Perfusion-Weighted Imaging

Recent work has looked at the two main imaging paradigms for producing MRI-based perfusion maps: dynamic susceptibility-weighted imaging and arterial spin labelling. The comparison between these techniques is outside of the scope of this chapter, but given the increasing evidence relating to gadolinium deposition within the brain, ASL does appear to be an attractive solution to producing perfusion maps within the brain in children. As previously discussed, in recent years we have had a change in the imaging paradigm relating to neuro-axis oncological assessment, and as such our differential diagnoses in such cases may exhibit anchoring bias based

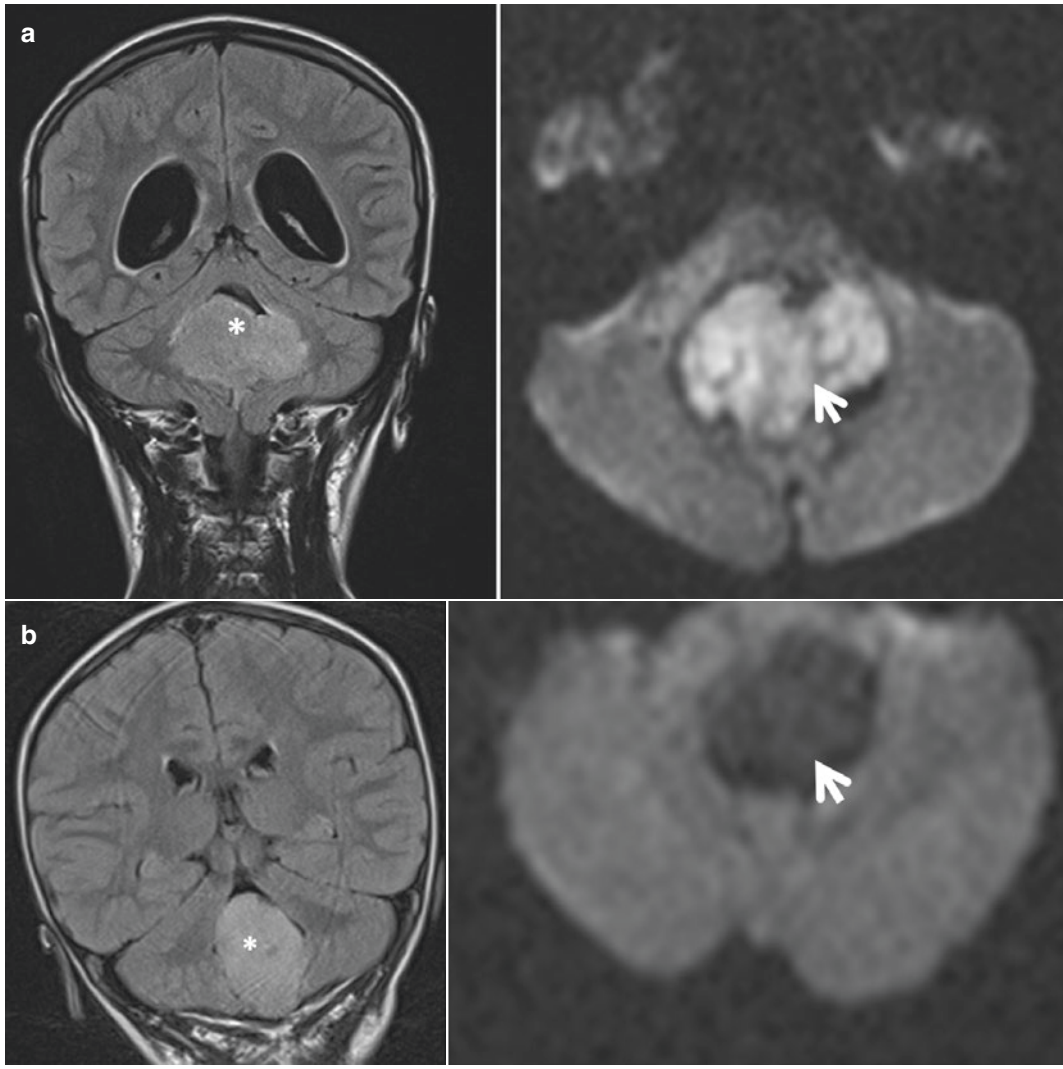

Fig. 13.10 Two patients with similar standard imaging appearances of their posterior fossa tumour as shown on their coronal FLAIR imaging (panels **a** and **b**, asterisks). There is clear difference in their diffusion patterns (with significant restriction in the medulloblastoma (panel **a**, white arrow) compared to the low-diffusivity pilocytic astrocytoma shown in panel **b** (white arrow). This is reflective of the difference in cellular density between the two tumour types

upon our previous teaching and experiences relating to diagnoses made on the basis of pattern recognition and anatomical location. An example of just such a case was discussed above, in which a presumed epidermoid lesion was in fact found to be a medulloblastoma.

The use of advanced radiologic techniques to develop any additional novel imaging metrics and characteristic imaging profiles must be welcomed in an effort to provide a more definitive characterisation of those lesions that either lack distinguishing qualities on conventional imaging or indeed have overlapping imaging features that can help in realigning our interpretation of a lesion away from such diagnostic approaches. In keeping with the other techniques previously discussed, perfusion imaging is just such a technique that can help to overcome some of the

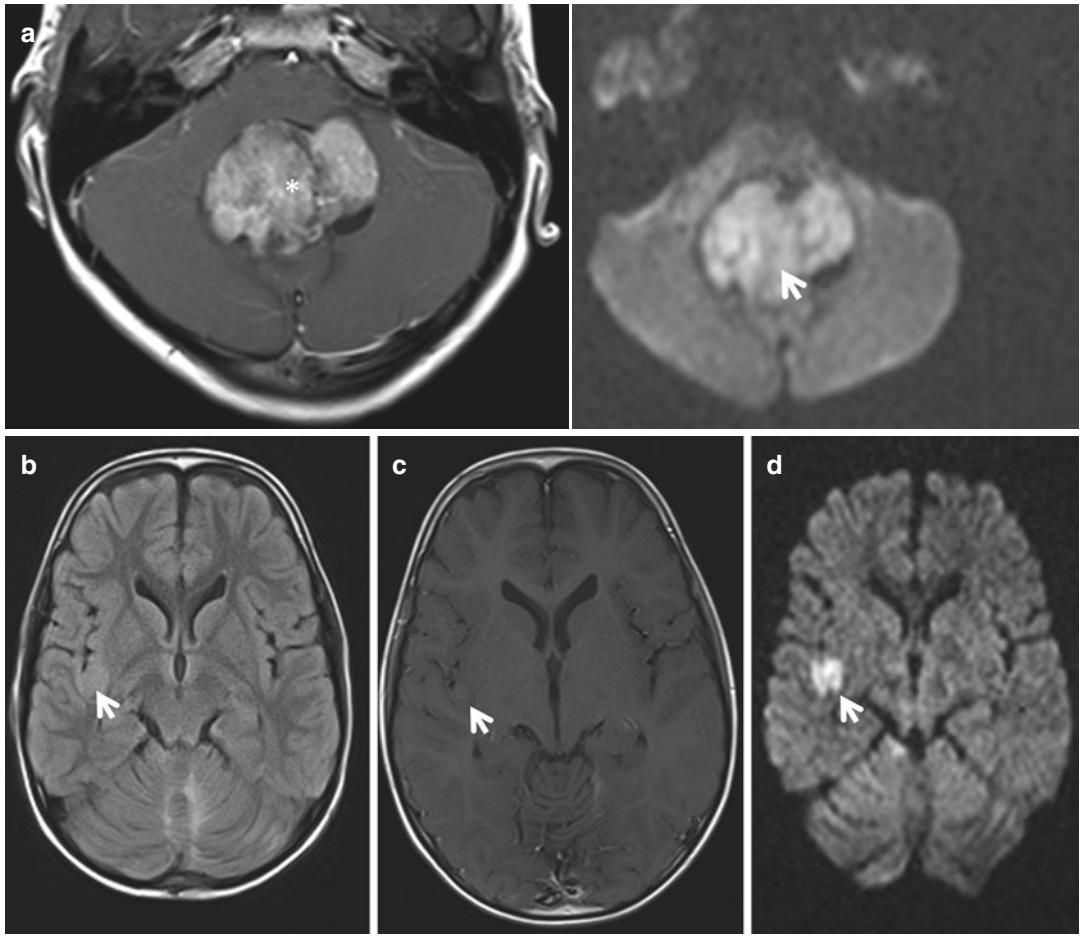

Fig. 13.11 At presentation (panel **a**), there was an intensely enhancing fourth ventricular mass (asterisk) with diffusion restriction throughout the lesion (white arrow) in keeping with a medulloblastoma which was confirmed at resection. At follow-up 2 years after surgical resection, there was very subtle change seen on FLAIR (panel **b**) with (unlike the primary tumour) no associated enhancement (panel **c**) but very significant diffusion restriction (panel **d**) in the right Sylvian fissure. The lesion was resected and histologically proven to be recurrent medulloblastoma. One can appreciate that in such a case, the DWI sequence is the most sensitive for identifying disease relapse unlike the standard imaging sequences

pitfalls of brain tumour imaging. An example of such would include intra-ventricular tumours [12] where the initial radiological imaging assessment would indicate a likely diagnosis of a choroid plexus lesion mainly due to intense enhancement and physical location of the tumour (Fig. 13.12). Diffusion-weighted imaging tends to have little benefit in such cases, and indeed imaging metrics for intra-ventricular tumours can be very similar. In this instance two vividly enhancing masses in female children aged 10 years and 13 years, respectively, are shown (Fig. 13.12). Note however a significant difference in their perfusion characteristics. This clearly introduces an imaging metric plane of separation that distinguishes between the imaging phenotypes of these two tumours, which at surgery were found to represent a meningioma and choroid plexus lesion, respectively.

We have discussed cases where cellular density was vital in the imaging follow-up of tumour subtypes. Similarly, perfusion imaging can be used to overcome the pitfall of an aggressive tumour which demonstrates no significant change

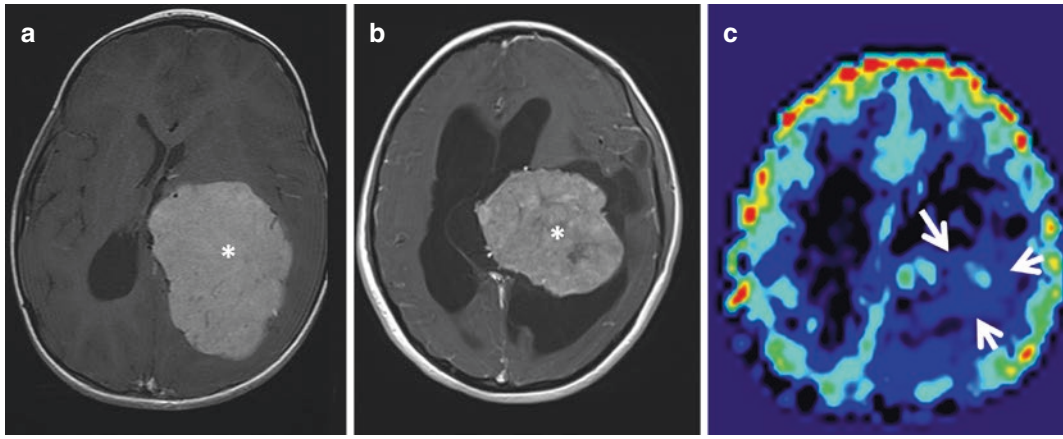

Fig. 13.12 Two different intra-ventricular tumours (post-contrast T1 images, panels **a** and **b**) have very similar imaging appearances (white asterisks). The only distinguishing feature between the two tumours was the perfusion imaging which was significantly high in patient A (not shown) and low in patient B (panel **c**). Meningiomas are known to have high perfusion as was confirmed for patient A, with the tumour in patient B representing a choroid plexus carcinoma

on conventional imaging yet shows an increase in perfusion imaging despite the lack of change using standard imaging metrics. In keeping with the other chapter on imaging follow-up in neuro-oncology, one can sometimes see similar improvement in patient follow-up using perfusion imaging rather than standard imaging metrics. In an age where we are moving towards more advanced treatment options including anti-angiogenic agents such as bevacizumab, we need to be aware of, and use in standard practice, these more subtle indicators of disease response to treatment.

One pitfall of imaging follow-up is how to interpret residual tissue at the site of primary or metastatic disease and how to interpret change in areas of the brain in which the therapy, be it surgical, radio-oncological or even chemotherapeutic, has caused derangement to the normal signal characteristics of the residual brain. In some instances the changes in the primary tumour appearance may be related to a dramatic change in both signal characteristics and morphology. This is shown in Fig. 13.13, where there is clearly progressive T2 signal and FLAIR derangement, accompanied by a focus of increasing perfusion within the resection cavity, which was the first indication of disease recurrence. Cases such as this emphasise that early changes in increased perfusion can confirm suspicious anatomic changes and should consider and present a clear indicator of disease relapse in such patients.

13.2.6 Summary

This chapter has hopefully identified and highlighted to the reader the importance of standardised imaging protocols in the setting of paediatric neuro-oncology. It has illustrated pitfalls relating to both imaging technique and timing of acquisition and follow-up and hopefully served to illustrate the benefits of multi-parametric imaging data acquisition within this domain.

As radiologists we do not take lightly the fact that undertaking an imaging study on a child is complex and for every study any risk needs to be outweighed by potential benefit. Such studies often require sedation, general anaesthesia and contrast injection and will by necessity result in anxiety to both patient and parent/guardian. Hence any imaging strategy that can improve the diagnostic and follow-up efficacy of a radiological examination should be welcomed, and this includes maximising the information gleaned

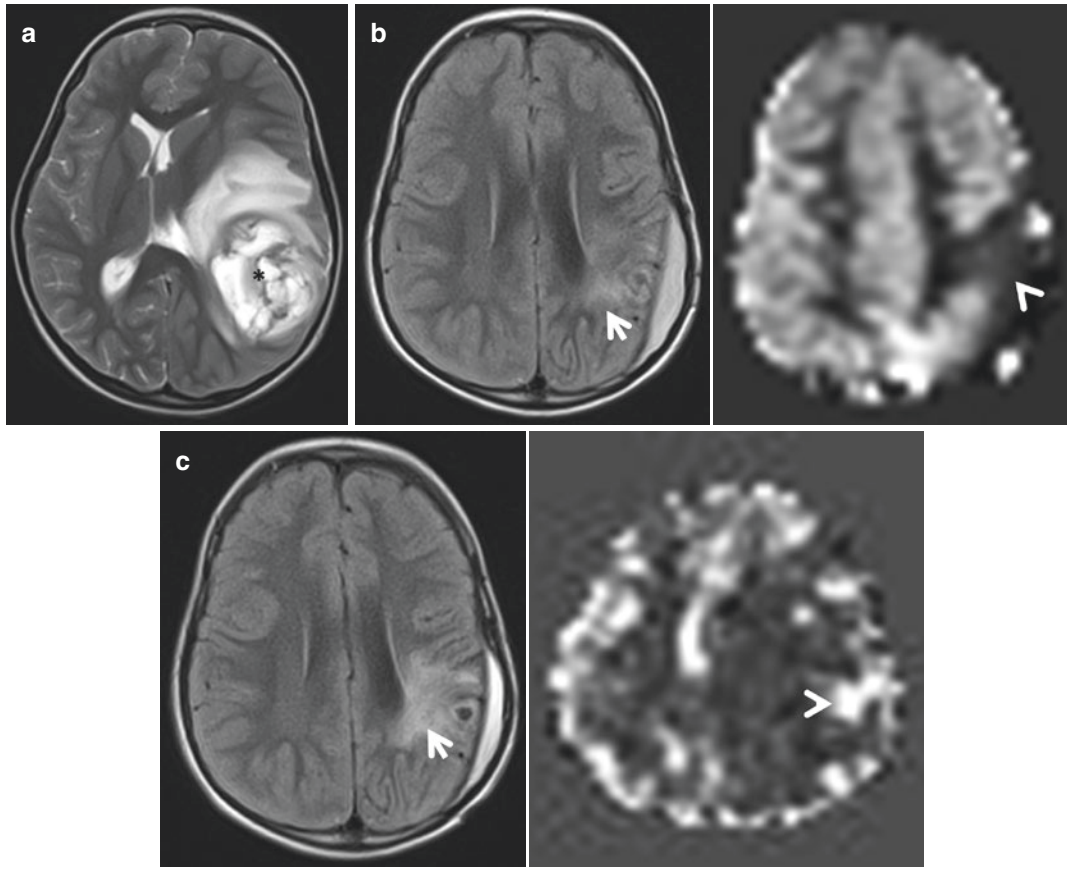

Fig. 13.13 A 12-year-old girl with histologically proven glioblastoma multiforme. Presentation imaging (panel **a**) shows a heterogeneous mass within the left parietal lobe (black asterisk). Following surgical resection there is some residual FLAIR signal change seen around the superior aspect of the resection cavity which is stable 6 months following surgery (panel **b**) white arrow. No abnormal perfusion is seen, and the peri-resection cavity actually has reduced perfusion, thought to represent postsurgical change (arrow head). Panel (**c**) is 3 months later and shows an increase in FLAIR signal (white arrow). Is this evolution of post radiotherapy change alone? The increasing perfusion within the mass (arrow head) suggests otherwise, and sadly this was indeed the case as this finding was the first harbinger of disease relapse

from such studies by employing multi-parametric assessment when necessary to try to reduce diagnostic and follow-up failure as much as is practicable.

References

1. Huisman TA. Tumor-like lesions of the brain. Cancer Imaging 2009;9(Spec No A):S10–S13. PubMed PMID: 19965288. Pubmed Central PMCID: 2797474.
2. Lorenzen A, Groeschel S, Ernemann U, Wilke M, Schuhmann MU. Role of presurgical functional MRI and diffusion MR tractography in pediatric low-grade brain tumor surgery: a single-center study. Childs Nerv Syst. 2018;34:2241. PubMed PMID: 29802593.
3. Fetit AE, Novak J, Rodriguez D, Auer DP, Clark CA, Grundy RG, et al. Radiomics in paediatric neuro-oncology: a multicentre study on MRI texture analysis. NMR Biomed. 2018;31(1). PubMed PMID: 29073725.
4. Tzika AA, Astrakas LG, Zarifi MK, Petridou N, Young-Poussaint T, Goumnerova L, et al. Multiparametric MR assessment of pediatric brain tumors. Neuroradiology. 2003;45(1):1–10. PubMed PMID: 12525947.
5. Colafati GS, Voicu IP, Carducci C, Miele E, Carai A, Di Loreto S, et al. MRI features as a helpful tool to predict the molecular subgroups of medulloblastoma: state of the art. Ther Adv Neurol Disord.

2018;11:1756286418775375. PubMed PMID: 29977341. Pubmed Central PMCID: 6024494.
6. Perreault S, Ramaswamy V, Achrol AS, Chao K, Liu TT, Shih D, et al. MRI surrogates for molecular subgroups of medulloblastoma. AJNR Am J Neuroradiol. 2014;35(7):1263–9. PubMed PMID: 24831600. Pubmed Central PMCID: 4819007.
7. Giordano M, Samii A, Lawson McLean AC, Bertalanffy H, Fahlbusch R, Samii M, et al. Intraoperative magnetic resonance imaging in pediatric neurosurgery: safety and utility. J Neurosurg Pediatr. 2017;19(1):77–84. PubMed PMID: 27791707.
8. Swinney C, Li A, Bhatti I, Veeravagu A. Optimization of tumor resection with intra-operative magnetic resonance imaging. J Clin Neurosci. 2016;34:11–4. PubMed PMID: 27469412.
9. Avula S, Jaspan T, Pizer B, Pettorini B, Parks C, Mallucci C. RA-13 comparison of final intra-operative MR scan and post-operative MRI performed 24 to 72 hours after brain tumour resection. Neuro Oncol. 2016;18(Suppl 3):iii167.
10. Bonneville F, Savatovsky J, Chiras J. Imaging of cerebellopontine angle lesions: an update. Part 2: intra-axial lesions, skull base lesions that may invade the CPA region, and non-enhancing extra-axial lesions. Eur Radiol. 2007;17(11):2908–20. PubMed PMID: 17569053.
11. Morana G, Alves CA, Tortora D, Severino M, Nozza P, Cama A, et al. Added value of diffusion weighted imaging in pediatric central nervous system embryonal tumors surveillance. Oncotarget. 2017;8(36):60401–13. PubMed PMID: 28947980. Pubmed Central PMCID: 5601148.
12. Zimny A, Sasiadek M. Contribution of perfusion-weighted magnetic resonance imaging in the differentiation of meningiomas and other extra-axial tumors: case reports and literature review. J Neurooncol. 2011;103(3):777–83. PubMed PMID: 21061142. Pubmed Central PMCID: 3116130.

14 Radioisotope Therapies: Iodine-131, I-131-MIBG, and Beyond

Neha S. Kwatra, Marguerite T. Parisi, and Barry L. Shulkin

14.1 Introduction

The value of radionuclides in cancer therapy has been recognized for several decades. The first use of radioisotope therapy in oncology was in the 1940s when radioactive iodine (I-131) was used to treat thyroid cancer [1–3]. Targeted radionuclide therapy involves the delivery of high-energy particles in close proximity to malignant cells, with their preferential uptake due to specific biologic features at the molecular or cellular level [4, 5]. The important considerations for physical characteristics of therapeutic radionuclide agents are their physical half-life (preferably between 6 h and 7 days), energy of radiation (high linear energy transfer radiations such as alpha and beta), daughter products, and method of production and radionuclide purity [6]. The biochemical characteristics that need to be considered are in vitro stability, tissue targeting, retention of radioactivity in the tumor, in vivo stability, and toxicity.

There has been a recent resurgence of interest in targeted radionuclide therapy due to the development of several new agents and the ability to combine these with both conventional and newer anticancer drugs in assorted multimodality treatment regimens. The noninvasiveness of radionuclide therapy and its relatively low toxicity in comparison to conventional chemotherapy and radiation therapy make it an attractive treatment modality. An increasing interest in targeted radionuclide therapy has also been related to the evolution of theranostics, which is the use of a compound labeled with a radionuclide initially for diagnostic imaging of a specific disease and then labeled with a different radionuclide for targeted therapy of that same disease process, including malignancies.

This chapter focuses on the relatively common pediatric applications of targeted radionuclide therapy including radioactive iodine (I-131) therapy of pediatric differentiated thyroid carcinoma (DTC) and I-131-metaiodobenzylguanidine (^{131}I-mIBG) therapy of high-risk neuroblastoma. A brief overview of other novel radionuclide agents that show promise for the treatment of neuroblastoma and other solid tumors of childhood is also provided.

N. S. Kwatra (✉)
Department of Radiology, Boston Children's Hospital, Boston, MA, USA
e-mail: Neha.Kwatra@childrens.harvard.edu

M. T. Parisi
Department of Radiology, University of Washington School of Medicine and Seattle Children's Hospital, Seattle, WA, USA
e-mail: meg.parisi@seattlechildrens.org

B. L. Shulkin
Department of Diagnostic Imaging, St. Jude Children's Research Hospital, Memphis, TN, USA
e-mail: Barry.Shulkin@STJUDE.ORG

S. D. Voss, K. McHugh (eds.), *Imaging in Pediatric Oncology*, Pediatric Oncology,
https://doi.org/10.1007/978-3-030-03777-2_14

14.2 Pediatric Thyroid Cancer Epidemiology

Thyroid cancer is a rare pediatric malignancy, with new cases of thyroid cancer in patients <20 years representing only 1.8% of all thyroid malignancies diagnosed in the United States [7, 8]. The incidence of thyroid cancer is 0.2 per 100,000 in children <10 years, 0.8 per 100,000 in children between 10 and 14 years of age, and 2.9 per 100,000 in the 15–19-year age group according to the Surveillance, Epidemiology, and End Results (SEER) program [7]. The incidence of childhood thyroid cancer is increasing by 1.1% per year [9, 10]. Prepubertal rates of thyroid cancer are similar in girls and boys, but in the postpubertal pediatric population, females are four times more likely to have thyroid cancer than males.

DTC, which includes the papillary and follicular types, constitutes the vast majority (90–95%) of thyroid cancers in children [11]. Medullary thyroid cancers comprise only 5–8%, and the undifferentiated thyroid cancers are very rare. Papillary thyroid carcinoma (PTC), which is the most common type of thyroid cancer, and follicular thyroid carcinoma (FTC) have some key differences. PTC is often bilateral, multifocal, and associated with the presence of regional lymph nodal metastases [8]. Hematogenous pulmonary metastases occur in up to 25% of cases, usually in patients with a significant nodal disease burden. FTC is usually unifocal and more likely to demonstrate hematogenous pulmonary and skeletal metastases. Nodal metastases are infrequent.

As compared to adults, children with DTC more frequently present with more advanced disease and are more likely to develop recurrence [12]. Lymph node involvement at diagnosis is present in 40–90% of children in comparison to 20–50% in adults. The prevalence of distant metastases in children is also higher, at 20–30%, in contrast to only 2–14% in adults. Multifocal disease is also more common in children. Even so, the mortality rates are lower in children than adults, with a 10-year mortality rate of <10% and overall survival of 98% [13–16].

14.3 Current Status of Radioactive Iodine (I-131) Therapy in Differentiated Thyroid Cancer

Traditional management of pediatric patients with DTC included postoperative I-131 therapy in all patients. The goal was ablation of any residual thyroid tissue in order to more effectively use serum thyroglobulin (Tg) as a biomarker for recurrent disease, to decrease the risk of recurrent disease, and to decrease mortality.

There are numerous reports of improved survival and decreased recurrence rates with postoperative I-131 therapy in both adults and children with advanced DTC [17–23]. However, in various adult studies, postoperative I-131 therapy has not clearly been shown to be of benefit to those with low-risk thyroid cancer after a complete surgical resection [24–28]. Further, there have been reports of an increasing incidence of secondary cancers in low-risk DTC patients treated with postoperative I-131 [25]. Based on the existing data, recent ATA recommendations suggest that thyroid remnant ablation can be withheld for such adult patients [8]. However, consensus has not been reached in the pediatric age group where there is conflicting data in regard to the benefit of thyroid remnant ablation in the low-risk thyroid cancer patient [15, 29, 30].

There is a growing awareness of the potential long-term risks associated with I-131 treatment including the development of secondary malignancies, among others [15, 31, 32]. Therefore, it is important to identify those children with DTC who have a high likelihood of benefit from I-131 therapy and to steer away from empiric administration to all patients. Recent guidelines from a pediatric thyroid cancer task force commissioned by the ATA have attempted to address this by developing risk-stratification groups for pediatric patients with DTC. This ATA task force developed three risk-stratification groups for children with PTC based on the use of the TNM classification system: low-, intermediate-, and high-risk groups (Table 14.1).

Definitive therapy for children with DTC includes thyroidectomy and, when appropriate, lymph node dissection and possible I-131 radio-

Table 14.1 American Thyroid Association risk levels in pediatric papillary thyroid carcinoma based on TNM classification of malignancies [1]

ATA pediatric-risk group	Disease description	TNM classification
Low	Disease grossly confined to the thyroid gland	T1, 2, or 3[a] No/Nx or incidental N1a M0
Intermediate	Patients with extensive nodal disease who are at low risk for distant metastatic disease, but at increased risk for incomplete nodal resection and persistent cervical disease	T1, 2, or 3[a] N1a or minimal N1b M0
High	Patients with locally invasive or regionally extensive disease, who are at highest risk for incomplete resection, persistent disease, and distant metastases	T4 Extensive N1b Any M

[a]The impact of the pathologic identification of microscopic extrathyroidal extension (ETE), T3 disease, on management and outcomes has not been well studied in pediatric patients with papillary thyroid cancer, but patients with minimal ETE are probably either ATA pediatric low- or intermediate-risk, depending on other clinical factors [16]

therapy for intermediate- and high-risk patients. Per the ATA pediatric guidelines, staging is usually performed within 12 weeks after total or subtotal thyroidectomy in order to identify patients who could benefit from more treatment, including additional surgery or I-131 therapy. ATA pediatric low-risk patients are initially assessed and followed only with physical examination and TSH-suppressed Tg levels, whereas both TSH-stimulated Tg levels and diagnostic whole-body scintigraphy (DxWBS) are typically recommended to assess for persistent disease in the intermediate- and high-risk patient groups. I-131 therapy is indicated for iodine-avid persistent locoregional and/or nodal disease that cannot be resected and iodine-avid distant metastases. In patients who have persistent disease following I-131 therapy, the decision to administer additional I-131 therapy should be based on prior response and clinical data in individual patients.

14.4 Diagnostic Whole-Body Scintigraphy

As mentioned above, per the recent ATA pediatric guidelines, diagnostic whole-body scintigraphy (DxWBS) is performed postoperatively in all patients with intermediate- and high-risk disease to help guide further management including the necessity for I-131 therapy. DxWBS is no longer recommended in the low-risk population, as was the practice previously. Whenever possible, I-123 rather than I-131 should be utilized for diagnostic imaging, using the lowest possible dose, due to several putative benefits including lower patient radiation exposure, improved image quality, and the ability to perform single-photon emission computed tomography (SPECT)/CT, as well as to avoid possible stunning [16].

DxWBS may also be included in surveillance imaging. Traditionally, sequential DxWBS at variable intervals had been utilized in routine surveillance to detect persistent or recurrent disease in children with DTC [33–36]. However, according to the recent ATA pediatric guidelines [8], there is no role for surveillance DxWBS in children with DTC who have not received I-131 therapy unless evidence exists for persistent or recurrent disease, based on physical examination, ultrasound, or serum Tg levels. Also, once a negative DxWBS is obtained, there is no benefit from serial DxWBS to survey for disease recurrence as long as the patient otherwise remains without clinical evidence of disease.

Follow-up DxWBS can be used in these situations [8]:

- In children suspected to have residual disease to determine the need for I-131 therapy and to aid in determination of the therapeutic dose to be administered
- To confirm the absence of iodine-avid disease in children with DTC who were previously treated with I-131 and who have no evidence of disease 1–2 years after initial therapy
- In children with high-risk disease who underwent I-131 therapy previously or are known to have iodine-avid metastatic disease based upon a previous posttreatment scan. The DxWBS

should be obtained after at least 12 months of clinical follow-up (unless there is a change in clinical status) and deferred even longer in children who continue to demonstrate a clinical response to previous treatment.

Patient preparation prior to DxWBS includes discontinuing levothyroxine (LT4) for 2–6 weeks. Liothyronine (LT3) supplementation may be given to reduce the duration of hypothyroidism during prolonged LT4 withdrawal or in patients who are sensitive to hypothyroid symptoms. LT3 can be administered up until 2 weeks of the scheduled whole-body imaging [16, 37]. Instead of thyroid hormone withdrawal, TSH stimulation can be performed by the use of recombinant human thyrotropin (rhTSH) stimulation. The experience using rhTSH in children is more limited than in adults but has been shown to be effective with no reported side effects [16, 38–40].

A low-iodine diet is also started about 2 weeks before imaging to maximize uptake within any potential residual iodine-avid disease. Laboratory studies that are typically obtained prior to DxWBS include serum TSH, stimulated Tg levels, antithyroglobulin antibodies (TgAb), and complete blood counts. TSH level >30 mIU/L is required to ensure adequate stimulation for imaging. A negative pregnancy test should be confirmed in all women of childbearing age.

DxWBS is typically performed at 24 h after the oral administration 2–4 mCi of I-123 NaI. Anterior and posterior whole-body images are acquired, with and without markers. It is important to recognize the physiologic sites of radiotracer uptake including some anatomic variants (Fig. 14.1). Physiologic thymic uptake is common in children

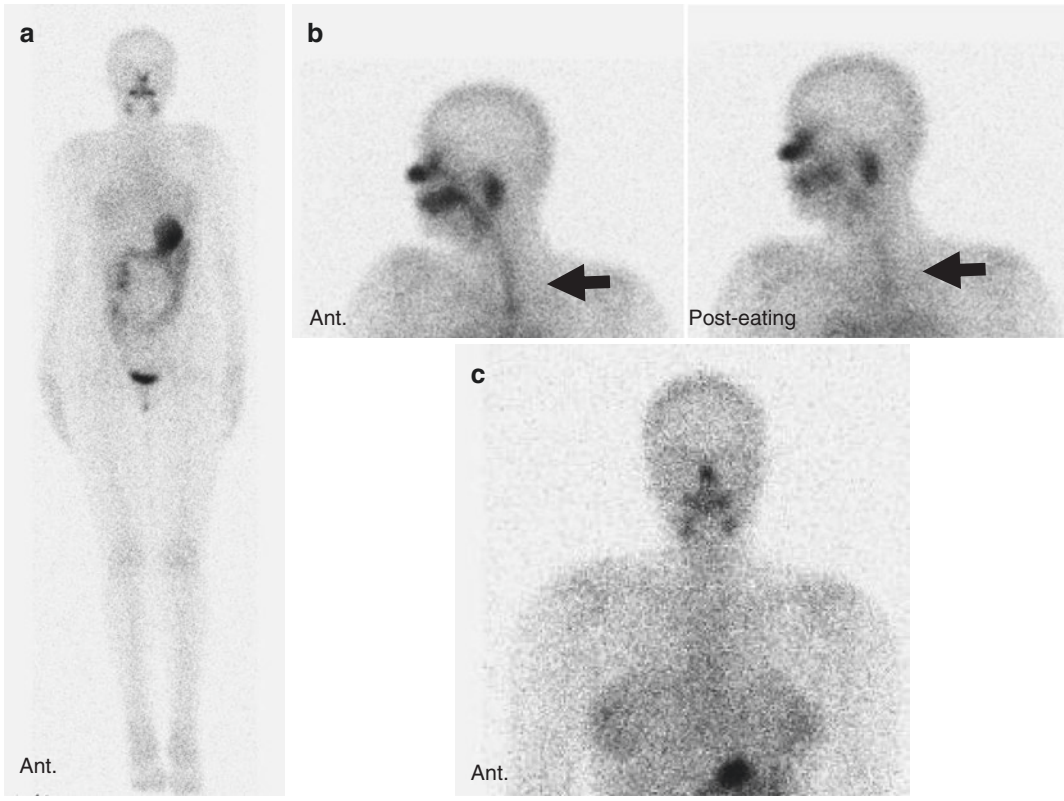

Fig. 14.1 Anterior whole-body image from a surveillance I-123 scan (**a**) demonstrates expected physiologic distribution of I-123 including activity within the salivary glands, nasal mucosa, oral cavity, gastrointestinal tract, and urinary system. Linear activity in the neck and chest on a I-123 scan in a different patient (**b**) demonstrates oral secretions within the esophagus that decreased following eating and drinking clear water. Anterior upper body image from a I-123 scan in a female patient (**c**) demonstrates physiologic uptake of iodine in normal breast tissue

with DTC, occurring in as many as 9% DxWBS and 30% post I-131 therapy whole-body scans (Fig. 14.2) [41]. The scan may demonstrate uptake within the thyroidectomy bed, which reflects thyroid remnant and/or thyroid bed disease, in locoregional nodes or at sites of possible distant metastases (Figs. 14.2, 14.3, and 14.4). Additional imaging, initially with SPECT/CT when available, or alternatively using anatomic modalities such as neck ultrasound (US), MRI, or CT without iodinated contrast can be used to accurately localize uptake noted on a DxWBS (Fig. 14.5).

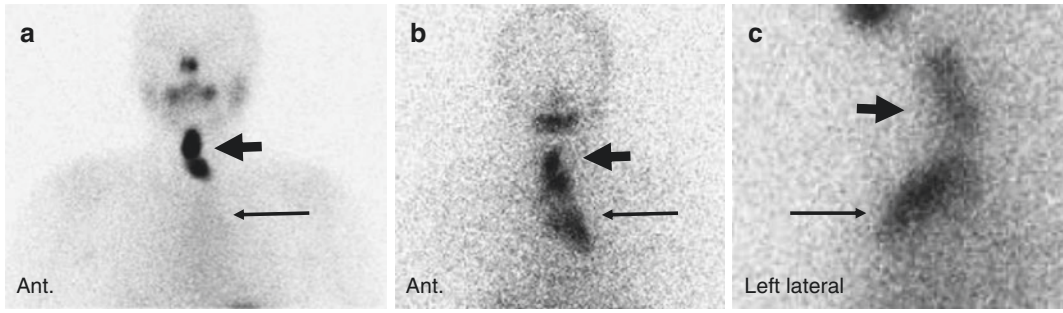

Fig. 14.2 A 12-year-old boy with papillary thyroid cancer, status post thyroidectomy. Anterior image from a postoperative I-123 scan (**a**) demonstrates two foci of intense uptake in the thyroid bed (thick arrow) most consistent with remnant thyroid. Faint diffuse uptake in the upper midline chest (long thin arrow) is consistent with thymic uptake, much more evident on the anterior (**b**) and lateral images (**c**) of the chest from a post I-131 therapy scan (long thin arrows). The uptake in the thyroid bed is demonstrated in (**b**) and (**c**) (thick arrows)

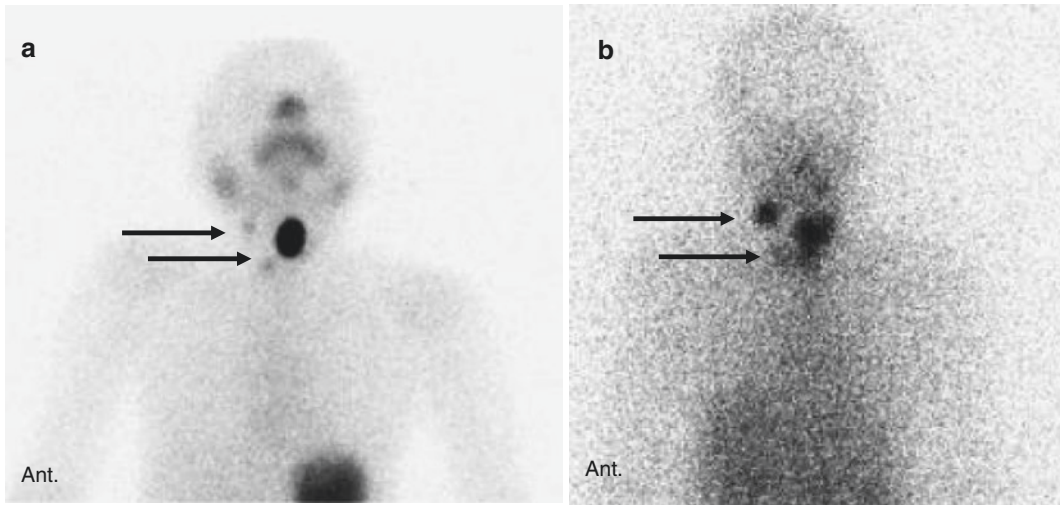

Fig. 14.3 An 11-year-old girl with papillary thyroid cancer, status post thyroidectomy. Anterior upper body images from postoperative I-123 scan (**a**) and post I-131 therapy scan (**b**) demonstrate an area of intense focal uptake in the expected location of the left thyroid bed, with the corresponding ultrasound image (**c**) demonstrating a circumscribed hypoechoic focus (white arrow), most consistent with remnant thyroid and/or residual disease in the thyroid bed. Two smaller foci of mild uptake in the right neck on images (**a**) and (**b**) (long thin arrows) are most consistent with nodal metastases, with one of the nodes in the right submandibular region (asterisk) shown on the corresponding ultrasound of the right neck (**d**)

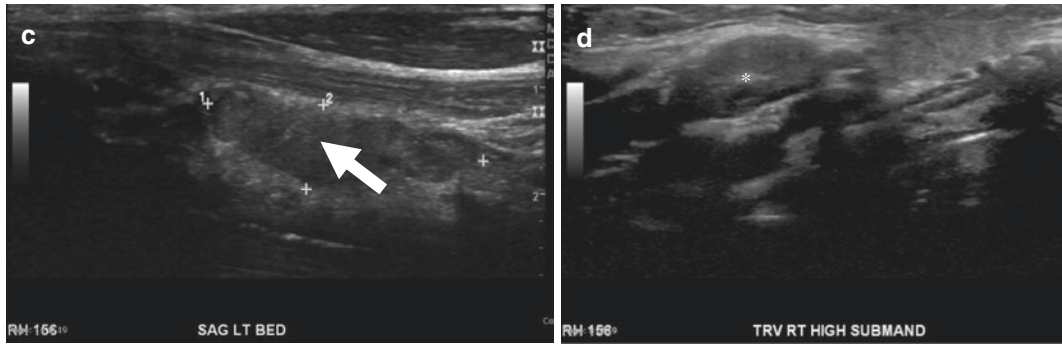

Fig. 14.3 (continued)

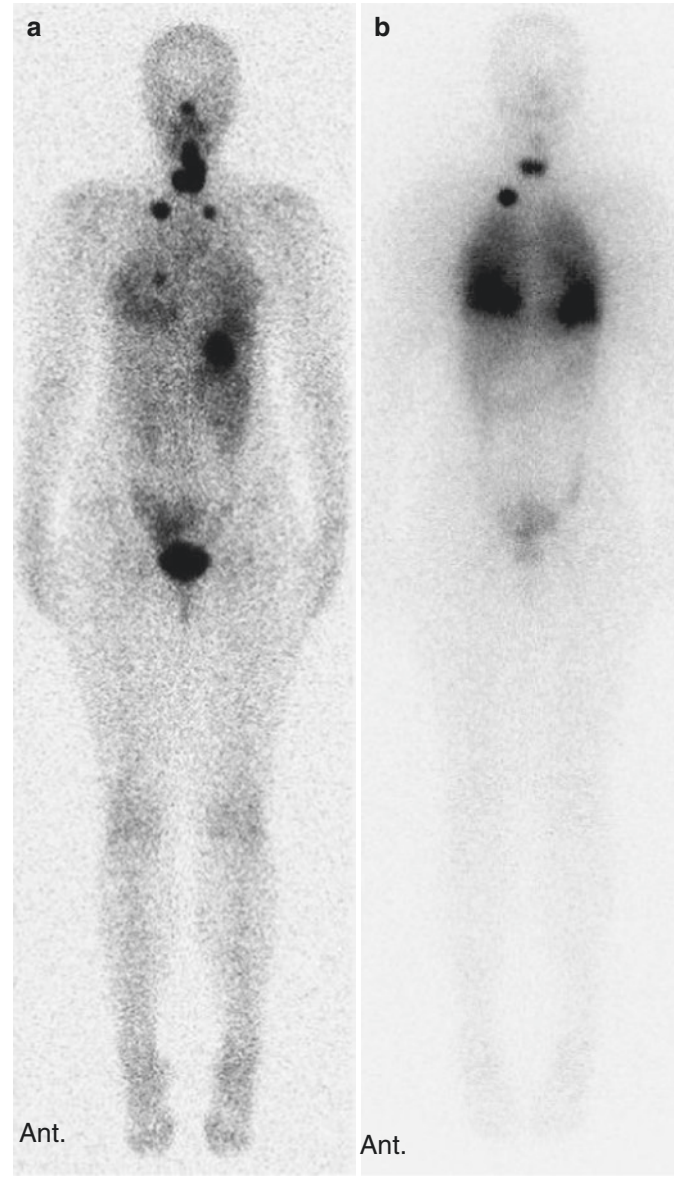

Fig. 14.4 An 18-year-old female status post thyroidectomy and left neck dissection for metastatic papillary thyroid cancer. Anterior whole-body image from a postoperative I-123 scan (**a**) demonstrates intense focal uptake within the thyroid bed consistent with remnant thyroid/residual disease. Two foci of uptake in the bilateral supraclavicular regions represent nodal metastases. A focus of uptake in the right lower chest is indicative of a pulmonary metastasis. Subtle diffuse lung uptake suggesting more widespread pulmonary involvement is also present. Anterior whole-body image from a I-131 post therapy scan performed 7 days after the oral administration of 155.3 mCi of I-131 (**b**) demonstrates diffuse intense bilateral lung uptake that is much more prominent compared to the pre-therapy I-123 scan. Note is made of mild hepatic uptake, consistent with functioning thyroid tissue (the result of radioiodine being assimilated into thyroxine in remnant thyroid tissue and then metabolized in the liver). The pattern of iodine uptake in the thyroid bed and the right supraclavicular node is similar to the pre-therapy scan. Iodine-avid left supraclavicular lymph node disease seen on the pre-therapy I-123 scan is not well appreciated

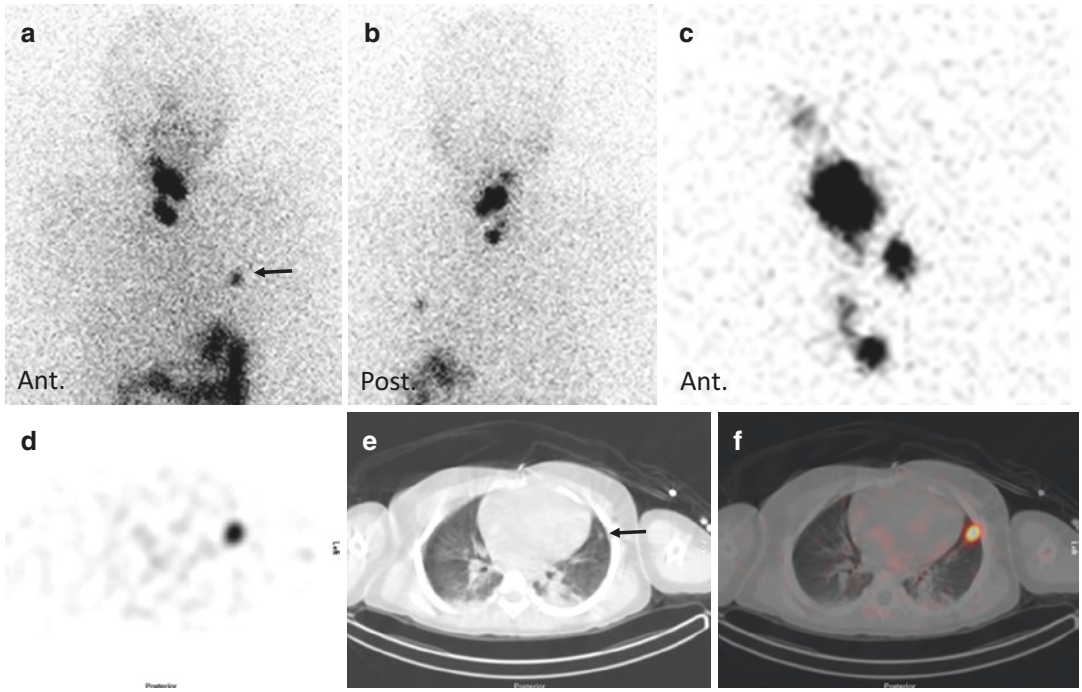

Fig. 14.5 A 6-year-old girl who underwent total thyroidectomy for a right-sided 4.2-cm papillary carcinoma with extra-thyroidal extension and angiolymphatic invasion. There was a right cervical 4-cm matted lymph node with extranodal extension. Anterior (**a**) and posterior (**b**) upper body images from a postoperative I-123 scan demonstrate considerable activity in the neck and a small focus of moderate uptake on the left side of the chest. Pinhole view of the thyroid (**c**) shows at least five foci of the uptake within the neck. Transverse SPECT (**d**), attenuation correction CT (**e**), and fusion (**f**) images through the mid-chest show markedly elevated uptake of I-123 in a small lingular nodule

14.5 Treatment-Related Considerations

14.5.1 I-131 Dose and Dosimetry

Approaches to choosing an appropriate dose of I-131 for treatment of DTC include empiric dosing or the use of dosimetry, which is typically based on bone marrow dose limits, but can be lesion-based as well. There are no standard administered activities of I-131 for the treatment of DTC in children. Further, there are no data that compare the safety or long-term outcomes using empiric and dosimetry-based treatment approaches or administered doses. Typically empiric dosing in children is based on adult guidelines, which are risk adapted to the pediatric population and adjusted for patient weight. In patients with remnant disease in the thyroidectomy bed alone, the dose may be as low as 30–50 mCi [16], but up to 100–150 mCi [33] depending on a variety of factors, whereas it is usually higher for those with cervical nodal disease (150–175 mCi and distant metastases (175–200 mCi)) [16, 33].

For children with diffuse lung uptake or extensive distant metastases, in those undergoing multiple I-131 treatments, or in children with potentially limited bone marrow reserve due to prior chemotherapy or radiation therapy, whole-body dosimetry can be used to calculate the largest possible administered dose of I-131. This allows practitioners to limit the absorbed activity to the blood to ≤200 rads (cGy) and whole-body retention at 48 h after administration to ≤4.44 GBq (120 mCi) in the absence, or 2.96 GBq (80 mCi) in the presence, of iodine-avid diffuse pulmonary

metastases, respectively [42–44]. Lesional dosimetry may aid in selecting effective activities of I-131 for children with substantial lung disease or large metastatic burden at other sites [43, 45–48]. Lesion-based toxicity constraints have not been validated in pediatrics and may potentially be higher in young children [8]. Additionally, these protocols are lengthy and not routinely available at all centers. The ATA pediatric task force recommended that all activities of I-131 should be calculated by experts with experience in dosing children due to differences in body size and iodine clearance in children in comparison to adults.

14.5.2 Outpatient Versus Inpatient Treatment Settings: Considerations

The current Nuclear Regulatory Commission (NRC) Patient Release Criteria allow the majority of the patients to undergo I-131 therapy for DTC as outpatients [49, 50]. A licensee is able to release patients, irrespective of administered activity, using dose rate measurements and total effective dose equivalent (TEDE) in mrem or mSv to meet NRC criteria. Patients can be released when the I-131 measured dose rate is ≤7 mrem per hour (h) at 1 m as measured by a dose rate meter [51]. Patients can also be released when the TEDE of a caretaker or family member is unlikely to exceed 500 mrem (5 mSv). If there is a possibility of the TEDE exceeding 100 mrem (1 mSv) in any person, relevant written and verbal precaution instructions are necessary [49, 52].

Inpatient therapy and consultation with the radiation safety officer (RSO) should be considered when [8, 50]:

1. Proposed treatment dose of I-131 is ≥200 mCi (7400 MBq) or TEDE is likely to exceed 500 mrem (5 mSv) to an adult family member or caregiver or to exceed 100 mrem (1 mSv) to a pregnant woman, child, or a member of the general public.
2. Patient is of a young age or unable to comprehend and comply with the tasks required for outpatient therapy.
3. Various other issues including incontinence, travel/housing limitations, cognitive/psychiatric limitations, etc.

In general, children and adolescents with PTC impart the highest dose of radiation to others during the initial 1–2 days following I-131 therapy. For young children, this may be especially problematic, particularly if they are not yet toilet trained or are unable to sleep alone.

14.5.3 Patient Preparation, Education, and Radiation Safety

The patient's ability to comply with preparatory regimens (described in the Sect. 14.4) should be established prior to therapy in order to maximize the efficacy of I-131 treatment. A negative pregnancy test needs to be confirmed in all females of childbearing age. Pregnancy and breast-feeding are absolute contraindications to I-131 therapy. Likewise, an appropriate response to withdrawal or r-TSH stimulation should be verified by demonstrating a serum TSH level of greater than 30 mIU/L. Risks (both short- and long-term side effects) and benefits of I-131 therapy need to be discussed and radiation safety instructions reviewed, with written educational materials provided. Written informed consent for I-131 treatment is obtained from the patient, parent, or legal guardian, depending on the age of the patient. After verification of the prescribed I-131 activity, the nuclear medicine physician (authorized user) should directly witness or administer the radioiodine to the patient orally. Just before the administration of I-131, the child is duly identified, preferably using two forms of identification. Those children who are candidates for outpatient treatment are discharged from the nuclear medicine department shortly after the administration of the therapeutic dose. For patients undergoing inpatient therapy, standard hospital orders are typically written by the admitting pediatric endocrinologist/oncologist. The radiation safety officer or nuclear medicine technologist obtains baseline patient radiation

emissions immediately following the oral administration of the I-131 dose and once every 12–24 h during the inpatient stay until release criteria are met and the patient discharged.

ATA pediatric guidelines recommend that all children receiving I-131 therapy for DTC receive adequate hydration in order to facilitate clearance of the radioisotope. Additional supportive care with antiemetic medications and stool softeners/laxatives can be administered as needed. Per these guidelines, sour candy or lemon drops may be given after I-131 treatment, but routine use of other adjunct agents such as lithium and amifostine is not recommended [8].

14.5.4 Posttreatment Whole-Body Scintigraphy

All patients undergoing I-131 therapy should be imaged 4–7 days after treatment [8] as there is a dose-related sensitivity of I-131 in disease detection [53, 54]. The post-therapy scans may detect new or additional foci of disease, although it remains unclear if this knowledge informs future treatment or outcomes (Fig. 14.6). The addition of SPECT/CT may aid in localizing uptake and particularly in distinguishing remnant thyroid tissue from nodal metastases in the thyroid bed [55].

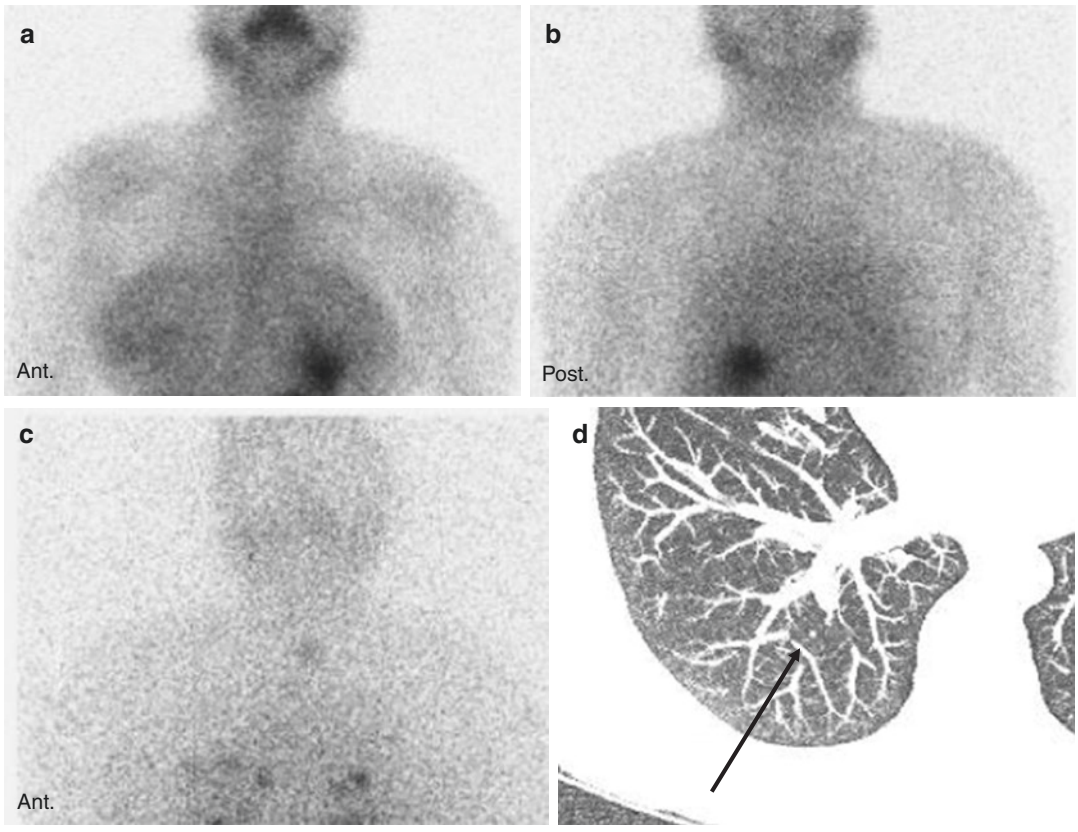

Fig. 14.6 A 19-year-old female with history of papillary thyroid cancer status post thyroidectomy, radioiodine therapy, and neck dissection, with interval decreased, but persistently detectable thyroglobulin. Anterior (**a**) and posterior (**b**) upper body images from a I-123 scan reveals no definite abnormal focal uptake. Anterior upper body image from a post-therapy I-131 scan (**c**) demonstrates a focus of mild tracer uptake in the midline neck in the thyroid bed that likely represents thyroid bed disease. Multiple foci of tracer activity within bilateral lungs are concerning for pulmonary metastases. Single transaxial image of the lower chest CT image (**d**) demonstrates a tiny right pulmonary nodule. Multiple similar appearing nodules were seen throughout both the lungs

14.5.5 Risks of I-131 Therapy

There can be early-, intermediate-, and long-term side effects related to I-131 therapy. Short- and intermediate-term risks include sialadenitis, xerostomia, thyroiditis, stomatitis, gastroenteritis, xerophthalmia, nasolacrimal duct obstruction, transient gonadal dysfunction, transient leukocytopenia and thrombocytopenia, and very rarely recurrent laryngeal nerve injury or acute radiation pneumonitis [8, 23, 56, 57]. Late side effects include chronic sialadenitis and xerostomia, xerophthalmia, decreased fertility, pulmonary fibrosis, bone marrow aplasia, genetic defects including chromosomal damage, and the development of second primary malignancies [23, 32, 58].

Even a single dose of I-131 may lead to permanent salivary gland dysfunction, an increased incidence of dental caries, and an increase risk of salivary gland malignancy [59, 60]. The use of preventative measures such as sour candies or lemon juice beginning 24 h following I-131 dosing in conjunction with robust hydration for 3–5 days [50] may prevent salivary gland dysfunction, although none of these prophylactic measures have been formally evaluated in children treated with I-131. Pain and swelling in thyroid remnant or nodal metastases are seen in 10–20% of cases. Transient leukocytopenia and thrombocytopenia occur in up to two-thirds of patients a few weeks after treatment, with return to baseline by 3 months [61]. Long-term bone marrow suppression is rare, but reported, and therefore it is essential to allow for recovery of bone marrow between I-131 treatments [62, 63].

Gonadal damage has been described in both women and men [64, 65]. Temporary menstrual irregularities including amenorrhea or oligomenorrhea may occur after I-131 therapy in about 8–27% of women. However, long-term rates for infertility, miscarriages, and fetal malformations do not appear to be increased in females after I-131 therapy, particularly when conception is delayed up to a year following I-131 treatment [64, 66–68]. In postpubertal males, a transient rise in follicle-stimulating hormone is common and may persist for up to 18 months [65, 68, 69]. Increasing cumulative activities of I-131 may lead to decreased spermatogenesis with postpubertal testes more vulnerable than prepubertal testes to these radiation effects [70]. Current guidelines recommend that males avoid attempts at conception for at least 4 months post I-131 therapy. Additionally, postpubertal males should be counseled and sperm banking considered for postpubertal males receiving cumulative activities of 400 mCi (14.8 GBq) [14].

Several recent studies have suggested the occurrence of genetic damage related to I-131 therapy, evidenced by an increase in the number of dicentric chromosomes in peripheral leukocytes as well as by the presence of chromosomal aberrations most prevalent in chromosomes 1, 4, and 10; such aberrations have persisted for up to 4 years after treatment [71–73].

Large long-term follow-up studies by Brown and Rubino et al. [31, 32] have confirmed that I-131 radiotherapy is associated with an increased risk of the development of second malignancies as well as with an increase in overall mortality for patients with DTC. The risk for the development of secondary malignancies was found to be greater in younger patients. An increased risk of both solid tumors and leukemias was found with increasing cumulative activities of I-131 administered [32]. A recent systematic review and metanalysis of the above two studies by Sawka et al. reported a small but significant increased relative risk of second primary malignancy, in particular leukemia, in patients treated with I-131 [74].

An important long-term effect of I-131 radiotherapy is the development of pulmonary fibrosis in patients with lung metastases. The risk of pulmonary fibrosis correlates with the intensity of I-131 uptake and is seen in 10% of children compared to only 1% of adults with DTC [21, 63]. The risk of pulmonary fibrosis appears to be dependent on the retained dose of I-131 in the lungs of patients with DTC and pulmonary metastases. Therefore it is recommended to obtain dosimetry, using a treatment limit of 80 mCi (2.96 GBq) whole-body retention of I-131 at 48 h in DTC patients with pulmonary metastases [16, 42, 75, 76].

14.6 Neuroblastoma Epidemiology

Neuroblastoma is the most common extracranial solid tumor in children and constitutes ~30% of infantile cancers [77–80]. The median age at diagnosis is 15 months. It is derived from primordial neural crest cells that inhabit the sympathetic ganglia and adrenal medulla. The most common sites of origin are the adrenal glands (48%), followed by extra-adrenal retroperitoneum (20%) and chest (16%), although it can occur anywhere along the sympathetic chain from the neck though the pelvis [81, 82]. Metastases most commonly involve the bone marrow or cortical bone, lymph nodes, and liver [83]. Approximately 50% of patients present with hematogenous metastases [78].

There are two different staging systems for neuroblastoma. The International Neuroblastoma Staging System (INSS), developed in 1988 [80, 84, 85], bases staging on the extent of residual disease following surgery. Features of the INSS are summarized in Table 14.2. Since the INSS is based on the degree of surgical resection and pathologic findings, it is not suitable for pretreatment risk classification of disease necessary for evaluating the success of large clinical trials. More recently, the International Neuroblastoma Risk Group Staging System (INRGSS) was developed to facilitate the comparison of risk-based clinical trials and published in 2009. Features of this image-based, pretreatment staging system are listed in Table 14.3 [80, 82, 86]. The INRGSS differs from the INSS in that the extent of disease is determined by the presence or absence of image-defined risk factors and metastatic disease at the time of diagnosis, prior to receiving any type of treatment including surgery. Image-defined risk factors are surgical risk factors, identified on imaging, that render total tumor resection risky or difficult at the time of diagnosis. In the INRGSS, localized tumors are classified as stage L1 when no image-defined risk factors are present; L2 disease is present if one or more image-defined risk factors are identified; stage M indicates disseminated disease, which is comparable to the INSS stage 4. Similar to the 4S category of the INSS system, the INRGSS also has a special MS category where metastases are confined to the liver, skin, and/or marrow in patients <18 months of age versus <12 months of age in INSS. Compared with the focus on surgical and pathologic findings in the INSS, the emphasis in the INRGSS has shifted to diagnostic imaging using either contrast-enhanced CT or MR of the primary tumor and ^{123}I-mIBG whole-body imaging as requisite evaluations to be obtained at diagnosis [86]. Since imaging records can be retrospectively reviewed, a system such as the INRGSS, which is based on preoperative imaging, is more reproducible and robust than one based on surgical findings. Additionally, experts can centrally review the imaging data, thus increasing the likelihood of uniform evaluation of disease extent and thus facilitating the comparison of risk-based clinical trials conducted in different centers worldwide by defining homogeneous pretreatment patient

Table 14.2 Summary of the International Neuroblastoma Staging System (INSS)

Stage	Description
1	Localized tumor with complete gross resection No regional lymph node involvement
2	Localized tumor with incomplete gross resection or ipsilateral lymph node involvement
3	Tumor crossing midline or contralateral lymph node involvement
4	Tumor with distant metastases
4S	Patient <12 months with localized tumor and metastases confined to the liver, skin, and/or bone marrow

Table reproduced with permission from Elsevier publishing company [80]

Table 14.3 International Neuroblastoma Risk Group Staging System (INRGSS)

Stage	Description
L1	Localized tumor not involving vital structures and confined to one body compartment (neck, chest, abdomen, or pelvis)
L2	Localized/regional tumor with one or more imaged-defined risk factors (i.e., involvement of two body compartments, encasement of major vascular structures, invasion of adjacent organs or intraspinal extension)
M	Tumor with distant metastases
MS	Patient <18 months with metastases confined to the liver, skin, and/or bone marrow

Table reproduced with permission from Elsevier publishing company [80]

cohorts. Of note, the INRGSS is not intended to be a substitute for the INSS, but rather, it is recommended that both systems be used in parallel.

The consensus INRG classification scheme includes the following criteria for risk group stratification—INRG stage, age, histologic category, grade of tumor differentiation, MYCN status, presence/absence of 11q aberrations, and tumor cell ploidy. Based on these criteria, children with neuroblastoma are placed in four different pretreatment risk subsets: very low risk (5-year event-free survival (EFS) >85%), low risk (5-year EFS >75–85%), intermediate risk (5-year EFS ≥50–75%), and high risk (5-year EFS<50%) [82]. The high-risk patients are generally treated with aggressive multimodality treatment regimens including chemotherapy, surgical resection, autologous stem cell transplant (SCT), external beam radiation, and minimal residual disease therapy that includes tumor-directed monoclonal antibody therapy and use of the differentiating agent 13-cis-retinoic acid [87, 88]. Despite the increasing intensities of therapy employed, prognosis for these patients remains poor.

When radiolabeled with either ^{131}I or preferably for diagnostic imaging ^{123}I, mIBG is concentrated by approximately 90% of neuroblastoma tumors, with uptake identified in primary soft tissue tumors as well as in sites of osseous and marrow metastases [89]. The physiologic distribution of mIBG includes uptake/activity in the salivary glands, heart, liver, adrenal glands, kidneys, urinary bladder, bowel, muscles, and occasionally brown fat and thyroid gland (if not blocked pharmacologically). The use of I-123 labeled mIBG in comparison to ^{131}I-mIBG allows for superior image quality and disease detection. With ^{123}I-mIBG, SPECT or SPECT/CT can be used, which helps increase the sensitivity of disease detection and allows for improved localization, particularly in the torso (Fig. 14.7). ^{123}I-mIBG is the cornerstone of staging and treatment response assessment in neuroblastoma.

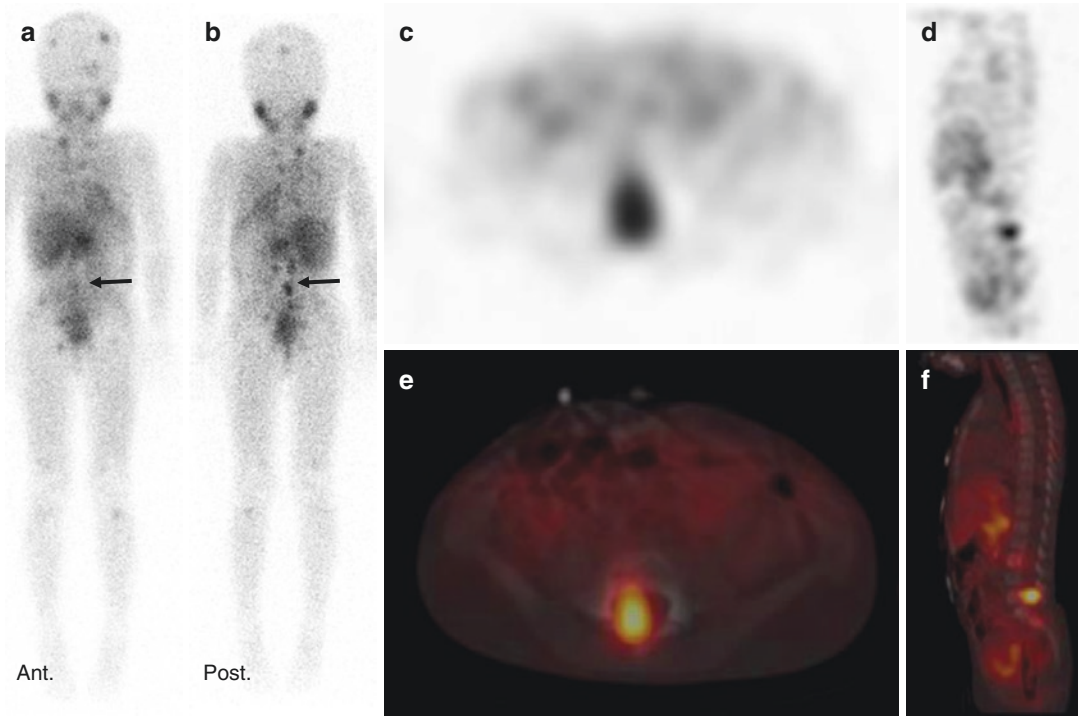

Fig. 14.7 A 5-year-old girl with recurrent neuroblastoma. Anterior (**a**) and posterior (**b**) whole-body images 24 h after injection of ^{123}I-mIBG reveal multifocal skeletal disease including a prominent focus in the midline lower abdomen, which appears to localize to the lower lumbar spine on these planar images. Transverse (**c**) and sagittal SPECT (**d**) and SPECT/CT (**e**, **f**) images localize this uptake within the vertebral canal at L5 rather than the vertebra itself

The high mIBG avidity and the known radiosensitivity of neuroblastoma combined with the poor prognosis of high-risk neuroblastoma make ^{131}I-mIBG an attractive targeted therapeutic agent in this patient group. ^{131}I-mIBG has been studied as a targeted therapy in the setting of both relapsed and newly diagnosed neuroblastoma. The combination of ^{123}I-mIBG for diagnostic and ^{131}I-mIBG for therapy of neuroblastoma is an example of theranostics.

14.7 Background and Current Status of ^{131}I-mIBG Therapy

Metaiodobenzylguanidine is a norepinephrine analog that concentrates in sympathetic nervous tissue. It was first developed and utilized for adrenal imaging by Wieland and Beierwaltes in 1979 [90, 91]. The cytocidal effect of beta-particle emission by ^{131}I-mIBG was recognized soon after its development leading to the prompt exploration of the use of ^{131}I-mIBG in the therapy of neuroendocrine tumors. ^{131}I-mIBG therapy was first attempted in pheochromocytoma patients in 1983 [92]. In 1986, the first report of the use of ^{131}I-mIBG to treat six children with neuroblastoma was published [93]. Since then, several trials using therapeutic ^{131}I-mIBG in patients with neuroblastoma have been performed.

14.7.1 Mechanism of ^{131}I-mIBG Uptake in Neuroblastoma

^{131}I-mIBG is an aralkylguanidine, which is a structural analog of the neurotransmitter norepinephrine (NE). ^{131}I-mIBG enters neuroendocrine cells by two different pathways, a specific uptake system (uptake-one) and a nonspecific uptake system. Uptake-one is an active process via a NE transporter (NET) with a high affinity but a low capacity for ^{131}I-mIBG. It is the predominant uptake system for ^{131}I-mIBG. The nonspecific uptake pathway is a passive diffusional mechanism [94–98]. Most neuroendocrine cells store ^{131}I-mIBG in neurosecretory granules, while in contrast, neuroblastoma cells typically store ^{131}I-mIBG in the cytoplasm and mitochondria [99, 100].

14.7.2 ^{131}I-mIBG Therapy: The Past and Present

^{131}I-mIBG remains an experimental agent in the treatment of high-risk neuroblastoma, although several phase I and phase II studies have demonstrated efficacy of ^{131}I-mIBG therapy for this disease. ^{131}I-mIBG therapy has been most widely studied in the setting of relapsed or refractory neuroblastoma, i.e., patients whose disease progressed after an initial response or those who failed to respond to induction chemotherapy. More recently, ^{131}I-mIBG has also been used as a first-line treatment (during induction) and in conjunction with myeloablative chemotherapy after response to initial chemotherapy (consolidation). A recent systematic review of ^{131}I-mIBG therapy in neuroblastoma by Wilson et al. [101] that included 30 studies previously reported in 51 publications concluded that even though the true effectiveness of ^{131}I-mIBG in comparison to other treatments remains unknown in the absence of randomized controlled trials, the high response rates of approximately 30% justify further studies of this agent in patients with relapsed or refractory high-risk neuroblastoma. The authors also concluded that it is difficult to adjudicate the role of ^{131}I-mIBG therapy during induction and consolidation given the limited existing data.

14.7.2.1 Relapsed/Refractory and Consolidation Studies

Several studies have used ^{131}I-mIBG therapy in the setting of relapsed or refractory high-risk neuroblastoma, either as a monotherapy or in combination with chemotherapy. A recent meta-analysis of 27 of these studies [101] reported an overall mean tumor response of 32%, although there was a wide variability ranging from 4% to 75%. Tumor-response rate was 39% (48/124) in patients who received chemotherapy concomitantly with ^{131}I-mIBG compared to 32% (199/629) for those receiving ^{131}I-mIBG alone.

Monotherapy: Historically, beginning around 1987, ^{131}I-mIBG had been used as single agent (monotherapy) in therapeutic trials in both Europe and North America. Multiple phase I and phase II trials have evaluated feasibility, toxicity,

and the most appropriate ^{131}I-mIBG treatment dose [102–113]. In 2007 Matthay et al. [114] reported the results of the largest trial using ^{131}I-mIBG as a monotherapy in patients with progressive, refractory, or relapsed high-risk ^{131}I-mIBG-avid neuroblastoma. In this three-institution phase II trial, 148 patients with cryopreserved stem cells available received 18 mCi/kg (666 MBq/kg) of ^{131}I-mIBG, whereas an additional 16 patients without available cryopreserved stem cells received 12 mCi/kg (444 MBq/kg) of ^{131}I-mIBG. Overall response rate to ^{131}I-mIBG therapy in this trial was 36%. An age-related response was also noted. The safety and efficacy of administering multiple doses of ^{131}I-mIBG (tandem infusions) have also been studied, with some evidence that the most benefit occurs with the first ^{131}I-mIBG treatment [115–117].

Combination therapies: To maximize the therapeutic effect of ^{131}I-mIBG therapy (and to avoid the development of resistant tumor clones), several groups have performed combination therapies of ^{131}I-mIBG with high-dose chemotherapy and autologous SCT. In a phase II trial of the New Approaches to Neuroblastoma Therapy (NANT) consortium, the largest ^{131}I-mIBG transplant trial to date, 12 mCi/kg (444 MBq/kg) of ^{131}I-mIBG in combination with a chemotherapy-conditioning regimen was incorporated into a myeloablative transplantation regimen in two cohorts of patients with refractory neuroblastoma. The addition of ^{131}I-mIBG therapy did not increase bone marrow or organ toxicity compared to the use of chemotherapy alone [118]. Klingebiel et al. [119] recruited 11 patients from the German Neuroblastoma Study NB90. These 11 patients who had INSS stage 4 disease and a response to initial chemotherapy received a single high dose of ^{131}I-mIBG, immediately followed by chemotherapy, stem cell support, and subsequent anti-GD2 antibody therapy. Objective tumor responses, assessed after recovery from stem cell transplantation, were identified in 4/11 patients, and 4/11 patients had a continued response from induction.

A useful approach to improve response to ^{131}I-mIBG therapy in high-risk neuroblastoma is to enhance the expression and function of NET by combining ^{131}I-mIBG, with other agents, which in turn increases mIBG uptake and therapeutic effect. Different strategies to augment NET expression include pretreatment with corticosteroids, gamma interferon, retinoic acid (in combination with gamma interferon), cisplatin, or doxorubicin; the use of radiosensitizers such as vorinostat, irinotecan, or topotecan; and the use of hyperbaric oxygen, gene therapy, or ionizing radiation from external beam radiation [120, 121].

14.7.2.2 First-Line Therapy

Although historically mIBG has been utilized in the treatment of relapsed or refractory high-risk neuroblastoma, small pilot studies suggest efficacy when given at the time of diagnosis when followed by surgery or in conjunction with induction chemotherapy, i.e., when ^{131}I-mIBG is used as a frontline treatment [122, 123]. The use of frontline radionuclide therapy helps to reduce overall tumor volume, thus enabling surgical resection; it decreases the toxicity associated with chemotherapy as well as decreases the likelihood of early drug resistance [124].

In an early study by Hoefnagel et al. [125], the response rate with ^{131}I-mIBG administered at diagnosis in 31 children with inoperable neuroblastoma was greater than 70% and resulted in significantly less side effects than traditional chemotherapeutic regimens. De Kraker et al. [124], administering two sequential fixed dose cycles of ^{131}I-mIBG treatment at induction in 44 patients with newly diagnosed high-risk neuroblastoma, reported a response rate of 73%. A recent retrospective multicenter analysis of a cohort pilot regimen of upfront ^{131}I-mIBG therapy in newly diagnosed stage IV neuroblastomas, prior to the standard German Pediatric Oncology Group neuroblastoma 2004 protocol, reported that induction therapy with ^{131}I-mIBG therapy was feasible, tolerable, effective, and induced early responses in this patient population [126]. Within the Children's Oncology Group (COG), ^{131}I-mIBG therapy during induction is currently being investigated in ANBL09P1, in which therapeutic doses of ^{131}I-mIBG are being administered after the fifth cycle of induction chemotherapy [120].

14.8 Establishment of a Multidisciplinary ^{131}I-mIBG Treatment Program

The administration of ^{131}I-mIBG therapy in neuroblastoma is presently being performed in more than 15 centers in North America. The planning and operational aspects of ^{131}I-mIBG therapy program have been published previously [120, 127–131], but it is important that each center develops an individualized program utilizing their institutional resources and strengths. Central considerations and processes that are involved in the development and execution of a successful ^{131}I-mIBG therapy program are described below.

14.8.1 Preliminary Planning

The first consideration in the establishment of an ^{131}I-mIBG therapy program is to determine the clinical need and the institutional resources available. Active commitment and participation of personnel across different specialties during both the planning and implementation phases of the ^{131}I-mIBG therapy program are the keys to developing a successful program. Pediatric oncologists who treat patients with neuroblastoma and identify a cohort eligible for ^{131}I-mIBG therapy typically drive the clinical demand for a therapy program and also take responsibility for the medical care of these patients during the inpatient admission for this treatment. Nuclear medicine staff, including physicians, technologists, and physicists, usually direct the receipt, handling, testing, and administration of the ^{131}I-mIBG. The institutional RSO needs to be involved not only in the planning process but in the operational processes as well. It may be useful to include a radiopharmacist in the planning stages depending on the commercial pharmacy supplying the ^{131}I-mIBG for treatment. Nursing managers and staff are integral members of the planning and operations team and often help facilitate scheduling and planning the patient admission as well as providing direct patient care conjointly with family members. Finally, hospital engineers and managers have a significant role in planning, facilitating, and supervising any needed facility renovations or new construction.

14.8.2 Treatment Room Location, Design, and Shielding

Both clinical and radiation safety criteria drive the location and design of the therapy room where the patient is treated on an inpatient basis. It is important to locate the treatment room on a clinical floor where the staff are familiar with caring for oncology patients. The treatment room should be designed to minimize the radiation to the caregivers and other individuals. In general, a private room with a dedicated bathroom and sink is required. The room should preferably be in a corner location or, if not feasible, be isolated to an area with limited patient and personnel occupancy in neighboring spaces. Determining the amount of shielding necessarily requires knowledge of the layout of the treatment room and adjacent areas as well as the radiation level allowable in the adjacent space, the latter being driven by its occupancy factor. It is useful to have an anteroom adjacent to the isolation room so that the caregiver(s) can stay close to but still be shielded from radiation exposure from the patient. The anteroom is also used for storage of radiation monitoring equipment and of the protective clothing that is worn when caregivers enter the therapy room. The floor plan of the treatment room and adjacent space at Boston Children's Hospital is provided in Fig. 14.8.

14.8.3 Operational Planning, Training, and Education

A multidisciplinary effort is indispensable in planning the operations and procedures of an ^{131}I-mIBG therapy program. As ^{131}I-mIBG is an investigational agent and entails the human administration of large doses of radioactivity, appropriate regulatory approval is necessary. An oncologist is typically the principal investigator on the research protocols required to administer ^{131}I-mIBG therapy, but in some settings, it may be

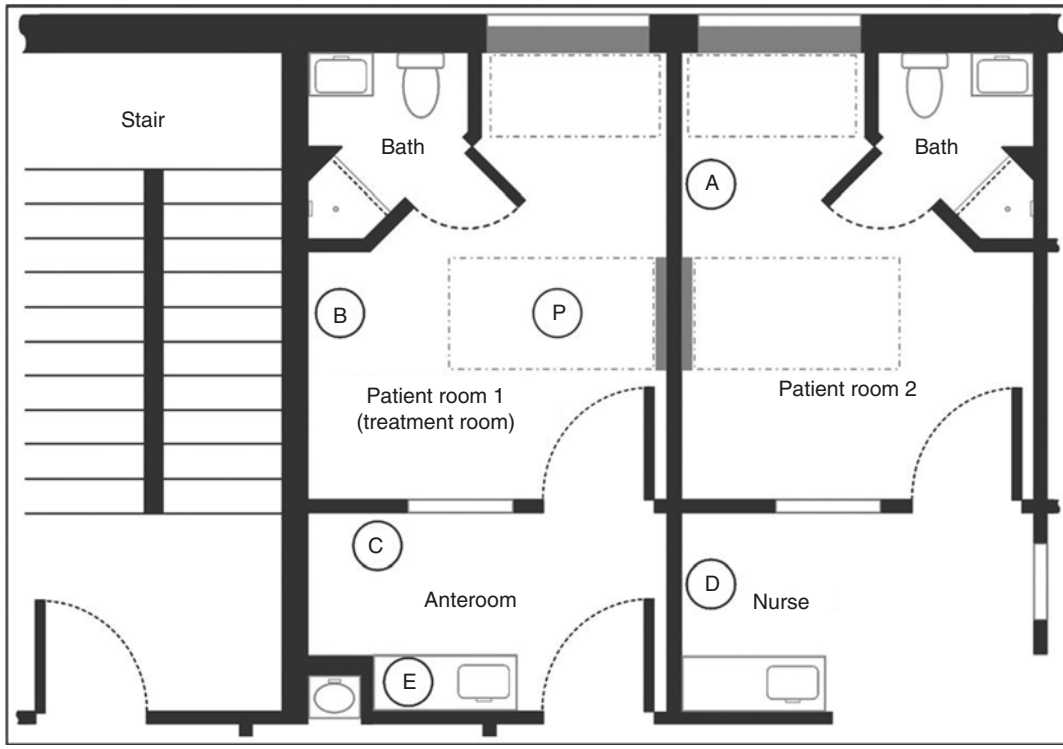

Fig. 14.8 Treatment room design. The ^{131}I-mIBG treatment room design at Boston Children's Hospital. There is an anteroom between the treatment room and hallway. The treatment room is located between another patient room (PATIENT ROOM 2) and a stairwell. On the floor above is a general space and below is a two-story high mechanical space. Shielding calculations were determined by the patient being located at point P, 1.2 m from the wall. On the basis of our calculations, the wall between the treatment room and the adjacent patient room (A) required 2.5 cm of lead, the wall adjacent to the stairwell (B) required 0.65 cm of lead, the wall between the treatment room and the anteroom (C) and the ceiling required 1.3 cm of lead, and the floor required 0.32 cm of lead. Walls D and E did not require additional shielding as adequate protection was afforded by the primary barriers and distance. Semin. Nucl. Med. 2011;41:354–63. Reproduced with permission from Elsevier

a nuclear medicine physician who undertakes this responsibility. Approval of the ^{131}I-mIBG therapy program from internal hospital committees, including the institutional review board for human subjects and the Radiation Safety Committee, should be obtained during the design process and before it is operational. In general, the RSO, supported by the Radiation Safety Committee, is the most suitable institutional liaison to interact with the governmental regulatory authorities when obtaining licensing of the facility.

Training and education are essential components in successful implementation of an ^{131}I-mIBG therapy program. Training includes developing medical, nursing, and radiation safety guidelines for the safe administration of this or other targeted radiotherapeutic agents to the patient. It also involves developing educational tools, including radiation safety training, for the patients, parents, and all staff involved in caring for these patients (Fig. 14.9).

14.8.4 Logistics of ^{131}I-mIBG Therapy Delivery to Patients

14.8.4.1 Nuclear Medicine and Clinical Care Processes

High-dose ^{131}I-mIBG therapy is administered on an inpatient basis and only to medically stable patients. Once the oncologist establishes the candidacy of a patient for ^{131}I-mIBG therapy, he or

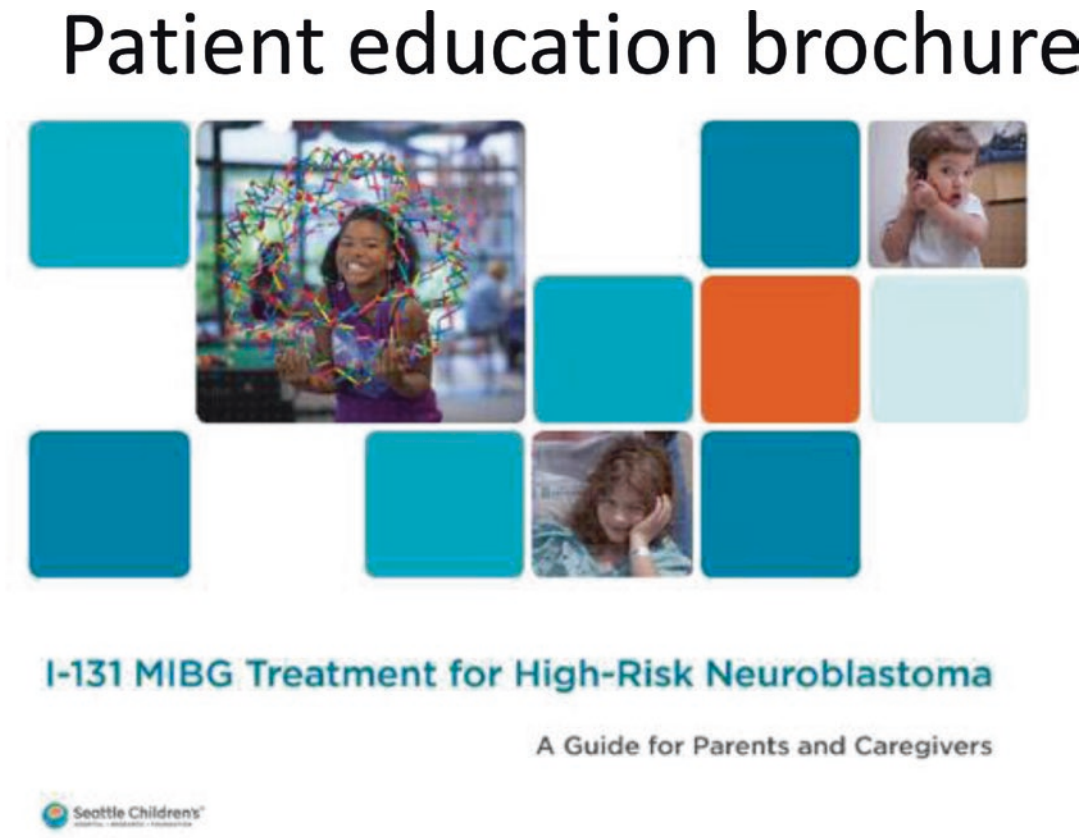

Fig. 14.9 Example of one of the educational slides created for family caregivers whose children are undergoing ^{131}I-mIBG therapy for neuroblastoma Semin. Nucl. Med. 2016;46:184–202. Reproduced with permission from Elsevier

she works with the nuclear medicine department to determine not only the date of treatment but the appropriate administered therapeutic activity. The administered dose is based on the requirements of the specific clinical trial protocol that the patient is enrolled in and typically varies from 5 to 18 mCi/kg at the investigators' discretion. Any dose ≥12 mCi/kg requires that the patient have stored stem cells available. Once all requirements are met, the nuclear medicine division contacts the appropriate radiopharmacy at such time as to order and ensure the availability of the required amount of ^{131}I-mIBG for the day of the therapy.

On the day of the treatment, the ^{131}I-mIBG is received and processed in the pharmacy of the receiving nuclear medicine department. Quality control testing should be performed at the receiving facility and/or at a contracted commercial radiopharmacy following appropriate established guidelines. The agent is diluted in normal saline and drawn into a syringe, which is placed in a shielded pump apparatus (Fig. 14.10). The dose is transported to the therapy room after verification of the activity in a dose calibrator and after completion of all steps ensuring the patient and staff are ready for the infusion. Informed written consent is obtained, and patient identification is performed prior to administration of the therapeutic agent by the nuclear medicine staff.

^{131}I-mIBG is infused intravenously over 90–120 min. EKG monitoring and automated blood pressure measurements are done during infusion. Younger patients are catheterized, while older patients are encouraged to void frequently. All caregivers are required to wear personal protective clothing and dosimeters to reduce direct radiation exposure, to monitor exposure levels,

Fig. 14.10 Shielded syringe pump. An example of a shielded syringe pump used for administration of ^{131}I-mIBG. The shielded syringe pump (Graseby Injection Pump Shield, Biodex) is located behind an L-block shield on a specially designed steel cart. The dose of ^{131}I-mIBG is drawn into a 30-mL syringe that is placed in the pump before transport to the treatment room. Semin. Nucl. Med. 2011;41:354–63. Reproduced with permission from Elsevier

and to prevent contamination of spaces outside the patient room. Within the patient isolation room, mobile lead shields are used to shield parents and personnel.

Since the majority of the direct care of the patient after ^{131}I-mIBG therapy is provided by one or two adult family members, they undergo training in basic patient care, appropriate use of personal protective clothing, handling and disposal of body fluids, and radiation safety issues. As neuroblastoma patients undergoing ^{131}I-mIBG therapy are typically young children who must stay in the hospital for several days during this procedure, it is extremely advantageous to have a child life specialist involved in the patient's care.

For most patients, discharge timing is driven by radiation safety concerns. Discharge generally depends on patient physiognomies as well as the administered dose and usually occurs 3–5 days after ^{131}I-mIBG administration. Criteria for discharge are determined by regulatory commitments made during the licensing process. Licensees are permitted to authorize discharge if the TEDE to any other individual from exposure to the released patient is not likely to exceed 500 mrem (5 mSv). The licensee is also required to provide the released individual or their family with specific instructions on recommended actions to maintain low doses to other individuals if the TEDE to any other individual is likely to exceed 100 mrem (1 mSv) [130]. Patients can also be released when the dose rate measured at 1 m has fallen to less than 7 mrem/h (0.07 mSv/h) [129].

14.8.4.2 Post-therapy Imaging

Whole-body imaging is obtained in the nuclear medicine department prior to patient discharge. Static images are usually obtained for 300,000–500,000 counts using a high-energy collimator. During this short imaging session, which is best performed early in the morning at the start of a regular workday, it is recommended that the adjacent imaging rooms be empty in order to minimize radiation exposure to other patients and staff and to minimize the likelihood of high-energy ^{131}I photons penetrating cameras/detectors in adjacent rooms and compromising image quality. These post-therapy images demonstrate the distribution pattern of the therapeutic dose within the body (Fig. 14.11). Often, post-therapy scans demonstrate physiologic uptake in the cerebellum and basal ganglia not appreciated on diagnostic ^{123}I-mIBG scans. Likewise, on post-therapy scans, mIBG uptake in the normal adrenal gland may be more pronounced than on diagnostic imaging. Further, as also occurs on post-therapy imaging of children with DTC, there is a dose-related sensitivity of disease detection on post-therapy ^{131}I-mIBG scans, which frequently demonstrate more sites of disease than appreciated on diagnostic pre-therapy scans [132–134].

14.8.5 Radiation Safety Considerations

14.8.5.1 Minimizing Radiation Exposure to Care Providers

The RSO is actively involved in planning and implementing each therapy admission including patient, parent, and staff education. Three important variables determine the amount of radiation exposure to an individual from a treated patient. These variables include the retained radioactivity in the patient, the distance of an individual from

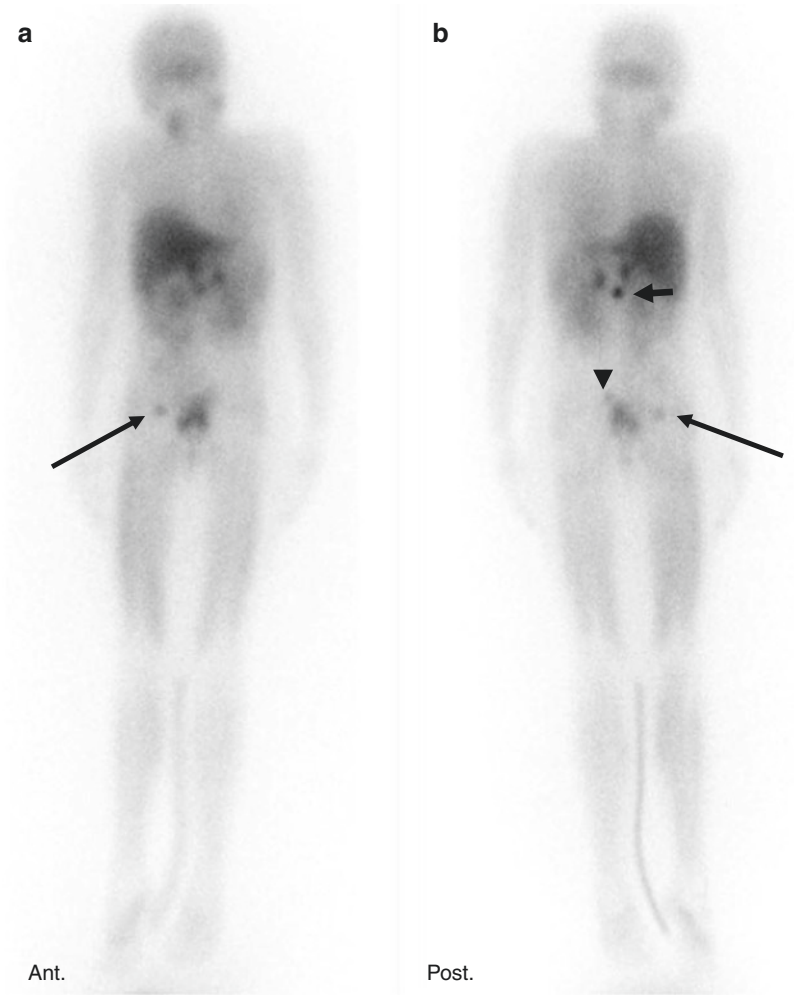

Fig. 14.11 An 11-year-old with recurrent neuroblastoma. Anterior (**a**) and posterior (**b**) whole-body images obtained 3 days status post high-dose ^{131}I-mIBG therapy reveal abnormal uptake in known osseous metastases in the L1 vertebra (short arrow) and in the right acetabulum (long arrow), better visualized than on diagnostic pre-therapy scans (not shown). There is also a subtle soft tissue lesion in the pelvis, cephalad to the bladder on the left (arrowhead), not seen on pre-therapy ^{123}I-mIBG imaging. As expected following high-dose mIBG therapy, there is physiologic uptake in the cerebellum and, when present, in bilateral adrenal glands

the treated patient, and the duration of the exposure to the treated patient [50]. Therefore much emphasis is placed on education about these factors to minimize the radiation exposures to family and staff caregivers [120]. All nursing staff and family caregivers involved in patient care should wear personal dosimeters. The staff and caregivers also can be trained to use a Geiger-Mueller-based radiation survey instrument that is located outside the therapy room. Caregivers should be encouraged to limit the time spent in the patient room whenever feasible and avoid, unless absolutely necessary subject to the patient's medical needs and age, sleeping in the therapy room. Family members who are not involved in patient care are not permitted to enter the treatment room. A recent study by Markelewicz et al. [135] determined that all the caregivers, including nursing staff, involved in ^{131}I-mIBG therapies received radiation doses well below the regulatory limit of 5 mSv. They concluded that sharing patient care among nurses and family caregivers is a safe and feasible treatment model to minimize radiation exposure.

14.8.5.2 Radiation Waste Disposal

Before the patient is admitted for ^{131}I-mIBG therapy, radiation safety staff members prepare the patient room by lining the floors, walls, and equipment with plastic covering to limit contamination. After the patient is discharged, the plastic covering is removed, and the room floor, fixtures, and equipment are surveyed for both fixed and removable contamination. The allowable limits for fixed

and removable contamination for release of items and areas for unrestricted use are based on criteria established during the licensing process. Waste materials should be segregated to limit the amount of material requiring radioactive waste management. Contaminated items and materials should be held in a dedicated storage space for decay.

14.8.6 Risks of ^{131}I-mIBG Therapy

The most common early side effects of ^{131}I-mIBG therapy are acute elevations in blood pressure and tachycardia during the infusion process [136]. Nausea and vomiting occur in 10–25% of patients within the first few hours and days following treatment [120].

Hematologic toxicity (notably thrombocytopenia) is the most frequent and serious side effect, commonly occurring with doses >12 mCi/kg (444 MBq/kg). Myelosuppression typically occurs within 2–4 weeks after therapy, with the nadir observed after 4–6 weeks. Autologous peripheral blood stem cell rescue is often necessary after higher administered doses to abrogate the hematologic toxicity [103, 114, 137].

Thyroid disorders, including hypothyroidism and thyroid nodules, are a late complication of ^{131}I-mIBG therapy and can occur despite thyroid blockade. Continued follow-up of neuroblastoma survivors after treatment with ^{131}I-mIBG for monitoring thyroid function and thyroid morphology (palpation or ultrasound) is therefore advised [138]. Another late radiation-induced toxicity includes the development of secondary malignancies, with acute myelogenous leukemia and myelodysplatic syndrome occurring at an overall frequency of 2–4% [137, 139, 140].

Gastrointestinal, renal, pulmonary, neurologic, and cardiac complications are rare, each occurring in less than 5% of patients receiving ^{131}I-mIBG monotherapy with doses ranging from 12 to 18 mCi/kg [120]. Organ toxicities increase when ^{131}I-mIBG is used in combination with myeloablative doses of chemotherapy [120]. Primary ovarian insufficiency has recently been reported in two children who were treated with ^{131}I-mIBG monotherapy suggesting that exposure to ^{131}I-mIBG alone may damage the female gonads [138].

14.9 Novel Radionuclide Therapies

14.9.1 Peptide Receptor Radionuclide Therapy

Somatostatin receptor expression is seen in pediatric embryonal tumors, in greater than 90% of neuroblastoma and medulloblastomas as well as in approximately 35% of Ewing sarcomas [141, 142]. Somatostatin analogs labeled with beta-emitting radionuclides are being investigated for therapy of these and other neuroendocrine tumors. The most common of these radiopharmaceuticals are ^{90}Y-DOTA^{0}-Tyr^{3}-octreotide (^{90}Y-DOTATOC) and ^{177}Lu-DOTA^{0}-Tyr^{3}-Thre^{8}-octreotide (^{177}Lu-DOTATATE). A few small pilot studies in children have recently evaluated the safety and feasibility of using these agents in the treatment of somatostatin-expressing refractory solid tumors and neuroblastoma. A phase 1 trial [143] of ^{90}Y-DOTATOC therapy in 17 children and young adults with somatostatin-receptor expressing refractory solid tumors demonstrated a 12% partial response and a 29% minor response rate. Although the dose-limiting factor for ^{90}Y-DOTATOC is renal radiation exposure, no dose-limiting toxicities were observed in the aforementioned phase I trial. In another pilot study [144] of eight children with refractory or relapsed high-risk neuroblastoma, ^{68}Ga-DOTATATE was found to be useful to image children with neuroblastoma and identify those suitable for molecular radiotherapy with ^{177}Lu-DOTATATE. Treatment with ^{177}Lu-DOTATATE was found to be feasible, practical, and well tolerated. In a recent study by Kong et al. [145] in eight patients, similar results were obtained with responses observed in patients with progression despite multimodality treatment. They found that a high proportion (6/8; 75%) of their neuroblastoma patients demonstrated sufficient somatostatin receptors indicating their suitability for targeted therapy.

14.9.2 Radionuclide Antibody Therapy

Radioimmunotherapy (RIT) for pediatric tumors has immense potential as a therapeutic modality. The radiation sensitivity of most pediatric tumors is a strong justification for exploring RIT as an adjunct to standard multimodality therapies. The use of RIT in pediatric cancer however remains limited. The largest number of children undergoing RIT has been patients with neuroblastoma treated with anti-GD2 (anti-glycolipid disialoganglioside) antibodies (^{131}I-3F8) [146]. The radiation toxicities of ^{131}I-3F8 were defined in a phase 1 dose-escalation study [147] performed in 24 high-risk neuroblastoma patients (aged 0.3–24.2 years at diagnosis) at Memorial Sloan Kettering Cancer Center. Acute toxicities included pain during infusion, fever, and mild diarrhea. No late extramedullary toxicities were reported, except for biochemical hypothyroidism. Based on the lack of extramedullary toxicities encountered in this phase I study, ^{131}I-3F8 at a dose of 740 MBq/kg was added to a multimodality program (N7) for all high-risk NB patients. With continued long-term follow-up (6–10 years from diagnosis) in this study, overall survival for this patient cohort was almost 40% [148].

Brentuximab vedotin (BV; SGN-35) uses a CD30 monoclonal antibody to cause apoptosis of targeted lymphoma cells. The initial experience with BV in children was limited to case reports of pediatric patients with relapsed or refractory Hodgkin or anaplastic large cell lymphoma (ALCL) [149]. The safety of BV was confirmed in a phase I/II study of pediatric patients with relapsed or refractory lymphomas with maximum tolerated dose determined to be 1.8 mg/kg administered every 3 weeks. The response to BV was documented among pediatric patients with Hodgkin lymphoma with overall response rates of 64%. The results for patients with ALCL included in that trial are not yet available [150, 151]. Currently, COG is conducting a randomized phase II trial of BV or crizotinib in combination with standard chemotherapy for newly diagnosed pediatric patients with ALCL [152].

The feasibility of using RIT in children with relapsed ALL has been tested in seven children (aged 3–16 years) with second or subsequent leptomeningeal relapse who received an intrathecal injection of anti-CD19 (^{131}I-HD37) or anti-CD10 (^{131}I-WCMH15.14) [153, 154]. The murine IgG1 ^{131}I-8H9, which recognizes a glycoprotein antigen expressed on a broad range of pediatric solid tumors, is also being studied [146]. A recently published experimental study [155] assessed the therapeutic potential of a novel radioiodinated alkyl-phospholipid ether analog (^{131}I-CLR1404) in rodent pediatric xenograft models. The authors found that single-dose intravenous injection of ^{131}I-CLR1404 significantly delayed tumor growth and extended survival, with a favorable side effect profile. ^{131}I-CLR1404 has already entered clinical trials in adults and may potentially become a tumor-targeted radiotherapeutic drug with broad applicability in pediatric oncology as well.

14.9.3 Palliative Bone-Seeking Radionuclide Therapies

Osteosarcoma, the most common primary bone tumor in children, is usually treated with chemotherapy and surgery. In palliative situations, bone-seeking radionuclide therapies (strontium-89 [Sr-89], rhenium-186 hydroxyethylene diphosphonate [Rh-186 HEDP], and samarium-153-ethylene diamine tetramethylene phosphonic acid [Sm-153-EDTMP]) may be offered to a subgroup of these patients with painful osseous metastases or in cases of recurrent sites of bone involvement inaccessible to local therapies such as surgery or external beam irradiation (Fig. 14.12). Radium-223 dichloride (Xofigo) is an alpha particle-emitting radiopharmaceutical which is now being used clinically in patients with metastatic castration-resistant prostate cancer. The same agent has generated interest for the treatment of progressive or recurrent osteosarcoma in children. A clinical trial at MD

Fig. 14.12 A 9-year-old boy with widely metastatic angiosarcoma treated with ^{153}Sm-EDTMP for intractable bone pain. Posterior maximal intensity projection image from FDG-PET scan (**a**) shows widespread abnormal skeletal uptake throughout the axial and appendicular skeleton. Posterior whole-body image from bone scan (**b**) shows abnormal uptake in the left humerus, pelvis, femora, and proximal tibia. Posterior whole-body image obtained 48 h after administration of 37 mCi of ^{153}Sm-EHDTP (**c**) shows distribution similar to bone scan. Note the lack of renal and bladder activity

Anderson is currently recruiting patients to determine the maximum tolerated dose of Ra-223 dichloride in those with progressive, locally recurrent, or metastatic osteosarcoma (https://clinicaltrials.gov/ct2/show/record/NCT01833520).

14.10 Conclusion

Radionuclide therapy continues to evolve as a complementary targeted treatment choice in selected pediatric tumors. Therapeutic radionuclides have a relatively safe toxicity profile in comparison to more traditional anticancer agents and can be utilized as monotherapy or in combination with other treatment modalities. I-131 therapy of differentiated thyroid cancer is the oldest and most widely used targeted therapy, with objective evidence of decreasing recurrence rates of DTC when administered following thyroidectomy in intermediate- and high-risk patient groups. ^{131}I-mIBG remains an experimental agent for treatment of neuroblastoma but has been demonstrated to be an effective and well-tolerated therapy in those patients with relapsed or refractory high-risk disease, both as a monotherapy and in combination with other multimodality treatments. ^{131}I-mIBG also shows promise as a frontline agent for therapy of high-risk neuroblastoma. Novel radionuclide therapies are actively being investigated in pediatric oncology, most prominently peptide receptor radionuclide therapy and radioimmunotherapy, for treatment of a variety of solid tumors. The current attention to well-established agents such as ^{131}I for DTC, and the successful implementation of ^{131}I-mIBG therapy for neuroblastoma and pheochromocytoma, coupled with the development of new as well as novel agents, has the potential to allow targeted radionuclide therapy achieve a tremendous impact in pediatric oncology in this era of personalized and precision medicine.

References

1. Fahey FH, Grant FD, Thrall JH. Saul Hertz, MD, and the birth of radionuclide therapy. EJNMMI Phys. 2017;4:15.
2. Means JH. The use of radioactive iodine in the diagnosis and treatment of thyroid diseases. Bull N Y Acad Med. 1948;24:273–86.
3. Seidlin SM, Marinelli LD, Oshry E. Radioactive iodine therapy; effect on functioning metastases of adenocarcinoma of the thyroid. JAMA. 1946;132:838–47.
4. Jadvar H. Targeted radionuclide therapy: an evolution toward precision cancer treatment. AJR Am J Roentgenol. 2017;209:277–88.
5. Zukotynski K, Jadvar H, Capala J, Fahey F. Targeted radionuclide therapy: practical applications and future prospects. Biomark Cancer. 2016;8:35–8.
6. Yeong C-H, Cheng M, Ng K-H. Therapeutic radionuclides in nuclear medicine: current and future prospects. J Zhejiang Univ Sci B. 2014;15:845–63.
7. Howlader N, Noone AM, Krapcho M, Miller D, Bishop K, Kosary CL, Yu M, Ruhl J, Tatalovich Z, Mariotto A, Lewis DR, Chen HS, Feuer EJ, Cronin KA, editors. SEER Cancer Statistics Review, 1975-2014. Bethesda, MD: National Cancer Institute; 2017. Available at https://seer.cancer.gov/csr/1975_2014/, based on November 2016 SEER data submission, posted to the SEER web site, April 2017. Accessed 10 Oct 2017.
8. Francis GL, Waguespack SG, Bauer AJ, Angelos P, Benvenga S, Cerutti JM, et al. Management guidelines for children with thyroid nodules and differentiated thyroid cancer. Thyroid. 2015;25:716–59.
9. Hogan AR, Zhuge Y, Perez EA, Koniaris LG, Lew JI, Sola JE. Pediatric thyroid carcinoma: incidence and outcomes in 1753 patients. J Surg Res. 2009;156:167–72.
10. LAG R, Smith MA, Gurney JG, Linet M, Tamra T, Young JL, Bunin GR, editors. Cancer incidence and survival among children and adolescents: United States SEER Program 1975-1995, SEER Program. NIH Pub. No. 99-4649. Bethesda, MD: National Cancer Institute; 1999. Available at https://seer.cancer.gov/archive/publications/childhood. Accessed 10 Oct 2017.
11. Kiratli PO, Volkan-Salanci B, Günay EC, Varan A, Akyüz C, Büyükpamukçu M. Thyroid cancer in pediatric age group: an institutional experience and review of the literature. J Pediatr Hematol Oncol. 2013;35:93–7.
12. Rivkees SA, Mazzaferri EL, Verburg FA, Reiners C, Luster M, Breuer CK, et al. The treatment of differentiated thyroid cancer in children: emphasis on surgical approach and radioactive iodine therapy. Endocr Rev. 2011;32:798–826.
13. Vergamini LB, Frazier AL, Abrantes FL, Ribeiro KB, Rodriguez-Galindo C. Increase in the incidence of differentiated thyroid carcinoma in children, adolescents, and young adults: a population-based study. J Pediatr. 2014;164:1481–5.
14. Pacini F. Thyroid cancer in children and adolescents. J Endocrinol Invest. 2002;25:572–3.
15. Hay ID, Gonzalez-Losada T, Reinalda MS, Honetschlager JA, Richards ML, Thompson GB. Long-term outcome in 215 children and adolescents with papillary thyroid cancer treated during 1940 through 2008. World J Surg. 2010;34:1192–202.
16. Parisi MT, Eslamy H, Mankoff D. Management of differentiated thyroid cancer in children: focus on the american thyroid association pediatric guidelines. Semin Nucl Med. 2016;46:147–64.

17. Brink JS, van Heerden JA, McIver B, Salomao DR, Farley DR, Grant CS, et al. Papillary thyroid cancer with pulmonary metastases in children: long-term prognosis. Surgery. 2000;128:881–6. discussion 886–887.
18. Chow S-M, Law SCK, Mendenhall WM, Au S-K, Yau S, Mang O, et al. Differentiated thyroid carcinoma in childhood and adolescence-clinical course and role of radioiodine. Pediatr Blood Cancer. 2004;42:176–83.
19. Giuffrida D, Scollo C, Pellegriti G, Lavenia G, Iurato MP, Pezzin V, et al. Differentiated thyroid cancer in children and adolescents. J Endocrinol Invest. 2002;25:18–24.
20. Pawelczak M, David R, Franklin B, Kessler M, Lam L, Shah B. Outcomes of children and adolescents with well-differentiated thyroid carcinoma and pulmonary metastases following ^{131}I treatment: a systematic review. Thyroid. 2010;20:1095–101.
21. Reiners C, Farahati J. 131I therapy of thyroid cancer patients. Q J Nucl Med. 1999;43:324–35.
22. Robbins RJ, Schlumberger MJ. The evolving role of (131)I for the treatment of differentiated thyroid carcinoma. J Nucl Med. 2005;46(Suppl 1):28S–37S.
23. Van Nostrand D. The benefits and risks of I-131 therapy in patients with well-differentiated thyroid cancer. Thyroid. 2009;19:1381–91.
24. Hay ID, Thompson GB, Grant CS, Bergstralh EJ, Dvorak CE, Gorman CA, et al. Papillary thyroid carcinoma managed at the Mayo Clinic during six decades (1940-1999): temporal trends in initial therapy and long-term outcome in 2444 consecutively treated patients. World J Surg. 2002;26:879–85.
25. Iyer NG, Morris LGT, Tuttle RM, Shaha AR, Ganly I. Rising incidence of second cancers in patients with low-risk (T1N0) thyroid cancer who receive radioactive iodine therapy. Cancer. 2011;117:4439–46.
26. Jonklaas J, Cooper DS, Ain KB, Bigos T, Brierley JD, Haugen BR, et al. Radioiodine therapy in patients with stage I differentiated thyroid cancer. Thyroid. 2010;20:1423–4.
27. Schlumberger M, Catargi B, Borget I, Deandreis D, Zerdoud S, Bridji B, et al. Strategies of radioiodine ablation in patients with low-risk thyroid cancer. N Engl J Med. 2012;366:1663–73.
28. Tuttle RM, Leboeuf R, Shaha AR. Medical management of thyroid cancer: a risk adapted approach. J Surg Oncol. 2008;97:712–6.
29. Jarzab B, Handkiewicz-Junak D, Wloch J. Juvenile differentiated thyroid carcinoma and the role of radioiodine in its treatment: a qualitative review. Endocr Relat Cancer. 2005;12:773–803.
30. Newman KD, Black T, Heller G, Azizkhan RG, Holcomb GW, Sklar C, et al. Differentiated thyroid cancer: determinants of disease progression in patients <21 years of age at diagnosis: a report from the Surgical Discipline Committee of the Children's Cancer Group. Ann Surg. 1998;227:533–41.
31. Brown AP, Chen J, Hitchcock YJ, Szabo A, Shrieve DC, Tward JD. The risk of second primary malignancies up to three decades after the treatment of differentiated thyroid cancer. J Clin Endocrinol Metab. 2008;93:504–15.
32. Rubino C, de Vathaire F, Dottorini ME, Hall P, Schvartz C, Couette JE, et al. Second primary malignancies in thyroid cancer patients. Br J Cancer. 2003;89:1638–44.
33. Hung W, Sarlis NJ. Current controversies in the management of pediatric patients with well-differentiated nonmedullary thyroid cancer: a review. Thyroid. 2002;12:683–702.
34. McClellan DR, Francis GL. Thyroid cancer in children, pregnant women, and patients with Graves' disease. Endocrinol Metab Clin North Am. 1996;25:27–48.
35. Parisi MT, Mankoff D. Differentiated pediatric thyroid cancer: correlates with adult disease, controversies in treatment. Semin Nucl Med. 2007;37:340–56.
36. Welch Dinauer CA, Tuttle RM, Robie DK, McClellan DR, Svec RL, Adair C, et al. Clinical features associated with metastasis and recurrence of differentiated thyroid cancer in children, adolescents and young adults. Clin Endocrinol (Oxf). 1998;49:619–28.
37. Treves ST. Pediatric nuclear medicine and molecular imaging. New York, NY: Springer; 2014.
38. WFE L, Zacharin MR, Waters K, Wheeler G, Johnston V, Hicks RJ. Management of paediatric thyroid carcinoma: recent experience with recombinant human thyroid stimulating hormone in preparation for radioiodine therapy. Intern Med J. 2006;36:564–70.
39. Luster M, Handkiewicz-Junak D, Grossi A, Zacharin M, Taïeb D, Cruz O, et al. Recombinant thyrotropin use in children and adolescents with differentiated thyroid cancer: a multicenter retrospective study. J Clin Endocrinol Metab. 2009;94:3948–53.
40. Luster M, Lippi F, Jarzab B, Perros P, Lassmann M, Reiners C, et al. rhTSH-aided radioiodine ablation and treatment of differentiated thyroid carcinoma: a comprehensive review. Endocr Relat Cancer. 2005;12:49–64.
41. Bural G, Drubach L, Treves ST, Grant F. Thymic uptake of radioiodine in children and young adults with thyroid cancer. J Nucl Med. 2010;51:489.
42. Benua RS, Cicale NR, Sonenberg M, Rawson RW. The relation of radioiodine dosimetry to results and complications in the treatment of metastatic thyroid cancer. Am J Roentgenol Radium Ther Nucl Med. 1962;87:171–82.
43. Lassmann M, Hänscheid H, Verburg FA, Luster M. The use of dosimetry in the treatment of differentiated thyroid cancer. Q J Nucl Med Mol Imaging. 2011;55:107–15.
44. Tuttle RM, Leboeuf R, Robbins RJ, Qualey R, Pentlow K, Larson SM, et al. Empiric radioactive iodine dosing regimens frequently exceed maximum tolerated activity levels in elderly patients with thyroid cancer. J Nucl Med. 2006;47:1587–91.
45. Lassmann M, Hänscheid H, Chiesa C, Hindorf C, Flux G, Luster M, et al. EANM Dosimetry

Committee series on standard operational procedures for pre-therapeutic dosimetry I: blood and bone marrow dosimetry in differentiated thyroid cancer therapy. Eur J Nucl Med Mol Imaging. 2008;35:1405–12.
46. Luster M, Lassmann M, Freudenberg LS, Reiners C. Thyroid cancer in childhood: management strategy, including dosimetry and long-term results. Hormones (Athens). 2007;6:269–78.
47. Maxon HR, Englaro EE, Thomas SR, Hertzberg VS, Hinnefeld JD, Chen LS, et al. Radioiodine-131 therapy for well-differentiated thyroid cancer--a quantitative radiation dosimetric approach: outcome and validation in 85 patients. J Nucl Med. 1992;33:1132–6.
48. Tuttle RM, Grewal RK, Larson SM. Radioactive iodine therapy in poorly differentiated thyroid cancer. Nat Clin Pract Oncol. 2007;4:665–8.
49. United States Nuclear Regulatory Commission Office of Federal and State. Material and environmental management programs 2009, 20555-0001. NRC Information Notice 2003-22, Supplement 1. Washington, DC: NRC; 2009. Available at www.nrc.gov/reading-rm/doc-collections/gen-comm/info-notices/2003/ml090500018.pdf. Accessed 10 Oct 2017.
50. American Thyroid Association Taskforce On Radioiodine Safety, Sisson JC, Freitas J, McDougall IR, Dauer LT, Hurley JR, et al. Radiation safety in the treatment of patients with thyroid diseases by radioiodine 131I : practice recommendations of the American Thyroid Association. Thyroid. 2011;21:335–46.
51. U.S. Nuclear Regulatory Commission Regulatory Guide 8.39. Release of patients administered radioactive materials. 1997. Available at www.nucmed.com/nucmed/ref/8_39.pdf. Accessed 10 Oct 2017.
52. United States Nuclear Regulatory Commission 2008 Standards for protection against radiation. Title 10, Code of Federal Regulations: Part 20, Subpart C—20.1201 Occupational dose limits for adults; 20.1207 Occupational dose limits for minors; Part 35, Subpart C—35.75 Release of individuals containing unsealed byproduct material or implants containing byproduct material. Available at www.nrc.gov/reading-rm/doc-collections/cfr. Accessed 10 Oct 2017.
53. Němec J, Röhling S, Zamrazil V, Pohunková D. Comparison of the distribution of diagnostic and thyroablative I-131 in the evaluation of differentiated thyroid cancers. J Nucl Med. 1979;20:92–7.
54. Waxman A, Ramanna L, Chapman N, Chapman D, Brachman M, Tanasescu D, et al. The significance of 1-131 scan dose in patients with thyroid cancer: determination of ablation: concise communication. J Nucl Med. 1981;22:861–5.
55. Ciappuccini R, Heutte N, Trzepla G, Rame J-P, Vaur D, Aide N, et al. Postablation (131)I scintigraphy with neck and thorax SPECT-CT and stimulated serum thyroglobulin level predict the outcome of patients with differentiated thyroid cancer. Eur J Endocrinol. 2011;164:961–9.
56. Goolden AW, Kam KC, Fitzpatrick ML, Munro AJ. Oedema of the neck after ablation of the thyroid with radioactive iodine. Br J Radiol. 1986;59:583–6.
57. Kloos RT, Duvuuri V, Jhiang SM, Cahill KV, Foster JA, Burns JA. Nasolacrimal drainage system obstruction from radioactive iodine therapy for thyroid carcinoma. J Clin Endocrinol Metab. 2002;87:5817–20.
58. Dottorini ME. Genetic risk assessment after iodine-131 exposure: an opportunity and obligation for nuclear medicine. J Nucl Med. 1996;37:612–5.
59. Klubo-Gwiezdzinska J, Van Nostrand D, Burman KD, Vasko V, Chia S, Deng T, et al. Salivary gland malignancy and radioiodine therapy for thyroid cancer. Thyroid. 2010;20:647–51.
60. Lee SL. Complications of radioactive iodine treatment of thyroid carcinoma. J Natl Compr Cancer Netw. 2010;8:1277–86. quiz 1287.
61. Verburg FA, Hänscheid H, Biko J, Hategan MC, Lassmann M, Kreissl MC, et al. Dosimetry-guided high-activity (131)I therapy in patients with advanced differentiated thyroid carcinoma: initial experience. Eur J Nucl Med Mol Imaging. 2010;37:896–903.
62. Van Nostrand D, Freitas J. Side effects of I-131 for ablation and treatment of Well- differentiated thyroid carcinoma. In: Wartofsky L, Van Nostrand D, editors. Thyroid Cancer: A Comprehensive Guide to Clinical Management. Totowa, NJ: Humana Press; 2006. p. 459–84.
63. Van Nostrand D, Neutze J, Atkins F. Side effects of "rational dose" iodine-131 therapy for metastatic well-differentiated thyroid carcinoma. J Nucl Med. 1986;27:1519–27.
64. Sawka AM, Lakra DC, Lea J, Alshehri B, Tsang RW, Brierley JD, et al. A systematic review examining the effects of therapeutic radioactive iodine on ovarian function and future pregnancy in female thyroid cancer survivors. Clin Endocrinol (Oxf). 2008;69:479–90.
65. Sawka AM, Lea J, Alshehri B, Straus S, Tsang RW, Brierley JD, et al. A systematic review of the gonadal effects of therapeutic radioactive iodine in male thyroid cancer survivors. Clin Endocrinol (Oxf). 2008;68:610–7.
66. Garsi J-P, Schlumberger M, Rubino C, Ricard M, Labbé M, Ceccarelli C, et al. Therapeutic administration of 131I for differentiated thyroid cancer: radiation dose to ovaries and outcome of pregnancies. J Nucl Med. 2008;49:845–52.
67. Dottorini ME, Lomuscio G, Mazzucchelli L, Vignati A, Colombo L. Assessment of female fertility and carcinogenesis after iodine-131 therapy for differentiated thyroid carcinoma. J Nucl Med. 1995;36:21–7.
68. Vini L, Hyer S, Al-Saadi A, Pratt B, Harmer C. Prognosis for fertility and ovarian function after treatment with radioiodine for thyroid cancer. Postgrad Med J. 2002;78:92–3.
69. Rosário PWS, Barroso AL, Rezende LL, Padrão EL, Borges MAR, Guimarães VC, et al. Testicular func-

tion after radioiodine therapy in patients with thyroid cancer. Thyroid. 2006;16:667–70.
70. Wallace WHB. Oncofertility and preservation of reproductive capacity in children and young adults. Cancer. 2011;117:2301–10.
71. Baugnet-Mahieu L, Lemaire M, Léonard ED, Léonard A, Gerber GB. Chromosome aberrations after treatment with radioactive iodine for thyroid cancer. Radiat Res. 1994;140:429–31.
72. Puerto S, Marcos R, Ramírez MJ, Galofré P, Creus A, Surrallés J. Equal induction and persistence of chromosome aberrations involving chromosomes 1, 4 and 10 in thyroid cancer patients treated with radioactive iodine. Mutat Res. 2000;469:147–58.
73. Richter HE, Lohrer HD, Hieber L, Kellerer AM, Lengfelder E, Bauchinger M. Microsatellite instability and loss of heterozygosity in radiation-associated thyroid carcinomas of Belarussian children and adults. Carcinogenesis. 1999;20:2247–52.
74. Sawka AM, Thabane L, Parlea L, Ibrahim-Zada I, Tsang RW, Brierley JD, et al. Second primary malignancy risk after radioactive iodine treatment for thyroid cancer: a systematic review and meta-analysis. Thyroid. 2009;19:451–7.
75. Rall JE, Alpers JB, Lewallen CG, Sonenberg M, Berman M, Rawson RW. Radiation pneumonitis and fibrosis: a complication of radioiodine treatment of pulmonary metastases from cancer of the thyroid. J Clin Endocrinol Metab. 1957;17:1263–76.
76. Van Nostrand D, Atkins F, Yeganeh F, Acio E, Bursaw R, Wartofsky L. Dosimetrically determined doses of radioiodine for the treatment of metastatic thyroid carcinoma. Thyroid. 2002;12:121–34.
77. Kaatsch P. Epidemiology of childhood cancer. Cancer Treat Rev. 2010;36:277–85.
78. Maris JM, Hogarty MD, Bagatell R, Cohn SL. Neuroblastoma. Lancet. 2007;369:2106–20.
79. Park JR, Eggert A, Caron H. Neuroblastoma: biology, prognosis, and treatment. Pediatr Clin North Am. 2008;55:97–120. x.
80. Sharp SE, Gelfand MJ, Shulkin BL. Pediatrics: diagnosis of neuroblastoma. Semin Nucl Med. 2011;41:345–53.
81. Brisse HJ, McCarville MB, Granata C, Krug KB, Wootton-Gorges SL, Kanegawa K, et al. Guidelines for imaging and staging of neuroblastic tumors: consensus report from the International Neuroblastoma Risk Group Project. Radiology. 2011;261:243–57.
82. Cohn SL, Pearson ADJ, London WB, Monclair T, Ambros PF, Brodeur GM, et al. The International Neuroblastoma Risk Group (INRG) classification system: an INRG Task Force report. J Clin Oncol. 2009;27:289–97.
83. DuBois SG, Kalika Y, Lukens JN, Brodeur GM, Seeger RC, Atkinson JB, et al. Metastatic sites in stage IV and IVS neuroblastoma correlate with age, tumor biology, and survival. J Pediatr Hematol Oncol. 1999;21:181–9.
84. Brodeur GM, Seeger RC, Barrett A, Berthold F, Castleberry RP, D'Angio G, et al. International criteria for diagnosis, staging, and response to treatment in patients with neuroblastoma. J Clin Oncol. 1988;6:1874–81.
85. Brodeur GM, Pritchard J, Berthold F, Carlsen NL, Castel V, Castelberry RP, et al. Revisions of the international criteria for neuroblastoma diagnosis, staging, and response to treatment. J Clin Oncol. 1993;11:1466–77.
86. Monclair T, Brodeur GM, Ambros PF, Brisse HJ, Cecchetto G, Holmes K, et al. The International Neuroblastoma Risk Group (INRG) staging system: an INRG Task Force report. J Clin Oncol. 2009;27:298–303.
87. Yu AL, Gilman AL, Ozkaynak MF, London WB, Kreissman SG, Chen HX, et al. Anti-GD2 antibody with GM-CSF, interleukin-2, and isotretinoin for neuroblastoma. N Engl J Med. 2010;363:1324–34.
88. Matthay KK, Villablanca JG, Seeger RC, Stram DO, Harris RE, Ramsay NK, et al. Treatment of high-risk neuroblastoma with intensive chemotherapy, radiotherapy, autologous bone marrow transplantation, and 13-cis-retinoic acid. Children's Cancer Group. N Engl J Med. 1999;341:1165–73.
89. Vik TA, Pfluger T, Kadota R, Castel V, Tulchinsky M, Farto JCA, et al. (123)I-mIBG scintigraphy in patients with known or suspected neuroblastoma: results from a prospective multicenter trial. Pediatr. Blood Cancer. 2009;52:784–90.
90. Wieland DM, Wu J, Brown LE, Mangner TJ, Swanson DP, Beierwaltes WH. Radiolabeled adrenergi neuron-blocking agents: adrenomedullary imaging with [131I]iodobenzylguanidine. J Nucl Med. 1980;21:349–53.
91. Wieland DM, Brown LE, Tobes MC, Rogers WL, Marsh DD, Mangner TJ, et al. Imaging the primate adrenal medulla with [123I] and [131I] metaiodobenzylguanidine: concise communication. J Nucl Med. 1981;22:358–64.
92. Sisson J, Shapiro B, Beierwaltes WH, Nakajo M, Glowniak J, Mangner T, et al. Treatment of malignant pheochromocytoma with a new radiopharmaceutical. Trans Assoc Am Physicians. 1983;96:209–17.
93. Treuner J, Klingebiel T, Feine U, Buck J, Bruchelt G, Dopfer R, et al. Clinical experiences in the treatment of neuroblastoma with 131I-metaiodobenzylguanidine. Pediatr Hematol Oncol. 1986;3:205–16.
94. Buck J, Bruchelt G, Girgert R, Treuner J, Niethammer D. Specific uptake of m-[125I]iodobenzylguanidine in the human neuroblastoma cell line SK-N-SH. Cancer Res. 1985;45:6366–70.
95. Jaques S, Tobes MC, Sisson JC, Baker JA, Wieland DM. Comparison of the sodium dependency of uptake of meta-lodobenzylguanidine and norepinephrine into cultured bovine adrenomedullary cells. Mol Pharmacol. 1984;26:539–46.
96. Jaques S, Tobes MC, Sisson JC. Sodium dependency of uptake of norepinephrine and m-iodobenzylguanidine into cultured human pheochromocytoma cells: evidence for uptake-one. Cancer Res. 1987;47:3920–8.

97. Tobes MC, Jaques S, Wieland DM, Sisson JC. Effect of uptake-one inhibitors on the uptake of norepinephrine and metaiodobenzylguanidine. J Nucl Med. 1985;26:897–907.
98. Smets LA, Loesberg C, Janssen M, Metwally EA, Huiskamp R. Active uptake and extravesicular storage of m-iodobenzylguanidine in human neuroblastoma SK-N-SH cells. Cancer Res. 1989;49:2941–4.
99. Gaze MN, Huxham IM, Mairs RJ, Barrett A. Intracellular localization of metaiodobenzyl guanidine in human neuroblastoma cells by electron spectroscopic imaging. Int J Cancer. 1991;47:875–80.
100. Lashford LS, Hancock JP, Kemshead JT. Metaiodobenzylguanidine (mIBG) uptake and storage in the human neuroblastoma cell line SK-N-BE(2C). Int J Cancer. 1991;47:105–9.
101. Wilson JS, Gains JE, Moroz V, Wheatley K, Gaze MN. A systematic review of 131I-meta iodobenzylguanidine molecular radiotherapy for neuroblastoma. Eur J Cancer. 2014;50:801–15.
102. Claudiani F, Garaventa A, Bertolazzi L, Villavecchia GP, Cabria M, Scopinaro G, et al. [131I]metaiodobenzylguanidine therapy in advanced neuroblastoma. J Nucl Biol Med. 1991;35:224–7.
103. DuBois SG, Messina J, Maris JM, Huberty J, Glidden DV, Veatch J, et al. Hematologic toxicity of high-dose iodine-131-metaiodobenzylguanidine therapy for advanced neuroblastoma. J Clin Oncol. 2004;22:2452–60.
104. Garaventa A, Bellagamba O, Lo Piccolo MS, Milanaccio C, Lanino E, Bertolazzi L, et al. 131I-metaiodobenzylguanidine (131I-MIBG) therapy for residual neuroblastoma: a mono-institutional experience with 43 patients. Br J Cancer. 1999;81:1378–84.
105. Hutchinson RJ, Sisson JC, Miser JS, Zasadny KR, Normolle DP, Shulkin BL, et al. Long-term results of [131I]metaiodobenzylguanidine treatment of refractory advanced neuroblastoma. J Nucl Biol Med. 1991;35:237–40.
106. Hutchinson RJ, Sisson JC, Shapiro B, Miser JS, Normole D, Shulkin BL, et al. 131-I-metaiodobenzylguanidine treatment in patients with refractory advanced neuroblastoma. Am J Clin Oncol. 1992;15:226–32.
107. Hoefnagel CA, Voûte PA, De Kraker J, Valdés Olmos RA. [131I]metaiodobenzylguanidine therapy after conventional therapy for neuroblastoma. J Nucl Biol Med. 1991;35:202–6.
108. Kang TI, Brophy P, Hickeson M, Heyman S, Evans AE, Charron M, et al. Targeted radiotherapy with submyeloablative doses of 131I-MIBG is effective for disease palliation in highly refractory neuroblastoma. J Pediatr Hematol Oncol. 2003;25:769–73.
109. Klingebiel T, Feine U, Treuner J, Reuland P, Handgretinger R, Niethammer D. Treatment of neuroblastoma with [131I]metaiodobenzylguanidine: long-term results in 25 patients. J Nucl Biol Med. 1991;35:216–9.
110. Lashford LS, Lewis IJ, Fielding SL, Flower MA, Meller S, Kemshead JT, et al. Phase I/II study of iodine 131 metaiodobenzylguanidine in chemoresistant neuroblastoma: a United Kingdom Children's Cancer Study Group investigation. J Clin Oncol. 1992;10:1889–96.
111. Lumbroso J, Hartmann O, Schlumberger M. Therapeutic use of [131I]metaiodobenzylguanidine in neuroblastoma: a phase II study in 26 patients. "Société Française d'Oncologie Pédiatrique" and Nuclear Medicine Co-investigators. J Nucl Biol Med. 1991;35:220–3.
112. Matthay KK, Huberty JP, Hattner RS, Ablin AR, Engelstad BL, Zoger S, et al. Efficacy and safety of [131I]metaiodobenzylguanidine therapy for patients with refractory neuroblastoma. J Nucl Biol Med. 1991;35:244–7.
113. Troncone L, Rufini V, Riccardi R, Lasorella A, Mastrangelo R. The use of [131I]metaiodobenzylguanidine in the treatment of neuroblastoma after conventional therapy. J Nucl Biol Med. 1991;35:232–6.
114. Matthay KK, Yanik G, Messina J, Quach A, Huberty J, Cheng S-C, et al. Phase II study on the effect of disease sites, age, and prior therapy on response to iodine-131-metaiodobenzylguanidine therapy in refractory neuroblastoma. J Clin Oncol. 2007;25:1054–60.
115. Howard JP, Maris JM, Kersun LS, Huberty JP, Cheng S-C, Hawkins RA, et al. Tumor response and toxicity with multiple infusions of high dose 131I-MIBG for refractory neuroblastoma. Pediatr Blood Cancer. 2005;44:232–9.
116. Johnson K, McGlynn B, Saggio J, Baniewicz D, Zhuang H, Maris JM, et al. Safety and efficacy of tandem 131I-metaiodobenzylguanidine infusions in relapsed/refractory neuroblastoma. Pediatr Blood Cancer. 2011;57:1124–9.
117. Matthay KK, Quach A, Huberty J, Franc BL, Hawkins RA, Jackson H, et al. Iodine-131--metaiodobenzylguanidine double infusion with autologous stem-cell rescue for neuroblastoma: a new approaches to neuroblastoma therapy phase I study. J Clin Oncol. 2009;27:1020–5.
118. Yanik GA, Villablanca JG, Maris JM, Weiss B, Groshen S, Marachelian A, et al. 131I-metaiodobenzylguanidine with intensive chemotherapy and autologous stem cell transplantation for high-risk neuroblastoma. A new approaches to neuroblastoma therapy (NANT) phase II study. Biol. Blood Marrow Transplant. J. Am. Soc. Blood Marrow Transpl. 2015;21:673–81.
119. Klingebiel T, Bader P, Bares R, Beck J, Hero B, Jürgens H, et al. Treatment of neuroblastoma stage 4 with 131I-meta-iodo-benzylguanidine, high-dose chemotherapy and immunotherapy. A pilot study. Eur J Cancer. 1998;34:1398–402.
120. Parisi MT, Eslamy H, Park JR, Shulkin BL, Yanik GA. ^{131}I-Metaiodobenzylguanidine theranostics in

neuroblastoma: historical perspectives; practical applications. Semin Nucl Med. 2016;46:184–202.
121. Streby KA, Shah N, Ranalli MA, Kunkler A, Cripe TP. Nothing but NET: a review of norepinephrine transporter expression and efficacy of 131I-mIBG therapy. Pediatr Blood Cancer. 2015;62:5–11.
122. De Kraker J, Hoefnagel CA, Caron H, Valdés Olmos RA, Zsiros J, Heij HA, et al. First line targeted radiotherapy, a new concept in the treatment of advanced stage neuroblastoma. Eur J Cancer. 1995;31A:600–2.
123. Mastrangelo S, Rufini V, Ruggiero A, Di Giannatale A, Riccardi R. Treatment of advanced neuroblastoma in children over 1 year of age: the critical role of ^{131}I-metaiodobenzylguanidine combined with chemotherapy in a rapid induction regimen. Pediatr Blood Cancer. 2011;56:1032–40.
124. de Kraker J, Hoefnagel KA, Verschuur AC, van Eck B, van Santen HM, Caron HN. Iodine-131-metaiodobenzylguanidine as initial induction therapy in stage 4 neuroblastoma patients over 1 year of age. Eur J Cancer. 2008;44:551–6.
125. Hoefnagel CA, De Kraker J, Valdés Olmos RA, Voûte PA. 131I-MIBG as a first-line treatment in high-risk neuroblastoma patients. Nucl Med Commun. 1994;15:712–7.
126. Kraal KCJM, Bleeker GM, van Eck-Smit BLF, van Eijkelenburg NKA, Berthold F, van Noesel MM, et al. Feasibility, toxicity and response of upfront metaiodobenzylguanidine therapy therapy followed by German Pediatric Oncology Group Neuroblastoma 2004 protocol in newly diagnosed stage 4 neuroblastoma patients. Eur J Cancer. 2017;76:188–96.
127. DuBois SG, Matthay KK. Radiolabeled metaiodobenzylguanidine for the treatment of neuroblastoma. Nucl Med Biol. 2008;35(Suppl 1):S35–48.
128. Grünwald F, Ezziddin S. 131I-metaiodobenzylguanidine therapy of neuroblastoma and other neuroendocrine tumors. Semin Nucl Med. 2010;40:153–63.
129. Sharp SE, Trout AT, Weiss BD, Gelfand MJ. MIBG in neuroblastoma diagnostic imaging and therapy. Radiogr Rev. 2016;36:258–78.
130. Shusterman S, Grant FD, Lorenzen W, Davis RT, Laffin S, Drubach LA, et al. Iodine-131-labeled meta-iodobenzylguanidine therapy of children with neuroblastoma: program planning and initial experience. Semin Nucl Med. 2011;41:354–63.
131. Taggart D, Dubois S, Matthay KK. Radiolabeled metaiodobenzylguanidine for imaging and therapy of neuroblastoma. Q J Nucl Med Mol Imaging. 2008;52:403–18.
132. Giammarile F, Lumbroso J, Ricard M, Aubert B, Hartmann O, Schlumberger M, et al. Radioiodinated metaiodobenzylguanidine in neuroblastoma: influence of high dose on tumour site detection. Eur J Nucl Med. 1995;22:1180–3.
133. Hickeson MP, Charron M, Maris JM, Brophy P, Kang TI, Zhuang H, et al. Biodistribution of post-therapeutic versus diagnostic (131)I-MIBG scans in children with neuroblastoma. Pediatr Blood Cancer. 2004;42:268–74.
134. Parisi MT, Matthay KK, Huberty JP, Hattner RS. Neuroblastoma: dose-related sensitivity of MIBG scanning in detection. Radiology. 1992;184:463–7.
135. Markelewicz RJ, Lorenzen WA, Shusterman S, Grant FD, Fahey FH, Treves ST. Radiation exposure to family caregivers and nurses of pediatric neuroblastoma patients receiving 131I-metaiodobenzylguanidine (131I-MIBG) therapy. Clin Nucl Med. 2013;38:604–7.
136. Wong T, Matthay KK, Boscardin WJ, Hawkins RA, Brakeman PR, DuBois SG. Acute changes in blood pressure in patients with neuroblastoma treated with ^{131}I-metaiodobenzylguanidine (MIBG). Pediatr Blood Cancer. 2013;60:1424–30.
137. Polishchuk AL, Dubois SG, Haas-Kogan D, Hawkins R, Matthay KK. Response, survival, and toxicity after iodine-131-metaiodobenzylguanidine therapy for neuroblastoma in preadolescents, adolescents, and adults. Cancer. 2011;117:4286–93.
138. Clement SC, Van Eck-Smit BLF, Van Trotsenburg ASP, Kremer LCM, Tytgat GAM, Van Santen HM. Long-term follow-up of the thyroid gland after treatment with 131I-Metaiodobenzylguanidine in children with neuroblastoma: importance of continuous surveillance. Pediatr Blood Cancer. 2013;60:1833–8.
139. Weiss B, Vora A, Huberty J, Hawkins RA, Matthay KK. Secondary myelodysplastic syndrome and leukemia following 131I-metaiodobenzylguanidine therapy for relapsed neuroblastoma. J Pediatr Hematol Oncol. 2003;25:543–7.
140. Garaventa A, Gambini C, Villavecchia G, Di Cataldo A, Bertolazzi L, Pizzitola MR, et al. Second malignancies in children with neuroblastoma after combined treatment with 131I-metaiodobenzylguanidine. Cancer. 2003;97:1332–8.
141. Albers AR, O'Dorisio MS, Balster DA, Caprara M, Gosh P, Chen F, et al. Somatostatin receptor gene expression in neuroblastoma. Regul Pept. 2000;88:61–73.
142. Frühwald MC, O'Dorisio MS, Pietsch T, Reubi JC. High expression of somatostatin receptor subtype 2 (sst2) in medulloblastoma: implications for diagnosis and therapy. Pediatr Res. 1999;45:697–708.
143. Menda Y, O'Dorisio MS, Kao S, Khanna G, Michael S, Connolly M, et al. Phase I trial of 90Y-DOTATOC therapy in children and young adults with refractory solid tumors that express somatostatin receptors. J Nucl Med. 2010;51:1524–31.
144. Gains JE, Bomanji JB, Fersht NL, Sullivan T, D'Souza D, Sullivan KP, et al. 177Lu-DOTATATE molecular radiotherapy for childhood neuroblastoma. J Nucl Med. 2011;52:1041–7.
145. Kong G, Hofman MS, Murray WK, Wilson S, Wood P, Downie P, et al. Initial experience with gallium-68 DOTA-octreotate PET/CT and peptide

receptor radionuclide therapy for pediatric patients with refractory metastatic neuroblastoma. J Pediatr Hematol Oncol. 2016;38:87–96.
146. Modak S, Cheung N-KV. Antibody-based targeted radiation to pediatric tumors. J Nucl Med. 2005;46(Suppl 1):157S–63S.
147. Cheung NK. Monoclonal antibody-based therapy for neuroblastoma. Curr Oncol Rep. 2000;2:547–53.
148. Cheung NK, Kushner BH, LaQuaglia M, Kramer K, Gollamudi S, Heller G, et al. N7: a novel multimodality therapy of high risk neuroblastoma (NB) in children diagnosed over 1 year of age. Med Pediatr Oncol. 2001;36:227–30.
149. Mikles B, Levine J, Gindin T, Bhagat G, Satwani P. Brentuximab vedotin (SGN-35) in a 3-year-old child with relapsed systemic anaplastic large cell lymphoma. J Pediatr Hematol Oncol. 2014;36:e85–7.
150. Neville KA, Rosolen A, Landman-Parker J, Aladjidi N, Beishuizen A, Daw S, et al. Phase 1/2 study of brentuximab vedotin in pediatric patients with relapsed or refractory (R/R) hodgkin lymphoma (HL) or systemic anaplastic large-cell lymphoma (sALCL): preliminary phase 2 data for brentuximab vedotin 1.8 Mg/Kg in the HL study arm. Blood. 2013;122:4378.
151. Neville K, Gore L, Mauz-Körholz C, Rosolen A, Landman-Parker J, Sanchez de Toledo J, et al. Phase I/II study of brentuximab vedotin in pediatric patients (pts) with relapsed or refractory (RR) Hodgkin lymphoma (HL) or systemic anaplastic large-cell lymphoma (sALCL): interim phase (ph) I safety data. J Clin Oncol. 2013;31:10028.
152. Sorge CE, McDaniel JK, Xavier AC. Targeted therapies for the treatment of pediatric non-hodgkin lymphomas: present and future. Pharmaceuticals (Basel) 2016;9(2).
153. Pizer BL, Kemshead JT. The potential of targeted radiotherapy in the treatment of central nervous system leukaemia. Leuk Lymphoma. 1994;15:281–9.
154. Pizer B, Papanastassiou V, Hancock J, Cassano W, Coakham H, Kemshead J. A pilot study of monoclonal antibody targeted radiotherapy in the treatment of central nervous system leukaemia in children. Br J Haematol. 1991;77:466–72.
155. Baiu DC, Marsh IR, Boruch AE, Shahi A, Bhattacharya S, Jeffery JJ, et al. Targeted molecular radiotherapy of pediatric solid tumors using a radioiodinated alkyl-phospholipid ether analog. J Nucl Med. 2018;59:244. https://doi.org/10.2967/jnumed.117.193748.

Interventional Radiology in Pediatric Oncology

15

Derek J. Roebuck and John M. Racadio

The role of interventional radiology (IR) in pediatric oncology is expanding. One of the most important IR techniques is image-guided biopsy, which is covered in a separate chapter. Many other IR procedures, such as central venous access, aspiration or drainage of fluid (such as nephrostomy, biliary drainage, paracentesis, or thoracocentesis), and enteral access (such as gastrostomy), are frequently necessary in the management of children with cancer, but are not specific to this patient group and are beyond the scope of this chapter. Some complications of oncology treatments are also amenable to IR techniques, such as superselective vesical artery embolization of hemorrhagic cystitis following cyclophosphamide therapy.

This chapter focuses on interventional oncology, which is the image-guided treatment of tumors. Interventional oncology procedures include percutaneous ablation and transarterial therapy, as well as a few others currently under investigation. Patients are typically referred to IR for these procedures following discussion in a multidisciplinary team meeting or tumor board. This underscores the importance of having a representative of IR present at these meetings. In children, all of these procedures usually require general anesthesia.

D. J. Roebuck (✉)
Perth Children's Hospital and University of Western Australia, Perth, Australia
e-mail: derek.roebuck@health.wa.gov.au

J. M. Racadio
Cincinnati Children's Hospital Medical Center, Cincinnati, OH, USA
e-mail: john.racadio@cchmc.org

15.1 Percutaneous Ablation

Percutaneous treatment of focal tumors may be performed with curative or palliative intent and without compromising the effectiveness of other modalities such as chemotherapy or radiation therapy. Several different forms of ablation are possible, and the choice of the right technique for the individual patient can be challenging and depends on many factors [1]. With all of the thermal ablation techniques, the possibility of injury to adjacent organs must be considered, and certain strategies may be used to minimize this risk. The simplest of these is "hydrodissection," which involves the injection of saline or very dilute local anesthetic between the tumor and adjacent sensitive structures (e.g., nerves), usually using ultrasound guidance. When protection of critical structures such as the spinal cord is a concern, some operators advocate the use of thermosensor needles. The evidence base for ablation in pediatric oncology is still quite limited [2].

15.1.1 Radiofrequency Ablation

Radiofrequency ablation (RFA) is the most common ablation technique in children and is used

S. D. Voss, K. McHugh (eds.), *Imaging in Pediatric Oncology*, Pediatric Oncology,
https://doi.org/10.1007/978-3-030-03777-2_15

most frequently for liver tumors and lung metastases [2–4]. In RFA, an electrode needle is inserted into the tumor, usually with image guidance, and alternating current is applied to cause thermal ablation. It is necessary to use one or more grounding pads large enough to allow sufficient current in the resulting electric circuit. In very small children (<10 kg), this may be technically challenging. Care must be taken to avoid skin burns [3].

15.1.2 Microwave Ablation

Microwave ablation (MWA) is a similar technique to RFA but uses much higher frequency electromagnetic waves (in the region of 2 GHz). One advantage over RFA is that no grounding pads are required. MWA has recently become the percutaneous treatment of choice for recurrent hepatoblastoma (Fig. 15.1).

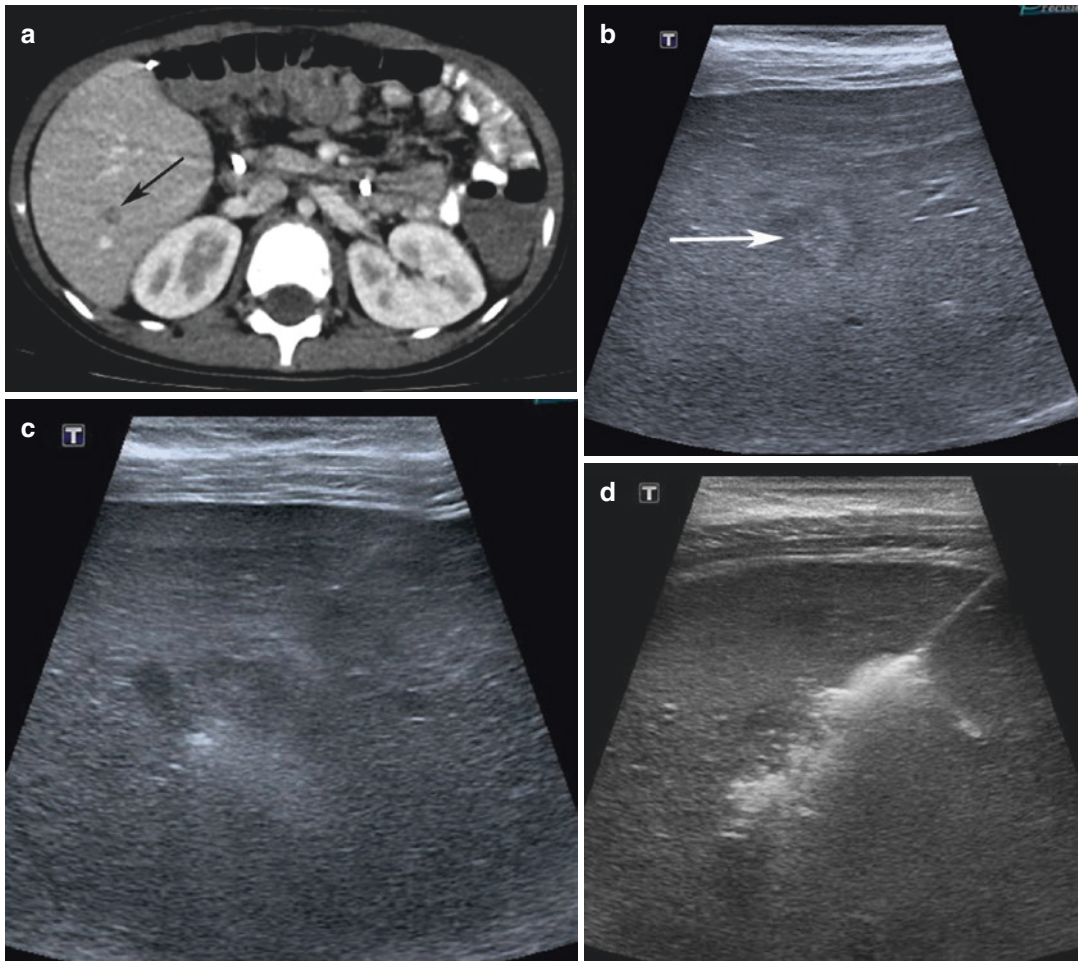

Fig. 15.1 Microwave ablation in a 7-year-old male status post left hepatic lobectomy for hepatoblastoma with a new lesion in the right lobe. (**a**) IV contrast-enhanced CT shows a hypodense lesion in the right hepatic lobe (arrow). (**b**) Transverse ultrasound of the right hepatic lobe shows a hyperechoic lesion with a hypoechoic halo corresponding to the lesion seen on CT. (**c**) Microwave ablation probe is placed across the lesion using ultrasound guidance. (**d**) Hyperechoic microbubbles form during microwave ablation

15.1.3 Cryoablation

Cryoablation causes cell death by generating extremely low temperatures (typically below −40 °C) within the tumor. Careful image guidance is needed, first to place the cryoablation probe(s) accurately and then to monitor the growth of the "iceball" to confirm effective tumor treatment and avoid damage to adjacent tissue (Fig. 15.2). Simple measures, such as hydrodissection and the application of sterile gloves filled with warm water, are sufficient to prevent injury to the overlying skin.

Established indications for cryoablation in adults include small renal tumors, bone and lung metastases, and extra-abdominal desmoid tumors [5, 6]. Currently, most potential indications in pediatrics are for treatment of nonmalignant conditions such as vascular malformations [7] including fibro-adipose vascular anomaly [8] and benign neoplasms, such as osteoid osteoma [9]. Nevertheless, cryoablation shows great promise as a potential treatment for recurrent or metastatic bone or soft tissue sarcomas [10] and may also have a role in the treatment of small renal tumors.

15.1.4 Other Forms of Percutaneous Ablation

Irreversible electroporation (IRE) changes the conductivity and permeability of the cell membrane by applying short pulses of electrical energy, causing cellular disruption and thermal injury [11]. Although IRE has been adopted in adults, for example, in the treatment of liver tumors and unresectable pancreatic cancer, its use in children with cancer has not yet been reported.

Percutaneous ethanol ablation is a cheap and simple technique, but its reported use in pediatric oncology appears to be limited to liver tumors [4, 12].

15.2 Transarterial Therapy

Intraarterial delivery of anticancer drugs or other treatment is attractive, in principle, because of the potential to deliver an increased local concentration of the therapeutic agent with less systemic toxicity.

15.2.1 Intraarterial Chemotherapy

The most important current application of intraarterial chemotherapy in pediatric oncology is in children with retinoblastoma [13]. Retinoblastoma is a tumor that rarely metastasizes outside the eye and is therefore ideally suited to local therapy. Following femoral artery access, an angiographic catheter is advanced to the ipsilateral internal carotid artery, and a coaxially inserted microcatheter is used to access the

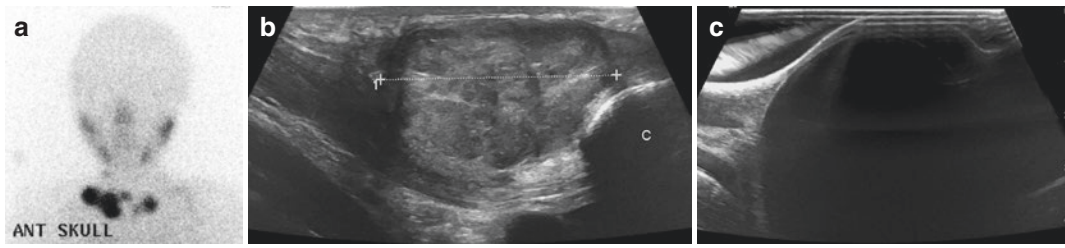

Fig. 15.2 Cryoablation in a 9-year-old girl with recurrent neuroblastoma. (**a**) ^{123}I-metaiodobenzylguanidine scintigraphy shows five avid lesions low in the neck. (**b**) Each lesion was targeted separately. Sagittal ultrasound shows the relationship of one lesion (cursors) to the clavicle (C). (**c**) Following cryoablation, the "iceball" is seen as a hypoechoic region completely covering the lesion

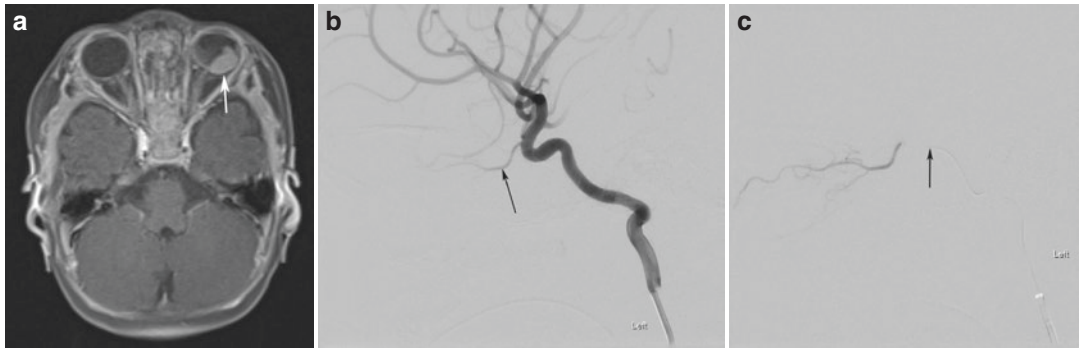

Fig. 15.3 Intraarterial chemotherapy in a 14-month-old girl with germline mutation in *RB1* and retinoblastoma. (**a**) Contrast-enhanced fat-saturated T1-weighted transverse image shows a left-sided intraocular tumor (arrow). (**b**) Lateral projection of left internal carotid artery angiogram shows a normal left ophthalmic artery (arrow). (**c**) Selective angiography performed through a microcatheter (arrow) shows that its tip lies in a suitable position for infusion of chemotherapeutic agents

ophthalmic artery (Fig. 15.3). A slow infusion of melphalan with or without topotecan is then administered. Multiple treatments may be required. Various technical problems may be encountered, including the need to access external carotid artery branches in children with variant anatomy [14] and the possibility of profound physiological reactions to the presence of the catheter in the internal carotid artery [15]. Good results in terms of eye salvage in advanced retinoblastoma have led to increased use of this technique [16].

15.2.2 Chemoembolization

It is possible that combining intraarterial chemotherapy with the occlusion (embolization) of arteries feeding the tumor may lead to slower washout of the drug from the tumor, as well as produce a potential ischemic effect. This technique has been used most often in children with liver tumors [17]. There are three potential indications: (1) to convert an unresectable tumor to a resectable one, (2) to control the tumor as a bridge to transplantation, and (3) palliation. Various chemoembolization agents have been used. Most experience internationally has been with a suspension of cisplatin (with or without doxorubicin) in ethiodized oil, followed by embolization with gelatin foam. This allows for recanalization of the occluded arteries in order to permit repeat chemoembolization. More recently, doxorubicin-eluting beads have been used for hepatic artery chemoembolization in children (Fig. 15.4). Most children develop manageable symptoms after chemoembolization, including anorexia, nausea and vomiting, fever, and pain. Transient biochemical derangements are also common. Other relatively minor complications include skin injury and arterial occlusion [18]. Potentially serious or fatal complications such as hepatic failure, liver abscess, cholecystitis, pancreatitis, gastric or duodenal injury, and pulmonary embolism are rare.

15.2.3 Radioembolization

Adults with hepatocellular carcinoma and liver metastases have for many years been treated with intraarterial delivery of yttrium-90 glass or resin microspheres for local radiation therapy. To date, radioembolization in children has been primarily reserved for relapsing tumor refractory to other treatments (Fig. 15.5). In addition

Fig. 15.4 Chemoembolization in a 6-year-old with relapsed hepatoblastoma refractory to systemic chemotherapy. (**a**) Coronal contrast-enhanced CT shows relapsed hepatoblastoma in the right hepatic lobe (arrows). (**b**) Right hepatic arteriogram demonstrates a mass with neovascularity. (**c**) Arteriogram through a microcatheter inserted in the feeding branch shows an ideal position for injection of 100–300 μm doxorubicin-eluting beads (DC Bead, BTG International, London, UK)

to many of the same complications seen with chemoembolization, radioembolization may also cause radiation pneumonitis and radiation-induced injury to the normal liver parenchyma or the gastrointestinal tract. For this reason, careful preprocedural planning is required. Selective angiography is performed in order to identify supply to nontarget regions of the gastrointestinal tract from branches of the hepatic arteries. Collateral supply to the stomach and duodenum (usually the gastroduodenal artery and right hepatic artery) can be occluded when this is appropriate. It may also be possible to occlude the intratumoral arteriovenous communications that are responsible for shunting to the lungs. Technetium-99m macroaggregated

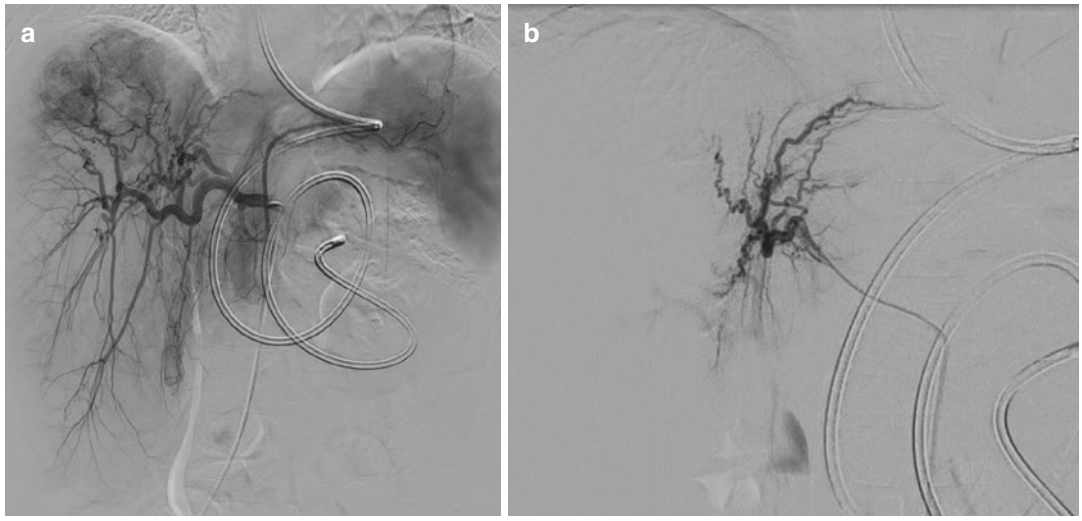

Fig. 15.5 Yttrium-90 (Y-90) radioembolization in a 5-year-old with relapsed hepatoblastoma. (**a**) Pre-embolization common hepatic arteriogram demonstrates hepatic dome hepatoblastoma with blood supply from both the left and right hepatic arteries. (**b**) Feeding branches were selected with a microcatheter, and Y-90 resin microspheres (SIR-Spheres, Sirtex Medical, Woburn, MA, USA) were injected

albumin is injected at the proposed point of radioembolization, and SPECT-CT is used to detect undesirable tracer deposition in normal liver, extrahepatic abdominal sites, and the lungs [19].

Radioembolization requires much more institutional infrastructure and regulatory oversight than chemoembolization but has been successfully used in children [20].

15.3 Other Interventional Oncology Treatments

High-intensity focused ultrasound (HIFU) is a noninvasive thermal ablation technique that allows delivery of energy to a targeted internal tumor, typically using magnetic resonance imaging for guidance. Preliminary work suggests that HIFU may have applications in desmoid fibromatosis [21], neuroblastoma [22], sarcomas [22], and liver tumors [23].

Other techniques currently being developed include treatment of focal tumors by image-guided injection of oncolytic viruses [24] or chimeric antigen receptor T-lymphocytes.

15.4 Conclusion

Various promising techniques have been employed in pediatric interventional oncology, although none of these have been adopted as the first-line treatment in international protocols. Further collaborative work is underway to try to identify the best applications for each of these techniques.

References

1. Hinshaw JL, Lubner MG, Ziemlewicz TJ, Lee FT Jr, Brace CL. Percutaneous tumor ablation tools: microwave, radiofrequency, or cryoablation--what should you use and why? Radiographics. 2014;34(5):1344–62.
2. Gomez FM, Patel PA, Stuart S, Roebuck DJ. Systematic review of ablation techniques for the treatment of malignant or aggressive benign lesions in children. Pediatr Radiol. 2014;44(10):1281–9.
3. Hoffer FA, Daw NC, Xiong X, Anghelescu D, Krasin M, Yan X, et al. A phase 1/pilot study of radiofrequency ablation for the treatment of recurrent pediatric solid tumors. Cancer. 2009;115(6):1328–37.
4. Liu B, Zhou L, Huang G, Zhong Z, Jiang C, Shan Q, et al. First experience of ultrasound-guided percutane-

ous ablation for recurrent hepatoblastoma after liver resection in children. Sci Rep. 2015;5:16805.
5. Cazzato RL, Garnon J, Ramamurthy N, Koch G, Tsoumakidou G, Caudrelier J, et al. Percutaneous image-guided cryoablation: current applications and results in the oncologic field. Med Oncol. 2016;33(12):140.
6. Schmitz JJ, Schmit GD, Atwell TD, Callstrom MR, Kurup AN, Weisbrod AJ, et al. Percutaneous cryoablation of extraabdominal desmoid tumors: a 10-year experience. AJR Am J Roentgenol. 2016;207(1):190–5.
7. Cornelis FH, Marin F, Labreze C, Pinsolle V, Le Bras Y, Midy D, et al. Percutaneous cryoablation of symptomatic venous malformations as a second-line therapeutic option: a five-year single institution experience. Eur Radiol. 2017;27(12):5015–23.
8. Shaikh R, Alomari AI, Kerr CL, Miller P, Spencer SA. Cryoablation in fibro-adipose vascular anomaly (FAVA): a minimally invasive treatment option. Pediatr Radiol. 2016;46(8):1179–86.
9. Whitmore MJ, Hawkins CM, Prologo JD, Marshall KW, Fabregas JA, Yim DB, et al. Cryoablation of osteoid osteoma in the pediatric and adolescent population. J Vasc Interv Radiol. 2016;27(2):232–7. quiz 238.
10. Lessard AM, Gilchrist J, Schaefer L, Dupuy DE. Palliation of recurrent Ewing sarcoma of the pelvis with cryoablation and somatosensory-evoked potentials. J Pediatr Hematol Oncol. 2009;31(1):18–21.
11. Lyu T, Wang X, Su Z, Shangguan J, Sun C, Figini M, et al. Irreversible electroporation in primary and metastatic hepatic malignancies: a review. Medicine (Baltimore). 2017;96(17):e6386.
12. Hara F, Kishikawa T, Tomishige H, Nishikawa O, Nishida Y, Kongo M. A child with adrenocortical carcinoma who underwent percutaneous ethanol injection therapy for liver metastasis. J Pediatr Surg. 2003;38(8):1237–40.
13. Abramson DH, Dunkel IJ, Brodie SE, Kim JW, Gobin YP. A phase I/II study of direct intraarterial (ophthalmic artery) chemotherapy with melphalan for intraocular retinoblastoma initial results. Ophthalmology. 2008;115(8):1398–404. 1404.e1391.
14. Bertelli E, Leonini S, Galimberti D, Moretti S, Tinturini R, Hadjistilianou T, et al. Hemodynamic and anatomic variations require an adaptable approach during intra-arterial chemotherapy for intraocular retinoblastoma: alternative routes, strategies, and follow-up. AJNR Am J Neuroradiol. 2016;37(7):1289–95.
15. Phillips TJ, McGuirk SP, Chahal HK, Kingston J, Robertson F, Brew S, et al. Autonomic cardiorespiratory reflex reactions and superselective ophthalmic arterial chemotherapy for retinoblastoma. Paediatr Anaesth. 2013;23(10):940–5.
16. Shields CL, Alset AE, Say EA, Caywood E, Jabbour P, Shields JA. Retinoblastoma control with primary intra-arterial chemotherapy: outcomes before and during the intravitreal chemotherapy era. J Pediatr Ophthalmol Strabismus. 2016;53(5):275–84.
17. Lungren MP, Towbin AJ, Roebuck DJ, Monroe EJ, Gill AE, Thakor A, et al. Role of interventional radiology in managing pediatric liver tumors. Part 1: Endovascular interventions. Pediatr Radiol. 2018;48(4):555–64.
18. Roebuck DJ. Alternative approaches for treatment. In: Zimmermann A, Perilongo G, Malogolowkin M, von Schweinitz D, editors. Pediatric liver tumors. Berlin: Springer; 2011. p. 177–88.
19. Gaba RC. Planning arteriography for yttrium-90 microsphere radioembolization. Semin Intervent Radiol. 2015;32(4):428–38.
20. Hawkins CM, Kukreja K, Geller JI, Schatzman C, Ristagno R. Radioembolisation for treatment of pediatric hepatocellular carcinoma. Pediatr Radiol. 2013;43(7):876–81.
21. Ghanouni P, Dobrotwir A, Bazzocchi A, Bucknor M, Bitton R, Rosenberg J, et al. Magnetic resonance-guided focused ultrasound treatment of extra-abdominal desmoid tumors: a retrospective multicenter study. Eur Radiol. 2017;27(2):732–40.
22. Shim J, Staruch RM, Koral K, Xie XJ, Chopra R, Laetsch TW. Pediatric sarcomas are targetable by MR-guided high intensity focused ultrasound (MR-HIFU): anatomical distribution and radiological characteristics. Pediatr Blood Cancer. 2016;63(10):1753–60.
23. Wang S, Yang C, Zhang J, Kong XR, Zhu H, Wu F, et al. First experience of high-intensity focused ultrasound combined with transcatheter arterial embolization as local control for hepatoblastoma. Hepatology. 2014;59(1):170–7.
24. Streby KA, Geller JI, Currier MA, Warren PS, Racadio JM, Towbin AJ, et al. Intratumoral injection of HSV1716, an oncolytic herpes virus, is safe and shows evidence of immune response and viral replication in young cancer patients. Clin Cancer Res. 2017;23(14):3566–74.

Tumour Tissue Sampling

16

Sam Stuart and Premal Amrishkumar Patel

16.1 Introduction

Indications for tumour biopsy include making the diagnosis of benign or malignant disease, staging malignancy and identifying or excluding infection. Image guidance allows accurate and specific sampling of tumours. The choice of imaging will depend on the location and nature of the tumour to be biopsied. Here we discuss patient work-up, the modality of imaging to use and possible complications and risks.

Image-guided percutaneous biopsy provides tissue for diagnosis and characterisation. Percutaneous biopsy is becoming more accepted as an appropriate and accurate way to obtain tissue for diagnosis and biological studies. Traditionally open surgical biopsy was thought of as the best way to obtain adequate tissue for diagnosis and biological characterisation. This method however is more invasive than IR-guided biopsy and is now rarely needed [1–3]. Percutaneous biopsy is also significantly cheaper to perform than open excision or surgical biopsy [4].

S. Stuart (✉) · P. A. Patel
Radiology Department, Great Ormond Hospital for Children, NHS Foundation Trust, London, UK
e-mail: Sam.Stuart@gosh.nhs.uk; Premal.Patel@gosh.nhs.uk

16.2 Patient Preparation/ Work-Up

16.2.1 Multidisciplinary Team Discussion

Prior to performing biopsy, it is ideal if the patient and the reasons for biopsy and choice of approach have been discussed in a multidisciplinary team meeting so that all parties can confirm the need for biopsy and choose the optimal approach. This, in many ways, is the most important part of the process of obtaining tissue. Discussion should also cover the amount of tissue required, particularly by the pathology team to make an accurate diagnosis and to perform biological tests to plan treatment. Whereas in adults only 1–2 cores of tissue are often obtained or needed, in children more tissue is often required for full characterisation of disease, and as many as 10–15 biopsy cores of tissue may be necessary to ensure adequate tissue is obtained. It is not only feasible but often very straightforward to obtain this significant number of biopsy cores and amount of tissue, thus avoiding the need for open or excisional biopsy.

It is important that the operator performing the image-guided procedure reviews the images prior to biopsy to ensure they are happy with the approach chosen and can plan their method. If ultrasound guidance is to be used, then ideally the operator should have performed the ultrasound or at least have reviewed the images.

S. D. Voss, K. McHugh (eds.), *Imaging in Pediatric Oncology*, Pediatric Oncology,
https://doi.org/10.1007/978-3-030-03777-2_16

16.2.2 Blood Tests

A normal coagulation profile, satisfactory haemoglobin level for the procedure and adequate platelet count are the most important blood results needed for solid organ biopsy. Platelet level of 50×10^9/L (50,000/μL) is satisfactory for most biopsies performed, but 100×10^9/L (100,000/μL) is often desirable for biopsies of masses within the liver. Cross-matched blood is rarely needed for the majority of procedures; however patients should have a valid blood group typing performed prior to the biopsy. Cross-matched blood should be available when performing biopsy of a mass within the liver or other lesions determined to be at high risk for haemorrhage.

16.2.3 Consent

Written consent for all percutaneous biopsies should be sought. The reason for needing a biopsy should be discussed as well as all of the other possible options including not having the procedure, percutaneous biopsy or FNA and surgical biopsy and the reason that the type of procedure being performed has been chosen. Risks of all biopsy procedures include haemorrhage, infection, pain and failure either to obtain tissue or to obtain adequate tissue for diagnosis. In our experience this is very rare. Tumour seeding along the biopsy tract is rarely seen but should be mentioned as a possible complication as this may result in the need for further treatment.

16.2.4 Sedation/Anaesthesia

Percutaneous biopsy in adults using local anaesthesia alone is an accepted technique. In children, however, and especially as most childhood cancers present in younger children, sedation or general anaesthesia may be needed. The use of local anaesthetic at the time of procedure can help improve postoperative pain.

16.2.5 Pre-procedure Imaging

Cross-sectional imaging (CT or MRI scan) is useful to review when planning a biopsy as it will allow identification of the most straightforward and safest lesion to biopsy. Imaging with ultrasound prior to the induction of general anaesthesia or sedation allows confidence that the chosen lesion is suitable for ultrasound-guided biopsy. Diffusion-weighted images (DWI) or ADC images on MRI are particularly useful to allow identification of areas of tumour that are likely to yield densely cellular tissue which is more useful for diagnostic tests than necrotic areas of a tumour. It is important to take at least some samples from the peripheral aspect of the tumour where viable tumour is likely to be found.

16.2.6 Contraindications

Contraindications to percutaneous image-guided tumour biopsy include there being no safe route to the lesion and uncorrectable bleeding diathesis. It should always be considered that other methods than a percutaneous image-guided biopsy may be available such as open surgical biopsy or endoscopic guided biopsy and that the risks and benefits of possible routes or approaches are considered. The safest route that is most likely to obtain the amount and type of tissue needed should be chosen.

16.3 Biopsy Device

16.3.1 Fine Needle Aspiration (FNA)

Fine needle aspiration involves passage of a needle into a lesion to yield a few cells for cytological analysis. It is not often used in paediatric oncology. FNA is usually only used to see if local lymph nodes are involved with metastatic spread. Structural information cannot be gleaned from the samples achieved using this sampling method. Additionally, the quantity of tissue obtained is inadequate for the numerous tests that may be needed to characterise and plan treatment for

primary tumours. The use of FNA will often be dictated by the preference or expertise of the local pathology department.

16.3.2 Core Needle Biopsy

Core needle biopsy is the most commonly performed method for obtaining tumour samples from soft tissue. There are many core needle biopsy devices available. Most are side-notch needles. These have a notch in a stylet which is advanced into the tissue to be sampled, and then a cutting cannula travels over the stylet and traps the tissue in the groove of the stylet (e.g. Medax Biiofeather™ Medax, Milan, Italy) (Fig. 16.1). There are numerous devices available; some are fully automated, in which a spring mechanism pushes the inner stylet forward, followed almost instantaneously by the outer cutting cannula. In the semiautomated systems, the inner stylet is advanced manually, and the spring mechanism advances the cutting cannula which travels over the stylet. Fully manual devices are also available. These devices generally can produce semicylindrical cores of 1 or 2 cm in length. The diameter of the core is dependent on the gauge of the device. An alternative to the side-notch needles is the automated end-cutting biopsy needle (e.g. BioPince; Angiotech Pharmaceuticals, Vancouver, BC). These are claimed to yield cylindrical cores that are slightly larger in diameter and volume for needles of similar gauge. They utilise a stylet which does not advance forwards; instead a coring cannula advances into the tissue to be sampled, over this an outer cannula with a pincer advances to cut the distal end of the sample and trap it with the cutting cannula.

Regardless of the device used, many cores are often needed for adequate tissue in paediatric tumours for diagnosis and biological characterisation. As a result a coaxial approach is often preferable (this is discussed further in Sect. 16.5).

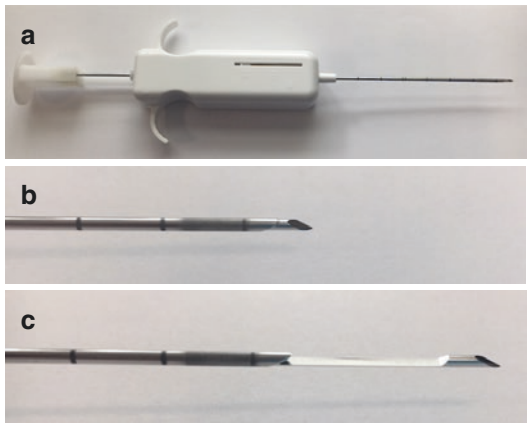

Fig. 16.1 (**a**) Semi-automatic spring loaded biopsy needle, (**b**) needle tip prior to advancement of biopsy tray, (**c**) needle tip after advancement of biopsy tray—ready for sample to be taken

16.3.3 Bone Biopsy Needles

For biopsy of bone lesions, there are number of specific bone biopsy needles which specifically allow ease of passage through bone while obtaining adequate specimens. Drill-assisted devices (e.g. The Arrow® OnControl® Powered Bone Access System, Teleflex, NC) can allow large diagnostic quality cores to be obtained with minimal physical exertion.

16.3.4 Vacuum-Assisted Biopsy Devices

Novel devices have found a role in adult practice. For example, vacuum-assisted biopsy devices (e.g. Vacora® Vacuum-Assisted Breast Biopsy System, BARD, Tempe, AZ) have been used to sample breast lesions in adults and to perform muscle biopsy in adults and children. They allow large volumes of tissue to be obtained quickly and under image guidance. Their role is not yet established in tumour biopsy in children.

16.3.5 Endoscopic Biopsy

Endoscopic biopsy or bronchoscopic biopsy is possible in larger children but not widely used. As mentioned earlier the young age of many children on presentation with childhood cancer means that these techniques may not be feasible.

16.4 Image Guidance

16.4.1 Ultrasound

Ultrasound will usually be the most useful and quickest method for guiding biopsy in the majority of tumours. Percutaneous ultrasound-guided biopsy is the go to method for superficial soft tissue tumours, lymph nodes and masses in the solid organs, including the kidney, liver and spleen.

Ultrasound has the advantages of being cheap relative to cross-sectional imaging and readily available; it allows real-time visualisation of the biopsy such that interpositioned bowel loops and other structures can be moved away from the biopsy path with compression. High-quality ultrasound images are usually straightforward to obtain in children. Additionally, unlike CT-guided procedures, it doesn't expose the child to ionising radiation.

With the majority of paediatric tumour biopsies, a high-frequency linear transducer can be used, and high-quality, high-resolution images are obtained. In larger patients with deeper lying tumours, lower-frequency curvilinear transducers may be needed to demonstrate the lesion clearly due to the limitations in the depth of view with high-frequency transducers.

Generally, if a lesion can be seen clearly on ultrasound, then it is likely to be suitable for ultrasound-guided biopsy, and this is likely to be the best modality to guide the biopsy. Most abdominal lesions, appendicular soft tissue lesions and neck lesions in children can be biopsied under ultrasound guidance. Ultrasound-guided biopsies in the thorax can be more difficult due to shadowing caused by the ribs and lack of ultrasound penetration through aerated lung. However, the intercostal spaces can be used to provide acoustic windows allowing ultrasound-guided biopsies within the thorax of pleurally based lesions and anterior mediastinal masses (Fig. 16.2).

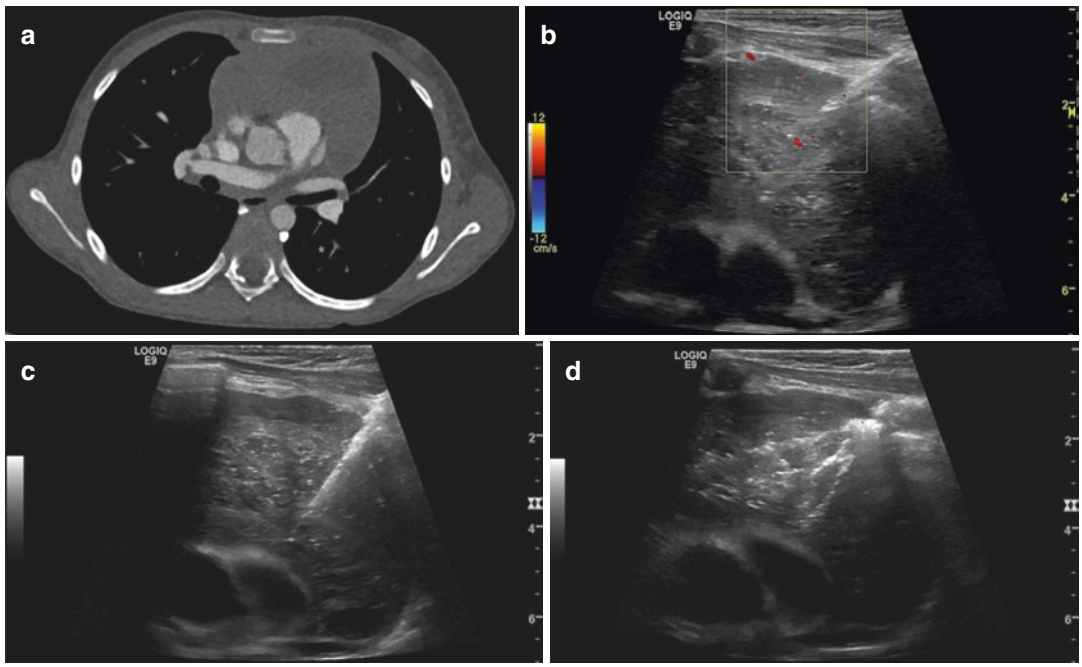

Fig. 16.2 A 9-year-old with an anterior mediastinal mass. (**a**) Axial image contrast-enhanced CT showing close relationship to aorta and pulmonary artery. Ultrasound-guided biopsy was performed. (**b**) demonstrates insertion of a coaxial needle into the lesion avoiding the internal mammary vessels. (**c**) demonstrates subsequent insertion of the biopsy needle. Eleven cores of tissue were taken. (**d**) Immediate post-biopsy image demonstrates numerous hyperechoic biopsy tracts though the lesion and a hyperechoic Gelfoam plug at the site of entry into the mass. The samples obtained resulted in a histological diagnosis of T-cell acute lymphoblastic lymphoma

16.4.2 Fluoroscopy

Fluoroscopy is used most often to guide bone lesion biopsies. It can be used alone if the lesion is readily visible on fluoroscopy. However, it is most often used in combination with cone beam CT (see below). It can also be used to judge needle depth when performing bone biopsy but doesn't often give as clear an image as to the location of the needle in a mass lesion as CT- or MRI-guided biopsy.

16.4.3 CT and Cone Beam CT

Bone and lung masses are primarily biopsied using CT guidance. Ultrasound will not penetrate through the bone or the air in the lungs so medullary bone and pulmonary lesions are particularly difficult to biopsy using ultrasound guidance alone. A combination of ultrasound and CT or fluoroscopic guidance can be useful with ultrasound used to identify the surface of the lesion and then fluoroscopy or CT to identify the depth of the biopsy. Most biopsy needles and devices have markers on them to demonstrate the depth of needle placement.

CT-guided biopsy can be performed in a conventional CT scanner either with the use of CT fluoroscopy or not. The use of CT is associated with a radiation burden [5]. CT fluoroscopy uses a relatively high dose of radiation so is not ideal when performing procedures on children. Dose levels can be kept at a minimum by only imaging the region of interest over a few contiguous slices. Cone beam CT (CB-CT) uses flat panel detectors to acquire real-time 3-D images in the interventional radiology suite. CB-CT is gaining popularity for performing CT-guided biopsy. This procedure can be performed in the interventional suite with comfort for the operator and anaesthetist, and the technical success and diagnostic accuracy are thought to be similar to traditional CT-guided biopsies with lower radiation dose and procedure time [6]. There are a number of additional dose reduction techniques being developed to further minimise the radiation burden from cone beam CT while maintaining image quality [7].

16.4.4 MRI

MRI-guided biopsy can be used for lesions that are not well visualised by ultrasound or CT. MRI-guided biopsy has disadvantages including that it is time consuming due to long image acquisition times. These long times mean that motion artefact, such as respiratory motion, can seriously degrade images. Special equipment, including an MRI compatible biopsy needle, is also needed that is safe within the locality of an MRI scanner and in particular the associated high-strength magnetic field. Limiting the area imaged and decreasing image quality such as spatial resolution can help images be obtained more quickly using MRI. Advantages of MRI-guided biopsy are that MRI can visualise some lesions not seen on CT or US or identify them more clearly, even without the use of intravenous contrast agents. There is no ionising radiation burden with MRI, and artefacts from bowel gas or bone that limit US image quality do not impact on MRI images. Focal liver lesions have been successfully biopsied in children using MRI guidance [8].

16.4.5 Contrast-Enhanced Ultrasound

Contrast-enhanced ultrasound can be useful, not only to allow imaging characterisation of lesions but also to increase lesion conspicuity to allow biopsy of a lesion that may not be easily seen with greyscale ultrasound [9]. It can demonstrate differential vascularisation to allow the differentiation between tumour and normal parenchyma. This not only makes the lesion easier to see but may also allow targeting of more vascular areas of the tumour rather than poorly perfused necrotic areas [10]. At present the ultrasound contrast agents that are approved for use are non-targeted; however molecularly targeted contrast microbubbles are being developed. In the future targeted ultrasound contrast agents may help target viable tumour tissue or areas of tumour with specified tumour biology. A molecular ultrasound contrast agent targeted at vascular endothelial growth factor receptor 2 has recently entered first in human clinical trials [11].

16.4.6 Image Fusion and Navigation

Image fusion methods can overlay CT or MRI images with CB-CT or ultrasound to allow lesions to be biopsied in an anatomical location even if they are not clearly visible on the imaging modality being used to guide the needle. Fusion of MRI images onto cone beam CT has been demonstrated to allow biopsy of lesions using real-time fluoroscopy that are only visible on MRI (Fig. 16.3) [12, 13]. Advantages of MR/CB-CT fusion techniques include the ability to perform the biopsy in a conventional interventional suite, three-dimensional planning of the needle trajectory using cross-sectional imaging, real-time fluoroscopic guidance for needle trajectory correction and the ability to target within heterogeneous lesions based on MR signal characteristics to maximise the potential biopsy yield [12]. Similarly for liver lesions not readily visible by ultrasound, electromagnetic tracking-based fusion imaging of real-time US and CT or MR images can be used to aid intervention (Fig. 16.4) [14]. If fusion with MR is being considered, the MRI should include an acquisition with isotropic voxels, which can be used for subsequent image registration. Additionally, fusion can be facilitated by scanning the patient with markers applied to the skin and using these later as landmarks to guide image registration.

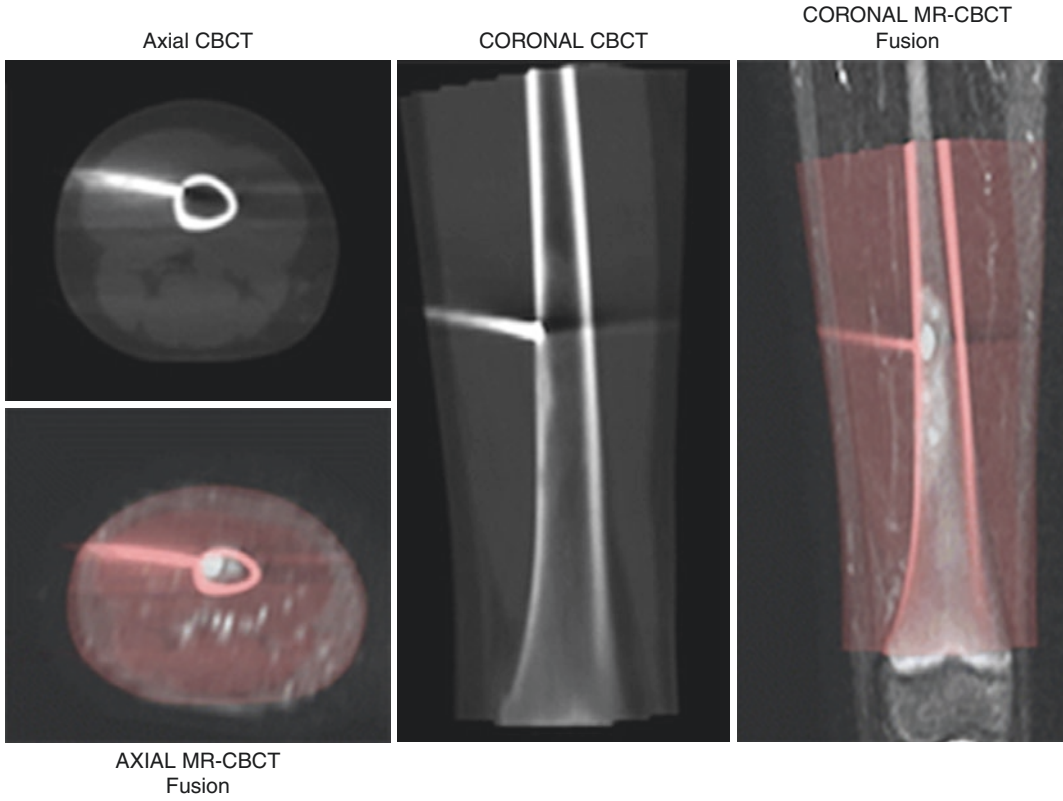

Fig. 16.3 Example of fusing MR to cone beam CT to biopsy a bone lesion. This lesion cannot be seen on the CT without image fusion. Axial and coronal cone beam CT and MR cone beam CT fusion images of a 6-year-old girl demonstrate a needle passage through a central area of high signal intensity within the bone lesion. Used with permission from Springer Nature (13)

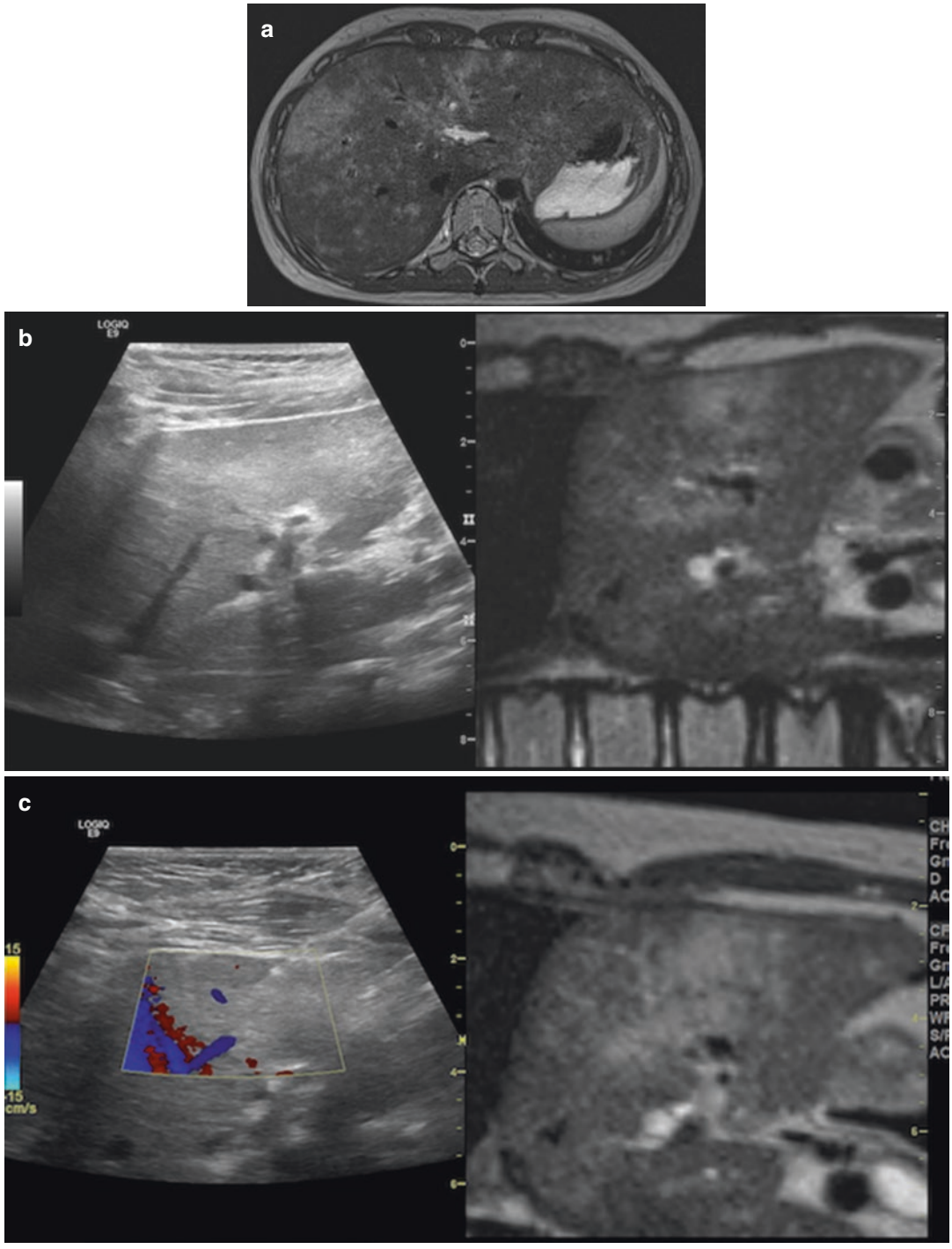

Fig. 16.4 A 9-year-old girl with ataxic telangiectasia and weight loss. Diffuse signal abnormality as seen on the axial T2-weighted MR image (**a**) was seen throughout the liver, predominately in a periportal distribution. This was not seen on ultrasound. (**b**) MRI fused with ultrasound to perform lesion biopsy. (**c**) MRI/ultrasound fusion imaging demonstrating insertion of biopsy needle into abnormal MR signal area

16.5 Biopsy Technique

Biopsy procedures under ultrasound guidance can either be performed freehand or using biopsy needle guides. Needle guides attach to the probes and help to guide the needle to the desired location. Operator preference usually dictates whether a needle guide will be used or the procedure performed freehand. A freehand approach allows more flexibility with regard to needle trajectory. More advanced techniques are becoming available including real-time guidance systems using electromagnetic needle tracking. This could allow guidance of needles into difficult to visualise areas. Similarly when using CB-CT to perform biopsies, a software-based needle guide system (e.g. Siemens syngo iGuide or Philips XperGuide) can be used.

16.5.1 Coaxial Approach

Tumour biopsies are usually performed using a coaxial technique (see above). This involves guiding an outer coaxial needle into the lesion, and then a biopsy needle is passed through the biopsy device multiple times. This allows multiple samples to ensure an adequate volume of tissues and allows sampling of multiple different areas of the lesion at different depths and locations by manipulating the outer coaxial needle. Care should be taken to ensure only one tract through normal tissue, and one pass is made through the tumour capsule or pseudo capsule. This helps to minimise complications such as bleeding and tract seeding. The coaxial technique has been studied for solid organ biopsy and been shown to be associated with a faster biopsies and decreased complication rate [15].

16.5.1.1 Gauge of Biopsy Needle

The authors advocate the following gauge of needle for biopsy of tumours in the following location:

- Liver, spleen and lung—18 g
- Renal or other abdominal masses, mediastinal lesions—16 g
- Lymph node or superficial lesions—14 g
- Bone biopsy—11 g

Tract Embolisation: If a coaxial biopsy needle is used, then the path that the needle has taken can be "plugged" using a substance to decrease the risk of bleeding. This is called tract embolisation. Absorbable gelatin sponge (Gelfoam®, Pfizer, NY) is the most commonly used agent. This can be deployed as pledgets or as a slurry down the coaxial needle. To minimise the risk of bleeding, the Gelfoam pledgets or slurry should cover the site of penetration of the capsule of the organ in which the tumour lies, if this is indeed the case. This may not only reduce haemorrhage but also reduce the risk of tumour seeding in the tract and the risk of pneumothorax after a transpleural path has been made, for example, in lung lesion biopsy. Studies have shown a significant decrease in pneumothorax rate post biopsy with the use of a plug for tract embolisation in patients undergoing transthoracic needle biopsy [16]. Ultrasound-guided percutaneous liver biopsy with gelatin sponge pledget tract embolisation has been shown to be associated with minimal complications [17]. Percutaneous liver biopsy with tract embolisation in a paediatric population even in the setting of coagulopathy has been shown to be as safe and effective as transjugular liver biopsy [18].

To reduce rates of pneumothorax post lung biopsy, an expanding hydrogel plug (Bio-Seal™, Angiotech, Vancouver, BC) has been developed and has been shown to significantly reduce rates of pneumothorax in patients undergoing CT-guided lung biopsy [19].

16.5.2 Special Considerations

There is sometimes no direct percutaneous route to a tumour. In such cases after consideration of alternatives, a biopsy may be performed by crossing other organs with the needle. For example, deep pelvic tumours can be biopsied using a transvesical percutaneous route or transrectal route under ultrasound guidance. Urine in the bladder will often provide a good sonographic window to visualise the mass to be targeted. Pancreatic-based masses usually require a trans-

gastric passage of the needle. Some upper abdominal masses may require passage of the biopsy needle through the pleural space; in such cases care should be taken to reduce potential contamination of the pleural cavity.

The presence of ascites in the abdomen and pleural effusion in the thorax can contribute to bleeding risk as haemorrhage can continue into the fluid without physical tamponade effect. Draining the ascites or pleural effusion prior to biopsy and plugging the biopsy tract with Gelfoam or similar product, either as pledgets or slurry, can reduce the post-procedure haemorrhage risk.

16.6 Vascular Access and Other Diagnostic Sampling

If general anaesthesia is used to facilitate biopsy, then further procedures that may be needed can be performed at the same time such as bone marrow aspiration and/or trephines, lumbar puncture and central venous access device insertion so that the patient can start treatment as soon as needed.

16.7 Post-procedure Care

Following biopsy patients should wait at least 6 h prior to discharge with 1–2 h of bed rest. This will differ between institutions, but some centres are happy to discharge patients the same day. There is a risk of delayed bleeding post liver lesion biopsy. Some institutions routinely check the haemoglobin level post biopsy to ensure there has been no significant decline. This is not routine practice at all institutions as haemodynamic and other changes such as increasing abdominal distension are likely to be noted earlier than a haemoglobin drop. Additionally, the pre-procedure haemoglobin is often taken in a fasted and partially dehydrated state pre-procedure, and the post-procedure haemoglobin is taken after fluids have been administered under general anaesthetic and the child has started drinking again. Haemodilutional effects thus have the potential to confound the comparison of these results. Following lung lesion biopsy, it is prudent to check for pneumothorax and perform chest X-ray an hour or more later to assess for pneumothorax or developing haemothorax.

16.8 Complications

Complications from image-guided biopsy are uncommon but can be life threatening when they occur. Haemorrhage requiring transfusion or intervention is rare. It is more common from the spleen than the other solid organs [2]. Patients should be monitored closely following biopsy to ensure that significant haemorrhage, although rare, is detected when it occurs. If haemorrhage occurs and does not settle with medical management, it may be possible to control by interventional radiological embolisation (see Chap. 15). There is always the possibility that non-diagnostic samples can be obtained, particularly from lesions with large amounts of necrotic or non-viable tissue. By sampling different areas of a lesion, identifying viable areas using imaging (vascular and enhancing areas or cellular areas on MRI) and taking adequate amount of tissue, then the non-diagnostic sample rate can be kept to a minimum. Tumour seeding is also possible but uncommon. In adults the tract seeding incidence is reported to be up to 3.4% based upon data mostly derived from hepatocellular carcinoma biopsies [2]. In our experience of tumour biopsies in children, it is significantly less than this. The biopsy route should always be planned with the possibility of tumour seeding in mind, and uninvolved areas should not be "contaminated" by the biopsy tract wherever possible as this could limit or impact on future resection margins or approaches. Damage to adjacent structures from needle path can be minimised by careful planning of the biopsy route and careful imaging at the time of biopsy.

16.9 Conclusion

Image-guided biopsy is becoming the mainstay of tissue sampling in paediatric oncology. Adequate pre-procedure imaging is vital for choosing the best technique to use, and discus-

sion in a multidisciplinary team (MDT) meeting format is useful for identifying the lesions or lesions from which tissue is needed and discussing the approach and amount of tissue required.

In summary, the steps to safely performing percutaneous biopsy include:

- Review imaging.
- Plan lesion to biopsy and method to perform biopsy ideally in MDT format. Discussions will highlight the amount of tissue required for investigations needed and how the samples should be prepared.
- Ensure blood work is within required limits and informed consent is obtained.
- Perform biopsy, preferably with coaxial needle, and consider plugging biopsy tract.
- Ensure samples are sent to appropriate place for investigations.

References

1. Sebire NJ, Roebuck DJ. Pathological diagnosis of paediatric tumours from image-guided needle core biopsies: a systematic review. Pediatr Radiol. 2006;36:426–31. https://doi.org/10.1007/s00247-006-0123-4.
2. Gupta S, Wallace MJ, Cardella JF, et al. Quality improvement guidelines for percutaneous needle biopsy. J Vasc Interv Radiol. 2010;21:969–75. https://doi.org/10.1016/j.jvir.2010.01.011.
3. Chowdhury T, Barnacle A, Haque S, et al. Ultrasound-guided core needle biopsy for the diagnosis of rhabdomyosarcoma in childhood. Pediatr Blood Cancer. 2009;53:356–60. https://doi.org/10.1002/pbc.22059.
4. Lachar WA, Shahab I, Saad AJ. Accuracy and cost-effectiveness of core needle biopsy in the evaluation of suspected lymphoma: a study of 101 cases. Arch Pathol Lab Med. 2007;131:1033–9. https://doi.org/10.1043/1543-2165(2007)131[1033:AACOCN]2.0.CO;2.
5. Brenner D, Elliston C, Hall E, Berdon W. Estimated risks of radiation-induced fatal cancer from pediatric CT. AJR Am J Roentgenol. 2001;176:289–96. https://doi.org/10.2214/ajr.176.2.1760289.
6. Shellikeri S, Setser RM, Hwang TJ, et al. Real-time fluoroscopic needle guidance in the interventional radiology suite using navigational software for percutaneous bone biopsies in children. Pediatr Radiol. 2017;47:963. https://doi.org/10.1007/s00247-017-3830-0.
7. Acord M, Shellikeri S, Vatsky S, et al. Reduced-dose C-arm computed tomography applications at a pediatric institution. Pediatr Radiol. 2017;47:1817. https://doi.org/10.1007/s00247-017-3964-0.
8. Smith EA, Grove JJ, Van Der Spek AFL, Jarboe MD. Magnetic-resonance-guided biopsy of focal liver lesions. Pediatr Radiol. 2017;47:750–4. https://doi.org/10.1007/s00247-017-3788-y.
9. Zhou J-H, Shan H-B, Ou W, et al. Contrast-enhanced ultrasound improves the pathological outcomes of US-guided core needle biopsy that targets the viable area of anterior mediastinal masses. Biomed Res Int. 2018;2018:9825709. https://doi.org/10.1155/2018/9825709.
10. Huang DY, Yusuf GT, Daneshi M, et al. Contrast-enhanced ultrasound (CEUS) in abdominal intervention. Abdom Radiol (NY). 2018;43:960–76. https://doi.org/10.1007/s00261-018-1473-8.
11. Abou-Elkacem L, Bachawal SV, Willmann JK. Ultrasound molecular imaging: moving toward clinical translation. Eur J Radiol. 2015;84:1685–93. https://doi.org/10.1016/j.ejrad.2015.03.016.
12. Thakor AS, Patel PA, Gu R, et al. MR cone-beam CT fusion image overlay for fluoroscopically guided percutaneous biopsies in pediatric patients. Pediatr Radiol. 2016;46:407–12. https://doi.org/10.1007/s00247-015-3479-5.
13. Shellikeri S, Setser RM, Vatsky S, et al. Prospective evaluation of MR overlay on real-time fluoroscopy for percutaneous extremity biopsies of bone lesions visible on MRI but not on CT in children in the interventional radiology suite. Pediatr Radiol. 2018;48:270–8. https://doi.org/10.1007/s00247-017-3995-6.
14. Lee MW. Fusion imaging of real-time ultrasonography with CT or MRI for hepatic intervention. Ultrasonography. 2014;33:227–39. https://doi.org/10.14366/usg.14021.
15. Babaei Jandaghi A, Lebady M, Zamani A-A, et al. A randomised clinical trial to compare coaxial and noncoaxial techniques in percutaneous core needle biopsy of renal parenchyma. Cardiovasc Intervent Radiol. 2017;40:106–11. https://doi.org/10.1007/s00270-016-1466-3.
16. Engeler CE, Hunter DW, Castaneda-Zuniga W, et al. Pneumothorax after lung biopsy: prevention with transpleural placement of compressed collagen foam plugs. Radiology. 1992;184:787–9. https://doi.org/10.1148/radiology.184.3.1509068.
17. Lungren MP, Lindquester WS, Seidel FG, et al. Ultrasound-guided liver biopsy with gelatin sponge pledget tract embolization in infants weighing less than 10 kg. J Pediatr Gastroenterol Nutr. 2016;63:e147–51. https://doi.org/10.1097/MPG.0000000000001429.
18. Tulin-Silver S, Obi C, Kothary N, Lungren M. Comparison of transjugular liver biopsy and percutaneous liver biopsy with tract embolization in pediatric patients. J Pediatr Gastroenterol Nutr. 2018;67:180. https://doi.org/10.1097/MPG.0000000000001951.
19. Zaetta JM, Licht MO, Fisher JS, Avelar RL. A lung biopsy tract plug for reduction of postbiopsy pneumothorax and other complications: results of a prospective, multicenter, randomized, controlled clinical study. J Vasc Interv Radiol. 2010;21:1235–1243.e3. https://doi.org/10.1016/j.jvir.2010.04.021.

17 Radiation Treatment Planning in Pediatric Oncology

Naomi A. Lavan and Henry C. Mandeville

17.1 Introduction

In the discipline of radiation oncology, the primary aim of treatment is to deliver ionizing radiation to the target while simultaneously minimizing dose delivered to adjacent normal tissues. The biological basis of radiotherapy (RT) includes cell- and tissue-specific inherent radiation sensitivity and the exploitation of the differences in tumor and normal tissue responses to ionizing RT. The balance between tumor control probability (TCP) and normal tissue complication probability (NTCP) is often referred to as the therapeutic ratio.

The interaction of ionizing radiation within the cells of the body produces direct effects and, more commonly, indirect effects on DNA mediated by free hydroxyl radicals produced through the ionization of water. DNA damage can be lethal (double-strand DNA breaks) or sublethal (single-strand DNA breaks, DNA cross-links, or base damage). Repair of sublethal damage in normal cells typically occurs within 6 h, and this forms the basis of fractionated delivery of RT. Normal cells are able to repair such damage correctly, whereas dysfunctional repair pathways are more likely to occur in tumor cells. Cells with cumulative chromosomal aberrations from poorly repaired DNA damage usually undergo cell death either soon after exposure or during subsequent cell divisions.

In pediatric radiation oncology, conventionally fractionated RT is delivered in five daily fractions of 1.5–1.8 Gy. The total prescribed dose is determined by the tumor type with doses ranging from as low as 10.5 Gy for Wilms tumor up to ~60 Gy for some sarcomas and brain tumors. Prescribed dose and fractionation vary according to tumor type; tumor burden, i.e., microscopic versus macroscopic disease; and treatment intent (radical versus palliative). The need for RT in children and young people is always carefully balanced between therapeutic effect and the risk of treatment-related morbidity. The vast majority of pediatric RT treatments are prescribed according to national or international trial protocols or guidelines.

RT can be delivered by external beam RT (EBRT) using photons, electrons, protons, or other particles and, internally, using brachytherapy and molecular RT. The following discussion will give an overview of these modalities with a primary focus on EBRT photon treatment as this is, at present, the most common mode of RT delivery for children and young people.

N. A. Lavan (✉) · H. C. Mandeville (✉)
The Royal Marsden NHS Foundation Trust and Institute of Cancer Research, Sutton, UK
e-mail: Henry.Mandeville@rmh.nhs.uk

S. D. Voss, K. McHugh (eds.), *Imaging in Pediatric Oncology*, Pediatric Oncology,
https://doi.org/10.1007/978-3-030-03777-2_17

17.2 The Radiotherapy Planning Process

The process of delivering an RT treatment course can be divided into three main parts: target definition, treatment planning, and treatment delivery. Cross-sectional imaging is integral to all stages.

There are particular elements in pediatric RT planning that make the pathway quite distinct from the treatment of adults. For example, very young children often require general anesthesia for simulation image acquisition and treatment. This generally applies to patients under the age of 3 and for a significant proportion of patients aged between 3 and 5 years. This age range can vary significantly between centers depending on their equipment, treatment times, and support staff; older children, or even teenagers and young adults, who are unable to comply with lying still for treatment due to learning or behavioral issues may also require anesthesia. Play specialists play an important role in the preparation and support of children and young people for RT, and their involvement can allow a child to proceed with treatment without the need for general anesthesia; this can have significant resource implications for an RT department.

Children are assumed to be inherently more radiation sensitive compared to adults, and this is reflected in the use of lower doses per fraction and lower overall total doses compared to fractionation schedules used for adult cancers [1]. Musculoskeletal late effects from RT can result in significant deformity so care is taken to irradiate vertebrae adjacent to a target volume homogenously to avoid future kyphosis or scoliosis. Radiation sensitivity also needs to be considered in the selection and modification of imaging parameters in order to minimize dose exposure from all imaging procedures as much as possible.

17.2.1 Common Terms in RT Treatment Planning

Internationally accepted terminology in RT treatment planning and additional commonly used terms that are referred to in this chapter are summarized in Table 17.1.

Table 17.1 Glossary of terms

EBRT	External beam RT
RTP	Radiotherapy planning scan
GTV	Gross tumor volume
CTV	Clinical target volume
ITV	Internal target volume
PTV	Planning target volume
PRV	Planning at risk volume
IM	Internal margin
SM	Setup margin
IGRT	Image guided radiotherapy
OAR	Organ at risk
Linac	Linear accelerator
MV	Megavoltage
KV	Kilovoltage
EPID	Electronic portal image dosimetry
CBCT	Cone beam computed tomography
MLC	Multileaf collimator

Guidance on conformal RT treatment planning and reporting is supplied by the International Commission on Radiation Units and Measurements (ICRU). ICRU 50, 62, and 83 were published in relation to conformal photon radiotherapy reporting and planning [2–4].

The GTV is the macroscopic visible tumor mass as defined on clinical examination and/or imaging. For many pediatric tumors, RT is given following surgery meaning that a GTV, according to the ICRU definition, may not be visible. In this instance, a "virtual" GTV is reconstructed with reference to preoperative imaging to define the areas of contact between tumor and surrounding normal tissues. The CTV represents the area of microscopic disease involvement; this is an anatomical expansion that can be confined by natural barriers of spread, e.g., uninvolved bone and muscle. The PTV is a geometric expansion of the CTV and constitutes a safety margin to account for systematic and random uncertainties in patient setup relative to the treatment beam geometry (setup margin) and in target position relative to the patient's bony anatomy (internal margin) [5]. Conventionally, large, population-based PTV margins are used to address such geometric uncertainty so that the clinical target volume (CTV) is positioned within the PTV with suitably high probability. The PTV can be defined by using mathematical "margin recipes" that take

such errors, for a representative patient population, into account [6].

17.2.2 Imaging Requirements for Target Definition

Once a multidisciplinary decision to treat a patient is made, and the patient has given written informed consent, the first step in the process is for the patient to have an RT planning (RTP) scan. This dataset is used to determine the target volume for RT and to calculate treatment dosimetry. In pediatrics this step requires intensive coordination and communication between members of the multidisciplinary team including radiologists, radiographers/technologists, play specialists, and anesthetists.

Computed tomography (CT) is the most common primary imaging modality used for this purpose. CT serves two important purposes, providing a three-dimensional (3D) representation of the tumor and patient's anatomy and also allowing direct computation of RT dose through the conversion of Hounsfield units to electron densities within treatment planning software (TPS) systems. The integration of volumetric CT images into RT treatment planning pathways allows dose delivery to be conformed to the patient's anatomy, so-called 3D conformal RT (3DCRT or CRT).

Despite significant technological developments within the field of radiation oncology, target delineation is well recognized as the weakest link in the precision and accuracy of the RT pathway [7, 8]. The challenge of accurate target definition is further compounded in pediatric RT where it is common to deliver RT after surgical resection of gross disease. The clinician is then tasked with the reconstruction of the preoperative tumor volume while respecting, often significant, changes in anatomy following surgery [9]. In pediatrics, RT guidelines within trial protocols along with the provision of central review aids standardized target delineation for this challenging treatment group [8]. International RT quality assurance programs for pediatric RT are well established in the United States and more recently implemented in Europe following the important recognition that protocol compliance is essential in the prospective evaluation of patient outcomes in the setting of clinical trials [8].

Efforts to standardize treatment volumes, particularly for common adult tumor types such as lung cancer, have been made through the development of consensus contouring guidelines and atlases, e.g., the Radiation Therapy Oncology Group (RTOG), training platforms provided by collaborative bodies such as the American Society for Radiation Oncology (ASTRO) and European Society for Radiotherapy and Oncology (ESTRO), and the integration of complementary imaging modalities in addition to CT. To determine the GTV, or "virtual" GTV, reference diagnostic imaging is consulted together with the RTP scan. Common modalities in pediatric RT planning include magnetic resonance imaging (MRI), positron emission tomography/computed tomography (PET/CT), and metaiodobenzylguanidine (MIBG) scintigraphy. Most TPS platforms enable image registration, allowing clinicians to utilize rigid fusion of multimodality imaging to further enhance GTV definition. The use of image fusion requires careful consideration of immobilization and positioning in both sets of images to minimize the introduction of significant geometric error because of differences in patient positioning between the fused image sets.

Given the fundamental importance of ensuring that the treatment target is correctly identified, collaboration between radiation oncologist and diagnostic imaging specialists is essential for accurate interpretation of imaging when determining the treatment target.

CT, though the mainstay of RT at present, offers only limited soft tissue contrast. The superior soft tissue contrast on MR makes it an attractive modality for use in RT. Many departments have the ability to perform MR RTP scans. These scans are performed with the same patient immobilization and setup relative to skin marks as RTP CT scan acquisition, enabling confident fusion of the two imaging modalities. At the present time, it is not yet possible to plan directly on MR, but with the availability of hybrid MR/RT treatment platforms [10–13], the development of MR-only workflows is an active area of research. Greater integration of MR into the RT pathway is expected to have significant benefits for young

patients as additional imaging will not result in additional radiation dose to the patient.

An overview of imaging modalities incorporated into RT planning of commonly occurring pediatric tumors is given in the table below (Table 17.2) as reflected in our institutional guidelines. The use of imaging modalities auxiliary to CT in RT planning can vary between institutions depending on available resources.

17.2.3 Motion Assessment

Internal organ motion can cause imaged structures to move in or out of the CT slice window during scan acquisition. This motion results in artifacts which are commonly seen in the thorax and upper abdomen, as these sites are susceptible to respiratory-related motion [14]. Such artifacts can distort the appearance of both target structures and organs at risk, thereby introducing systematic delineation errors into the RT planning process. 4DCT was developed as a means to reduce motion-related image artifact seen on 3DCT [15, 16].

Internal motion also represents a significant source of residual error in treatment delivery. Motion of tumor and motion of the organ at risk (OAR) in the thorax and abdomen of children and young people are increasingly described in the literature [17–23]. Though of smaller magnitude than observed in adults [21], 4DCT, the current gold standard for motion assessment in adults, is increasingly used to generate individualized margins in pediatric patients [17, 23]. 4DCT imaging results in increased dose delivered to the patient, but the use of low-dose protocols looks to maintain the ALARA principle of dose exposure [23].

Despite the time-resolved nature of 4DCT, there are accepted limitations in its application, such as in the setting of irregular breathing patterns. The ability of a single 4DCT to fully characterize respiratory-related motion is potentially limited as irregular breathing can result in improper "binning" in retrospective sorting methods.

Alternative imaging modalities with potential to derive motion information include ultrasound (US) and magnetic resonance imaging (MRI), but, as yet, there are limited published results relating to their use in children [18, 24].

Table 17.2 Royal Marsden Hospital, Sutton, UK, guidelines for target definition is given as an illustrative example of the integration of imaging into the RT planning pathway

Tumor type	Target definition of GTV/CTV on contrast-enhanced CT and adjunctive imaging[a] for additional anatomical information
CNS (high grade)	Surgical cavity and any residual enhancement visible on gadolinium-enhanced T1-weighted MRI (Fig. 17.1)
CNS (low grade)	High signal intensity on T2-weighted or fluid-attenuated inversion recovery (FLAIR) MRI
CNS (cranio-spinal)	T1-weighted MRI is used to identify the thecal sac
Hodgkin lymphoma	All areas of disease according to PET-CT at the time of diagnosis (Fig. 17.2a, b) Boost is indicated to areas of persistent FDG avidity on late response assessment PET-CT
Neuroblastoma	"Virtual GTV" reconstructed with reference to preoperative CT or MR ^{123}I mIBG, ^{68}Gallium DOTATOC/DOTATATE PET-CT may be used to give additional anatomical information
Wilms tumor	"Virtual GTV" reconstructed with reference to preoperative CT or MR
Soft tissue sarcoma	"Virtual GTV" reconstructed with reference to diagnostic and preoperative CT or MR
Ewing sarcoma	"Virtual GTV" reconstructed with reference to diagnostic and preoperative CT or MR

[a]May be fused with RTP CT scan

17.2.4 Treatment Planning

With treatment targets defined, the next step in the RT pathway is treatment dosimetry, the iterative process of determining appropriate beam arrangements for treatment delivery. Each beam delivers a proportion of the prescribed dose, and the trajectory of each beam is depicted on the RTP scan. For many pediatric tumor sites, conformal RT using anterior and posterior directions suffice, but in some cases more sophisticated beam

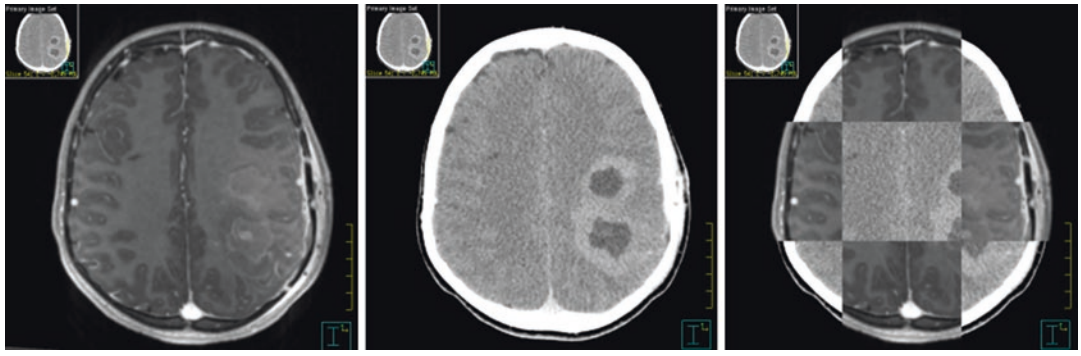

Fig. 17.1 Example T2-weighted MRI (left), contrast-enhanced RTP CT (middle), and fused MR/RTP CT (right)

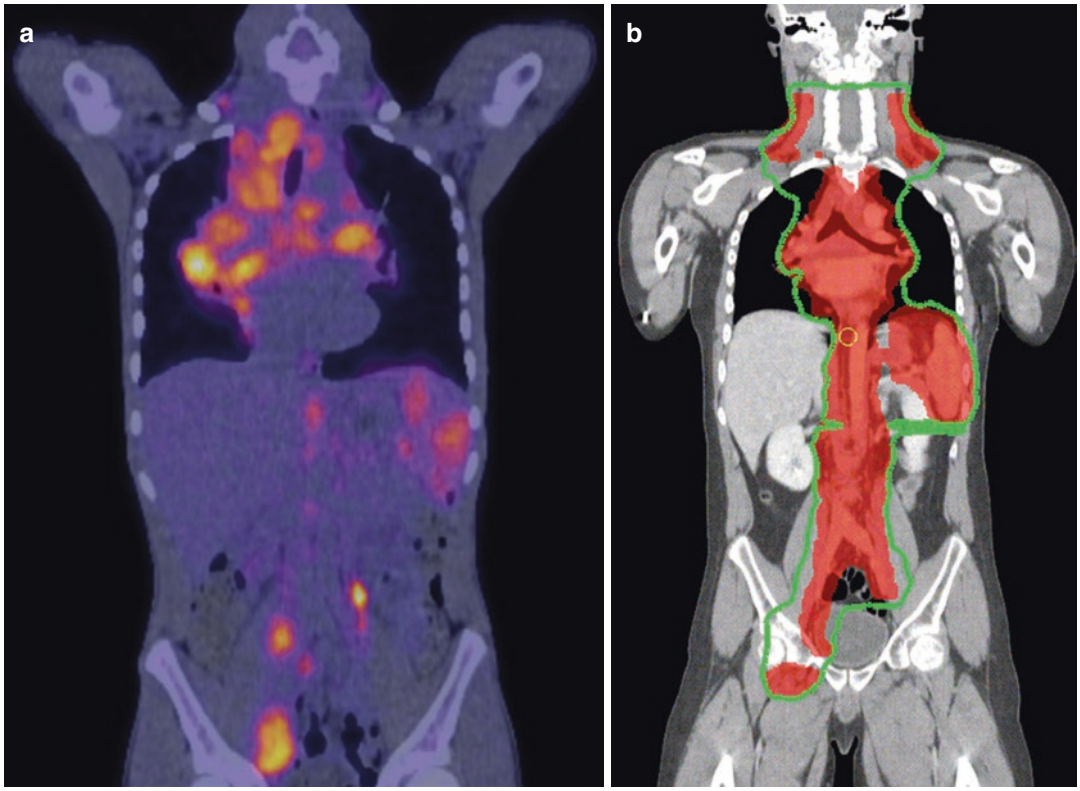

Fig. 17.2 A 15-year-old patient with a diagnosis of stage IVB classical Hodgkin lymphoma (patient had bone involvement). (**a**) Diagnostic PET/CT images depicting abnormal FDG uptake within the supraclavicular, mediastinal, para-aortic, and bilateral iliac nodal regions and uptake within the spleen. (**b**) RT treatment volumes (red-shaded area) with associated dose distribution (green line). Note different arm positions in diagnostic PET-CT compared to RT treatment position

arrangements and delivery techniques might be preferred, for example, complex target shapes adjacent to critical normal tissue. In recent decades, developments within the field of RT have enabled increasingly conformal dose distributions to be generated, called intensity-modulated RT (IMRT). IMRT is now readily available in the clinic.

The output of the dosimetry process is the combined dose distribution of all beams presented as a plan on the RTP scan and its associated dose volume histogram (DVH). A DVH is a graphical representation of the radiation dose received by segmented tissues, normal and tumor, within the beam trajectories. Known tolerance doses for OAR are reflected in RT guidelines within clinical trials. Data for normal tissue tolerances in RT are frequently extrapolated from laboratory or animal studies. Normal tissue tolerance is often multifactorial, but guidance is taken from the quantitative analysis of normal tissue effects in the clinic (QUANTEC) reports in adults [25–40]. Given the accepted physiological differences between children and adults, pediatric-specific guidance is warranted and awaited [41].

17.3 Treatment Delivery

The reference RTP CT on which the treatment plan is generated is the geometric representation of the patient's anatomy at an arbitrary snapshot in time. The TPS-generated RT plan and its dose distribution are defined relative to a treatment machine reference point (usually the isocenter). A plan can become suboptimal if the location of the target relative to the planned dose distribution changes during treatment. As previously mentioned, such changes can result from variation in patient setup relative to the beam isocenter (setup errors) and variation in the target position relative to the patient's bone anatomy (target volume changes). These changes have systematic or random components that can occur during or between treatment fractions (intra- and inter-fraction, respectively) and represent the geometric uncertainties involved in RT delivery.

The ability to confidently deliver increasingly conformal dose distributions depends on accurate and precise knowledge of the target position. This process of harnessing image guidance to manage geometric uncertainty in RT treatment delivery is called IGRT, and the clinical benefit derived from normal tissue sparing and/or dose escalation as a result of increasing accuracy has been demonstrated in a number of adult tumor sites [42].

Patient position at the time of treatment is verified relative to the reference CT dataset (i.e., the planned position) using skin marks/tattoos and lasers aligned to an external coordinate system. Setup error can be reduced through the use of patient positioning systems and rigid immobilization devices. Appropriate use of current patient immobilization devices (vacuum bag, alpha cradle) can now attain patient setup reproducibility in the region of 3–5 mm [1]. However, it is well recognized that internal anatomy may not be well correlated to external skin marks.

Modern linear accelerators are integrated with in-room IGRT systems, such as planar imaging, cone beam CT, and more recently MRI, together with automated couch correction, summarized in Table 17.3 (adapted from [43]). IGRT imaging allows the quantification of some geometric uncertainties, and the assessment of inter- and intra-fraction error in pediatric RT delivery is well described [44–51]. IGRT imaging protocols require adaptation to deliver the minimal additional dose to the pediatric patient [52].

Motion information extracted from 4DCT can be verified at the time of treatment delivery by imaging of the tumor itself via, e.g., fluoroscopy or respiratory-correlated 4D-CBCT [53], imaging of fiducial markers implanted in the tumor, inferring tumor position from a surrogate breathing motion signal, and non-radiographic tracking of a marker implanted in the tumor [7]. Treatment delivery can be gated, where treatment delivery is interrupted when the anatomy is out of position, or tracked, where motion is compensated by the machine using dynamic multileaf collimators (MLC) or moving the treatment couch and machine, e.g., CyberKnife (Accuray Inc., Sunnyvale, CA, USA) [54].

In addition to identifying target position, IGRT imaging can identify anatomical changes that could adversely affect the delivered dose. Replanning prompted by observed anatomical changes is referred to as adaptive RT (ART). This

Table 17.3 Radiation-based in-room IGRT systems and non-ionizing modalities

Imaging modality	Dose per image	Geometric accuracy	Type of tissue match used for treatment localization
EPID MV/KV	1–3 mGy	1–2 mm	Bone match 2D planar imaging
CBCT KV/MV	30–50 mGy	≤1 mm	Soft tissue match Tomographic reconstruction from a series of planar images obtained in one rotation of the gantry around the patient providing volumetric anatomical information Time-resolved CBCT reconstruction possible
"CT-on-rails"	10–50 mGy	≤1 mm	Soft tissue match Diagnostic quality volumetric images
Fan beam MV CT	10–30 mGy	≤1 mm	Soft tissue match Volumetric
Stereoscopic KV	0.10–200 mGy 0.33–0.55 mGy	<1 mm	2D Match based on implanted fiducial markers or bone anatomy Match based on bone anatomy, six degree of freedom correction of translational and rotational setup corrections
Ultrasound	No dose	3–5 mm	Soft tissue match Clinically available for prostate (Clarity™)
MR	No dose	1–2 mm	Soft tissue match

EPID electronic portal image dosimetry, *2D* two-dimensional, *MV* megavoltage, *KV* kilovoltage, *CBCT* cone beam CT

has been described in the setting of pediatric craniopharyngioma where changes in cyst volume during a treatment course and the potential adverse dosimetric impact of not replanning based on changes in target size have been described [48].

17.4 Other Therapeutic RT Delivery Techniques

17.4.1 Stereotactic Ablative Radiotherapy

Stereotaxis is the use of an external, three-dimensional frame of reference for localization. This ability has been incorporated into photon-based EBRT in the form of stereotactic radiosurgery (SRS) and stereotactic ablative radiotherapy (SABR). SRS and SABR involve the delivery of large doses of radiation over one or few treatment fractions. Large doses of RT are delivered with the aim of ablating the target tissue. The delivery of single-fraction SRS relies on the induction of cell death and necrosis in the target tissue without biologic sparing of normal tissues contained within the treatment target. A number of clinically available platforms are capable of delivering SRS and SABR. Some require a frame-based localization system; others do not. With the delivery of such high doses and such treatment effect, IGRT is a prerequisite for delivering these treatments where applied safety margins may be negligible.

The use of SABR/SRS has been reported for select pediatric tumors, primarily CNS tumors [55]. Due to the ability to treat using small safety margins, SABR is an attractive option for use in the re-irradiation setting; and its application has been described in this setting for ependymoma and other CNS tumors [55–57]. There is also increasing interest in the use of ablative RT in extracranial sites, e.g., the spine and lung, and also in the management of oligometastatic disease [58].

17.4.2 Proton Beam Therapy (PBT)

The physical characteristics of the charged proton beam result in negligible exit dose as the particles have a finite range. It is also possible to deliver conformal dose distributions with fewer beams (equivalent arc) using PBT compared to conformal photon RT. PBT delivers increased conformity of treatment delivery and exposes

smaller volumes of normal tissue to moderate- or low-dose radiation [59]. These advantages are likely to translate into less long-term morbidity from normal tissue late effects and second malignancy induction, and so, even in the absence of randomized evidence, many pediatric tumors, particularly in the CNS, are treated with PBT.

The body of evidence for PBT use in children comes from dosimetric studies and case series with now increasing follow-up. Dosimetric studies have demonstrated favorable sparing of normal tissue, primarily in CNS tumors but also for cranio-spinal delivery. From published case series, disease control is equivalent to photon EBRT, and late toxicity, when reported, is favorable.

The geometric uncertainties in treatment delivery already described could have greater impact on PBT delivery as the dose deposition is affected by particle range and radiological depth of the target. Until recently, PBT in-room IGRT equipment lagged behind parallel developments of photon IGRT platforms [60]. Planar imaging was, and still is, frequently used for PBT image guidance. Intensity-modulated treatments are deliverable with current PBT technology. With this, advances in IGRT platforms for PBT will likely follow those seen for photon delivery.

Furthermore, it is clear that the biological effects of PBT are distinctly different from photon EBRT. The relative biological effectiveness (RBE) of PBT is taken to be 1.1 relative to photon beam therapy. It is now increasingly apparent that the RBE changes along the beam trajectory and in fact increases toward the end of the particle range [61].

Though PBT is now preferentially chosen for many pediatric tumors, it will be important to confirm the advantages with an evidence base of mature survivorship data [62].

17.4.3 Brachytherapy

Brachytherapy (BT) is an RT modality that involves the placement of radioactive sources within a body cavity (intracavity) and within tissue (interstitial) or surface molds that can be sculpted to a tumor bed. BT is characterized by the ability to deliver high biologically effective doses, relative to EBRT, with very steep dose gradients. The latter is a result of both the low-energy radiation of BT and the inverse square law that dictates that dose at a distance from a radioactive source is inversely proportional to the square of that distance.

The dose profiles of BT can achieve local control with better organ and function preservation than could be achievable with EBRT for certain tumor sites. Pediatric tumor sites, in which the use of BT is best described, include rhabdomyosarcoma (extremity, genitourinary, and head and neck sites), other soft tissue sarcoma subtypes arising along the trunk or extremities, and retinoblastoma. BT can be delivered as the sole local therapy or as a boost following EBRT. BT can be delivered using pulse dose rate (PDR) techniques or remote high-dose rate (HDR), either fractionated or intraoperative.

Due to the highly skilled nature of BT, it is delivered within specialized centers and only for a select proportion of pediatric patients. The principles of BT are similar for both adult and pediatric indications.

Cross-sectional imaging has revolutionized BT and is now routinely incorporated in BT, with CT, MR, ultrasound, and fluoroscopy all playing a role in BT for various anatomical sites. Cross-sectional imaging aids in the placement of radioactive sources and applicators, thereby improving treatment dosimetry and aiding the definition of target volumes and OAR.

17.4.4 Molecular Radiotherapy

Molecular RT (MRT) is a modality of treatment, whereby unsealed radioactive sources are delivered systemically to the patient. MRT can be used in the treatment of malignant, e.g., neuroendocrine cancer, and benign disease, e.g., hyperthyroidism. Molecular RT requires collaboration between nuclear medicine clinicians, diagnostic imaging specialists, and oncologists. In the setting of neuroendocrine tumors, the rate of treatment success can be predicted by pre-therapy imaging, and new tracers offer potential to improve the sensitivity and specificity for uptake in cancer cells [63].

The interdependence of diagnostic imaging and molecular RT delivery is illustrated in two contemporary studies in the field recruiting with in the United Kingdom. In pediatric patients with metastatic neuroblastoma, a novel imaging practice using I-124 as a PET tracer instead of the standard I-123 tracer is being investigated. The study's hypothesis is that the superior spatial resolution of PET imaging will allow greater precision in localizing small foci of metastatic disease and allow reliable and reproducible quantitative assessment of the extent of disease. If successful, I-124 imaging will offer improved disease evaluation and could be utilized for treatment planning with 131-I MIBG [64]. 177Lu-DOTATATE is being investigated in a phase IIA study in children with primary refractory or relapsed high-risk neuroblastoma. Eligible patients for therapy undergo diagnostic imaging using radiolabeled 68Ga-DOTATATE PET/CT which allows higher sensitivity and improved spatial resolution for disease assessment. Pre- and post-therapy quantitative imaging is used to provide patient-specific absorbed dose [65].

The potential benefit of therapeutic 131-I MIBG therapy in high-risk neuroblastoma, for patients with a poor response to induction therapy, will be explored in the SIOPEN VERITAS study [66]. If positive, this would expand the indication for MRT in high-risk neuroblastoma.

17.5 Future Directions

Adaptive RT (ART) and the introduction of MR-guided RT will see further development in the integration of imaging and RT. For a discipline conventionally reliant on CT imaging, adopting an MR-only workflow will necessitate even greater communication between diagnostic imaging specialists and radiation oncologists to ensure correct interpretation of imaging for planning and treatment purposes. There may even be a need to incorporate a broader scope of formal diagnostic imaging education modules into postgraduate training for radiation oncology as our reliance on MR and other auxiliary imaging modalities intensifies. As an example, ultrasound has real untapped potential for RT image guidance [67, 68], but it is widely acknowledged that its success as an image guidance tool is operator dependent; to integrate this modality training, both clinicians and therapeutic radiographers will be necessary. Both MR and ultrasound are of particular relevance for young patients given the absence of additional radiation dose, and their development should be made a focus of pediatric RT research and development.

References

1. Olch AJ. Pediatric radiotherapy planning and treatment. London: CRC Press; 2013.
2. Jones D. ICRU report 50—prescribing, recording and reporting photon beam therapy. Med Phys. 1994;21(6):833–4.
3. Landberg T, Chavaudra J, Dobbs J, Gerard JP, Hanks G, Horiot JC, et al. Report 62. J Int Comm Radiat Units Meas. 1999;32(1):1–52.
4. ICRU. Report 83. J Int Comm Radiat Units Meas. 2010;10(1):1–106.
5. International Commission on Radiation Units and Measurements (ICRU). Report 62. Prescribing, recording and reporting photon beam therapy (supplement to ICRU report 50). Bethesda, MD: ICRU; 1999.
6. van Herk M, Remeijer P, Rasch C, Lebesque JV. The probability of correct target dosage: dose-population histograms for deriving treatment margins in radiotherapy. Int J Radiat Oncol Biol Phys. 2000;47(4):1121–35.
7. Keall PJ, Mageras GS, Balter JM, Emery RS, Forster KM, Jiang SB, et al. The management of respiratory motion in radiation oncology report of AAPM Task Group 76. Med Phys. 2006;33(10):3874–900.
8. Gaze MN, Boterberg T, Dieckmann K, Hormann M, Gains JE, Sullivan KP, et al. Results of a quality assurance review of external beam radiation therapy in the International Society of Paediatric Oncology (Europe) Neuroblastoma Group's High-risk Neuroblastoma Trial: a SIOPEN study. Int J Radiat Oncol Biol Phys. 2013;85(1):170–4.
9. Chen AB, Killoran J, Kim H, Mamon H. Treatment planning for resected abdominal tumors: differences in organ position between diagnostic and radiation-planning computed tomography scans. Int J Radiat Oncol Biol Phys. 2005;63(5):1613–20.
10. Keall PJ, Barton M, Crozier S. The Australian magnetic resonance imaging–linac program. Semin Radiat Oncol. 2014;24(3):203–6.
11. Mutic S, Dempsey JF. The ViewRay system: magnetic resonance–guided and controlled radiotherapy. Semin Radiat Oncol. 2014;24(3):196–9.

12. Lagendijk JJW, Raaymakers BW, van Vulpen M. The magnetic resonance imaging–linac system. Semin Radiat Oncol. 2014;24(3):207–9.
13. Fallone BG. The rotating biplanar linac–magnetic resonance imaging system. Semin Radiat Oncol. 2014;24(3):200–2.
14. Chen GT, Kung JH, Beaudette KP. Artifacts in computed tomography scanning of moving objects. Semin Radiat Oncol. 2004;14(1):19–26.
15. Vedam SS, Keall PJ, Kini VR, Mostafavi H, Shukla HP, Mohan R. Acquiring a four-dimensional computed tomography dataset using an external respiratory signal. Phys Med Biol. 2003;48(1):45–62.
16. Rietzel E, Pan T, Chen GT. Four-dimensional computed tomography: image formation and clinical protocol. Med Phys. 2005;32(4):874–89.
17. Pai Panandiker AS, Sharma S, Naik MH, Wu S, Hua C, Beltran C, et al. Novel assessment of renal motion in children as measured via four-dimensional computed tomography. Int J Radiat Oncol Biol Phys. 2012;82(5):1771–6.
18. Uh J, Krasin MJ, Li Y, Li X, Tinkle C, Lucas JT Jr, et al. Quantification of pediatric abdominal organ motion with a 4-dimensional magnetic resonance imaging method. Int J Radiat Oncol Biol Phys. 2017;99(1):227–37.
19. Huijskens SC, van Dijk IW, Visser J, Rasch CR, Alderliesten T, Bel A. Magnitude and variability of respiratory-induced diaphragm motion in children during image-guided radiotherapy. Radiother Oncol. 2017;123:263.
20. Huijskens SC, van Dijk IWEM, de Jong R, Visser J, Fajardo RD, Ronckers CM, et al. Quantification of renal and diaphragmatic interfractional motion in pediatric image-guided radiation therapy: a multicenter study. Radiother Oncol. 2015;117(3):425–31.
21. van Dijk IW, Huijskens SC, de Jong R, Visser J, Fajardo RD, Rasch CR, et al. Interfractional renal and diaphragmatic position variation during radiotherapy in children and adults: is there a difference? Acta oncologica. Stockholm: Sweden; 2017. p. 1–7.
22. Nazmy MS, Khafaga Y, Mousa A, Khalil E. Cone beam CT for organs motion evaluation in pediatric abdominal neuroblastoma. Radiother Oncol. 2012;102(3):388–92.
23. Kannan S, Teo BK, Solberg T, Hill-Kayser C. Organ motion in pediatric high-risk neuroblastoma patients using four-dimensional computed tomography. J Appl Clin Med Phys. 2017;18(1):107–14.
24. Beltran C, Pai Panandiker AS, Krasin MJ, Merchant TE. Daily image-guided localization for neuroblastoma. J Appl Clin Med Phys. 2010;11(4):3388.
25. Bhandare N, Jackson A, Eisbruch A, Pan CC, Flickinger JC, Antonelli P, et al. Radiation therapy and hearing loss. Int J Radiat Oncol Biol Phys. 2010;76(3):S50–S7.
26. Dawson LA, Kavanagh BD, Paulino AC, Das SK, Miften M, Li XA, et al. Radiation-associated kidney injury. Int J Radiat Oncol Biol Phys. 2010;76(3):S108–S15.
27. Deasy JO, Moiseenko V, Marks L, Chao KSC, Nam J, Eisbruch A. Radiotherapy dose-volume effects on salivary gland function. Int J Radiat Oncol Biol Phys. 2010;76(3):S58–63.
28. Gagliardi G, Constine LS, Moiseenko V, Correa C, Pierce LJ, Allen AM, et al. Radiation dose-volume effects in the heart. Int J Radiat Oncol Biol Phys. 2010;76(3):S77–85.
29. Kavanagh BD, Pan CC, Dawson LA, Das SK, Li XA, Ten Haken RK, et al. Radiation dose-volume effects in the stomach and small bowel. Int J Radiat Oncol Biol Phys. 2010;76(3):S101–S7.
30. Kirkpatrick JP, van der Kogel AJ, Schultheiss TE. Radiation dose-volume effects in the spinal cord. Int J Radiat Oncol Biol Phys. 2010;76(3):S42–S9.
31. Lawrence YR, Li XA, el Naqa I, Hahn CA, Marks LB, Merchant TE, et al. Radiation dose-volume effects in the brain. Int J Radiat Oncol Biol Phys. 2010;76(3):S20–S7.
32. Marks LB, Bentzen SM, Deasy JO, Kong F-M, Bradley JD, Vogelius IS, et al. Radiation dose-volume effects in the lung. Int J Radiat Oncol Biol Phys. 2010;76(3):S70–S6.
33. Mayo C, Martel MK, Marks LB, Flickinger J, Nam J, Kirkpatrick J. Radiation dose-volume effects of optic nerves and chiasm. Int J Radiat Oncol Biol Phys. 2010;76(3):S28–35.
34. Mayo C, Yorke E, Merchant TE. Radiation associated brainstem injury. Int J Radiat Oncol Biol Phys. 2010;76(3):S36–41.
35. Michalski JM, Gay H, Jackson A, Tucker SL, Deasy JO. Radiation dose-volume effects in radiation-induced rectal injury. Int J Radiat Oncol Biol Phys. 2010;76(3):S123–S9.
36. Pan CC, Kavanagh BD, Dawson LA, Li XA, Das SK, Miften M, et al. Radiation-associated liver injury. Int J Radiat Oncol Biol Phys. 2010;76(3):S94–S100.
37. Rancati T, Schwarz M, Allen AM, Feng F, Popovtzer A, Mittal B, et al. Radiation dose-volume effects in the larynx and pharynx. Int J Radiat Oncol Biol Phys. 2010;76(3):S64–S9.
38. Roach M III, Nam J, Gagliardi G, El Naqa I, Deasy JO, Marks LB. Radiation dose-volume effects and the penile bulb. Int J Radiat Oncol Biol Phys. 2010;76(3):S130–S4.
39. Viswanathan AN, Yorke ED, Marks LB, Eifel PJ, Shipley WU. Radiation dose-volume effects of the urinary bladder. Int J Radiat Oncol Biol Phys. 2010;76(3):S116–S22.
40. Werner-Wasik M, Yorke E, Deasy J, Nam J, Marks LB. Radiation dose-volume effects in the esophagus. Int J Radiat Oncol Biol Phys. 2010;76(3):S86–93.
41. PENTEC. Available from: https://www.pentecradiation.org/.
42. Dawson LA, Jaffray DA. Advances in image-guided radiation therapy. J Clin Oncol. 2007;25(8):938–46.
43. De Los Santos J, Popple R, Agazaryan N, Bayouth JE, Bissonnette JP, Bucci MK, et al. Image guided radiation therapy (IGRT) technologies for radiation

therapy localization and delivery. Int J Radiat Oncol Biol Phys. 2013;87(1):33–45.
44. Beltran C, Pegram A, Merchant TE. Dosimetric consequences of rotational errors in radiation therapy of pediatric brain tumor patients. Radiother Oncol. 2012;102(2):206–9.
45. Beltran C, Krasin MJ, Merchant TE. Inter- and intrafractional positional uncertainties in pediatric radiotherapy patients with brain and head and neck tumors. Int J Radiat Oncol Biol Phys. 2011;79(4):1266–74.
46. Beltran C, Merchant TE. Dependence of intrafraction motion on fraction duration for pediatric patients with brain tumors. J Appl Clin Med Phys. 2011;12(4):3609.
47. Beltran C, Sharma S, Merchant TE. Role of adaptive radiation therapy for pediatric patients with diffuse pontine glioma. J Appl Clin Med Phys. 2011;12(2):3421.
48. Beltran C, Naik M, Merchant TE. Dosimetric effect of target expansion and setup uncertainty during radiation therapy in pediatric craniopharyngioma. Radiother Oncol. 2010;97(3):399–403.
49. Beltran C, Naik M, Merchant TE. Dosimetric effect of setup motion and target volume margin reduction in pediatric ependymoma. Radiother Oncol. 2010;96(2):216–22.
50. Beltran C, Trussell J, Merchant TE. Dosimetric impact of intrafractional patient motion in pediatric brain tumor patients. Med Dosim. 2010;35(1):43–8.
51. Altunbas C, Hankinson TC, Miften M, Tello T, Plimpton SR, Stuhr K, et al. Rotational setup errors in pediatric stereotactic radiation therapy. Pract Radiat Oncol. 2013;3(3):194–8.
52. Beltran C, Lukose R, Gangadharan B, Bani-Hashemi A, Faddegon BA. Image quality & dosimetric property of an investigational imaging beam line MV-CBCT. J Appl Clin Med Phys. 2009;10(3):3023.
53. Sonke JJ, Zijp L, Remeijer P, van Herk M. Respiratory correlated cone beam CT. Med Phys. 2005;32(4):1176–86.
54. Jaffray DA. Image-guided radiotherapy: from current concept to future perspectives. Nat Rev Clin Oncol. 2012;9(12):688–99.
55. Murphy ES, Chao ST, Angelov L, Vogelbaum MA, Barnett G, Jung E, et al. Radiosurgery for pediatric brain tumors. Pediatr Blood Cancer. 2016;63(3):398–405.
56. Hoffman LM, Plimpton SR, Foreman NK, Stence NV, Hankinson TC, Handler MH, et al. Fractionated stereotactic radiosurgery for recurrent ependymoma in children. J Neurooncol. 2014;116(1):107–11.
57. Saran F, Baumert BG, Creak AL, Warrington AP, Ashley S, Traish D, et al. Hypofractionated stereotactic radiotherapy in the management of recurrent or residual medulloblastoma/PNET. Pediatr Blood Cancer. 2008;50(3):554–60.
58. Brown LC, Lester RA, Grams MP, Haddock MG, Olivier KR, Arndt CA, et al. Stereotactic body radiotherapy for metastatic and recurrent ewing sarcoma and osteosarcoma. Sarcoma. 2014;2014:418270.
59. Yock TI, Tarbell NJ. Technology insight: proton beam radiotherapy for treatment in pediatric brain tumors. Nat Clin Pract Oncol. 2004;1(2):97–103. quiz 1 p following 11.
60. Alcorn SR, Chen MJ, Claude L, Dieckmann K, Ermoian RP, Ford EC, et al. Practice patterns of photon and proton pediatric image guided radiation treatment: results from an International Pediatric Research consortium. Pract Radiat Oncol. 2014;4(5):336–41.
61. Peeler CR, Mirkovic D, Titt U, Blanchard P, Gunther JR, Mahajan A, et al. Clinical evidence of variable proton biological effectiveness in pediatric patients treated for ependymoma. Radiother Oncol. 2016;121(3):395–401.
62. Merchant TE. Clinical controversies: proton therapy for pediatric tumors. Semin Radiat Oncol. 2013;23(2):97–108.
63. National Cancer Research Institute (NCRI). CTRad: identifying opportunities to promote progress in molecular radiotherapy research in the UK, vol. 2016. London: NCRI; 2016.
64. Phase I/II study of [124I]mIBG PET/CT in neuroblastoma. Available from: https://www.hra.nhs.uk/planning-and-improving-research/application-summaries/research-summaries/phase-iii-study-of-124imibg-petct-in-neuroblastoma/.
65. LuDo. Available from: http://www.cancerresearchuk.org/about-cancer/find-a-clinical-trial/a-trial-looking-177-lutetium-dotatate-neuroblastoma-children-young-people-ludo.
66. Trial Evaluating and Comparing Two Intensification Treatment Strategies for Metastatic Neuroblastoma Patients With a Poor Response to Induction Chemotherapy (VERITAS). 2017. Accessed on 1 Oct 2017. Available from: https://clinicaltrials.gov/ct2/show/NCT03165292.
67. O'Shea T, Bamber J, Fontanarosa D, van der Meer S, Verhaegen F, Harris E. Review of ultrasound image guidance in external beam radiotherapy part II: intra-fraction motion management and novel applications. Phys Med Biol. 2016;61(8):R90–R137.
68. Fontanarosa D, van der Meer S, Bamber J, Harris E, O'Shea T, Verhaegen F. Review of ultrasound image guidance in external beam radiotherapy: I. Treatment planning and inter-fraction motion management. Phys Med Biol. 2015;60(3):R77–114.

18 Radiation Dose Considerations in Pediatric Oncologic Imaging

Karen E. Thomas and Frederic H. Fahey

18.1 Introduction

Imaging plays a key role in diagnosis, staging, therapeutic response monitoring, detection of complications, and long-term surveillance in pediatric oncology. At every stage of a patient's clinical course, decisions are made which are significantly influenced by the results of imaging studies. Many of the diagnostic imaging modalities utilized—CT, nuclear medicine, radiography, and fluoroscopy—involve low-dose ionizing radiation. Interventional imaging procedures such as placement of peripherally inserted central catheters (PICC), central venous lines (CVL), gastrostomy tubes, biopsies, and embolization procedures also commonly involve fluoroscopy and occasionally CT.

Over the past 15 years, increased awareness among medical professionals and the wider public of the potential future risk of malignancy associated with the use of ionizing radiation in imaging has led to a more widespread culture of benefit/risk assessment when considering imaging in children. The principle of balancing potential benefit against potential risk or side effects has always been an integral part of oncological management, a subject very familiar to both physicians and patients' families making decisions on chemotherapy regimens, radiotherapy, and surgical interventions, many of which have significant potential acute and long-term complications. Recent concerns related to diagnostic and interventional imaging can and should be seen in this wider context.

Survival rates for childhood malignancy continue to improve, with a current overall 5-year survival rate of 82% and rates of 95% or above for Hodgkin lymphoma, thyroid carcinoma, gonadal germ cell tumor, and retinoblastoma [1]. The resultant expectation, namely, that the majority of children will grow up to lead long and full lives, means that the need to minimize potential long-term side effects from previous therapy is now central to the design of new treatment regimens and the driving force for much ongoing research. Although the potential risk from ionizing imaging modalities is less clearly defined than many well-documented side effects of disease therapy, and any manifestations are expected to have a long latency of several decades, all aspects of patient care should be included in our efforts to reduce the future impact of a child's cancer treatment on their teenage and adult lives. The design of imaging regimens and optimization of technical settings are essential parts of this effort.

K. E. Thomas
Department of Diagnostic Imaging,
Hospital for Sick Children, Toronto, ON, Canada
e-mail: karen.thomas@sickkids.ca

F. H. Fahey (✉)
Division of Nuclear Medicine and Molecular Imaging, Department of Radiology,
Boston Children's Hospital, Boston, MA, USA
e-mail: frederic.fahey@childrens.harvard.edu

S. D. Voss, K. McHugh (eds.), *Imaging in Pediatric Oncology*, Pediatric Oncology,
https://doi.org/10.1007/978-3-030-03777-2_18

Particular challenges and considerations exist in pediatric oncology patients that make the assessment of potential risk versus benefit from ionizing imaging studies more complex than in other patient cohorts. These include patient exposure to other known carcinogens. Radiotherapy is a well-established risk factor for secondary malignant neoplasms in survivors of childhood cancer [2, 3], the magnitude of which outweighs any possible contribution from imaging. Chemotherapy also appears to potentiate the effects of irradiation [4]. The relative lack of quantitative radiation dose data from imaging studies until recent years, the ongoing rarity and difficulty of conducting truly blinded studies of imaging regimens, and the consideration of individuals with specific radiosensitivity syndromes and cancer predisposition genes present additional challenges.

Even without these complicating factors, there is a wider ongoing debate and uncertainty about the level of risk associated with ionizing radiation in medical imaging, as discussed more in the following section. This is likely to be the case for the foreseeable future and something that we will have to "live with" and make prudent decisions accordingly. Overall, the consensus of opinion is that the level of risk is low, but likely not zero, and in view of this, oncologists and oncologic imaging specialists should be familiar with the background issues and means to reduce the overall radiation burden from imaging. This chapter will review the utility of ionizing imaging modalities and current risk models for potential future malignancy risk, consider dose-saving technologies and strategies, and discuss some aspects of communication of these issues with patients and their families.

18.2 Potential Long-Term Risks from Ionizing Radiation

Many of the radiologic imaging modalities used in oncologic patients including radiography, fluoroscopy, CT, nuclear medicine, and PET utilize ionizing radiation to produce their images. As a result, our patients receive radiation dose to many of their organs including those that have been shown to be susceptible to adverse health effects from radiation. Much of our current knowledge regarding the long-term effects of radiation in humans is based on the Life Span Study (LSS) from the Radiation Effects Research Foundation, a collaborative endeavor of US and Japanese investigators. Ozasa et al. reported on the most recent results from these data [5]. As of 2003, over 86,000 subjects of both sexes and a wide range of age at the time of exposure have been followed for almost 60 years. This study is often characterized as a "high-dose" study; however, over a third of the subjects received an estimated radiation dose of less than 5 mGy. Another third received a dose between 5 and 100 mGy which is the dose range perhaps of most interest to those practicing medical imaging. In the 86,000 subjects, there have been almost 11,000 deaths with an estimated 530 excess deaths due to radiation exposure. In the 30,000 subjects receiving 5–100 mGy, there were 3600 total deaths with an excess 49 deaths due to radiation exposure. Although most of the subjects received less than 100 mGy, most of the excess deaths were in subjects receiving more than 200 mGy. These data along with their uncertainties are summarized in Fig. 18.1. In this figure, weighted colon dose was used as a surrogate for whole body dose. The red arrow indicates the 100 mGy level, below which we are most interested with regard to medical imaging. Although a linear model

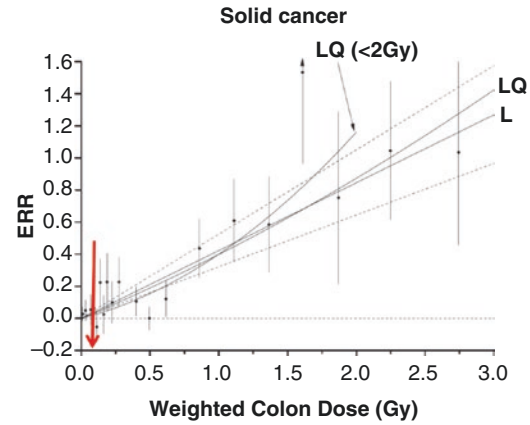

Fig. 18.1 Excess relative risk (ERR) for all solid cancers versus weighted colon dose (in Gy, a surrogate for whole body dose). ERR represents the excess risk attributable to radiation such that a value of 0.0 indicates no demonstrable risk above background cancer incidence levels. The red arrow indicates the 0.1 Gy (100 mGy) level, a reasonable limit for the radiation dose from a series of radiologic procedures. Used with permission from Radiation Research

describes these data particularly at doses above 200 mGy, the uncertainties associated with the effects below 100 mGy include the possibility of no effect.

In general, the LSS findings have been corroborated by a variety of other epidemiologic studies including those involving occupational, medical, and environmental exposures. The current knowledge regarding potential health effects of ionizing radiation from both epidemiologic and biological studies has been reviewed and summarized by expert panels assembled by several organizations including the US National Academy of Sciences (NAS) and the United Nations Scientific Committee on the Effects of Atomic Radiation (UNSCEAR). In 2006, NAS published the Phase 2 report of the 7th edition of the Biological Effects of Ionizing Radiation (BEIR VII Phase 2) [6]. Considering the state of knowledge at that time, this report recommended that the linear no-threshold (LNT) model was appropriate for solid tumors, whereas a linear-quadratic model was appropriate for leukemia when considering adverse health effects in the context of radiation safety. The report provided mathematical models for estimating the risk associated with radiation for a variety of parameters including the cancer of concern, the age at the time of exposure, and the magnitude of exposure. Although the use of the LNT model may remain controversial [7], particularly regarding its accuracy for estimating risk at very low doses, it may still be considered prudent with respect to children who may be at higher risk than adults. According to the BEIR VII models, a 10-year-old child may be at twice the cancer risk, and a 1-year-old three times the risk of a 40-year-old adult at a given radiation dose level. UNSCEAR notes that these cancer risks vary across different tumor types for children as compared to adults [8].

18.3 Typical Radiation Doses

Numerous parameters exist relating radiation dose from imaging studies. Readers will encounter a wide variety of measurements and units varying from absorbed doses such as surface and organ doses (mGy), radionuclide administered activity (MBq), and tube output measures such as volume CT dose index (CTDI) and dose length product (DLP) in CT or dose area product (DAP) in fluoroscopy. The complexities of dosimetry are beyond the scope of this chapter, but we will briefly consider a few examples. For the administration of radioisotopes, the radiation dose to the patient depends on a variety of factors associated with both the radiopharmaceutical and the patient. The radionuclide associated with the radiopharmaceutical (e.g., ^{99m}Tc or ^{18}F) determines the radiations emitted (gamma rays, beta particles, positrons, etc.) and the physical half-life. The chemical to which it is labeled (e.g., FDG, MDP, MIBG, etc.) along with the patient's own physiology will determine to which source organs the radiopharmaceutical will distribute and how long it will stay there (i.e., the biological half-life). Given this information and knowing the size and shape of the patient, one can make a reasonable estimate of radiation dose to all pertinent target organs within the body. In most instances, dosimetry is not based on the physiology or anatomy of a specific patient but rather on patient models of comparable size and physiology.

For CT, one can estimate $CTDI_{vol}$ (reported in mGy) based on the CT acquisition parameters. It is noted that $CTDI_{vol}$ is not the estimate of the radiation dose delivered to the patient, but rather the dose to a standard phantom (16- or 32-cm-diameter Plexiglas cylinders) based on the acquisition parameters. However, $CTDI_{vol}$ can be scaled to the size of the patient and reported as the size-specific dose estimate (SSDE). DLP (in mGy-cm) is determined by multiplying $CTDI_{vol}$ by the axial extent of the CT scan. For fluoroscopy, the entrance radiation dose or DAP can be used to assess the potential of a detrimental health effect such as skin damage.

Although all of these dosimetric parameters have valuable roles in radiation physics and quality assurance processes, they do not easily allow comparison of the relative "dose impact" of studies from different modalities and/or body regions, information which is often requested by physicians and families. For example, assessment of the relative dose of a skull radiographic series compared to a head CT. A concept called effective

dose can provide some broad guidance on relative dose, but the reader must be aware of its very considerable limitations in methodology and application.

Effective dose was originally developed as a tool for occupational and public radiation protection, and not for medical use [9, 10]. It is defined by the International Commission on Radiological Protection (ICRP) as the sum of the absorbed doses in all exposed tissues and organs of the body, each weighted according to its radiation sensitivity. Endeavors or procedures where part of the body is exposed to ionizing radiation are presumed to carry a similar risk to an equivalent, whole body exposure with the same effective dose. A single value, expressed in millisieverts (mSv), is derived as a very broad guide to potential stochastic radiation determination. It is not a physical, measured quantity; there are many levels of estimation and extrapolation with an uncertainty of up to ±40%, and its "very broad estimate" nature should be appreciated [9]. The weighting factors are based on broad population averages across age and gender, and therefore effective dose estimates must be considered in terms of populations of similar demographics undergoing a particular procedure. As a result, effective dose estimates should not be used for individual risk assessment [11]. For this, organ dose calculations by a medical physicist with regard to patient age, gender, and mass are necessary.

In 2008, a compilation of typical effective doses for more than 50 radiological procedures was published, which provides an understanding of the relative dose associated with radiographic, nuclear medicine, CT, and fluoroscopic studies in adults [12]. For pediatric patients, there are greater complexities of dosimetry with the necessity to consider cohorts of varying ages and sizes. No corresponding pediatric compilation is yet available. Some typical effective doses for 5–10-year-old children are provided in Table 18.1, based on several sources [13–17].

Radiation dose variability between institutions may be considerable and is well documented in both adult and pediatric studies. Two- to threefold variability in dose associated with a particular study is frequent, and ranges up to 25-fold have been reported in some cases [18, 19]. Typical doses can also be expected to change over time, usually trending downward with advances in dose-saving technologies, and published data may become outdated relatively quickly in some areas [20]. In interventional radiology, the range of possible dose associated with a procedure is wider than most diagnostic studies as study length and complexity are significantly influenced by individual patient anatomy and disease extent.

Table 18.1 Typical effective dose estimates for commonly performed imaging studies considering 5–10-year-old children

Radiographs	*Fluoroscopy/interventional*
CXR (2 views)	Upper GI series
0.02–0.03 mSv	0.4– 0.8 mSv
AXR (2 views)	Voiding cystourethrogram
0.1–0.4 mSv	0.1– 0.7 mSv
Ankle XR (3 views)	PICC/CVL insertion
<0.01 mSv	0.05–0.15 mSv[a]
Nuclear medicine	*CT*
^{99m}Tc MDP bone scan	CT head (1 phase)
2.5–4 mSv	1.5–2.5 mSv
^{99m}Tc MAG3 renal scan	CT head (2 phases)
1–2 mSv	3–5 mSv
^{123}I MIBG scan	CT chest
3.5–4.5 mSv	2–3.5 mSv
^{18}F FDG-PET + Dx CT	CT abdomen/pelvis
11–16 mSv	3–7 mSv
^{18}F FDG-PET + AC CT	CT neck/chest/abdomen/pelvis
6–8 mSv	6–10 mSv

Adapted from References [13–17] and institutional dose estimates from the Hospital for Sick Children, Toronto
[a]May vary by order(s) of magnitude related to procedure length
Dx CT = diagnostic CT
AC CT = attenuation correction CT

Several cumulative dose studies involving cohorts of pediatric oncology patients have been published. Effective dose estimates have been summated over several years from the time of initial diagnosis, in some cases from all ionizing modalities [13, 14, 21, 22] and in others limited to CT and PET/CT [23, 24]. As discussed previously, effective dose should not be used to assess individual radiation exposure or risk. It may however provide insight into the relative dose contribution of different imaging modalities, regimens or specific studies, the relative contribution of therapy-related and surveillance imaging, and the degree and etiology of imaging

variability within a cohort. Opportunities may be found to improve imaging algorithms, such as targeting specific higher dose frequently performed studies for dose-reduction efforts, removing studies of limited clinical utility, or reviewing the frequency and modality of follow-up studies.

18.4 Dose-Reduction Strategies

Strategies for dose reduction in medical imaging require a multidisciplinary collaborative approach and can be categorized into three major elements: education, justification, and optimization. Input from all stakeholders including radiologists, referring physicians and other caregivers, radiographers and technologists, medical physicists, equipment vendors, patients and their families, the wider public, and regulatory authorities is necessary to achieve success in imaging radiation safety (Table 18.2). Over the past 15 years, there have been considerable advances in knowledge and awareness of the potential risks associated with ionizing radiation among the medical and allied health professions [25]. This can be attributed to a proliferation of professional literature, local educational efforts, widespread media coverage, and, importantly, to several international educational campaigns that have raised the profile of radiation safety in medical imaging. The Image Gently campaign was created by the Alliance for Radiation Safety in Pediatric Imaging, founded in 2007 by the Society for Pediatric Radiology (SPR), the American Society of Radiologic Technologists (ASRT), the American College of Radiology (ACR), and the American Association of Physicists in Medicine (AAPM) [26]. Acting primarily through social marketing, the Campaign advocates for children, with the aim of improving pediatric imaging practice in North America and around the world. The Alliance has grown to become a coalition of more than 90 professional societies and organizations and has broadened its target audience beyond its original audience of radiologists, technologists, and medical physicists, to include government and international agencies, parents, the public, and equipment vendors. Information for all stakeholders is available on its website (www.imagegently.org), including translations in multiple languages.

Table 18.2 Principles of radiation safety in oncologic imaging

- Education of all stakeholders
- Justification of every imaging study
- Avoid repeating studies performed elsewhere
- Utilization of non-ionizing modalities (ultrasound, MRI)
- Adaptation of technical factors to patient size and clinical indication
- Utilization of modality-specific dose-saving technologies
- Medical physicist input to dose optimization
- Regular review of national/international oncologic imaging protocols
- Use of institutional and/or national Dose Reference Levels/Ranges
- International advocacy campaigns, e.g., Image Gently
- Legislative and regulatory requirements

Six major campaigns have targeted radiation safety and process improvements in CT, interventional radiology, fluoroscopy, nuclear medicine, radiography, and dental radiology. The Image Wisely campaign has been subsequently launched by the Joint Task Force on Adult Radiation Protection of the Radiological Society of North America (RSNA) and the ACR and provides similar educational resources to improve radiation safety in adult patients [27]. The EuroSafe Imaging campaign (www.EuroSafeimaging.org) is an initiative of the European Society of Radiology, also providing information to referring physicians and patients' families in addition to heading several international collaborative projects including clinical decision support systems and European dose reference levels (DRLs) for pediatric imaging.

Justification is a central element to radiation safety. Every imaging study should be warranted, with the potential benefit to the patient outweighing the small potential future risk. As stated in the dose optimization statement of the Society of Nuclear Medicine and Molecular Imaging, the right test with the right dose should be given to the right patient at the right time [28]. Oncology patients will undergo a mix of protocol-mandated

imaging studies to assess acute treatment response and provide imaging surveillance as well as a (usually smaller) number of additional clinically driven studies depending on individual clinical course or treatment complications. The major international oncological societies and study groups face many challenges in formulating clinical trial imaging protocols. There are relatively few true evidence-based guidelines to determine optimal imaging frequency or choice of modality [29]. CT technology has changed quickly, with improved sensitivity and/or lower radiation dose of new techniques. New MRI sequences such as diffusion-weighted imaging may provide valuable information without the use of ionizing radiation, and advanced hybrid imaging capabilities such as PET-MR have become possible. Newer techniques are sometimes incorporated into clinical practice without removing previous studies from routine protocols, perhaps with duplication or unnecessary radiation exposure. Discussion around optimal imaging is particularly pertinent in the surveillance phase where the assessment of potential benefit and risk is most complex. In some tumors, recurrence most frequently presents clinically despite imaging surveillance; in others, earlier detection of relapse by imaging may not improve survival [2]. The psychological effects of intensive surveillance should also be considered, both of reassurance and of anxiety, including the impact of false-positive results. The greater stratification of surveillance imaging regimens according to disease characteristics, tumor stage, grade, and perhaps genomic profile, is an important and challenging need for the future [14, 29, 30].

Non-ionizing imaging modalities, namely, ultrasound and MRI, play an increasing role in oncological imaging and are especially valuable in long-term surveillance when regular interval imaging is required. Ultrasound is well suited to the pediatric body habitus and provides a sensitive high-quality imaging modality that is portable and cost-effective and has not been associated with any significant safety concerns. It is, however, operator dependent to a greater degree than other modalities, its breadth of use varies with local experience and expertise, and it has limitations for some primary tumor locations such as intrathoracic and primary osseous sites. Ultrasound is most frequently utilized for intra-abdominal solid organ, bowel, and gynecological imaging, detection of vascular thrombosis, and assessment of superficial structures such as the thyroid, testes, and soft tissue masses. The advent of ultrasound contrast agents is likely to extend its role and specificity in tumor diagnosis.

MRI is now the mainstay of neuro-oncology and musculoskeletal tumor imaging due to its exceptional soft tissue characterization, as well as having a significant and increasing role in abdominal, gynecologic, and some thoracic malignancies. This reflects both the advances in sequence development and acquisition speed that have occurred over the past decade and the more widespread availability of this technology. Hepatocyte-specific contrast agents have improved diagnostic confidence in the characterization of liver masses, and diffusion-weighted sequences hold potential in many areas, particularly tumor response assessment and whole body screening in cancer predisposition syndromes [31]. The desire to reduce ionizing radiation exposure to a cohort of patients who will undergo multiple imaging procedures has undoubtedly led to a shift toward MRI and away from CT as the imaging modality of choice in many cases. However, the duration of most MRI studies is still longer than CT and often requires patient sedation or general anesthetic in children under 6–8 years of age.

Concerns have been raised related to adverse neurocognitive effects of anesthetic agents on young children which are particularly relevant to oncology patients who may undergo repeated close interval sedation or anesthesia for both imaging- and therapy-related procedures [32]. Potential long-term toxicities from the use of gadolinium contrast agents have also emerged, initially related to the rare association with nephrogenic systemic fibrosis and, more recently, to the documented although as yet uncertain clinical significance of intracerebral retained gadolinium [33–35]. These concerns serve as a reminder that all imaging studies, regardless of modality, must be considered and justified with an awareness of potential adverse effects as well as potential benefits to the patient,

in a manner similar to our consideration of medical therapies and interventions.

Computed tomography remains the most sensitive modality for the detection of pulmonary metastases, fungal lung parenchymal disease, and pulmonary emboli, as well as often being the imaging modality at initial presentation, at times of acute clinical deterioration, and part of hybrid functional PET/CT imaging. The role of nuclear medicine continues to evolve, with potential for quantitative FDG-PET imaging, use of other ^{18}F-based isotopes and hybrid PET-MRI. In the interventional suite, recent developments include the application of cone beam CT technology for biopsy procedures and, at many pediatric oncology centers, an increasingly comprehensive fluoroscopy and angiography service ranging from PICC and CVL insertions to complex angiography, chemoembolization, radioembolization, and radiofrequency ablation procedures [36]. It is clear that despite the increasing use of ultrasound and MRI, pediatric oncology patients will still require imaging that involves ionizing radiation at various stages from diagnosis to surveillance.

A fundamental principle of the Image Gently campaign is that the lowest dose of ionizing radiation should be used for a given examination, while still assuring that the diagnostic and /or therapeutic aims of the study are achieved. This is known as the ALARA (As Low As Reasonably Achievable) principle Technical parameters and protocols must therefore always be tailored to patient size and clinical indication, optimized to achieve the necessary image quality with consideration of dose implications. This can be a challenging balance to address. Many of the dose-saving techniques available to radiologists are image quality neutral or, in the case of some technical advances, may result in improved image quality; however, others may have a negative impact on image quality which must be considered in the context of the clinical needs of the study. For example, the spatial resolution required in a patient with concern for subtle secondary liver lesions may be higher than other patients in whom the study aim is detection of low likelihood and relatively easily visualized, retroperitoneal nodal enlargement [37]. Collaboration and exchange of information between oncologist and radiologist is central to achieving the desired outcome for the patient.

Comprehensive review of the range of dose-saving techniques for all modalities is beyond the scope of this chapter, and the reader is referred to more detailed sources [17, 38–43]. As an overview, strategies in CT are based on the principles of child-sizing technical parameters such as mAs and kVp, limiting field of coverage, avoiding the use of multiple scan phases whenever possible, adapting dose to clinical indication, and utilizing the many technical advances now available. These include tube current modulation, adaptive collimation, organ collimation, dual tube technology, more sensitive detector materials, and iterative reconstruction techniques. As a result, typical CT doses have gradually declined and can be expected to continue to do so. Arguably, the most important dose-saving advance in diagnostic and interventional fluoroscopy has been pulse fluoroscopy, the intermittent "pulsing" of the X-ray beam several times per second rather than its continuous use. Depending on the task, and therefore the image quality needed, the rate of beam pulsing and hence degree of dose reduction can be varied. Together with greater consideration of patient positioning with respect to beam source, careful collimation, and restriction of magnification mode use, significantly lower radiation doses for many diagnostic and interventional studies have been achieved.

In nuclear medicine, advances in detector and collimator technology and in reconstruction algorithms have improved image quality at lower counts, the benefit of which can be translated into either lower administered isotope activity or faster image acquisition time. It is in the area of standardization of procedures that pediatric nuclear medicine has led in radiation protection. In 2008 and 2010, respectively, the European Association of Nuclear Medicine and the North American Consensus Guidelines (a collaboration of the Society of Nuclear Medicine, Society for Pediatric Radiology, and the American College of Radiology working with the Image Gently campaign) published recommendations for size-based scaling of administered activity for the most frequently performed pediatric nuclear medicine

studies [44]. In 2014 and 2016, harmonized guidelines between the North American and European groups were published [45, 46]. These consensus protocols have undoubtedly improved consistency of approach between imaging centers, although further dissemination is still needed and efforts toward global standardization are underway [47].

18.5 Communication with Patients and Families

Over the past 15 years, there have been a number of articles in both the medical literature and the popular press regarding the potential adverse health effects associated with exposure to ionizing radiation. As a result, many of our patients and their families have questions and concerns. This includes teens who have often studied the effects of radiation in school. In addition, today's patients are less satisfied with the notion that medical imaging is inherently safe. Therefore, it is incumbent upon nuclear medicine physicians, radiologists, and oncologists to be prepared to discuss the potential risks as well as the benefits of ionizing imaging modalities with their patients and families. It is essential to discuss both benefit and risk as the patient's questions often come back to "Why do I need this test anyway?" Thus, it is important to discuss the value of the procedure to the patient's clinician as well as any potential risks, and also explain to the patient that every effort will be made to adhere to the principles of ALARA. In 2012, the SNMMI issued a statement that if the right test with the right dose (is) given to the right patient at the right time, the benefits of the procedure very far outweigh the potential risks, and if an appropriate procedure—one that can provide the physician with clinical information essential to the patient's treatment—is not performed when necessary due to fear of radiation, it can be detrimental to the patient. In order to communicate well, it is imperative we present the potential risks in an understandable and straightforward manner in the context of the benefits of the procedure.

Although there may be some patients or parents who are interested in the effective dose and the number of millisieverts, most parents want us to provide context. One reasonable discussion with the patient may be to indicate that the level of exposure from a particular procedure may be similar to that from a number of X-rays or equivalent to exposure to 1 or 2 years of background radiation. The exposure may also be comparable to that received by the technologist performing the study in each year of their career. In nuclear medicine, parents often wish to stay with their small children during procedures, and so the question of exposure to a parent may also require discussion. Except for leaving the room during the acquisition of the CT component of PET/CT or SPECT/CT, it is reasonable to allow the parent to stay in the room but request that they stay at least 1 m from their child. If this is the case, the exposure of the parent is most likely less than exposure one receives from a cross-continental flight.

Relating the level of potential risk can be particularly challenging. Many patients and their families are easily confused when the risk is presented numerically. For example, some might think 1 in a 1000 is a higher risk than 1 in a 100 since 1000 is a larger number. Others might confuse 0.05% with 5%. For these reasons, many practitioners in the field suggest communicating risk either graphically or by comparison to other risks of everyday living instead. Let's assume as an example that the radiation risk associated with a MDP bone scan in a 10-year-old using ^{99m}Tc MDP is approximately one fatal cancer in 2500 administrations. In Fig. 18.2, there are 2500 small circles representing the number of 99mTc MDP administrations. The red star in the lower right represents the single case of fatal cancer in these 2500 administrations. Also shown in this figure are 550 dark blue circles which represent those individuals that will naturally die of cancer (22%). It is hoped that this figure conveys to the patient that the risk of a fatal cancer resulting from an imaging study is truly very small. Table 18.3 compares the 1 in 2500 risk described above to the lifetime risk associated with other

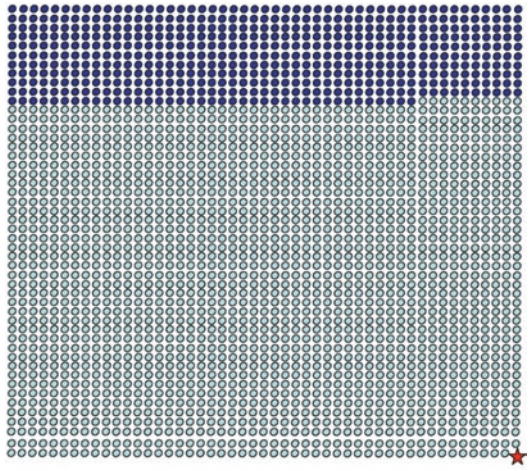

Fig. 18.2 This figure shows 2500 small circles representing the number of ^{99m}Tc MDP administrations. The red star in the lower right represents the single case of fatal cancer in these 2500 administrations. Also shown in this figure are 550 dark blue circles which represent those individuals that will naturally die of cancer (22%). Used with permission from the Journal of Nuclear Medicine

Table 18.3 Lifetime risk of death from everyday activities in the United States

Activity	Lifetime risk
Assault	214
Accident while riding in a car	304
Accident as a pedestrian	652
Choking	894
Accidental poisoning	1030
Drowning	1127
Exposure to fire or smoke	1181
Falling down stairs	2024
Cancer from 99mTc MDP bone scan (10-year-old)	2500
All forces of nature	3190
Accident while riding a bike	4734
Cancer from 99mTc MDP bone scan (40-year-old)	4760
Accidental firearms discharge	6333
Accident while riding in a plane	7058
Falling off ladder or scaffolding	10,606
Hit by lightning	84,388

Note: Lifetime risk of 304 for "accident while riding in a car" indicates that 1 out of every 304 Americans will die as a result of an accident while driving in a car during their lifetime

activities of daily life. As a comparison, the probability of an individual dying as a result of falling down the stairs is about 1 in 2000, and thus this is slightly more risky than the example of receiving a ^{99m}Tc MDP bone scan. Again, these comparisons may be helpful for some patients and their families as they try to put radiation risk in context.

18.6 Summary

Imaging plays a central role in the diagnosis and staging of pediatric malignancies, assessment of response to therapy, detection of treatment-related complications, and subsequent disease surveillance. The past decade has seen a considerable shift toward greater utilization of non-ionizing modalities in both CNS and non-CNS tumor imaging due to concerns regarding potential risks of ionizing radiation and to technical advances particularly in MRI sequences and acquisition time. However, the emergence of potential MRI contrast agent toxicities and anesthetic-related neurocognitive concerns have highlighted the complexity of benefit and risk assessment in imaging. With large numbers of pediatric cancer patients now reaching adulthood and leading full lives, the minimization of any long-term effects related to childhood therapy, including imaging, has become increasingly important. It is our responsibility as oncology caregivers to have an understanding of the background to current ionizing radiation risk models, an overview of the relative radiation dose of commonly performed imaging studies, and to become comfortable with patient and family discussions around benefit and risk, despite the many challenges. Several international advocacy campaigns for radiation safety in imaging have driven a multidisciplinary approach toward optimizing radiation dose and image quality in all modalities, and further downward trends in dose can be anticipated.

References

1. NCI. SEER cancer statistics review, 1975-2014. Bethesda, MD: National Cancer Institute; 2017. https://seer.cancer.gov/csr/1975_2014/, based on November 2016 SEER data submission, posted to the SEER web site, April 2017.
2. McHugh K, Roebuck DJ. Pediatric oncology surveillance imaging: two recommendations. Abandon CT scanning, and randomize to imaging or solely clinical follow-up. Pediatr Blood Cancer. 2014;61(1):3–6.
3. Bhatia S, Yasui Y, Robison LL, et al. High risk of subsequent neoplasms continues with extended follow-up of childhood Hodgkin's disease: report from the Late Effects Study Group. J Clin Oncol. 2003;21(23):4386–94.
4. Garwicz S, Anderson H, Olsen JH, et al. Second malignant neoplasms after cancer in childhood and adolescence: a population-based case-control study in the 5 Nordic countries. The Nordic Society for Pediatric Hematology and Oncology. The Association of the Nordic Cancer Registries. Int J Cancer. 2000;88(4):672–8.
5. Ozasa K, Shimizu Y, Suyama A, et al. Studies of the mortality of atomic bomb survivors, Report 14, 1950-2003: an overview of cancer and noncancer diseases. Radiat Res. 2011;177(3):229–43.
6. National Research Council. Committee to assess health risks from exposure to low levels of ionizing radiation. Health risks from exposure to low levels of ionizing radiation: Beir VII Phase II. Washington, DC: National Academic Press; 2006.
7. Siegel JA, Pennington CW, Sacks B. Subjecting radiologic imaging to the linear no-threshold hypothesis: a non sequitur of non-trivial proportion. J Nucl Med. 2017;58(1):1–6.
8. UNSCotEoAR. Effects of radiation exposure of children. Vol II Annex B. New York, NY: UNSCEAR, United Nations; 2013.
9. Martin CJ. Effective dose: how should it be applied to medical exposures? Br J Radiol. 2007;80(956):639–47.
10. Harrison JD, Balonov M, Martin CJ, et al. Use of effective dose. Ann ICRP. 2016;45(1 Suppl):215–24.
11. Fisher DR, Fahey FH. Appropriate use of effective dose in radiation protection and risk assessment. Health Phys. 2017;113(2):102–9.
12. Mettler FA Jr, Huda W, Yoshizumi TT, Mahesh M. Effective doses in radiology and diagnostic nuclear medicine: a catalog. Radiology. 2008;248(1):254–63.
13. Ahmed BA, Connolly BL, Shroff P, et al. Cumulative effective doses from radiologic procedures for pediatric oncology patients. Pediatrics. 2010;126(4):e851–8.
14. Owens C, Li BK, Thomas KE, Irwin MS. Surveillance imaging and radiation exposure in the detection of relapsed neuroblastoma. Pediatr Blood Cancer. 2016;63(10):1786–93.
15. Glatz AC, Purrington KS, Klinger A, et al. Cumulative exposure to medical radiation for children requiring surgery for congenital heart disease. J Pediatr. 2014;164(4):789–794.e710.
16. WHO. Communicating radiation risks in paediatric imaging: information to support health care discussions about benefit and risk. Geneva: World Health Organization; 2016.
17. Fahey FH, Treves ST, Adelstein SJ. Minimizing and communicating radiation risk in pediatric nuclear medicine. J Nucl Med. 2011;52(8):1240–51.
18. Smith-Bindman R, Lipson J, Marcus R, et al. Radiation dose associated with common computed tomography examinations and the associated lifetime attributable risk of cancer. Arch Intern Med. 2009;169(22):2078–86.
19. Thomas KE. CT update: use, dose variability and diagnostic reference levels. Diagn Imaging Eur. 2012;(July):27–30.
20. Lee C, Pearce MS, Salotti JA, et al. Reduction in radiation doses from paediatric CT scans in Great Britain. Br J Radiol. 2016;89(1060):20150305.
21. Chong AL, Grant RM, Ahmed BA, Thomas KE, Connolly BL, Greenberg M. Imaging in pediatric patients: time to think again about surveillance. Pediatr Blood Cancer. 2010;55(3):407–13.
22. Pierobon J, Webber CE, Nayiager T, Barr RD, Moran GR, Gulenchyn KY. Radiation doses originating from diagnostic procedures during the treatment and follow-up of children and adolescents with malignant lymphoma. J Radiol Prot. 2011;31(1):83–93.
23. Chawla SC, Federman N, Zhang D, et al. Estimated cumulative radiation dose from PET/CT in children with malignancies: a 5-year retrospective review. Pediatr Radiol. 2010;40(5):681–6.
24. Nievelstein RA, Quarles van Ufford HM, Kwee TC, et al. Radiation exposure and mortality risk from CT and PET imaging of patients with malignant lymphoma. Eur Radiol. 2012;22(9):1946–54.
25. Boutis K, Thomas KE. Radiation dose awareness and disclosure practice in paediatric emergency medicine: how far have we come? Br J Radiol. 2016;89(1061):20160022.
26. Goske MJ, Applegate KE, Boylan J, et al. Image Gently(SM): a national education and communication campaign in radiology using the science of social marketing. J Am Coll Radiol. 2008;5(12):1200–5.
27. Mayo-Smith WW, Morin RL. Image wisely: the beginning, current status, and future opportunities. J Am Coll Radiol. 2017;14(3):442–3.
28. SNMMI position statement on dose optimization for nuclear medicine and molecular imaging procedures. 2012. Accessed 22 Dec 2017. http://snmmi.files.cms-plus.com/docs/SNM_Position_Statement_on_Dose_Optimization_FINAL_June_2012.pdf.
29. Weiser DA, Kaste SC, Siegel MJ, Adamson PC. Imaging in childhood cancer: a Society for Pediatric Radiology and Children's Oncology Group Joint Task Force report. Pediatr Blood Cancer. 2013;60(8):1253–60.

30. Seibel NL, Janeway K, Allen CE, et al. Pediatric oncology enters an era of precision medicine. Curr Probl Cancer. 2017;41(3):194–200.
31. Towbin AJ, Trout AT, Roebuck DJ. Advances in oncologic imaging. Eur J Pediatr Surg. 2014;24(6):474–81.
32. Rappaport BA, Suresh S, Hertz S, Evers AS, Orser BA. Anesthetic neurotoxicity--clinical implications of animal models. N Engl J Med. 2015;372(9):796–7.
33. Weller A, Barber JL, Olsen OE. Gadolinium and nephrogenic systemic fibrosis: an update. Pediatr Nephrol. 2014;29(10):1927–37.
34. Kanal E, Tweedle MF. Residual or retained gadolinium: practical implications for radiologists and our patients. Radiology. 2015;275(3):630–4.
35. Ramalho J, Semelka RC, Ramalho M, Nunes RH, AlObaidy M, Castillo M. Gadolinium-based contrast agent accumulation and toxicity: an update. AJNR Am J Neuroradiol. 2016;37(7):1192–8.
36. Racadio JM. Controlling radiation exposure during interventional procedures in childhood cancer patients. Pediatr Radiol. 2009;39(Suppl 1):S71–3.
37. Goske MJ, Frush DP, Brink JA, Kaste SC, Butler PF, Pandharipande PV. Curbing potential radiation-induced cancer risks in oncologic imaging: perspectives from the 'image gently' and 'image wisely' campaigns. Oncology (Williston Park). 2014;28(3):232–8. 243.
38. Nievelstein RA, van Dam IM, van der Molen AJ. Multidetector CT in children: current concepts and dose reduction strategies. Pediatr Radiol. 2010;40(8):1324–44.
39. Strauss KJ, Goske MJ, Kaste SC, et al. Image gently: ten steps you can take to optimize image quality and lower CT dose for pediatric patients. AJR Am J Roentgenol. 2010;194(4):868–73.
40. Nelson TR. Practical strategies to reduce pediatric CT radiation dose. J Am Coll Radiol. 2014;11(3):292–9.
41. Hernanz-Schulman M, Goske MJ, Bercha IH, Strauss KJ. Pause and pulse: ten steps that help manage radiation dose during pediatric fluoroscopy. AJR Am J Roentgenol. 2011;197(2):475–81.
42. Willis CE. Strategies for dose reduction in ordinary radiographic examinations using CR and DR. Pediatr Radiol. 2004;34(Suppl 3):S196–200. discussion S234–141.
43. Connolly B, Racadio J, Towbin R. Practice of ALARA in the pediatric interventional suite. Pediatr Radiol. 2006;36(Suppl 2):163–7.
44. Grant FD, Gelfand MJ, Drubach LA, Treves ST, Fahey FH. Radiation doses for pediatric nuclear medicine studies: comparing the North American consensus guidelines and the pediatric dosage card of the European Association of Nuclear Medicine. Pediatr Radiol. 2015;45(5):706–13.
45. Lassmann M, Treves ST, Group ESPDHW. Paediatric radiopharmaceutical administration: harmonization of the 2007 EANM paediatric dosage card (version 1.5. 2008) and the 2010 North American consensus guidelines. Eur J Nucl Med Mol Imaging. 2014;41(5):1036–41.
46. Treves ST, Gelfand MJ, Fahey FH, Parisi MT. 2016 update of the North American Consensus Guidelines for pediatric administered radiopharmaceutical activities. J Nucl Med. 2016;57(12):15N–8N.
47. Fahey FH, Bom HH, Chiti A, et al. Standardization of administered activities in pediatric nuclear medicine: a report of the first nuclear medicine global initiative project, Part 2-Current standards and the path toward global standardization. J Nucl Med. 2016;57(7):1148–57.

Pediatric Molecular Imaging

19

Benjamin L. Franc
and Heike Elisabeth Daldrup-Link

19.1 Introduction

Molecular imaging technologies enable in vivo detection, characterization, and quantification of cellular and molecular abnormalities that control cancer development, progression and treatment response. Genetic profiling and liquid biopsies are being increasingly integrated in diagnostic workups of children with cancer predisposition syndromes and children with cancer. Examples include screening for molecular tumor biomarkers and the determination of MYC oncogene expression in patients with neuroblastoma, α-fetoprotein (AFP) in patients with malignant liver tumors, and AFP and/or β-human chorionic gonadotropin (HCG) levels in patients with germ cell tumors. If tumor biomarkers are positive, imaging plays a crucial role to determine the presence, location, and extent of an underlying tumor. However, as malignant tumors are being detected earlier based on blood biomarkers, the sensitivity and specificity of conventional imaging technologies might not be sufficient any more (Fig. 19.1). Novel molecular imaging technologies can provide more specific information compared to traditional imaging approaches. Molecular imaging biomarkers can interact with specific biological targets and dynamically assess gene, protein, and cell functions of malignant tumors [1]. This provides more sensitive and more specific information about the transition from healthy tissues to the earliest stages of cancer as well as the type, grade, and stage of established cancers than is currently available [2]. Molecular imaging technologies thereby improve the in vivo detection, characterization, and quantification of cellular and molecular abnormalities that control cancer development, progression, and treatment response. The obtained information can be used to prescribe personalized therapies and personalized treatment monitoring options. Future trends aim toward integrating cancer staging approaches for the primary tumor, and the whole body such that a comprehensive diagnosis can be generated with one single exam. This is not only convenient for the patient but also saves direct and indirect health-care costs by streamlining procedures and minimizing lost school and work time. Closer cross-disciplinary collaboration between oncologists, laboratory

B. L. Franc
Pediatric Molecular Imaging Program, Department of Radiology, Stanford University, Stanford, CA, USA
e-mail: Benjamin.franc@ucsf.edu

H. E. Daldrup-Link (✉)
Pediatric Molecular Imaging Program, Department of Radiology, Stanford University, Stanford, CA, USA

Hematology/Oncology Section, Department of Pediatrics, Stanford University, Stanford, CA, USA
e-mail: heiked@stanford.edu;
http://daldrup-link-lab.stanford.edu/

S. D. Voss, K. McHugh (eds.), *Imaging in Pediatric Oncology*, Pediatric Oncology,
https://doi.org/10.1007/978-3-030-03777-2_19

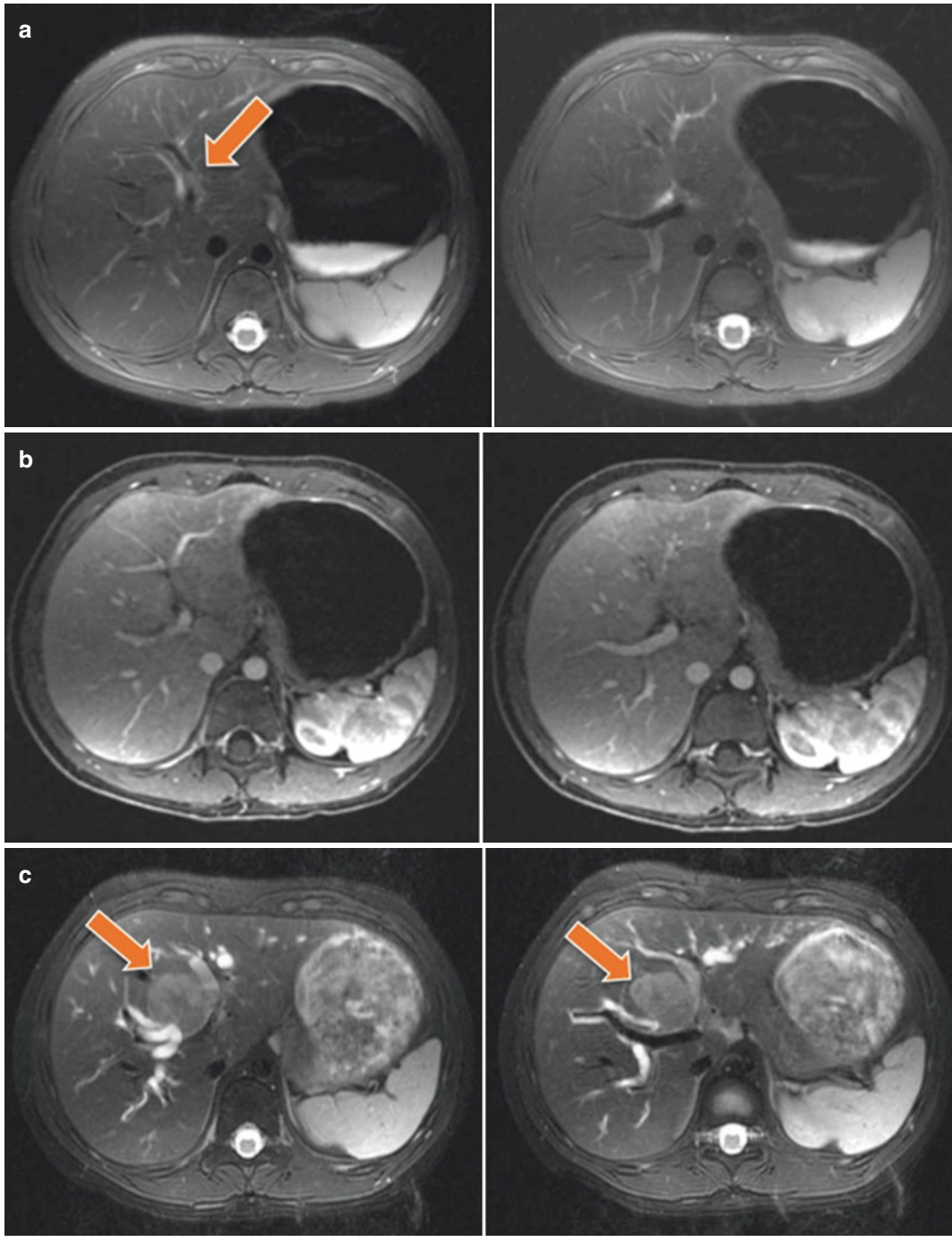

Fig. 19.1 Axial T2-weighted fast spin echo (FSE) images (**a**) in a 5-year-old patient with chronic hepatitis B and rising AFP shows questionable tiny, 2 mm lesion along the proximal left portal vein (orange arrow), which does not show any contrast enhancement on gadobutrol (Gadavist)-enhanced T1-weighted LAVA images (**b**). The patient was lost to follow up and returned 5 years later with abdominal pain and jaundice. The MRI 5 years later shows a large, inhomogenous T2-hyperintense mass at the bifurcation of the portal vein (orange arrow), which causes marked biliary duct compression and intrahepatic biliary duct dilatation (**c**). The lesion is hypovascular compared to surrounding liver parenchyma on early arterial (**d**) and delayed (**e**) gadobutrol (Gadavist) enhanced T1-weighted LAVA images. Biopsy proved a hepatocellular carcinoma. More sensitive and specific imaging technologies are needed to detect early-stage cancers

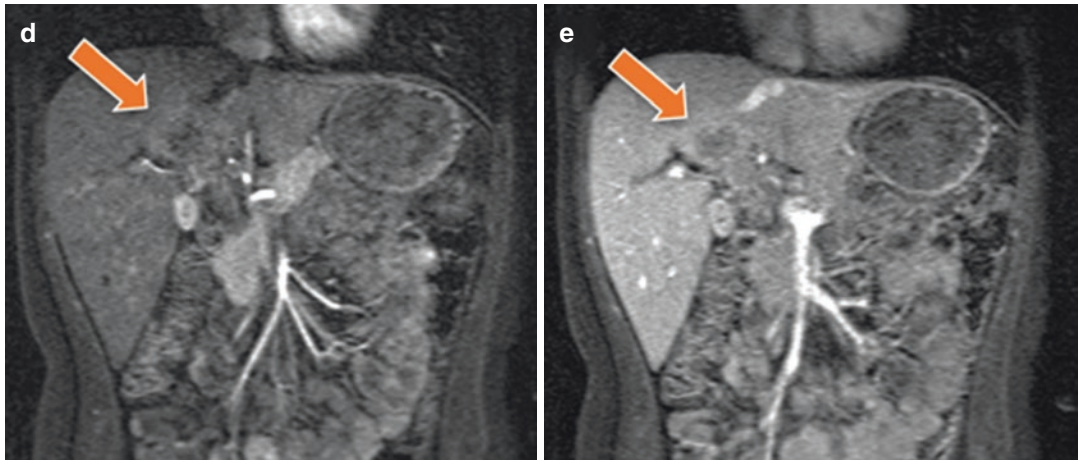

Fig. 19.1 (continued)

medicine physicians, and radiologists will enable "one stop" cancer staging and restaging, with imaging, blood and tissue samples obtained at once in the same facility and with one office visit.

19.2 Ultrasound

Ultrasound (US) is the workhorse of the clinical pediatric radiologist to date. US is widely available, noninvasive, and easy to apply. The portability of US makes it possible to bring this technology to the patient rather than the patient to the technology. This could, in theory, make it possible to train parents and other family members to perform simple screening exams of their child with portable ultrasound scanners at home, in order to bridge weeks of uncertainty between routinely scheduled imaging exams in the clinic. At the same time, US exams in cancer centers are becoming increasingly sophisticated. 3D/4D US imaging has gained widespread use in prenatal imaging. Cancer imaging experts have only recently started to harness 3D/4D US and microbubble contrast-enhanced US for the benefit of pediatric cancer patients. Examples include preoperative assessment of liver tumor resectability [3] and planning hepatectomies in patients with hepatoblastoma [4].

Microbubble contrast agents can increase the sensitivity and specificity of US exams for imaging cancer and inflammation, and some are approved by the Food and Drug Administration (FDA) in the United States [5–7]. Microbubbles are perfluorobutane and nitrogen-containing spheres of phospholipids with diameters of 1–4 μm, which is slightly smaller than a red blood cell. A recent retrospective analysis of 34 pediatric cancer patients who had received microbubble-enhanced US showed that this procedure is safe and well tolerated in the pediatric oncology population [8]. Targeted microbubbles can provide more specific enhancement of cancers and other pathologies [5–7, 9]. A first in human investigation of microbubbles targeted to the kinase insert domain receptor (KDR, a key regulator of angiogenesis) on ovarian and breast cancers in adult patients showed the feasibility of imaging KDR receptor expression in vivo with US. Microbubble-enhanced US images matched well with immunohistochemistry as the gold standard (93% of breast and 85% of ovarian malignant lesions) [10]. There is a pressing need to pursue similar prospective clinical trials on the comparative diagnostic value and efficacy of unenhanced and contrast-enhanced US as well as nontargeted and targeted microbubbles in the pediatric oncology population [11, 12]. Young patients in particular would benefit from this technology as it could reduce the need for more invasive procedures and anesthesia.

19.3 Photoacoustic Imaging

Photoacoustic imaging is an emerging new imaging modality which is radiation free, highly adaptable, and noninvasive [1]. Photoacoustic scanners typically operate through handheld transducers, which deliver pulsed laser light into the tissue of interest. The laser light is absorbed and causes thermo-elastic expansion of the target tissue, which leads to emission of ultrasound waves ("light in—ultrasound out"). Advantages compared to ultrasound include less image noise and higher sensitivity for the detection of targeted probes (picogram compared to microgram for US). Advantages compared to optical imaging include deeper tissue penetration (up to 5 cm) and increased spatial resolution. A practical limitation that we encountered with first-generation photoacoustic systems was that the pulsed laser in these systems is very expensive, appears to be short-lived, and can only be exchanged by the vendor. Technical improvements would benefit from longer laser life times and a possibility for the user and/or a service person to exchange laser parts on site.

Nevertheless, photoacoustic systems provide a number of interesting applications: A recent study in patients with non-melanoma skin cancers found accurate measures of lesion dimensions and depths with three-dimensional spatial resolution up to 80 μm, which correlated with postsurgical histopathology as the standard of reference [13]. New technologies enable photoacoustic microscopy of tumor resection margins, creating real-time histology-like images of tissue surfaces [14]. Another study of freshly excised thyroid specimens collected from 50 patients who underwent thyroidectomy found that radiofrequency photoacoustic signals and two-dimensional photoacoustic images could be used to differentiate malignant, benign, and normal thyroid tissue. [15] Multispectral photoacoustic imaging combined with the FDA-approved near-infrared fluorophore indocyanine green reliably visualized sentinel lymph nodes in 20 patients with melanoma, with up to 5-cm penetration and 100% concordance with ^{99m}Tc-labeled tracer-based lymphoscintigraphy for sentinel lymph node identification [16]. A variety of advanced photoacoustic imaging agents have been developed which can target specific cancer characteristics [1] or provide combined diagnostic and therapeutic (theranostic) applications [17].

19.4 Optical Imaging

Optical imaging (OI) is another inexpensive, noninvasive, rapid (<1 min), and radiation-free imaging technique with molecular sensitivity, close to that of radiotracer imaging [1, 18]. For many years, optical coherence tomography (OCT), which renders an in vivo cross-sectional view of the retina, has been used for retinal imaging [19]. Several studies described the value of OCT for the detection of retinoblastoma: OCT could differentiate hamartomas and retinoblastoma, monitor tumor progression, and monitor treatment response [20, 21]. An interesting recent article describes the use of OCT for the diagnosis of interferon-induced retinopathy [22]. OI and OCT can generate images of oxygenated hemoglobin, which is inherently fluorescent. This can be utilized for noninvasive monitoring of tumor oxygenation. Intravenously injected fluorescent probes are being used to enhance tumors on OI and OCT images, similar to other contrast-enhanced imaging technologies. The FDA-approved fluorescent label, indocyanine green (ICG) [23, 24], has been applied in patients for noninvasive OI detection of breast lesions [25], intraoperative detection of peritoneal metastases [26], and intraoperative brain tumor delineation combined with functional brain mapping [27]. A variety of tumor-targeted imaging agents [28, 29] and handheld OI transducers [30] are currently being developed for intraoperative tumor delineation in patients.

19.5 Single-Photon Emission Computed Tomography (SPECT)

Computed tomography has limited utility for molecular imaging applications as a "stand-alone" technology, because of its low sensitivity and low soft tissue contrast. However, CT can provide background anatomic information for radiophar-

maceutical localization and correlation with other imaging modalities. In addition, data from CT is used in the processing of SPECT and PET emission images, to correct for various physical factors such as soft tissue attenuation. SPECT imaging utilizes single-photon radionuclides (e.g., ^{99m}Tc, ^{111}In, ^{123}I, ^{201}Tl, ^{133}Xe), which emit noncoincident gamma rays at different energy levels, thereby potentially allowing multiplexing (simultaneous detection of multiple tracers). Traditional nuclear gamma cameras utilize scintillation-based detectors. However, advances in higher sensitivity semiconductor cadmium-zinc-telluride (CZT) detectors have enabled reduced imaging times and/or reduced levels of radioactivity for certain applications requiring only a small field of view [31, 32]. Recent technical developments include handheld gamma cameras for intraoperative detection of small tumors [33].

SPECT imaging studies used for the detection of pediatric cancers in the settings of baseline diagnosis and/or staging include ^{123}I-metaiodobenzylguanidine (MIBG) SPECT, a well-established clinical study used for detection of neuroblastomas, and which has also been used in guiding the treatment of neuroblastoma [34]. ^{111}In-DTPA-octreotide (DTPA, diethylenetriamine pentaacetate) is used to image somatostatin receptor expression and enables the differentiation of neuroendocrine tumors from other tumor types or from scar in the treated patient [35, 36].

Following diagnosis and staging, SPECT has a limited role in evaluating response to therapy. Uptake of ^{123}I-MIBG on nuclear imaging is part of the response criteria for neuroblastoma [37]. ^{99m}Tc-annexin V SPECT has been explored for imaging tumor apoptosis in response to therapy [38]. In adult patients, the vascular endothelial growth factor (VEGF) isoform $VEGF_{165}$ has been labeled with ^{123}I and used for imaging pancreatic carcinomas and brain cancer [39, 40]. However, the high radiation dose delivered to the thyroid via the ^{123}I radiotracer limits corresponding applications in children. Radiolabeling of non-radioactive therapies provides the capability to track their tissue localization in vivo. For example, ^{111}In-labeled anti-VEGF antibody (bevacizumab) has been tracked to malignant brain tumors and osteosarcomas [39, 41].

19.6 Positron Emission Tomography (PET) and PET/CT

PET systems coincidently detect two photons emitted from a positron annihilation and are generally more sensitive than gamma camera/SPECT-based techniques, due in part to lower soft tissue attenuation of the high energy (511 keV) gamma photons and the inherently higher resolution images that result from coincidence photon detection. PET imaging systems are most often integrated with CT in a single PET/CT system with the dual purpose of attenuation correction of the PET emission images and gathering background anatomic data.

PET/CT is widely used in the settings of diagnosis and staging of pediatric cancers. ^{18}F-fluorodeoxyglucose (FDG)-PET/CT is the established clinical imaging modality for staging and restaging of a number of malignant tumors in pediatric patients, including lymphoma [42–44] (Fig. 19.2) and soft tissue sarcomas [45, 46] (Fig. 19.3). In these applications, ^{18}F-FDG-PET/CT has demonstrated sufficient sensitivity and accuracy to supplant some traditional non-imaging methods of staging. For example, in patients with Hodgkin lymphoma, ^{18}F-FDG-PET/CT is more sensitive than bone marrow biopsy in detecting bone marrow involvement, providing an opportunity for pediatric patients to avoid an invasive procedure in many cases [47, 48].

Indications for ^{18}F-FDG-PET/CT in the staging of other tumors are decided on an individual basis, such as bone sarcomas [45, 46], head and neck cancers [49] and, rarely, Wilms tumor [50]. Several studies have demonstrated improved sensitivities and specificities of ^{18}F-FDG-PET/CT compared to all collective standard staging procedures [45, 49, 51–55]. In pediatric patients with suspected malignancy, dual time point ^{18}F-FDG-PET/CT has been used to improve discrimination between malignant and benign tumors [56]. Additional benefits to using ^{18}F-FDG-PET/CT in the diagnosis/staging timeframe is the ability to target biopsy to non-necrotic portions of the tumor, as in the case of soft tissue sarcomas [57]. In addition to simply detecting the presence of a malignant focus, the level of ^{18}F-FDG uptake can also provide long-term prognostic data,

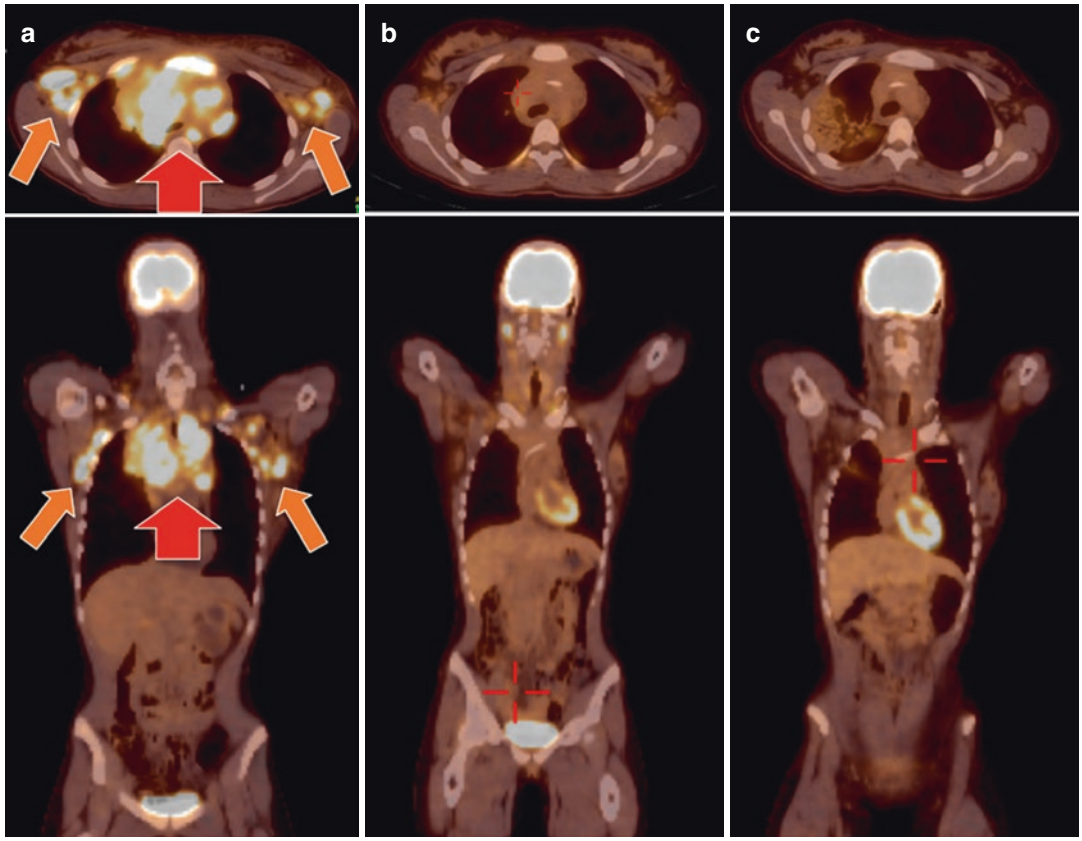

Fig. 19.2 Axial and coronal ^{18}F-FDG PET-CT images of a 16-year-old female with non-Hodgkin lymphoma demonstrate intensely hypermetabolic mediastinal (red arrow) and axillary (orange arrows) lymph nodes at baseline (**a**) that decrease significantly in size and metabolic activity following two cycles of ABVD therapy (**b**). After completion of therapy (**c**), ^{18}F-FDG PET-CT demonstrates complete metabolic response to therapy with small residual non-FDG-avid soft tissue mass. Mildly hypermetabolic density in the right upper lung field represented a pneumonia that resolved after antibiotic treatment

Fig. 19.3 ^{18}F-FDG PET-CT staging exam of a rhabdomyosarcoma in the left masseter muscle in a 6-year-old boy. Sagittal fused ^{18}F-FDG PET-CT (**a**) and PET MIP (**b**) images demonstrate the primary malignancy (red arrow). Additional osseous metastases along the posterior aspect of the spine are evident on the PET MIP (blue arrows). Metabolically active lung metastases (orange arrows) evident on axial ^{18}F-FDG PET-CT (**c**), emission PET (**d**), and CT images (**e**)

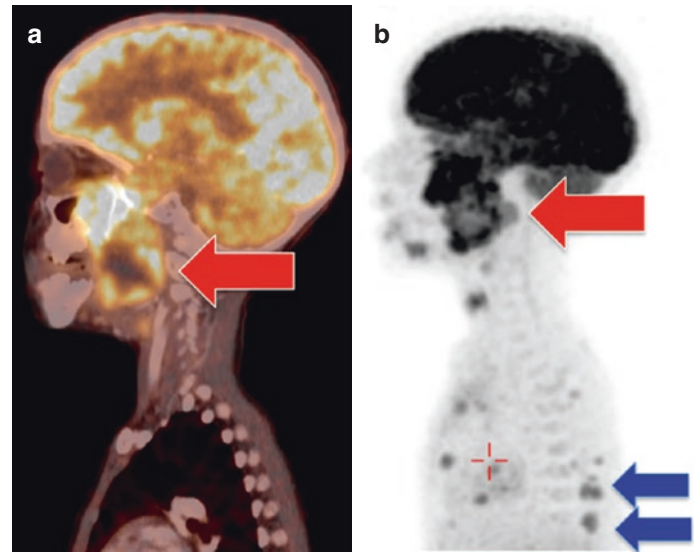

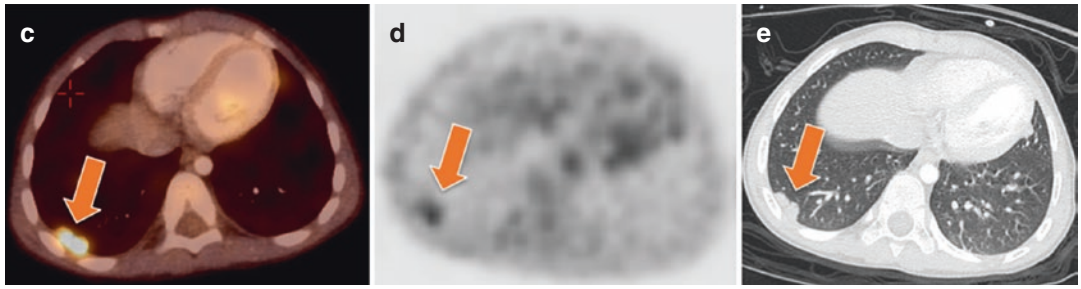

Fig. 19.3 (continued)

which is helpful in long-term patient management of certain cancers, such as low-grade astrocytoma [58]. In the case of asymptomatic patients with neurofibromatosis type 1 (NF-1), ^{18}F-FDG-PET/CT can assist in early identification of malignant peripheral nerve sheath tumors (MPNST) [59].

Novel whole-body staging applications in pediatric cancer patients using radiotracers other than ^{18}F-FDG include ^{18}F-NaF for imaging of bone metastases [60, 61] as well as ^{124}I-MIBG PET [62] (Fig. 19.4) and ^{18}F-DOPA PET/CT [53, 63] for staging of neuroblastoma, possibly eventually replacing ^{123}I-MIBG SPECT. ^{18}F-DOPA and ^{124}I-MIBG PET/CT have recently shown higher overall accuracy than ^{123}I-MIBG scintigraphy [53, 64]. In addition, ^{124}I-MIBG PET studies are useful in dosimetry studies, calculating radiation dose for ^{131}I-MIBG radiotracer therapy of neuroblastomas and pheochromocytomas [65, 66].

^{18}F-labeled agents targeting sympathetic neurons, such as ^{18}F-fluoropropylbenzylguanidine (FPBG), ^{18}F-FHBG, and ^{18}F-MFBG have several advantages such as wide availability and improved imaging characteristics over isotopes like ^{124}I, and initial published experience in neuroblastoma looks promising [67, 68]. ^{18}F-DOPA has also proved valuable in the diagnosis and evaluation of the extent of paraganglioma and pheochromocytoma, though malignant forms of these tumors rarely present in childhood [69].

^{68}Ga-1,4,7,10-tetraazacyclododecane-1,4,7,10-tetraacetic acid (DOTA)-octreotate (DOTATATE) has also been explored as a highly sensitive means of detecting sites of disease in neuroblastoma patients and has recently been approved by the FDA for imaging neuroendocrine tumors [70]. Other radiolabeled somatostatin analogues utilized to image pediatric neuroendocrine tumors include ^{68}Ga-DOTA-edotreotide (DOTATOC) and ^{68}Ga-DOTA-1-Nal3-octreotide (DOTANOC) [71].

Combining molecular imaging information from multiple PET radiopharmaceuticals is not possible in a single image acquisition but can be accomplished in a single day using a combination of short-lived isotopes, such as ^{11}C, and longer-lived isotopes, such as ^{18}F or ^{89}Zr. Risk stratification for neuroblastoma patients has been demonstrated using metabolic tumor volume (MTV) and total lesion glycolysis (TLG) from ^{18}F-FDG PET/CT combined with dopaminergic tumor volume (DTV) and total lesion ^{18}F-DOPA activity (TLDA) on ^{18}F-FDOPA PET/CT [72].

PET-CT is also useful in planning and monitoring therapy. ^{18}F-FDG-PET/CT is used in radiation treatment planning in pediatric Hodgkin lymphoma, particularly in those cases with extensive involvement [73]. ^{124}I-MIBG PET studies were useful to calculate radiation dose for ^{131}I-MIBG radiotracer therapy of neuroblastomas and pheochromocytomas [65, 66]. Similarly, ^{124}I PET/CT-based dosimetry can impact patient management when performed prior to ^{131}I radioiodine therapy for differentiated thyroid cancer [74].

In lymphoma, ^{18}F-FDG-PET/CT is now being integrated into consensus-based treatment response criteria [75]. ^{18}F-FDG uptake associated with sites of Hodgkin disease on PET/CT following completion of therapy is indicative of poor progression-free and overall survival, and ^{18}F-FDG-PET/CT at this time point can be a critical tool for the oncologist to plan next steps in the patient's management [76, 77]. In adult patients with relapsed or refractory Hodgkin lymphoma undergoing autologous stem cell transplant, a

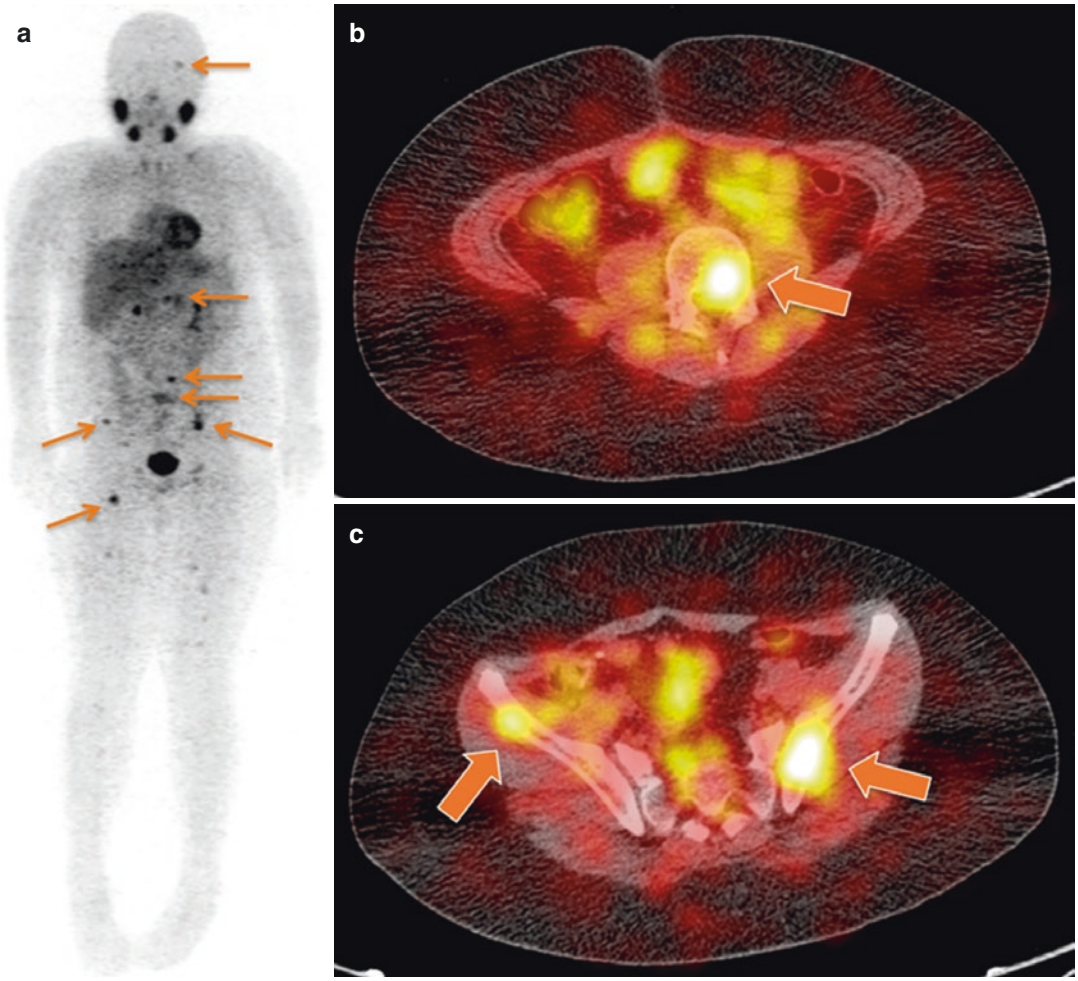

Fig. 19.4 ^{124}I-MIBG PET scan of a 9-year-old girl with recurrent neuroblastoma, presenting for treatment planning prior to administration of ^{131}I-MIBG therapy. PET MIP image (**a**) demonstrates numerous osseous metastases, which localize to the spine (**b**) and osseous pelvis (**c**) on fused axial PET-CT images. (*This figure was kindly provided by Youngho Seo, Ph.D., University of California, San Francisco)

negative pretransplant ^{18}F-FDG-PET/CT predicts a favorable response. Pediatric patients with negative findings on pretransplant imaging with ^{18}F-FDG-PET/CT or ^{67}Ga nuclear imaging also appear to have a good prognosis [78]. In pediatric patients with Burkitt lymphoma, ^{18}F-FDG-PET/CT can assist in confirming complete response following induction chemotherapy, potentially limiting cases requiring biopsy of the residual mass [79] (Fig. 19.5).

^{18}F-FDG-PET/CT's potential role in predicting pathologic response of some solid tumors early in the treatment course has also been evaluated. Semiquantitative changes in ^{18}F-FDG uptake between PET/CT scans at baseline and after 10 weeks of therapy are predictive of histologic response in osteosarcoma, potentially allowing a change of therapy in patients with anticipated poor response [80]. ^{18}F-FDG-PET/CT-based response assessment has also been explored in Wilms tumor [81]. However, since almost all Wilms tumors are resected, undergo histological evaluation, and have an excellent prognosis, ^{18}F-FDG-PET/CT is of limited utility in this patient population. ^{18}F-FDG-PET/CT might provide important information about tumor extent in rare cases of tumor recurrences.

^{18}F-deoxy-fluorothymidine (FLT) is a marker of tumor cell proliferation, which can be used to monitor treatment response to cancer therapy [82]. In

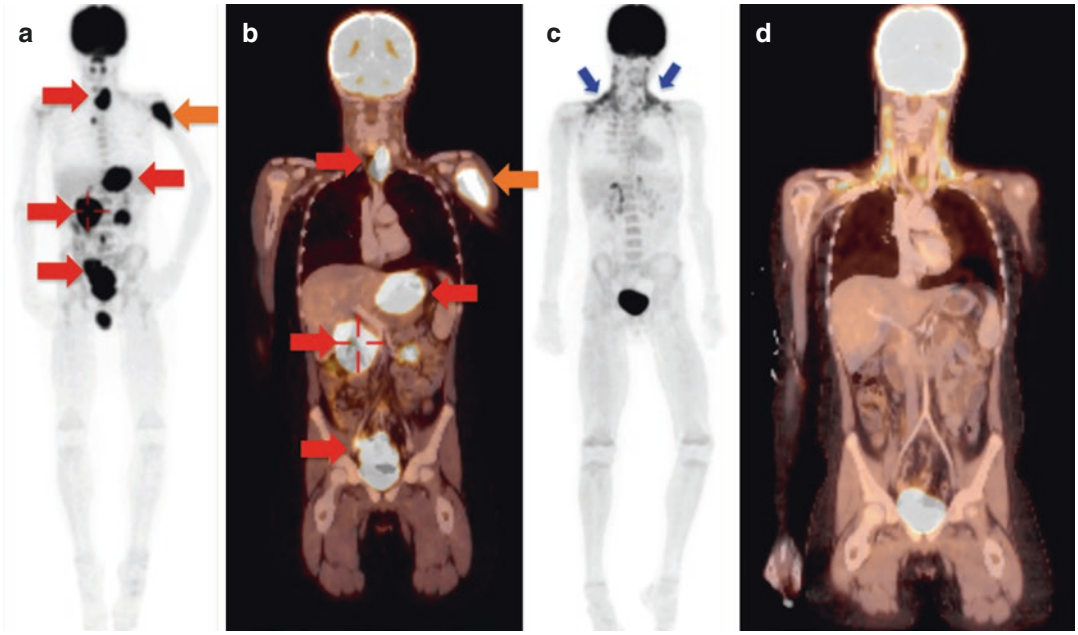

Fig. 19.5 ^{18}F-FDG PET/CT of a 9-year-old boy with Burkitt lymphoma. ^{18}F-FDG PET MIP (**a**) and coronal fused PET-CT (**b**) show multiple intensely hypermetabolic masses, scattered throughout the soft tissues of the thyroid bed, right kidney, gastrohepatic ligament, and pelvis (red arrows) as well as the left proximal humerus (orange arrow). Posttreatment ^{18}F-FDG PET MIP (**c**) and coronal fused PET-CT (**d**) show complete response by both metabolic and anatomic criteria. New ^{18}F-FDG activity in the supraclavicular regions on posttreatment scans was consistent with ^{18}F-FDG uptake in benign brown fat (blue arrows)

pediatric patients with primary brain tumors, ^{18}F-FLT–PET was useful in primary staging and response assessment [83]. Conversely, ^{18}F-FLT tumor uptake did not correlate with response of metastatic germ cell tumors to cisplatin therapy [84].

Other emerging PET radiotracers may predict response even prior to beginning therapy, as they characterize the expression of specific molecular markers on the surface of cancer cells or highlight processes that may render a tumor resistant to therapy. P-glycoprotein overexpression, which leads to activation of ATP-dependent drug-efflux pumps in cancer cells and multidrug resistance, can be detected with various PET tracers, including ^{11}C-verapamil [85] and ^{11}C-colchicine [86]. P-glycoprotein overexpression has been described in high risk and advanced stage neuroblastomas, malignant sarcomas, and hepatoblastomas, among others [87–90]. ^{64}Cu-DOTA-NHS-IL12, a radiolabeled immunocytokine that targets areas of tumor necrosis, is being explored as a means of characterizing solid tumors following radiation therapy to evaluate potential efficacy of immunotherapeutics [91]. ^{89}Zr-bevacizumab is being studied as a means to select glioma patients with tumors overexpressing VEGF, the target of the bevacizumab therapeutic antibody [92]. ^{124}I-EGFR and ^{124}I-CD44v6 may have a future role in measuring in vivo activity of therapeutics targeting heat shock protein 90 (HSP90), a component critical to the activation and stabilization of several oncogenic proteins [93, 94]. ^{89}Zr-onartuzumab, a tracer based on a therapeutic antibody targeting cancers with upregulated expression of the receptor to hepatocyte growth factor, c-MET, has demonstrated promise in monitoring changes in c-MET levels during therapy with inhibitors of epidermal growth factor receptor (EGFR) tyrosine kinase and HSP90 [95].

Apart from identifying and characterizing sites involved in malignancy, PET/CT is finding new applications by identifying other processes that may affect management of the pediatric cancer patient. For example, graft versus host disease (GVHD) is a significant complication in pediatric patients undergoing cord blood- or bone marrow hematopoietic stem cell

transplantation [96]. PET/CT with ^{18}F-fluoro-9-beta-D-arabinofuranosylguanine (^{18}F-AraG), a radiopharmaceutical that targets two salvage kinase pathways and preferentially accumulates in activated primary T cells, holds promise to identify GVHD in its acute phase, when treatments are most effective [97].

19.7 Magnetic Resonance (MR) Imaging and PET/MR

MR imaging is ionizing radiation free and the current clinical standard for local staging of most solid primary tumors in children, including tumors of the CNS, abdomen, pelvis, and musculoskeletal system [98, 99]. MR imaging can measure tumor physiology in addition to the inherent anatomical data, such as proton diffusion as an indirect marker of tumor cell density [2, 98, 100–102], blood and tissue oxygenation [103, 104], and drug or metabolite concentrations [105–107].

Whole-body diffusion-weighted MRI has shown equivalent sensitivities compared to ^{18}F-FDG-PET/CT for staging of children with cancer [101, 102, 108–111]. The degree of proton diffusion (or Brownian motion) in the tumor tissue can be quantified as the apparent diffusion coefficient (ADC) [112], which is directly associated with tumor grade and anaplastic progression [113]. In sarcomas, the degree of restricted diffusion [114, 115] and metabolic activity of the primary tumor at baseline have been linked to overall survival [51, 116, 117]. Diffusion-weighted MR showed increasing ADC values (= increasing proton diffusion) in response to therapy, which correlated with decreasing ^{18}F-FDG uptake in some cancers [114, 115].

Integrated PET/MRI systems combine the high soft tissue contrast of MRI with the high sensitivity of PET while exposing patients to significantly less ionizing radiation compared to PET/CT [118–125]. In addition to obviating the need for CT acquisition associated with PET/CT, reductions in doses of radiopharmaceuticals administered for the PET portion of PET/MR are also being explored as a means of reducing radiation exposure [126]. A variety of T1- and T2-weighted pulse sequences have been used for co-registration of PET and MRI data of pediatric patients [121–125]. Recent studies found that pediatric tumors can be equally well delineated on Gd-enhanced T1-weighted scans and unenhanced T2-weighted scans [127]. However, if the faster T1-weighted scans were applied, intravenous contrast agent injection improved vessel and tumor delineation compared to unenhanced scans [128]. This was particularly useful for accurate tumor measurements and surgical planning. Unfortunately, small molecular gadolinium chelates did not provide sufficient long-lasting vessel enhancement for whole-body PET/MR scans, especially when local staging and whole-body staging scans were combined in one session.

To solve this problem, our team uses the FDA-approved iron supplement ferumoxytol "off-label" for MR contrast enhancement [129–134] (Fig. 19.6). Ferumoxytol is composed of iron oxide nanoparticles, which provide long-lasting

Fig. 19.6 In vivo biodistribution and MR signal effects of intravenously administered superparamagnetic iron oxide nanoparticles (SPIO) with hydrodynamic diameters in the order of 30–40 nm: (**a**) After intravenous injection, SPIO initially distribute in the blood pool, where they show a strong T1-effect. This effect can be used for long-lasting vessel enhancement on T1-weighted MR images. (**b**) Due to their large size, nanoparticles do not extravasate across intact vascular endothelia in most normal organs. However, the nanoparticles leak across hyperpermeable sinus in organs of the reticuloendothelial system (RES), such as bone marrow, liver, spleen, and lymph nodes. This leads to a hypointense signal effect of normal RES tissues on T2- and T2*-weighted MR images. Nanoparticle extravasation occurs at a relatively slower rate into the interstitium of malignant tumors. Therefore, tumors in RES organs can be depicted as T2-hyperintense lesions on relatively early postcontrast scans (yellow arrows). (**c**) SPIO do slowly extravasate across discontinuous microvessels in tumors, a process that takes many hours. In the tumor interstitium, SPIO are phagocytosed by tumor-associated macrophages (TAM). This leads to a T2-enhancement of tumors on delayed postcontrast scans (yellow arrows). TAM-bound SPIO in solid tumor tissue can be differentiated from free SPIO in tumor necrosis because intracellular SPIO in TAM exert a hypointense MR signal effect on both T1- and T2-weighted MR images, while extracellular SPIO in tumor necrosis demonstrate T1-hyperintense and T2-hypointense signal. Within macrophages, SPIO undergo a slow metabolization. Baseline MR signal intensities in RES organs and tumors are regained after several weeks

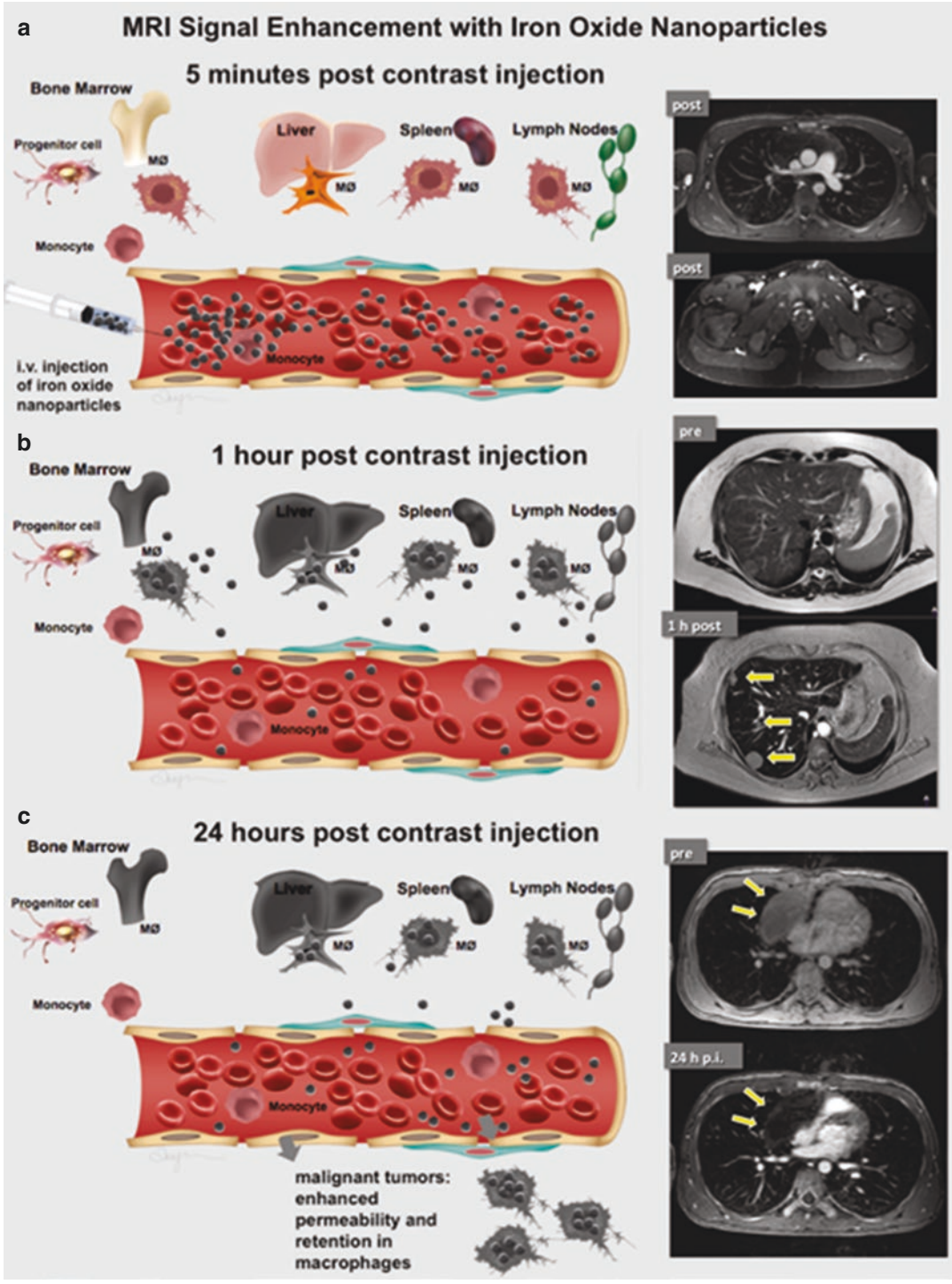
a
MRI Signal Enhancement with Iron Oxide Nanoparticles
5 minutes post contrast injection
Bone Marrow
Progenitor cell
MØ
Liver
Spleen
Lymph Nodes
Monocyte
i.v. injection of iron oxide nanoparticles
post
post
b
1 hour post contrast injection
pre
1 h post
c
24 hours post contrast injection
pre
24 h p.i.
malignant tumors: enhanced permeability and retention in macrophages

blood pool enhancement with a blood half-life of approximately 10 h [134]. In addition, ferumoxytol nanoparticles are slowly phagocytosed by macrophages, which can be used for improved MRI detection of tumor deposits in liver, lymph nodes, and bone marrow [130] or diagnoses of tumor-associated inflammation [135] (Fig. 19.6). Ferumoxytol is metabolized in the liver and therefore, can be applied in patients with renal insufficiency [130, 131]. However, ferumoxytol nanoparticles can rarely cause severe anaphylactic reactions, with a reported incidence of 0.1–0.2% [136, 137, 138]. Therefore, when using iron oxide nanoparticles for diagnostic or theranostic purposes, it is important that the care team has experience with prevention and treatment of allergic reactions, should they occur. We are currently developing a predictive blood test to determine an individual patient's risk to develop an allergic reaction against ferumoxytol. Patients with a positive test could then receive appropriate pretreatment conditioning prior to a ferumoxytol MRI. Ferumoxytol-enhanced ^{18}F-FDG PET/MR provided exquisite contrast between vessels and malignant lymph nodes in patients with lymphomas (Figs. 19.7 and 19.8) and exquisite delineation of malignant soft tissue sarcomas (Fig. 19.9) [139].

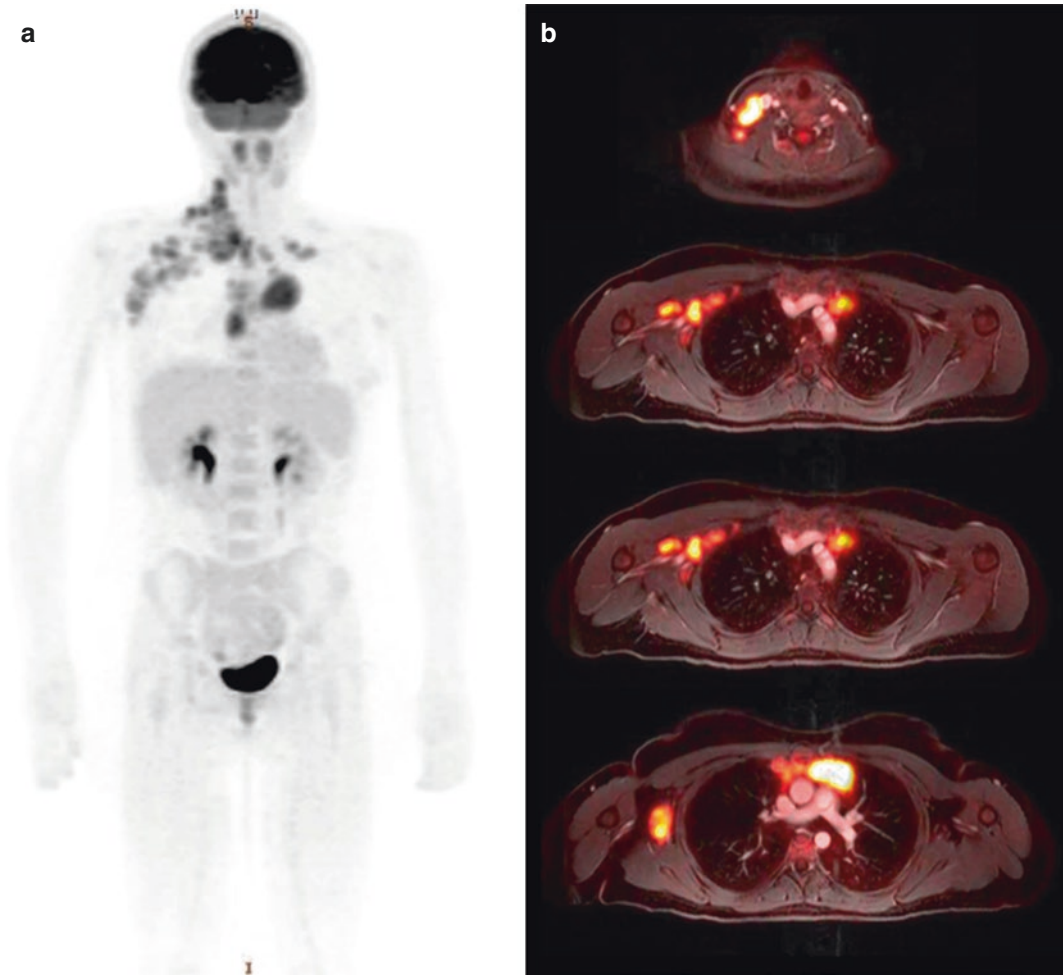

Fig. 19.7 ^{18}F-FDG PET/MR of an 18-year-old girl with Burkitt lymphoma: ^{18}F-FDG PET MIP shows multiple hypermetabolic and enlarged lymph nodes of the right neck, right axilla, and the mediastinum (**a**). Axial ferumoxytol-enhanced T1-weighted LAVA sequences fused with ^{18}F-FDG PET images provide accurate delineation and localization of hypermetabolic lymph nodes with regard to vessels in the neck, axilla, and mediastinum (**b**)

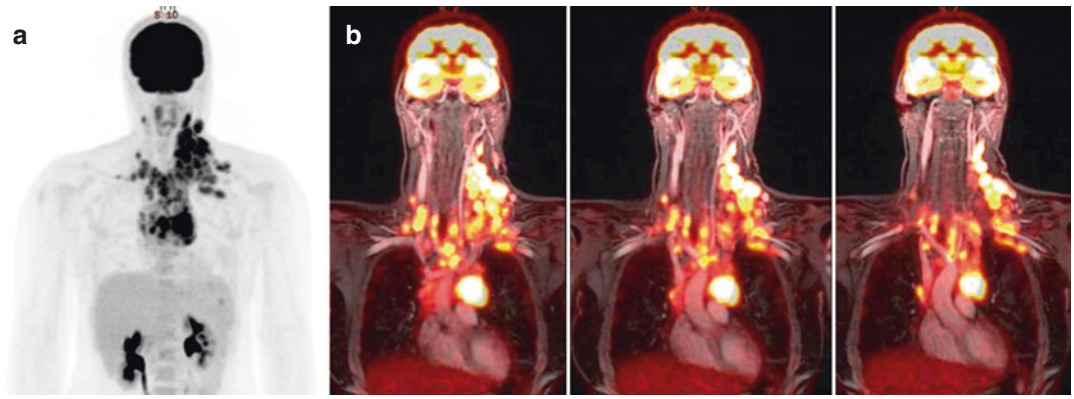

Fig. 19.8 ^{18}F-FDG PET/MR of a 15-year-old girl with Burkitt lymphoma: ^{18}F-FDG PET MIP shows multiple hypermetabolic and enlarged lymph nodes of the neck bilaterally and the mediastinum (**a**). Axial ferumoxytol-enhanced T1-weighted LAVA sequences, which were simultaneously obtained within a 30 s breathhold during PET data acquisition, were reformatted in a coronal plane and fused with ^{18}F-FDG PET images (**b**). These images provide accurate delineation and localization of hypermetabolic lymph nodes with regard to vessels in the neck and mediastinum, without additional scan time

Iron oxide nanoparticles can be used as "Trojan Horses" to shuttle therapeutic drugs into tumors through the enhanced permeability and retention (EPR) effect and/or through specific targeting mechanisms: Several clinically translatable theranostic nanoparticles have been developed for combined diagnosis and therapy of cancers [140, 141] and could be monitored through image-guided drug delivery [142–144]. Other innovative developments are under way with orally administered nanoparticle compounds, which are absorbed, enter the blood pool, bind to specific cancer-related molecules in the bloodstream, and can be detected by wearable devices [145–148]. These new biomolecules need to be validated against and integrated with traditional diagnostic approaches.

One of the first clinical applications of PET/MR has been imaging brain tumors. Very specific localization of signal on PET to a lesion on MRI can be highly valuable in the case of small intracranial tumors. Amino acid-based PET radiotracers are most often employed to initially characterize intracranial lesions as well as to evaluate changes during or following therapy. The most commonly used of these are ^{11}C-methionine (MET), ^{18}F-fluoroethyl-tyrosine (FET), ^{18}F-FDOPA, and ^{11}C-alpha-methyl-L-tryptophan (AMT). Each tracer depends on a different metabolic pathway and therefore is employed to answer a specific molecular question. For example, ^{11}C-AMT has recently been applied to evaluate levels of tumor expression of indoleamine 2,3-dioxygenase (IDO), a key metabolic step in the kynurenine pathway that contributes to immunoresistance [149]. Combined ^{18}F-fluroethyl-choline (FEC) PET/MR has been explored as a tool for diagnosis and treatment response assessment of astrocytic tumors [150] and intracranial nongerminomatous germ cell tumors (NGGCT) [151].

Novel radiotracers mentioned above for whole-body PET/CT applications can be also applied to PET/MR applications. Examples include ^{18}F-FDG-DOPA for evaluation of persistent hyperinsulinemic hypoglycemic infants and detection of insulinomas, ^{18}F-fluoride for staging of osteosarcoma, ^{124}I for iodine-positive thyroid cancer, ^{18}F-DOPA for medullary thyroid carcinoma, ^{68}Ga-DOTATOC for neuroendocrine tumors, and ^{124}I-MIBG for neuroblastoma, among others.

While whole-body PET/MR is relatively new as a combined imaging modality, applications that take advantage of the collection of PET data and MRI data contemporaneously are rapidly evolv-

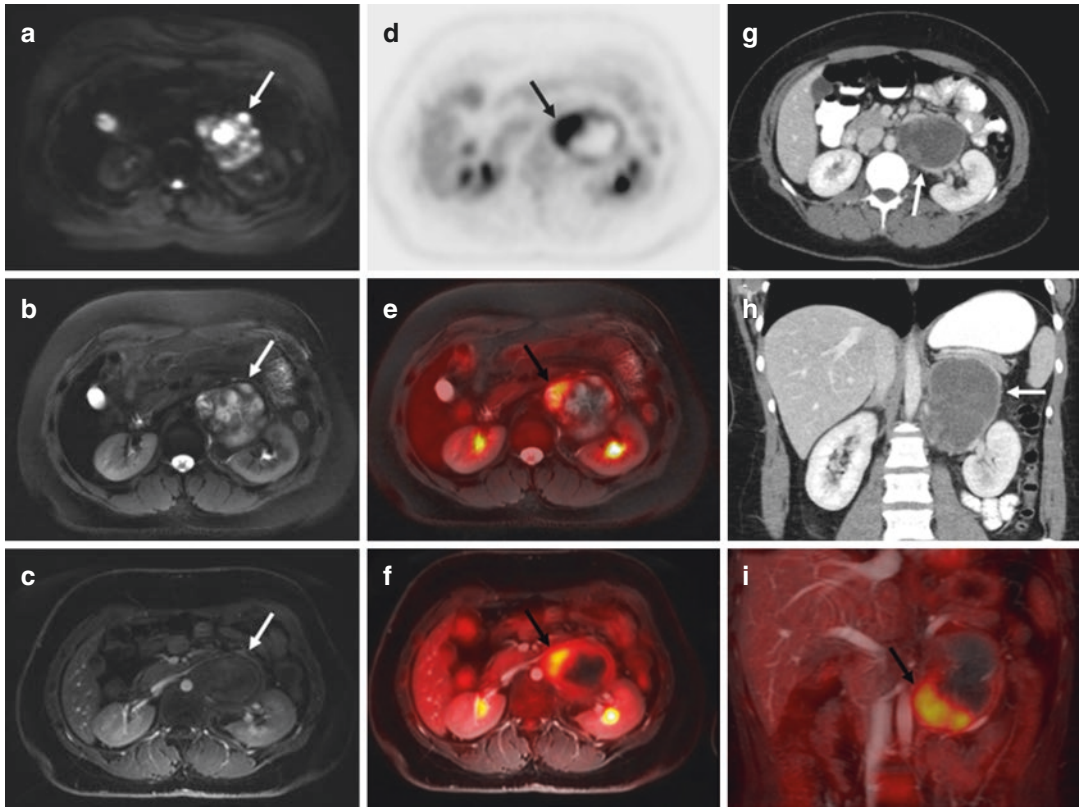

Fig. 19.9 ^{18}F-FDG PET/MR and CT findings in a 25-year-old female with soft tissue sarcoma in the left retroperitoneum (arrows). (**a**) Axial diffusion-weighted imaging (TR/TE/*b*-value: 7770/56.1/50,600) shows restricted diffusion (white arrow) in the tumor, (**b**) axial T2 PROPELLER (TR/TE/Flip angle: 8000/95.8/142) shows inhomogeneous hyperintense tumor signal; (**c**) ferumoxytol-enhanced T1-weighted LAVA scan (TR/TE/Flip angle: 4.2/1.7/15) shows close relation between the tumor and renal vessels. (**d**) Axial ^{18}F-FDG PET, (**e**) ^{18}F-FDG PET superimposed on T2-weighted FSE scan, and (**f**) ^{18}F-FDG PET superimposed on T1-weighted LAVA scan show that the tumor contains hypermetabolic medial and caudal areas (black arrow). (**g**, **h**) Axial and coronal CT shows a rather featureless, slightly inhomogeneous mass (white arrow); (**i**) Coronal ^{18}F-FDG PET superimposed on T1-weighted LAVA scan again shows the hypermetabolic caudal tumor part (black arrow). At surgery, this anterior and caudal tumor part was found to be adherent to adjacent vascular structures (reprint with permission from ref. [139])

ing [152, 153] (Fig. 19.9). Combining data from both PET and MR enables acquisition of multiplexed signals and can yield characterization of several tissue features in a single test. For example, combining information from T2-weighted, diffusion-weighted, and contrast-enhanced MRI scans with information from FDG-PET scans provided new information about the complex microenvironment of soft tissue sarcomas and could be linked to tumor aggressiveness and prognosis. In glioblastoma, a combination of specific MRI and ^{11}C-AMT PET characteristics have been associated with amplification of the epidermal growth factor receptor [EGFR] and methylation of the O6-methylguanine-DNA methyltransferase [MGMT] promoter, both prognostic indicators [154]. Co-temporal acquisition of MRI information has proved valuable in the interpretation of levels of uptake of PET molecular imaging agents, such as in the case of pseudoprogression of intracranial malignancies after proton beam therapy [155].

Collection of multiple molecular signals contemporaneously with PET/MR will also benefit from the development of hyperpolarized MR spectroscopic imaging (HMRSI).

HMRSI is an exciting, relatively new area of molecular MR imaging, currently studied in adult patients. For clinical applications, ^{13}C-labeled molecules are polarized into an antiparallel orientation, far beyond their thermal equilibrium, using a "dynamic nuclear polarization" (DNP) system outside of the MR magnet. Since the hyperpolarization of the probe decays rapidly, the probe has to be transported within few minutes to the patient and injected intravenously, followed by spectroscopic MR imaging of ^{13}C-containing metabolites [1, 156]. Hyperpolarized MRI of [1-^{13}C] pyruvate enables dynamic mapping of oncogene expression in vivo through detection of increased aerobic glycolysis and diminished oxidative phosphorylation (Warburg effect) in tumors. This enables early detection of de novo tumor formations and therapy-induced tumor regression [157].

19.8 Summary and Outlook

For children with cancer, an accurate diagnosis and therapy response assessment are critical for prescription of personalized treatment protocols and optimized outcomes. Since molecular imaging technologies can provide a variety of highly specific measures, molecular imaging has a unique opportunity to contribute both to the prediction and detection of cancer through identification and validation of existing and new biomarkers and assessment of their impact on treatment decisions and outcomes. Pediatric molecular imaging biomarkers should have both immediate and long-term value for a significant number of children. Future developments will focus on further increasing the sensitivity and specificity of imaging tests through more specific biomarkers and integration of genomic and proteomic data, reducing radiation exposures, and improving the safety, efficiency, and yield of novel multimodality imaging tests. The diagnosis of tumor recurrence remains a wide open area of investigation. Data suggest that the disappearance of molecular clones of tumors (e.g., lymphomas) may lag behind the disappearance of morphologic evidence of disease [158]. Thus, surveillance exams will likely require a combination of serum biomarkers and targeted imaging of selected patients. Examples include alpha-fetoprotein (AFP) as biomarker for hepatoblastomas and human chorionic gonadotropin (HCG) as biomarker for non-seminomatous germ cell tumors (GCT), lactate dehydrogenase (LDH) for patients with lymphoma and *vanillylmandelic acid* (VMA), and norepinephrine for neuroblastoma and pheochromocytoma [159]. Imaging approaches for the detection of residual disease, recurrent disease, and secondary tumor development will have to be refined to integrate genetic testing and serum biomarkers into modern diagnostic workups.

Acknowledgment The work described here was in part supported by a grant from the Eunice Kennedy Shriver National Institute of Child Health and Human Development, grant number R01 HD081123. There is no conflict of interest or industry support for this project. We thank Eileen Misquez and Becki Perkins for administrative assistance, and we thank Praveen Gulaka, Anne Muehe, Ashok Theruvath, Dawn Holley, and Harsh Gandhi from the Pediatric Molecular Imaging team at Stanford for their help with acquisition of PET/MR scans. We thank the members of the Franc and Daldrup-Link labs for valuable discussions.

References

1. James ML, Gambhir SS. A molecular imaging primer: modalities, imaging agents, and applications. Physiol Rev. 2012;92:897–965.
2. Voss SD. Pediatric oncology and the future of oncological imaging. Pediatr Radiol. 2011;41(Suppl 1):S172–85.
3. Su L, Dong Q, Zhang H, et al. Clinical application of a three-dimensional imaging technique in infants and young children with complex liver tumors. Pediatr Surg Int. 2016;32:387–95.
4. Zhang G, Zhou XJ, Zhu CZ, Dong Q, Su L. Usefulness of three-dimensional(3D) simulation software in hepatectomy for pediatric hepatoblastoma. Surg Oncol. 2016;25:236–43.
5. Kiessling I, Bzyl J, Kiessling F. Molecular ultrasound imaging and its potential for paediatric radiology. Pediatr Radiol. 2011;41:176–84.
6. Lindner JR. Microbubbles in medical imaging: current applications and future directions. Nat Rev Drug Discov. 2004;3:527–32.

7. Willmann JK, Cheng Z, Davis C, et al. Targeted microbubbles for imaging tumor angiogenesis: assessment of whole-body biodistribution with dynamic micro-PET in mice. Radiology. 2008;249:212–9.
8. Coleman JL, Navid F, Furman WL, McCarville MB. Safety of ultrasound contrast agents in the pediatric oncologic population: a single-institution experience. AJR Am J Roentgenol. 2014;202:966–70.
9. Willmann JK, Paulmurugan R, Chen K, et al. US imaging of tumor angiogenesis with microbubbles targeted to vascular endothelial growth factor receptor type 2 in mice. Radiology. 2008;246:508–18.
10. Willmann JK, Bonomo L, Carla Testa A, et al. Ultrasound molecular imaging with BR55 in patients with breast and ovarian lesions: first-in-human results. J Clin Oncol. 2017;35:2133.
11. Rennert J, Georgieva M, Schreyer AG, et al. Image fusion of contrast enhanced ultrasound (CEUS) with computed tomography (CT) or magnetic resonance imaging (MRI) using volume navigation for detection, characterization and planning of therapeutic interventions of liver tumors. Clin Hemorheol Microcirc. 2011;49:67–81.
12. Stenzel M, Mentzel HJ. Ultrasound elastography and contrast-enhanced ultrasound in infants, children and adolescents. Eur J Radiol. 2014;83:1560–9.
13. Attia ABE, Chuah SY, Razansky D, et al. Noninvasive real-time characterization of non-melanoma skin cancers with handheld optoacoustic probes. Photoacoustics. 2017;7:20–6.
14. Wong TTW, Zhang R, Hai P, et al. Fast label-free multilayered histology-like imaging of human breast cancer by photoacoustic microscopy. Sci Adv. 2017;3:e1602168.
15. Sinha S, Dogra VS, Chinni BK, Rao NA. Frequency domain analysis of multiwavelength photoacoustic signals for differentiating among malignant, benign, and normal thyroids in an ex vivo study with human thyroids. J Ultrasound Med. 2017;36:2047.
16. Stoffels I, Morscher S, Helfrich I, et al. Metastatic status of sentinel lymph nodes in melanoma determined noninvasively with multispectral optoacoustic imaging. Sci Transl Med. 2015;7:317ra199.
17. Gao W, Li S, Liu Z, et al. Targeting and destroying tumor vasculature with a near-infrared laser-activated "nanobomb" for efficient tumor ablation. Biomaterials. 2017;139:1–11.
18. Sutton EJ, Henning TD, Pichler BJ, Bremer C, Daldrup-Link HE. Cell tracking with optical imaging. Eur Radiol. 2008;18:2021–32.
19. Ahmad M, Kaszubski PA, Cobbs L, Reynolds H, Smith RT. Choroidal thickness in patients with coronary artery disease. PLoS One. 2017;12:e0175691.
20. Seider MI, Grewal DS, Mruthyunjaya P. Portable optical coherence tomography detection or confirmation of ophthalmoscopically invisible or indeterminate active retinoblastoma. Ophthalmic Surg Lasers Imaging Retina. 2016;47:965–8.
21. Lee H, Proudlock FA, Gottlob I. Pediatric optical coherence tomography in clinical practice-recent progress. Invest Ophthalmol Vis Sci. 2016;57:OCT69–79.
22. Mastropasqua L, Borrelli E, Amodei F, et al. Optical coherence tomography angiography in the multimodal imaging evaluation of interferon-associated retinopathy: a case report. Ophthalmic Surg Lasers Imaging Retina. 2017;48:498–504.
23. Meier R, Krug C, Golovko D, et al. ICG-enhanced imaging of arthritis with an integrated optical imaging/X-ray system. Arthritis Rheum. 2010;62:2322.
24. Meier R, Thuermel K, Moog P, et al. Detection of synovitis in the hands of patients with rheumatological disorders: diagnostic performance of optical imaging in comparison to MRI. Arthritis Rheum. 2012;64:2489.
25. Roblyer D, Ueda S, Cerussi A, et al. Optical imaging of breast cancer oxyhemoglobin flare correlates with neoadjuvant chemotherapy response one day after starting treatment. Proc Natl Acad Sci U S A. 2011;108:14626–31.
26. Sheth RA, Upadhyay R, Stangenberg L, Sheth R, Weissleder R, Mahmood U. Improved detection of ovarian cancer metastases by intraoperative quantitative fluorescence protease imaging in a pre-clinical model. Gynecol Oncol. 2009;112:616–22.
27. Prakash N, Uhlemann F, Sheth SA, Bookheimer S, Martin N, Toga AW. Current trends in intraoperative optical imaging for functional brain mapping and delineation of lesions of language cortex. Neuroimage. 2009;47(Suppl 2):T116–26.
28. Predina JD, Okusanya O, DN A, Low P, Singhal S. Standardization and optimization of intraoperative molecular imaging for identifying primary pulmonary adenocarcinomas. Mol Imaging Biol. 2018;20:131.
29. Harmsen S, Teraphongphom N, Tweedle MF, Basilion JP, Rosenthal EL. Optical surgical navigation for precision in tumor resections. Mol Imaging Biol. 2017;19:357–62.
30. Zhao Q, Jiang H, Cao Z, Yang L, Mao H, Lipowska M. A handheld fluorescence molecular tomography system for intraoperative optical imaging of tumor margins. Med Phys. 2011;38:5873–8.
31. Herzog BA, Buechel RR, Katz R, et al. Nuclear myocardial perfusion imaging with a cadmium-zinc-telluride detector technique: optimized protocol for scan time reduction. J Nucl Med. 2010;51:46–51.
32. Nkoulou R, Fuchs TA, Pazhenkottil AP, et al. Absolute myocardial blood flow and flow reserve assessed by gated SPECT with cadmium-zinc-telluride detectors using 99mTc-tetrofosmin: head-to-head comparison with 13N-ammonia PET. J Nucl Med. 2016;57:1887–92.
33. Van Haren RM, Fitzgerald TL. Intraoperative hand held gamma probe detection of a recurrent nonfunctional neuroendocrine tumor. JOP. 2008;9:704–7.
34. Taggart D, Dubois S, Matthay KK. Radiolabeled metaiodobenzylguanidine for imaging and therapy

of neuroblastoma. Q J Nucl Med Mol Imaging. 2008;52:403–18.
35. Vaccarili M, Lococo A, Fabiani F, Staffilano A. Clinical diagnostic application of 111In-DTPA-octreotide scintigraphy in small cell lung cancer. Tumori. 2000;86:224–8.
36. O'Dorisio MS, Khanna G, Bushnell D. Combining anatomic and molecularly targeted imaging in the diagnosis and surveillance of embryonal tumors of the nervous and endocrine systems in children. Cancer Metastasis Rev. 2008;27:665–77.
37. Park JR, Bagatell R, Cohn SL, et al. Revisions to the international neuroblastoma response criteria: a consensus statement from the National Cancer Institute Clinical trials planning meeting. J Clin Oncol. 2017;35:2580–7.
38. Belhocine T, Steinmetz N, Hustinx R, et al. Increased uptake of the apoptosis-imaging agent (99m)Tc recombinant human Annexin V in human tumors after one course of chemotherapy as a predictor of tumor response and patient prognosis. Clin Cancer Res. 2002;8:2766–74.
39. Heneweer C, Grimm J. Clinical applications in molecular imaging. Pediatr Radiol. 2011;41:199–207.
40. Cortes-Funes H. The role of antiangiogenesis therapy: bevacizumab and beyond. Clin Transl Oncol. 2009;11:349–55.
41. Aguilera DG, Goldman S, Fangusaro J. Bevacizumab and irinotecan in the treatment of children with recurrent/refractory medulloblastoma. Pediatr Blood Cancer. 2011;56:491–4.
42. Cheng G, Chen W, Chamroonrat W, Torigian DA, Zhuang H, Alavi A. Biopsy versus FDG PET/CT in the initial evaluation of bone marrow involvement in pediatric lymphoma patients. Eur J Nucl Med Mol Imaging. 2011;38:1469–76.
43. Riad R, Omar W, Kotb M, et al. Role of PET/CT in malignant pediatric lymphoma. Eur J Nucl Med Mol Imaging. 2010;37:319–29.
44. Morimoto T, Tateishi U, Maeda T, Arai Y, Nakajima Y, Edmund Kim E. Nodal status of malignant lymphoma in pelvic and retroperitoneal lymphatic pathways: comparison of integrated PET/CT with or without contrast enhancement. Eur J Radiol. 2008;67:508–13.
45. Tateishi U, Yamaguchi U, Seki K, Terauchi T, Arai Y, Kim EE. Bone and soft-tissue sarcoma: preoperative staging with fluorine 18 fluorodeoxyglucose PET/CT and conventional imaging. Radiology. 2007;245:839–47.
46. Walter F, Czernin J, Hall T, et al. Is there a need for dedicated bone imaging in addition to 18F-FDG PET/CT imaging in pediatric sarcoma patients? J Pediatr Hematol Oncol. 2012;34:131–6.
47. Hassan A, Siddique M, Bashir H, et al. 18F-FDG PET-CT imaging versus bone marrow biopsy in pediatric Hodgkin's lymphoma: a quantitative assessment of marrow uptake and novel insights into clinical implications of marrow involvement. Eur J Nucl Med Mol Imaging. 2017;44:1198–206.
48. Agrawal K, Mittal BR, Bansal D, et al. Role of F-18 FDG PET/CT in assessing bone marrow involvement in pediatric Hodgkin's lymphoma. Ann Nucl Med. 2013;27:146–51.
49. Boktor RR, Omar WS, Mousa E, et al. A preliminary report on the impact of (1)(8)F-FDG PET/CT in the management of paediatric head and neck cancer. Nucl Med Commun. 2012;33:21–8.
50. Begent J, Sebire NJ, Levitt G, et al. Pilot study of F(18)-Fluorodeoxyglucose positron emission tomography/computerised tomography in Wilms' tumour: correlation with conventional imaging, pathology and immunohistochemistry. Eur J Cancer. 2011;47:389–96.
51. Baum SH, Fruhwald M, Rahbar K, Wessling J, Schober O, Weckesser M. Contribution of PET/CT to prediction of outcome in children and young adults with rhabdomyosarcoma. J Nucl Med. 2011;52:1535–40.
52. Ricard F, Cimarelli S, Deshayes E, Mognetti T, Thiesse P, Giammarile F. Additional Benefit of F-18 FDG PET/CT in the staging and follow-up of pediatric rhabdomyosarcoma. Clin Nucl Med. 2011;36:672–7.
53. Piccardo A, Lopci E, Conte M, et al. Comparison of 18F-dopa PET/CT and 123I-MIBG scintigraphy in stage 3 and 4 neuroblastoma: a pilot study. Eur J Nucl Med Mol Imaging. 2012;39:57–71.
54. London K, Stege C, Cross S, et al. 18F-FDG PET/CT compared to conventional imaging modalities in pediatric primary bone tumors. Pediatr Radiol. 2012;42:418–30.
55. Tateishi U, Hosono A, Makimoto A, et al. Comparative study of FDG PET/CT and conventional imaging in the staging of rhabdomyosarcoma. Ann Nucl Med. 2009;23:155–61.
56. Costantini DL, Vali R, Chan J, McQuattie S, Charron M. Dual-time-point FDG PET/CT for the evaluation of pediatric tumors. AJR Am J Roentgenol. 2013;200:408–13.
57. Eary JF, Conrad EU. Imaging in sarcoma. J Nucl Med. 2011;52:1903–13.
58. Kruer MC, Kaplan AM, Etzl MM Jr, et al. The value of positron emission tomography and proliferation index in predicting progression in low-grade astrocytomas of childhood. J Neurooncol. 2009;95:239–45.
59. Azizi AA, Slavc I, Theisen BE, et al. Monitoring of plexiform neurofibroma in children and adolescents with neurofibromatosis type 1 by [18 F]FDG-PET imaging. Is it of value in asymptomatic patients? Pediatr Blood Cancer. 2018;65(1)
60. Li Y, Schiepers C, Lake R, Dadparvar S, Berenji GR. Clinical utility of (18)F-fluoride PET/CT in benign and malignant bone diseases. Bone. 2012;50:128–39.
61. Lin FI, Rao JE, Mittra ES, et al. Prospective comparison of combined (1)(8)F-FDG and (1)(8) F-NaF PET/CT vs. (1)(8)F-FDG PET/CT imaging for detection of malignancy. Eur J Nucl Med Mol Imaging. 2012;39:262–70.

62. Vaidyanathan G, Affleck DJ, Zalutsky MR. Validation of 4-[fluorine-18]fluoro-3-iodobenzylguanidine as a positron-emitting analog of MIBG. J Nucl Med. 1995;36:644–50.
63. Lopci E, Piccardo A, Nanni C, et al. 18F-DOPA PET/CT in neuroblastoma: comparison of conventional imaging with CT/MR. Clin Nucl Med. 2012;37:e73–8.
64. Lee CL, Wahnishe H, Sayre GA, et al. Radiation dose estimation using preclinical imaging with 124I-metaiodobenzylguanidine (MIBG) PET. Med Phys. 2010;37:4861–7.
65. Maraninchi D, Vey N, Viens P, et al. A phase II study of interleukin-2 in 49 patients with relapsed or refractory acute leukemia. Leuk Lymphoma. 1998;31:343–9.
66. Matthay KK, Weiss B, Villablanca JG, et al. Dose escalation study of no-carrier 131-MIBG for relapsed or refractory neuroblastoma: new approaches to neuroblastoma therapy (NANT) trial. J Nucl Med. 2012;53:1155.
67. Suh M, Park HJ, Choi HS, So Y, Lee BC, Lee WW. Case report of PET/CT imaging of a patient with neuroblastoma using 18F-FPBG. Pediatrics. 2014;134:e1731–4.
68. Pandit-Taskar N, Zanzonico P, Staton KD, Carrasquillo JA, Reidy-Lagunes D, Lyashchenko S, Burnazi E, Zhang H, Lewis JS, Blasberg R, Larson SM, Weber WA, Modak S. Biodistribution and dosimetry of 18F-meta-fluorobenzylguanidine: a first-in-human PET/CT imaging study of patients with neuroendocrine malignancies. J Nucl Med. 2018;59(1):147–53. https://doi.org/10.2967/jnumed.117.193169.
69. El-Rabadi K, Weber M, Mayerhofer M, et al. Clinical value of 18F-fluorodihydroxyphenylalanine positron emission tomography/contrast-enhanced computed tomography (18F-DOPA PET/CT) in patients with suspected paraganglioma. Anticancer Res. 2016;36:4187–93.
70. Kong G, Hofman MS, Murray WK, et al. Initial experience with gallium-68 DOTA-octreotate PET/CT and peptide receptor radionuclide therapy for pediatric patients with refractory metastatic neuroblastoma. J Pediatr Hematol Oncol. 2016;38:87–96.
71. Degnan AJ, Tadros SS, Tocchio S. Pediatric neuroendocrine carcinoid tumors: review of diagnostic imaging findings and recent advances. AJR Am J Roentgenol. 2017;208:868–77.
72. Liu CJ, Lu MY, Liu YL, et al. Risk stratification of pediatric patients with neuroblastoma using volumetric parameters of 18F-FDG and 18F-DOPA PET/CT. Clin Nucl Med. 2017;42:e142–e8.
73. Paulino AC, Margolin J, Dreyer Z, Teh BS, Chiang S. Impact of PET-CT on involved field radiotherapy design for pediatric Hodgkin lymphoma. Pediatr Blood Cancer. 2012;58:860–4.
74. Freudenberg LS, Jentzen W, Marlowe RJ, Koska WW, Luster M, Bockisch A. 124-iodine positron emission tomography/computed tomography dosimetry in pediatric patients with differentiated thyroid cancer. Exp Clin Endocrinol Diabetes. 2007;115:690–3.
75. Younes A, Hilden P, Coiffier B, et al. International Working Group consensus response evaluation criteria in lymphoma (RECIL 2017). Ann Oncol. 2017;28:1436.
76. Ozuah NW, LaCasce AS. How to approach a patient with limited stage hodgkin lymphoma who remains PET positive at the end of chemotherapy: radiation therapy? Clin Lymphoma Myeloma Leuk. 2017;17:710.
77. Bakhshi S, Bhethanabhotla S, Kumar R, et al. Posttreatment PET/CT rather than interim PET/CT using deauville criteria predicts outcome in pediatric hodgkin lymphoma: a prospective study comparing PET/CT with conventional imaging. J Nucl Med. 2017;58:577–83.
78. Ozuah NW, Dahmoush HM, Grant FD, et al. Pretransplant functional imaging and outcome in pediatric patients with relapsed/refractory Hodgkin lymphoma undergoing autologous transplantation. Pediatr Blood Cancer. 2017;65(1)
79. Bailly C, Eugene T, Couec ML, et al. Prognostic value and clinical impact of (18)FDG-PET in the management of children with burkitt lymphoma after induction chemotherapy. Front Med. 2014;1:54.
80. Davis JC, Daw NC, Navid F, et al. FDG uptake during early adjuvant chemotherapy predicts histologic response in pediatric and young adult patients with osteosarcoma. J Nucl Med. 2018;59:25.
81. Qin Z, Tang Y, Wang H, et al. Use of 18F-FDG-PET-CT for assessment of response to neoadjuvant chemotherapy in children with wilms tumor. J Pediatr Hematol Oncol. 2015;37:396–401.
82. Soloviev D, Lewis D, Honess D, Aboagye E. [(18)F] FLT: an imaging biomarker of tumour proliferation for assessment of tumour response to treatment. Eur J Cancer. 2012;48:416–24.
83. Gilles R, Vogel WV, Gidding CE, Janssens GO, van der Vliet TM, Oyen WJ. (18)F-fluoro-L-thymidine-PET for the evaluation of primary brain tumours in children: a report of three cases. Nucl Med Commun. 2010;31:482–7.
84. Pfannenberg C, Aschoff P, Dittmann H, et al. PET/CT with 18F-FLT: does it improve the therapeutic management of metastatic germ cell tumors? J Nucl Med. 2010;51:845–53.
85. Hendrikse NH, Vaalburg W. Dynamics of multidrug resistance: P-glycoprotein analyses with positron emission tomography. Methods. 2002;27:228–33.
86. Levchenko A, Mehta BM, Lee JB, et al. Evaluation of 11C-colchicine for PET imaging of multiple drug resistance. J Nucl Med. 2000;41:493–501.
87. Chan HS, Haddad G, Thorner PS, et al. P-glycoprotein expression as a predictor of the outcome of therapy for neuroblastoma. N Engl J Med. 1991;325:1608–14.
88. Chan HS, Thorner PS, Haddad G, Ling V. Immunohistochemical detection of P-glycoprotein:

prognostic correlation in soft tissue sarcoma of childhood. J Clin Oncol. 1990;8:689–704.
89. Baldini N, Scotlandi K, Barbanti-Brodano G, et al. Expression of P-glycoprotein in high-grade osteosarcomas in relation to clinical outcome. N Engl J Med. 1995;333:1380–5.
90. Kucerova H, Sumerauer D, Drahokoupilova E, Piskova M, Bednricek J, Eckschlager T. Significance of P-glycoprotein expression in childhood malignant tumors. Neoplasma. 2001;48:472–8.
91. Eckert F, Schmitt J, Zips D, et al. Enhanced binding of necrosis-targeting immunocytokine NHS-IL12 after local tumour irradiation in murine xenograft models. Cancer Immunol Immunother. 2016;65:1003–13.
92. Jansen MH, Lagerweij T, Sewing AC, et al. Bevacizumab targeting diffuse intrinsic pontine glioma: results of 89Zr-bevacizumab PET imaging in brain tumor models. Mol Cancer Ther. 2016;15:2166–74.
93. Haylock AK, Spiegelberg D, Mortensen AC, et al. Evaluation of a novel type of imaging probe based on a recombinant bivalent mini-antibody construct for detection of CD44v6-expressing squamous cell carcinoma. Int J Oncol. 2016;48:461–70.
94. Spiegelberg D, Mortensen AC, Selvaraju RK, Eriksson O, Stenerlow B, Nestor M. Molecular imaging of EGFR and CD44v6 for prediction and response monitoring of HSP90 inhibition in an in vivo squamous cell carcinoma model. Eur J Nucl Med Mol Imaging. 2016;43:974–82.
95. Pool M, Terwisscha van Scheltinga AGT, Kol A, Giesen D, de Vries EGE, Lub-de Hooge MN. 89Zr-Onartuzumab PET imaging of c-MET receptor dynamics. Eur J Nucl Med Mol Imaging. 2017;44:1328–36.
96. Rocha V, Wagner JE Jr, Sobocinski KA, et al. Graft-versus-host disease in children who have received a cord-blood or bone marrow transplant from an HLA-identical sibling. Eurocord and International Bone Marrow Transplant Registry Working Committee on Alternative Donor and Stem Cell Sources. N Engl J Med. 2000;342:1846–54.
97. Ronald JA, Kim BS, Gowrishankar G, et al. A PET imaging strategy to visualize activated T cells in acute graft-versus-host disease elicited by allogenic hematopoietic cell transplant. Cancer Res. 2017;77:2893–902.
98. Kaste SC. Imaging pediatric bone sarcomas. Radiol Clin North Am. 2011;49:749–65. vi–vii.
99. Brisse HJ, McCarville MB, Granata C, et al. Guidelines for imaging and staging of neuroblastic tumors: consensus report from the International Neuroblastoma Risk Group Project. Radiology. 2011;261:243–57.
100. Chavhan GB, Babyn PS. Whole-body MR imaging in children: principles, technique, current applications, and future directions. Radiographics. 2011;31:1757–72.
101. Kwee TC, Fijnheer R, Ludwig I, et al. Whole-body magnetic resonance imaging, including diffusion-weighted imaging, for diagnosing bone marrow involvement in malignant lymphoma. Br J Haematol. 2010;149:628–30.
102. Kwee TC, Takahara T, Vermoolen MA, Bierings MB, Mali WP, Nievelstein RA. Whole-body diffusion-weighted imaging for staging malignant lymphoma in children. Pediatr Radiol. 2010;40:1592–602. quiz 720–1.
103. Hyder F, Rothman DL. Quantitative fMRI and oxidative neuroenergetics. Neuroimage. 2012;62:985.
104. Jacobs J, Rohr A, Moeller F, et al. Evaluation of epileptogenic networks in children with tuberous sclerosis complex using EEG-fMRI. Epilepsia. 2008;49:816–25.
105. Bendini M, Marton E, Feletti A, et al. Primary and metastatic intraaxial brain tumors: prospective comparison of multivoxel 2D chemical-shift imaging (CSI) proton MR spectroscopy, perfusion MRI, and histopathological findings in a group of 159 patients. Acta Neurochir. 2011;153:403–12.
106. Paldino MJ, Faerber EN, Poussaint TY. Imaging tumors of the pediatric central nervous system. Radiol Clin North Am. 2011;49:589–616.
107. Kim H, Catana C, Ratai EM, et al. Serial magnetic resonance spectroscopy reveals a direct metabolic effect of cediranib in glioblastoma. Cancer Res. 2011;71:3745–52.
108. Punwani S, Taylor SA, Bainbridge A, et al. Pediatric and adolescent lymphoma: comparison of whole-body STIR half-Fourier RARE MR imaging with an enhanced PET/CT reference for initial staging. Radiology. 2010;255:182–90.
109. Krohmer S, Sorge I, Krausse A, et al. Whole-body MRI for primary evaluation of malignant disease in children. Eur J Radiol. 2010;74:256–61.
110. Kwee TC, van Ufford HM, Beek FJ, et al. Whole-body MRI, including diffusion-weighted imaging, for the initial staging of malignant lymphoma: comparison to computed tomography. Invest Radiol. 2009;44:683–90.
111. Kwee TC, Takahara T, Ochiai R, et al. Whole-body diffusion-weighted magnetic resonance imaging. Eur J Radiol. 2009;70:409–17.
112. Padhani AR, Koh DM, Collins DJ. Whole-body diffusion-weighted MR imaging in cancer: current status and research directions. Radiology. 2011;261:700–18.
113. Cuccarini V, Erbetta A, Farinotti M, et al. Advanced MRI may complement histological diagnosis of lower grade gliomas and help in predicting survival. J Neurooncol. 2016;126:279.
114. Padhani AR, Liu G, Koh DM, et al. Diffusion-weighted magnetic resonance imaging as a cancer biomarker: consensus and recommendations. Neoplasia. 2009;11:102–25.
115. Afaq A, Andreou A, Koh DM. Diffusion-weighted magnetic resonance imaging for tumour response assessment: why, when and how? Cancer Imaging. 2010;10(Spec No A):S179–S188.

116. Franzius C, Bielack S, Flege S, Sciuk J, Jurgens H, Schober O. Prognostic significance of (18) F-FDG and (99m)Tc-methylene diphosphonate uptake in primary osteosarcoma. J Nucl Med. 2002;43:1012–7.
117. Brenner W, Conrad EU, Eary JF. FDG PET imaging for grading and prediction of outcome in chondrosarcoma patients. Eur J Nucl Med Mol Imaging. 2004;31:189–95.
118. Drzezga A, Souvatzoglou M, Eiber M, et al. First clinical experience with integrated whole-body PET/MR: comparison to PET/CT in patients with oncologic diagnoses. J Nucl Med. 2012;53:845.
119. Samarin A, Burger C, Wollenweber SD, et al. PET/MR imaging of bone lesions - implications for PET quantification from imperfect attenuation correction. Eur J Nucl Med Mol Imaging. 2012;39:1154.
120. Schwenzer NF, Stegger L, Bisdas S, et al. Simultaneous PET/MR imaging in a human brain PET/MR system in 50 patients-current state of image quality. Eur J Radiol. 2012;81:3472.
121. Hirsch FW, Sattler B, Sorge I, et al. PET/MR in children. Initial clinical experience in paediatric oncology using an integrated PET/MR scanner. Pediatr Radiol. 2013;43:860–75.
122. Schafer JF, Gatidis S, Schmidt H, et al. Simultaneous whole-body PET/MR imaging in comparison to PET/CT in pediatric oncology: initial results. Radiology. 2014;273:220–31.
123. Ponisio MR, McConathy J, Laforest R, Khanna G. Evaluation of diagnostic performance of whole-body simultaneous PET/MRI in pediatric lymphoma. Pediatr Radiol. 2016;46:1258–68.
124. Bezrukov I, Schmidt H, Gatidis S, et al. Quantitative evaluation of segmentation- and atlas-based attenuation correction for PET/MR on pediatric patients. J Nucl Med. 2015;56:1067–74.
125. Purz S, Sabri O, Viehweger A, et al. Potential pediatric applications of PET/MR. J Nucl Med. 2014;55:32S–9S.
126. Gatidis S, Schmidt H, la Fougere C, Nikolaou K, Schwenzer NF, Schafer JF. Defining optimal tracer activities in pediatric oncologic whole-body 18F-FDG-PET/MRI. Eur J Nucl Med Mol Imaging. 2016;43:2283–9.
127. Klenk C, Gawande R, Tran VT, et al. Progressing toward a cohesive pediatric 18F-FDG PET/MR protocol: is administration of gadolinium chelates necessary? J Nucl Med. 2016;57:70–7.
128. Daldrup-Link H. How PET/MR can add value for children with cancer. Curr Radiol Rep. 2017;5(3)
129. Khurana A, Chapelin F, Beck G, et al. Iron administration before stem cell harvest enables MR imaging tracking after transplantation. Radiology. 2013;269:186–97.
130. Klenk C, Gawande R, Uslu L, et al. Ionising radiation-free whole-body MRI versus (18) F-fluorodeoxyglucose PET/CT scans for children and young adults with cancer: a prospective, non-randomised, single-centre study. Lancet Oncol. 2014;15:275–85.
131. Lu M, Cohen MH, Rieves D, Pazdur R. FDA report: ferumoxytol for intravenous iron therapy in adult patients with chronic kidney disease. Am J Hematol. 2010;85:315–9.
132. Neuwelt EA, Varallyay CG, Manninger S, et al. The potential of ferumoxytol nanoparticle magnetic resonance imaging, perfusion, and angiography in central nervous system malignancy: a pilot study. Neurosurgery. 2007;60:601–11. discussion 11–2.
133. Simon GH, von Vopelius-Feldt J, Fu Y, et al. Ultrasmall supraparamagnetic iron oxide-enhanced magnetic resonance imaging of antigen-induced arthritis: a comparative study between SHU 555 C, ferumoxtran-10, and ferumoxytol. Invest Radiol. 2006;41:45–51.
134. Stabi KL, Bendz LM. Ferumoxytol use as an intravenous contrast agent for magnetic resonance angiography. Ann Pharmacother. 2011;45:1571–5.
135. Daldrup-Link HE, Golovko D, Ruffel B, et al. MR Imaging of tumor associated macrophages with clinically-applicable iron oxide nanoparticles. Clin Cancer Res. 2011;17:5695.
136. Muehe AM, Feng D, von Eyben R, et al. Safety report of ferumoxytol for magnetic resonance imaging in children and young adults. Invest Radiol. 2016;51:221–7.
137. Clement O, Siauve N, Cuenod CA, Frija G. Liver imaging with ferumoxides (Feridex): fundamentals, controversies, and practical aspects. Top Magn Reson Imaging. 1998;9:167–82.
138. Corot C, Robert P, Idee JM, Port M. Recent advances in iron oxide nanocrystal technology for medical imaging. Adv Drug Deliv Rev. 2006;58:1471–504.
139. Muehe AM, Theruvath AJ, Lai L, et al. How to provide gadolinium-free PET/MR cancer staging of children and young adults in less than 1 h: the Stanford approach. Mol Imaging Biol. 2018;20:324.
140. Ansari C, Tikhomirov GA, Hong SH, et al. Cancer therapy: development of novel tumor-targeted theranostic nanoparticles activated by membrane-type matrix metalloproteinases for combined cancer magnetic resonance imaging and therapy (small 3/2014). Small. 2014;10:417.
141. Mohanty S, Chen Z, Li K, et al. A novel theranostic strategy for MMP-14 expressing glioblastomas impacts survival. Mol Cancer Ther. 2017;16:1909.
142. Cole AJ, Yang VC, David AE. Cancer theranostics: the rise of targeted magnetic nanoparticles. Trends Biotechnol. 2011;29:323–32.
143. Pan D, Caruthers SD, Chen J, et al. Nanomedicine strategies for molecular targets with MRI and optical imaging. Future Med Chem. 2010;2:471–90.
144. Yu Y, Sun D. Superparamagnetic iron oxide nanoparticle 'theranostics' for multimodality tumor imaging, gene delivery, targeted drug and prodrug delivery. Exp Rev Clin Pharmacol. 2010;3:117–30.
145. Swan M. Emerging patient-driven health care models: an examination of health social networks,

consumer personalized medicine and quantified self-tracking. Int J Environ Res Public Health. 2009;6:492–525.
146. Chenu O, Vuillerme N, Bucki M, Diot B, Cannard F, Payan Y. TexiCare: an innovative embedded device for pressure ulcer prevention. Preliminary results with a paraplegic volunteer. J Tissue Viability. 2013;22:83–90.
147. Torrado-Carvajal A, Rodriguez-Sanchez MC, Rodriguez-Moreno A, et al. Changing communications within hospital and home health care. Conf Proc IEEE Eng Med Biol Soc. 2012;2012:6074–7.
148. Ali SM, Aijazi T, Axelsson K, Nur O, Willander M. Wireless remote monitoring of glucose using a functionalized ZnO nanowire arrays based sensor. Sensors (Basel). 2011;11:8485–96.
149. Juhasz C, Dwivedi S, Kamson DO, Michelhaugh SK, Mittal S. Comparison of amino acid positron emission tomographic radiotracers for molecular imaging of primary and metastatic brain tumors. Mol Imaging. 2014;13:7290201400015.
150. Fraioli F, Shankar A, Hargrave D, et al. 18F-fluoroethylcholine (18F-Cho) PET/MRI functional parameters in pediatric astrocytic brain tumors. Clin Nucl Med. 2015;40:e40–5.
151. Tsouana E, Stoneham S, Fersht N, et al. Evaluation of treatment response using integrated 18F-labeled choline positron emission tomography/magnetic resonance imaging in adolescents with intracranial non-germinomatous germ cell tumours. Pediatr Blood Cancer. 2015;62:1661–3.
152. Morana G, Piccardo A, Milanaccio C, et al. Value of 18F-3,4-dihydroxyphenylalanine PET/MR image fusion in pediatric supratentorial infiltrative astrocytomas: a prospective pilot study. J Nucl Med. 2014;55:718–23.
153. Morana G, Piccardo A, Puntoni M, et al. Diagnostic and prognostic value of 18F-DOPA PET and 1H-MR spectroscopy in pediatric supratentorial infiltrative gliomas: a comparative study. Neuro Oncol. 2015;17:1637–47.
154. Bosnyak E, Michelhaugh SK, Klinger NV, et al. Prognostic molecular and imaging biomarkers in primary glioblastoma. Clin Nucl Med. 2017;42:341–7.
155. Korchi AM, Garibotto V, Ansari M, Merlini L. Pseudoprogression after proton beam irradiation for a choroid plexus carcinoma in pediatric patient: MRI and PET imaging patterns. Childs Nerv Syst. 2013;29:509–12.
156. Gallagher FA, Bohndiek SE, Kettunen MI, Lewis DY, Soloviev D, Brindle KM. Hyperpolarized 13C MRI and PET: in vivo tumor biochemistry. J Nucl Med. 2011;52:1333–6.
157. Hu S, Balakrishnan A, Bok RA, et al. 13C-pyruvate imaging reveals alterations in glycolysis that precede c-Myc-induced tumor formation and regression. Cell Metab. 2011;14:131–42.
158. Cheson BD, Pfistner B, Juweid ME, et al. Revised response criteria for malignant lymphoma. J Clin Oncol. 2007;25:579–86.
159. Sandoval JA, Malkas LH, Hickey RJ. Clinical significance of serum biomarkers in pediatric solid mediastinal and abdominal tumors. Int J Mol Sci. 2012;13:1126–53.

Imaging of Children with Cancer Predisposition Syndromes

20

Sudha A. Anupindi, Ethan A. Smith, and Nancy A. Chauvin

20.1 Introduction

Most pediatric solid tumors are sporadic; however, there is a subset of pediatric cancers that occur in association with known clinical syndromes. Patients with a genetic predisposition are thought to account for between 5% and 10% of all pediatric cancers [1]. In these patients, screening with clinical tests (physical examination, laboratory evaluations) or imaging examinations may be performed. The primary goal of screening is to detect disease at an earlier stage which should allow for more limited therapy, less treatment-associated morbidity, and ultimately improved outcomes and survival [2]. The purpose of this chapter is to discuss special considerations in screening pediatric patients with cancer predisposition syndromes (CPS), as well as to discuss imaging techniques used in screening. The chapter will also review select cancer predisposition syndromes of particular interest in pediatric oncology and radiology, focusing on the most frequent cancer predisposition syndromes encountered, including Wilms tumor predisposition syndromes, Li-Fraumeni syndrome, and neurofibromatosis type 1, as well as more rare syndromes that have specific features, including DICER1 mutations, familial paraganglioma syndromes, and multiple endocrine neoplasia syndromes.

20.2 Background

Successful models for cancer screening have been established in adult populations. The most widely known of these cancer screening programs that rely on imaging is the use of screening mammography to detect breast cancer in women. Breast cancer is the most common cancer among American women and the second leading cause of cancer-related death. Through successful screening programs, age-adjusted breast cancer mortality rates decreased by 36% over the period between 1989 and 2012 [3]. Other successful screening programs include those for cervical cancer and colorectal cancer, while development of a lung cancer screening program for at-risk individuals is underway. As shown by these examples, cancer screening in an at-risk population can reduce mortality rates and improve outcomes.

However, cancer screening programs also have potential drawbacks and risks that must be

S. A. Anupindi (✉)
Department of Radiology, Children's Hospital of Philadelphia, Philadelphia, PA, USA
e-mail: Anupindi@email.chop.edu

E. A. Smith
Department of Radiology, Cincinnati Children's Hospital Medical Center, Cincinnati, OH, USA
e-mail: ethan.smith@cchmc.org

N. A. Chauvin
Department of Radiology, Hershey Children's Hospital, Hershey, PA, USA
e-mail: nchauvin@pennstatehealth.psu.edu

S. D. Voss, K. McHugh (eds.), *Imaging in Pediatric Oncology*, Pediatric Oncology,
https://doi.org/10.1007/978-3-030-03777-2_20

acknowledged. Although a disease such as breast cancer may be sufficiently common in a population of women, most women undergoing screening mammography will never develop a breast cancer. The inconvenience, anxiety provoked by testing, and the financial cost to society in these patients must be considered. In addition, screening tests will have a certain number of false-positive results—instances where the screening test is positive, but on further work-up, no cancer is found. In these instances, the emotional and financial costs to the patient, as well as the increased risk of procedural complications and/or side effects, can be significant. Similar considerations must be made in pediatric patients with cancer predisposition syndromes. The advantages of screening must outweigh the costs both to the patient and their family and to the healthcare system as a whole.

20.2.1 Screening Test Characteristics

A screening test, by definition, is performed on asymptomatic individuals in a population at risk for a certain disease [2]. The objective of a screening test is to detect disease at an earlier stage, allowing for less disease and treatment-related morbidity and mortality. If a screening test is positive, the patient often must undergo additional testing to confirm the test as a true positive (e.g., exclude a false-positive result) and to further characterize and diagnose the disease process.

Cancer screening takes on many forms, including physical examination, laboratory tests, and imaging studies. Some screening tests, especially laboratory testing, can be defined as either positive or negative (e.g., an elevated prostate-specific antigen, PSA). Others, including most tests that involve imaging, require interpretation by a trained individual. In this setting, intra- and interobserver variability and bias may become important factors that must be considered [2].

The primary goal of a screening test is earlier disease detection. The sensitivity of the test (e.g., finding all cases of disease) is usually emphasized over the specificity. An example of the emphasis on sensitivity can be seen with screening mammography. It is accepted that there will be multiple false-positive screening mammograms (as defined by the need for further testing, including ultrasound and biopsy) to find one true positive test (i.e., biopsy-confirmed breast cancer). It is important to keep in mind that the sensitivity and specificity of any test also depend on the prevalence of the disease in the screening population [2]. This is an important consideration in pediatric cancer predisposition syndromes, where despite the relative predisposition of these patients to developing cancer, the actual incidence of malignancy may still be quite low across the screened population.

An additional consideration in the implementation of a screening test are the manifestations of the disease itself and the feasibility and safety of performing the screening test. The risks and cost of the screening test must be weighed against the potential benefit to the patients being screened. For example, a test that carried a significant risk of harm and was not able to diagnose a cancer at a clinically significant earlier stage would not be an effective screening test. Likewise, a test that is prohibitively expensive, or that is only available to a small portion of the population, would not be an effective screening test. An ideal screening test would be noninvasive, have a very low risk of harm to the patient, and be relatively inexpensive and widely available to the screening population.

20.2.2 Special Considerations in Pediatrics

20.2.2.1 Radiation

While the true risk posed by ionizing radiation remains unknown, as long as there is some potential for harm due to ionizing radiation, the ALARA principle (As Low As Reasonably Achievable) should be followed, especially in children. As such, the risks and potential benefits of any imaging test used for cancer screening must be weighed against any risks posed by ionizing radiation. The potential risks of ionizing radiation may be especially relevant in certain patients with cancer

predisposition syndromes, such as Li-Fraumeni syndrome [4]. With this in mind, most recommendations for imaging screening in pediatric cancer predisposition syndromes focus on the use of nonionizing modalities, including ultrasound and magnetic resonance imaging (MRI), even at the cost of some loss of sensitivity and specificity. For example, contrast-enhanced computed tomography (CT) can be more sensitive and specific than ultrasound for small renal masses; however, in patients with Wilms tumor predisposition syndromes, routine screening is performed with ultrasound in order to avoid repeated exposure to ionizing radiation [5].

20.2.2.2 Sedation and Anesthesia

Although the risks are not clearly defined, there is developing evidence that exposure to anesthesia in young children may have some deleterious effects on cognitive development and behavior [6]. Very young children often require anesthesia to undergo MRI and sometimes CT, due to their inability to tolerate the length of the studies (as in MRI), to overcome fear/anxiety, and to avoid excessive motion artifacts. In a screening population (patients at risk for a disease, but who do not have the disease), avoidance of repeated exposure to anesthetics is appropriate to minimize any potential risk of cognitive or behavioral effects. Like potential risks of ionizing radiation, the need to avoid repeated anesthesia exposure may guide the choice of imaging screening performed in patients with cancer predisposition syndromes, especially in younger patients. In these populations, although MRI may be more sensitive and specific than ultrasound, screening ultrasound may be preferred as the initial imaging modality of choice in order to avoid the risk of repeated anesthesia exposure.

20.2.2.3 Parental Fear/Anxiety

The knowledge that a child has an increased risk of cancer can cause a significant amount of fear and anxiety in parents and caregivers of the child. Anxiety can be caused by the fear of missing an important diagnosis but also by the uncertainty caused by false-positive tests and repeated exposure to medical imaging and other interventions. When considering screening tests in these patients, there must be some standardization in terms of how often patients are imaged to reassure parents and caregivers that the time interval between imaging is appropriate to avoid missing an important diagnosis. Likewise, there must be some guidance and standardization as to appropriate follow-up if a suspected cancer is found, as well as expectations for management of potential false-positive and incidental findings.

20.2.3 Practical Considerations of Ultrasound for Screening in CPS

20.2.3.1 Ultrasound

Ultrasound (US) using gray scale and color Doppler is the first line of imaging in a child with a potential mass/tumor [7, 8]. US is widely available, has lower cost than CT and MRI, and obviates the need for sedation/general anesthesia or ionizing radiation [7]. Standard US is practical and can provide details about the solid or cystic components of the mass, location, internal vascularity, and effect on adjacent vascular structures [8]. Contrast-enhanced US is emerging as a safe, reliable adjunctive imaging tool to further characterize tumors in children but is not yet in widespread use in the United States [9, 10]. Ultrasound is not a stand-alone imaging tool for CPS but needs to be used in conjunction with genetic testing, physical examination, and biochemical testing.

20.2.3.2 Pitfalls of Ultrasound, Interpretation, and Communication

Although there are many advantages to using US for the evaluation of pediatric tumors, there are limitations. Ultrasound can be limited in children with large body habitus. In addition, in very large tumors, the organ of origin can be difficult to identify, and US can underestimate the full depth and burden of disease.

Ultrasound is very operator dependent, and interpretation of the imaging is best performed in real time to provide accurate results. In many

pediatric practices, ultrasound examinations are performed by technologists, with representative images reviewed by pediatric radiologists who have the responsibility of rescanning areas of question. Each case is scrutinized, and the radiologist has a checklist of which images must be acquired for a given examination protocol. Again, this may not be the case in all practices and is institution specific. However, this systematic approach is important when undertaking cancer surveillance in high-risk groups such as those with overgrowth syndromes (i.e., Beckwith-Wiedemann) or other CPS, so as not to overlook potential sites of pathology. Structured reporting is equally important to a methodical assessment of the ultrasound images. A structured report can allow for easy comparison with prior studies and is reproducible and consistent [11]. Communication of findings should be made in a clear and concise format. This type of systematic written and verbal communication among the entire team can help minimize false-positive findings and triage appropriately the cases that need additional work-up and possibly invasive testing.

20.2.4 Practical Considerations of Whole-Body MRI for Screening CPS

20.2.4.1 Whole-Body MRI (WBMRI)

In the last decade, whole-body MRI (WBMRI) has gained more acceptance and is widely being used in North America and elsewhere as an imaging tool for screening pediatric cancer predisposition syndromes [12]. This population of children has very few other whole-body screening options at the current time. Although PET-MRI is on the horizon, it is not widely available and still exposes patients to ionizing radiation with the PET component. PET-MRI is discussed in more detail in Chapter 4 of this textbook. WBMRI can also provide wide anatomic coverage and excellent contrast resolution across a variety of tissues, allowing evaluation of the solid organs, soft tissues, and bone marrow with a single test [11, 12].

Previous publications have advocated using WBMRI in conjunction with other biochemical tests and not as a stand-alone examination [13, 14]. A detailed description regarding the WBMRI technique is beyond the scope of this discussion and is covered in Chapter 7 of this textbook. Currently, there is no consensus on the imaging protocols to be used [11, 12]. In general, the workhorse sequences for WBMRI imaging for oncology indications include coronal inversion recovery and T1-weighted (nonfat saturated) sequences.

The main disadvantages of WBMRI are those inherent to MRI itself including cost, availability, length of exam, and safety due to use of sedation/general anesthesia. A significant recognized pitfall of WBMRI is frequency of false-positive findings [12]. However, when WBMRI is interpreted by experienced pediatric radiologists, these false positives can be minimized [12]. An encouraging advantage of WBMRI for CPS is the very high negative predictive value (100%) as reported [12]. Ideally, radiologists familiar with WBMRI examinations and tumors commonly seen in the setting of CPS are best suited to interpret these examinations. However, this is site specific, and in some institutions without experienced radiologists, images from WBMRI examinations may be sent to a central review site for interpretation, as suggested by Greer et al. [11].

20.2.4.2 Interpretation and Pitfalls

Each abnormality identified on a WBMRI should be discussed with the oncologist and geneticist to determine which findings require further evaluation with additional imaging or biopsy and which can be conservatively followed [11]. Anupindi and colleagues have suggested a risk stratification methodology to scrutinize abnormalities on a WBMRI [11, 12]. In this manner, unnecessary interventions can be avoided and thereby reduce anxiety to patients and families. Lesions on WBMRI which fall into the high-risk group should be further evaluated, whereas low-risk lesions would not require additional imaging or tissue diagnosis.

20.2.4.3 Communication

WBMRI screenings may cause patients and their families a tremendous amount of anxiety and stress. Direct communication with the oncologist

regarding any findings on the WBMRI is vital. Landier et al. recently reported consensus guidelines developed by the Children's Oncology Group (COG) regarding patient and family education for newly diagnosed cancer patients [15]. This report emphasized the need for a family-centered approach with direct communication of results and plans across all multidisciplinary departments [15]. COG guidelines also emphasize the standardization of educational content to patient and families and dissemination of information over several time points, as opposed to overwhelming both families and clinical teams with too much complex information in a single sitting [15].

20.2.4.4 Reporting

Structured reporting is also important as it provides a checklist to avoid errors and highlights the important imaging features in a concise way that makes it easy for the oncology team to understand, compare, and implement treatment [16]. Using report templates is another method to "standardize content" especially for institutions where the families receive and have access to their reports routinely [15].

20.2.5 Common Cancer Predisposition Syndromes

20.2.5.1 Li-Fraumeni Syndrome

Li-Fraumeni syndrome (LFS) is a rare autosomal dominant cancer predisposing condition that leads to an increased risk of six common "core" cancers which include soft tissue sarcomas, osteosarcomas, premenopausal breast cancer, central nervous system (CNS) tumors, adrenocortical carcinomas, and leukemia (Fig. 20.1). In addition, a wide spectrum of other benign and malignant neoplasms may also occur [17]. LFS is caused by a mutation in the gene encoding the TP53 (tumor protein p53) transcription factor [18]. TP53 plays a critical role in cellular growth by regulating the expression of numerous genes involved in cell cycle arrest, apoptosis, DNA repair, and senescence in response to cellular stressors [19].

The risk for germline mutation carriers to develop one or more neoplasms is estimated to be 50% by age 30–31 years for women and age 46 years for men [20]. Unfortunately, a significant number of cancers occur at an early age (Fig. 20.2). A recent study of 214 LFS families [21] showed that 22% of cancers were diagnosed

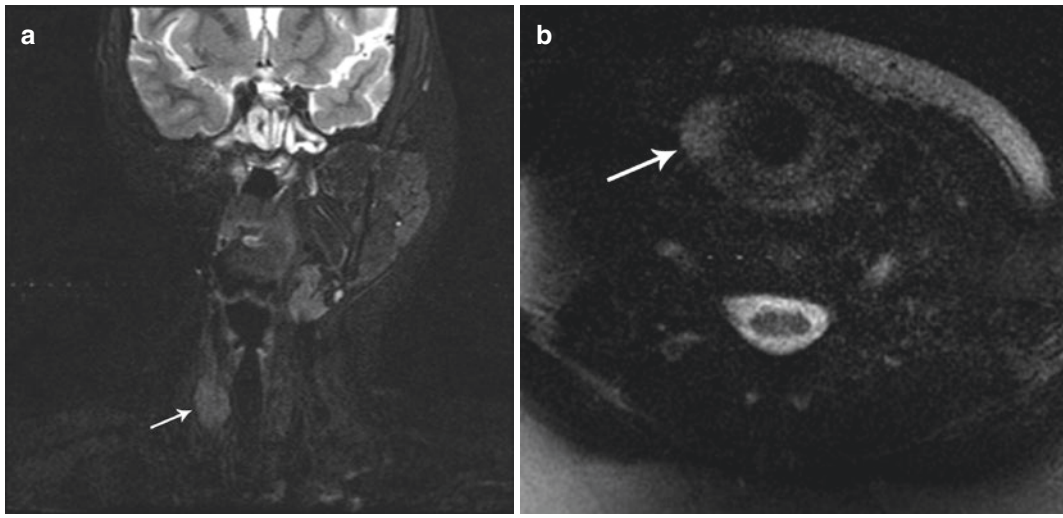

Fig. 20.1 15-year-old with Li-Fraumeni syndrome and history of prior right maxillary rhabdomyosarcoma and right mandibular osteosarcoma for which she had right-sided radiation and facial surgery with resection of the right mandible and hardware placement resulting in susceptibility artifact. Routine surveillance brain and neck imaging was performed without intravenous contrast due to renal failure. (**a**) Coronal inversion recovery image of the neck and (**b**) axial T2-weighted single-shot fast-spin echo sequence shows a mass (*arrows*) which has bright signal in the right lobe of the thyroid gland (pathology proven to be papillary thyroid carcinoma)

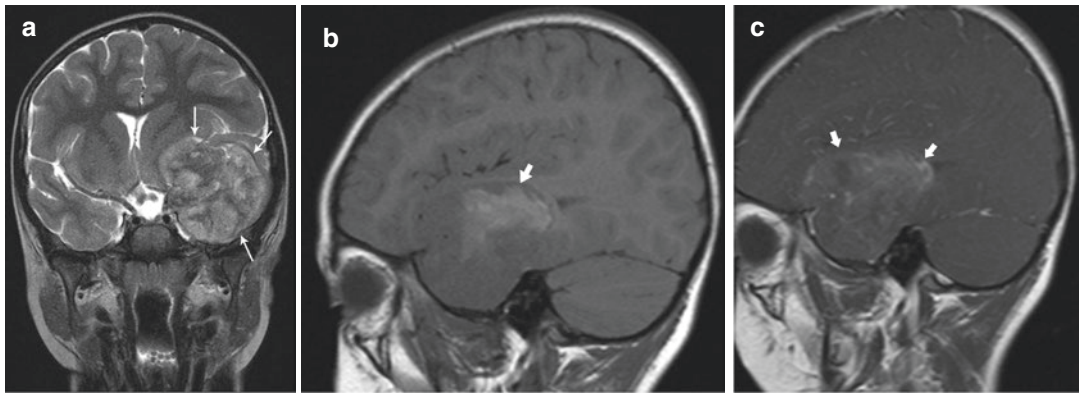

Fig. 20.2 4-year-old female with Li-Fraumeni syndrome found to have a brain tumor on routine surveillance imaging. (**a**) Coronal T2-weighted image from a brain MRI shows a large heterogeneous mass in the left temporal lobe (*white arrows*) with mass effect on the adjacent brain parenchyma and mild effacement of the left frontal horn, (**b**) sagittal T1-weighted image of the mass shows it contains T1 bright hemorrhage (*arrowhead*), (**c**) on sagittal T1-weighted post-contrast image, there is patchy enhancement of the mass (*arrowhead*). This was biopsy proven to be an atypical teratoid rhabdoid tumor

by 5 years of age and 41% before age 18 years. Notably, 4% of their study population developed cancer within the first year of life. The most common tumor in children with LFS was osteosarcoma (30%) with adrenal cortical carcinoma, brain tumors, and soft tissue tumors occurring at 27%, 25%, and 23%, respectively. In both children and adults, 40% of patients encountered a second malignancy, often in a prior radiation field [21] (Fig. 20.1). These results were supported by investigators from the National Cancer Institute (NCI), who found that almost 50% of their study population developed a second malignancy, with a median time to occurrence of 10 years [20]. Hisada et al. [22] determined that the relative risk of developing a second cancer was 83 times higher for individuals with LFS who developed a malignancy during childhood [22].

Goals of cancer surveillance in LFS patients are aimed primarily at early detection and treatment of solid tumors. With early detection of malignancy, small tumors can be resected with often reduced or no requirement for chemotherapy or radiation, which, in theory, may reduce the risk of second cancers [17]. Previous prospective work following the feasibility and outcomes of screening children and adults using a multimodality protocol has been coined the "Toronto protocol" [14, 23] and provided compelling evidence in support of a systematic approach for disease surveillance in at-risk populations of patients. Investigators detected 40 tumors in 19 of 59 patients undergoing systematic surveillance over a median follow-up period of 32 months (mostly low-grade or premalignant lesions) in contrast to 61 tumors that were detected in 43 of 49 patients who elected to not undergo surveillance. There was a much higher overall 5-year survival in the surveillance group versus the non-surveillance group (88.8% versus 59.6%). Despite false-negative results ($n = 2$), false-positive results ($n = 2$), and incidental findings detected on WBMRI in the population, WBMRI screening was recommended for all LFS patients [14, 23]. In 2016, the American Association for Cancer Research (AACR) expert panel recommended a LFS screening imaging protocol (Table 20.1) [4]. Of note, recommended physical examinations, laboratory tests, and endoscopy recommendations were not included in Table 20.1.

Screening should begin as soon as a genetic diagnosis (proven TP53 mutation carrier status) or clinical diagnosis (phenotype fitting the classic LFS definition) has been established [4] (Fig. 20.2). Currently, the AACR expert panel advocates that modifications to the surveillance

Table 20.1 Recommended LFS imaging screening protocol [adapted based on the Toronto Protocol by Villani and colleagues in their 2011 and 2016 publications]

Children (birth to age 18 years)
Adrenal cortical carcinoma—US of the abdomen and pelvis every 3–4 months
Brain tumor—annual brain MRI (first MRI with intravenous contrast; thereafter without contrast if previous MRI normal and no new abnormalities)
Soft tissue and bone sarcoma—annual WBMRI
Adults
Breast cancer—annual breast MRI screening (ages 20–75 years)
Brain tumor—annual brain MRI (first MRI with intravenous contrast; thereafter without contrast if previous MRI normal and no new abnormalities)
Soft tissue and bone sarcoma—annual WBMRI with US of the abdomen and pelvis every 12 months (at least one scan every 6 months)

recommendations based on phenotype-genotype correlations are at this point premature, and more information is needed before recommendations may be modified [4].

20.2.5.2 Beckwith-Wiedemann Syndrome

Beckwith-Wiedemann syndrome (BWS) is the most common imprinting disorder and, consequently, one of the most common cancer predisposition disorders. BWS affects at least 1 in 11,000 children. However the clinical features are variable which can make the clinical diagnosis and molecular diagnosis challenging [24]. BWS results from the variable association of overgrowth, abdominal wall defects (omphalocele, umbilical hernia, diastasis recti), macroglossia, nephrourologic malformations, hemihyperplasia, hyperinsulinemic hypoglycemia, ear anomalies, capillary malformations, and organomegaly [25]. The wide range of clinical features due to genetic and epigenetic changes on chromosome 11p15 has led to the use of the term "11p Overgrowth Spectrum" [24]. While the specific molecular anomalies at chromosome 11p15 are found in 75–80% of BWS cases, the diagnosis is clinical [26].

The cumulative risk of embryonal tumors occurring during the first decade of life is approximately 8–10%, with the highest likelihood during infancy and progressively declining during the first 10 years of age. Wilms tumor (nephroblastoma) represents the most common tumor (43%) (Fig. 20.3), while hepatoblastoma (20%), adrenal adenoma/carcinoma (7%), neuroblastoma, rhabdomyosarcoma, pancreatoblastoma, and leukemia make up the remaining associated malignancies [27]. It is known that BWS molecular subgroups are characterized by relevant differences in cancer risk with patients having a molecular abnormality involving the telomeric domain (pUPD) and H19 gain of methylation (GOM) typically having a higher risk and patients with abnormalities in the centromeric domain having a lower risk of malignancy. Maas et al. [28] determined the relative tumor risks for each subgroup in their cohort (n = 229) and proposed a tumor surveillance system based on the genetic disturbance. However, this system has not been universally adopted pending larger international investigations. At this time, current screening recommendations do not differ based on the genetic cause of BWS, although some clinicians may follow patients in the higher-risk groups more closely or react to potential screening abnormalities more urgently [24].

Tumor surveillance should be initiated as soon as BWS is diagnosed [27]. The average age of diagnosis for a unilateral Wilms tumor is 38 months, with 75% of Wilms tumors occurring before age 5 years [29]. Current imaging surveillance recommendations include ultrasounds of the abdomen and pelvis every 3 months until age 8 years [24, 30] (Fig. 20.3). The aim of frequent imaging is to provide an early diagnosis of Wilms tumor and allow for more conservative, nephron-sparing treatment. In addition to imaging, BWS patients undergo routine alpha-fetoprotein (AFP) measurements at intervals ranging from 6 weeks to 3 months until the age of 4 years to detect hepatoblastoma, while patients with *CDKN1C* mutations are screened for neuroblastoma with urine HVA/VMA levels [24]. It should be noted that other syndromes in addition to BWS predispose to Wilms tumor and other embryonal tumors [31]. Non-syndromic hemihypertrophy syndrome (asymmetric overgrowth of one or more body parts) is also associated with Wilms tumor [31].

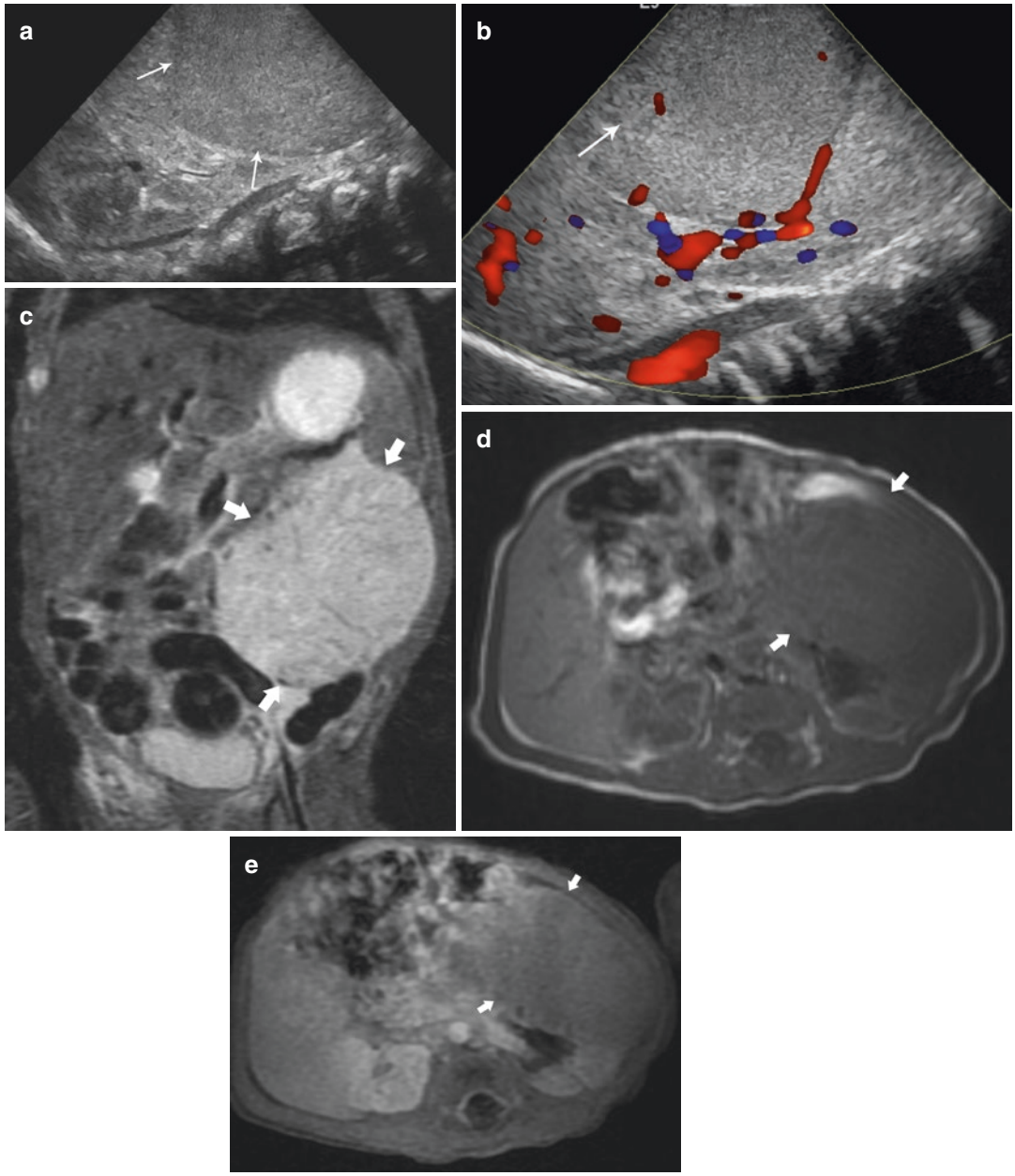

Fig. 20.3 3-day-old female with large renal mass. Initial ultrasound shows the mass incompletely and difficult to discern the organ of origin and further evaluation with MRI aided in characterizing the mass. (**a**, **b**) Sagittal gray scale (**a**) and color Doppler (**b**) images from the initial ultrasound show a solid vascular homogeneous mass (*arrows*) which appears to be arising from the left kidney; (**c**, **d**) coronal T2-weighted and (**d**) axial T1-weighted images from an abdominal MRI show the large retroperitoneal solitary mass is T2 bright (**c**) and T1 dark (**d**) and is arising from the left kidney (*arrows*); (**e**) axial T1-weighted post-contrast image shows minimal enhancement of the mass (*arrows*). The mass was surgically removed and proven to be Wilms tumor, and subsequent genetic testing confirmed the infant has Beckwith-Wiedemann syndrome

20.2.5.3 Von Hippel-Lindau

Von-Hippel Lindau (vHL) disease is a multisystem tumor predisposition syndrome which is associated with both benign and malignant tumors, including central nervous system and retinal hemangioblastomas, clear cell renal carcinoma, pheochromocytoma, pancreatic neuroendocrine tumors (pancreatic NET), endolymphatic sac tumor, and epididymal and broad ligament cystadenoma, as well as renal and pancreatic cysts [32]. The incidence of vHL is estimated at 1 in 36,000 with a lifetime penetrance of 100% by age 75 years [33].

Many of the vHL-associated lesions present within the third and fourth decades of life; however the age range of initial manifestations is wide. While most of the vHL-related tumors are benign, sequelae related to mass effect on adjacent structures (i.e., visual loss from retinal hemangioma) and operative/postoperative complications can be associated with high morbidity [34]. Children with hemangioblastomas and pheochromocytomas can remain clinically occult until tumors become sufficiently large and symptoms become severe, increasing the risks related to surgical resection. Surveillance programs leading to early recognition have been associated with reduced morbidity [35, 36]. Lifelong surveillance is recommended, and an expert consensus has recently compiled recommendations for children. In addition to routine physical examinations, blood pressure screening, ophthalmology and audiology evaluations, annual plasma, or urine metanephrine levels, imaging plays an important role. By 8 years of age, biennial MRI of the brain and spine should be undertaken to monitor for CNS hemangioblastomas (Fig. 20.4). Although the incidence of CNS hemangioblastomas is relatively low in this age group, these tumors can cause substantial morbidity with progression (Fig. 20.4) [34]. Rednam et al. [34] also suggest consideration for annual screening with MRI of the brain and entire spinal cord to start in mid-adolescence. For all age groups, MR imaging should include thin high spatial resolution images through the internal auditory canals, to evaluate for endolymphatic sac tumors which, while rare in the general population, occur with increased frequency in vHL patients.

New surveillance guidelines for visceral manifestations of vHL (renal cell carcinoma and pancreatic NET) have also been proposed, including the recommendation for annual abdominal MRI starting at age 10 years [34]. For detection of renal cell carcinoma, a dynamic contrast-enhanced MRI renal protocol should be considered as part of the screening protocol and in follow-up. Ultrasound may be utilized to complement MRI or where MRI is contraindicated. Given the high sensitivity of biochemical screening measures for detecting pheochromocytomas, routine surveillance imaging for this tumor in vHL patients is not advocated [34].

20.2.5.4 Hereditary Pheochromocytoma-Paraganglioma Syndrome

Hereditary pheochromocytoma-paraganglioma (HPP) syndrome is an autosomal dominantly inherited disease with incomplete penetrance that consists of rare, usually benign neural crest tumors that are symmetrically distributed along the paravertebral axis from the skull base and neck to the pelvis [37]. These tumors tend to hypersecrete catecholamines; however, it should be noted that paragangliomas found around the neck region are frequently nonsecretory. Approximately 25% of pheochromocytomas/paragangliomas are malignant, with metastases most commonly occurring in the bone, liver, lymph nodes, and lung [38]. Additionally, patients can develop gastrointestinal stromal tumors (GIST), pituitary adenomas, renal cancers, and other rare tumor types [34]. In addition, pheochromocytoma/paraganglioma occur with increased frequency in other hereditary predisposition syndromes and are associated with the *RET*, *VHL*, *NF1*, and *FH* genes [34].

Consensus guidelines from an expert panel recommend initiating tumor surveillance at around age 8 years. Since silent (nonsecretory) tumors occur more frequently in HPP compared with vHL, radiologic screening is recommended in addition to biochemical surveillance. Current

Fig. 20.4 16-year-old male presented with 2 weeks of headaches and visual changes. Contrast-enhanced brain MRI was performed showing the following: (**a**) axial T1-weighted image reveals bilateral mixed cystic and solid cerebellar masses (*white arrows*) with associated large tortuous vessels (*curved arrows*), (**b**) axial T2-weighted images confirm the T2-hyperintense cystic nature of the lesions with hypointense foci (*white block arrows*) containing blood products, (**c**) post-contrast axial image shows enhancement (*white block arrows*) of the nodules only, and (**d**) sagittal T1-weighted fat suppressed image of the thoracic spine shows a bright intramedullary mass (*white arrow*) in the thoracic spine at T6 level in keeping with hemangioblastoma. Given these hallmark findings, the patient went on to be diagnosed with von Hippel-Lindau disease

imaging recommendations for patients with HPP include biennial WBMRI with optional dedicated neck MRI with and without IV contrast to begin at age 6–8 years [34]. Currently, data does not support routine imaging for depiction of GISTs in high-risk patients; however CT with contrast or FDG-PET should be performed in symptomatic patients with gastric bleeding or anemia [34].

20.2.5.5 Neurofibromatosis

The neurofibromatoses consist of at least three autosomal dominantly inherited disorders: neurofibromatosis 1 (NF1), neurofibromatosis 2 (NF2), and schwannomatosis. While NF1 and NF2 share similar names, the two conditions are distinct and represent separate clinical and molecular entities with their respective genes localizing to chromosomes 17q and 22q, respectively. Recommendations for tumor surveillance of gene carriers were proposed in the 2016 AACR Childhood Cancer Predisposition Workshop [39].

The clinical course of NF1 varies widely. Typical features include cognitive problems, café au lait macules, axillary and groin freckling, Lisch nodules, and cutaneous and deeper neurofibromas which occur along peripheral nerves. Approximately 2–3% of NF1 patients have plexiform tumors which can be disfiguring. The deeper fusiform subcutaneous and plexiform tumors may undergo degeneration into malignant peripheral nerve sheath tumor (MPNST) which can occur beginning in adolescence, with a peak between the ages of 20 and 35 years and an overall lifetime risk of 8–13% [39, 40]. Rapidly growing tumors associated with pain or neurologic deficit need to be evaluated for a MPNST. MRI often shows a heterogeneous tumor, and ^{18}F-FDG PET imaging is useful in differentiating a benign plexiform neurofibroma from malignant transformation into MPNST (Fig. 20.5) [39].

Patchy hyperintense T2-weighted brain lesions may be seen and are thought to be caused by aberrant myelination or gliosis and are pathognomonic of NF1. Gliomas are the predominant tumor in NF1 and can occur in all parts of the nervous system, with a predilection for the optic pathways, brain stem, and cerebellum. Optic pathway gliomas (OPG) are grade 1 pilocytic astrocytomas and occur in 15% of children with NF1 and may result in impaired visual acuity, abnormal color vision, visual field loss, pupillary abnormalities, pale optic disc, proptosis, and hypothalamic dysfunction. Symptomatic OPGs are most frequent in children younger than 7 years of age [40]. NF1 is also associated with juvenile myelomonocytic leukemia, embryonal rhabdomyosarcoma, gastrointestinal tumors, pheochromocytomas, duodenal carcinoid, and glomus tumors in the nail beds [39].

In childhood, routine MRI surveillance is not currently recommended unless patients are symptomatic or have a previously diagnosed tumor. Given that early detection of an asymptomatic OPG has not been shown to reduce the incidence of visual loss, routine screening brain MRI does not have added value. Physical examinations with complete ophthalmic assessments every 6–12 months from birth to age 8 years are recommended. If visual impairment is detected, a repeat test in 2 weeks is recommended. If the visual loss is persistent, a brain MRI is indicated. As children transition into adulthood, women need to be advised of the increased breast cancer risk associated with NF-1 (four- to fivefold higher than the general population) and should seek breast cancer screening for moderate (20%) lifetime risk. In addition, because of the risk of MPNST, WBMRI should be considered, with screening to commence between the ages of 16 and 20 years to assess for internal tumor burden (Fig. 20.5) [39].

NF2 predisposes to the development of benign nerve sheath tumors, predominately schwannomas, meningiomas, and low-grade ependymomas. The hallmark of NF2 is bilateral often multifocal eighth cranial nerve schwannomas which lead to hearing loss and balance disturbance. NF2 typically presents in adulthood. Children, however, with NF2 may present due to an isolated meningioma or non-cranial schwannoma [41, 42].

The expert panel from 2016 AACR Childhood Cancer Predisposition Workshop recommends annual brain MRI with and without IV gadolinium contrast starting at 10 years of age (consider twice yearly in the first year for signs of rapid growth). Screening may begin earlier in patients with high-risk genotypes or symptomatic

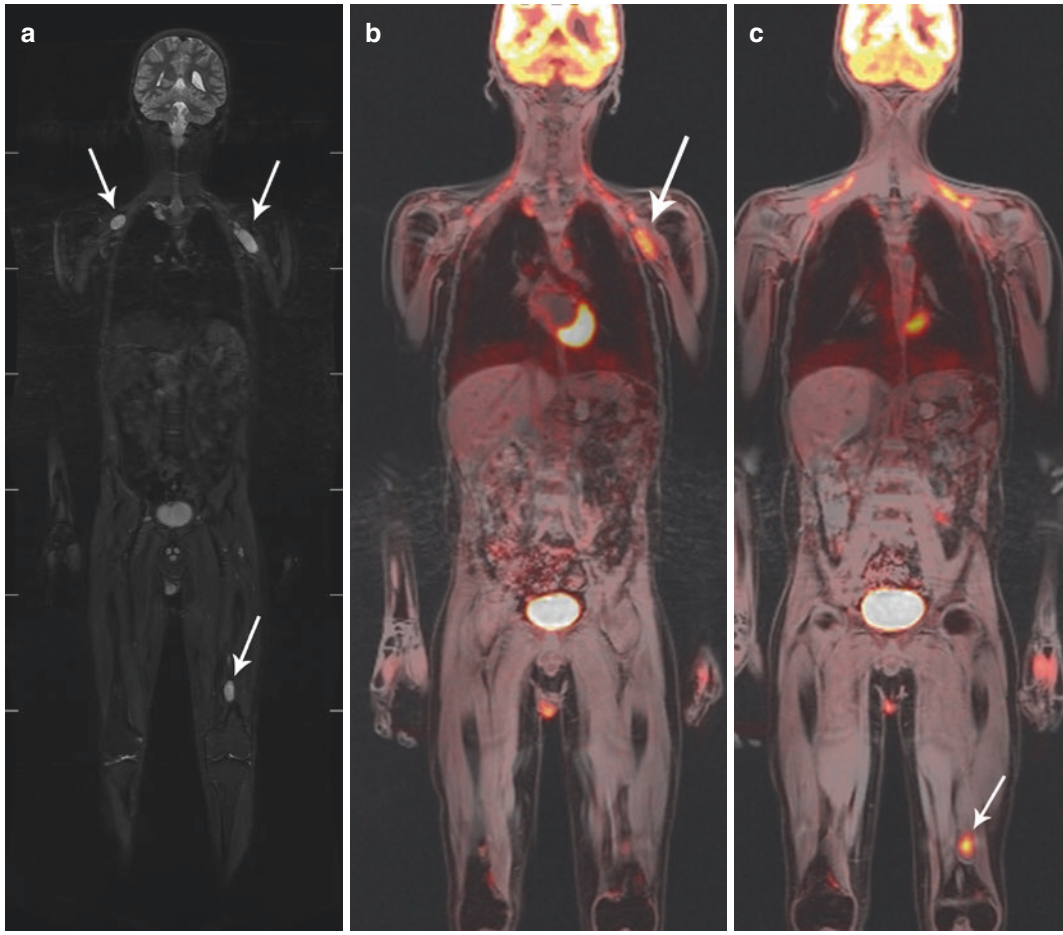

Fig. 20.5 19-year-old male with NF1 had a whole-body PET-MR. (**a**) Coronal inversion recovery image shows neurofibromas in both axillary regions (*white arrows*) left greater than right and one in the left distal thigh (*arrows*); (**b**, **c**) Coronal whole-body images from the fused portion of the PET/MR reveal that the lesions in left axilla and distal thigh are FDG-avid (*arrows*) suggesting possible malignant potential and a biopsy was recommended

diagnoses. If baseline imaging does not demonstrate NF2 findings, frequency of surveillance may be reduced to brain MRI every 2 years. Protocols should include high resolution (1–3 mm slice thickness) through the internal auditory canals, preferably in at least two orthogonal planes. If an NF2 lesion (vestibular schwannoma) is detected, follow-up imaging should be obtained at 6 months to assess tumor growth, with subsequent screening intervals based on lesion stability. At 10 years of age, spine MR imaging with and without IV gadolinium contrast is recommended with surveillance at 24–36-month intervals. If an NF2 lesion (peripheral schwannoma) is detected, follow-up imaging should also be obtained at 6 months to assess tumor growth. WBMRI examinations may be obtained depending on symptoms and known sites of disease [41].

20.2.5.6 DICER1 Syndrome

The *DICER1* gene is located on chromosome 14q32 and encodes an enzyme that is involved in the biogenesis of microRNAs (miRNAs) which play a key role in oncogenesis. Germline *DICER1* mutations identified in 2009 have been shown to cause familial pleuropulmonary blastoma (PPB), ovarian Sertoli-Leydig cell tumor, uterine cervix embryonal rhabdomyosarcoma, pituitary

blastoma, pineoblastoma, multinodular goiter, cystic nephroma, and intraocular medulloepithelioma [43, 44] (Fig. 20.6). Slade et al. [44] determined that the risk of tumor in *DICER1* mutation carriers is low and that most carriers do not develop tumors. Given the pleiotropic nature of *DICER1* and modest penetrance, the issue of surveillance becomes complex. At this time, healthy known *DICER1* mutation carriers are not routinely screened. As more information is learned regarding the molecular mechanisms of DICER1 and the clinical course, surveillance including WBMRI may become an integral part of managing this syndrome in the future [11].

20.2.5.7 Hereditary Retinoblastoma

Retinoblastoma (RB) is the most frequent malignant intraocular tumor in childhood with an incidence of

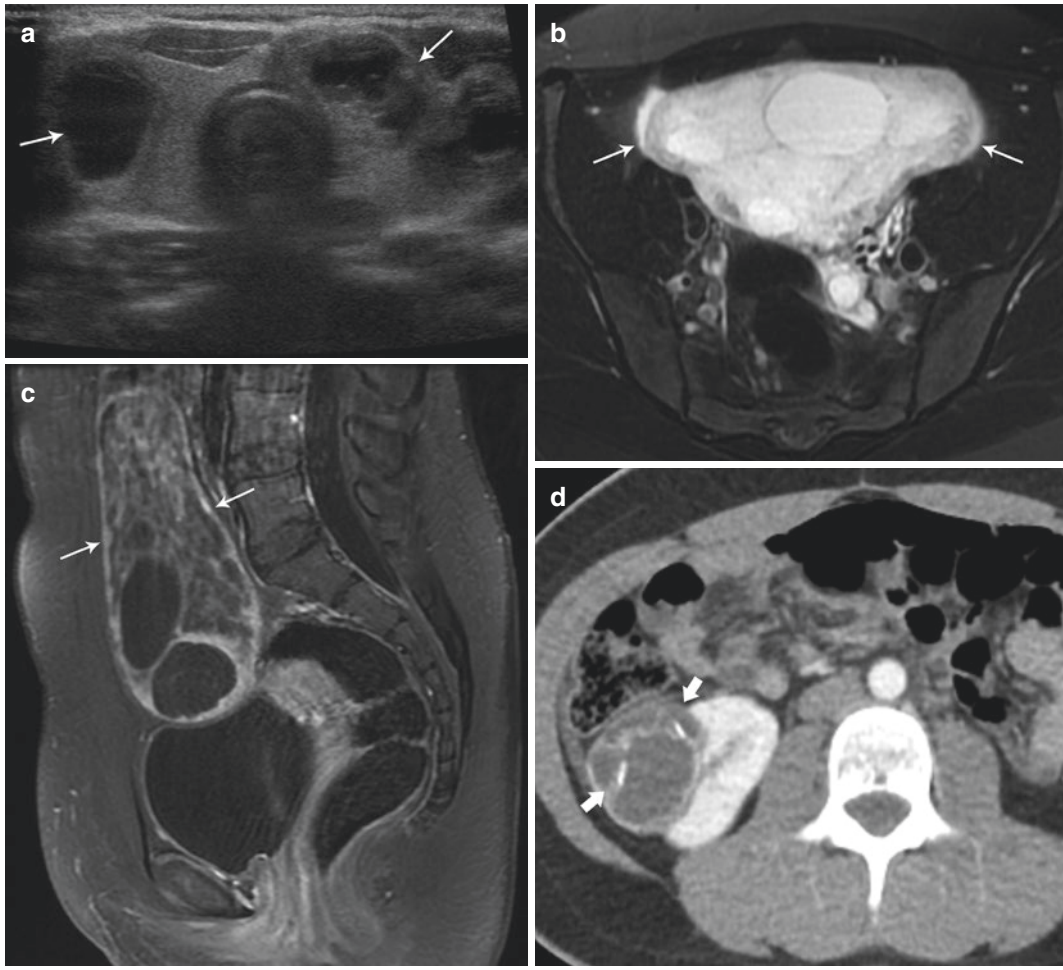

Fig. 20.6 17-year-old female diagnosed with DICER 1 with multiple tumors (multinodular goiter, multilocular cystic nephroma, and Sertoli-Leydig cell tumor) characteristics of this germline mutation. (**a**) Transverse gray-scale ultrasound image shows mixed solid and cystic masses in each lobe of the thyroid gland (*white arrows*) representing a multinodular goiter; (**b**) axial T2-weighted MRI image through the pelvis shows a large multilocular cystic mass arising from the left ovary (*white arrows*); (**c**) sagittal post-contrast image demonstrates enhancement of the stroma interspersed between the cysts of the mass (*white arrows*). This was pathologically proven to be a Sertoli-Leydig cell tumor. CT of the chest, abdomen, and pelvis was obtained for further disease staging. Axial CT (**d**) and coronal reformatted CT images (**e**) reveal a cystic mass (*white block arrows*) in the lower pole of the right kidney with peripheral curvilinear calcifications and no enhancement of the cystic components, consistent with multilocular cystic nephroma

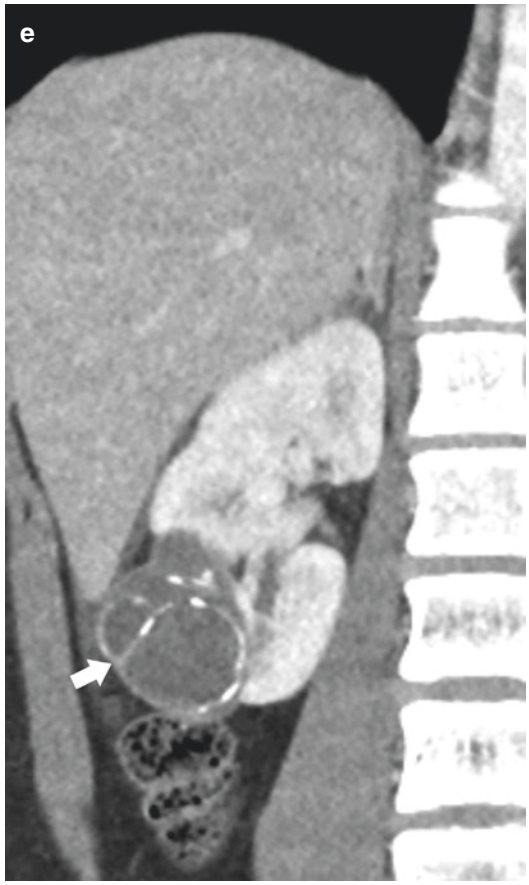

Fig. 20.6 (continued)

1 in 17,000 births; however considerable geographic variation has been reported [45, 46]. While most cases are sporadic, approximately 10% of retinoblastomas are familial. All cases of bilateral RB and up to 10% of unilateral RB are expected to carry a germline mutation in the *RB1* gene and thus may transmit the disease to future offspring [45]. Rarely hereditary RB is caused by a somatic *MYCN* amplification [46]. Almost two thirds of retinoblastomas are diagnosed before the age of 2 years, and 95% are diagnosed by age 5 years [47]. In addition to RB, children with hereditary RB are also at risk for developing a midline intracranial primitive neuroectodermal tumor (PNET). Those with hereditary RB continue to have a higher risk of developing a second primary tumor, often therapy related, such as an osteosarcoma, soft tissue sarcoma, skin cancer, brain tumor, and tumors of the nasal cavity, eye, and orbit. The median age to develop a secondary primary tumor is between 15 and 17 years of age [46].

An expert panel at the AACR Childhood Cancer Predisposition Workshop developed a surveillance protocol for children with known RB predisposition [46]. In addition to genetic testing and intraocular screening, surveillance imaging is an important component. While some authors advocate for the use of maternal US and fetal MRI for prenatal detection of RB in at-risk fetuses [48], the expert panel concluded that more data is necessary to support this practice. Once the diagnosis of a RB mutation is established, a brain MRI is indicated with many experts in the United States advocating for routine brain MR imaging every 6 months until the age of 5 years, although this practice is not universally accepted. No established imaging guidelines are set for the evaluation of second malignancies in RB survivors. Given the increased risks for bone and soft tissue sarcomas, some authors have recommended considering annual WBMRI after 8–10 years of age [46] although consensus guidelines are lacking.

20.2.5.8 Multiple Endocrine Neoplasias (MEN)

MEN1

MEN syndromes (MEN1 and MEN2 and MEN4) are autosomal dominant disorders where patients can develop both non-endocrine and endocrine tumors. MEN1 subtype is caused by a germline mutation in the gene locus on chromosome 11q13, whereas the MEN2 subtype is a result of a mutation in the proto-oncogene on the locus of chromosome 10q11 [49, 50]. MEN4 is a newly described group comprised of individuals at risk of developing parathyroid and pituitary tumors [50]. The focus of this discussion will be on MEN1 and MEN2 syndromes.

MEN1 patients can commonly develop tumors of the anterior pituitary, parathyroid gland, and endocrine pancreas (usually gastrinomas and insulinomas) with less frequent occurrence of adrenal tumors, carcinoids, schwannomas, and ovarian tumors [49, 51, 52]. Tumors in MEN1 patients

were initially thought to present in adulthood, but there are reports of tumors occurring in these genetically predisposed individuals as early as age 5 [52, 53]. Approximately 17% of MEN1 tumors present before 21 years of age [52]. The most common clinical manifestation of the MEN1-associated neoplasms is primary hyperparathyroidism (PHPT) and hypercalcemia related to parathyroid adenomas; however, the greatest morbidity and death result from the presence of malignant pancreatic neuroendocrine tumors [52].

Genetic testing for possible MEN1 syndrome is indicated for any individual with two or more of the primary MEN1 tumors, any person with one MEN1 tumor and a first-degree relative with MEN1, and individuals under the age of 30 who develop PHPT or who have a pancreatic islet tumor regardless of family history [52]. Monsalve et al. in 2011 have reported guidelines for MEN1 syndromes where US of the pancreas was a screening option starting at age 5 [49]. Updates to these guidelines have evolved. Based on a recent publication by Wasserman and colleagues, in addition to clinical screening, annual biochemical testing of glucose, insulin, and prolactin levels begins by age 5 and calcium levels at age 8. By age 10 years, levels of glucagon, proinsulin, and pancreatic polypeptide are checked (identifiers for endocrine pancreatic tumors) [52]. These guidelines were established based on published reports of these tumors occurring in the earliest pediatric age groups. Imaging plays a role in the evaluation of specific tumors at various ages, for example, MRI examinations of the brain and abdomen are recommended for the assessment of pituitary, pancreatic, or adrenal neoplasms, respectively. Currently, there is no role for routine ultrasound or whole-body MRI screening in the MEN1 population at this time based on recent consensus statement by the AACR [11].

MEN2

MEN2 syndrome is comprised of three subsets, MEN2A, MEN2B, and familial medullary thyroid carcinoma (MTC). The common thread among these subsets is MTC which occurs in all individuals with 100% penetrance [50]. MEN2A individuals are at risk for developing MTC, pheochromocytomas, and parathyroid adenomas/hyperplasia [50]. MEN2B individuals also develop MTC and pheochromocytomas but in addition are at risk for mucosal neuromas and intestinal ganglioneuromas [51]. Although various authors quantify the risk for development of these tumors, the actual risk profile is codon specific to the *RET* mutation [54, 55]. Therefore, genetic evaluation needs to be thorough and codon specific to risk stratify patients.

Screening of Medullary Thyroid Carcinoma in MEN2

MTC occurs in early childhood in patients with MEN2B and later in adolescence and early adulthood for those with MEN2A. MEN2 patients are risk stratified into *highest-, high-*, and *moderate-risk* profiles [54–56]. In general, screening consists of serial thyroid ultrasound (US) and serum calcitonin levels. The age of onset of MTC and the risk stratification level are keys to determining what screening tests are performed and to guide management. Those in the *highest-risk* category are recommended to have a thyroidectomy by the age of 1 year regardless of ultrasound imaging or serum calcitonin values [55]. Children in the *high-risk* category are advised to have an annual thyroid US and blood tests for calcitonin levels starting at age 3 (Fig. 20.7) [55]. Thyroidectomy is recommended at age 5 or earlier if there are elevated calcitonin levels [55]. Delaying thyroidectomy is a desirable goal as the surgery is not without significant risk. However, annual screening is anxiety provoking and burdensome particularly for families of children falling into the moderate-risk category, and they may opt for early thyroidectomy. Recently a publication by Morris et al. [54] examined the sensitivity of US in determining presence of MTC in asymptomatic children with MEN2A and found that US is not sensitive in detecting MTC and should not be used to falsely reassure families or guide management over serum calcitonin levels. The report by Morris et al. [54] and other publications [57, 58] do not recommend any additional imaging studies but still advocate performing a pre-thyroidectomy thyroid ultrasound. Currently, there is also no role for WBMRI for MTC [11].

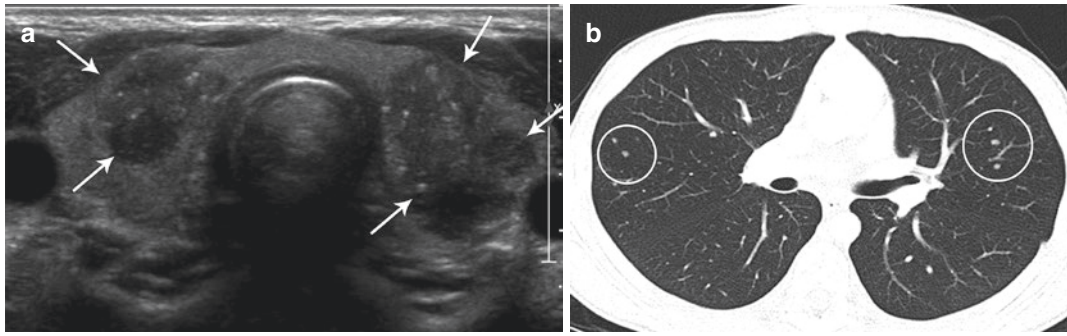

Fig. 20.7 13-year-old male with MEN2 was found to have an elevated calcitonin level and went on to have a thyroid ultrasound. (**a**) Transverse gray-scale US image of the thyroid gland demonstrates heterogeneous large hypoechoic masses containing punctate echogenic foci in each lobe of the thyroid gland (*arrows*); (**b**) non-contrast CT scan of the chest was performed as part of the metastatic work-up; axial image shows multiple tiny lung nodules in both lungs (*white circles*) representing metastatic disease

Screening for Pheochromocytoma in MEN2

Pheochromocytomas in MEN2 are commonly bilateral and benign and clinically present with labile hypertension [50]. Approximately 50% of patients with MEN2A and MEN2B develop pheochromocytomas [50]. There are no large studies on the incidence of pheochromocytomas in children with MEN2 but rather multiple case reports emphasizing its rarity [59]. Because of a single case report of pheochromocytoma occurring in an 8-year-old with MEN2A, initial American Thyroid Association (ATA) guidelines initially recommended screening to start at this young age [56, 59]. However, revised 2015 ATA guidelines have modified the age for screening, utilizing a risk category. For children with the highest- or high-risk category, screening is recommended to begin at age 11 years, and those in a moderate-risk category can begin screening at age 16 years. Screening is biochemical testing of either free plasma metanephrine and normetanephrines or a 24-h urine metanephrine and normetanephrine level [55]. If biochemical tests are elevated, then complementary information is needed with a contrast-enhanced abdominal CT or MRI [55]. MRI is preferred as it is advantageous due to its lack of ionizing radiation, multi-planar capability, and high tissue contrast. Currently WBMRI is not recommended for routine pheochromocytoma screening in this population of patients [11].

20.3 Conclusion

In this chapter, we have discussed the characteristics and considerations of a screening test and presented a review of specific imaging techniques, particularly those pertaining to ultrasound and WBMRI. Imaging plays a key role in the cancer screening recommendations for children with cancer predisposition syndromes, and imaging guidelines are being modified as we further understand the genetic component of these syndromes. However, imaging alone is not sufficient. A thorough physical examination, biochemical testing, and genetic testing are needed along with imaging for a comprehensive evaluation. Although early detection of cancers is crucial to improved outcome in this population, this does not come without a cost to the patient and family. It is important to have a standardized approach to image interpretation and direct communication with the oncology team to ensure the overall best care for patients and their families.

References

1. Garber JE, Offit K. Hereditary cancer predisposition syndromes. J Clin Oncol. 2005;23(2):276–92.
2. Maxim LD, Niebo R, Utell MJ. Screening tests: a review with examples. Inhal Toxicol. 2014;26(13):811–28.

3. Smith RA, Andrews KS, Brooks D, Fedewa SA, Manassaram-Baptiste D, Saslow D, et al. Cancer screening in the United States, 2017: a review of current American Cancer Society guidelines and current issues in cancer screening. CA Cancer J Clin. 2017;67(2):100–21.
4. Kratz CP, Achatz MI, Brugieres L, Frebourg T, Garber JE, Greer MC, et al. Cancer screening recommendations for individuals with Li-Fraumeni syndrome. Clin Cancer Res. 2017;23(11):e38–45.
5. Reiman TA, Siegel MJ, Shackelford GD. Wilms tumor in children: abdominal CT and US evaluation. Radiology. 1986;160(2):501–5.
6. Vutskits L, Davidson A. Update on developmental anesthesia neurotoxicity. Curr Opin Anaesthesiol. 2017;30(3):337–42.
7. Sood S, Hryhorczuk AL, Rissmiller J, Lee EY. Spectrum of syndromic disorders associated with pediatric tumors: evolving role of practical imaging assessment. Radiol Clin North Am. 2017;55(4):869–93.
8. Yikilmaz A, George M, Lee EY. Pediatric hepatobiliary neoplasms: an overview and update. Radiol Clin North Am. 2017;55(4):741–66.
9. Rafailidis V, Deganello A, Watson T, Sidhu PS, Sellars ME. Enhancing the role of paediatric ultrasound with microbubbles: a review of intravenous applications. Br J Radiol. 2017;90(1069):20160556.
10. Sidhu PS, Cantisani V, Deganello A, Dietrich CF, Duran C, Franke D, et al. Role of contrast-enhanced ultrasound (CEUS) in paediatric practice: an EFSUMB position statement. Ultraschall Med. 2017;38(1):33–43.
11. Greer MC, Voss SD, States LJ. Pediatric cancer predisposition imaging: focus on whole-body MRI. Clin Cancer Res. 2017;23(11):e6–e13.
12. Anupindi SA, Bedoya MA, Lindell RB, Rambhatla SJ, Zelley K, Nichols KE, et al. Diagnostic performance of whole-body MRI as a tool for cancer screening in children with genetic cancer-predisposing conditions. AJR Am J Roentgenol. 2015;205(2):400–8.
13. Villani A, Malkin D. Biochemical and imaging surveillance in Li-Fraumeni syndrome - authors' reply. Lancet Oncol. 2016;17(11):e473.
14. Villani A, Shore A, Wasserman JD, Stephens D, Kim RH, Druker H, et al. Biochemical and imaging surveillance in germline TP53 mutation carriers with Li-Fraumeni syndrome: 11 year follow-up of a prospective observational study. Lancet Oncol. 2016;17(9):1295–305.
15. Landier W, Ahern J, Barakat LP, Bhatia S, Bingen KM, Bondurant PG, et al. Patient/family education for newly diagnosed pediatric oncology patients. J Pediatr Oncol Nurs. 2016;33(6):422–31.
16. Sahni VA, Silveira PC, Sainani NI, Khorasani R. Impact of a structured report template on the quality of MRI reports for rectal cancer staging. AJR Am J Roentgenol. 2015;205(3):584–8.
17. Valdez JM, Nichols KE, Kesserwan C. Li-Fraumeni syndrome: a paradigm for the understanding of hereditary cancer predisposition. Br J Haematol. 2017;176(4):539–52.
18. Correa H. Li-Fraumeni syndrome. J Pediatr Genet. 2016;5(2):84–8.
19. Reinhardt HC, Schumacher B. The p53 network: cellular and systemic DNA damage responses in aging and cancer. Trends Genet. 2012;28(3):128–36.
20. Mai PL, Best AF, Peters JA, DeCastro RM, Khincha PP, Loud JT, et al. Risks of first and subsequent cancers among TP53 mutation carriers in the National Cancer Institute Li-Fraumeni syndrome cohort. Cancer. 2016;122(23):3673–81.
21. Bougeard G, Renaux-Petel M, Flaman JM, Charbonnier C, Fermey P, Belotti M, et al. Revisiting Li-Fraumeni syndrome from TP53 mutation carriers. J Clin Oncol. 2015;33(21):2345–52.
22. Hisada M, Garber JE, Fung CY, Fraumeni JF Jr, Li FP. Multiple primary cancers in families with Li-Fraumeni syndrome. J Natl Cancer Inst. 1998;90(8):606–11.
23. Villani A, Tabori U, Schiffman J, Shlien A, Beyene J, Druker H, et al. Biochemical and imaging surveillance in germline TP53 mutation carriers with Li-Fraumeni syndrome: a prospective observational study. Lancet Oncol. 2011;12(6):559–67.
24. Kalish JM, Deardorff MA. Tumor screening in Beckwith-Wiedemann syndrome-to screen or not to screen? Am J Med Genet A. 2016;170(9):2261–4.
25. Eggermann T, Algar E, Lapunzina P, Mackay D, Maher ER, Mannens M, et al. Clinical utility gene card for: Beckwith-Wiedemann syndrome. Eur J Hum Genet. 2014;22(3)
26. Ibrahim A, Kirby G, Hardy C, Dias RP, Tee L, Lim D, et al. Methylation analysis and diagnostics of Beckwith-Wiedemann syndrome in 1,000 subjects. Clin Epigenetics. 2014;6(1):11.
27. Mussa A, Molinatto C, Baldassarre G, Riberi E, Russo S, Larizza L, et al. Cancer risk in Beckwith-Wiedemann syndrome: a systematic review and meta-analysis outlining a novel (Epi)genotype specific histotype targeted screening protocol. J Pediatr. 2016;176:142–9 e1.
28. Maas SM, Vansenne F, Kadouch DJ, Ibrahim A, Bliek J, Hopman S, et al. Phenotype, cancer risk, and surveillance in Beckwith-Wiedemann syndrome depending on molecular genetic subgroups. Am J Med Genet A. 2016;170(9):2248–60.
29. Davidoff AM. Wilms' tumor. Curr Opin Pediatr. 2009;21(3):357–64.
30. Zarate YA, Mena R, Martin LJ, Steele P, Tinkle BT, Hopkin RJ. Experience with hemihyperplasia and Beckwith-Wiedemann syndrome surveillance protocol. Am J Med Genet A. 2009;149A(8):1691–7.
31. Dumoucel S, Gauthier-Villars M, Stoppa-Lyonnet D, Parisot P, Brisse H, Philippe-Chomette P, et al. Malformations, genetic abnormalities, and Wilms tumor. Pediatr Blood Cancer. 2014;61(1):140–4.

32. Chittiboina P, Lonser RR. Von Hippel-Lindau disease. Handb Clin Neurol. 2015;132:139–56.
33. Poulsen ML, Budtz-Jorgensen E, Bisgaard ML. Surveillance in von Hippel-Lindau disease (vHL). Clin Genet. 2010;77(1):49–59.
34. Rednam SP, Erez A, Druker H, Janeway KA, Kamihara J, Kohlmann WK, et al. Von Hippel-Lindau and hereditary pheochromocytoma/paraganglioma syndromes: clinical features, genetics, and surveillance recommendations in childhood. Clin Cancer Res. 2017;23(12):e68–75.
35. Priesemann M, Davies KM, Perry LA, Drake WM, Chew SL, Monson JP, et al. Benefits of screening in von Hippel-Lindau disease--comparison of morbidity associated with initial tumours in affected parents and children. Horm Res. 2006;66(1):1–5.
36. Prasad R, Johnston LB, Savage MO, Martin L, Perry LA, Storr HL. Pediatric endocrine screening for von Hippel-Lindau disease: benefits and the challenge of compliance. J Endocrinol Invest. 2011;34(4):296–9.
37. Santos P, Pimenta T, Taveira-Gomes A. Hereditary pheochromocytoma. Int J Surg Pathol. 2014;22(5):393–400.
38. Fishbein L, Nathanson KL. Pheochromocytoma and paraganglioma: understanding the complexities of the genetic background. Cancer Genet. 2012;205(1-2):1–11.
39. Evans DGR, Salvador H, Chang VY, Erez A, Voss SD, Schneider KW, et al. Cancer and central nervous system tumor surveillance in pediatric neurofibromatosis 1. Clin Cancer Res. 2017;23(12):e46–53.
40. Ferner RE, Huson SM, Thomas N, Moss C, Willshaw H, Evans DG, et al. Guidelines for the diagnosis and management of individuals with neurofibromatosis 1. J Med Genet. 2007;44(2):81–8.
41. Evans DGR, Salvador H, Chang VY, Erez A, Voss SD, Druker H, et al. Cancer and central nervous system tumor surveillance in pediatric neurofibromatosis 2 and related disorders. Clin Cancer Res. 2017;23(12):e54–61.
42. Evans DG, Huson SM, Donnai D, Neary W, Blair V, Newton V, et al. A clinical study of type 2 neurofibromatosis. Q J Med. 1992;84(304):603–18.
43. Schultze-Florey RE, Graf N, Vorwerk P, Koscielniak E, Schneider DT, Kratz CP. DICER1 syndrome: a new cancer syndrome. Klin Padiatr. 2013;225(3):177–8.
44. Slade I, Bacchelli C, Davies H, Murray A, Abbaszadeh F, Hanks S, et al. DICER1 syndrome: clarifying the diagnosis, clinical features and management implications of a pleiotropic tumour predisposition syndrome. J Med Genet. 2011;48(4):273–8.
45. Rothschild PR, Levy D, Savignoni A, Lumbroso-Le Rouic L, Aerts I, Gauthier-Villars M, et al. Familial retinoblastoma: fundus screening schedule impact and guideline proposal. A retrospective study. Eye (Lond). 2011;25(12):1555–61.
46. Kamihara J, Bourdeaut F, Foulkes WD, Molenaar JJ, Mosse YP, Nakagawara A, et al. Retinoblastoma and neuroblastoma predisposition and surveillance. Clin Cancer Res. 2017;23(13):e98–e106.
47. Parkin DM, Stiller CA, Draper GJ, Bieber CA. The international incidence of childhood cancer. Int J Cancer. 1988;42(4):511–20.
48. Staffieri SE, McGillivray G, Elder JE, Bristowe A, Cole S, McKenzie JD, et al. Managing fetuses at high risk of retinoblastoma: lesion detection on screening MRI. Prenat Diagn. 2015;35(2):174–8.
49. Monsalve J, Kapur J, Malkin D, Babyn PS. Imaging of cancer predisposition syndromes in children. Radiographics. 2011;31(1):263–80.
50. Grajo JR, Paspulati RM, Sahani DV, Kambadakone A. Multiple endocrine neoplasia syndromes: a comprehensive imaging review. Radiol Clin North Am. 2016;54(3):441–51.
51. Shinagare AB, Giardino AA, Jagannathan JP, Van den Abbeele AD, Ramaiya NH. Hereditary cancer syndromes: a radiologist's perspective. AJR Am J Roentgenol. 2011;197(6):W1001–7.
52. Wasserman JD, Tomlinson GE, Druker H, Kamihara J, Kohlmann WK, Kratz CP, et al. Multiple endocrine neoplasia and hyperparathyroid-jaw tumor syndromes: clinical features, genetics, and surveillance recommendations in childhood. Clin Cancer Res. 2017;23(13):e123–e32.
53. Farrell WE, Azevedo MF, Batista DL, Smith A, Bourdeau I, Horvath A, et al. Unique gene expression profile associated with an early-onset multiple endocrine neoplasia (MEN1)-associated pituitary adenoma. J Clin Endocrinol Metab. 2011;96(11):E1905–14.
54. Morris LF, Waguespack SG, Edeiken-Monroe BS, Lee JE, Rich TA, Ying AK, et al. Ultrasonography should not guide the timing of thyroidectomy in pediatric patients diagnosed with multiple endocrine neoplasia syndrome 2A through genetic screening. Ann Surg Oncol. 2013;20(1):53–9.
55. Wells SA Jr, Asa SL, Dralle H, Elisei R, Evans DB, Gagel RF, et al. Revised American Thyroid Association guidelines for the management of medullary thyroid carcinoma. Thyroid. 2015;25(6):567–610.
56. American Thyroid Association Guidelines Task F, Kloos RT, Eng C, Evans DB, Francis GL, Gagel RF, et al. Medullary thyroid cancer: management guidelines of the American Thyroid Association. Thyroid. 2009;19(6):565–612.
57. Elisei R, Romei C, Renzini G, Bottici V, Cosci B, Molinaro E, et al. The timing of total thyroidectomy in RET gene mutation carriers could be personalized and safely planned on the basis of serum calcitonin: 18 years experience at one single center. J Clin Endocrinol Metab. 2012;97(2):426–35.
58. Rohmer V, Vidal-Trecan G, Bourdelot A, Niccoli P, Murat A, Wemeau JL, et al. Prognostic factors of disease-free survival after thyroidectomy in 170 young patients with a RET germline mutation: a multicenter study of the Groupe Francais d'Etude des Tumeurs Endocrines. J Clin Endocrinol Metab. 2011;96(3):E509–18.
59. Rowland KJ, Chernock RD, Moley JF. Pheochromocytoma in an 8-year-old patient with multiple endocrine neoplasia type 2A: implications for screening. J Surg Oncol. 2013;108(4):203–6.

Surveillance Imaging in Pediatric Oncology

21

Martijn V. Verhagen, Kieran McHugh, and Stephan D. Voss

21.1 Introduction

Over the past 60 years, improvements in the diagnosis and treatment of pediatric malignancy have led to increases in both event-free survival (EFS) and overall survival (OS) for the majority of childhood cancers. More than 80% of the children diagnosed with cancer today will be 5-year survivors, and many of these will be cured of their disease [1]. This presents unique new challenges for both the clinician and the imaging specialist in determining how best to monitor patients for disease recurrence. It would seem sensible and intuitive that diseases that historically had universally poor outcomes should now require some type of post-therapy imaging surveillance. Surveillance imaging, by definition, commences when patients have completed all of their intended therapy and are either free of demonstrable disease or have reached a point of disease stability for which further aggressive treatment is no longer indicated. For the purposes of this review, surveillance imaging will refer primarily to those patients who are free of disease at completion of therapy. For surveillance imaging to be useful, of course, it should lead to an improved survival benefit. To date that is largely unproven, but the value of surveillance is being evaluated in many current studies.

Developing an algorithm for both clinical and imaging surveillance is an essential aspect of these patients' follow-up care and demands knowledge of the patient's primary disease, which includes an understanding of the initial stage of disease, tumor location, presence of metastatic disease, and response to initial therapy. Also important are historical data that inform us on the likelihood and typical time course of disease recurrence based on the above characteristics of the tumor. For example, low-stage, low-grade tumors that have been completely resected (e.g., stage 1 Wilms tumor) or that have enjoyed a complete response to therapy (e.g., non-bulky stage 2a Hodgkin disease) may require a less intensive post-therapy surveillance regimen. In contrast, a patient with relapsed high-risk stage 4 neuroblastoma who is now free of disease following aggressive relapse therapy has a much greater likelihood of early disease recurrence and may require more intensive off-treatment imaging surveillance. This approach assumes that detection of relapse will lead to a better outcome, but that remains unproven for many pediatric tumors. What imaging modalities should be used, how frequently imaging should be performed, and the relative risks and benefits of different

M. V. Verhagen · K. McHugh
Great Ormond Street Hospital for Children, London, UK
e-mail: Kieran.McHugh@gosh.nhs.uk

S. D. Voss (✉)
Boston Children's Hospital, Harvard Medical School, Boston, MA, USA
e-mail: Stephan.Voss@childrens.harvard.edu

S. D. Voss, K. McHugh (eds.), *Imaging in Pediatric Oncology*, Pediatric Oncology,
https://doi.org/10.1007/978-3-030-03777-2_21

surveillance imaging strategies will be the focus of this review.

A related topic is the approach to imaging surveillance for patients with cancer predisposition syndromes. The technologic advances in whole genomic screening techniques, coupled with a rapidly expanding list of tumor-specific molecular genetic markers, have led to the increasing use of genetic testing to identify inherited gene mutations that might put a person at higher risk of developing certain types of cancer. The imaging approaches used to screen patients with known cancer predisposition syndromes share many features with the off-therapy surveillance imaging used to monitor patients who have already been treated for cancer. In both instances patients are free of disease but have a finite risk of developing either new or recurrent cancer, and the imaging modalities used and frequency with which imaging is performed must be tailored to the specific disease or syndrome [2]. Because of the increasing number of recognized cancer predisposition syndromes, and the unique features that characterize many of these syndromes, features that in turn dictate the approach to radiologic screening, a separate chapter in this textbook has been dedicated to the imaging of cancer predisposition syndromes; the reader is referred to this section (Chap. 20) for a more comprehensive treatise on this important subject.

In order to decide on appropriate methods of surveillance, it is necessary to study both the contribution and usefulness of radiological and clinical findings. The effects on event-free survival (EFS) and overall survival (OS) need to be taken into consideration, and these must be weighed against the potential disadvantages of the available radiological techniques. For example, the more frequent use of imaging surveillance in low-risk/low-stage patients with a very good prognosis, for whom treatment intensity is being reduced and who may thus experience increased rates of relapse, may be justifiable, despite the likelihood of a good overall outcome that may not be affected by earlier detection of recurrence. In contrast, there are certain high-risk patients for whom risk of relapse remains high after completion of therapy and for whom there are no good alternative treatment options. In these patients, identifying recurrent disease earlier with frequent surveillance imaging will likely not impact outcome, and the approach to imaging surveillance may require additional consideration. In both populations of patients, the decision to undertake a specific surveillance imaging strategy should follow from a discussion between the treating clinician and the radiologist, so as to balance the risks and benefits of the various techniques.

In recent years, with improvement in outcome for children with cancer, the aim has shifted to reducing treatment-related toxicity and general long-term comorbidity associated with many of the therapies used to treat pediatric patients [3, 4]. The result has been a judicious reduction in the intensity of cytotoxic therapies and a shift toward use of molecularly targeted agents. At the same time, radiologists and oncologists have become increasingly aware of the high cumulative radiation doses children may receive from CT scans and nuclear medicine studies obtained during and after their treatment, doses which—when added to the toxicity of chemotherapy and radiotherapy—have caused many to express concern that these heavily treated and intensively imaged children may be receiving unnecessarily high doses of ionizing radiation as a result of surveillance imaging [5–8].

For children whose cancers have been successfully treated, imaging surveillance—when indicated—is only one aspect of comprehensive end-of-therapy monitoring. The need for regular clinical follow-up is essential, despite relatively low overall rates of tumor recurrence detected during routine clinic visits. Indeed, one study reported that 804 clinic visits were needed to detect one tumor recurrence [9]. Nonetheless, clinic visits are useful for patient and family reassurance, and in many instances, the findings on physical examination, when coupled with other laboratory tests, complement the results obtained from surveillance imaging, and together each plays an important role in pediatric oncology surveillance.

This chapter describes the basic principles of disease surveillance in medicine and places them in the context of pediatric oncology. Posttreatment surveillance is discussed with a focus on imaging and the potential risks related to anesthesia and

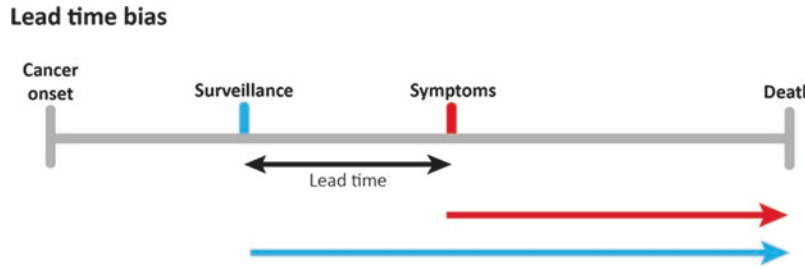

Fig. 21.1 Because of lead-time bias, measured survival is longer for disease detected by surveillance (blue arrow) compared to symptomatic disease (red arrow)

exposure to ionizing radiation versus the benefits that accrue from early detection of disease. Available literature on specific types of malignancy is presented with the aim of elucidating the usefulness of surveillance with different tumors. In those situations where radiological surveillance is needed, we suggest to replacing CT with MRI when appropriate, with the addition of diffusion-weighted imaging (DWI) [10, 11], and routine ultrasound examinations wherever possible.

21.2 Problems with Surveillance

We all know the mantra: early detection is the best protection. Intuitively, short-term imaging surveillance should lead to earlier detection of disease recurrence in posttreatment oncological patients as compared to clinical surveillance alone, with a resultant improvement in overall outcome. This, however, depends on two factors: firstly that the imaging modality being used for surveillance (e.g., MRI, ultrasound, CT) has sufficient sensitivity and specificity in detecting disease before clinical signs or symptoms appear and secondly that early radiological detection of disease recurrences improves outcome as compared to clinical detection [12–15].

In evaluating the efficacy of surveillance imaging for detecting disease and improving outcome, an understanding of lead-time and length-time bias is fundamental. Lead-time bias relates to the time between detection of cancer by imaging and the time point of clinical detection. When determining the impact of early detection on survival, the modality that leads to earlier detection will always appear to result in a longer survival time. Therefore, even if early detection by imaging surveillance does not actually improve overall survival, the earlier diagnosis by imaging and the resultant increase in time to progression will appear favorable when compared to clinical surveillance [13–15] (Fig. 21.1). Diagnosing a disease earlier does not automatically make patients live longer; instead they merely live for a longer time with the disease label. Put another way, survival appears longer because the disease clock starts earlier [16]. Such lead-time bias can be overcome, however, by analyzing the results by date of birth instead of age at diagnosis.

Length-time bias refers to the amount of time needed for a malignancy to manifest clinically, versus being detected by imaging. If, as typically is the case for aggressive tumors, this length of time is less than the interval between surveillance imaging exams, the cancer will present clinically and surveillance imaging will have little apparent impact. Because of this, there will be a bias toward surveillance imaging detecting malignancies that are inherently less aggressive and slower-growing (Fig. 21.2). Length-time bias can therefore result in recurrences detected by surveillance imaging correlating with longer survival, when in fact surveillance imaging may simply be detecting less aggressive, more indolent tumors [13–15].

21.3 Lessons from Neuroblastoma Screening

Experience with historical screening for neuroblastoma is instructive in several ways. Survival rates for affected children depend on factors such

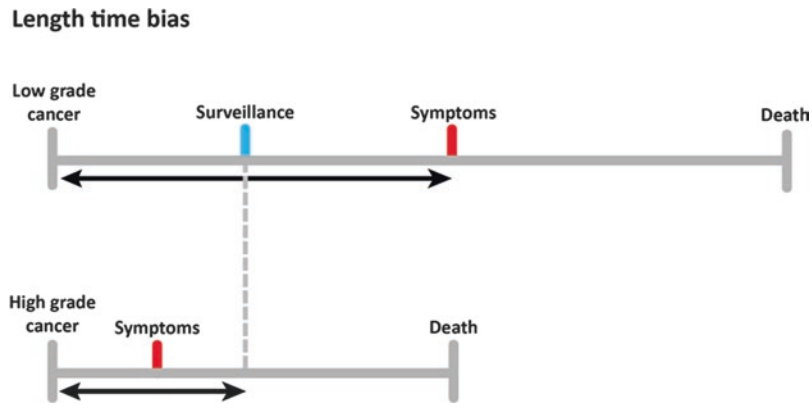

Fig. 21.2 Due to its shorter length time (time between onset and symptoms, black arrows), high-grade cancer may present with symptoms before the surveillance time point is reached. Therefore aggressive cancer is less often included in surveillance studies

as the age of the child, which part of the body is affected, how widely disseminated the tumor is when diagnosed, and biological parameters. The overall 5-year survival rate of children aged 1–4 years at diagnosis is around 50–60%. In addition, it is a well-known idiosyncrasy of neuroblastoma, particularly when diagnosed in infancy, that the tumor can undergo complete spontaneous regression without treatment.

Neuroblastoma was therefore a tempting target for screening for four reasons: (1) children who are diagnosed before the age of 1 year are known to have a better outlook than those who are diagnosed later; (2) children with advanced disease fare much worse than those with early disease; (3) there was a simple and cheap screening test that can be carried out by blotting wet diapers and measuring catecholamines in the urine; and (4) the test detects nine out of ten children with neuroblastoma.

Mass screening of infants for neuroblastoma at 6 months of age was first introduced in Japan in 1985 without the benefit of any evidence from clinical trials. Based on the above considerations, it seemed a sensible and logical approach to screen for a tumor which historically often had a poor prognosis. During the first 3 years of nationwide screening, over 337 infants were diagnosed, 97% of whom were alive in 1990 following treatment. But 20 years later, there was no evidence that neuroblastoma screening had reduced the number of children dying from this cancer [17]. How could that be?

When the evidence on which screening had been introduced and promoted in Japan was scrutinized, it turned out that there were serious flaws but a ready explanation. The impressive 97% survival rate illustrates the effect of length-time bias—meaning that screening works best at picking up slowly developing conditions (slow-growing tumors in this case). By contrast, fast-growing tumors are, of course, less likely to be picked up by screening but will lead to clinical signs in the infant such as abdominal distension or a palpable mass, either of which will rapidly be brought to a doctor's attention. These fast-growing tumors are potentially much more serious than slow-growing ones. Slow-growing neuroblastomas usually have a good outcome, and spontaneous regression is observed in many patients up to 18 months of age.

So the 337 cases diagnosed by screening would mostly have had a good outcome anyway and would not have included infants with the worst potential outcomes. Furthermore screening would have detected some neuroblastomas that would have disappeared spontaneously. Without screening no one would ever have known that these tumors existed; with screening, this overdiagnosis turned the affected babies into patients, who then went on to be exposed to unnecessary harms associated with treatment and management.

In addition, the encouraging results from small studies that had led to the nationwide screening in Japan had initially been analyzed by looking at length of survival from the date of diagnosis of neuroblastoma, not at length of survival from date of birth. This is important because diagnosing a disease earlier does not automati-

cally make patients live longer—they merely live for a longer time with the disease. Put another way, survival appears longer because the disease happened to be picked up earlier. As mentioned above this is lead-time bias, and it can be overcome by analyzing results by date of birth instead of age at diagnosis.

By contrast, when unbiased evidence was obtained from clinical trials done in Canada and Germany, involving about three million children in all, researchers were unable to detect any benefit from screening [17]. But, there were apparent potential harms that resulted from screening, including unjustified surgery and chemotherapy, both of which can have serious unwanted side effects. In light of this evidence, infant screening for neuroblastoma in Japan was stopped in 2004.

At the same time, infants in New South Wales in Australia were fortunately spared from neuroblastoma screening, which had been planned in the 1980s after the encouraging early Japanese studies. When an Australian expert reanalyzed the Japanese results from dates of birth of the infants rather than from dates of diagnosis, this analysis did not detect any difference in the survival rates between the screened and the unscreened infants. That study convinced the New South Wales authorities to abandon their proposed screening program, thereby saving infants from unnecessary treatments and the health service from unnecessary expense [16].

The lesson here is we should not assume early detection is always worthwhile. Screening for neuroblastoma illustrates how easily one can fall into the trap of assuming that because a disease can be detected early, screening must be beneficial. The studies above demonstrate not only how neuroblastoma screening provided no value in terms of patient outcome but also how a well-intentioned but ill-conceived screening program led to overdiagnosis and in many cases identified tumors that would have spontaneously regressed.

Going forward the significance of lead-time bias and length-time bias on the interpretation of the various other retrospective observational case-based and small population studies available in the pediatric oncology literature is uncertain. Prospective randomized studies that seek to minimize lead-time and length-time bias are needed to assess the true sensitivity and specificity of the various surveillance imaging approaches. The degree to which imaging surveillance may improve overall survival will be similarly challenging to unequivocally demonstrate, and caution is needed when interpreting such studies. With these considerations in mind, the available literature will be presented with a focus on determining the necessity and usefulness of surveillance imaging in pediatric oncology.

21.4 Risks and Benefits of Imaging Surveillance

21.4.1 Ionizing Radiation Risks

Exposure to low doses of ionizing radiation for diagnostic imaging (in particular CT and nuclear medicine) can amount to significant cumulative radiation doses in childhood malignancy [18–20]. The cumulative effective dose (CED) varies depending on diagnosis, local protocols, individual disease stage, and clinical course. One study [18] reported the CEDs in a population consisting of 150 patients with five cancer groups (leukemia, lymphoma, brain tumors, neuroblastoma, and assorted tumors). They found a median CED of 61 mSv with a range of <1 mSv to 642 mSv. The leukemia subgroup had the lowest median CED (5 mSv), while the neuroblastoma and lymphoma groups—groups that typically undergo intensive multimodality imaging throughout their treatment course—were highest (median 213 mSv and 191 mSv, respectively) [18].

Over the past two decades, radiologists have become increasingly aware of the potential risks associated with cumulative exposure to ionizing radiation related to diagnostic imaging examinations. It should be noted at the outset that the doses associated with diagnostic imaging are orders of magnitude less than the doses used for radiation therapy, the latter being doses that are delivered with therapeutic and potentially curative intent. This caveat aside, radiologists and clini-

cians are increasingly mindful of the ALARA (As Low As Reasonably Achievable) principle, which asserts that the use of radiation-based imaging techniques should be justified, the imaging protocols should be optimized, and the doses should be kept to the minimum needed to achieve the necessary diagnostic goals. This principle is based on extrapolation from epidemiologic studies that investigated the potential danger of relatively "low-dose" radiation exposure. The first study was the continuing Life Span Study (LSS) of the survivors of the atomic bombings in 1945 in Japan. This cohort consisted of approximately 100,000 people, in which 30,000 were exposed to doses ranging from 5 to 125 mSv (average 34 mSv) [6, 21]. This lowest-dose subgroup demonstrates a statistically significant ERR (excess relative risk) of developing cancer following exposure to doses of ionizing radiation that may overlap with the CED related to diagnostic imaging. While the validity of extrapolating population-based epidemiologic data in order to estimate lifetime cancer mortality risk attributable to radiation exposures encountered in diagnostic imaging has been challenged and is vigorously debated, the notion that cumulative exposures to low doses of ionizing radiation may have untoward health effects is supported by a recent study that showed an increased relative risk (RR) for leukemia and brain tumors in children with a CED of 30 mGy and 50–74 mGy, respectively [8]. Another study followed 680,211 patients and found an increase in incidence of cancer after CT exposure, where the average effective radiation dose was estimated at 4.5 mSv (5). Interestingly, reanalysis of one population-based cohort revealed that underlying unreported conditions might have introduced bias into the cancer risk assessments for CT, resulting in overestimates of relative risk [22]. Furthermore, not all cancers have an increased incidence in patients exposed to low doses of ionizing radiation: a recent epidemiologic study of 178,601 patients showed no association between radiation dose from pediatric CT scans and risk of developing Hodgkin lymphoma [23].

While applying the principles of ALARA seems appropriate and supports the accepted ethical and moral imperatives to do what is best for the patient, the discussion around whether low-dose radiation is truly harmful is still under discussion [21, 24]. Proponents of the linear no-threshold (LNTH) model argue that biologic injury from ionizing radiation is directly proportional to dose, that risk increases with cumulative exposure, and that there is no dose threshold below which risk is absent. Others have argued that the risks of ionizing radiation cannot be evaluated by traditional epidemiologic methods because the data are imprecise and contain methodological errors. Such studies refute the validity of the LNTH model at effective doses below 100 mSv, submitting that a finite, although not universally agreed upon, radiation threshold must be achieved for risk to be present. Supporters of this so-called threshold model also point to evidence that biological repair mechanisms exist to correct radiation-induced DNA damage [25, 26].

While the acceptance of a single unifying hypothesis for carcinogenesis risk from exposure to low doses of radiation inducing cancer seems unlikely in the near future, given the ongoing debate in the literature, adherence to the ALARA principle needs to be upheld as long as the effects of low-dose radiation are not fully understood. CT remains a very effective modality for diagnosing and characterizing many pediatric malignancies. With the introduction of improved CT detector technology and advanced iterative reconstruction techniques, we can now push the ALARA principles toward routinely achieving high-quality diagnostic CT scans at sub-mSv effective doses. This is particularly important for situations where CT is the best modality for optimal imaging (e.g., for lung nodule detection) or analysis of comorbidity of treatment (e.g., chest fungal infection). These are situations when we should not refrain from performing CT but should rather strive toward optimizing our CT technique. With regard to surveillance imaging, the question is not only whether surveillance imaging should be performed, but also how. Whenever imaging is necessary, the modality that is the most effective at identifying and characterizing disease with the least toxicity should be used [3]. For example, initial and follow-up CT—when appropriate—can often be replaced by ultrasound and

MRI. Particularly with the increasing use of ultrasound contrast agents, diffusion-weighted MR imaging (DWI), and development of new fast, sensitive, and tissue-specific MR imaging techniques, other imaging modalities frequently provide diagnostic information that is similar or superior to CT with no associated radiation burden [10, 11, 20].

A comprehensive discussion of second malignant neoplasms (SMNs) is outside of the scope of this review but bears mention since they can occur in survivors of pediatric cancer and are most likely related to the cumulative toxicities that accompany treatment with cytotoxic chemotherapy and radiation therapy. The degree to which the relatively low cumulative effective doses of ionizing radiation derived from repeated diagnostic imaging examinations contribute to increases in the attributable risk of developing a SMN is unknown, but should not be discounted. SMNs are not tumor recurrence per se. These malignancies are unrelated histologically to the first cancer that was treated and may occur many years after the first tumor treatment. Survivors of childhood cancer are reported to have a life expectancy which is 4–18 years shorter compared to the normal population, with 50% of non-recurrence mortality caused by another cancer (20). Chemotherapy causes less treatment-related risks for SMN than radiotherapy but appears to potentiate the effect of irradiation (21). One paper studying Hodgkin lymphoma (HL) post-treatment SMN reported breast carcinoma as most common, followed by thyroid carcinoma, bone, colorectal, lung, and stomach tumors. Younger age and use of radiation therapy were important risk factors; the risk of an SMN was 10% at 20 years and 26% at 30 years (22). Abdominopelvic radiation therapy has been shown to increase the risk of gastrointestinal carcinoma and colorectal carcinoma in patients who as children had Wilms tumor or HL (23). Despite the importance of SMNs in the overall long-term health and well-being of pediatric cancer survivors, because of the relatively low incidence of SMNs and their long latency period for development, routine imaging surveillance is not advocated for early detection of SMN, with reliance rather on regular thorough clinical examination for follow-up.

21.4.2 Sedation Risks

Risks associated with diagnostic imaging are not limited to ionizing radiation. There is increasing awareness that repeated exposures to sedation and anesthesia are associated with potential risks in the pediatric population. These risks include the immediate or short-term risk of anesthesia exposure and long-term neurocognitive effects related to repeated exposures to sedation/anesthesia. The immediate, or short-term, risks relate primarily to medical management issues that accompany an episode of sedation or anesthesia and include airway management, hemodynamic instability, allergic reactions, as well as managing the coexisting medical issues that are commonplace in children being treated for cancer. Long-term neurocognitive deficits related to exposure to sedation/anesthesia medications have been increasingly recognized as leading to potential adverse health outcomes. While these concerns are based primarily on preclinical data, there are some human epidemiologic studies that suggest there may be detrimental effects in patients who have had anesthesia early in life. The FDA, acknowledging these concerns, has warned that "repeated or lengthy use of general anesthetic and sedation drugs during surgeries or procedures in children younger than 3 years or in pregnant women during their third trimester may affect the development of children's brains," although they do note that further research is needed to fully characterize how early life anesthetic exposure affects children's brain development.

These concerns are particularly important for surveillance imaging [27]. Weighing the relative risks of carcinogenesis from ionizing radiation against the potential risks of anesthesia is challenging and demands a thoughtful approach from both the clinician and the radiologist. It has been our tendency to simply replace CT imaging, whenever possible, with MRI, an approach that may not be best for every patient. This is particularly true

when CT and MRI exams are diagnostically equivalent and an ultrafast sub-mSv CT scan can be performed without sedation versus an MRI that requires 30–60 min of sedation and/or general anesthesia to obtain a high-quality motion-free exam. In addition, a contrast-enhanced MRI scan carries with it another complicating factor, namely gadolinium deposition in the brain, with its unknown long-term consequences [28].

With these considerations in mind, when developing a surveillance strategy, the modalities chosen should reflect an understanding of the underlying disease, the sensitivity and specificity of the different imaging modalities for the disease being imaged, and the potential risks and benefits of the options available for surveillance imaging.

21.5 Surveillance for Relapse in Children with Malignancy

Advances in treatment have led to prolonged EFS and in many cases improvements in OS for many pediatric malignancies. This has resulted in a heretofore unprecedented need to re-evaluate the strategies we employ when monitoring for tumor recurrence [29]. For surveillance to be useful and justifiable, there should be evidence not only that the chosen imaging modality has sufficient sensitivity and specificity for detecting disease but also that early detection of recurrence leads to improved outcome. The most recent and relevant literature on surveillance imaging are reviewed below, with a focus on those pediatric malignancies for which posttreatment surveillance imaging either has been, or is becoming, an important consideration.

21.5.1 Neurological/CNS Tumors

Surveillance imaging for neurological tumors is most effectively performed with MRI [15]; however when to initiate imaging surveillance and with which frequency remain the subject of investigation. One study [15] reported medulloblastoma relapse detection by MRI in 17 out of 24 patients, with prolonged median survival from the time of relapse to 44 months, as compared to the seven patients whose relapse was identified based on clinical symptoms and who died between scans. They found that the relapses detected by surveillance imaging were less advanced, and more amenable to salvage therapy, accounting for the improvements in outcome. Another study [30] had similar results, showing longer time to recurrence in those patients for whom initial relapse was detected by imaging surveillance compared to clinical relapse. These patients included children with malignant glioma (7.8 months versus 4.3 months, $p = 0.041$) and medulloblastoma (23.6 months versus 8.9 months, $p = 0.0006$) but not ependymoma (19.5 months versus 13.3 months, $p = 0.19$). This was confirmed in a study that reported longer post-treatment EFS and longer OS for the cohort of medulloblastoma patients whose disease recurrence was detected by surveillance imaging as compared to those who presented with clinical symptoms. The mean EFS for patients whose asymptomatic recurrence was detected by imaging was 26.1 months, with a mean OS from the time of recurrence of 8.0 months. This contrasted with mean EFS of 19.1 months and OS of 3.6 months for patients with symptomatic recurrence [31].

Surveillance imaging for CNS tumors, therefore, appears to detect at least a portion of the asymptomatic relapses. These comprise approximately one-third of relapses, which in turn may create opportunities for alternative therapies or investigational agent trials [30]. All studies showed a longer time to relapse and longer survival when relapses were detected by imaging. Two studies found that detection rates for asymptomatic tumor recurrences were 1.59–2.1% for surveillance imaging [31, 32]; the degree to which this reflects early detection of less aggressive disease is uncertain. This has led some to speculate that longer survival might in part be a reflection of lead-time and length-time bias [31], with more indolent tumors presenting later than more aggressive tumors, and thus some question whether first year imaging surveillance is truly effective [30].

21.5.2 Hodgkin Lymphoma

Young patients diagnosed with Hodgkin lymphoma (HL) enjoy early event-free and overall

survival rates that often exceed 90%. As such, the usefulness and cost-effectiveness of surveillance imaging for HL have been reassessed. One study [33] reported a relapse rate of 11.6% in 216 children with HL, with a median time to relapse of 7.6 months. Detection of disease relapse was based on clinical examination in 76% and by surveillance imaging in 24% of patients. Surprisingly, the primary determinant of overall survival was time to relapse, not how the relapse was detected. Deaths only occurred in children whose relapses occurred during the first year following completion of therapy. Patients whose relapses occurred beyond 1 year, regardless how those relapses were detected, responded to salvage therapy with no impact on OS. Another study [34] found that only 9% of relapses were detected with CT in a young adult age group (median age 33 years); however this accounted for 29% of the total cost of follow-up. A study of non-HL patients found that CT also had a low relapse detection rate of 5.7% in asymptomatic patients [35], and a similarly low rate has been reported in adult HL surveillance studies [36]. Rathore et al. [37] reported relapses in 13 of 99 children (13%), 11 of which occurred within 5 months of treatment. They also reported a low detection rate of relapse based on surveillance imaging of 1.3% (17 out of 1358 scans).

The mean radiation dosages reported in a pediatric HL surveillance study ranged from 31.97 to 51.35 mSv depending on disease stage and treatment protocol [37]. As described above, these exposures, while relatively low when compared to the doses delivery for radiotherapy, may still be contributing to an excess relative risk of developing delayed secondary tumors and a decreased lifetime expectancy [29, 38]. This was reaffirmed by an earlier study [39] which reported an 18.5-fold increased risk of developing SMNs compared with the general population in 1380 children with HL during long-term follow-up (median 17.0 years). The degree to which the additional exposure to ionizing radiation from multiple CT scans and nuclear medicine studies during the off-therapy surveillance period contributed to the SMNs is uncertain.

A study comparing MRI and PET/CT showed that there was very good agreement between MRI and the enhanced PET/CT for nodal and extranodal staging (k = 0.96 and 0.86, respectively). They found that sensitivity and specificity of MR were 98% and 99% for nodal disease and 91% and 99% for extranodal disease [40]. Although not widely employed for HL imaging or surveillance, with improvements in MR imaging techniques in the thorax (which is the primary site of disease in the majority of patients with HL), MRI is increasingly being used in place of CT whenever possible. Fortunately, HL patients tend to be adolescents and older teenagers and thus do not require anesthesia for MRI.

Because the majority of pediatric HL relapses occur within the first year after therapy, this time period should be the focus of end-of-therapy imaging surveillance. Based on the principle that surveillance imaging should be cost-effective and sensitive for disease detection and that early detection of relapse should improve overall outcome, the evidence that has emerged over the past 5 years indicates that CT scanning has been overutilized in the management of HL, with little impact on outcome. With the majority of HL relapses occurring clinically and with radiation doses employed for lymphoma being among the highest in pediatric oncology, an alternative strategy for imaging surveillance in HL has been proposed [33]. This surveillance scheme for routine post-therapy surveillance in HL has been incorporated into ongoing Children's Oncology Group HL protocols, with a substantial reduction in post-therapy CT scanning being embraced by both clinical oncologists and radiologists [4].

21.5.3 Neuroblastoma

Posttreatment survival and risk of recurrence in neuroblastoma (NBL) vary greatly, depending on stage and risk classification at the time of diagnosis, with a reported range of 27.3–58.9% [41, 42]. For example, stage 4S (MS) represents a subset of low-risk disease—occurring in children under 1 year with a localized primary site of disease and metastases limited to the liver, skin, and up to

10% of bone marrow. These children were recognized as having an excellent overall outcome, often without the need for chemotherapy or surgical resection of the primary mass [43]. These children have relatively frequent monitoring early on in the course of treatment/observation but then require only minimal disease surveillance once response has been established. In contrast, for higher-stage, high-risk patients (risk stratification being determined based on age, disease stage, histology, and molecular pathology), certain end-of-therapy surveillance imaging protocols require children to receive numerous CT or MR scans and MIBG evaluations, as often as every 3 months for the first year, followed by biannual and eventually annual surveillance for up to 5 years [1]. One study reported a CED of 214 mSv [18], which is higher than many children received during the atomic bombings in Japan in 1945 [6, 21], potentially increasing the risk of SMN and a resulting shortened life span [39].

For neuroblastoma patients with higher-risk disease, the value of early relapse detection is uncertain. In one study, median progression-free survival following relapse was reported as 8.4 months for high-risk patients and 11.8 months for those with intermediate-risk disease [44]. In the high-risk group, 80% of the relapses occurred within 2 years, compared to 50% for the intermediate-risk group. Given results such as these for difficult to treat cancers such as neuroblastoma, where salvage regimen options are limited and are often not curative [1], the impact on survival following early detection of recurrence is unclear.

As with many pediatric malignancies, relapse in neuroblastoma often presents with symptoms or is identified by laboratory or non-CT imaging techniques such as routine outpatient ultrasound. In one study of patients with non-thoracic primary neuroblastoma, thoracic relapses were rare, and the majority presented with symptoms or were identified by other non-CT imaging modalities; only 14% of the thoracic recurrences were detected in asymptomatic children [41], indicating that elimination of routine surveillance chest CT imaging can substantially decrease radiation exposure without compromising disease detection. Another study [42] noted that 74% of patients had clinically evident recurrence or that relapse was detected by X-ray, ultrasound, or urinary catecholamines. Sixteen percent of relapses were detected by MIBG scintigraphy, with only 10% using cross-sectional imaging (CT/MRI), although it should be noted that monitoring tumor markers alone (VMA and HVA) is not sufficiently sensitive to serve as the only means of monitoring for relapse [45]. Patients with neuroblastoma are heavily treated and are at increased risk of developing treatment-related morbidities, including development of second malignancies. As such, efforts have been made to understand the impact of reducing the intensity of routine CT imaging surveillance. One study reported a CED from imaging in neuroblastoma of 214 mSv [18], while other studies have shown that reducing or eliminating routine CTs from surveillance imaging protocols could lead to dose savings of 30–40% [41].

Because the extent and frequency of surveillance imaging for children with neuroblastoma are so variable, it is difficult to present a single evidence-based recommendation for disease surveillance. It seems reasonable, following the principles outlined in this review, that for low-risk abdominal NBL and stage 4S disease, the potential for recurrence can be reliably monitored in most cases with ultrasound, combined with clinical observation and tumor markers. Monitoring children with high-risk disease is more challenging. Patients who achieve early complete response to chemotherapy and surgical resection based on MIBG and CT/MRI have better outcomes as compared to those with residual MIBG avid disease. A response-based algorithm could therefore be considered, reserving more intensive surveillance for those patients with greater likelihood of relapse. Whether this could be accomplished with a single comprehensive whole-body examination remains to be determined [43, 46].

While the utility of surveillance imaging for neuroblastoma patients continues to be the subject of debate [42, 47], there is currently no compelling data to support the elimination of imaging surveillance in low-/intermediate-risk patients, for whom treatment intensity is being reduced and who may experience increased rates of relapse, or in high-risk patients, for whom risk of relapse

after completion of therapy remains high. In both populations of patients, however, it is unclear which poses a greater risk to the patient: the cumulative radiation dose from surveillance CT scans performed on modern equipment with low-dose techniques or—as was noted earlier—the multiple exposures to anesthetics for serial MRI examinations. Further work is clearly needed.

21.5.4 Wilms Tumor

Survival of Wilms tumor patients is one of the best in pediatric oncology. Overall 10-year survival rates for stages 1–3 range from 96% to 89%, decreasing to 81% for stage 4 (hematogenous metastases to the lungs and liver) and 78% for stage 5 (bilateral renal tumor) [48]. Differences in treatment between Europe and America may impact local recurrence rates and strategies for end-of-therapy surveillance. The International Society of Pediatric Oncology (SIOP), based in Europe, prefers preoperative chemotherapy prior to surgery, resulting in downstaging of some patients, which in turn makes surgical resection easier with less risk of tumor spillage. Children who are downstaged from stage 3 will avoid radiotherapy and thus avoid the potential long-term sequelae related to radiotherapy [47]. When compared to COG studies, in which up-front surgical resection, followed by chemotherapy and radiation, is the preferred approach, SIOP studies report slightly higher recurrence rates, although these radiotherapy-naïve patients do appear to have high salvage rates [49].

Recurrence in Wilms tumor occurs most frequently in the lungs [50–52], with abdominal and pelvic recurrences seen in only ~10% of patients [50]. Survival after relapse of Wilms tumor is 50–80% depending on therapy [50, 52]. One study [53] reported recurrence in 10/53 patients receiving 210 CT examinations. Eight of the recurrences were apparent through clinical symptoms, radiographs, or ultrasound. Only two patients with recurrence in the chest were found by CT and not by plain radiograph, although the relationship between early detection of pulmonary recurrence by CT and survival in these patients was not established. Another study [54] reported on 80 patients who underwent a total of 605 routine pelvic surveillance CTs. Sixteen children (15%) relapsed after a median of 11.3 months (range 5 months to 7.3 years) after diagnosis, of whom four died. Three of the 16 patients had relapses detected on pelvic CT; however these patients also had clinical evidence of recurrence and all survived. These authors concluded that pelvic CT could be omitted from routine Wilms tumor follow-up, a conclusion supported by another more recent study [55]. Omitting pelvic CT would have saved on 30.5–44.9% of radiation dose (depending on age). In this study two additional patients died of SMN, and one developed a desmoid tumor of the abdominal wall.

Despite the low incidence of asymptomatic pelvic and chest recurrences, routine chest and abdominal CT or MRI has historically been an integral part of Wilms tumor trials in the Children's Oncology Group [56]. However, in a recent COG study of 281 patients with relapsed unilateral favorable histology Wilms tumor treated on the fifth National Wilms Tumor Study (NWTS-5) protocol, detection of relapse with CT was not associated with improved survival compared to detection with CXR/US, and the authors concluded that eliminating CT scans from surveillance programs would result in substantial reduction in radiation exposure and health-care costs without compromising overall survival [57]. Whether these recommendations can be extended to higher-risk patients or incorporated into risk-adapted off-treatment monitoring programs remains to be studied.

Based on available data, therefore, it seems appropriate to refrain from routine chest CTs and abdomen/pelvic CTs in low risk, low stage Wilms tumor, with abdominal US or MRI as a reasonable surveillance imaging alternative if indeed surveillance imaging is indicated. In agreement with this approach, the SIOP recommendations for nonmetastatic Wilms tumor surveillance are to follow up with chest X-rays and abdominal ultrasound. We are not aware of any evidence to suggest that patients with Wilms tumors in SIOP trials relapse with more advanced disease [56], based on delays in detection.

21.5.5 Hepatoblastoma

As with many other pediatric solid tumors, children with hepatoblastoma often undergo frequent and long-term surveillance imaging, which can contribute to significant cumulative exposures to ionizing radiation, in addition to repeated exposures to sedation and anesthesia agents. One study [58] reported a median recurrence time after initial diagnosis of 12 months (range 4–115 months) in 12% of patients after complete remission, resulting in 59 patients with recurrence. Twenty-seven of these children had recurrences in the lung, 21 in the liver, and five in both the liver and lung. Fifty out of 59 patients had increased alpha fetoprotein (AFP) at the time of recurrence. Thirty-one out of 59 patients achieved secondary complete remission, and 3-year OS was 43%. Another study [59] found increased AFP in the 5/26 patients in whom recurrence was identified; none of the patients, despite intensive surveillance imaging, had their recurrences detected by imaging alone, prior to AFP elevation. They reported two false-positive AFP levels and 15 false-positive imaging exams, and when compared to either FDG PET/CT or CT, AFP elevation was significantly more accurate in detecting recurrence. Another small study [60] in which no recurrences were detected by pelvic CT further supports the recommendations to reduce the use of routine CT for hepatoblastoma surveillance. Rather, serum AFP appears to be the preferred method of surveillance in children with hepatoblastoma. It is important to note, however, that imaging surveillance, ideally with MRI for liver tumors, must still be tailored to the individual patient and should be considered in high-risk patients for whom early detection of relapse may affect surgical resectability and impact survival [59, 61].

21.5.6 Bone and Soft Tissue Sarcomas

Surveillance imaging recommendations following treatment of osteosarcoma, Ewing sarcoma, rhabdomyosarcoma, and other more rare pediatric sarcomas are based mainly on results from both adult and pediatric trials. The only prospective randomized controlled trial that included children and examined the impact of surveillance imaging in sarcoma patients was published by Puri et al. [62]. The purpose of this study, which included 500 nonmetastatic extremity sarcoma (bone and soft tissue) patients (median age 20 years, range 3–65 years), was to determine the impact of a less intense post-therapy follow-up regimen on 3-year OS. This study showed no difference in outcome for patients undergoing surveillance with chest radiographs at 3 or 6 month intervals versus those receiving a more intensive CT surveillance regimen at similar 3 or 6 month intervals; local control/primary site imaging was similar for all groups. Furthermore, almost 90% of the local recurrences were identified clinically. Although this study included both children and adults, their findings provide a high level of evidence to justify eliminating chest CT from routine follow-up in nonmetastatic sarcoma patients and provide further evidence to support the use of clinical exam findings and symptoms for initial detection of local disease recurrence.

Another study [63] of adult sarcoma patients found a 47% relapse rate in patients with a soft tissue extremity sarcoma (mean age 51, range 13–88). Local recurrences were detected clinically in 30/31 patients; MRI identified one local recurrence. Twenty-eight patients developed isolated lung metastases; these were detected by CXR in 19 patients, chest CT in three patients, and clinically in 11 patients. More than 80% of the relapses occurred in the first 2 years of follow-up. In some settings (i.e., nonmetastatic localized disease), therefore, clinical examination appears to be an important means of detecting relapse. However, in a study of mixed soft tissue or bone sarcoma patients, only half (14/29) of the relapses that occurred were detected clinically [64], although this study did not find that regular imaging surveillance improved OS.

Körholz et al. [65] looked specifically at a population of pediatric osteosarcoma patients. Twenty-eight of their 72 patients demonstrated recurrence, of which 90% occurred within 3 years following primary therapy. Recurrence was

detected primarily by clinical examination, CXR, and chest CTs. Bone scintigraphy was important for detection of distant metastases; routine radiographs of the primary tumor site did not detect any recurrence. While they recommended routine CXR, chest CT, and clinical examination for at least the first 3 years, they noted that the impact of early recurrence detection on overall survival was uncertain. The COG bone tumor committee recommendations for imaging osteosarcoma and Ewing sarcoma call for a fairly intensive, albeit decreasing frequency of chest CT scans, performed every 3 months in the first year, every 6 months in the second and third years, and yearly in the fourth and fifth years, followed by yearly chest radiographs during post-chemotherapy surveillance [66]. The committee acknowledged, however, that there was a "lack of evidence to support this guideline," responding to concerns raised by Dauer et al. [12] who stated that frequent and repeated chest CTs during post-chemotherapy surveillance for osteosarcoma are not adequately justified.

Another challenge is when and how to incorporate new imaging modalities into existing surveillance regimens and whether to eliminate historical modalities. For example, FDG-PET imaging has been required along with a bone scan for metastatic disease evaluation in several trials of pediatric bone and soft tissue sarcoma. However, a study that compared FDG PET/CT and bone scintigraphy in 29 children (mean age 12 ± 5 years), of whom 72% had bone sarcoma and 28% a soft tissue sarcoma, found an accuracy of 100% for FDG PET/CT, compared to 82–90% for bone scintigraphy, providing compelling evidence for eliminating bone scintigraphy from surveillance regimens [67].

The soft tissue sarcomas present a separate challenge when developing evidence-based surveillance imaging recommendations, given the different histologic subtypes, age at diagnosis, location of primary disease, and presence of both locoregional nodal and metastatic spread. Children with rhabdomyosarcoma were specifically studied by Lin et al. [68]. OS was compared between recurrence detected clinically (28/47 children) and by imaging (15/47 children). Three-year survival rates in this cohort of patients were poor, and did not differ significantly ($p = 0.38$) between the groups, with 20% 3-year OS for imaging-based detection and 11% for clinical detection.

21.6 Conclusion

Surveillance imaging plays an important role in the end-of-treatment care of patients with cancer. As more patients become long-term survivors of their childhood malignancies, we must continually work to improve our approach to imaging these patients, being mindful of the risks and benefits that accompany any radiologic examination. Although disease surveillance has received much recent attention, the available evidence on how to best perform routine surveillance imaging is limited and largely based on small retrospective observational studies; more prospective studies are clearly needed. Going forward it would be ideal, albeit difficult to implement, if posttreatment surveillance studies were established whereby children are randomized to clinical and imaging surveillance versus clinical surveillance alone (omitting repeated radiologic imaging) [47]. While some families find a normal follow-up surveillance study to be reassuring, this needs to be balanced with the need for and hazards of ionizing radiation, potential for follow-on testing related to false-positive results, and, particularly in young children, risks of repeated anesthesia.

There are some unfortunate children who present with high-risk metastatic disease for which, if relapse occurs after completion of treatment, there is no further salvage therapy available. While this represents a minority of pediatric oncology patients, it may be appropriate to consider sparing these families the additional burden of repeated surveillance imaging that will have little impact on outcome.

As we have emphasized here, evidence has begun to emerge showing little to no benefit from routinely performed surveillance imaging in patients who are otherwise asymptomatic, particularly when viewed against the yardstick of disease-free survival. For many reasons, it

can still be argued that early detection of disease when it is likely to occur is important, both for individual patients and in certain diseases where retrieval therapies exist. However, the choice of imaging modality, surveillance imaging frequency, and duration of surveillance should be part of a thoughtful consideration between the patient, the radiologist, and the treating oncologist, to ensure the most appropriate use of imaging for a given patient's disease.

References

1. Weiser DA, Kaste SC, Siegel MJ, Adamson PC. Imaging in childhood cancer: a Society for Pediatric Radiology and Children's Oncology Group Joint Task Force report. Pediatr Blood Cancer. 2013;60(8):1253–60. https://doi.org/10.1002/pbc.24533.
2. Greer MC, Voss SD, States LJ. Pediatric cancer predisposition imaging: focus on whole-body MRI. Clin Cancer Res. 2017;23(11):e6–e13. https://doi.org/10.1158/1078-0432.CCR-17-0515.
3. Kaste SC. Oncological imaging: tumor surveillance in children. Pediatr Radiol. 2011;41(Suppl 2):505–8. https://doi.org/10.1007/s00247-011-2108-1.
4. Voss SD. Surveillance imaging in pediatric Hodgkin Lymphoma. Curr Hematol Malig Rep. 2013;8(3):218–25. https://doi.org/10.1007/s11899-013-0168-z.
5. Goske MJ, Applegate KE, Bulas D, Butler PF, Callahan MJ, Coley BD, Don S, Frush DP, Hernanz-Schulman M, Kaste SC, Morrison G, Sidhu M, Strauss KJ, Treves ST, Alliance for Radiation Safety in Pediatric I. Image gently: progress and challenges in CT education and advocacy. Pediatr Radiol. 2011;41(Suppl 2):461–6. https://doi.org/10.1007/s00247-011-2133-0.
6. Hall EJ, Brenner DJ. Cancer risks from diagnostic radiology. Br J Radiol. 2008;81(965):362–78. https://doi.org/10.1259/bjr/01948454.
7. Mathews JD, Forsythe AV, Brady Z, Butler MW, Goergen SK, Byrnes GB, Giles GG, Wallace AB, Anderson PR, Guiver TA, McGale P, Cain TM, Dowty JG, Bickerstaffe AC, Darby SC. Cancer risk in 680,000 people exposed to computed tomography scans in childhood or adolescence: data linkage study of 11 million Australians. BMJ. 2013;346:f2360. https://doi.org/10.1136/bmj.f2360.
8. Pearce MS, Salotti JA, Little MP, McHugh K, Lee C, Kim KP, Howe NL, Ronckers CM, Rajaraman P, Sir Craft AW, Parker L, Berrington de Gonzalez A. Radiation exposure from CT scans in childhood and subsequent risk of leukaemia and brain tumours: a retrospective cohort study. Lancet. 2012;380(9840):499–505. https://doi.org/10.1016/S0140-6736(12)60815-0.
9. Howell L, Mensah A, Brennan B, Makin G. Detection of recurrence in childhood solid tumors. Cancer. 2005;103(6):1274–9. https://doi.org/10.1002/cncr.20896.
10. Gawande RS, Gonzalez G, Messing S, Khurana A, Daldrup-Link HE. Role of diffusion-weighted imaging in differentiating benign and malignant pediatric abdominal tumors. Pediatr Radiol. 2013;43(7):836–45. https://doi.org/10.1007/s00247-013-2626-0.
11. Humphries PD, Sebire NJ, Siegel MJ, Olsen OE. Tumors in pediatric patients at diffusion-weighted MR imaging: apparent diffusion coefficient and tumor cellularity. Radiology. 2007;245(3):848–54. https://doi.org/10.1148/radiol.2452061535.
12. Dauer LT, St Germain J, Meyers PA. Let's image gently: reducing excessive reliance on CT scans. Pediatr Blood Cancer. 2008;51(6):838.; author reply 839-840. https://doi.org/10.1002/pbc.21725.
13. Fletcher RH, Fletcher SW, Wagner EH. Clinical epidemiology, the essentials. 5th ed. Philadelphia, PA: Lippincott Williams & Wilkins; 2012.
14. Mckenzie K, Powell H. Health screening. Learn Disab Pract. 2004;7(10):34–8.
15. Roebuck DJ, Villablanca JG, Maher K, Nelson MD Jr. Surveillance imaging in children with medulloblastoma (posterior fossa PNET). Pediatr Radiol. 2000;30(7):447–50. https://doi.org/10.1007/s002470000235.
16. Evans I, Thornton H, Chalmers I, Glasziou P. Earlier is not necessarily better. In: Testing treatments. 2nd ed. London: Pinter & Martin; 2011.
17. Marcus PM, Prorok PC, Miller AB, DeVoto EJ, Kramer BS. Conceptualizing overdiagnosis in cancer screening. J Natl Cancer Inst. 2015;107(4) https://doi.org/10.1093/jnci/djv014.
18. Ahmed BA, Connolly BL, Shroff P, Chong AL, Gordon C, Grant R, Greenberg ML, Thomas KE. Cumulative effective doses from radiologic procedures for pediatric oncology patients. Pediatrics. 2010;126(4):e851–8. https://doi.org/10.1542/peds.2009-2675.
19. Chong AL, Grant RM, Ahmed BA, Thomas KE, Connolly BL, Greenberg M. Imaging in pediatric patients: time to think again about surveillance. Pediatr Blood Cancer. 2010;55(3):407–13. https://doi.org/10.1002/pbc.22575.
20. Robbins E. Radiation risks from imaging studies in children with cancer. Pediatr Blood Cancer. 2008;51(4):453–7. https://doi.org/10.1002/pbc.21599.
21. Hendee WR, O'Connor MK. Radiation risks of medical imaging: separating fact from fantasy. Radiology. 2012;264(2):312–21. https://doi.org/10.1148/radiol.12112678.
22. Berrington de Gonzalez A, Salotti JA, McHugh K, Little MP, Harbron RW, Lee C, Ntowe E, Braganza MZ, Parker L, Rajaraman P, Stiller C, Stewart DR, Craft AW, Pearce MS. Relationship between paediatric CT scans and subsequent risk of leukaemia and

brain tumours: assessment of the impact of underlying conditions. Br J Cancer. 2016;114(4):388–94. https://doi.org/10.1038/bjc.2015.415.
23. Berrington de Gonzalez A, Journy N, Lee C, Morton LM, Harbron RW, Stewart DR, Parker L, Craft AW, McHugh K, Little MP, Pearce MS. No association between radiation dose from pediatric CT scans and risk of subsequent Hodgkin lymphoma. Cancer Epidemiol Biomarkers Prev. 2017;26(5):804–6. https://doi.org/10.1158/1055-9965.EPI-16-1011.
24. Andronikou S. Letting go of what we believe about radiation and the risk of cancer in children. Pediatr Radiol. 2017;47(1):113–5. https://doi.org/10.1007/s00247-016-3697-5.
25. Ulsh BA. Checking the foundation: recent radiobiology and the linear no-threshold theory. Health Phys. 2010;99(6):747–58. https://doi.org/10.1097/HP.0b013e3181e32477.
26. Guillerman RP. From 'Image Gently' to image intelligently: a personalized perspective on diagnostic radiation risk. Pediatr Radiol. 2014;44(Suppl 3):444–9. https://doi.org/10.1007/s00247-014-3037-6.
27. Callahan MJ, MacDougall RD, Bixby SD, Voss SD, Robertson RL, Cravero JP. Ionizing radiation from computed tomography versus anesthesia for magnetic resonance imaging in infants and children: patient safety considerations. Pediatr Radiol. 2017;48:21. https://doi.org/10.1007/s00247-017-4023-6.
28. Soares BP, Lequin MH, Huisman T. Safety of contrast material use in children. Magn Reson Imaging Clin N Am. 2017;25(4):779–85. https://doi.org/10.1016/j.mric.2017.06.009.
29. Yeh JM, Nekhlyudov L, Goldie SJ, Mertens AC, Diller L. A model-based estimate of cumulative excess mortality in survivors of childhood cancer. Ann Intern Med. 2010;152(7):409–17., W131–408. https://doi.org/10.7326/0003-4819-152-7-201004060-00005.
30. Minn AY, Pollock BH, Garzarella L, Dahl GV, Kun LE, Ducore JM, Shibata A, Kepner J, Fisher PG. Surveillance neuroimaging to detect relapse in childhood brain tumors: a Pediatric Oncology Group study. J Clin Oncol. 2001;19(21):4135–40. https://doi.org/10.1200/JCO.2001.19.21.4135.
31. Yalcin B, Buyukpamukcu M, Akalan N, Cila A, Kutluk MT, Akyuz C. Value of surveillance imaging in the management of medulloblastoma. Med Pediatr Oncol. 2002;38(2):91–7.
32. Kovanlikaya A, Karabay N, Cakmakci H, Uysal K, Olgun N, Ergor G. Surveillance imaging and cost effectivity in pediatric brain tumors. Eur J Radiol. 2003;47(3):188–92.
33. Voss SD, Chen L, Constine LS, Chauvenet A, Fitzgerald TJ, Kaste SC, Slovis T, Schwartz CL. Surveillance computed tomography imaging and detection of relapse in intermediate- and advanced-stage pediatric Hodgkin's lymphoma: a report from the Children's Oncology Group. J Clin Oncol. 2012;30(21):2635–40. https://doi.org/10.1200/JCO.2011.40.7841.
34. Dryver ET, Jernstrom H, Tompkins K, Buckstein R, Imrie KR. Follow-up of patients with Hodgkin's disease following curative treatment: the routine CT scan is of little value. Br J Cancer. 2003;89(3):482–6. https://doi.org/10.1038/sj.bjc.6601052.
35. Guppy AE, Tebbutt NC, Norman A, Cunningham D. The role of surveillance CT scans in patients with diffuse large B-cell non-Hodgkin's lymphoma. Leuk Lymphoma. 2003;44(1):123–5. https://doi.org/10.1080/1042819021000040323.
36. Torrey MJ, Poen JC, Hoppe RT. Detection of relapse in early-stage Hodgkin's disease: role of routine follow-up studies. J Clin Oncol. 1997;15(3):1123–30. https://doi.org/10.1200/JCO.1997.15.3.1123.
37. Rathore N, Eissa HM, Margolin JF, Liu H, Wu MF, Horton T, Kamdar K, Dreyer Z, Steuber P, Rabin KR, Redell M, Allen CE, McClain KL, Guillerman RP, Bollard CM. Pediatric Hodgkin lymphoma: are we over-scanning our patients? Pediatr Hematol Oncol. 2012;29(5):415–23. https://doi.org/10.3109/08880018.2012.684198.
38. Meadows AT, Friedman DL, Neglia JP, Mertens AC, Donaldson SS, Stovall M, Hammond S, Yasui Y, Inskip PD. Second neoplasms in survivors of childhood cancer: findings from the Childhood Cancer Survivor Study cohort. J Clin Oncol. 2009;27(14):2356–62. https://doi.org/10.1200/JCO.2008.21.1920.
39. Bhatia S, Yasui Y, Robison LL, Birch JM, Bogue MK, Diller L, DeLaat C, Fossati-Bellani F, Morgan E, Oberlin O, Reaman G, Ruymann FB, Tersak J, Meadows AT, Late Effects Study G. High risk of subsequent neoplasms continues with extended follow-up of childhood Hodgkin's disease: report from the Late Effects Study Group. J Clin Oncol. 2003;21(23):4386–94. https://doi.org/10.1200/JCO.2003.11.059.
40. Punwani S, Taylor SA, Bainbridge A, Prakash V, Bandula S, De Vita E, Olsen OE, Hain SF, Stevens N, Daw S, Shankar A, Bomanji JB, Humphries PD. Pediatric and adolescent lymphoma: comparison of whole-body STIR half-Fourier RARE MR imaging with an enhanced PET/CT reference for initial staging. Radiology. 2010;255(1):182–90.
41. Federico SM, Brady SL, Pappo A, Wu J, Mao S, McPherson VJ, Young A, Furman WL, Kaufman R, Kaste S. The role of chest computed tomography (CT) as a surveillance tool in children with high-risk neuroblastoma. Pediatr Blood Cancer. 2015;62(6):976–81. https://doi.org/10.1002/pbc.25400.
42. Owens C, Li BK, Thomas KE, Irwin MS. Surveillance imaging and radiation exposure in the detection of relapsed neuroblastoma. Pediatr Blood Cancer. 2016;63(10):1786–93. https://doi.org/10.1002/pbc.26099.
43. Papaioannou G, McHugh K. Neuroblastoma in childhood: review and radiological findings. Cancer Imaging. 2005;5:116–27. https://doi.org/10.1102/1470-7330.2005.0104.
44. Basta NO, Halliday GC, Makin G, Birch J, Feltbower R, Bown N, Elliott M, Moreno L, Barone G, Pearson AD, James PW, Tweddle DA, McNally RJ. Factors

associated with recurrence and survival length following relapse in patients with neuroblastoma. Br J Cancer. 2016;115(9):1048–57. https://doi.org/10.1038/bjc.2016.302.
45. Simon T, Hero B, Hunneman DH, Berthold F. Tumour markers are poor predictors for relapse or progression in neuroblastoma. Eur J Cancer. 2003;39(13):1899–903.
46. Guimaraes MD, Noschang J, Teixeira SR, Santos MK, Lederman HM, Tostes V, Kundra V, Oliveira AD, Hochhegger B, Marchiori E. Whole-body MRI in pediatric patients with cancer. Cancer Imaging. 2017;17(1):6. https://doi.org/10.1186/s40644-017-0107-7.
47. McHugh K, Roebuck DJ. Pediatric oncology surveillance imaging: two recommendations. Abandon CT scanning, and randomize to imaging or solely clinical follow-up. Pediatr Blood Cancer. 2014;61(1):3–6. https://doi.org/10.1002/pbc.24757.
48. Davidoff AM. Wilms tumor. Adv Pediatr. 2012;59(1):247–67. https://doi.org/10.1016/j.yapd.2012.04.001.
49. Kembhavi SA, Qureshi S, Vora T, Chinnaswamy G, Laskar S, Ramadwar M, Arora B. Understanding the principles in management of Wilms' tumour: can imaging assist in patient selection? Clin Radiol. 2013;68(7):646–53. https://doi.org/10.1016/j.crad.2012.11.012.
50. Green DM. Considerations in the diagnosis and management of pediatric patients with favorable histology wilms tumor who present with only pulmonary nodules. Pediatr Blood Cancer. 2016;63(4):589–92. https://doi.org/10.1002/pbc.25840.
51. Malogolowkin M, Cotton CA, Green DM, Breslow NE, Perlman E, Miser J, Ritchey ML, Thomas PR, Grundy PE, D'Angio GJ, Beckwith JB, Shamberger RC, Haase GM, Donaldson M, Weetman R, Coppes MJ, Shearer P, Coccia P, Kletzel M, Macklis R, Tomlinson G, Huff V, Newbury R, Weeks D, National Wilms Tumor Study G. Treatment of Wilms tumor relapsing after initial treatment with vincristine, actinomycin D, and doxorubicin. A report from the National Wilms Tumor Study Group. Pediatr Blood Cancer. 2008;50(2):236–41. https://doi.org/10.1002/pbc.21267.
52. Breslow N, Sharples K, Beckwith JB, Takashima J, Kelalis PP, Green DM, D'Angio GJ. Prognostic factors in nonmetastatic, favorable histology Wilms' tumor. Results of the Third National Wilms' Tumor Study. Cancer. 1991;68(11):2345–53.
53. Wilimas JA, Hammond E, Douglass EC, Champion J, Parvey L, Coburn T. The value of computerized tomography as a routine follow-up procedure for patients with Wilms' tumor. Med Pediatr Oncol. 1984;12(3):221–3.
54. Kaste SC, Brady SL, Yee B, McPherson VJ, Kaufman RA, Billups CA, Daw NC, Pappo AS. Is routine pelvic surveillance imaging necessary in patients with Wilms tumor? Cancer. 2013;119(1):182–8. https://doi.org/10.1002/cncr.27687.
55. Mirza W, McHugh K, Aslam M, Sajjad Z, Abid W, Youssef T, Ali A, Fadoo Z. CT pelvis in children; should we routinely scan pelvis for wilms tumor and hepatoblastoma? Implications for imaging protocol development. J Coll Physicians Surg Pak. 2015;25(10):768770–695. https://doi.org/08.2014/JCPSP.768770
56. Dumba M, Jawad N, McHugh K. Neuroblastoma and nephroblastoma: a radiological review. Cancer Imaging. 2015;15:5. https://doi.org/10.1186/s40644-015-0040-6.
57. Mullen EA, Chi YY, Hibbitts E, Anderson JR, Steacy KJ, Geller JI, Green DM, Khanna G, Malogolowkin MH, Grundy PE, Fernandez CV, Dome JS. Impact of surveillance imaging modality on survival after recurrence in patients with favorable-histology wilms tumor: a report from the Children's Oncology Group. J Clin Oncol. 2018;18:JCO1800076. https://doi.org/10.1200/JCO.18.00076.
58. Semeraro M, Branchereau S, Maibach R, Zsiros J, Casanova M, Brock P, Domerg C, Aronson DC, Zimmermann A, Laithier V, Childs M, Roebuck D, Perilongo G, Czauderna P, Brugieres L. Relapses in hepatoblastoma patients: clinical characteristics and outcome--experience of the International Childhood Liver Tumour Strategy Group (SIOPEL). Eur J Cancer. 2013;49(4):915–22. https://doi.org/10.1016/j.ejca.2012.10.003.
59. Rojas Y, Guillerman RP, Zhang W, Vasudevan SA, Nuchtern JG, Thompson PA. Relapse surveillance in AFP-positive hepatoblastoma: re-evaluating the role of imaging. Pediatr Radiol. 2014;44(10):1275–80. https://doi.org/10.1007/s00247-014-3000-6.
60. Kan JH, Hwang M, Lowas SR, Hernanz-Schulman M. Impact of pelvic CT on staging, surveillance, and survival of pediatric patients with Wilms tumor and hepatoblastoma. AJR Am J Roentgenol. 2011;196(5):W515–8. https://doi.org/10.2214/AJR.10.5179.
61. Shelmerdine SC, Roebuck DJ, Towbin AJ, McHugh K. MRI of paediatric liver tumours: how we review and report. Cancer Imaging. 2016;16(1):21. https://doi.org/10.1186/s40644-016-0083-3.
62. Puri A, Gulia A, Hawaldar R, Ranganathan P, Badwe RA. Does intensity of surveillance affect survival after surgery for sarcomas? Results of a randomized noninferiority trial. Clin Orthop Relat Res. 2014;472(5):1568–75. https://doi.org/10.1007/s11999-013-3385-9.
63. Rothermundt C, Whelan JS, Dileo P, Strauss SJ, Coleman J, Briggs TW, Haile SR, Seddon BM. What is the role of routine follow-up for localised limb soft tissue sarcomas? A retrospective analysis of 174 patients. Br J Cancer. 2014;110(10):2420–6. https://doi.org/10.1038/bjc.2014.200.
64. Postovsky S, Barzilai M, Meller I, Kollander Y, Futerman B, Ben Arush MW. Does regular follow-up influence the survival of patients with sarcoma after recurrence? The Miri Shitrit pediatric oncology department experience. J Pediatr Hematol

Oncol. 2008;30(3):189–95. https://doi.org/10.1097/MPH.0b013e31815d88fa.

65. Korholz D, Verheyen J, Kemperdick HF, Gobel U. Evaluation of follow-up investigations in osteosarcoma patients: suggestions for an effective follow-up program. Med Pediatr Oncol. 1998;30(1):52–8.
66. Meyer JS, Nadel HR, Marina N, Womer RB, Brown KL, Eary JF, Gorlick R, Grier HE, Randall RL, Lawlor ER, Lessnick SL, Schomberg PJ, Kailo MD. Imaging guidelines for children with Ewing sarcoma and osteosarcoma: a report from the Children's Oncology Group Bone Tumor Committee. Pediatr Blood Cancer. 2008;51(2):163–70. https://doi.org/10.1002/pbc.21596.
67. Walter F, Czernin J, Hall T, Allen-Auerbach M, Walter MA, Dunkelmann S, Federman N. Is there a need for dedicated bone imaging in addition to 18F-FDG PET/CT imaging in pediatric sarcoma patients? J Pediatr Hematol Oncol. 2012;34(2):131–6. https://doi.org/10.1097/MPH.0b013e3182282825.
68. Lin JL, Guillerman RP, Russell HV, Lupo PJ, Nicholls L, Okcu MF. Does routine imaging of patients for progression or relapse improve survival in rhabdomyosarcoma? Pediatr Blood Cancer. 2016;63(2):202–5. https://doi.org/10.1002/pbc.25750.

Perspectives and Future Directions

22

Stephan D. Voss and Kieran McHugh

The imaging of children with cancer has evolved significantly over the past 30 years. In developing this textbook, it seemed fitting that the last chapter should focus on surveillance imaging approaches in pediatric oncology. In years past, surveillance imaging was a topic that had little place in the pediatric oncology imaging literature. Most of our efforts were directed at improving diagnoses and assessing responses to treatment. Although survival rates were improving, patients were still not reaching a point where long-term imaging surveillance was a topic of discussion—survival from the primary malignancy was the main concern.

Over the past two decades, we have seen trends toward increasing survival in pediatric oncology. The outcomes for children with cancer have significantly improved, and more than 80% of children diagnosed with cancer are now alive at 5 years from the time of diagnosis and are considered cancer survivors, with the hope for a long life free of cancer [1]. For those tumors with a particularly good outcome such as Wilms tumor, for example, treated patients would expect a near normal life expectancy. These improvements in survival have been the result of numerous collaborative international clinical trials. In addition active programs in pediatric oncologic drug development have taken place and include the recent discovery of novel targeted therapies with fewer short-term and long-term toxicities, molecularly targeted therapeutics, and the increasing wealth of genetic information to develop personalized approaches to treating pediatric cancer. The continued success of these efforts to reduce childhood cancer mortality will require new treatment paradigms that build on an increased understanding of the molecular processes that promote growth and survival of specific childhood cancers.

The ongoing development of novel therapeutic agents has necessitated an evolution in our approach to imaging. As was discussed in several chapters, radiologic imaging had historically been focused on morphologic characterization of malignancies and pattern recognition. Today, new imaging technologies are readily available, with hybrid imaging techniques such as PET/CT, PET/MR, and SPECT/CT now in routine clinical use in nearly every pediatric practice. How we use the tools and apply them to address specific clinical concerns related to diagnosis and response assessment has been the topic of several chapters. Functional imaging advances using diffusion-weighted imaging and MR spectroscopy, coupled with the ability to perform high-quality radiation-

S. D. Voss (✉)
Boston Children's Hospital, Harvard Medical School, Boston, MA, USA
e-mail: Stephan.Voss@childrens.harvard.edu

K. McHugh
Great Ormond Street Hospital for Children, London, UK
e-mail: Kieran.McHugh@gosh.nhs.uk

S. D. Voss, K. McHugh (eds.), *Imaging in Pediatric Oncology*, Pediatric Oncology,
https://doi.org/10.1007/978-3-030-03777-2_22

free whole-body MRI examinations, have further contributed to increasing opportunities to apply the best imaging methods to the management of specific diseases and tumor types. With these new imaging techniques come concerns about the risks and benefits associated with the commonly used imaging modalities, driving the development of other techniques such as contrast-enhanced ultrasound. We are still charged with making rigorous measurements in order to assess tumor response to treatment. Many newer treatments are not primarily cytotoxic and thus may not cause tumor shrinkage but rather are targeted to specific receptors, intracellular signaling pathways, and tumor metabolic activity; thus, novel approaches are needed to assess tumor response, and many have been presented here.

As patients make the transition from being actively treated for their cancer to being survivors of pediatric cancer, we are becoming increasingly aware of complications to treatment that we never before had an opportunity to witness. Comprehensive survivorship programs are actively enrolling patients in most cooperative groups, and imaging plays a role as we seek to better understand long-term toxicities and late effects such as the development of second malignant neoplasms. Similarly, we are beginning to incorporate newer imaging-directed therapies into routine treatment algorithms, such as radioisotope therapies and novel imaging-directed radiation treatment approaches. Interventional radiology techniques have similarly contributed to transforming imaging in pediatric oncology, with percutaneous biopsies and targeted minimally invasive therapies now being delivered by interventional radiologists. These new approaches carry challenges, particularly with regard to understanding potential radiation-related risks associated with the use of imaging; it is our responsibility to communicate these considerations, along with a candid discussion of potential risks and benefits, to patients receiving these new targeted therapies.

Since the sequencing of the human genome, we have the ability to generate genetic profiles from individual patient's tumors and correlate these genotypes with specific tumor and patient phenotypes to drive drug development. For example, the Children's Oncology Group (COG), in partnership with the National Cancer Institute (NCI), is planning a trial entitled the COG-NCI Pediatric Molecular Analysis for Therapeutic Choice (Pediatric MATCH) protocol in which tumor-specific biomarker profiles will be used to direct enrollment onto phase II trials of targeted therapies [2]. With data such as these, we are beginning to recognize a need to correlate patient-specific genetic information with our approaches to imaging. In particular, the need for surveillance imaging in patients with genetically identified cancer predisposition syndromes has recently become an important topic, and the choice of imaging technique, examination frequency, and age of surveillance onset represent fruitful new areas for investigation and application of our imaging expertise.

Other challenges facing pediatricians, oncologists, and radiologists caring for children with cancer have not been fully addressed in this textbook and will undoubtedly require further research. For example, how we identify and define pulmonary metastatic disease remains a topic of discussion. Chest CT is an efficient and sensitive modality for detecting lung nodules, and yet we know that many of the small sub-centimeter nodules identified in children are not malignant [3]. Furthermore, in children with solid malignancies, the ability of experienced pediatric radiologists to correctly predict malignant lung nodule histology on the basis of CT features is limited, with accuracy ranging from 57% to 67% [4]. Because the identification of pulmonary metastatic disease can be important for directing therapy and predicting outcome, some groups have sought to directly assess the impact of so-called indeterminate pulmonary nodules on outcome. In one such trial from the European Pediatric Soft Tissue Sarcoma Study Group (EpSSG), patients with one pulmonary nodule less than 1 cm in diameter or only a few lung nodules less than 5 mm were classified as having "indeterminate" lung nodules and were treated as having localized, not metastatic, disease. The outcome of this cohort after 10 years of fol-

low-up is similar to those patients with normal chest CTs at diagnosis [5]. Similar efforts to revise the classification of pulmonary nodules are being explored in patients with Wilms tumor, and these collective attempts to better define pulmonary metastatic disease in children with solid tumors indicate that there is much exciting work to be done in this area.

A separate challenge worthy of future study relates to the observation that diagnostic rates vary, between and possibly within countries, for some childhood cancers. Research has shown, for example, that Wilms tumors are significantly larger in volume and have a more advanced tumor stage at diagnosis in the UK as compared to Germany [3, 6]. As a consequence there is a small (3%) difference in event-free and overall survival between the two countries. International benchmarking data within the same clinical trial provided good evidence that a higher proportion of children with renal tumors in Germany are diagnosed asymptomatically as compared with the UK [6]. One interpretation is that patients have easier access to a pediatrician in Germany. Earlier diagnoses are thus made, which in turn are associated with a lower Wilms tumor stage at diagnosis and overall better outcomes. These data suggest that the system of primary care available to children could contribute to making the early diagnosis of an abdominal mass in a child with no or vague symptoms. Results such as these could have implications for other tumors as well and are likely to stimulate active debate around the efficacy and cost-effectiveness of screening programs aimed at earlier discovery of pediatric malignancies.

We would be remiss if we did not address how we report on the imaging studies that demand so much of our time and attention. The complexity of medical imaging has increased dramatically over the past few decades, providing radiologists with an ever-increasing number of images to interpret and more imaging modalities to compare. Individual reporting styles are generally the norm, but an alternative to free-form reporting is structured reporting, which involves the presentation of a standard set of concepts and findings in a standard sequence [7]. Structured reports use a template with standardized headings analogous to a checklist of necessary report elements. In addition, structured reports often use standardized language, such as the standardized lexicon called RadLex that is being developed by the Radiological Society of North America [7]. The use of such standardized language not only reduces the chances of miscommunication but also makes the reports more accessible for data mining and research. Recognizing the advantages of structured reporting, the US Food and Drug Administration mandated the use of the Breast Imaging Reporting and Data System for all mammography reports nearly two decades ago. In one oncology study, referring clinicians and radiologists found that structured reports had better content and greater clarity than conventional reports [7]. It is the editors' view that structured reporting would probably improve diagnostic accuracy, and as a consequence tumor staging, in pediatric oncology.

Some of the most important lessons that have come from these collective efforts relate not just to our better understanding of tumor biology but also to how imaging can be directed toward supporting and increasing the efficacy of newer pediatric specific drugs. Just as important has been the rich and collaborative environment that has emerged to support those of us working in pediatric oncology. As this textbook has shown, investigators from around the world have contributed their insights and expertise, and it is through such collaborative efforts that we can continue to strive toward making further improvements in pediatric cancer survival. While survival rates for many cancers continue to trend upward, nearly approaching 100% for certain childhood cancers, there is still much work to be done, particularly for cancers such as high-risk neuroblastoma and pediatric brain tumors, where morbidity and mortality still remain high. Much of this work will be done in the setting of national and international cooperative groups. There will be many opportunities to share data and harmonize approaches used among the different groups in order to best compare the efficacy of different treatment para-

digms. Similarly, there will be an opportunity to evaluate new technologies and imaging agents, for example, radionuclide tracers, many of which receive approval in Europe prior to being trialed in the USA. Our ability to accelerate these developments and bring them quickly into clinical practice will remain an important goal for the future.

Finally, in reflecting back over the many chapters in this text, it is worth pausing and remembering that the figures presented throughout this textbook, depicting characteristic features of particular tumor types, or showing the results of novel approaches to therapy or complications thereof, all contain images from individual children being treated for cancer. These children come to us with the expectation that the examinations we perform and the complex investigations that we undertake will help guide current therapies, as well as inform future management once their disease has been successfully treated. It is to these children that this textbook is dedicated, in the hopes that future editions will reveal additional new and more effective imaging techniques in order to provide the greatest benefit for those patients in the greatest need.

References

1. Adamson PC. Improving the outcome for children with cancer: development of targeted new agents. CA Cancer J Clin. 2015;65:212–20.
2. Allen CE, Laetsch TW, Mody R, et al. Target and agent prioritization for the Children's Oncology Group-National Cancer Institute Pediatric MATCH trial. J Natl Cancer Inst. 2017;109(5)
3. McHugh K, Pritchard J. Problems in the imaging of three common paediatric solid tumours. Eur J Radiol. 2001;37:72–8.
4. McCarville MB, Lederman HM, Santana VM, et al. Distinguishing benign from malignant pulmonary nodules with helical chest CT in children with malignant solid tumors. Radiology. 2006;239:514–20.
5. Vaarwerk B, Bisogno G, McHugh K, Brisse HJ, Morosi C, Corradini N, Jenney M, Orbach D, Chisholm JC, Ferrari A, Zanetti I, De Salvo GL, van Rijn RR, Merks JHM, on behalf of the EpSSG Radiology Group. Indeterminate pulmonary nodules at diagnosis in rhabdomyosarcoma: are they clinically significant? A report from the European Paediatric Soft tissue sarcoma Study Group. 2019. J Clin Oncol https://doi.org/10.1200/JCO.18.01535, in press.
6. Pritchard-Jones K, Graf N, van Tinteren H, et al. Evidence for a delay in diagnosis of Wilms' tumour in the UK compared with Germany: implications for primary care for children. Arch Dis Child. 2016;101:417–20.
7. Schwartz LH, Panicek DM, Berk AR, et al. Improving communication of diagnostic radiology findings through structured reporting. Radiology. 2011;260:174–81.